Mehrphasensysteme in der Geotechnik - Experiment und Simulation

Habilitationsschrift

vorgelegt am 05.02.2013
der Fakultät Bauingenieurwesen

der Bauhaus-Universität Weimar
von
Dr.-Ing. Frank Wuttke

geb. am 22.04.1971 in Erfurt/Thüringen

Gutachter:

1. Prof.Dr.-Ing.habil. Carsten Könke / Bauhaus-Universität Weimar
2. Prof.Dr.-Ing.habil. Stavros Savidis / Technische Universität Berlin

Erteilung der Habilitation am 12.02.2014

Vorwort des Verfassers

Die vorliegende Arbeit entstand während meiner Tätigkeit als postdoktoraler Mitarbeiter an der Professur für Bodenmechanik und als Juniorprofessor für Modellierung in der Geomechanik der Bauhaus-Universität Weimar.

Herrn Professor Dr.-Ing. habil. C. Könke von der Bauhaus-Universität Weimar und Herrn Professor Dr.-Ing. habil. S. Savidis von der Technischen Universität Berlin danke ich recht herzlich für die Übernahme des Berichts.

Hinsichtlich der vielen und langen Diskussionen zu den unterschiedlichen Fragestellungen im Fachgebiet der Geotechnik und Geomechanik, möchte ich ganz besonders Herrn Prof. J.C. Santamarina vom Georgia Institute of Technology, Frau Prof. P. Dineva von der Bulgarischen Akademie der Wissenschaften, Herrn Prof. G.D. Manolis von der Aristotle University of Thessaloniki, Herrn Prof. T. Schanz von der Ruhr-Universität Bochum als auch Herrn Dr. H.-G.Schmidt für die lange Zusammenarbeit danken.

Meinen Doktoranden, den Kolleginnen und Kollegen sowie dem technischen Personal vom Bereich Geotechnik, möchte ich für die gute Zusammenarbeit und anregenden Diskussionen während meiner Tätigkeit an den Forschungsthemen danken. Mit ihren Studien- und Masterarbeiten haben auch Herr M.Sc. Kafle, Herr M.Sc. Rizvi und Herr M.Sc. Asslan einen Beitrag zum Fortgang dieser Arbeit geleistet.

Ganz besonders herzlich möchte ich mich bei meiner Familie, insbesondere bei meiner Frau und meinen Kindern für die Geduld und das Verständnis bedanken, welches sie immer wieder aufbringen mussten.

Frank Wuttke

Inhaltsverzeichnis

Abbildungsverzeichnis

Kapitel 1

Einführung

Die vorliegende Habilitationsarbeit wurde vom Autor als eine kumulative Habilitation konzipiert. Für den besseren Überblick und die Gewährleistung eines 'roten Fadens' in dieser Arbeit, wurde eine Abhandlung der wichtigsten Bestandteile verkürzt zusammengefasst und die Kopplung derer dargelegt. Es ist natürlich nicht möglich, in dem gekürzten Text das Gesamtgebiet in allen Punkten abzuhandeln. Dazu wird auf die benannten Publikationen am Ende jedes Kapitels verwiesen.

Die einzelnen Kapitel wurden so strukturiert, dass die getätigten Arbeiten der zugrunde liegenden Publikationen aufgeführt und insbesondere die neuen Erkenntnisse und Entwicklungen vorgestellt wurden. Auf umfangreiche begleitende Erläuterungen zu den Grundlagen einzelner Methoden und Verfahren wurde an dieser Stelle bewusst verzichtet, um keinen Charakter eines Lehrbuches zu erzeugen. Dieses bewirkt allerdings auch, dass Teile der Habilitationsarbeit mitunter nur kurz ausgeführt wurden und zum tieferen Verständnis nachgeschlagen werden müssen.

1.1 Präambel and Motivation

Die Geotechnik ist eines der umfangreichsten Fachgebiete innerhalb des konstruktiven Bauingenieurwesens. Sie umfasst neben dem Materialverhalten, der Boden-Bauwerk-Interaktion, den Bauwerksgründungen, der Umweltgeotechnik auch den Erdbau oder das geotechnischen Erdbebeningenieurwesen, um nur einige der Gebiete zu benennen. Gleichzeitig sind die Modellierungen im Boden in der Regel dreidimensional, mehrphasig, als granulares Medium zu tätigen und die auftretenden Belastungen sind statischer und dynamischer Natur.

Neben der Modellierung und numerischen Simulationen nimmt das Monitoring von Parameter- oder Zustandsänderungen einen immer größeren Bereich in der Geo-

technik ein. Diese Notwendigkeit der Ist-Zustandbewertung steigt, da die Bauwerke immer kostensparender entworfen, umgebaut und der Altbestand saniert, ertüchtigt und an neue Lastbedingungen angepasst werden muss, wodurch genaue Zustands- und Schädigungsbewertungen im Zusammenhang mit den Prognosemethoden notwendig werden.

Aus geotechnischer Sicht existiert ein Mangel an Prognosemethoden bezüglich des Last-Verformungsverhalten von statischen, zyklischen und dynamischen Belastungssituationen. Dieses Problem resultiert aus der Komplexität geotechnischer Aufgabenstellungen. Bislang erfolgte vorrangig die Entwicklung von Grenztragfähigkeitsnachweisen, um die Realisierung des Bauwerkes prinzipiell zu ermöglichen. Gebrauchtstauglichkeitsnachweise bedingen prognosefähige Theorien und Simulationsmodelle, an welchen ein grundsätzlicher Mangel vorhanden ist. Für die Durchführung von Prognoserechnungen wird in der Geotechnik in der Regel die Finite-Elemente-Methodik genutzt, da die Struktur sehr gut in den vorhandenen Details abgebildet werden kann. Problematisch wird diese Vorgehensweise, wenn die Notwendigkeit besteht, die komplexen Details des Bodens, der Interaktionsgrenzfläche und der Struktur möglichst genau abzubilden, auch im Hinblick auf nichtlineare Materialgesetze zu hinterlegen. Durch die inhärente Heterogenität, mögliche Anisotropie, Partikeleinfluss und Mehrphasigkeit des Bodens, der Komplexität von Interaktionsausbildung und -prozess, der nichtlinearen Material- und Kontaktbedingungen zwischen Bauwerk und Boden sowie der mehrdimensionalen Belastung ist eine solche Anzahl an hochkomplexen Beziehungen vorhanden, dass eine detaillierte Abbildung oft schwierig oder nicht möglich ist. Behelfsmäßig können an dieser Stelle empirische Beziehungen oder die in der Arbeit aufgegriffenen Makroelement-Modelle genutzt werden.

In der modernen Geotechnik sind die Eigenschaften von Geomaterialien ein extrem wichtiger Faktor für die Realisierung von Bauwerken im Bereich der erneuerbaren Energien, der Energiespeicherung, der Realisierung von Offshore-Konstruktionen, der Abdichtung von Endlagern sowie die Ermittlung von Bodenkennwerten für geeignete Prognosemodelle. Dabei sollte die Bodenkennwertanalyse unter verschiedenen Belastungen, der Zustandsbeschreibung und dem Strukturänderungsmonitoring unter dem Einfluss gekoppelter Felder, wie Temperatur, Hydraulik, Mechanik, Chemie und auch der Biologie, immer Bestandteil der Untersuchungen sein. Konventionelle geotechnische Untersuchungen können diese Aussagen nicht in dem Umfang leisten. Dazu müssen neue Methoden und Techniken entwickelt und vorhandene Verfahren anderer Fachdisziplinen genutzt werden. Diesbezüglich wird seit geraumer Zeit die integrierte Standort- und Kennwertanalyse propagiert und durchgeführt. Aus den redundanten und komplementären Daten unterschiedlicher Methoden und Techniken soll eine möglichst umfassende Aussage getätigt werden.

Eine weitere Notwendigkeit neben den erweiterten Analysen von Bodenmaterialien, -strukturen sowie Gründungselementen sind Untersuchungen im Hinblick auf Extremereignisse auch unter dem Blickwinkel der Klimaänderung erforderlich. Jedes Jahr sind hohe Personenverluste allein durch Versagen von geotechnischen Strukturen durch Extremereignissen zu beklagen. Zu diesen Versagensfällen zählen neben vielfältigen Böschungsbrüchen, Schlamm- und Gerölllawinen, der geotechnischen Erdbebengefährdung auch der Schutz gegen Damm- und Deichbrüche durch Hochwasser. Gegen die Extremereignisse selber wird es keinen Schutz geben, aber die Bauwerke und Materialien können so ausgelegt und entworfen werden, dass sie einen maximalen Schutz gegen ein Versagen bieten. Dazu müssen die globalen Mechanismen der Struktur oder der Interaktion verstanden werden, welche eine unbedingte Weiterentwicklung des vorhandenen Wissens erfordert, da natürliche Ereignisse und auftretende Schäden diese Notwendigkeit immer wieder verdeutlichen.

1.2 Ziel und Inhalte der Habilitationsarbeit

Das Ziel der Arbeit ist die Weiterentwicklung von theoretischen und experimentellen Methoden und Theorien in der Geotechnik unter der besonderen Berücksichtigung von ungesättigten Materialien. Da bereits eine Vielzahl unterschiedlicher Methoden in Experiment und Theorie auf diesen Gebiet existieren, wurden vom Autor bewusst offene Lücken in dem Fachgebiet herausgegriffen und die entsprechenden Modelle und Methoden hierfür entwickelt. Für die Entwicklung werden Methoden und Erkenntnisse aus der Dynamik und Statik gleichermaßen eingesetzt, um den Erkenntnisgewinn zu erhalten. Die gemeinsame Nutzung ergibt neue progressive Verfahren, um existierende Probleme zu lösen.

Mit der Umsetzung der Arbeit als kumulative Habilitationsarbeit wird der Stand der Forschung und Entwicklung kurz in den jeweiligen Kapiteln und ausführlicher in den beiliegenden Publikationen abgehandelt. Eine explizite Zusammenstellung als gesondertes Kapitel wird nicht eingearbeitet, da die jeweiligen Referenzen für die behandelten Themen einen breiten Raum einnehmen und in einer Zusammenfassung den Rahmen sprengen würden.

In dem zweiten Kapitel dieser Arbeit erfolgt die Entwicklung von dynamischen, teilsättigungs- und wellenbasierten Methoden für die Ermittlung von *small-strain* Steifigkeiten, die verbesserten Analyse von frequenzabhängigen Phänomenen im Boden und von Methoden zum Strukturmonitoring. Insbesondere nehmen die Methodenentwicklungen zur Detektion von Strukturänderungen einen wichtigen Platz ein und stellen einen komplett neuen Methodenvorrat für die Untersuchungen in der Geotechnik dar. Die getätigten Entwicklungen zur Strukturänderungsidentifikation,

wie das Spannungsmonitoring, das Saugspannungsmonitoring oder die Analyse des Kriechens von granularen Materialien, waren bislang nicht möglich und werden für zukünftige Untersuchungen ein hilfreiches Werkzeug darstellen. Für die Entwicklung der Monitoringmethoden wurden zur Validierung und für die indirekte Bestimmung der Parameter und Zustände, die Hertz-Kontakttheorie herangezogen. Änderungen auf der Mikroskala, wie Spannung, Sättigung oder Zementierung, können mit den getätigten Entwicklungen als funktionale Zusammenhänge abgebildet werden. Für limitierte Abbildungsmodelle wurden eigene Erweiterungen als Ergebnis des Zustandsmonitorings in die Modellbildung eingebunden.

In dem dritten Kapitel wird die komplexe Interaktion von Boden und Bauwerk unter elasto-plastischen Verformungen für die Statik und Dynamik in ungesättigten Böden behandelt. Um den komplexen Bodenbedingungen, Lasten und Interaktionen gerecht zu werden und prognosefähiges Werkzeug zu erhalten, wird dazu die Makroelement-Modellierung genutzt. Es werden Lösungen für ein Flachfundament auf ein- und mehrphasigem Boden vorgestellt, welche methodisch auch auf andere Fundamentkonzeptionen übertragen werden können. Für prognosefähige Simulationsmodelle von zyklisch und dynamisch belastete Strukturen, ist die Wahl von Makroelement-Modellen eine Möglichkeit, um die komplexen Mechanismen für eine Modellierung beherrschbar zu machen und realitätsnahe Ergebnisse zu erhalten. Aber auch für statische Belastungen können diese Modelle einen wertvollen Beitrag bei mehrdimensionalen Einwirkungen, nichtlinearer Interaktion und komplexen Bodenverhältnissen leisten. Die Grundidee dafür ist die Reduktion der Modellkomplexität, welche für den Fall der Interaktion immer mehrere gekoppelte Teilmodelle beinhalten würde.

In dem vierten Kapitel wird die Modellierung von hybriden mehrphasigen numerischen Modellen für die Ausbreitung von Wellenfeldern in großräumigen geologischen Strukturen abgehandelt. Dabei wird der Aspekt der hybriden Modellierung genutzt, um unterschiedliche Modelle miteinander zu koppeln, so dass die Analyse dieser sehr großen Strukturen überhaupt realisiert werden kann. In einem hybriden Modell werden die Vorteile von unterschiedlichen Methoden miteinander gekoppelt. Einschränkungen der jeweiligen numerischen Verfahren werden damit verringert oder beseitigt. Für die Realisierung wurden in einem ersten Schritt ein Wellenzahlintegrationsverfahren für großräumige, geschichtete Strukturabbildung und die Randintegralgleichungsmethode für die Abbildung einer lokalen, beliebig geschichten, heterogenen Struktur gekoppelt, validiert und analysiert. Zukünftige weitere Kopplungen zu kleinen, elasto-plastischen, oberflächennahen Strukturen stehen noch aus. Insgesamt ist das Ziel, den Gesamteinflussbereich, seismische Quelle, seismischer Pfad, heterogenes, mehrphasiger mittlerer Nahfeldbereich und plastischer direkter Interaktionsbereich einer geotechnischen Erdbebenbelastung abzubilden. Zusätzlich

zu der Entwicklung der hybriden Methodik erfolgte die Erweiterung beider Methoden auf eine fluidgesättigte Zweiphasenbeschreibung. Für die Realisierung und Abbildung der Phänomene von fluidgesättigtem Bodenverhalten, wurde ein viskoser Ansatz nach Bardet im Frequenzbereich genutzt. Dabei wird das geänderte Materialschwingungs- und Materialdämpfungsverhalten durch viskose Analogien realisiert.

Die abgehandelten Themen stellen einen Ausschnitt aus dem geotechnischen Fachgebiet dar, in welchen neue Entwicklungen in der Arbeit getätigt wurden. Die Entwicklungen sind untereinander in der Nutzung als Validierung, als Eingangskennwerte oder funktionale Beschreibung für die Simulation verflochten.

Die Entwicklung von geeigneten Identifikationswerkzeugen, der Detektion von Abhängigkeiten ungesättigter Bodenparameter ist wesentlich für die Weiterentwicklung von prognosefähigen Simulationsmethoden. Die Erweiterung von Simulationsmethoden bezüglich des Last-Deformationsverhaltes ist unabdingbar für geotechnische Deformationsprognosen oder die Erfassung von zyklischem Akkumulationsverhalten. Insbesondere ungesättigte Bodenbedingungen haben einen großen Effekt auf das Last-Deformationsverhalten, so dass Saugspannungs-Wassergehalt-Beziehungen diesbezüglich analysiert und erfasst werden müssen. Die in dieser Arbeit genutzte Definition der Makroelemente als Interaktionsmodell sind über einen sehr großen Bereich des geotechnischen Design nutzbar, liefern gute Prognosen und sind numerisch stabil. Gleichzeitig können die Elemente in einem FEM Netz genutzt werden, um komplexes plastisches Last-Verformungsverhalten abbilden zu können. Damit stehen alle Entwicklungen der einzelnen Kapitel eng miteinander in Verbindung und die Ergebnisse, Methoden sind aufeinander aufbauend und ergänzend.

Kapitel 2

Experimentelle Methoden, Charakterisierung und Prozessmonitoring in mehrphasigen Geomaterialien

2.1 Einleitung und Motivation

Für die experimentelle Analyse, die Bodencharakterisierung und das Monitoring von sich ändernden Materialstrukturen in mehrphasigen Böden stehen dem Ingenieur eine Vielzahl von experimentellen Methoden aus der konventionellen, der modernen Geotechnik und der Geophysik zur Verfügung. Das bedeutet, dass neben dem üblichen experimentellen Equipment aus der Geotechnik eine Vielzahl von speziell entwickelten Sensoren und Instrumenten für die Analyse von mehrphasigen Böden und seit einigen Jahren mehr und mehr die Untersuchungsmethoden der Geophysik zur Analyse von physikalischen Feldern zur Verfügung steht. Die Gesamtheit der Untersuchungen liefert einige redundante, in der Mehrzahl komplementäre Daten, welche in ihrer gemeinsamen Interpretation zur Zustandsbeschreibung der Böden führen. Oft sind die gemessenen Daten indirekt mit dem gewünschten Parameter gekoppelt, so dass zur Ermittlung eine inverse Berechnung unter Nutzung von Simulationsmodellen erforderlich ist. Diese Tatsache beschränkt nicht den Aussagebereich der Ergebnisse, denn oftmals sind überhaupt keine anderen Möglichkeiten für die Ermittlung von Informationen möglich, es erfordert nur eine detailierte Analyse hinsichtlich möglicher bzw. auftretender Varianzen für die weiterführende Nutzung in Designroutinen. In dem nachfolgenden Kapitel sollen eigene neu entwickelte experimentelle Verfahren, neue Wege in der Charaterisierung und des Strukturmonitorings in der Geotechnik vorgestellt werden. Die Laborentwicklungen erfolgten, um Phänomene auf der Mikroskala detailliert und kontrolliert untersuchen zu können. Diese Analyse soll

eine Antwort geben, welche Prozesse für die vorhandenen effektiven Parameter auf der Makroskala von geotechnischen Studien verantwortlich sind. Damit liefern diese Methoden Aussagen und Verknüpfungspunkte für die getätigten Entwicklungen in den nachfolgenden Kapiteln.

2.2 Laborequipment für mehrphasige Materialien

Für das Studium mehrphasiger Böden wurde eine Reihe von speziellen, bereits existierenden Methoden genutzt, welche kurz vorgestellt werden sollen, da diese später nur aufgegriffen und nicht weiter erläutert werden. Für die Bestimmung von Matrix-Saugspannungen innerhalb der Laborversuche werden Tensiometer genutzt, bei welchen die entstehenden Saugspannung direkt durch eine Keramik mit hohen Lufteintrittspunkt als Druck gemessen wird (Lu & Likos 2004). Die Tensiometer werden innerhalb der Technikumsversuche für die Untersuchungen und Modellierung der Makroelemente verwendet.

Für die Bestimmung der Saugspannungs-Sättigungs-Kurve der Böden wird die Achsen-Translations-Technik genutzt. Dabei werden die natürlichen ungesättigten Bedingungen von effektiver Bodenspannung, Luft- und Wasserspannung ($u_w < 0$) in kontrollierte effektive Bodenspannungen, Luft- und Wasserspannungen ($u_w > 0$) im Labor überführt. Das bedeutet, dass die Saugspannung ($u_a - u_w$) und Nettospannung ($\sigma - u_a$) durch die Kontrolle der aufgebrachten Drücke bestimmt werden kann. Für normale nichtbindige Böden wurde dazu eine modifizierte Druckzelle ähnlich einer Ödometerzelle (Lins, Fredlund & Schanz 2009), für Böden mit höherem Feinkornanteil ein spezieller Hochdruckbehälter (Lu & Likos 2004) genutzt. Zur Durchführung der seismischen Analysen wurde eine Triaxialzelle umgebaut bzw. erweitert, so dass neben der Wellenanregung auch die Wasser- und Luftdrücke kontrolliert, gemessen und damit die Netto- und Saugspannungen bestimmt werden konnten. Letztlich ist diese Vorgehensweise relativ einfach zu realisieren, sie benötigt nur in Abhängigkeit vom Bodentyp, dem darin enthaltenen Feinkornanteil bzw. der hydraulischen Leitfähigkeit einen hohen Zeitaufwand.

Die Bestimmung des zeitabhängigen Wassergehaltes erfolgte auf eine indirekte Art durch die Anwendung von Sensoren der Zeitbereichsreflektrometrie (TDR - time domain reflectometry), welche üblicherweise ortsstationär und in erweiterter Form ortsaufgelöst durchgeführt werden kann (Scheuermann 2012). In den Technikumsversuchen wurden normale TDR-Sensoren eingesetzt. Der Einsatz von erweiterte TDR-Sensoren, ortsstationär und punktuell bzw. ortsveränderlich und punktuell, erfolgte innerhalb der Versuche in (Al-Janabi, Wagner & Wuttke 2013).

2.3 Erweiterte dynamische Laboranalysen

Für die zeitlich und örtlich hochauflösende Analyse von Böden, für das Verständnis von Teilsättigungseinflüssen auf das Last-Verformungsverhalten von Böden im sehr kleinen Deformationsbereich als auch für das Verständnis des Prozessmonitorings, d.h. des Strukturänderungsmonitorings, sind erweiterte dynamische und geoelektrische Laboruntersuchungen unerlässlich.

Die Bereitstellung von sogenannten 'initialen' Bodensteifigkeiten, also Steifigkeiten bei sehr kleinen Dehnungen, ist eine wichtige Voraussetzung für die Bestimmung von zutreffenden Prognosen zum Deformationsverhalten von Böden. Moderne komplexe Stoffgesetzmodellierungen beinhalten diesen Parameter aus experimentellen dynamischen oder verfeinerten statischen Bodenuntersuchungen. Die korrekte Ermittlung dieser Funktion besteht aus der Startwertermittlung im ungestörten, natürlichen Boden und den kontrollierten Untersuchung zu Einflüssen aus Rand,- Struktur und Belastungsbedingungen. Bei den dynamischen Methoden nehmen die wellenbasierten Methoden eine Sonderstellung ein, da diese sehr gute Ergebnisse unter fast beliebigen Rand- bzw. Strukturbedingungen erbringen und einen sehr großen Einsatzbereich aufweisen. In den Laboren werden dazu piezoelektrische Elemente in bodenmechanischen Standard- und Spezialgeräten eingesetzt.

Die Literatur zeigt, dass fast alle wellenbasierten Untersuchungen auf der Analysen von einfachen Laufzeitmessungen für den Informationsgewinn (Jovicic, Coop & Simic 1996, Arulnathan & Boulanger 1998) beruhen. Schwierig und auch immer „subjektiv“ ist dabei die Ermittlung des Ersteinsatzes der Welle, mit welcher die tatsächliche Wellengeschwindigkeit bestimmt wird. Diesbezüglich sind in (Greening & Nash 2004) vergleichende Untersuchungen vorgenommen worden, welche dokumentieren, dass bei Zeitbereichstechniken (Peak-to-Peak u.a.) die Zeitdifferenz zwischen gesendetem und empfangenem Signal unterschätzt bzw. damit die resultierenden Wellengeschwindigkeiten und damit auch die abgeleiteten initialen Steifigkeiten G_0 überschätzt wird. Die prozentualen Abweichungen, welche der Literatur entnommen werden können, zeigen einen großen Schwankungsbereich. Es fehlen Methoden, welche eine eindeutige Bestimmung der Wellenlaufzeiten ermöglichen.

Korrelationstechniken können diesbezüglich einen Verbesserung darstellen, jedoch sind diese auf den Vergleich ähnlicher Signalformen begrenzt, da sie andernfalls eine methodenbasierte Dispersion im Ergebnis aufweisen. Ebenso weisen frequenzbasierte Korrelationstechniken Probleme im Anfangs- und Endbereich des Phasengangs auf, wodurch eine Fehlinterpretation des Phasengangs auftreten kann (Wuttke, Markwardt & Schanz 2012). Neben diesen Methoden können seismische Wellen ebenfalls durch die Anwendung von Zeit-Frequenz-Transformationen auf ein Sweepsignal ausgewertet

werden. Diese neueren Transformationstechniken werden in der Geotechnik bislang nur wenig oder überhaupt nicht angewendet. Der Energiegehalt kann im Idealfall über alle Anregungsfrequenzen gleich verteilt und damit die Frequenzabhängkeit der Wellengeschwindigkeiten des Bodens detektiert werden.

Alle vorgenannten Methoden haben nicht die Sensitivität sehr kleine Struktur- oder Materialänderungen zu detektieren. Die Entwicklung der Codawellen Interfereometrie (Snieder 2002, Snieder 2006) basiert auf der Auswertung diffuser, mehrfach gestreuter Wellenfelder innerhalb eines streuenden Mediums. Diese mehrfach gestreuten, überlagerten und das Medium durchlaufenen Wellenfelder weisen eine extreme Sensitivität gegenüber kleinen Strukturstörungen auf (Cowan, Jones & Weitz 2002), (Gret, Snieder & Scales 2006). Die in (Wuttke, Asslan & Schanz 2012) entwickelte Methodik, basierend auf der Codawellen Interferometrie, ist in der Lage, ein Prozessmonitoring von sehr kleinen Strukturänderungen nachzuverfolgen und mit Hilfe der Hertz'schen Kontaktmodelle in zustandsbeschreibende Aussagen zu überführen (Dai, Wuttke & Santamarina 2012), (Wuttke 2012).

Aus dem Blickwinkel der Geotechnik betrachtet, können zwei wesentliche Entwicklungen aus der Analyse von Wellenfeldern abgeleitet werden. Durch die Auswertung des kohärenten Wellenfeldabschnittes werden im allgemeinen makroskopische Parameter, wie z.B. Elastizitätsmoduli, abgeleitet. Dem entsprechend beeinflusst der Boden das anfängliche Wellenfeld als ein quasi „Effektivwert-Filter“ in der Übertragung von Wellen. Der dem kohärenten Abschnitt nachfolgende diffuse Abschnitt des Wellenfeldes, welcher wesentlich sensitiver gegenüber Spannungs-, Struktur- oder Wassergehaltsänderung ist, wird durch die mikroskopischen Einflüsse der Struktur beeinflusst.

Geotechnisches Laborequipment für mechanische Wellen

Für die Erzeugung von Wellen im Labormaßstab werden in der Regel Piezosensoren genutzt, welche im Ultra- oder normalen Schallbereich arbeiten. Diese Sensoren, welche höher bis hochfrequente Wellen anregen, werden bevorzugt in Laborgeräten eingesetzt, um entsprechend kleine Wellenlängen für eine Wellenausbreitung in dem Material bzw. innerhalb der Laborgeräte anzuregen (Wuttke, Markwardt & Schanz 2009). Für die Erzeugung einer umkehrbaren mechanischen, zeitabhängigen Verformung aus elektrischen Signalen wird der Piezoeffekt genutzt. Die entsprechend des Wellentyps angepassten Sensoren werden in entsprechend modifizierten Geräten paarweise eingebaut und können unter laufendem Betrieb genutzt werden. Für die Untersuchung der Wellenausbreitung unter teilgesättigten Versuchsrandbedingungen wurden die Zellen so erweitert, dass zusätzlich zu den Umgebungsdrücken auch der Porenwasser- und Porenluftdruck kontrolliert werden kann (Wuttke & Schanz 2012, Wuttke 2012).

Erweiterte TDR-Messungen

Neben den oben bereits erwähnten Saugspannungsmessungen wird vielfach die Zeitbereichsreflektometrie angewandt, um den Wassergehalt zu bestimmen. Die Messungen von elektromagnetischen Signalen beruht dabei auf der Analyse der frequenzabhängigen komplexen Permittivität bzw. Dielektrizitätszahl des porösen Mediums. In der gemeinsamen Betrachtung mit seismischen Messungen, insbesondere in der gemeinsamen Anwendung von TDR und Codawellen-Interferometrie, lassen sich neue Erkenntnisse hinsichtlich der Struktur bzw. der Strukturänderung ableiten. Grundlage der Messungen sind diese frequenzabhängigen Eigenschaften des Bodens, welche sich in Abhängigkeit von der mehrphasigen Bodenstruktur, wie Porosität, Wassergehalt, Porenwasserionengehalt und die Fluidtemperatur, unterscheiden (Klein & Santamarina 2003),(Wagner, Emmerich, Bonitz & Kupfer 2011). In (Al-Janabi et al. 2013) wurden die TDR Messungen genutzt, um das Kollapspotential ungesättigter Böden genauer zu analysieren. Dadurch, das die elektromagnetischen Wellen mit der frequenzabhängigen komplexen Permittivität ein starke Abhängigkeit von dem Wassergehalt und der Porenstruktur besitzen, existiert eine direkte Beziehung zwischen den makroskopischen Phänomenen und den mikrostrukturellen Ursachen.

2.4 Angewandte Signalanalyse - Absolutwertverfahren

Bei der Untersuchung von Wellenfeldern kann in die Analyse des kohärenten und eines weitgehend zufällig überlagerten, verrauschten Wellenfeldteil unterschieden werden (Lomax 1999, Somfai, Roux, Snoeijer, Van Hecke & Van Saarloos 2005). Dieser erste Wellenfeldteil wird dabei durch den direkten Weg der Korn-zu-Korn-Kontakte als ballistische Wellenfront übertragen, wodurch sich eine direkte Wellengeschwindigkeit in der Analyse ergibt. Der zweite Wellenfeldteil (Coda) entsteht durch die multiple Überlagerung von reflektierten und refraktieren Wellenfronten hin zu einem diffusen Wellenfeld, welches das Medium mehrfach durchlaufen hat und in der Auswertung einen Geschwindigkeitsgradienten liefern, siehe Abbildung 2.1. Die Bestimmung absoluter Wellengeschwindigkeiten können dabei in den Ersteinsatz (time-of-flight) und den Phasen- bzw. Gruppengeschwindigkeit der kohärenten Wellenfront (Greening & Nash 2004) unterschieden werden. Allgemein sind die Phasen- und Gruppengeschwindigkeiten sehr viel näher an der Analyse des Mikrostrukturverhaltens, da die dabei auftretende Frequenzabhängigkeit (Dispersion) ein Ergebnis des mikroskopischen Mehrphasensystems sind.

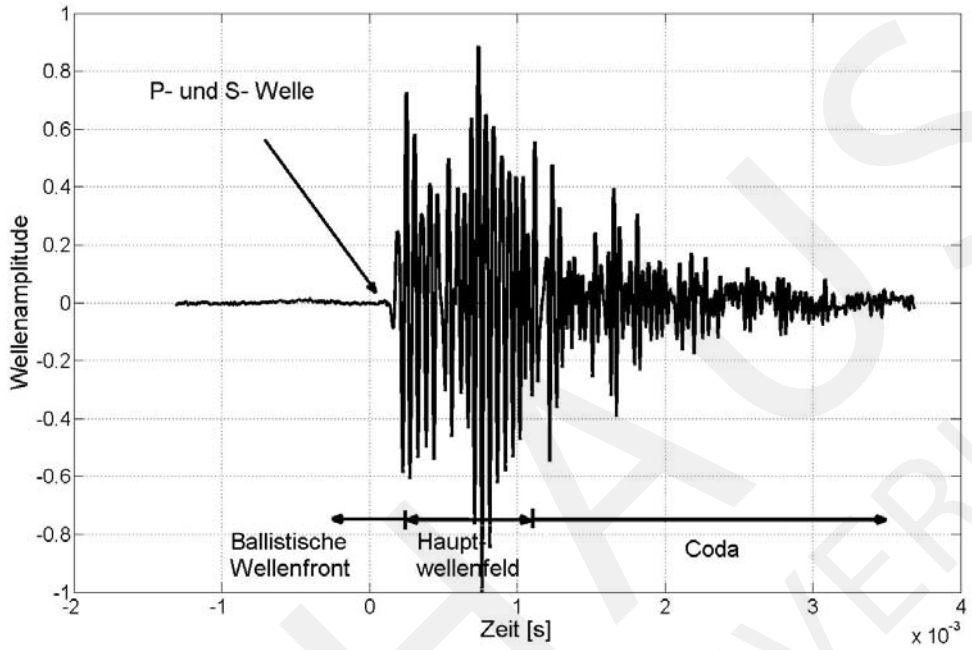

Abbildung 2.1: Abbildung eines Wellenfeldes in Laboruntersuchungen mit dem ballistischen Ersteinsätzen (P- und S-Wellenlaufzeiten), dem Hauptwellenfeld (Phasen- und Gruppenlaufzeiten) und dem Codawellenfeld.

2.4.1 Stationäre Signale

In der geotechnischen Analyse von Wellenfeldern wird bislang fast immer von einer stationären Signalform ausgegangen. Es werden Ersteinsätze bzw. Signalähnlichkeiten zwischen zwei zu vergleichende Signalen bestimmt. Diese Analysen werden entweder im Zeit- oder im Frequenzbereich durchgeführt. Diese Verfahren, der Auto- und Kreuzkorrelation, sind numerisch sehr robust und werden in vielen Analysemethoden genutzt. Insbesondere die Kreuzkorrelation zweier Signale mit

$$(f \circledast g) = \int_{-\infty}^{\infty} f^*(t)\; g(\tau + t)\, dt \;\rightarrow\; \mathfrak{F}\,(f \circledast g) = r_{ij} = (\mathfrak{F}\,\{f\})^* \cdot (\mathfrak{F}\,\{g\}) \qquad (2.1)$$

wird für die Filterung der gespeicherten Wellenfeldinformationen, z.B. Amplituden und Phasenänderung, sehr häufig genutzt. Dabei sind die Signale f und g im Zeitbereich um τ verschoben $(f \circledast g)$ oder nach der Transformation in den Frenquenzbereich $\mathfrak{F}\,\{f\}$ mit dem gültigen Verschiebungssatz im Frequenzbereich komplex konjugiert multipliziert. Diese Anwendung der Kreuzkorrelation setzt, wie bereits besagt, eine Signalähnlichkeit voraus, welche nicht immer gegeben ist. Zudem kann eine Zeitabhängigkeit der Frequenzgehaltsänderung nicht analysiert werden. Vorteilhaft in

der Anwendung der Korrelationstechniken ist die Tatsache, die Wellenfeldhauptgruppe, den größten Anteil der Energie führt (Wuttke 2005). Dieses basiert auf dem physikalischen Hintergrund, dass die Energie bevorzugt durch die Eigenformen des Systems transportiert wird. Die zu bestimmenden Phasengeschwindigkeiten v_{ph} in dem Wellenfeld sind die diskreten Eigenwerte des Systems und stehen mit den im Wellenfeld auftretenden Gruppengeschwindigkeiten v_{gr} in folgendem physikalischen Zusammenhang

$$\begin{aligned} v_{ph} &= \frac{\omega}{k} = \lambda \cdot f \quad \text{mit} \quad f,\, k \in \mathbb{R} \\ v_{gr} &= \frac{\partial \omega}{\partial k} = v_{ph} + k \cdot \frac{\partial v_{ph}}{\partial k}, \end{aligned} \tag{2.2}$$

wobei λ die Wellenlänge, f die Frequenz, ω die Kreisfrequenz und k die Wellenzahl darstellt. Wird das Wellenfeld in den Frequenzbereich transformiert, so kann die Phasen- und Gruppengeschwindigkeit zur jeweiligen Frequenz bestimmt werden durch

$$v_{ph}\left(f_i\right) = L \frac{2\pi\, f_i}{tan^{-1} \frac{\Im(r_{ij}(f_i))}{\Re(r_{ij}(f_i))}} \tag{2.3}$$

$$v_{gr}\left(f_i\right) = 2\pi L \frac{df}{d\varphi\left(f_i\right)},$$

mit L als die Aufpunktentfernung zwischen den beiden Signalen.

Nachteilig bei allen bisherigen Analysen ist der große 'subjektive' Anteil in der Bestimmung der jeweiligen Wellengeschwindigkeit. Die Bestimmung des Ersteinsatzes kann durch Nahfeldeffekte, elektrische Ladungs-"Cross-talks" und durch einfaches Rauschen sehr schnell unmöglich oder zu einer 'subjektiven' Wahl werden. Die Anwendung von Korrelationsmethoden erfordert eine ähnliche Signalform oder -verläufe, welche nicht immer gegeben ist. Zusätzlich zu dieser oft nicht gegebenen Signalähnlichkeit besitzen seismische Quellen eine Bandpass begrenzte Anregungsfrequenz. Damit besteht für Verfahren, basierend auf der Phasendifferenz zwischen zwei Signalen, eine unklare Zuordnung der Phasenwechsel im tieferen und hohen Frequenzbereich. Die Fehlinterpretation durch 'subjektive' Zuordnungen ziehen Abweichungen in der Wellengeschwindigkeit nach sich, siehe Abbildung 2.2. Zur Beseitigung dieser Schwierigkeiten sowie zur verbesserten Analyse der Frequenzabhängigkeit und um tiefere Aussagen zu Mikrostrukturänderungen zu ermöglichen, wurde durch (Wuttke, Markwardt & Schanz 2012) eine Methodik basierend auf der Zeit-Frequenz- und Zeit-Skalierungs-Transformation entwickelt.

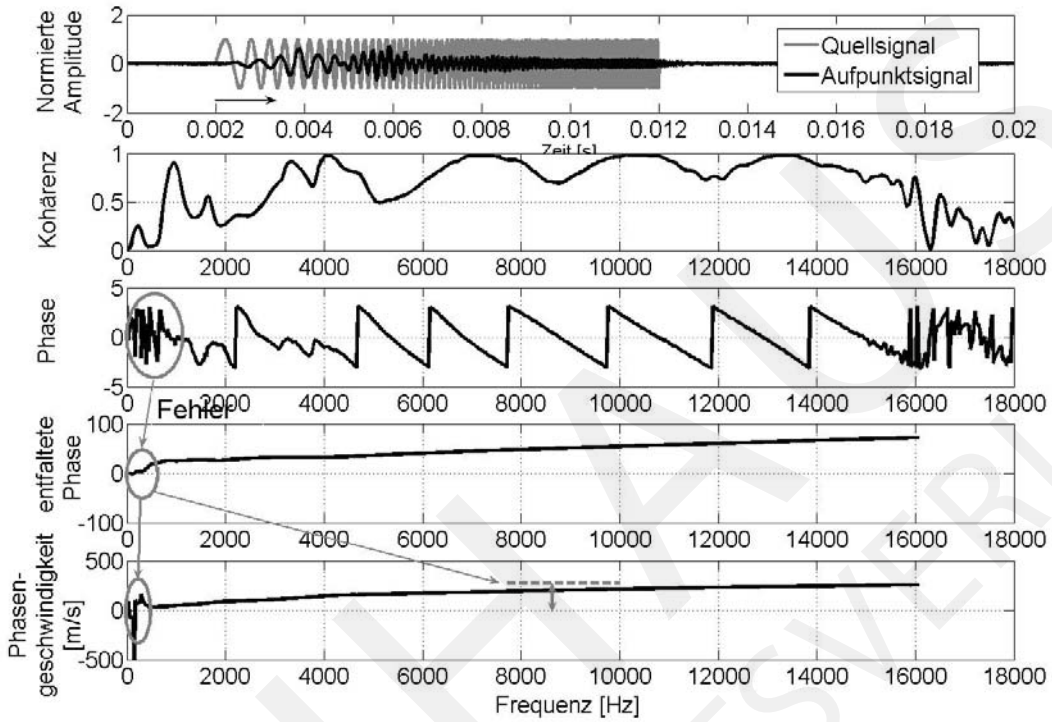

Abbildung 2.2: Fehlerausbildung in der Phasendifferenzenmethode als Ursache mangelhafter Energieanregung im tiefen Frequenzbereich, nach (Wuttke, Markwardt & Schanz 2012).

2.4.2 Nichtstationäre Signale

Die Entwicklung der Zeit-Frequenz-Analyse eines Signal gehen auf die gefensterten Fourieranalyse zurück (Bath 1974). Durch Grossmann und Morlet (Grossmann & Morlet 1984) wurden die Grundlagen der Wavelet-Analyse gelegt. Diese Transformation basiert auf der Anwendung von skalierten und verschobenen „Wavelets“. Das Wavelet-System $\psi_{s,\tau}$ als multiple Kopie des Original-Wavelet ψ, ist durch den Faktor s skaliert und wird per Zeitversatz τ positioniert.

Für die Anwendung der Zeit-Frequenz- und Zeit-Skalierungs-Transformationen bei geotechnischen Problemstellungen sind die spezifischen geotechnischen Versuchsrandbedingungen in die Methoden zu integrieren und die Methodik der Zielstellung anzupassen. Erste Aussagen zu der Methodik hinsichtlich geotechnischer Laborexperimenten erfolgten durch (Arroyo 2007) bezüglich der Identifikation eines propagierenden Impulses. Ausgangspunkt für die eigenen Überlegungen zur Anwendung von Waveletanalysen waren die Untersuchungen von (Greening & Nash 2004). In diesen Untersuchungen erfolgte die Nutzung eines linearen Sweepsignals für die

Anregung eines Frequenzbandes, welches noch auf der Basis von Phasendifferenzenverfahren, mit den inhärenten Zuordnungsproblemen (Abbildung 2.2), analysiert wurde. Mehrphasige, granulare Geomaterialien können in Abhängigkeit von den Rand- und Zustandsbedingungen der Materialstruktur ein frequenzabhängiges Verhalten abbilden. Daher war es aus der Sicht des Autors für weiterführende Identifikationsanalysen erforderlich, die Analysen zur Dispersionscharateristik hinsichtlich Zeit- und Frequenzabhängigkeit zu erweitern (Wuttke, Markwardt & Schanz 2009). Ausgangspunkt für die getätigten Betrachtungen ist die kontinuierlich Wavelet Transformation, welche mit $s > 0,\ \tau \in \mathbb{R}$ und den entsprechenden Wavelet-Funktionen ψ in Gl. (2.4) definiert ist

$$\mathcal{W}(s,\tau) = \frac{1}{\sqrt{s}} \int_{-\infty}^{\infty} f(t)\, \psi^* \left(\frac{t-\tau}{s} \right) dt. \tag{2.4}$$

In Gl. 2.4 sind s der Skalierungsparameter, τ der zeitliche Versatzparameter und ψ^* die komplex konjugierte Funktion von ψ (Wuttke, Markwardt & Schanz 2012). Der Faktor $\frac{1}{\sqrt{s}}$ dient ausschließlich der Normierung des Energiegehaltes.

Infolge der höheren Redundanz der transformierten Signale eignet sich eine kontinuierliche Wavelet-Transformation (CWT) prinzipiell gut für die Analyse von nichtstationären Meßsignalen. Hierbei sind für die zu analysierenden seismischen Signale komplexwertige „Mutter - Wavelets“, insbesondere das Morlet-Wavelet, besonders gut geeignet. Das Morlet-Wavelet kann durch den gekoppelten Real- und Imaginärteil störende Oszillationen in dem Transformationsbereich vermeiden. Um die günstigen Eigenschaften der Morlet-Wavelets zu nutzen und gleichzeitig den Rechenaufwand zu verringern, wurde die CWT in den Frequenzbereich transformiert mit dem Ziel, die Vorteile des mathematischen Frequenzbereichs für eine schnellere Wavelet-Transformation auszunutzen. Eine wesentliche Grundlage dafür war die analytische Transformierbarkeit des Morlet-Wavelets.

Zeit-Skalierungs-Transformation

Kontinuierliche Wavelet Transformation CWT Folgt man der obigen Definition der kontinuierlichen Wavelet-Transformation

$$\mathcal{W}(s,\tau) = \mathcal{W}_{s,\tau} = \frac{1}{\sqrt{s}} \int_{-\infty}^{\infty} f(t)\, \psi^* \left(\frac{t-\tau}{s} \right) dt \ \ ,(s>0)\,, \tag{2.5}$$

so kann ein komplexwertiges Morlet-Wavelet $\psi_{_M}(t)$ als modulierte Gaußfunktion betrachtet werden, welches die Signale und deren Zeit-Frequenz-Inhalt in Real-, Imaginärteil oder als Magnitude abbilden kann. Das so gewählte Mutterwavelet ergibt sich zu

$$\psi_{_M}(t) = \pi^{-\frac{1}{4}}\, e^{j\omega_c t}\, e^{-\frac{1}{2}t^2}, \quad \omega_c = 2\pi\, \xi_c, \quad |\psi_{_M}(t)|^2 = \frac{e^{-t^2}}{\sqrt{\pi}}\,, \quad \|\psi_{_M}\| = 1, \tag{2.6}$$

wobei die Norm des Morlet-Wavelet $\|\psi_{_M}\|$ im Zeit- und Frequenzbereich identisch ist. Mit der Definition des Wavelet in Gl.(2.6) und der CWT nach Gl.(2.5) stellt sich die komplette Wavelet-Transformation wie folgt dar

$$W_{s,\tau} = \pi^{-\frac{1}{4}}\, s^{-\frac{1}{2}} \int_{-\infty}^{\infty} f(t)\; e^{-j\omega_c \frac{t-\tau}{s}}\, e^{-\frac{1}{2}\left(\frac{t-\tau}{s}\right)^2} dt. \tag{2.7}$$

Für eine numerische Implementierung müssen die Variablen durch eine Zeitschrittdefinitionen substituiert werden

$$t \mapsto t_i = i \cdot \Delta t, \quad \tau \mapsto \tau_b = b \cdot \Delta t, \quad s \mapsto s_a = a \cdot \Delta t, \quad f_i = f(i \cdot \Delta t)$$

womit sich die entsprechende numerische Abbildung ergibt

$$W_{s_a,\tau_b} = \pi^{-\frac{1}{4}} \left(\frac{\Delta t}{a}\right)^{\frac{1}{2}} \sum_{i=0}^{N-1} f_i\, e^{j\omega_c \frac{b-i}{a}}\, e^{\frac{1}{2}\left(\frac{b-i}{a}\right)^2}, \quad a \in \mathbb{N},\; b \in \mathbb{N}_0. \tag{2.8}$$

Mit den so gegeben Skalierungs- und Zeitparametern, a und b, wurden die numerischen und experimentellen Analysen in (Wuttke, Markwardt & Schanz 2012) durchgeführt. Die grafische Abbildung des Skalierungsparameters s_a gegenüber dem Frequenzparameter f_i ergibt letztlich das Zeit-Frequenz-Spektrum des Signals f. Die Auswertungen zeigen durch die vorhandenen Redundanzen eine sehr scharfe Zeit-Frequenz-Auflösung im tieferen Frequenzbereich, wonach die Zeit-Frequenz-Auflösung in breitere Unschärfebereiche mit zunehmender Frequenz übergeht.

Im Allgemeinen besteht eine hoher zeitintensiver numerische Berechnungsaufwand in der Anwendung der Methodik. Die Anwendungsfähigkeit während des laufenden Laborbetriebs für Zeitverläufe von mehr als 5000 Samples ist nicht mehr gegeben. Neben den methodischen Besonderheiten der Wavelet-Transformation ist während der Durchführung zu beachten, dass die grundlegende und allgemeingültige Unschärferelation nach Heisenberg besteht, Gl. 2.9.

$$\Delta t \cdot \Delta f \geq \frac{1}{4\pi}. \tag{2.9}$$

Diese inhärente Eigenschaft bedeutet, dass die Zeit-Frequenz-Auflösung nicht kleiner als $\frac{1}{4\pi}$ werden kann. Somit geht eine höhere Zeitauflösung immer mit einer verringerte Frequenzauflösung einher und umgekehrt.

Kontinuierliche Wavelet Transformation im Frequenzbereich Für die Verringerung der Berechnungszeit in der kontinuierlichen Wavelet-Transformation wird die CWT nachfolgend in den Frequenzbereich übertragen. Analysen diesbezüglich finden sich in der Literatur nur sehr wenige. Torrence (Torrence & Compo 1998) zeigt

eine Transformation zur Analyse von Klimadaten, wodurch das Wavelet spezielle Anpassungen enthält und nicht in eigenen Implementationen weiter genutzt wurde. Folgt man der Fouriertransformation, so ergibt sich das Morlet-Wavelet nach Gl.2.6 im Frequenzbereich mit $\omega = 2\pi f$ und $\omega_c = 2\pi f_c$ (f_c Mittenfrequenz) zu

$$\hat{\psi}_M(\omega) = \pi^{-\frac{1}{4}} \int_{-\infty}^{\infty} e^{-\frac{1}{2}t^2}\ e^{j\,(\omega_c-\omega)\,t}\,dt = \pi^{-\frac{1}{4}} \int_{-\infty}^{\infty} e^{-\frac{1}{2}t^2}\ e^{-j\,(\omega-\omega_c)\,t}\,dt$$
$$= \pi^{-\frac{1}{4}} \int_{-\infty}^{\infty} e^{-\frac{1}{2}t^2}\ e^{-j\,\xi\,t}\,dt$$

wobei der Term $\xi = \omega - \omega_c$ genutzt wird. Das fouriertransformierte Morlet-Wavelet ist nach (Wuttke, Markwardt & Schanz 2012) definiert als

$$\hat{\psi}_M(\omega) = \sqrt{2}\ \sqrt[4]{\pi}\ e^{-\frac{(\omega-\omega_c)^2}{2}} \tag{2.10}$$

womit die komplette Wavelet-Transformation im Frequenzbereich definiert werden kann zu

$$\mathfrak{F}_\tau\{\mathcal{W}(s,\tau,t)\} = \hat{f}(\omega)\cdot\sqrt{s}\,\hat{\psi}_M(s\,\omega) = \sqrt{2\,s}\ \sqrt[4]{\pi}\ \hat{f}(\omega)\ e^{-\frac{(s\,\omega-\omega_c)^2}{2}}. \tag{2.11}$$

Mit der Einführung der Diskretisierungsparameter $s = a \cdot \Delta t$ zu den jeweiligen Zeitschritten Δt erhält man die numerisch nutzbare Form der Wavelet-Transformation im Frequenzbereich unter Berücksichtigung von $\omega = 2\pi f$

$$\mathfrak{F}\,\{\mathcal{W}\} = \sqrt[4]{\pi}\ \sqrt{2\,\Delta t}\ \sqrt{a}\ \hat{f}(\omega)\ \exp\left(-\frac{(a\,\Delta t\,\omega-\omega_c)^2}{2}\right).$$

Eigene Analysen in laufenden Laboruntersuchungen erbrachten eine Reduktion der Berechnungszeit um den Faktor 50 und mehr gegenüber der im Zeitbereich definierten Methode.

Zeit-Frequenz-Transformation

Nachteilig in der Nutzung von Zeit-Skalierungs-Transformationen ist die Zunahme der Unschärfen mit ansteigender Frequenz. Um diesen Effekt zu verringern, werden Zeit-Frequenz-Transformationen hinsichtlich der Eignung analysiert. In Vergleich zu den Zeit-Skalierungs-Transformation basieren diese Transformationen nicht auf einer Skalierung der jeweiligen zeit- und frequenzverschobenen Fenster- bzw. Wavelet-Funktion, wodurch Leaking-Effekte vermieden werden können. Allerdings können sogenannte Kreuzterme „Fehlstellen“ im Spektrum der transformierten Variablen auftreten. Für die genutzte lineare Zeit-Frequenz-Funktion im Sweepsignals bietet sich die Wigner-Ville-Verteilung (Wigner-Ville-Distribution WVD) für die numerische

Analyse an. Prinzipiell existieren unterschiedliche, an die zu analysierende Signalform angepasste Zeit-Frequenz-Transformationen (Kiencke, Schwarz, & Weickert 2008) und (Hammond & White 1996).

Ausgehend von der Kurzzeit-Fourier-Transformation eines Signals $X(\tau,\omega) = \int_{-\infty}^{\infty} x(t)w(t-\tau)e^{-j\omega t}dt$, welches noch die Eigenschaften des genutzten Zeitfensters $w(t)$ verschoben um τ in der Transformation enthält, wird der Fensterterm und das Argument der Signalfunktion durch das zeitlich verschobene, komplex konjugierte Signal ersetzt $X(\tau,\omega) = \int_{-\infty}^{\infty} x(t+\frac{\tau}{2})x(t-\frac{\tau}{2})^* e^{-j\omega\tau}d\tau$ und nach dem Zeitversatz τ integriert (Allen & Mills 2004). Methodisch stellen die kleinen symmetrischen überlappenden Zeitfenster als das innere Produkt, die Fourieranalyse von τ in $x\left(t+\frac{\tau}{2}\right)x^*\left(t-\frac{\tau}{2}\right)$ bezüglich der aktuellen, momentanen Autokorrelationsfunktion dar.

Um die „ähnlichen“ Bestandteile des durch die Bodeneigenschaften zeit- und frequenzverschobenen Empfangssignals zu bestimmen, wird der Versatz in zwei symmetrische Teile, einmal nach dem zu untersuchenden Zeit- und nach dem Frequenzmittenpunkt zerlegt. Die so entstehende 2-dimensionale Fouriertransformation, entsprechend eines Zeitversatzes

$$W_{xx}(t,f) = \int_{-\infty}^{\infty} x\left(t+\frac{\tau}{2}\right)x^*\left(t-\frac{\tau}{2}\right)e^{-j2\pi f\tau}d\tau \tag{2.12}$$

oder bezüglich eines Frequenzversatzes

$$W_{xx}(t,f) = \int_{-\infty}^{\infty} x\left(f+\frac{\vartheta}{2}\right)x^*\left(f-\frac{\vartheta}{2}\right)e^{-j2\pi\vartheta t}d\vartheta. \tag{2.13}$$

ist die WVD. Die außergewöhnliche Zeit-Frequenz-Auflösung der WVD wurde in unterschiedlichen Analysen (Wuttke, Markwardt & Schanz 2009, Wuttke, Markwardt & Schanz 2012) dokumentiert. Einschränkend gegenüber der CWT ist der limitierende Korrelationsansatz, welcher ausschließlich auf Maximierung der Auflösung ausgelegt ist. Demgegenüber bietet die CWT durch den analytischen Ansatz und den bereits vorhandenen theoretischen, mathematischen Rahmen weitere Perspektiven in der Applikation.

2.5 Angewandte Signalanalyse - Gradientenverfahren

2.5.1 Coda wave interferometry

Wie bereits beschrieben, besitzt ein Wellenzug neben dem kohärenten Zeitabschnitt einen verrauschten, stochastischen Zeitabschnitt, die Coda. Durch das mehrfache Durchlaufen der Welle durch das Material erhält diese eine hohe Sensitivität gegenüber kleinsten Änderungen in dieser Struktur. Während des Durchlaufens einer Welle durch ein granulares Medium wird das Wellenfeld mehrfach gebrochen, reflektiert und überlagert. Die einzelnen Wellenpfade werden durch die vorhanden Partikel in dem Wellenweg geändert und interferieren später wieder. Später ankommende Wellen im registrierten Zeitverlauf hatten dementsprechend einen längeren Laufweg als die eher ankommenden Wellenfronten. Wird in die Struktur des Materials eine kleine Störung eingetragen, so ändert sich der Laufweg minimal in der Partikelstruktur. Es wird das Verhalten der minimalen und akkumulierenden Zeitverzögerung innerhalb des neuen Signals nach der Störung sichtbar, siehe Abbildung 2.3.

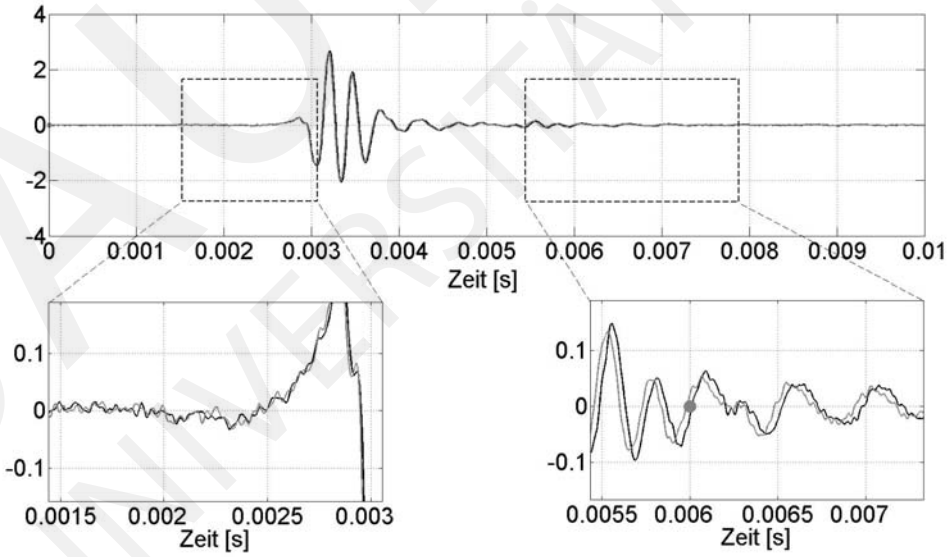

Abbildung 2.3: Abbildung der Zeitverzögerung innerhalb der Coda des Wellenfeldes.

Dieser akkumulierende Zeitversatz im Zeitverlauf zwischen dem Signal vor und nach der kleinen Störung hat die Ursache in den sich nacheinander akkumulierenden, interferierenden Wellenanteilen. Die unterschiedlich durch das Medium propagierenden Wellenfronten speichern auf dem jeweiligen Laufweg die Änderung der Struktur in einer Laufzeitänderung ab, interferieren erneut und bilden so eine durchschnittliche,

konstante Änderung im Phasenversatz der Wellenform ab. Durch die Codawellen-Interferometrie wird die Information wieder aus dem Zeitverlauf extrahiert.

Die Grundlage der Codawellen-Interferomtrie (CWI) ist die Bestimmung der relativen Geschwindigkeitsänderung zwischen beiden Zuständen. Die Umsetzung der CWI kann entsprechend drei unterschiedlicher Lösungswege erfolgen:

- gefensterte Codawellen-Interferometrie
- gedehnte Codawellen-Interferometrie
- frequenztransformierte Codawellen-Interferometrie

Alle drei Wege ergeben ein analoges Ergebnis hinsichtlich der Geschwindigkeitsänderung. Eine ausführliche Beschreibung und Herleitung der Methoden ist in (Wuttke, Asslan & Schanz 2012, Dai et al. 2012) abgebildet. Der gebräuchlichste Analyseweg ist die gefensterte Codawellen Interferometrie nach Gl. (2.14), welche in der Signalanalyse eine gefensterte, normierte Kreuzkorrelation darstellt

$$R^{t,T}(t_s) := \frac{\int_{t-T}^{t+T} u_{unp}(t')\ u_{per}(t'+t_s)\,dt'}{\left[\int_{t-T}^{t+T} u_{unp}^2(t')\,dt' \int_{t-T}^{t+T} .u_{per}^2(t')\,dt'\right]^{\frac{1}{2}}}. \tag{2.14}$$

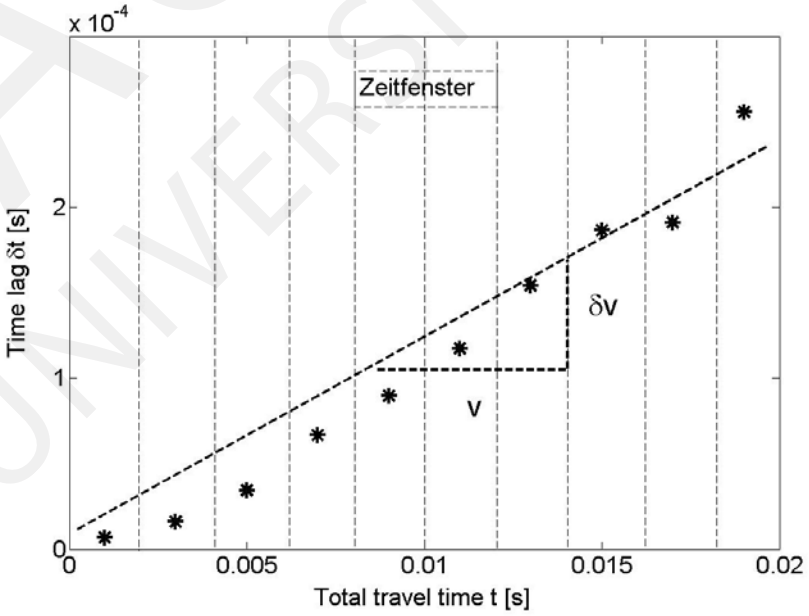

Abbildung 2.4: Abbildung zur Bestimmung des Geschwindigkeitsgradienten aus den einzelnen Laufzeitverzögerungen innerhalb der Zeitfenster, nach (Wuttke, Asslan & Schanz 2012).

Darin ist u_{unp} das Wellenfeld in der ungestörten Struktur, u_{per} das Wellenfeld in der gestörten Struktur, T die Fensterlänge und t_s die Zeitabschnitte. Aus der Signalanalyse ergibt sich neben dem Zeitversatz zwischen den Signalen auch die normierte Magnitude, wodurch nach (Snieder 2006) die auftretenden Varianzen bestimmt werden können. Die Kopplung der einzelnen Zeitverzögerungen zwischen den Signalen jedes Fensterabschnitts und der Zeitachse weist einen Anstieg in der Zeitverzögerung auf. Dieser Anstieg entspricht dem Verhältnis der Geschwindigkeitsänderung $\frac{\delta v}{v}$, siehe Abbildung 2.4.

Die numerischen Schritte zur Durchführung der CWI können in folgenden Schritten wiedergegeben werden:

1. Sensor-stationäre Zeitverlaufsmessungen an der Struktur (vor / nach der Störung)
2. Korrektur der Signale in Glättung und Nullachsenabweichung
3. Fensterung aller Zeitverläufe und Analyse aufeinanderfolgender Signale
4. Abbildung der Zeitverzögerung und der Geschwindigkeitsunterschiede zwischen den Signalen
5. Kumulative Abbildung der Änderungsevolution

2.5.2 Hertz-Kontakt-Theorien

In der Interpretation von Labormessungen werden immer Theorien benötigt, um die Ergebnisse zu validieren oder gewünschte, aber indirekte Parameter abzubilden. Dabei bieten sich speziell für granulare Materialien, Hertz-Kontakt-Modelle an, da diese die Phänomene auf der Mikroskala und in der Simulation die Laborexperimente gut abbilden können. In der Weiterentwicklung dieser Theorien würden partikelbasierte numerische Methoden, wie Discret-Element Methoden entstehen (O'Sullivan 2011), welche in dieser Arbeit allerdings nicht herangezogen werden. Bereits aus den einfachen Beziehungen, basierend auf den Hertz-Kontakt-Modellen, lassen sich eine Vielzahl der getätigten Exerimenten mit unterschiedlichen Randbedingungen validieren. Für die Untersuchung der unterschiedlichen geotechnischen Materialbedingungen, müssen der Umgebungsdruck in der Kornstruktur, die Kornrauhigkeit bzw. -form, die vorhanden Kapillarkräfte von ungesättigten Materalien, kohäsive Inter-Partikelkräfte und mögliche Inter-Partikel-Zementierungen modellierbar sein. Diesbezüglich eignen sich Hertz-Kontakt-Modelle gut, um in Verbindung mit dem Steifigkeitsmodul auch eine direkte Progose zur Wellengeschwindigkeit unter diesen Einflüssen abzugeben. Basierend auf dem Hertz-Kontakt-Modellen existieren für granulare Materialien existieren eine Vielzahl von unterschiedlichen Modellen. Die bekanntesten Modelle sind

das Hertz-Mindlin-Model (Marion 1990), das Brandt-Modell (Brandt 1955) oder das Dvorkin-Nur-Modell (Bachrach, Dvorkin & Nur 2000).

Inter-Partikel Kräfte und Kontaktflächen

Alle mikroskaligen Beschreibungen, wie die Hertz-Kontakt-Theorien gehen von der Beschreibung der Kräfte und deren Kontaktflächen zwischen den Partikeln aus, um die Spannungen und auftretenden Steifigkeiten an den Grenzflächen zu definieren. Diese Kräfte widerspiegeln die unterschiedlichen Interaktionen und Art der Kornkontakte auf der Mikroskala. Nach (Cho & Santamarina 2001) ist die Kontaktkraft für zwei Sphären in einem kubischen Haufwerk $N = 4R^2\sigma_0$ bzw. für die mittlere Normalkraft N, dem mittleren Kornradius R und dem Umgebungsdruck σ_0 in einem zufällig angeordneten Haufwerk monodisperser Sphären $N = 4R^2\sigma_0 \frac{\pi}{(1-n)cn}$, mit n als Porenzahl und cn als Koordinationszahl der Partikelkontakte $cn \geq \pi\,(1+e)$. Als Radius der Kontaktfläche ergibt sich für $a = \left[\frac{3NR}{8G}\,(1-\nu)\right]$, wobei G und ν die Poissonparameter darstellen.

Zementierte Böden besitzen durch die Anlagerung von Zementierungsbrücken zwischen den Körnern eine Vergrößerung der Kontaktfläche. Nach (Mavko, Mukerji & Dvorkin 2009) kann die Vegrößerung durch das Verhältnis $\alpha = a/R$ zwischen dem Radius der Zementierung und dem Radius des Korns berücksichtigt werden, wobei die unterschiedliche Steifigkeit von Korn und Zementierung eingeht. Nach (Santamarina, Klein & Fam 2001) ergibt sich unter Annahme der gleichen mechanischen Parameter für Korn und Zementierung eine vereinfachte Kontaktfläche $a = R\sqrt{(CC+1)^{2/3} - 1 + \left(\frac{3(1-\nu_g)\sigma}{2G_g}\right)^{2/3}}$, mit ν_g als Poissonzahl des Korns, CC das Gewichtsverhältnis zwischen Zement und Partikel, G_g der Schubmodul des Korns und σ der Umgebungsdruck.

Die Modellierung von ungesättigten granularen Medien ist nur bedingt gelöst, da nur geringe Sättigungsbedingungen von $w \leq 6\%$ mit dem Modell erfasst werden können. Die Gründe liegen in der Modellierung eines Wassermeniskus an den Korn-Kontaktflächen, als zusätzliche Zugspannung zwischen den Körnern. Diese Menisken werden nur bei recht geringen Wassergehältern nach dem residualen Wassergehalt ausgebildet. In der Übergangszone zwischem dem Lufteintrittspunkt und dem residualen Wassergehalt sind lokale Zonen von gesättigten und ungesättigten Bereichen zufällig verteilt, welches die Erfassung der Mechanismen deutlich erschwert. Diese Abfolge ist deutlich sichtbar, wenn sättigungssensitive Kompressionswellen für ein Monitoring der Strukturänderung genutzt werden. Zwischen dem Lufteintrittspunkt und dem residualen Wassergehalt sind die Wellenfelder chaotisch, stark von der hydraulischen Situation beeinflusst und lassen sind nur schlecht interpretieren. Vor dem Lufteintrittspunkt und nach der residualen Sättigung ist das Änderungsverhalten

der Kompressionswellenfelder in Form und Frequenz glatter und weniger stochastisch, wodurch eine Interpretation möglich ist. Entsprechend (Lu & Likos 2004) ist die Saugspannung entlang des Meniskus durch $(u_a - u_w) = T_s \left(\frac{1}{r_1} - \frac{1}{r_2}\right)$ definiert. Die Radien r_1 und r_2 entsprechen dem Radius von Kornmitte zum Meniskus und der äußeren Meniskuskrümmung, T_s ist die Oberflächenspannung zwischen Wasser und Luft. Die kapillare Kontaktkraft zwischen den Körnern folgt nach (Cho & Santamarina 2001) zu $N = \Delta u \left(\pi r_2^2\right) + T_s \left(2\pi r_2\right)$ bzw. $N = T_s R\pi \left(2 - \left(8/9wG_s\right)^{1/4}\right)$.

2.5.3 Ableitung makroskopischer Moduli aus Kornstrukturen

Die Bestimmung makroskopischer Moduli resultiert aus der Ableitung der elastischen Moduli aus den Spannungen der Kornkontaktflächen. Vereinfacht kann dazu auf die parabolische Spannungsbeschreibung des Hertz'schen Kontaktes zurückgegriffen werden

$$\sigma_{contact}\left\{a, r\right\} = \sigma_0 \sqrt{1 - \left(\frac{r}{a}\right)^2} \; mit \; \sigma_0 = \frac{3N}{2\pi a^2}, \tag{2.15}$$

wobei der Kontaktradius $a = \sqrt[3]{\frac{3(1-\nu)NR}{8G_g}}$ berücksichtigt wird (Marion 1990).

Die Steifigkeit ergibt sich aus der Ableitung der Normal- oder Schubspannung nach der Dehnung oder Scherdehnung. Dieser Zusammenhang wird im Hertz-Mindlin-Modell durch die Terme, $S_n = \frac{4aG}{1-\nu}$ für die Normalkräfte und $S_\tau = \frac{8aG}{2-\nu}$ für die Scherkräfte aufgegriffen. Nach (Mavko et al. 2009) können effektive, makroskopische Kompressions- und Schermoduli für eine zufällige Struktur von runden Körnern (Sphären) in Abhängigkeit von der durchschnittlichen Anzahl der Kornkontakte (Koordinationszahl cn) eines Einzelkorns für das Hertz-Mindlin-Modell angegeben werden zu

$$\begin{aligned} G_{eff,Skelett} &= \tfrac{cn(1-n)}{20\pi R}\left(S_n + 1.5S_{tau}\right) \\ K_{eff,Skelett} &= \tfrac{cn(1-n)}{12\pi R} S_n \end{aligned} \tag{2.16}$$

Die entsprechenden Geschwindigkeiten werden durch die kontinuumsmechanische Definition der Geschwindigkeiten $c_s^2 = \frac{G_{eff}}{\rho_{eff}}$ bzw. $c_p^2 = \frac{E_{s,eff}}{\rho_{eff}}$ definiert. Durch die Definitionen der Partikelkontaktfläche a von ungesättigten oder zementierten granularen Lockerböden können Wellengeschwindigkeiten auch für diesen Bedingungen prognostiziert werden.

Als empirische Beziehung der Wellengeschwindigkeit, basierend auf Hertz'schen Analogien und unter Berücksichtigung weiterer stochastischer Bodeneigenarten, wie Kornform, Heterogenitäten etc., wird die Kraft-Verschiebungsrelation entsprechend eines Exponentialgesetzes $N = \nu r^\theta$ mit experimentell zu bestimmenden Konstanten ν

und θ definiert (Santamarina et al. 2001). Über die Ableitung der Kraft N nach der Verschiebung r kann die allgemeine Form der Wellengeschwindigkeit für $c_p = \nu\sigma^{\chi}$ bzw. $c_s = \alpha\sigma^{\beta}$ angegeben werden. Die Konstanten beinhalten spezielle Randbedingungen der unterschiedlichen granularen Kornstrukturen, z.B. elastische Sphären, natürliche Kornform und -rauhigkeit, Phasenausbildung und andere schwer modellierbare Bodeneigenarten.

2.6 Charakterisierung und Prozessmonitoring von mehrphasigen Lockerböden

2.6.1 Identifikation von frequenzabhängigem Materialverhalten

In (Wuttke, Asslan & Schanz 2010, Wuttke, Markwardt & Schanz 2012) wurde eine Methodik, die auf Zeit-Frequenz- oder Zeit-Skalierungs-Transformationen basiert, zur hochauflösenden Ermittlung der Gruppengeschwindigkeit entwickelt, um Frequenzabhängigkeiten in Geomaterialien genauer und zeiteffektiv sowie Geschwindigkeiten ohne „subjektive“ Einflüsse analysieren zu können. Dazu erfolgt die Analyse eines sweepangeregten Signals vor und nach dem zu untersuchenden Bodenbereich im Zeit-Frequenz-Bereich. Durch die Sweepanregung kann ein breiter Frequenzbereich entsprechend angeregt werden und gleichzeitig die Effektivität der Methoden genutzt werden. Aus der zeitlichen Differenz der Spektralamplituden im Zeit-Frequenz-Spektrum können die Gruppengeschwindigkeiten frequenzabhängig ermitteln werden, siehe Abbildung 2.5.

Aufbauend auf dieser Methodik erfolgt die Anwendung und Analyse anhand numerischer und experimenteller Untersuchungen von Geomaterialien in (Wuttke, Markwardt & Schanz 2012). Die Analysen erfolgen anhand simulierter dispersiver Wellenfeldern, experimentell anhand von Glaskugeln und Hostun-Sand (Wuttke et al. 2010). Die Simulationsanalysen sollen die prinzipielle Anwendungsfähigkeit demonstrieren. Als wesentliches Ergebnis zeigt sich, dass keine numerische Dispersion durch die Analyse hervorgerufen wird. Die Auflösung der CWT war für die numerischen Beispiele stabiler und genauer als die der WVD. Die experimentellen Untersuchungen wurden innerhalb einer Triaxialzelle durchgeführt, kontrolliert im Frequenzbereich durch Korn- und Probengröße hinsichtlich der Vermeidung von Nahfeldeffekte bzw. Zerstreuung des Signals. Die Geometrie der Probe verursachte inhärente Wellenfeldstörungen durch Reflexionen und Interferenzen, welche die Analysequalität mitunter beeinträchtigen können. Für weitere Untersuchungen unter Vermeidung dieser Berandungseinflüsse wurde ein Großversuchsstand mit innenliegenden Sensoren konzipiert, so dass das außenliegende Material die reflektierten Wellen dämpfen kann.

Unter harmonischen oder langen Sweepanregungen wurde die Probe in Biegeschwingungen versetzt, wodurch die Antwort entsprechend der Anregung von Eigenwerten und -formen erfolgt (Arroyo 2007). Zum Vergleich wurden numerisch bestimmte Eigenwerte eines entsprechenden Modells in (Wuttke, Markwardt & Schanz 2012) den experimentell ermittelte Dispersionsgeschwindigkeiten, welche experimentell ermittelten Eigenwerte repräsentieren, gegenübergestellt. Allerdings sind noch weitere Untersuchungen erforderlich, um das hervorgerufene Proben-Eigenschwingverhalten für eine Identifikation der Struktur auch unter Mehrphasigkeit zu nutzen. Prinzipiell konnte im Gegensatz zu den bisherigen Untersuchungsmethoden auf „subjektive“ Abschätzungen oder Auswahl von Abtastpunkten verzichtet werden.

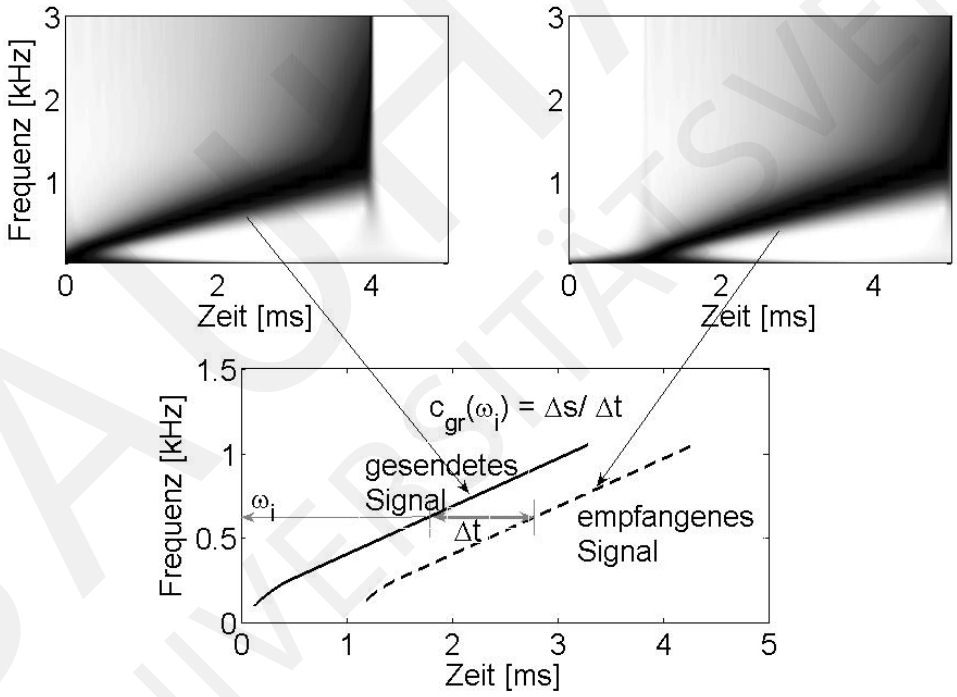

Abbildung 2.5: Bestimmung der Gruppengeschwindigkeit aus der Zeit-Frequenz-Analyse zwischen dem gesendeten und empfangenen Sweepsignal.

2.6.2 Prozessmonitoring von Spannungsabhängigkeit

Für die Analyse der Spannungsänderung in granularen Geomaterialien erfolgte die Überführung der Geschwindigkeitsänderungen in Druckspannungsänderung, die auf der Wellengeschwindigkeitsabbildung durch Hertz'sche Kontaktmodelle basieren. Für das Monitoring einer Spannungsänderung wurden unterschiedliche Experimente

aufbauend auf einem 5kPa Spannungsänderungsprozess durchgeführt. Kumulativ abgebildet ergibt sich die Geschwindigkeitsevolution, siehe (Wuttke, Asslan & Schanz 2012, Wuttke 2012). Zur Validierung der Vorgehensweise erfolgte ein Vergleich mit synthetisch generierten Ergebnissen eines Hertz-Kontakt-Modells.

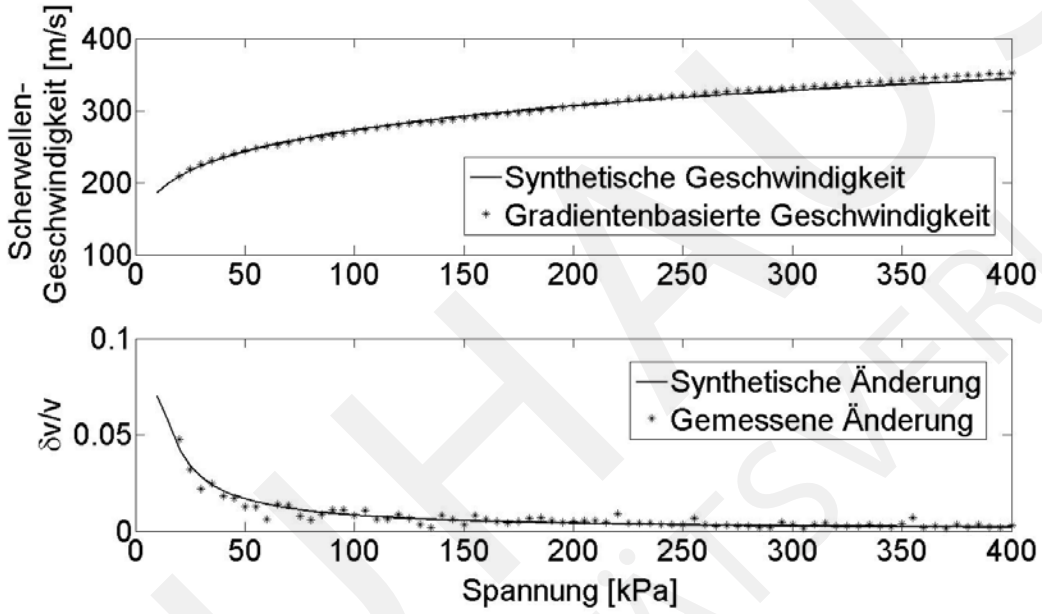

Abbildung 2.6: Bestimmung der Spannungsänderung anhand der Änderung des Geschwindigkeitsänderung, nach (Wuttke, Asslan & Schanz 2012)

Die Wellengeschwindigkeit kann dabei durch folgende Gleichung beschrieben werden: $v = \alpha \cdot \sigma^{\beta}$, wobei α und β materialabhängige Parameter sind. So wird der Exponent für elastische runde Partikel zu 1/6 und für kantige Partikel zu 1/4 gesetzt (Santamarina et al. 2001). Unter Berücksichtigung der Gradientendefinition $\delta v/v$ ergibt sich für das Hertzkontakt-Gradientenmodell folgende Gl. (2.17)

$$\frac{\delta v}{v} = \beta \frac{\delta \sigma}{\sigma}. \tag{2.17}$$

Für die Bestimmung der Spannung aus den gemessenen Geschwindigkeitsgradienten ist die Gl. (2.17) nach σ umzustellen

$$\sigma = \frac{\delta \sigma}{\beta \frac{\delta v}{v}}. \tag{2.18}$$

Die Abbildung 2.6, siehe auch (Wuttke, Asslan & Schanz 2012), (Wuttke 2012) und (Dai et al. 2012), zeigen, dass diese Methodik für jede Änderung des Spannungsverlaufs eingesetzt werden kann und sowohl für Simulationen als auch für Experimente einen sehr guten Verlauf der tatsächlich applizierten Spannungen wiedergeben konnte.

2.6.3 Prozessmonitoring von Saugspannungsänderung

Im Studium ungesättigter Böden stellt die Nutzung von wellenbasierten Werkzeugen einen wesentlichen Forschungspunkt dar. Bislang ist das Verhalten von Wellen durch ungesättigte Geomaterialien weitestgehend unerforscht. Mit den Arbeiten von (Albers 2010), (Steeb, Frehner & Schmalholz 2010) und (Gatmiri & Jabbari 2005) wurden die Anfänge der theoretischen Modellierung als Kontinuumsmodell durchgeführt. Mikromechanische Modelle, wie Partikelmodelle, sind derzeit in der Entwicklungen für Zwei-Phasen-Materialien. Vereinfachte Hertz-Kontaktmodelle existieren durch die Entwicklungen von (Cho & Santamarina 2001), allerdings nur mit einem Gültigkeitsbereich von bis zu 6% Materialsättigung. Allgemeingültigere Modelle sind in der Forschung und Entwicklung derzeit nicht existent.

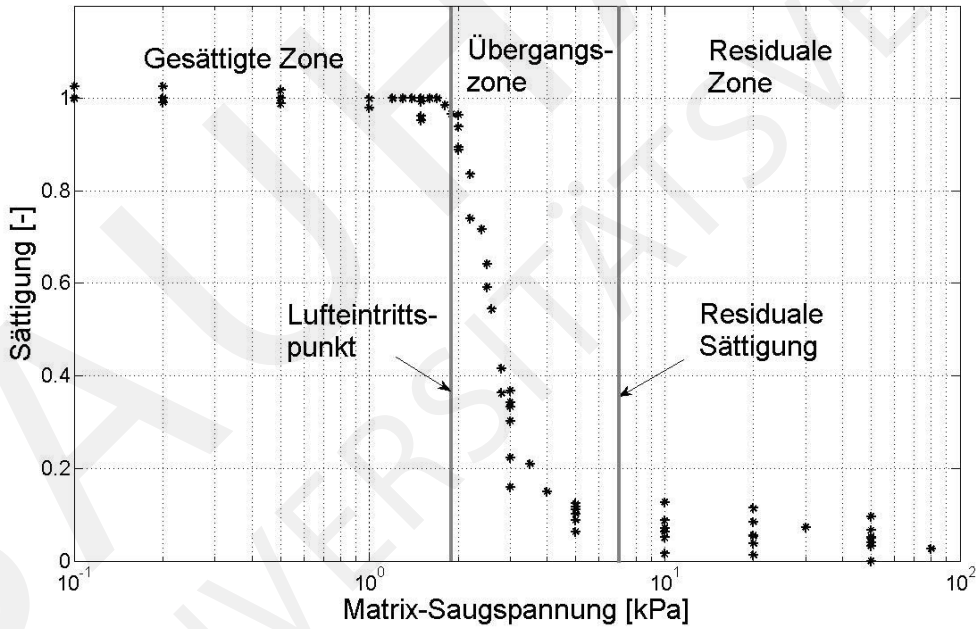

Abbildung 2.7: Abbildung der Saugspannungs-Sättigungs-Kurve für Hostun-Sand

In den nachfolgenden Analysen wird eine Möglichkeit zur Ableitung der Änderung der Scherwellengeschwindigkeit und damit der small-strain Bodensteifigkeiten in Abhängigkeit von der vorhanden Saugspannung vorgestellt, (Wuttke 2012), (Wuttke & Schanz 2012). Zur Entwicklung dieser Ansätze wurden spezielle experimentelle Laboruntersuchungen durchgeführt. Eine Triaxialzelle wurde so modifiziert, dass neben dem Zelldruck auch der Porenwasser- und Porenluftdruck innerhalb der Probe kontrolliert werden konnte. Ausgehend von dem Aufbringen kontrollierter Saugspannung-Inkremente vom gesättigten bis zum nahezu trockenen Probenzustand

erfolgten die seismischen Labormessungen. Neben den Daten der Wellengeschwindigkeitsänderungen war der Verlauf der Saugspannung-Sättigungs-Funktion ermittelt worden. Die Saugspannung-Sättigungs-Funktion (Soil-Water-Characteristic Curve SWCC) ist eine der wichtigsten Informationen für die Erläuterung des Verhaltens von ungesättigten Böden, für jeden Boden unterschiedlich und damit quasi der ungesättigte Fingerabdruck des Materials, siehe Abbildung 2.7.

Im Vergleich beider Kurven (Wuttke 2012) ist zu bemerken, dass das Änderungsverhalten der Saugspannungs-Sättigungs-Funktion und der Scherwellengeschwindigkeitsänderungen sehr ähnlich und innerhalb der kumulativen Funktionen fast identisch sind, siehe Abbildung 2.8. Dieses impliziert die Möglichkeit einer recht einfachen Übertragung der Saugspannungs-Sättigungs-Gesetzmäßigkeiten auf die Entwicklung der Scherwellengeschwindigkeit über einen großen Bereich der Materialsättigung.

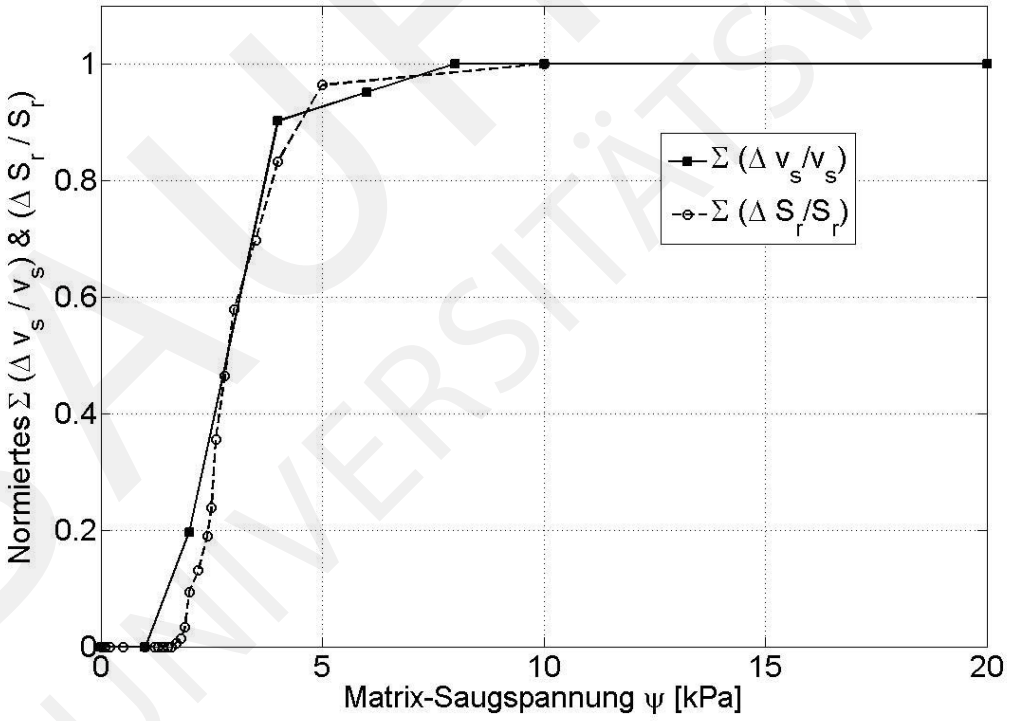

Abbildung 2.8: Bestimmung der Saugspannungsänderung anhand der Änderung des Geschwindigkeitsänderung, nach (Wuttke 2012).

Unter Annahme eines funktionalen Verlaufs der Saugspannungs-Sättigungs-Gesetzmäßigkeiten nach Van Genuchten (Van Genuchten 1980), $\theta(\psi) = [1 + (\alpha\psi)^n]^{-m}$, mit θ als volumetrischem Wassergehalt, ψ als Saugspannung und n, m als materialabhängige

Parameter, kann der Wellengeschwindigkeitsgradient aus dem Saugspannungsgradient $\frac{\delta\theta}{\delta\psi}$ abgeleitet werden

$$\frac{\delta v}{v} = \frac{\delta\theta}{\theta} = 1 - \frac{(1+\alpha\psi_i^n)^m}{(1+\alpha\psi_{i+1}^n)^m}. \tag{2.19}$$

Derzeit ist der Gültigkeitsbereich der Gleichungen auf ein granulares, enggestuftes Material ohne Feinkornanteil und Scherwellen begrenzt. Auftretende Zementierungen durch Feinkornanteile während des Trocknungsvorgangs verstärken die Zunahme der Geschwindigkeitsänderungen deutlich und müssen berücksichtigt werden. Zukünftig müssen noch folgende Punkt untersucht werden, um die Methodik allgemeingültiger zu gestalten: a) die Quantifizierung des Einflusses des Feinkornanteils und b) die Analyse von Kompressionswellen im Bereich des Lufteintrittspunktes - dem Entstehen einer nicht-kontinuierlichen Fluidphase bis zum residualen Wassergehalt, durchzuführen.

2.6.4 Bestimmung von Kriechfunktionen in granularen Böden

Für das Kriechen von Böden wird oft eine viskoser Ansatz in der Beschreibung des speziellen Materialverhaltens genutzt. Bislang wurden die Modelle auf bindige Böden begrenzt, da die auftretenden Amplituden relativ groß und gut erfassbar sind. Rollige oder nichtbindige Böden sind als Böden weitestgehend ohne Kriechverhalten bekannt. Jedoch weisen auch diese Böden ein Kriechverhalten auf, nur viel kleiner. Interessant wird diese Fragestellung, wenn das zyklische Verhalten eines nichtbindigen Boden unter Schwelllast zu untersuchen ist. Zyklisch belastete Böden weisen immer eine Verformungsakkumulation auf, (Wichtmann 2005). Je nach Verdichtungsgrad, Kornform und anderen mikroskopische Einflusse wird diese Akkumulation größer oder kleiner ausfallen. Nichtbindige Böden weisen ein Kriechen auf, welches durch die leichte Änderung der Struktur, Abbruch von Kornkanten oder Änderung der Anzahl der Korn-zu-Korn-Kontakte, d.h. der Koordinationsanzahl im Strukturtensor, beeinflusst wird. Letztlich wird eine Kopplung aus dem statischen Lastanteil in der Schwelllast und der zyklischen Wechsellast vorhanden sein. Der statische Anteil führt damit ebenfalls zum Kriechen des Bodens.

In (Dai, Wuttke & Santamarina 2012) erfolgt eine Studie zum Monitoring und zur Modellierung der Kriechfunktion von granularen Bodenmaterialien unter einer statischen Belastung. Dazu wurde eine Ottawa-Sandprobe unter anderem mit einer konstanten statischen Last für 8 Stunden belastet. Die Durchschallung erfolgte mit einem zunehmenden Zeitabstand. Das Kriechen des Bodens war deutlich in der Coda durch die Zunahme der Wellengeschwindigkeitsänderungen sichtbar, (Dai et al. 2012). Ausgehend von der Geschwindigkeitsänderungsfunktion wurde das Potenzgesetz $c_p = a(t/t_{ref})^b$, unter empirischer Bestimmung der Konstanten a und b, für die

gegebenen Umgebungsbedingungen und Materialcharakteristika definiert. Dieser Verlauf wurde der zeit- und spannungsabhängigen Wellenschwindigkeitsgleichung gegenübergestellt

$$c_p = \sqrt{\frac{E}{\rho}} = \sqrt{\frac{G_m}{\rho\,(1-\nu_m)}} \left(\frac{k \cdot t_{ref}}{1-n}\right)^{\frac{1}{4}} \left(\frac{\sigma'}{\sigma_{ref}}\right)^{\frac{m}{4}} \left(\frac{t}{t_{ref}}\right)^{\frac{l-n}{4}}. \tag{2.20}$$

Durch Vergleich von vorhanden Kriechkonstanten in der Kriechfunktion und der zuvor bestimmten experimentellen Gleichung konnten die fehlenden Parameter zur Definition des Kriechgesetzes eines granularen Materials ermittelt werden.

2.7 Zusammenfassung

Das Kapitel 2 behandelte die Grundlagen und neue Entwicklungen in der experimentellen Analyse von ungesättigten, granularen Materialien. Insbesondere die Untersuchung und Weiterentwicklung von wellenbasierten Analysemethoden war im Fokus der Entwicklungen. Das Ziel dieser Forschungen waren die Entwicklung neuer Ansätze, Methoden und Ergebnisse für ungesättigte, nichtbindige Böden, um die bestehenden Methoden und Materialbeziehungen zu erweitern. Weitere Zielsetzung war ebenso die Erstellung eines funktionalen Zusammenhangs und fehlender Eingangsparameter für die theoretischen Modelle und Simulationen in den Kapiteln 3 und 4. Die Kenntnis der small-strain Steifigkeit in Abhängigkeit von der Sättigung komplettiert die Prognosefähigkeit hinsichtlich des Last-Verformungsverhaltens unter veränderlichen Sättigungsgraden. Dieses Wissen ist nicht nur in der Prognose von statischen Last-Verformungs-Problemen wichtig, vielmehr ist es in der Behandlung zyklischer und dynamische Problemstellungen eine wesentliche Eingangsnotwendigkeit, um die Setzungsakkumulation unter Wechsellast richtig zu erfassen.

2.8 Beigelegte eigene Publikationen zu Kapitel 2

Dai, S., Wuttke, F., Santamarina, J.C. (2013) Coda Wave Analysis to Monitor Processes in Soils, *ASCE Journal of Geotechnical and Geoenvironmental Engineering*, vol. 139, no.9, pp.1504-1511

Wuttke, F., Markwardt, K., Schanz, T. (2012) Dispersion analysis in Geotechnical Laboratory Tests: Time-frequency and time-scale signal transforms, *ASTM Geotechnical Testing Journal*, vol.35, no.5

Wuttke, F., Schanz, T. (2012) Zustandsänderungsmonitoring von granularen, mehrphasigen Böden mittels Codawellen Interferometrie, *4. VDI Tagung Baudynamik*,

Kassel

Wuttke, F., Asslan, M., Schanz, T. (2011) Time-lapse monitoring of fabric changes in granular materials by Coda Wave Interferometry, *ASTM Geotechnical Testing Journal*, vol.35, no.2

Wuttke, F., Asslan, M., Schanz, T. (2010) Wave velocity analysis of state parameter changes in multi-phase granular material, *5th UNSAT International Conference on Unsaturated Soils*, Barcelona

Kapitel 3

Modellbildung und Simulation der Boden-Bauwerk-Interaktion

3.1 Einleitung und Motivation zur Makro-Element Theorie

Das Studium von Phänomenen komplexer Boden-Bauwerk-Interaktionsmechanismen unter Berücksichtigung von Mehrphasigkeit der Bodenmaterials und mehrdimensionalen und zeitabhängigen Belastungen ist nach dem heutigen Stand der numerischen Simulationsmodelle eine hohe und zum Teil auch noch ungelöste Herausforderung für realistische Prognoserechnungen. Die korrekte Prognose ist allerdings von fundamentaler Bedeutung für den Entwurf und die wirtschaftliche Bemessung. Für die Modellierung von komplexen Gesamtmodellen müssen die jeweiligen Partialmodelle weitgehend das physikalische Experiment widerspiegeln und zugleich verlustfrei miteinander interagieren. Als Partialmodelle müssen für die Boden-Bauwerk-Interaktion das konstitutive Bodenmodell, das konstitutive Boden-Bauwerk-Interface-Modell und das Modell der Konstruktion erstellt und miteinander gekoppelt werden. Durch die numerischen Fehler dieser Modelle, welche insbesondere für die Simulation von zeitabhängigen Belastungen vorhanden sind, würde eine FEM Simulation numerisch mindestens sehr aufwendig sein bzw. falsche Ergebnisse liefern.

Eine andere Art der Beschreibung von komplexen Boden-Bauwerk-Interaktion, welche speziell für zyklisch, dynamische aber auch komplexe statische Problemstellungen immer mehr Bedeutung bekommt, ist die Nutzung von Makro-Element-Modellen. Diese Modelle stellen eine Reduktion der gekoppelten Gesamtmodellkomplexität dar, da die oben benannten unterschiedlichen Modelle in einer Beschreibung zusammengefasst und damit ein makroskopisches Systemverhalten abgebildet wird. Die Makroelementbeschreibung in der klassischen Geotechnik bzw. des geotechnischen Erdbebeningenieurwesens folgen der ursprünglichen Entwicklung von (Nova

& Montrasio 1991, Montrasio & Nova 1997) als eine der ersten Beschreibung des klassischen Grundbruchs durch die 2D Definition eines Makroelements für ein Streifenfundament. Durch (Butterfield & Gottardi 1994) wurde eine Erweiterung in 3D Formulierungen vorgenommen. In den folgenden Jahren erfolgte eine Vielzahl von Publikationen zu unterschiedlichen Konstruktionen unter kombinierten und komplexen, statischen Lastsituationen (Houlsby & Cassidy 2002, Houlsby, Kelly, Huxtable & Byrne 2005, Kisse 2008). Zeitgleich wurden Makroelementmodelle für dynamische Boden-Bauwerk-Interaktionssysteme entwickelt (Cremer, Pecker & Davenne 2001, Pender 2006, Chatzigogos, Pecker & Salencon 2009). In (Muir-Wood 2004) ist ein Überblick über die Herangehensweise zur Modellierung von geotechnischen Interaktionsproblemen sowie deren Makroelementmodellierung gegeben. Eine Modellierung von mehrpasigen Problemstellungen oder die Einbeziehung von sehr kleinen bis großen Dehnungen von statisch oder zyklisch, dynamisch belasteten Gründungen für realistischere Prognosemodelle in der Geotechnik und dem geotechnischen Erdbebeningenieurwesen sind derzeit ausstehend.

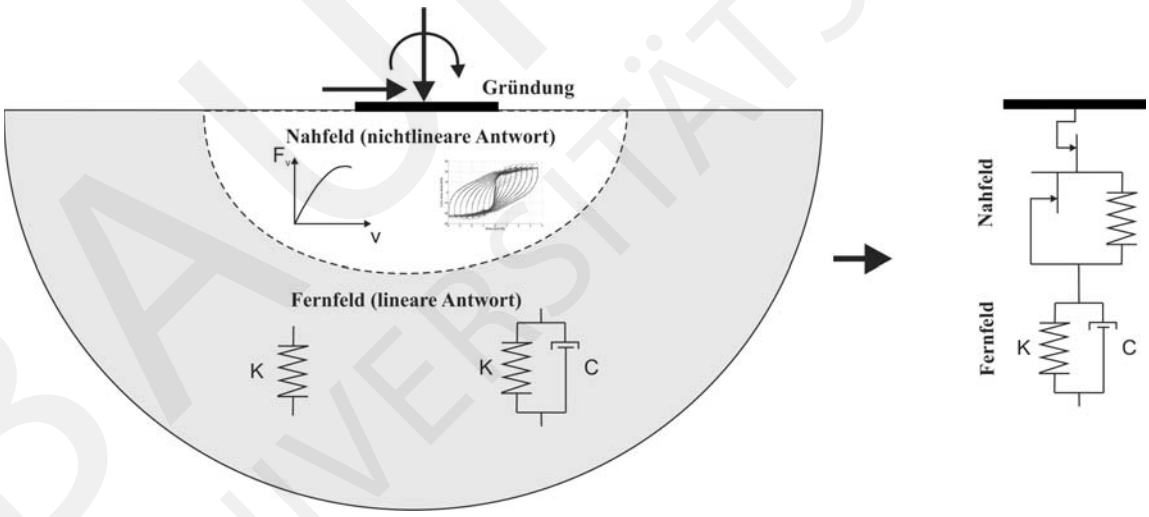

Abbildung 3.1: Räumliche Konzeption eines Makroelements

Die Grundidee eines Makroelements in der Geotechnik umfasst die Gründungsstruktur und Lasten, die Interaktionsgrenzfläche und den umgebenden Boden in einer übergreifenden konstitutiven Elementbeschreibung. Dieser Ansatz kann als direkte Beziehung zwischen den externen Lasten und Momenten als generalisierte Abbildung der Spannungen sowie Verformungen und Rotationen als generalisierte Dehnungen betrachtet werden (Nova & di Prisco 2003).

3.2 Makroelement einer statisch belasteten Flachgründung auf einphasigen Boden

Anhand eines Streifenfundaments werden nachfolgend die Grundprinzipien der Modellierung dargelegt und in nachfolgenden Unterkapiteln auf die speziellen Randbedingungen erweitert. Im Gegensatz zu den üblichen konstitutiven Formulierungen im Spannungs-Dehnungs-Bereich werden Makroelement-Modellierungen auf Basis von Last-Verschiebungs-Beschreibungen definiert, die mathematischen Grundformulierungen sind im Wesentlichen aber kongruent. Für die elasto-plastische, verfestigende Beschreibung von Bodenmaterialien sind die totalen Verschiebungen aus der Summe von elastischen und plastischen Verschiebungen definiert, $\delta\mathbf{q} = \delta\mathbf{q}^e + \delta\mathbf{q}^p$. Analog zu den elasto-plastischen Stoffgesetzen werden in den Makroelementen für Flachgründungen ebenfalls die Konstruktionselemente, elastische Eigenschaften, Fließ- und Versagensfläche, plastisches Potential und plastische Verfestigungsregel genutzt. Die normierten Belastungs- und Verschiebungsvektoren, $\mathbf{Q}$ und $\mathbf{q}$ sind

$$\mathbf{Q} = \begin{Bmatrix} \bar{V} \\ \bar{H} \\ \bar{M} \end{Bmatrix} = \frac{1}{V_m} \begin{Bmatrix} V \\ \frac{H}{\mu} \\ \frac{M}{\psi_m B} \end{Bmatrix} \qquad \mathbf{q} = \begin{Bmatrix} \bar{v} \\ \bar{u} \\ \bar{\theta} \end{Bmatrix} = V_m \begin{Bmatrix} v \\ \mu u \\ \psi\theta_m B \end{Bmatrix} \tag{3.1}$$

mit H, V, M als horizontale, vertiale Last und das Moment, μ als Anstieg der Versagensfläche zwischen H-V, ψ_m als als Anstieg der Versagensfläche zwischen M-V, B der Fundamentbreite, u, v, θ_m als Horizontal-, Vertikalverschiebung und der Fundamentverdrehung. Die elasto-plastische Formulierung der inkrementellen Kräfte ist durch

$$\delta\mathbf{Q} = D\delta\mathbf{q} - \Lambda D\frac{\delta g}{\delta\mathbf{Q}}, \tag{3.2}$$

definiert.

Die dreidimensionale Versagensfläche $f(\mathbf{Q}) = 0$, siehe Abbildung 3.2, unter der gegebenen dreidimensionalen Belastung ergibt sich nach (Nova & Montrasio 1991, Gottardi & Butterfield 1995)

$$\bar{H}^2 + \bar{M}^2 - \bar{V}^2\left(1 - \bar{V}\right)^{2\beta} = 0, \tag{3.3}$$

wobei β ein Kontrollparameter bezüglich der Form der Versagensfläche und des Fließkriteriums ist. Auf Grundlage der Konsistenzbedingung $\left(\frac{\partial f}{\partial\sigma}\right)^T \delta\sigma + \frac{\partial f}{\partial\rho_c}\delta\rho_c = 0$ mit $\rho_c(\mathbf{q}^p)$ nach (Hicher & Shao 2008) und der Fließregel $f(\mathbf{Q}, \rho_c) = 0$ und $\frac{\partial f}{\partial\mathbf{Q}}\delta\mathbf{Q} > 0$ mit $\delta\mathbf{q}^p = \Lambda\frac{\partial g}{\partial\mathbf{Q}}$, ergibt sich das Fließkriterium $f(\mathbf{Q}, \rho_c) = 0$ als Erweiterung der

Versagensfläche um die Verfestigungsfunktion $\rho_c(\mathbf{q}^p)$ für isotrope Verfestigung zu

$$\delta f = \left(\frac{\partial f}{\partial \mathbf{Q}}\right)^T \delta\mathbf{Q} + \Lambda \frac{\partial f}{\partial \rho_c}\left(\frac{\partial \rho_c}{\partial \mathbf{q}^p}\right)^T \frac{\partial g}{\partial \mathbf{Q}} = \frac{\partial f}{\partial \mathbf{Q}}\delta\mathbf{Q} - \Lambda H = 0, \tag{3.4}$$

mit $H = -\frac{\partial f}{\partial \rho_c}\left(\frac{\partial \rho_c}{\partial \mathbf{q}^p}\right)^T \frac{\partial g}{\partial \mathbf{Q}}$.

Die Funktion des Fließkriteriums abgeleitet von der Versagensfläche ergibt sich zu

$$f(\mathbf{Q}, \rho_c) = \bar{H}^2 + \bar{M}^2 - \bar{V}^2\left[1 - \frac{\bar{V}}{\rho_c}\right]^{2\beta} = 0, \tag{3.5}$$

mit ρ_c als Verfestigungsfunktion, $\rho_c \in \mathbb{R}, 0 < \rho_c \leq 1$. Entsprechend (Nova & Montrasio 1991) ist die Verfestigungsfunktion ρ_c in Abhängigkeit von den Kräften und Momenten definiert zu

$$\rho_c = \frac{\bar{V}}{1 - \left(\frac{\bar{H}^2 + \bar{M}^2}{\bar{V}^2}\right)^{2\beta}}, \tag{3.6}$$

in Abhängigkeit von den Dehnungen lautet diese

$$\rho_c = 1 - exp\left[-\frac{R_0}{V_m^2}\sqrt{\bar{u}^2 + \left(\alpha\frac{|\bar{v}|}{\mu}\right)^2 + \left(\gamma\frac{\left|\bar{\theta}\right|}{\psi}\right)^2}\right], \tag{3.7}$$

und in inkrementeller Schreibweise nach (Shirato 2008)

$$\delta\rho_c = (1 - \rho_c)\frac{R_0}{V_m^2}\left[\delta\bar{u} + \alpha\frac{\delta|\bar{v}|}{\mu} + \gamma\frac{\delta\left|\bar{\theta}\right|}{\psi}\right]. \tag{3.8}$$

Das plastische Verformungsinkrement ergibt sich nach Gl. 3.2 zu

$$\delta\mathbf{q}^p = \Lambda\frac{\partial g}{\partial \mathbf{Q}}, \tag{3.9}$$

wobei der plastische Multiplikator Λ aus der Gl.3.2 und Gl.3.4 bestimmt werden kann

$$\Lambda = \frac{\left(\frac{\partial f}{\partial \mathbf{Q}}\right)^T D\delta\mathbf{q}}{\left(\frac{\partial f}{\partial \mathbf{Q}}\right)^T D\frac{\partial g}{\partial \mathbf{Q}} + H}. \tag{3.10}$$

Die plastische Potentialfunktion $g(\mathbf{Q})$ ist nach (Mestat, Bourgeois & Reiffsteck 2002) definiert zu

$$g(\mathbf{Q}, \rho_g) = \lambda^2\bar{H}^2 + \chi^2\bar{M}^2 - \bar{V}^2\left[1 - \frac{\bar{V}}{\rho_g}\right]^{2\beta} = 0. \tag{3.11}$$

Durch Substitution der Gl.3.10 in Gl.3.2 ergibt sich die komplette Beschreibung der inkrementelle Last

$$\delta\mathbf{Q} = D\delta\mathbf{q} - \frac{D\frac{\partial g}{\partial \mathbf{Q}}\frac{\partial f}{\partial \mathbf{Q}}D}{\frac{\partial f}{\partial \mathbf{Q}}D\frac{\partial g}{\partial \mathbf{Q}} + H}\delta\mathbf{q} = D^{ep}\delta\mathbf{p} \tag{3.12}$$

bzw. aus Gl.3.9 und Gl.3.4 das plastische Verformungsinkrement in Abhängigkeit von der Verfestigungsfunktion H

$$\delta\mathbf{q}^p = -\frac{\left(\frac{\partial f}{\partial \mathbf{Q}}\right)^T \frac{\partial g}{\partial \mathbf{Q}}\delta\mathbf{Q}}{\underbrace{\frac{\partial f}{\partial \rho_c}\left(\frac{\partial \rho_c}{\partial \mathbf{q}^p}\right)^T \frac{\partial g}{\partial \mathbf{Q}}}_{H}} \tag{3.13}$$

als isotropes, verfestigendes, konstitutives Einflächenmodell, siehe Abbildung 3.2 und (Wuttke, Kafle, Lins & Schanz 2012).

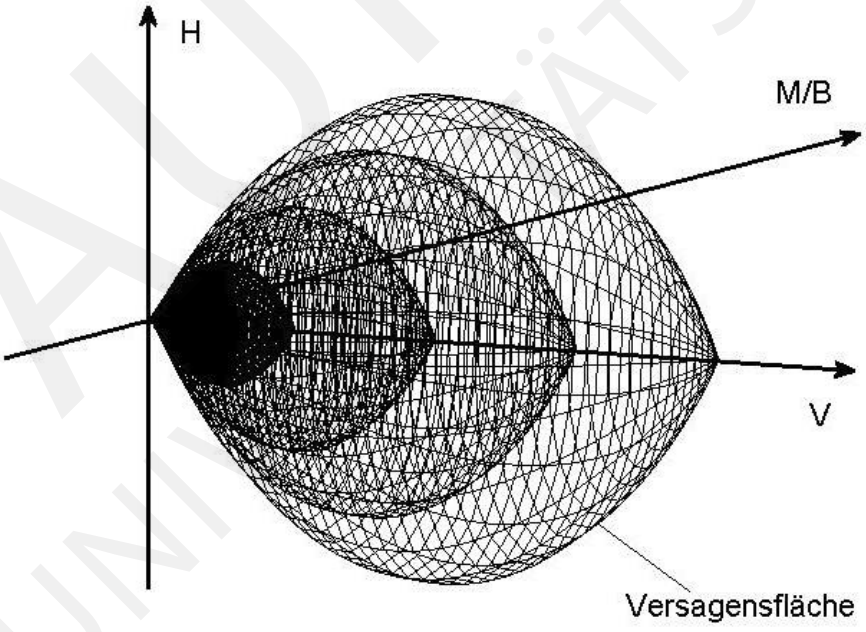

Abbildung 3.2: Darstellung der isotropen Verfestigung bis zur Versagensfläche des Modells, nach (Wuttke, Kafle, Lins & Schanz 2012).

Treten für die vorhandenen Last-Deformationskurven nun geringfügige elastische Deformation auf, so kann anstelle der Beschreibung der kompletten inkrementelle

Last nach Gl. 3.12 das elastische Inkrement vernachlässigt werden. Oft wird auf diese Weise gegeben Ableitungen auf die Beschreibung der plastischen Verformungen reduziert. Beide Sachverhalte treffen das tatsächliche Bodenverhalten nicht zu, der Boden ist weder rein elastisch noch reicht die alleinige plastische Nachweisführung aus. Das small-strain Bodenverhalten, welches gerade in den kleinen Dehnungsbereichen maßgeblich wird, ist in beiden Beschreibungen nicht gegeben. In Kapitel 3.4 wird die Implementierung dieses Verhaltens in das hier definierte Bodenmodell dargelegt, um diese Lücke zu schließen.

3.3 Makroelement einer statisch belasteten Flachgründung auf mehrphasigen, ungesättigten Boden

Zur Erweiterung der Ansätze für die Definition eines Makroelements von einem Flachfundament, ruhend auf einem ungesättigten Boden, werden die Definitionen und Ableitungen eines Ein-Phasen-Modells aufgegriffen. Für die Erstellung des Modells wurden eine Vielzahl von experimentellen Versuchen durchgeführt, um die Abhängigkeiten der Variablen von der Mehrphasigkeit zu bestimmen. Während der experimentellen Versuche erfolgte neben der Aufzeichnung der Last-Verformungs-Funktionen die Registrierung der vorhandenen Saugspannungen $\psi = (u_a - u_w)$ im Modellboden, wobei u_a und u_w die anstehenden Luft- bzw. die Wasserdrücke beschreiben.

Die Schwierigkeit bei den durchgeführten 1g-Versuchen besteht in der Kontrolle bzw. Aufzeichnung der Saugspannung über die Tiefe des Bodens. Im Gegensatz zu saugspannungskontrollierten Elementversuchen in geschlossen Laborzellen ist der 1g-Versuch nach oben offen und mit dem Umgebungsluftdruck, $u_a = 100kPa$, in Verbindung. Die über die Tiefe veränderliche Saugspannung wird durch die Höhe des Grundwasserspiegels eingestellt. Dieses kann vereinfacht als Verlängerung der hydrostatischen Abnahmefunktion nach $(u_a - u_w) = \rho_w g h_c$, (Fredlund & Rahardjo 1993) erfolgen, wobei h_c die Kapillarhöhe ist, welche von Porenradius der Bodenstruktur abhängig ist $h_c = \frac{2T_s}{\rho_w g r}$, mit T_s als der Oberflächenspannung des Wassers ($T_s = 72.75\, mN/m\ bei\ 20°C$), ρ_w der Dichte des Wassers, g der Erdbeschleunigung und r als dem Kapillarradius. Der tatsächliche Verlauf der Saugspannungen unter dem Fundament ist wesentlich komplexer, hängen von dem umgebenen Klima, baulichen Details und vom Last-Verformungs-Verlauf ab. Es können lokale Zonen der Saugspannungserhöhung aber auch der Abnahme über die Tiefe vorhanden sein, welche durch den Verdichtungs- und Auflockerungsvorgang während der Belastung bis zum Bruch verstärkt bzw. induziert werden. Somit muss die getätigte Annahme

als gemittelter Wert gesehen werden, welcher in der Prognoserechnung genutzt wird.

Die Saugspannung nimmt dabei von der Oberfläche bis zum anstehenden Wasserspiegel hin ab und ist an diesem Null. Diese Vorgehensweise entspricht der vorhandenen Situation natürlicher Böden, welche immer mehr oder weniger ungesättigt sind. Nachteilig bei dieser Vorgehensweise ist der Sachverhalt, dass die vorhandene tiefenabhängige und -veränderliche Saugspannung eine Definition der konstitutiven Gleichungen nach Saug- oder Matrixspannung erschwert. Die Veränderung der hydraulischen Zustände während des Versuches, von kleinen Deformationen bis hin zum Grundbruch, unter dem Modellfundament können nur schlecht oder überhaupt nicht erfasst und in das Modell überführt werden. Stattdessen wird eine äquivalente Tiefe angesetzt, hier von der $1,5$-fachen Tiefe der Fundamentbreite, zu welcher die Saugspanungen punktuell erfasst werden. Sinnvoller ist eine Überführung der konstitutiven Abhängigkeiten in den anstehenden Wasserspiegel, welcher für die Ausbildung der Saugspannungen verantwortlich ist. Über die Tiefe, die Permeabilität und die vorhandene hydraulischen Beziehungen der Saugspannungs-Sättigungskurve können die vorhandenen Saugspannungen über die Tiefe bestimmt werden. Da die Veränderung der hydraulischen Bedingungen direkt unter dem Fundament Bestandteil des aufgezeichneten Last-Deformationsverhaltens für den jeweilig anstehenden Bodentyp und Grundwasserstand sind, ergibt sich das sättigungsabhängige Last-Verformungsverhalten aus diesen Informationen, siehe Abbildung 3.3.

Die Untersuchung des Grundbruchverhaltens in Abhängigkeit vom ungesättigten Verhalten des Bodens wurde bereits durch (Vanapalli & Mohamed 2007) studiert. Die Auswirkungen auf die Grundbruchlast waren eindeutig. In Abhängigkeit vom Sättigungsgrad war die Grundbruchlast deutlich höher als im trockenen oder gesättigten Zustand. Die Beschreibung dieser Abhängigkeit vom Sättigungsgrad bzw. der vorhandenen Saugspannung erwies sich als nicht einfach zu implementieren. Zum Einen erfolgte die Implementation in das übliche Effektivwert-Spannungskonzept mit der Matrixspannung $(u_a - u_w)$ und Nettospannung $(\sigma_n - u_a)$, wonach die Mohr-Coulomb-Bedingung zur Beschreibung der Scherfestigkeit (Fredlund, Morgenstern & Widger 1978) definiert zu

$$\tau_f = c^{'} + (\sigma_n - u_a)\, tan\varphi^{'} + (u_a - u_w)\, tan\varphi^{b}, \tag{3.14}$$

und zum anderen erfolgte die Implementierung direkt in die Gleichungen der Grundbruchlast nach (Vanapalli & Mohamed 2007)

$$\begin{aligned} q_u = \left[c^{'} + (u_a - u_w)_b \left(1 - s^{\psi}\right) tan\varphi^{'} + (u_a - u_w)_{avr}\, s^{\psi} tan\varphi^{'}\right] N_c S_s i_c d_c + \\ q N_q S_q i_q d_q + \frac{1}{2}\gamma_1 B N_{\gamma_S} \gamma_i \gamma_d \gamma, \end{aligned} \tag{3.15}$$

mit S als Sättigung, $(u_a - u_w)_b$ als Matrixspannung zum Lufteintrittspunkt, $(u_a - u_w)_{avr}$ als durchschnittliche Saugspannung über $1.5B$ und ψ als empirischer Parameter abhängig von dem Plastizitätsindex I_p.

Der Berechnungsansatz liefert ausschließlich Bruchspannungen, welche allerdings im höheren Saugspannungsbereich, nach dem residualen Sättigungs- bzw. Saugspannungswert, einen falschen Trend der Bruchwerte durch weiter ansteigende Bruchwerte mit zunehmender Sättigung liefert. Experimentelle Untersuchungen zum Grundbruchverhalten zeigen, dass die Werte a) nach dem Erreichen der der Bruchlast absinken und b) ebenso mit zunehmender Saugspannung wieder absinken, wenn die Saugspannungen den residualen Wert überschreiten, Abbildung 3.3 bzw. nach (Wuttke, Kafle, Lins & Schanz 2012) und (Schanz, Lins & Vanapalli 2011).

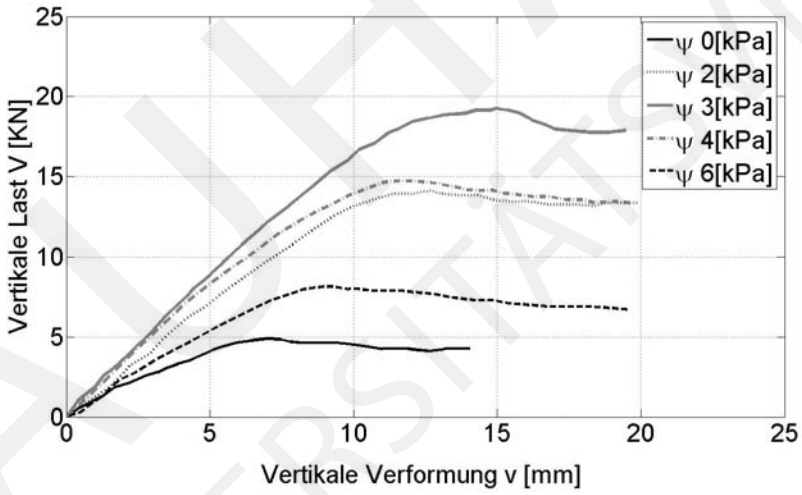

Abbildung 3.3: Darstellung der Abhängigkeit der experimentellen Last-Verformungskurve von der Teilsättigung im Bodeneinflussbereich, nach (Wuttke, Kafle, Lins & Schanz 2012).

Durch die Nutzung von Makroelementen kann sowohl der Bruchwert als auch der Last-Verformungsverlauf bis zur Bruchspannung abgebildet werden. Mit dieser Kenntnis und der Notwendigkeit der Verbesserung der Last-Verformungsbeschreibung einschließlich der Grundbruchlastabbildung für ungesättigte Böden wurde das statische Modell des Makroelements entsprechend erweitert.

Ausgehend von dieser Zielstellung wurden die Abhängigkeit der vertikalen Bruchlast und Last-Verformungsverhalten von der gemittelten Saugspannung über die Tiefe der 1.5-fachen Fundamentbreite bestimmt und in die obigen Gleichungen des statischen Makroelement des Ein-Phasen-Materials implementiert, (Wuttke, Kafle, Lins &

Schanz 2012). Das Versagenskriterium mit den normierten Belastungen lautet damit

$$\begin{aligned} f(\mathbf{Q},\psi) &= \left[\tfrac{H}{\mu V_m(\psi)}\right]^2 + \left[\tfrac{M}{V_m(\psi)\psi_m(\psi)B}\right]^2 - \left[\tfrac{V}{V_m(\psi)}\right]^2 \left[1-\tfrac{V}{V_m(\psi)}\right]^{2\beta(\psi)} = 0 \\ &= \left[\bar{H}(\psi)\right]^2 + \left[\bar{M}(\psi)\right]^2 - \left[\bar{V}(\psi)\right]^2 \left[1-\bar{V}(\psi)\right]^{1\beta(\psi)} = 0, \end{aligned} \tag{3.16}$$

wobei $h(\psi)$ die sättigungsabhängige, maximale, normierte Horizontallast, $m(\psi)$ das sättigungsabhängige, maximale, normierte Moment, $\xi(\psi)$ die sättigungsabhängige, maximale, normierte Vertikallast und $\beta(\psi)$ der Steuerparameter für die Form der dreidimensionalen Versagensfläche darstellt, siehe Abbildung 3.4. Die sättigungs- bzw. saugspannungsabhängige Fließfläche ergibt sich damit zu

$$f(Q,\rho_c,\psi) = \left[\bar{H}(\psi)\right]^2 + \left[\bar{M}(\psi)\right]^2 - \left[\bar{V}(\psi)\right]^2 \left[1-\frac{\bar{V}(\psi)}{\rho_c}\right]^{2\beta(\psi)} = 0, \tag{3.17}$$

das plastische Potential abhängig von der Saugspannung

$$g(Q,\rho_g,\psi) = \left[\lambda\bar{H}(\psi)\right]^2 + \left[\chi(\psi)\bar{M}(\psi)\right]^2 - \left[\bar{V}(\psi)\right]^2 \left[1-\frac{\bar{V}(\psi)}{\rho_g}\right]^{2\beta(\psi)} = 0, \tag{3.18}$$

und die Verfestigungsfunktion zu

$$\rho_c(\psi) = 1 - exp\left(-\frac{R_0(\psi)\sqrt{v^2 + (\alpha_h u) + (\gamma_h(\psi) B\theta_m.)^2}}{V_m(\psi)}\right). \tag{3.19}$$

Somit kann das saugspannungsabhängige plastische Verformungsinkrement analog den vorhergehenden Ableitung für ein einphasiges Material definiert werden zu

$$d\boldsymbol{q}^p(\psi) = -\frac{\left(\frac{\partial \boldsymbol{f}(\psi)}{\partial \boldsymbol{Q}(\psi)}\right)^T \frac{\partial \boldsymbol{g}(\psi)}{\partial \boldsymbol{Q}(\psi)} d\boldsymbol{Q}(\psi)}{\left[\frac{\partial f(\psi)}{\partial \rho_c}\right]\left[\frac{\partial \rho_c(\psi)}{\partial|\boldsymbol{q}(\psi)|}\right]^T \left[\frac{\partial g(\psi)}{\partial \boldsymbol{Q}(\psi)}\right]}. \tag{3.20}$$

Das elasto-plastische Last-Verformungs-Verhalten ist damit in Abhängigkeit von den Saugspannungen bis zum Versagen des Bodens beschrieben, (Wuttke, Kafle, Lins & Schanz 2012). Für die Abbildung des korrekten Verformungsverhaltens ist der anfängliche Anstieg der Verformung R_0 ein wesentlicher Parameter und wird ebenfalls durch die Sättigung beeinflusst, mit $R_0(\psi) = R_{sat}\left(1+\alpha\psi^b S^c\right)$ als empirische Gleichung. Ein Ergebnis der Analysen war, dass die Vertikalkraft und das Moment sättigungsabhängig sind, während die Horizontallast für den hier analysierten Fall der nicht eingebettete Fundamente weitgehend unabhängig vom Sättigungsverhalten abgebildet werden kann.

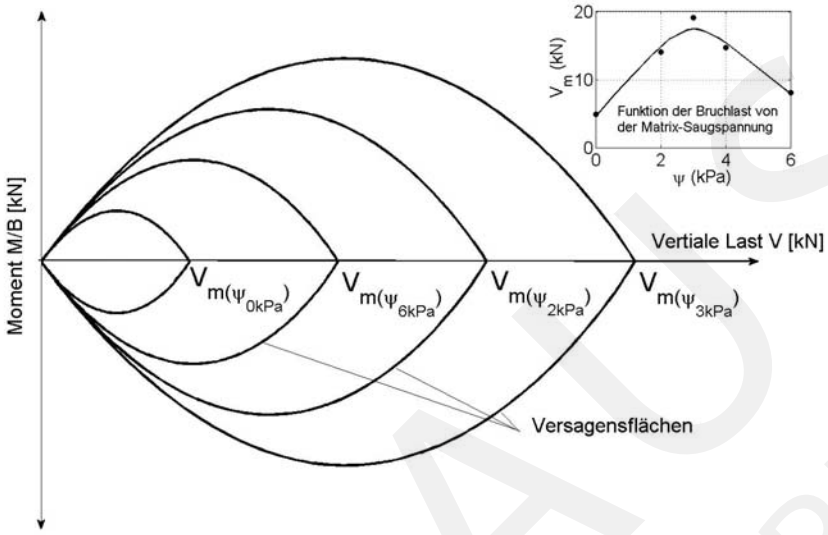

Abbildung 3.4: Darstellung der Abhängigkeit der Versagensfläche von der Teilsättigung im Bodeneinflussbereich, nach (Wuttke, Kafle, Lins & Schanz 2012).

Eine weitere wesentliche Tatsache hinsichtlich der aufnehmbaren Grundbuchlast nach Abbildung 3.3 bzw. nach (Wuttke, Kafle, Lins & Schanz 2012) ist, dass das Maximum der Bruchlast kurz vor der residualen Saugspannung erreicht wird. Danach fällt die Bruchlast wieder ab, wobei der trockene Boden eine geringfügig höhere Bruchlast als der gesättigte Boden aufweist. Dieses Verhalten übertragen auf eine Bemessung bedeuten, dass im Fall einer Bemessung gegen Versagen immer ein trockener oder gesättigter Zustand angesetzt werden muss, um den veränderlichen Zustand einer Teilsättigung im Boden während des Bauzustandes auszuschließen. Im Falle einer Deformationsprognose muss sehr wohl der Sättigungszustand des Boden berücksichtigt werden, um die deutlich unterschiedlichen Verformungsbeträge bei gleicher Belastung und unterschiedlicher Sättigung nachvollziehen zu können.

Der Parameter R_0 wurde in (Wuttke, Kafle, Lins & Schanz 2012), hinsichtlich der vorhandenen Saugspannungsabhängigkeit quantifiziert und beschrieben. Die Ermittlung zu R_0-Werten zu sehr kleinen Verformungen erfordern sehr genaue Verformungsmessungen im Bereich von 10^{-5} oder kleiner, welche derzeit technisch nur schwierig realisierbar sind. Für eine Kontrolle von R_0 ist es günstiger die Analogie zum Steifigkeitsverhalten im sehr kleinen Dehnungsbereich, E_0, G_0 zu nutzen. Mit der möglichen Überführung einer seismisch ermittelten Steifigkeit E_{S0} bzw. G_0 in einem ungesättigten Boden, definiert in Kapitel 2.5.3, in eine anfängliche Steifigkeit, ist es möglich das Verfestigungsverhalten der Last-Verformungs-Funktion in allen Punkten eindeutig und funktional abhängig vom Saugpannungswert zu definieren.

3.4 Makroelement einer statisch belasteten Flachgründung auf einphasigen Boden und sehr kleinem Verformungsbereich

Ausgehend von dem Ziel der Verbesserung der Prognosegenauigkeit ist das Einbeziehen des Dehnungsverhaltens im kleinen Dehnungsbereich wesentlich. Theoretische Überlegungen (Atkinson 2000, Burland 1989), experimentelle Ergebnisse und numerische Studien (Benz 2007) haben diese Effekte untermauert. In statischen Lastfällen wird die absolute Deformationsamplitude des Halbraums korrekt abgebildet und im Fall von zyklischen Belastungen ermöglicht dieses Verhalten eine korrekte Setzungsakkumulation in dem Deformationsbereich. Aus diesen Gründen ist es notwendig die bisherigen Makroelementmodelle hinsichtlich eines small-strain-Verhaltens zu erweitern. Übliche elasto-plastische verfestigende Modellgesetze nehmen in dem Bereich der kleinen Dehnungen entweder ein elastisches Verhalten an oder sie bilden den Bereich erst überhaupt nicht ab, da Steifigkeiten mit konventionellen Laboruntersuchungen erst ab einem Dehnungsniveau von 10^{-3} ermittelbar sind. Unter Beachtung eines umgebenden Halbraum, der sich dadurch stark vergrößernden Spannungsfläche bzw. verringernden Deformationen mit zunehmender Entfernung, nehmen die Steifigkeiten infolge der Deformationsabhängigkeit deutlich zu und erreichen schnell den small-strain Regionen, wodurch Prognoserechnungen ohne diese Berücksichtigung falsche Werte liefern.

Einige wenige Stoffmodelle, wie die 'Continuous Hyperplastic'-Beschreibung (Houlsby & Puzrin 2006), das Small-Strain Hardening Soil (Benz 2007) oder (Elhakim 2005), berücksichtigen dieses Bodenverhalten. Grundsätzlich bestehen Erkenntnisse über das small-strain Bodenverhalten seit vielen Jahren für das statische und dynamische Verhalten von Böden (Jardine, Potts, Fourie & Burland 1986), (Prevost & Keane 1990), (Fahey & Carter 1993), (Puzrin & Burland 1996), (Atkinson 2000). Allerdings ist die mathematischen Abbildung hinsichtlich der Stoffmodellierungen unterschiedlich, die small-strain Beschreibung basiert auf der hyperbolischen Beschreibung der Steifigkeitsreduktion mit zunehmender Dehnung, die elasto-plastische verfestigende Beschreibung basiert auf der iterativen Beschreibung der bodenabhängigen Spannungs-Dehnungsfunktion durch eine inkrementellen Bestimmung der Dehnungen oder Spannungen.

Einen interessanten Ansatz bietet Niemunis (Niemunis, Prada-Sarmiento & Grandas-Tavera 2011) in der Kopplung eines paraelastischen Ansatzes von (Hueckel & Nova 1979) zu einer hybriden Stoffmodellierung für zyklische Belastungssimulationen. In dieser Formulierung wird für die Spannungs-Dehnungs-Funktion im small-strain Bereich $10^{-7}...10^{-4}$ eine Abhängigkeit von der hyperbolischen Steifigkeitsfunktion, hier

als empirische Funktion $H = E\,(1 - f d^{\chi})$ genutzt. Die Parameter f und χ wurden aus Versuchen bestimmt. Das Spannungsinkrement ergibt sich aus der Kopplung des genutzten hypoplastischen Stoffmodell für große Dehnungen und der paraelastischen Beschreibung für sehr kleine Dehnungen. Die Ansätze sind in (Hueckel & Nova 1979) definiert, wonach die paraelastische Dehnung ϵ_{pe} in diesem Dehnungsbereich die Summe aus den elastischen Dehnungen ϵ_e und den mikroplastischen Dehnungen ϵ_{mp} darstellt, $\epsilon_{pe} = \epsilon_e + \epsilon_{mp}$.

Angewendet auf die obigen Gleichungen in Abschnitt 4.1.1 und 4.1.2 bedeutet dies, dass die Last-Verformungs-Funktionen in gekoppelte Abhängigkeit zu dem hysteretischen Verhalten der Steifigkeitsfunktion im kleinen Dehnungsbereich gebracht werden, siehe Abbildung 3.5. Nach (Houlsby & Puzrin 2006) gilt für die Fließflächen im small-strain Bereich die assozierte Fließregel.

Mit dieser Aussage und der Wichtungskopplung von (Niemunis et al. 2011) kann die plastische Verformung des Makroelements definiert werden zu

$$d\boldsymbol{q}_p = (1 - w)\left(\Lambda \frac{\partial g}{\partial \boldsymbol{Q}}\right)^{a} + w\left(\Lambda \frac{\partial g}{\partial \boldsymbol{Q}}\right)^{na}, \tag{3.21}$$

wobei die Indizes a und na die assoziierte und nicht-assoziierte Fließregeln kennzeichnen.

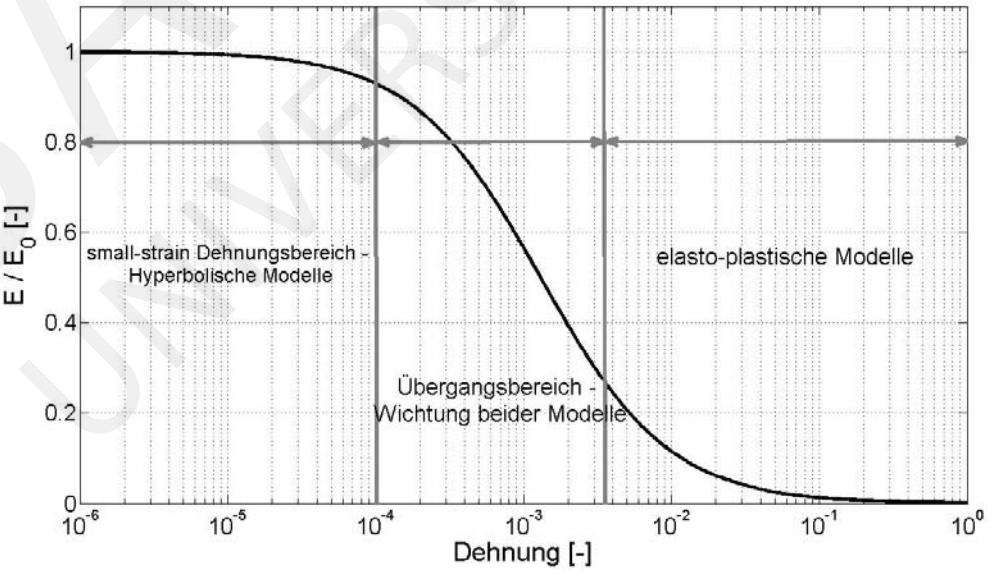

Abbildung 3.5: Abbildung der Steifigkeitsdegradation und der konstitutiven Simulationsbereiche, nach (Wuttke & Kafle 2013)

Das erste Produkt von plastischem Multiplikator und plastischem Potential wird für den Bereich bis max. 10^{-4} angesetzt, danach erfolgt ein Übergangsbereich mit einer Wichtung beider Terme, siehe Abbildung 3.6,

$$w = \left(\frac{\epsilon - d_0}{d_L - d_0}\right)^{\beta} = \left(\frac{v - d_0}{d_L - d_0}\right)^{\beta} \tag{3.22}$$

mit $d_L = 0.005$, $d_0 = 10^{-4}$ β zwischen 0.25 ... 2.5, entsprechend (Niemunis et al. 2011). Im Wesentlichen beeinflusst die hyberbolische Beschreibung den Verlauf der Verfestigungsfunktion ρ_c innerhalb der konstitutiven Stoffmodellierung. Das bedeutet, dass unter dem Ansatz der assoziierten Fließregel das plastische Potential unabhängig von der Verfestigungsfunktion ρ_c ist und ausschließlich der plastische Multiplikator nach Gl. 3.10 von ρ_c abhängig ist.

Wird für Beschreibung der hyberbolischen Reduktionsfunktion vereinfachend eine semi-empirische Darstellung genutzt (Bai 2011)

$$E = E_{max} \frac{1}{a + b\epsilon^m}, \tag{3.23}$$

mit $\epsilon = \delta v / v$ und $a,\ b,\ m$ als Versuchskennwerte und v als Verformungsbetrag, so kann die Verfestigungsfunktion ρ_c in Abhängigkeit von der hyperbolischen Funktion definiert werden.

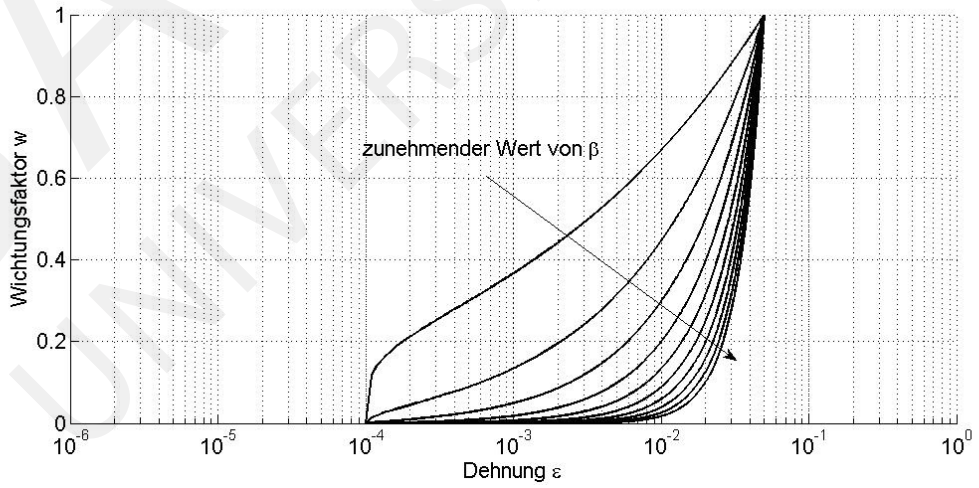

Abbildung 3.6: Darstellung des Verlaufs der Wichtungsfaktoren nach (Niemunis et al. 2011)

Ausgehend von der eindimensionalen Beschreibung der Verfestigungsfunktion nach

(Nova & Montrasio 1991)

$$\frac{V}{V_m} = 1 - exp\left\{ - \underbrace{R_0}_{konstant} \cdot \underbrace{\frac{v}{V_m}}_{iterativ} \right\}, \tag{3.24}$$

wird die Gl.3.23 für die hyberbolische Beschreibung anstelle der negativen Exponentialfunktion genutzt. Zu vermerken ist, dass die Verfestigungsfunktion von dem Verformungsinkrement und der Exponentialfunktion gesteuert wird, die Anstiegsfunktion R_0, also die Steifigkeit bleibt konstant. Für die Skalierung und Steuerung der eindimensionale Verfestigungsfunktion mit hyberbolischer Beschreibung wird ein anderer Ansatz genutzt. Bei diesem Ansatz wird als Steuerungsparameter die normierte, hyperbolische Funktion der deformationsabhängigen Steifigkeit genutzt, die Verschiebung wird als ein konstanter Wert der Magnitude angesetzt, damit ist die Verfestigungsfunktion definiert ist zu

$$\left(\frac{V}{V_b}\right) = 1 - -\frac{E(v)v_r}{V_b} = 1 - \underbrace{\frac{E_{max}}{a + b\epsilon(\delta v)^m}}_{iterativ} \cdot \underbrace{\frac{v_r}{V_b}}_{konstant} . \tag{3.25}$$

Anstelle der vorherigen Versagensgröße V_m wird nun der Kontrollwert V_b als „virtuelle“ Versagensgröße zu den jeweilig definierten virtuellen Bereiche innerhalb der Reduktionskurve eingeführt, Abbildung 3.5. Die Werte V_b entsprechen zugehörigen Deformationen innerhalb der Reduktionskurve, wodurch jeder Teilbereich numerisch eindeutig eine eigene Versagensfläche zugewiesen bekommt und die darin gültigen Verfestigungsregeln kontrolliert werden können, siehe Abbildung 3.7.

Die Parameter v_r und V_b, als Peak-wert der jeweiligen „virtuellen“ Versagensfläche, ergeben sich aus der jeweiligen Reduktionskurve zu den Umkehrpunkten des Anstiegs in der Kurve. dadurch können in Abhängigkeit der jeweilig experimentell ermittelten Kurve die Parameter a, b und m bestimmt werden und unterschiedliche Reduktionskurven eingebunden werden. Erweitert auf die dreidimensionale Schreibweise ergibt sich die Verfestigungsfunktion zu

$$\rho_c = 1 - \frac{v_r}{V_b} \cdot \frac{E_{max}}{a + b\left(\frac{1}{V_b}\sqrt{\bar{v}^2 + \bar{u}^2 + \bar{\theta}}\right)^m}. \tag{3.26}$$

Für die Bestimmung des plastischen Multiplikators können die entsprechenden partiellen Ableitungen der Verfestigungsfunktion Gl.3.4 nach den Verschiebungsgrößen, $\frac{\partial \rho_c}{\partial \bar{v}}$, $\frac{\partial \rho_c}{\partial \bar{u}}$ bzw. $\frac{\partial \rho_c}{\partial \bar{\theta}}$, bestimmt werden. Damit ist der Übergang zwischen der hyperbolischen und der elasto-plastischen Last-Verformungs-Beschreibung definiert (Wuttke & Kafle 2013).

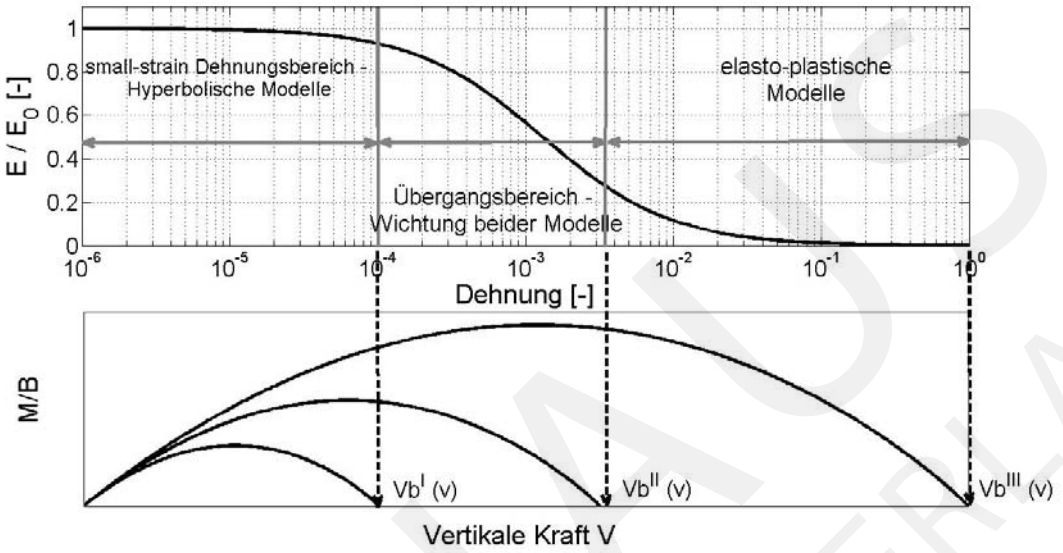

Abbildung 3.7: Darstellung des definierten Bereiche für die Verfestigungsfunktion in Abhängigkeit von den Dehnungsbereichen der hyberbolischen Reduktionskurve, nach (Wuttke & Kafle 2013).

3.5 Modellierung der Verformungsakkumulation eines zyklisch belasteten Flachfundaments auf einphasigen Boden

Für die zyklische Belastung eines Makroelements wird in der Beschreibung für einphasige Böden der Notation von (di Prisco, Nova & Sibilia 2002) gefolgt. Dabei ist die elasto-plastische Beschreibung durch ein 'Bounding Surface' Modell mit einem beweglichen, elastischen Bereich als ein Kegel mit Kappe innerhalb der plastischen 'Bounding Surface' definiert, siehe Abbildung 3.8. Die Versagensfläche ist analog dem statischen Fall mit $f(\mathbf{Q}) = \left[\bar{H}\right]^2 + \left[\bar{M}\right]^2 - \left[\bar{V}\right]^2 \left[1 - \bar{V}\right]^{2\beta} = 0$ gegeben. Ausgehend von den normierten Last- und Verformungsvektoren

$$\mathbf{Q} = \left\{ \begin{array}{c} \bar{v} \\ \bar{H} \\ \bar{M} \end{array} \right\} = \frac{1}{V_m} \left\{ \begin{array}{c} V \\ H\ \mu \\ M\ \psi_m B \end{array} \right\}, \qquad \mathbf{q} = \left\{ \begin{array}{c} \bar{v} \\ \bar{u} \\ \bar{\theta} \end{array} \right\} = V_m \left\{ \begin{array}{c} v \\ \mu u \\ \psi \theta_m B \end{array} \right\}$$

und deren Kopplung durch die Nachgiebigkeitsmatrix C, $d\mathbf{q} = Cd\mathbf{Q}$ ist das plastische Potential analog dem statischen Fall definiert. Entsprechend (di Prisco et al. 2002), sind die verallgemeinerten plastischen Dehnungen unter Berücksichtigung einer zu-

sätzlichen Memory-Matrix $\boldsymbol{\phi}_c$ definiert zu

$$d\mathbf{q}^p = \Lambda\left(\mathbf{Q}_I\right)\boldsymbol{\phi}_c\left(\delta,\rho_k\right)\frac{\partial g}{\partial \mathbf{Q}}Q_I. \tag{3.27}$$

Dementsprechend erfolgt analog zur statischen Beschreibung die Fließbedingung $f\left(\mathbf{Q},\rho_c\right) = \bar{H}^2 + \bar{M}^2 - \bar{V}^2\left[1-\frac{\bar{V}}{\rho_c}\right]^{2\beta} = 0$ und die plastische Potentialfunktion $g\left(\mathbf{Q},\rho_g\right) = \lambda^2\bar{H}^2 + \chi^2\bar{M}^2 - \bar{V}^2\left[1-\frac{\bar{V}}{\rho_g}\right]^{2\beta} = 0$. Die zyklische Lastfunktion $\boldsymbol{\phi}_c\left(\delta,\rho_k\right)$ für trockene Materialien ist

$$\phi_{c,ii} = exp^{-\left[\zeta\sqrt{\frac{\delta\rho_c}{\xi}}+\kappa_i\rho_k\right]} \tag{3.28}$$

mit $\boldsymbol{\phi}_{c,ii} =$

$$\begin{bmatrix} exp\left\{-\left[\zeta_{\bar{v}}\sqrt{\frac{\delta\rho_c}{\xi}}+\kappa_{\bar{v}}\rho_k\right]\right\} & 0 & 0 \\ 0 & exp\left\{-\left[\zeta_{\bar{u}}\sqrt{\frac{\delta\rho_c}{\xi}}+\kappa_{\bar{u}}\rho_k\right]\right\} & 0 \\ 0 & 0 & exp\left\{-\left[\zeta_{\bar{\theta}}\sqrt{\frac{\delta\rho_c}{\xi}}+\kappa_{\bar{\theta}}\rho_k\right]\right\} \end{bmatrix}$$

und die Verfestigungsfunktion in der zyklischen Lastfunktion definiert ist zu:

$$d\rho_k = \left(1-\rho_k\right)\frac{R_0}{V_m^2}\left[du + \alpha\frac{d\left|v\right|}{\mu} + \gamma\frac{d\left|\theta\right|}{\psi_M}\right]. \tag{3.29}$$

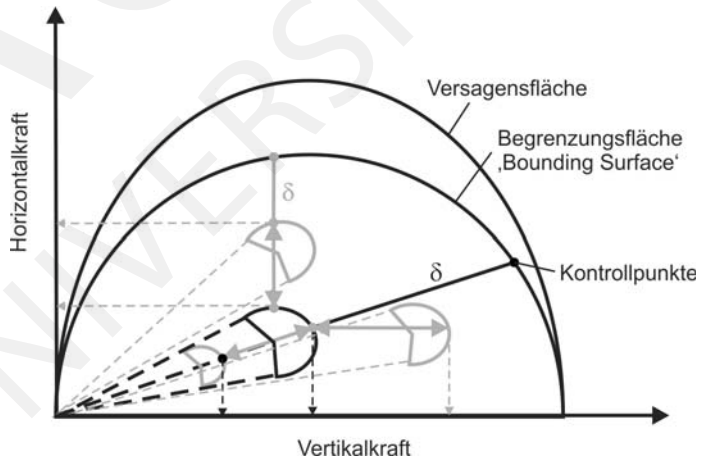

Abbildung 3.8: Abbildung der Bewegung der elastischen „Blase“ innerhalb der Bounding- und Versagensflächen des zyklischen Systemmodells, nach (Kafle & Wuttke 2013) bzw. (di Prisco et al. 2002).

In der Anwendung des Modells in Simulationen ist die Akkumulation der Verformung mit zunehmenden Zyklenzahlen deutlich sichtbar, siehe Abbildung 3.9. Erste Anwendungen an einem praktischen Beispiel erfolgte in (Wuttke, Schmidt, Zabel,

Kafle & Stade 2011). Weiterführende Betrachtungen hinsichtlich der numerischen Simulation einer zyklischen Modellierung in Abhängigkeit von den Saugspannungen ψ im ungesättigten Boden wurden in (Kafle & Wuttke 2013), (Kafle, Wuttke, Sextos, Faraonis & Kilanitis 2013) durchgeführt.

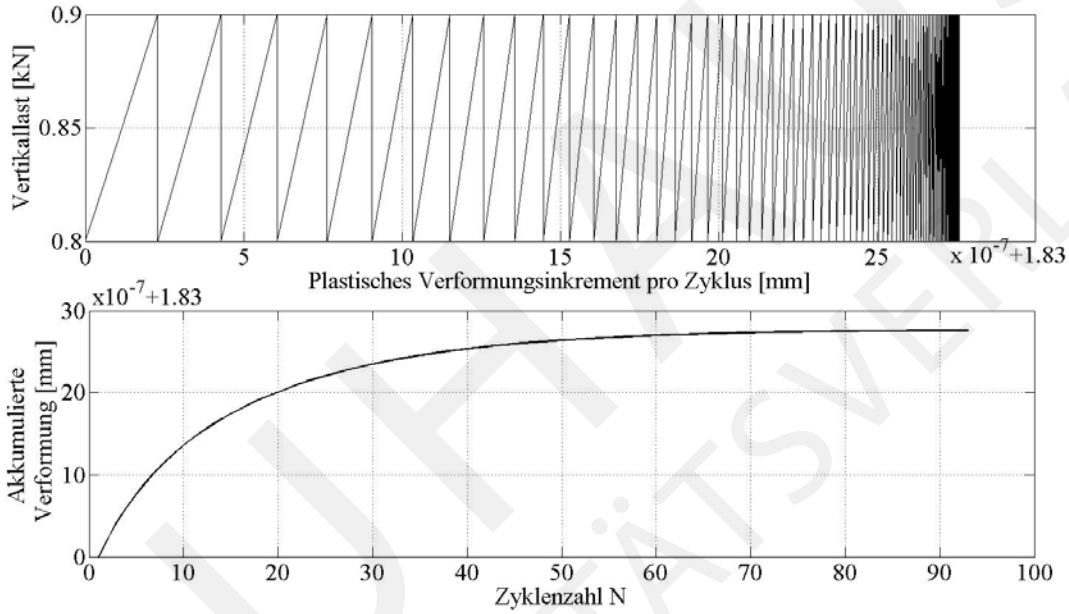

Abbildung 3.9: Simulation der Verformungsakkumulation über die Anzahl der Zyklen, nach (Kafle & Wuttke 2013)

3.6 Zusammenfassung

In dem Kapitel 3 erfolgte die Beschreibung und Weiterentwicklung von existierenden Makroelementmodellen. Dazu wurden die bestehenden Theorie aufgegriffen und mit den Randbedingungen für ungesättigte Böden sowie das small-strain Bodenverhalten erweitert. Für die Umsetzung und Implementierung dieser Randbedingungen wurden Versuchsmethoden und Ergebnisse aus dem Kapitel 1 genutzt. Die so definierten Makroelemente können problemlos in FEM Untersuchungen zur Simulation komplexer Last- und Randbedingungen eingesetzt werden. Insbesondere für Fragestellungen im zyklisch, dynamischen Lastbereich sind Simulationen heutzutage noch schwierig, sehr zeitaufwendig bzw. weisen noch starke numerische Fehler auf. An dieser Stelle können Systemmodellierungen als „Zwischenlösung“ einen sehr nützlichen Beitrag für den Entwurf von Bauwerken mit einer realitätsnahen Prognosemöglichkeit liefern.

3.7 Beigelegte eigene Publikationen zu Kapitel 3

Wuttke, F., Kafle, B., Lins, Y., Schanz, T. (2013), A macro-element for static loaded shallow strip foundation resting on unsaturated soil, *International Journal of Geomechanics*, vol.13, no.5, pp.557-564

Wuttke, F., Schmidt, H.G., Zabel, V., Kafle, B., Stade, I. (2011) Vibration induced building settlement assessement and calculation, *8th International Conference on Structural Dynamics EURODYN*, Leuven, Belgium

Kafle, B., Wuttke, F. (2013) Cyclic Macro-element for shallow footing over unsaturated sand, *1st Pan-American Conference on Unsaturated Soils*, Columbia

Wuttke, F., Kafle, B. (2013) A hybrid small to large strain stiffness macroelement for shallow foundations, *Computer and Geotechnics* (submitted)

Kapitel 4

Modellbildung und Simulation der Wellenausbreitung durch poröse Geomaterialien

4.1 Einleitung und Motivation

Die Modellierung von dynamisch belasteten Gründungs- und Gebäudestrukturen auf komplexen Bodenverhältnissen ist ein bislang noch nicht ausreichend analysiertes und auch modelliertes Fachgebiet. Die dynamische Interaktionen zwischen Boden und Gebäude können dabei aktiv durch Erdbeben oder passiv durch Gebäudeschwingungen angeregt werden. In beiden Fällen spielt der Boden eine maßgebliche Rolle, dabei sind die elasto-plastischen, zyklischen und dynamischen Eigenschaften ein Faktor in der Interaktion, die Wellenausbreitung im Gebäudenah- und Gebäudefernfeld eine weiterer Faktor der Interaktion. Wellen, interagieren durch ihre Zeit- und Ortsabhängigkeit mit nahen und entfernten Bodenstrukturen, bewirken elastische und plastische Deformationen und Verstärken sich durch konstruktive Interferenz. Bei bestimmten Phänomenen spielt ebenfalls die Mikrostruktur eine große Rolle, so beeinflusst die Mehrphasigkeit maßgeblich das Amplifikations- und Dämpfungsverhalten des Untergrundes und vorhandene wassergesättigte, granulare Böden können während des Wellendurchlaufs verflüssigen. Es existieren damit eine Vielzahl von Problemstellungen, welche im Zusammenhang mit einer Wellenausbreitung von hohem wissenschaftlichen und praktischem Interesse sind.

In den nachfolgenden Kapitel wird auf getätigte Forschungsergebnisse eingegangen, welche ein Baustein in einem umfangreicheren und langfristigen Forschungsvorhaben sind. Die Zielstellung ist die Entwicklung eines hybriden Gesamtmodells zur effektiven Analyse von Wellenausbreitungsproblemen unter Berücksichtigung der Einflussfaktoren, wie seismische Quelle, großskaliger Wellenpfad, lokaler komplexer

Nahfeldbereich, zyklisch belasteter und elasto-plastischer Interaktionsbereich inklusive der Gründungsstruktur, wie in Kapitel 3 beschrieben. Diesbezüglich sind auch die mikroskopischen Phänomene der Wellenausbreitung durch ungesättigte Materialien ein wichtiger Forschungsschwerpunkt, welcher nur im Labor unter kontrollierten Bedingungen analysiert werden kann. Die Laboruntersuchungen aus Kapitel 2 liefern dazu einen wichtigen Informationsgewinn und entsprechende Eingangsparameter für die numerische Simulation. Neben den physikalischen Beziehungen hinsichtlich der Wellengeschwindigkeits-Saugspannungsrelation ist die Ermittlung der korrekten Eingangsparameter in die Numerik eine weitere wichtige Information für die numerischen Simulationen.

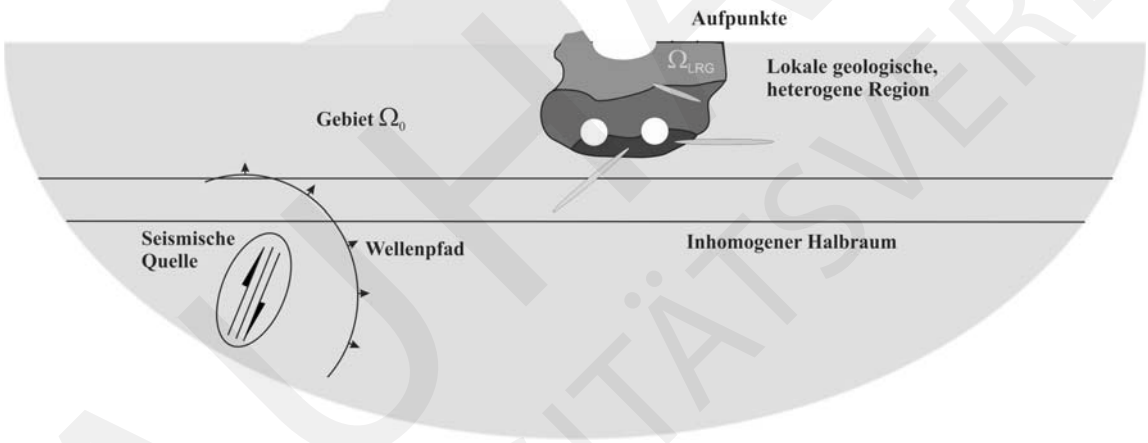

Abbildung 4.1: Darstellung des hybriden Gesamtmodells: seismische Quelle, Wellenpfad, lokale Region.

Um die Wellenausbreitung in unbgrenzten, aber komplexen Gebieten realisieren zu können, wurde eine hybride Modellierung entwickelt. Dabei erfolgt die Simulation des geologisch komplexen Nahbereichs durch die Randintegralgleichungsmethode, welche mit der Wellenausbreitung im Fernfeld durch eine Wellenzahlintegration, inklusive der Einbettung einer seismischen Quelle, gekoppelt wurde, siehe Abbildung 4.1. Das Gesamtmodell beinhaltet folgende wesentliche Randbedingungen: (1) eine laterale Inhomogenität in lokalen, geologischen Bodenstrukturen mit beliebig geschichteten oder gefalteten Bodentypen und topografischen Oberflächenstrukturen und (2) einen geschichteten inhomogenen Halbraum mit der eingebetteten, lokalen geologischen Struktur und der seismischen Quelle. Die Schwerpunkte lagen in der Entwicklung, Validierung und numerische Implementierung einer (a) neuen hybriden, numerischen Randelement-Wellenzahlintegrations-Methode, (b) der Erhöhung der Ergebnisgenauigkeit unter Reduzierung der Berechnungszeit und des Speicherbedarfs gegenüber konventionellen numerischen Methoden und (c) der Fähigkeit, effektiv die

Partialmodelle – seismische Quelle, inhomogener Wellenpfad zwischen Quelle und oberflächennaher urbaner Region und die stark heterogene, komplexe urbane Region – in der numerischen Simulationen zu berücksichtigen.

4.2 Randintegralgleichungsmethode - BIEM und Elastodynamik

Die Randelementemethode als numerisches Verfahren zur Lösung von Feldgleichungen besitzt Vorteile in der Simulation von unbegrenzten Gebieten. Für Wellenausbreitungsprobleme wird diese Fragestellung von entscheidenter Relevanz. Alle Simulationsmodelle müssen die Sommerfeld'sche Abstrahlungsbedingung erfüllen. Numerische Methoden mit Gebietsdiskretisierungen, wie FEM, besitzen an dieser Stelle einen Defizit. Die Randintegralgleichungsmethodik diskretisiert nicht nur den Rand und ist damit um eine Dimension kleiner als die FEM, sie nutzt auch Fundamentallösungen als Wichtungsfunktionen, wodurch die Feldgleichungen exakt erfüllt werden und damit in der Elastodynamik auch die Sommerfeld'schen Abstrahlungsbedingungen. Ausgehend von der Grundgleichung der Elastodynamik

$$\left(\alpha_l^2 - \beta_l^2\right) u_{j,ji}\left(x,z,t\right) + \beta_l^2 u_{j,jj}\left(x,z,t\right) = \ddot{u}_i\left(x,z,t\right) \tag{4.1}$$

wobei die Indizes $(i,j = x,z)$ die partiellen Dimensionsableitungen, u den Verschiebungsvektor und α, β die Kompressions- und Scherwellengeschwindigkeit kennzeichnen, werden die nachfolgenden Ableitungen im frequenztransformierten Abbildungsbereich getätigt. Durch Anwendung der Fouriertransformation ergeben sich die zeitunabhängigen, partiellen Differentialgleichungen - die Helmholtz'schen Gleichungen, welche die Grundlage der nachfolgenden Studien bilden.

$$\begin{aligned}\left(\frac{k_s^2}{k_p^2} - 1\right)\left[u_{z,xz} + u_{x,xx}\right] + \left[u_{x,xx} + u_{x,zz}\right] &= -k_p^2 u_x \\ \left(\frac{k_s^2}{k_p^2} - 1\right)\left[u_{x,xz} + u_{z,zz}\right] + \left[u_{z,xx} + u_{z,zz}\right] &= -k_p^2 u_z\end{aligned} \tag{4.2}$$

Die Wellenzahlen sind durch $k_p = \frac{\omega}{\alpha}$ und $k_s = \frac{\omega}{\beta}$, mit ω als Kreisfrequenz definiert. Die Fundamentallösung, welche die Sommerfeld'sche Abstrahlungsbedingung erfüllt, ergibt sich aus den Helmholtzgleichungen (Rus & Gallego 2005) zu

$$U_{ij}^{*} = \frac{1}{2\pi\mu}\left(\psi\delta_{ij} - \chi r_{,i}r_{,j}\right). \tag{4.3}$$

$$\begin{aligned} P_{ij}^{*} = \frac{1}{2\pi}\Bigg[&\left(\psi_{,r} - \frac{\chi}{r}\right)\left(\frac{\partial r}{\partial n}\delta_{ij} + r_{,j}n_i\right) - 2\frac{\chi}{r}\left(n_j r_{,i} - 2r_{,i}r_{,j}\frac{\partial r}{\partial n}\right) \\ &-2\chi_{,r}r_{,i}r_{,j}\frac{\partial r}{\partial n} + \left(\frac{c_p^2}{c_s^2} - 2\right)\left(\psi_{,r} - \chi_{,r} - \frac{\chi}{r}\right)r_{,i}n_j\Bigg] \end{aligned} \tag{4.4}$$

wobei die Terme ψ und χ folgende Ausdrücke beschreiben

$$\begin{aligned} \psi &= K_0\left(ik_s r\right) + \frac{1}{ik_s r}\left[K_1\left(ik_s r\right) - \frac{c_s}{c_p}K_1\left(ik_p r\right)\right] \\ \chi &= K_2\left(ik_s r\right) - \frac{c_s^2}{c_p^2}K_2\left(ik_p r\right) \end{aligned} \tag{4.5}$$

Der Term δ_{ij} repräsentiert das Konecker-delta, $r_i = x_i - z_i$, $r = \sqrt{x^2 + z^2}$ den Aufpunkt, $r_{,i} = \frac{\partial r}{\partial x_i}$ und $K_n\left(ik_s r\right)$ beschreibt die Besselfunktion der Ordnung n des Argumentes $(ik_s r)$. Ausgehend von der Darstellung des Greenschen Satzes und der Anwendung des Gaußschen Integralsatzes erhält man das bekannte System von Randintegralgleichungen

$$\begin{aligned} &C_{ij}u_i(x,z,\omega) = \\ &\int_{\Omega_m} U_{ij}^{*}(x,z,x_0,z_0,\omega)p_j(x_0,z_0,\omega)d\Gamma - \int_{\Omega_m} P_{ij}^{*}(x,z,x_0,z_0,\omega)u_j(x_0,z_0,\omega)d\Gamma, \end{aligned} \tag{4.6}$$

in welchem die Verschiebungs- und Spannungs-Fundamentallösungen, U_{ij}^{*} und P_{ij}^{*}, vorhanden sind. Nach Umstellen des Integralgleichungssystems nach den gesuchten Verschiebungs- bzw. Spannungsgrößen kann das Gleichungssystem entsprechend der numerischen Algebra gelöst werden. Nach Summation über alle diskrete Knotenpunkte und Umstellen der Gleichung

$$C_{ij}u_i + \sum_{j=1}^{N}\left(\underbrace{\int_{\Omega_m} P_{ij}^{*}d\Gamma}_{\hat{H}}\right)u_j = \sum_{j=1}^{N}\left(\underbrace{\int_{\Omega_m} U_{ij}^{*}d\Gamma}_{\hat{G}}\right)p_j \tag{4.7}$$

erhält ergibt sich ein Matrixgleichungssystem

$$C_{ij}u_i + \sum_{j=1}^{N}\hat{H}_{ij}u_j = \sum_{j=1}^{N}\hat{G}_{ij}p_j, \tag{4.8}$$

welches nach den unbekannten Termen umgestellt und gelöst werden kann.

Durch Übertragung auf die Problemstellung des hybriden Gesamtmodell auf Gl.4.2, muss für die Abbildung des heterogenen komplexen geologischen Bereiches, das komplexe, zerstreute Wellenfeld bestimmt werden $u_i^{sc} = u_i^{total} - u_i^{fr}$, $p_i^{sc} = p_i^{total} - p_i^{fr}$.

$$\begin{aligned} C_{ij} \left(u_j^{total}(x,z) - u_j^{fr}(x,z) \right) \Big|_{\Lambda^{external}} = \\ \int_{\Lambda^{external}} U_{ij}^*(x,z,x_0,z_0,\omega) \left(p_j^{total}(x_0,z_0) - p_j^{fr}(x_0,z_0) \right) d\Gamma - \\ \int_{\Lambda^{external}} P_{ij}^*(x,z,x_0,z_0,\omega) \left(u_j^{total}(x_0,z_0) - u_j^{fr}(x_0,z_0) \right) d\Gamma \end{aligned} \tag{4.9}$$

Die Terme u^{fr}, u^{sc} und u_{total} kennzeichnen dabei die Verschiebungen des Freifeldes, des zerstreuten Wellenfeldes innerhalb des lokalen Bereiches und des totalen Wellenfeldes in dem Anregungsbereich als konstruktive, interagierende Überlagerung aus Freifeld und zerstreuten Wellenfeld.

4.3 Wellenzahlintegration und seismische Quelle

Für die Formulierung des großräumigen geologischen Bereiches von einer seismischen Quelle bis zu einem lokalen, oberflächennahen, das Bauwerk beeinflussenden geologischen Bereich, müssen andere Methoden als die vorher beschriebene Randelementmethodik genutzt werden, da der numerische Aufwand in den gegebenen Skalen für numerische Lösungen, wie FE- und BE-Methode, deutlich zu groß sein würde. In Abhängigkeit von der geologischen Formation kann der Wellenpfad mehrere zehn Kilometer betragen. Eine Möglichkeit der Simulation für diese Skalengröße ist die Wellenzahlintegration, welche der Gruppe der Matrixrekursionsalgorithmen zugerechnet werden kann und auf der Methodik der allgemeinen Reflexions- und Transmissionskoeffizienten basiert (Wuttke 2005), (Chen 1993) und (Luco & Apsel 1983). Neben der Realisierung großer Skalen ohne numerische Instabilität (Chen 2001) kann auch eine seimische Quelle in die Methodik integriert werden, so dass realitätsnahe Simulationen möglich sind (Hisada 1994), Abbildung 4.3. Die Wellenzahlintegration behandelt die Wellenausbreitung durch ein beliebig geschichteten Halbraum, wobei die Sommerfeld'schen Abstrahlungsbedingungen a priori in den Definitionen vorhanden sind.

Ausgehend von der partiellen Differentialgleichung der Elastodynamik einphasiger Medien $\mu \Delta u + (\mu + \lambda) \nabla \nabla u = \rho \ddot{u}$ und der Lösung durch Anwendung des Helmoltz'schen Darstellungssatz, kann die entkoppelte Potentiallösung durch Anwendung einer mehrdimensionalen Integraltransformation nach Raum und Zeit in eine einfache Differentialgleichung überführt und gelöst werden $\left\{ \tilde{f} \right\} = \mathbf{E\Lambda}(z) \{\mathbf{C}\}$,

(Wuttke 2005). Die Matrix $\mathbf{E}$ beinhaltet die Struktur- und Steifigkeitsvariablen μ bzw. β, α, die Matrix $\mathbf{\Lambda}$ die tiefenabhängigen Exonenten $z \in \left(z^{l-1}, z^{l}\right)$ und $\mathbf{C}$ die Wellenamplituden.

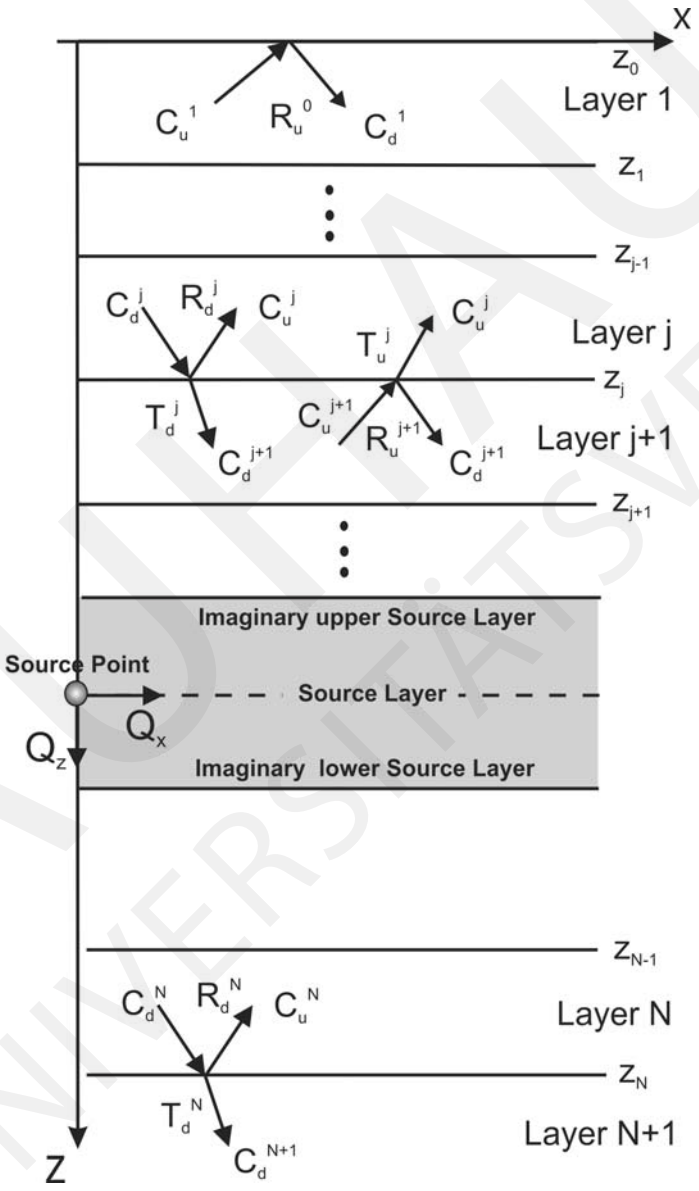

Abbildung 4.2: Darstellung der Einbettung einer Dipol-Verwerfungsquelle innerhalb des geschichteten Halbraums zur Berechnung der Green'schen Funktionen im Frequenzbereich, nach (Wuttke, Dineva & Schanz 2009) und (Hisada 1994)

Die Freifeld-Verschiebungs- und Spannungensvektoren $u^{l,fr}\left(k, z, \omega, S\right)$, $\Sigma^{l,fr}\left(k, z, \omega, S\right)$ können in Abhängigkeit von der Quell- und Aufpunkttiefe, -entfernung sowie der Quelle für die jeweilige Schicht l angegeben werden

$$\mathbf{u}^{1,fr}(x,z,\omega,S) = \frac{1}{2\pi}\int_{-\infty}^{\infty}\left(\mathbf{E}^1_{11}\mathbf{\Lambda}^1_d\hat{\mathbf{R}}^0_u + \mathbf{E}^1_{12}\mathbf{\Lambda}^1_u\right)\hat{\mathbf{T}}^1_u\hat{\mathbf{T}}^2_u ... \hat{\mathbf{T}}^{S-1}_u\left(\mathbf{B}^{S+}\mathbf{D}^S - \mathbf{B}^{S-}\right)^{-1}\Delta\mathbf{Q}e^{(ikx)}dk \tag{4.10}$$

$$\mathbf{\Sigma}^{1,fr}(x,z,\omega,S) = \frac{1}{2\pi}\int_{-\infty}^{\infty}\left(\mathbf{E}^1_{21}\mathbf{\Lambda}^1_d\hat{\mathbf{R}}^0_u + \mathbf{E}^1_{22}\mathbf{\Lambda}^1_u\right)\hat{\mathbf{T}}^1_u\hat{\mathbf{T}}^2_u ... \hat{\mathbf{T}}^{S-1}_u\left(\mathbf{B}^{S+}\mathbf{D}^S - \mathbf{B}^{S-}\right)^{-1}\Delta\mathbf{Q}e^{(ikx)}dk. \tag{4.11}$$

Die Integranden sind abhängig von der Wellenzahl k, der Frequenz ω, der seismischen Punkt- oder Linienquelle S und den elastischen Konstanten in den jeweiligen Schichten l. Die verallgemeinerten Reflexion- und Transmissionskoeffizienten sind durch $\hat{\mathbf{R}}^l_u = \mathbf{R}^l_u + \mathbf{T}^l_d\hat{\mathbf{R}}^{l-1}_u\hat{\mathbf{T}}^l_u$ und $\hat{\mathbf{T}}^l_u = \left(\mathbf{I} - \mathbf{R}^l_d\hat{\mathbf{R}}^{l-1}_u\right)^{-1}\mathbf{T}^l_u$, $l = 1,\ldots,S-1$ für Schichten oberhalb der seismischen Quelle sowie $\hat{\mathbf{R}}^l_d = \mathbf{R}^l_d + \mathbf{T}^l_u\hat{\mathbf{R}}^{l+1}_d\hat{\mathbf{T}}^l_d$ und $\hat{\mathbf{T}}^l_d = \left(\mathbf{I} - \mathbf{R}^l_u\hat{\mathbf{R}}^{l+1}_d\right)^{-1}\mathbf{T}^l_d$, $l = M-1,\ldots,S$ für die Schichten unterhalb der Quelle definiert. In der Beschreibung der Quellfunktion ΔQ kann eine Einzel- oder Linienquelle ($\Delta Q = [-P_x, 0]^T$ bzw. $\Delta Q = [0, -P_z]^T$) in beliebiger Richtung abgebildet werden (Hisada 1995). Die Verschiebung- und Spannungsmatrizen sind definiert zu

$$\begin{aligned}\mathbf{u}^{l,fr}(k,z,\omega) &= \mathbf{E}^l_{11}\mathbf{\Lambda}^l_d\mathbf{C}^l_d + \mathbf{E}^l_{12}\mathbf{\Lambda}^l_u\mathbf{C}^l_u\\ \mathbf{\Sigma}^{l,fr}(k,z,\omega) &= \mathbf{E}^l_{21}\mathbf{\Lambda}^l_d\mathbf{C}^l_d + \mathbf{E}^l_{22}\mathbf{\Lambda}^l_u\mathbf{C}^l_u,\end{aligned} \tag{4.12}$$

wobei der Index u und d die in $-z$ bzw. $+z$-Richtung laufenden Wellen durch die jeweiligen Schichten kennzeichnet. In den numerischen Simulationen wird eine komplexe Wellengeschwindigkeit angesetzt. Die komplexe Wellengeschwindigkeit repräsentiert die übliche durch die hysteretische Materialdämpfung modifizierten Wellengeschwindigkeiten. Der Ansatz der komplexen Wellengeschwindigkeiten in obigen Gleichungen hat den Effekt, das die Integrale in die komplexe Integrationsebene hinein verschoben werden, so dass die dort vorhandenen Singuaritäten umgangen und während der numerischen Integration nicht gesondert betrachtet werden müssen. Die Verschiebungen und Spannungen ergeben sich durch die Integration aller Wellenzahlen k entlang des Integrationspfades.

4.3.1 Simulation der seismischen Verwerfung und synthetische Seismogramme

Die Modellierung und Simulation einer seismischen Quelle kann auf unterschiedliche komplexe Art und Weise erfolgen. Der einfachste Fall ist eine dynamisch wirkende Einzellast, wobei Lamb (Lamb 1904) erstmals das Randwertproblem einer dynamischen

Einzellast auf einem Halbraum analytisch löste. Für Simulation von realistischen seismischen Verwerfungen kann diese Modellierung nicht direkt genutzt werden, da die Modellierung zu stark vereinfacht ist. Es ist üblich, die seismischen Quelle als gekoppelte Doppel-Dipolquelle zu simulieren. Das bei einer Verwerfung wirkende seismische Moment aus Kraft und Hebelarm ist im seismischen Momententensor zusammengefasst

$$M_{kj} = \begin{bmatrix} M_{xx} & M_{xy} & M_{xz} \\ M_{yx} & M_{yy} & M_{yz} \\ M_{zx} & M_{zy} & M_{zz}. \end{bmatrix}$$

Die Momentenkomponenten M_{kj} sind lineare Dipolquellen mit einem Hebelarm und einer Kraft in gleicher Richtung. Die darin vorkommenden Kräftepaare beschreiben Kräfte in der $\pm k$-Richtung. Die während einer Verwerfung auftretenden Momente, hervorgerufen durch die vorhandenen Körperkräfte der Bodenmassen, werden durch das Kräftepaar aus Einzelkräften abgebildet. Die resultierenden Verschiebungen u_i sind das Produkt der Faltung $u_i = M_{kj} * G_{ik,j}$ zwischen Momentenanregungsfunktion und Green'scher Funktion $G_{ik,j}$ eines geschichteten Mediums zu den frequenzabhängigen Verschiebungen u_i.

Nach (Miksat 2006) ergeben sich die Verschiebungskomponenten für den 2D Fall

$$\begin{aligned} u_x &= M_{xx} * G_{xx,x} + M_{xz} * G_{xx,z} + M_{zx} * G_{xz,x} + M_{zz} * G_{xz,z} \\ u_y &= M_{yx} * G_{yy,x} + M_{yz} * G_{yy,z} \\ u_z &= M_{xx} * G_{zx,x} + M_{xz} * G_{zx,z} + M_{zx} * G_{zz,x} + M_{zz} * G_{zz,z} \end{aligned} \tag{4.13}$$

mit $M_0 = G_0 AD$ als das auftretende skalare Moment M_0 der Verwerfung unter Nutzung der Verwerfungsfläche A, der durchschnittlichen Verschiebung D und der Schubsteifigkeit G. Die auftretenden seismischen Momente in Gl.(4.13) sind durch folgende geometrische Beziehungen abgebildet

$$\begin{aligned} M_{xx} &= -M_0 \left(sin\delta cos\lambda sin2\phi + sin2\delta sin\lambda sin^2\phi \right) \\ M_{yy} &= M_0 \left(sin\delta cos\lambda sin2\phi - sin2\delta sin\lambda cos^2\phi \right) \\ M_{zz} &= M_0 \left(sin2\delta sin\lambda \right) \\ M_{xy} &= M_0 \left(sin\delta cos\lambda cos2\phi + \frac{1}{2} sin2\delta sin\lambda sin\phi \right) \\ M_{xz} &= -M_0 \left(cos\delta cos\lambda cos\phi + cos2\delta sin\lambda sin\phi \right) \\ M_{yz} &= -M_0 \left(cos\delta cos\lambda sin\phi - cos2\delta sin\lambda cos\phi \right). \end{aligned} \tag{4.14}$$

Sythetische Seismogramme Zur Berechnung des synthischen Seismogramms können verschiedene Lösungsmöglichkeiten genutzt werden. In dem vorliegenden Algorithmus wird die Lösung nach Gl.(4.13) als Green'sche Funktion im Frequenzbereich mit der seismischen Herdlösung im Frequenzbereich gefaltet. Die Rücktransformation

dieser Ergebnisse in den Zeitbereich wird durch die Anwendung der inversen Fouriertransformation realisiert (Wuttke 2005). Für die Durchführung der Faltung zwischen Green'scher Funktion und Herdlösung müssen bestimmte numerische Zeit-Frequenz-Randbedingungen der Anregungsfunktion berücksichtigt werden.

Die Applikation des seismischen skaleren Momentes $M_0(t)$ folgt einer zeitlichen Abhängigkeit, da die Kraft während des Verwerfungsvorgangs aufgebaut wird und während des Verschiebungsvorgangs wieder abfällt. Dabei ist die Bruchlänge l proportional zur Inversen der maximalen Eckfrequenz f_c des seismischen Momentes. Das bedeudet, dass der seismische Momentenverlauf einer Impulsfunktion einer Abklingkurve auf die maximale Eckfrequenz f_c folgt $M_0(t)(\infty)\left[1-(1+tf_c)\,e^{-tf_c}\right]$. Durch diese Funktion ergibt sich als Ergebnis der Faltung von seismischem Moment und GREEN'scher Funktionen ein Ausklingen mit ansteigender Frequenz, wodurch die numerische Stabilität sichergestellt wird.

4.4 Hybride WNI-BIE-Formulierung

Für die Wellenausbreitung in einem unbegrenzten Gebiet müssen besondere Simulationsmethoden bereitgestellt werden. Die Einflüsse von entfernten Bereichen werden im Wellenfeld gespeichert. Das Wellenfeld wird dadurch modifiziert und weist Besonderheiten nahe der Oberflächen auf, so dass ein möglichst großer geologischer Bereich in der Simulation erfasst werden muss. Für die numerische Simulation dieser großen geologischen Skalen von Quelle, Pfad, geologischem Nahfeld und Interaktionsbereich gibt es zwei mögliche Wege: a) die Abbildung aller Teilmodelle in einer numerischen Simulation, welches große Rechenleistung und Zeit braucht (Borsutzky 2007), oder b) die Kombination unterschiedlicher Partialmodelle zu einem hybriden Gesamtmodell.

Der zweite Weg soll im Nachfolgenden analysiert und entwickelt werden, da diese Vorgehensweise unterschiedliche Vorteile besitzt und zukünftig noch weiter an Bedeutung gewinnen wird. Hybride Methoden sind immer dann angebracht, wenn das Gesamtmodell zwei oder mehrere Teile mit einer deutlich unterschiedlichen Komplexität besitzen. Diese Situation ist für den Fall von propagierenden Wellen zu einem oberflächennahen Bauwerk gegeben. Die hybride Mehrmodelltechnik wurde erstmalig durch (Alterman & Karal 1968) als „Domain-coupling“ für die Simulation und Modellierung einer Wellenausbreitung mit Hilfe von Finite Differenzen genutzt. Diese Herangehensweise wurde durch eine Vielzahl von Autoren in der Kopplung unterschiedlicher Wellenausbreitungsmodelle, wie Modal Summation, Ray methods, Finite Elemente und Finite Differenzen aufgegriffen (Fah, Suhadolc & Panza 1990, Fah 1992, Fah, Suhadolc & Panza 1993, Fah, Suhadolc, Muller & Panza 1994, Zahradnik & Moczo 1996). Durch (Robertsson & Chapman 2000)

wurde der Begriff „wave injection“ geprägt, trifft es doch die Wirkungsweisen an der Grenzfläche zwischen beiden Modellen. In (Wuttke, Schanz & Dinava 2010) sind weitere Beispiele und Autoren für hybride Modelle gegeben. Zusammenfassend kann gesagt werde, dass hybride Modelle mit BIEM Kopplungen nur sehr wenig und mehrphasige Lösungen nicht in der Literatur vorhanden sind, wodurch sich ein Mangel in den Simulationsmethoden ergibt. Dieser Mangel wird in eigenen Untersuchungen aufgegriffen und einige Lösungen werden bereitgestellt. Zusätzlich wurde in den getätigten Analysen eine realitätsnahe seismische Quelle implementiert, wogegen die meisten numerischen Simulationen alleinig den Einfall einer ebenen Körperwellenfront betrachten, welches nicht den tatsächlichen Bedingungen entspricht. Der Schwerpunkt der getätigten Untersuchungen lag in der Kopplung der BIE- und der WNI-Methode unter Einbeziehung a) einer seismischer Quelle, b) eines inhomogenen Wellenpfades, c) einer Mehrphasigkeit in Pfad und lokaler Region und d) einer lokale, komplexe geologische Region und e) einer vorhandenen Topographie an der Oberfläche.

Die Kopplung der beiden Modelle erfolgt in zwei Schritten. In einem ersten Schritt wird das Wellenfeld im Freifeld u_i^{fr} und p_i^{fr} an allen Punkten im Feld berechnet. Insbesondere die Ergebnisse entlang der virtuellen Anregungsgrenze bzw. -berandung werden in den Interaktionsknoten $\Lambda^{excitation}$ als Anregung abgespeichert. Die so bestimmten Verschiebungen u_i^{fr} und Spannungen p_i^{fr} bilden die Freifeldbewegung des horizontal geschichteten Mediums für große Skalen ab. Die Anregungsgrenze ist variabel und vor dem eigentlichen lokalen, heterogenen geologischen Bereich positioniert. Der zweite Schritt beinhaltet die Modellierung der stark heterogenen, beliebig geschichteten, komplexen geologischen Übergangs- oder Anregungszone. In diesem Bereich existiert ein totales Wellenfeld u_i^{total} und p_i^{total}, welches durch die multiplen Reflexionen und Transmissionen des Freifeld-Wellenfeldes und des gestreuten, lokalen Wellenfeld in der heterogenen Zone ausgebildet wird. Das gestreutes Wellenfeld $u_i^{scattered}$ und $p_i^{scattered}$ ist innerhalb und außerhalb des regionalen Bereiches vorhanden. Das gestreute Wellenfeld innerhalb der geologischen Heterogenität ist die Differenz zwischen totalem Wellenfeld und Freifeld-Wellen, $u_i^{sc} = u_i^{total} - u_i^{fr}$ und $p_i^{sc} = p_i^{total} - p_i^{fr}$. Diese Felder sind in dem Bereich zwischen der variablen Anregungsgrenze und Grenze zur lokalen geologischen Region miteinander gekoppelt (Wuttke, Schanz & Dinava 2010). Der Übergangsbereich besitzt die gleichen Parameter wie das Freifeld, wird allerdings durch die BIE-Methode mit abgebildet, so dass dort eine wechselseitige Interaktion stattfinden kann. Durch die variable geometrische Größe der Heterogenität, der gegebenen Material- und geometrischen Dämpfungen muss das Wellenfeld an der Anregungsgrenze $u_i^{total} = u_i^{fr}$ und $p_i^{total} = p_i^{fr}$ ergeben, wodurch die Voraussetzungen für die Anwendung des Modells gegeben sind.

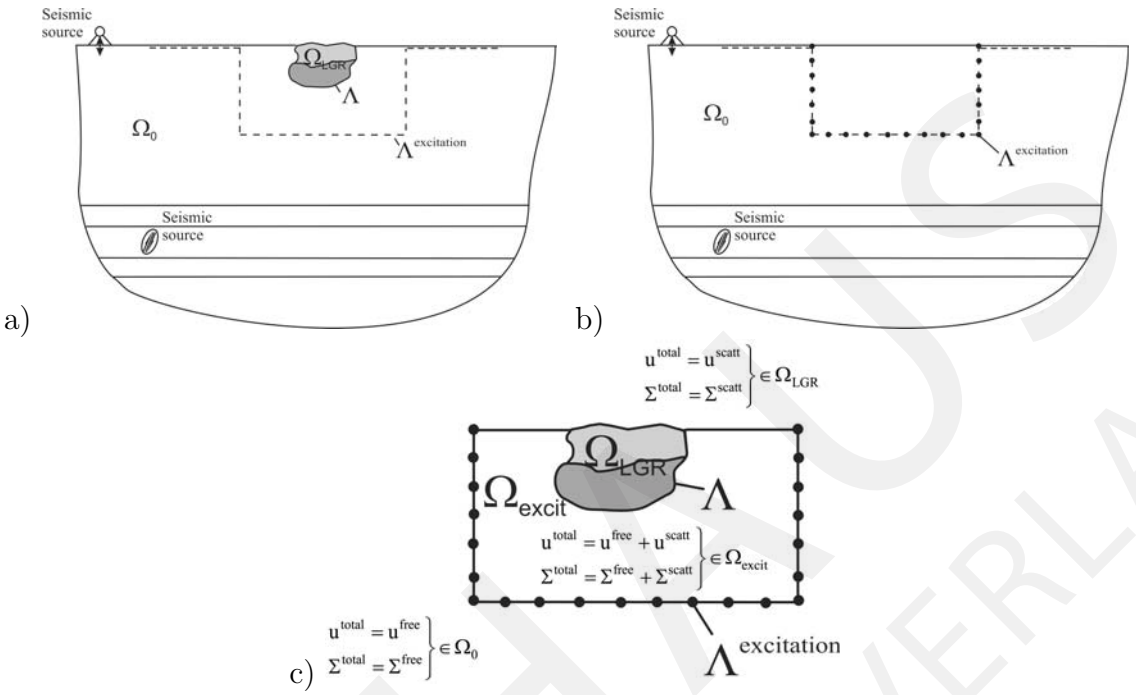

Abbildung 4.3: Zusammensetzung der Partialmodelle zu einem hybriden Gesamtmodell, nach (Wuttke, Dineva & Schanz 2011).

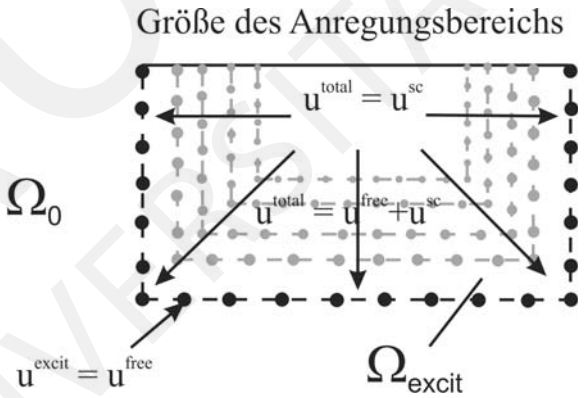

Abbildung 4.4: Variation des Übergangsbereichs zur Erfüllung der Randbedingung $u_i^{total} = u_i^{fr}$ und $p_i^{total} = p_i^{fr}$.

4.5 Modellierung poroelastischer, fluidgesättigter Materialien

Für die Erweiterung der bestehenden elasto-dynamischen Theorien hinsichtlich einer Wellenausbreitung durch zwei- oder dreiphasige Materialien existieren unterschiedliche Herangehensweisen. Zum einen können die kompletten Beziehungen, basierend auf den Biot'schen Grundlagen, im Zeitbereich gelöst und implementiert werden

(Schanz 2001) bzw. die Biot'schen Theorien für fluidgesättigte Materialien durch Nutzung der Theorie poröser Medien (Albers 2010) zur Abbildung ungesättigter Materialien erweitert werden. Ein anderer numerisch günstiger Ansatz ist die Nutzung von visko-elastischen Isomorphismen der Biot'schen Poroelastizität im Frequenzbereich.

Poroelastisches Modell nach Bardet Der Ursprung der Untersuchungen zur Wellenausbreitung durch poroelastische Materialien wurde durch (Biot 1956*a*, Biot 1956*b*) und (Frenkel 1944) begründet. Seitdem haben viele Autoren dieses Problem aufgegriffen und immer waren die Phänomene der Wellenausbreitung durch ein fluidgesättigtes, homogenes Zweiphasenmedium besonderer Gegenstand der Untersuchungen (Chen & Dargush 1995, Schanz & Diebels 2003, Lin, Lee & Trifunac 2005). Das fluidgesättigte, poröse Medium bewirkt eine zusätzliche Energiedissipation während der Wellenausbreitung und eine weitere zweite, langsamere Kompressionswelle zu den bereits existierenden Kompressions- und Scherwellen in einem einphasigen, elastischen Kontinuum. Diese zusätzliche Welle war und ist speziell für hochfrequente Anregungen ein besonderer Gegenstand der Untersuchungens, wie die Analyse von Oberflächenwellen innerhalb gesättigter, poroelastischer Halbräume (Wilmanski 2005, Schanz & Pryl 2004) als Grundlage für unterschiedliche Identifikationsaufgaben belegen. Infolge mangelnder Fundamentallösungen zu poroelastischen Problemstellungen existieren relative wenige Publikationen zu numerischen BIEM-Lösungen (Schanz 2001) und (Gatmiri & Jabbari 2005).

Einen anderen Ansatz als die transiente Lösung und Implementation der Biot'schen Gleichungen, bieten visko-elastische Analogien, (Simon, Zienkewicz & Paul 1984). Danach induziert ein poroelastisches und ein viskoelastisches Material eine ähnliche Wellenfeldänderung im Signal. Bardet (Bardet 1992, Bardet 1995) leitet dazu ein lineares, viskoelastisches Kelvin-Voigt-Modell aus dem Biot'schen Modell ab und weist nach, dass dieser Ansatz unter gewissen Gültigkeitsgrenzen analoge Phänomene wie das transiente, poroelastische Zweiphasenmodell ergibt. Durch die mikroskopischen Materialkonstanten des Biot'schen Modells werden die Wellengeschwindigkeiten zu komplexwertigen Variablen. Die numerische Implementation ist im Vergleich zu transienten Lösungen nach (Schanz 2001) einfacher und die numerische Stabilität entspricht der normalen viskoelastischen Lösung.

Die partiellen Differentialgleichungen der Elastodynamik sind für ein lineares, viskoelastisches Kelvin-Voigt-Modell im Frequenzbereich wie folgt definiert

$$\begin{aligned}\left(\frac{k_s^2}{k_p^2}-1\right)\left[u_{y,xy}+u_{x,xx}\right]+\left[u_{x,xx}+u_{x,yy}\right]+k_p^2 u_x=0\\ \left(\frac{k_s^2}{k_p^2}-1\right)\left[u_{x,xy}+u_{y,yy}\right]+\left[u_{y,xx}+u_{y,yy}\right]+k_p^2 u_y=0\end{aligned} \tag{4.15}$$

mit k_p, k_s als die Wellenzahlen der Longitudinal- und Scherwelle und u_i als die Verschiebung in x- und y-Richtung. Innerhalb der jeweiligen Bodenschicht und ergeben sich die von der Materialstruktur abhängigen Wellenzahlen

$$k_p^2=\frac{\omega^2}{\bar{c}_p^2}=\frac{\omega^2}{c_p^2\left(1-i\omega D_p\right)} \text{ und } k_s^2=\frac{\omega^2}{\bar{c}_s^2}=\frac{\omega^2}{c_s^2\left(1-i\omega D_s\right)}. \tag{4.16}$$

Für kleine Frequenzen und Dämpfungen $\omega D_p << 1$ bzw. $\omega D_s << 1$ gelten die Approximationen

$$k_p^2\approx\frac{\omega}{c_p\left(1-i\omega D_p\right)} \text{ bzw. } k_s^2\approx\frac{\omega}{c_s\left(1-i\omega D_s\right)}. \tag{4.17}$$

welche ähnlich den hysteretischen Dämpfungen eines normalen Bodenmaterials als komplexe Variablen definiert sind. Die in den Wellengeschwindigkeiten und Dämpfungen enthaltenen poroelastischen Parameter sind durch die folgenden mikrostrukturellen Relationen bestimmt

$$c_p=\sqrt{\frac{P+2Q+R}{\bar{\rho}}} \text{ und } c_s=\sqrt{\frac{N}{\bar{\rho}}} \tag{4.18}$$

sowie

$$D_p=\frac{\bar{\rho}}{b}\left(\frac{Q+R}{P+2Q+R}\frac{\bar{\rho}_{12}+\bar{\rho}_{22}}{\bar{\rho}}\right) \text{ und } D_s=\frac{\bar{\rho}}{b}\left(\frac{\bar{\rho}_{12}+\bar{\rho}_{22}}{\bar{\rho}}\right). \tag{4.19}$$

In den Gl.4.18 und 4.19 sind $\bar{\rho}=(1-n)\,\rho_s+n\rho_f$ die effektive Dichte, mit n als Porenzahl der Feststoffmatrix, ρ_f und ρ_g die Fluid- und Korndichte, $b=n^2 g\rho_f/k$ der Dämpfungskoeffizient und k die hydraulische Permeabilität im Bodenmaterial. Die Dichten $\bar{\rho}_{12}$ und $\bar{\rho}_{22}$ ergeben sich zu $\bar{\rho}_{12}=0.5(1-n)\rho_f$ und $\bar{\rho}_{12}=0.5(n+1)\rho_f$. Die bekannten Biot'schen Konstanten P, Q, N und R werden durch die Moduli der Feststoffmatrix K_{dry}, des Korns K_g und des Fluids K_f für $\omega\bar{\rho}/b << 1$ definiert.

$$\begin{aligned}P=\frac{3\left(1-\nu\right)}{1+\nu}K_{dry}+\frac{Q^2}{R},\ Q=\frac{n\left(1-n-\frac{K_{dry}}{K_g}\right)}{1-n-\frac{K_{dry}}{K_g}+n\frac{K_g}{K_f}}K_g,\ N=\frac{3}{2}\frac{(1-2\nu)}{1+\nu}K_{dry}\\ R=\frac{n^2}{1-n-\frac{K_{dry}}{K_g}+n\frac{K_g}{K_f}}K_g,\ K_{dry}=\frac{2}{3}\frac{G\left(1+\nu\right)}{1-2\nu}.\end{aligned} \tag{4.20}$$

Mit den obigen Definitionen wird das zweiphasige, poroelastische dynamische Verhalten durch ein dynamisches Verhalten eines einphasigen, viskoelastischen Materials approximiert.

4.6 Numerische Studien

Unterschiedliche Studien in (Wuttke, Schanz & Dinava 2010), (Wuttke, Dineva & Schanz 2011), (Dineva, Wuttke & Manolis 2012*b*) und (Dineva, Wuttke & Manolis 2012*a*), wurden im Zusammenhang mit einer hybriden Modellierung zum Studium der Abhängigkeiten von dem Typ der seismischen Quelle, dem Wellenpfad, der Oberflächenstruktur (Wuttke, Dineva & Schanz 2011) aber auch von der Porosität und der Sättigung (Wuttke, Schanz & Dinava 2010) durchgeführt.

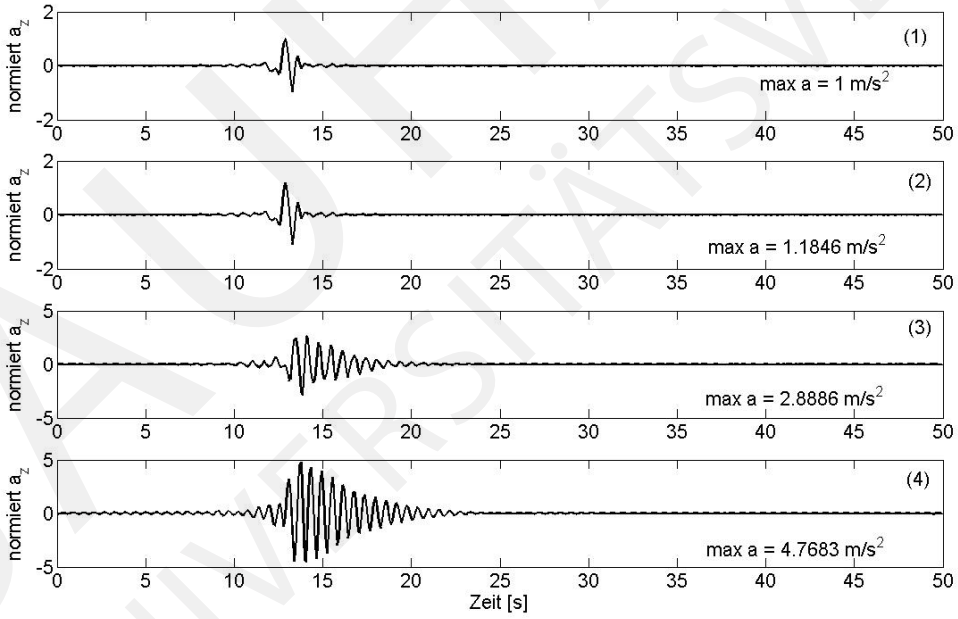

Abbildung 4.5: Darstellung der vertikalen Beschleunigungskomponente für die Simulationsbeispiele 1 bis 4, nach (Wuttke, Schanz & Dinava 2010)

Als Beispiel für die Einflüsse von porösen, gesättigten oder trockenen Material soll nachfolgend aus den zitierten Publikationen ein Beispiel, Abbildung (4.5), zu den Abhängigkeiten von dem Porenanteil und der Sättigung abgebildet werden. Die Abbildungen umfassen unterschiedliche Simulationen, so das Beispiel-1 als ein horizontal geschichteter Halbraum ohne laterale Heterogenität, das Beispiel-2 als ein hybrides Modell eines horizontal geschichteten Halbraums mit einer lateral,

poroelastischer, trockenen Heterogenität, das Beispiel-3 als ein horizontal geschichteter, poroelastischer, gesättigter Halbraum ohne laterale Heterogenität und das Beispiel-4 als ein hybrides Modell eines horizontal geschichteten, poroelastischen, trockenen Halbraums und lateral inhomogener Heterogenität.

4.7 Zusammenfassung

Im Kapitel 4 wurde die Entwicklung eines hybriden numerischen Algorithmus zur Simulation von propagierenden Wellenfeldern in großskaligen geologischen Gebieten und der Einbeziehung von lokalen, oberfächennahen heterogenen Bereichen vorgestellt. Derartige Entwicklungen sind die Grundlage für weiterführende Boden-Bauwerks-Interaktionsstudien unter Nutzung realitätsnaher einfallender Wellenfelder. Neben der Applikationsfähigkeit wurde auch der Einfluss von fluidgesättigten Materialien auf die Simulation von Wellenfelder studiert und abgebildet, wobei die Parameter für die Simulation durch Anwendung der Methoden aus Kapitel 2 bestimmt werden können. In weiterführenden Entwicklungen kann die Kopplung zur FEM für den unmittelbaren Interaktionsbereich und dem Einsatz von elasto-plastischen Makroelementen für die Interaktion durchgeführt werden, um die Auswirkungen einer hybriden Wellenausbreitung durch komplexe Bodenbedingungen auf Bauwerksstrukturen direkt zu studieren.

4.8 Beigelegte eigene Publikationen zu Kapitel 4

Dineva, P., Wuttke, F., Manolis, G. D. (2012) Elastic wave scattering and stress concentration effects in non-homogeneous poroelastic geological media with discontinuities, *Soil Dynamics and Earthquake Engineering*, vol.41, pp.102-118

Dineva, P., Wuttke, F., Manolis, G. D. (2012) Elastic wave evaluation in discontinuous poroelastic media by BEM: SH-waves, *Journal of Theoretical and Applied Mechanics*, vol. 42, no.3, pp.75-100

Wuttke, F., Dineva, P., Schanz, T. (2011) Seismic wave propagation in laterally inhomogeneous geological region via a new hybrid approach, *Journal of Sound and Vibration*, vol.330, no.4, pp.664-684

Wuttke, F., Schanz, T., Dineva, P. (2010) Hybride Modellierung seismischer Wellenausbreitung in geologischen, fluidgesättigten Materialien, *Bauingenieur*, vol.85, pp.288-295

Kapitel 5

Zusammenfassung und Ausblick

Wie in der Einleitung der Arbeit bereits erläutert wurde, ist das Ziel die Weiterentwicklung von experimentellen Methoden und von Simulationsverfahren, um Lösungen für existierende Schwachstellen und „Lücken“ auf dem Gebiet der Geotechnik anzubieten. Als Hauptthema ziehen sich Mehrphasensysteme in der Geotechnik und die Modellierung und Simulation dieser durch die unterschiedlichen Themenkomplexe. Eine Grundphilosophie der Arbeit ist, nicht zwischen „*dynamischem*“ oder „*statischem*“ Verhalten in der Analyse von Materials oder der Strukturen abzugrenzen. Wie in der Arbeit gezeigt, ergibt die gemeinsame Nutzung neue experimentelle und numerische Verfahren, welche in der Lage sind anstehende Probleme in der Geotechnik zu lösen.

Nachfolgend soll ein kurzer Überblick der vorgestellten Entwicklungen als Resümee und ein abgeleiteter Ausblick der Arbeit getätigt werden. Die Arbeit gliedert sich in 3 wesentliche Schwerpunkte:

1. Im zweiten Kapitel werden neue Entwicklungen zu experimentellen Verfahren vorgestellt. Das Ziel dieser Methoden ist es, verbesserte Aussagen in der Struktur- und Zustandserkennung ungesättigter granularer Materialien zu erhalten. Insbesondere wellenbasierte Methoden waren im Fokus der Entwicklungen, da diese neben anderen geophysikalischen Verfahren ein großes Potential hinsichtlich neuer Erkenntnisse zu Geomaterialien besitzen. Diese Aussage basiert auf dem Hintergrund, dass die unterschiedlichen Analyseverfahren letztlich das gleiche Material untersuchen. Oftmals extrahierten die Verfahren jedoch nur unterschiedliche physikalische Informationen ohne diese in Verknüpfung zu bringen. Die Motivation war, dass mit dem Gelingen einer Überführung dieser unterschiedlichen Informationen in eine gemeinsame Aussage, ein deutlicher Mehrwert aus dem geotechnischen Experiment zu erwarten ist.

   Den obigen Aussagen entsprechend, erfolgte die Einbeziehung des gesamten Wellenfeldes in die Analysen. Das Ergebnis der Entwicklungen sind neue

Verfahren zur Analyse von frequenzabhängigem Materialverhalten und eine neue Methodenklasse mit sehr hohem Potential hinsichtlich des Zustandsmonitorings und abgeleitete Analysen zur Beschreibung der Materialänderung. Letztlich wurde damit eine komplett neue Analysemethode zum Monitoring kleinster Strukturänderungen von Geomaterialien entwickelt und validiert. Als abgeleitete, funktionale Zusammenhänge wurden Relationen hinsichtlich der Spannungsänderung gegenüber dem Zeitversatz in der Coda, bezüglich der Saugspannungsänderung im Boden über den vollständigen hydraulischen Bereich und die Ableitung der funktionalen Beschreibung von zeitabhängigen, viskosen Materialänderungen vorgestellt und diskutiert. Ein Informationstransfer der Ergebnisse wurde bereits durch die Nutzung der Steifigkeitsbeschreibung zu sehr kleinen Dehnungen und der Änderung dieser in Abhängigkeit in der konstitutiven Modellierung der Makroelemente realisiert. Weiterer zukünftiger Erkenntnisgewinn für die Weiterentwicklung anderer konstitutiver Modelle und in den Zustandsidentifikationen kann nicht hoch genug eingeschätzt werden, da diese sensitiven und in der Auswertung eindeutigen experimentelle Methoden bislang nicht zur Verfügung standen.

2. Im dritten Kapitel wurde der Fokus auf die Entwicklungen zur Boden-Bauwerk-Interaktion gelegt. Um komplexe Situationen realitätsnah in Prognoserechnungen beschreiben zu können, erfolgte die Modellbildung als Makroelement. Für unterschiedlichen Randbedingungen eines statisch belasteten Flachfundamentes, wie Sättigungsabhängigkeit, „*small-strain*“ Dehnungsbereich, erfolgte die Modellierung und Simulation. Übertragen wurden diese Erkenntnisse auf die Modellierung eines zyklisch belasteten Gründung. Dabei sind die entwickelten Ansätze von unmittelbarer Notwendigkeit, da die zyklische Problemstellung nicht Prognosefähig ohne die Berücksichtigung der getätigten Entwicklungen ist.

   Mit der Weiterentwicklung der Makroelemente wurde versucht die „Lücke“ von prognosefähigen Modellen zu verkleinern und eine einfache, aber belastbare Lösung mit dieser kompakten Modellbildung anzubieten. Insgesamt weist die Modellierung unterschiedliche Vorteile gegenüber einer herkömmlichen konstitutiven Modellierung auf. Neben komplizierten Belastungsfällen, wie mehrdimensionale, zeitabhängige oder dynamische Lasten, können relativ einfach mehrphasige Materialstrukturen einbezogen werden. Analog wie bei der ursprünglichen konstitutiven Modellierung, gelten die experimentellen Aussagen für das jeweilige Material und in dieser Modellierung auch für das System. Der numerische Anwender verliert nur die Freiheit in der Systemmodellierung, gewinnt dafür die Möglichkeit, unter den benannten komplexen Randbedingungen, ein prognosefähiges Modell zu erhalten.

3. Im vierten Kapitel wurde die Entwicklung eines hybriden numerischen Al-

gorithmus zur Simulation von Wellenfeldern in großen geologischen, porösen Geomaterialien dargelegt. Diese Entwicklung resultiert aus dem Mangel an numerischen Methoden zur Beschreibung dieser Problemstellung. Existierende Methoden sind nicht für diese großskaligen Dimensionen entwickelt worden. Mit der Aufgabe eine realitätsnahe Simulation unter Einbeziehung aller Pfadeffekte bis hin zur Interaktionszone durchzuführen, müssen diese Verfahren weiterentwickelt werden.

Für die Simulation eines porösen, fluidgesättigten Materials wurde eine vereinfachte viskoelastische Lösung anstelle der komplexen Biot'schen Ansätze in der numerischen Simulation genutzt. Mit dem Ziel den gesamten Wellenpfad zu simulieren, wurde eine seismische Doppledipol-Quelle als Verwerfung implementiert. Das hybride Modell wurde anhand unterschiedlicher Beispiele verifiziert und kann nunmehr in weiteren Kopplungen bis zur Interaktionszone ausgedehnt werden.

Betrachtet man die getätigten Entwicklungen, so ist leicht erkennbar, dass diese in einem laufenden Forschungsrahmen stehen. Während der Bearbeitung dieser Themen ergaben sich natürlich eine Vielzahl an weiteren Fragestellungen. Für die Entwicklungen im Kapitel 4 ist es sinnvoll, die Methoden direkt miteinander in Verbindung zu bringen und dabei die matrixbasieren Rekursionsalgorithmen in eine Randelement-Formulierung bringen, so dass eine echte Kopplung gewährleistet ist, ohne die Vorteile der matrixbasierten Methoden zu verlieren. Zusätzlich sollte neben der Schichtung eine Lösung auf spannungsbasierten Steifigkeitsgradienten als auch eine Überführung in dreidimensionale Abbildungen realisiert werden. Im Kapitel 3 sollten für zyklische und dynamische Problemstellungen die Bandbreite vorhandenen der Makroelement-Lösungen ausgebaut werden, da diese speziell für dynamische Problemstellung die einfache prognosefähige Simulation für praktische Fragen und Applikationen darstellen. Die statischen Makroelemente sollten für unterschiedliche Bodentypen und Gründungskonstruktionen erweitert werden, um die Anwendungsbreite zu erweitern. Die Entwicklungen in Kapitel 2 haben bereits einen sehr hohen Stand erreicht. Es ist hier wichtiger am Transfer der Informationen in geotechnische Aussagen zukünftig zu arbeiten. Einige Lösungen wurden bereits vorgestellt, das enorme Potential allerdings noch lange nicht ausgeschöpft. Da die gradientenbasierten Methoden regelrecht „automatisiert“ werden können und eindeutige Ergebnisse geben, sind diese für zukünftige Monitoringfragen bestens geeignet.

Literaturverzeichnis

Al-Janabi, A., Wagner, N. & Wuttke, F. (2013), 'Mirco and macro hydro-mechanical behaviour of natural and compacted collapsible soils', *European Journal of Environmental and civil engineering* **submitted**.

Albers, B. (2010), *Modeling and Numerical Analysis of Wave Propagation in Saturated and Partially Saturated Media*, Vol. 48 of *Veröffentlichungen des Grundbauinstitutes der Technischen Universität Berlin*, Shaker.

Allen, R. L. & Mills, D. (2004), *Signal Analysis: Time, Frequency, Scale and Structure*, IEEE, Piscataway.

Alterman, Z. & Karal, F. (1968), 'Propagation of elastic waves in layered media by finite difference methods', *Bulletin of the Seismological Society of America* **58**, 367–398.

Arroyo, M. (2007), 'Wavelet based analysis of pulse tests in soil samples', *Rivista Italiana di Geotecnica* **2**, 25–38.

Arulnathan, R. & Boulanger, R. (1998), 'Analysis of bender elements', *Geotechnical Testing Journal* **21**(2), 120–131.

Atkinson, J. (2000), 'Non-linear soil stiffness in routine design', *Geotechnique* **50**(5), 487–508.

Bachrach, R., Dvorkin, J. & Nur, A. (2000), 'Seismic velocities and poisson's ratio of shallow unconsolidated sands', *Geophysics* **65**(2), 559–564.

Bai, L. (2011), Preloading Effects on Dynamic Sand Behaviour by Resonant Column Tests, PhD thesis, Technische Universität Berlin.

Bardet, J. (1992), 'A viscoelastic model for the dynamic behaviour of saturated poroelastic soils', *Trans. of the ASME* **59**, 128–135.

Bardet, J. (1995), 'The damping of saturated poroelastic soils during steady-state vibrations', *Applied Mathematics and Computation* **67**, 3–31.

Bath, M. (1974), *Spectral Analysis in Geophysics*, Vol. 7, developments edn, Elsevier Science.

Benz, T. (2007), Small strain stiffness of soils and its numerical consequences., PhD thesis, Universität Stuttgart.

Biot, M. (1956*a*), 'Theory of propagation of elastic waves in a fluid saturated solid. i. low frequency range.', *Journal of Acoustical Socitiety of America* **28**(2), 168–178.

Biot, M. (1956*b*), 'Theory of propagation of elastic waves in a fluid saturated solid. ii. higher-frequency range.', *Journal of Acoustical Socitiety of America* **28**(2), 179–191.

Borsutzky, R. (2007), Seismic Risk Analysis of Buried Lifelines, PhD thesis, Technische Universität Braunschweig.

Brandt, H. (1955), 'A study of the speed of sound in porous granular media', *Journal of Applied Mechanics* **22**, 479–485.

Burland, J. (1989), 'Small is beautiful - the stiffness of soils at small strains', *Canadian Geotechnical Journal* (9th Laurits Bjerrum Lecture).

Butterfield, R. & Gottardi, G. (1994), 'A complete three dimensional failure envelope for shallow footings on sand', *Geotechnique* **44**, 181–184.

Chatzigogos, C., Pecker, A. & Salencon, J. (2009), 'Macroelement modeling of shallow foundations', *Soil Dynamics and Earthquake Engineering,* **29**, 765–781.

Chen, J. & Dargush, D. (1995), 'Boundary element method for dynamic poroelastic and thermoelastic analyses', *International Journal of Solids Structures* **35**(15), 2257–2278.

Chen, X. (1993), 'A systematic and efficient method of computing normal modes for multilayered media', *Geophysical Journal International* **115**, 391–409.

Chen, X. (2001), Osculation of dispersion curves. Persönliche Kommunikation.

Cho, G. & Santamarina, J. C. (2001), 'Unsaturated particulate materials - particle-level studies', *Journal of Geotechnical and Geoenvironmental Engineering* **127**(1).

Cowan, M., Jones, I. & Weitz, D. (2002), 'Diffusing acoustic wave spectroscopy', *Physical Reviews E* **65**, 066605.

Cremer, C., Pecker, A. & Davenne, L. (2001), 'Cyclic macro-element for soil-structure interaction: material and geometrical non-linearities.', *International Journal for Numerical and Analytical Methods in Geomechanics* **25**, 1257–1284.

Dai, S., Wuttke, F. & Santamarina, J. (2012), 'Coda wave analysis to monitor processes in soils', *ASCE Journal of Geotechnical and Geoenvironmental Engineering* p. in print.

di Prisco, C., Nova, R. & Sibilia, A. (2002), Analysis of soil-structure interaction of towers under cyclic loading, *in* G. Pande & S. Pietruszczak, eds, 'NUMOG VIII', A.A. Balkema, Rome.

Dineva, P., Wuttke, F. & Manolis, G. (2012*a*), 'Elastic wave evaluation in discontinuous poroelastic media by bem: Sh-waves', *Journal of Theoretical and Applied Mechanics* **42**(3), 75–100.

Dineva, P., Wuttke, F. & Manolis, G. D. (2012*b*), 'Elastic wave scattering and stress concentration effects in non-homogeneous poroelastic geological media with discontinuities', *Soil Dynamics and Earthquake Engineering* **41**, 102–118.

Elhakim, A. F. (2005), Evaluation of shallow foundation displacement using soil small-strain stiffness, PhD thesis, Georgia Institute of Technology.

Fah, D. (1992), A Hybrid Technique for the Estimation of Strong Ground Motion in Sedimentary Basins, PhD thesis, Swiss Federal Institute of Technology.

Fah, D., Suhadolc, P., Muller, S. & Panza, G. (1994), 'A hybrid method for the estimation of ground motion in sedimentary basins: quantitative modelling for mexico city', *Bulletin of the Seismological Society of America* **84**(2), 383–399.

Fah, D., Suhadolc, P. & Panza, G. (1990), Estimation of strong ground motion in laterally heterogeneous media: modal summation - finite differences, *in* 'Proceedings of the 9th European Conference of Earthquake Engineering', Moscow, USSR, p. 100–109.

Fah, D., Suhadolc, P. & Panza, G. (1993), 'Variability of seismic ground motion in complex media: the case of a sedimentary basin in the fruili italy area', *Journal* **30**, 131–148.

Fahey, M. & Carter, J. (1993), 'A finite element study of the pressuremeter test in sand using a nonlinear elastic plastic model', *Canadian Geotechnical Journal* **30**(2), 348–362.

Fredlund, D., Morgenstern, N. & Widger, R. (1978), 'The shear strength of unsaturated soils', *Canadian Geotechnical Journal* **15**(3), 313–321.

Fredlund, D. & Rahardjo, H. (1993), *Soil Mechnics for Unsaturated Soils*, Wiley.

Frenkel, J. (1944), 'On the theory of seismic and seismoelectric phenomena in moist soil', *Journal of Physics* **3**(4), 230–241.

Gatmiri, B. & Jabbari, E. (2005), 'Time-domain green's functions for unsaturated soils, two dimensionl solution.', *International Journal of Solid Structure* **42**, 5971–6002.

Gottardi, G. & Butterfield, R. (1995), 'The displacement of a model rigid surface footing on dense sand under general planar loading', *Soil and Foundation* **35**(3), 71–82.

Greening, P. & Nash, D. (2004), 'Frequency domain determination g_{max} using bender elements', *Geotechnical Testing Journal* **27**(3), 288–294.

Gret, A., Snieder, R. & Scales, J. (2006), 'Time-lapse monitoring of rock properties with coda wave interferometry', *Journal of Geohysical Research* **111**, B03305.

Grossmann, A. & Morlet, J. (1984), 'Decomposition of hardy functions into square integrable wavelets of constant shape', *SIAM Journal on Mathematical Analysis* **15**(4), 723–736.

Hammond, J. & White, P. (1996), 'The analysis of nonstationary signals using time-frequency methods', *Journal of Sound and Vibrations* **190**(3), 419–447.

Hicher, P.-Y. & Shao, J.-F. (2008), *Constitutive Modeling of Soils and Rocks*, ISTE, Wiley.

Hisada, Y. (1994), 'An efficient method for computing green's functions for a layered half space without sources and receivers at close depth', *BSSA* **84**(5), 1456–1472.

Hisada, Y. (1995), 'An efficient method for computing green's functions for a layered half space with sources and receivers at close depth', *BSSA* **85**(4), 1080–1093.

Houlsby, G. & Cassidy, M. (2002), 'A plasticity model for the behaviour of footings on sand under combined loading', *Geotechnique* **52**(2), 117–129.

Houlsby, G., Kelly, R., Huxtable, J. & Byrne, B. (2005), 'Field trials od suction caissons in clay for offshore wind turbine foundations', *Geotechnique* **55**(4), 287–296.

Houlsby, G. & Puzrin, A. (2006), *Principles of Hyperplasticity*, Springer.

Hueckel, T. & Nova, R. (1979), 'Some hysteresis effects of the behaviour of geological media', *International Journal of Solids and Structures* **15**, 625–642.

Jardine, R., Potts, D., Fourie, A. & Burland, J. (1986), 'Studies of the influence of non-linear stress-strain characteristics in soil-structure interaction.', *Geotechnique* **36**(3), 377–396.

Jovicic, V., Coop, M. & Simic, M. (1996), 'Objective criteria for determining gmax from bender element tests', *Geotechnique* **46**(2), 357–362.

Kafle, B. & Wuttke, F. (2013), Cyclic macro-element for shallow footing over unsaturated sand, *in* '1st Pan-American Conference on Unsaturated Soils', Columbia.

Kafle, B., Wuttke, F., Sextos, A., Faraonis, P. & Kilanitis, I. (2013), A realistic consistent model for cyclic loaded shallow foundation over multiphase granular material, *in* 'CompDyn', Greece.

Kiencke, U., Schwarz, M., & Weickert, T. (2008), *Signalverarbeitung: Zeit-Frequenz-Analyse und Schaetzverfahren*, Oldenbourg.

Kisse, A. (2008), Eintwicklung eines Systemgesetzes yur Beschreibung der Boden-Bauwerk-Interaktion Flachgegründeter Fundamente auf Sand, PhD thesis, University of Duisburg-Essen.

Klein, K. & Santamarina, J. (2003), 'Electrical conductivity in soils: Underlying phenomena', *Journal of Environmental and Engineering Geophysics* **8**(4).

Lamb, H. (1904), 'On the propagation of tremors over the surface of an elastic solid,', *Philosophical Transactions of the Royal Society of London, Series A* **203**.

Lin, C.-H., Lee, V. & Trifunac, M. (2005), 'The reflection of plane waves in a poroelastic half-space saturate with inviscid fluid', *Soil Dynamic and Earthquake Engineering* **25**, 205–223.

Lins, Y., Fredlund, D. G. & Schanz, T. (2009), 'Modified pressure plate apparatus and column testing device for measuring hydraulic properties of an unsaturated sand', *ASTM Geotechnical Testing Journal* **32**(4), 450–464.

Lomax, A. (1999), 'Path-summation wave forms', *Geophysical Journal International* **138**, 702–716.

Lu, N. & Likos, W. J. (2004), *Unsaturated Soil Mechanics*, Wiley.

Luco, E. & Apsel, R. J. (1983), 'On the green's function for a layered half-space', *BSSA* **73**(4), 909–929.

Marion, D. (1990), Acoustical, Mechanical and Transport Properties of Sediments and Granular Materials, PhD thesis, Stanford University.

Mavko, G., Mukerji, T. & Dvorkin, J. (2009), *The Rock Physics Handbook*, Cambridge University Press.

Mestat, P., Bourgeois, E. & Reiffsteck, P. (2002), *Constitutive modelling of soils and rocks*, hicher p. y. and shao, j. f. edn, John Wiley & Sons Inc., chapter 3, pp. 77–138.

Miksat, J. (2006), Modellierung der Bodenbewegung von krustalen und mitteltiefen Erdbeben, PhD thesis, Universität Karlsruhe.

Montrasio, L. & Nova, R. (1997), 'Settlement of shallow foundaitons on sand: geometrical effects', *Geotechnique* **47**, 49–60.

Muir-Wood, D. (2004), *Geotechnical Modelling*, Applied Geotechnics, Spon Press Taylor & Francis Group.

Niemunis, A., Prada-Sarmiento, L. F. & Grandas-Tavera, C. E. (2011), 'Paraelasticity', *Acta Geotechnica* **6**(6), 67–80.

Nova, R. & di Prisco, C. (2003), The macroelement concept and its application in geotechnical engineering, *in* J.-P. Magnan & N. Droniuc, eds, 'FONDSUP International Symposium sur les fondations superficielles', Paris.

Nova, R. & Montrasio, L. (1991), 'Settlement of shallow foundations on sand', *Geotechnique* **41**(2), 243–256.

O'Sullivan, C. (2011), *Particulate Discrete Element Modelling*, Vol. 4 of *Applied Geotechnics*, Spon Press.

Pender, M. (2006), Integrated design of structure-foundation systems: Role of shallow foundation bearing strength surfaces, *in* M. Pender & M. Cubrinovski, eds, 'Proceedings of 2006 New Zealand Earthquake Geotechnical Engineering Workshop'.

Prevost, J. & Keane, C. (1990), 'Shear stress-strain curve generation from simple material parameters.', *Journal of Geotechnical and Geoenvironmental Engineering* **116**(8), 1250–1254.

Puzrin, A. & Burland, J. (1996), 'A logarithmic stress-strain function for rocks and soils', *Geotechnique* **46**(1), 157–164.

Robertsson, J. & Chapman, C. (2000), 'An efficient method for calculating finite-difference seismograms after model alterations', *Geophysics* **65**, 907–918.

Rus, G. & Gallego, R. (2005), 'Boundary integral equation for inclusion and cavity shape sensitivity in harmonic elastodynamics', *Engineering Analysis with Boundary Elements* **29**, 77–91.

Santamarina, J., Klein, K. A. & Fam, M. (2001), *Soils and Waves*, Wiley.

Schanz, M. (2001), *Wave propagation in viscoelastic and poroelastic continua. A Boundary Element Approach*, Lecture Notes in applied Mechanics, Springer.

Schanz, M. & Diebels, S. (2003), 'A comperative study of biot's theory and the linear theory of porous media for wave propagation problems.', *Acta Mechanica* **161**, 213–235.

Schanz, M. & Pryl, D. (2004), 'Dynamic fundamental solutions for compressible and incompressible modeled poroelastic continua', *International Journal of Solids and Structures* **41**, 4047–4073.

Schanz, T., Lins, Y. & Vanapalli, S. (2011), Bearing capacity of a strip footing on an unsaturated sand, *in* E. Alonso & A. Gens, eds, 'Processdings of the 5th International Conference on Unsaturated Soils', Taylor & Francis Group, pp. 1195–1200.

Scheuermann, A. (2012), 'Ortsaufgelöste zeitbereichsreflektometrie in geohydraulik und geomechanik'.

Shirato, M. (2008), 'Numerical simulation of model tests of pier shallow foundation systems subjected to earthquake loads using an elasto-uplift-plastic macroelement', *Soils and Foundations* **48**(5), 693–711.

Simon, B., Zienkewicz, O. & Paul, D. (1984), 'An analytical solution for the transient resonse of saturated porous elastic solids.', *International Journal for Numerics and Analytical Methods in Geomechanics.* **8**, 381–398.

Snieder, R. (2002), 'Coda wave interferometry and equilibrium of energy in elastic media', *Physical Review* **66**(4), 1–8.

Snieder, R. (2006), 'The theory of coda wave interferometry', *Pure and Applied Geophysics* **163**, 455–473.

Somfai, E., Roux, J., Snoeijer, J., Van Hecke, M. & Van Saarloos, W. (2005), 'Elastic wave propagation in confined granular systems', *Physical Review E* **72**, 1539–3755.

Steeb, H., Frehner, M. & Schmalholz, S. (2010), 'Waves in residual-saturated porous media', *Mechanics of Generalized Continua* **21**, 179–187.

Torrence, C. & Compo, G. (1998), 'A practical guide to wavelet analysis', *Bulletin of American Meteorological Society* **79**(1), 61–78.

Van Genuchten, M. (1980), 'A closed-form equation for predicting the hydraulic conductivity of unsaturated soils', *Journal of Soil Science Society of America* **44**, 892–898.

Vanapalli, S. K. & Mohamed, F. M. O. (2007), Bearing capacity of model footings in unsaturated soil., *in* T. Schanz, ed., 'Experimental unsaturated soil mechanics', Springer Proceedings in Physics 112, pp. 483–493.

Wagner, N., Emmerich, K., Bonitz, F. & Kupfer, K. (2011), 'Experimental investigations on the frequency and temperature dependent dielectric material properties of soil', *IEEE Transactions on Geoscience and Remote Sensing* **47**(7), 2518–2530.

Wichtmann, T. (2005), Explicit accumulation model for non-cohesive soils under cyclic loading„ PhD thesis, Ruhr-University Bochum.

Wilmanski, K. (2005), *Surface waves in geomechanics:direct and inverse modeling for soils and rocks*, Vol. 481, Springer, chapter Elastic modeling of surface waves in single and multicomponent systems.

Wuttke, F. (2005), Beitrag zur Standortindentifizierung mit Oberflächenwellen, PhD thesis, Bauhaus-Universität Weimar.

Wuttke, F. (2012), Physical relation between coda wave analysis and fabric change in multiphase, granular material, *in* 'International Conference of Quantitative Nondestructive Evaluation, Special Session on Coda Wave Interferometry', Denver, Colorado.

Wuttke, F., Asslan, M. & Schanz, T. (2010), Determination of g_0 via high resolution timefrequency nalysis in dry, saturated and partially saturated sands, *in* '5th UNSAT International Conference on Unsaturated Soils', Barcelona.

Wuttke, F., Asslan, M. & Schanz, T. (2012), 'Time-lapse monitoring of fabric changes in granular materials by coda wave interferometry', *Geotechnical Testing Journal* **35**(2), GTJ103546.

Wuttke, F., Dineva, P. & Schanz, T. (2009), 'Seismische wellenausbreitung in lateral heterogenen medien mittels eines hybriden modells', *Bauingenieur* **3**.

Wuttke, F., Dineva, P. & Schanz, T. (2011), 'Seismic wave propagation in laterally inhomogeneous geological region via a new hybrid approach', *Journal of Sound and Vibration* **330**(4), 664–684.

Wuttke, F. & Kafle, B. (2013), 'A hybrid small to large strain stiffness macroelement for shallow foundations', *Computer and Geotechnics* **submitted**.

Wuttke, F., Kafle, B., Lins, Y. & Schanz, T. (2012), 'A macro-element for static loaded shallow strip foundation resting on unsaturated soil', *ASCE International Journal of Geomechanics* **in print**.

Wuttke, F., Markwardt, K. & Schanz, T. (2009), Anwendung der wavelet transformation in geotechnischen in - und ex situ untersuchungen, *in* 'VDI Tagung Baudynamik', Kassel.

Wuttke, F., Markwardt, K. & Schanz, T. (2012), 'Dispersion analysis in geotechnical laboratory tests: Time-frequency and time-scale signal transforms', *ASTM Geotechnical Testing Journal* **35**(5).

Wuttke, F. & Schanz, T. (2012), Zustandsänderungsmonitoring von granularen, mehrphasigen böden mittels codawellen interferometrie, *in* '4. VDI Tagung Baudynamik', Kassel.

Wuttke, F., Schanz, T. & Dinava, P. (2010), 'Hybride modellierung seismischer wellenausbreitung in geologisch fluidgesättigten materialien', *Bauingenieur* **85**(6), 288–295.

Wuttke, F., Schmidt, H.-G., Zabel, V., Kafle, B. & Stade, I. (2011), Vibration induced building settlement assessment and calculation, *in* '8th International Conference on Structural Dynamics EuroDyn', Leuven, Belgium.

Zahradnik, J. & Moczo, P. (1996), 'Hybrid seismic modelling based on discrete wave number and finite difference methods', *PAGEOPH* **148**(1/2), 21–38.

Anhang A

Beigelegte eigene Publikationen zur kumulativen Habilitationsschrift

Publikationen zum Kapitel 2

Coda Wave Analysis to Monitor Processes in Soils

Sheng Dai, S.M.ASCE[1]; Frank Wuttke[2]; and J. Carlos Santamarina, M.ASCE[3]

Abstract: Small-strain elastic wave propagation is a constant-fabric phenomenon ideally suited to monitor processes in soils. However, the determination of very small changes in travel time limits our ability to resolve changes in soil stiffness caused by internal processes or changes in boundary conditions. The first-arrival reflects the fastest path between the source and receiver of the propagating wave field; later arrivals in the coda correspond to longer paths after multiple boundary reflections and internal scattering. Therefore, time shifts between the codas of two consecutive signals are longer and easier to detect than between the signals' first arrivals. Slight changes in coda waves can be determined by cross-correlating time windows, time-stretched signals, or frequency-stretched spectra. Basic coda analysis assumes a homogeneous velocity change throughout the medium, propagation modes (P, S) that are equally affected by the process and the preservation of V_P/V_S ratio during the process. The resolving power of coda wave interferometry is explored in an experimental study conducted with quartzitic sand subjected to loading, creep, and unloading stages. The results reveal that coda wave analysis can be used to detect changes in wave velocity on the order of $\Delta V/V < 0.1\%$ (this corresponds to a stress change smaller than $\Delta\sigma'/\sigma' \approx 1\%$ in uncemented soils). Such a high velocity resolution permits the study of creep, aging, and diagenetic processes even in relatively short duration tests. **DOI: 10.1061/(ASCE)GT.1943-5606.0000872.** © *2013 American Society of Civil Engineers.*

CE Database subject headings: Sand (soil type); Stiffness; Creep; Wave propagation.

Author keywords: Coda wave interferometry; Cross correlation; Ottawa sand; Stiffness-stress response; Creep; Aging.

Introduction

The characterization of natural soils is inherently challenging due to their particulate nature and the effect of the measurement process on measured properties. Small-strain measurements using elastic waves provide valuable soil information without altering the soil fabric; examples include small-strain stiffness and attenuation, spatial variability, and soil changes during internal or boundary-imposed processes.

A salient problem in wave measurements is the determination of the first arrival in wave fields. Recommended criteria vary for different experimental configurations (examples for bender element tests can be found in Lee and Santamarina 2005; Arroyo et al. 2006; Youn et al. 2008). Furthermore, changes in first arrivals can often fall below detection limits when monitoring phenomena such as diagenesis, creep, and aging.

On the other hand, the signal tail or coda captures multiple scattered and reflected waves that arrive after the fastest wavefront (Aki 1969; Aki and Chouet 1975; Snieder 2006). These later wavefronts have traveled longer paths and accumulated larger time shifts. Therefore, coda analysis or coda wave interferometry may provide process information even when changes in first arrivals are below resolution. Coda wave analysis has been used to evaluate slight changes in fields, such as earthquake engineering, volcano monitoring, fault movement, and material characterization (Snieder et al. 2002; Gret 2004; Shapiro et al. 2005; Snieder 2006; Otheim et al. 2011; Schurr et al. 2011; Wuttke et al. 2012).

This study identifies and compares algorithms for basic coda wave analysis, highlights underlying assumptions in coda interpretation, and demonstrates the methodology using experimental data gathered to assess the stiffness evolution of a uniform quartzitic sand specimen during loading, creep, and unloading processes. Eventually, the enhanced signal processing methodology provides new insight into soil behavior.

Analysis of Seismic Codas

The concept of coda wave analysis is introduced herein. For clarity, the sampling interval Δt is the time separation between two contiguous discrete values in a digital signal, and a time window is a signal segment between two predefined times.

Consider two consecutive P wave signals A and B obtained for a sandy specimen under isotropic confinement, the first one at 67.6 kPa (9.8 psi) and the second one at 68.9 kPa (10 psi), as shown in Fig. 1(a). The time for the first arrival t_D is identical in both signals ($t_D \approx 200$ μs), yet time windows taken in the range of 1,800−2,200 μs (i.e., 9–11 times the travel time for the first arrival t_D) and 3,600−4,000 μs (i.e., 18−20 times t_D) show that coda waves accumulate time shifts.

The time delay for a given event in the two signals increases linearly with travel distance l, that is, with the event time $t = l/V$, as shown in Fig. 1(b). The slope of the trend in Fig. 1(b) is $\theta = \Delta t/t$. For a velocity change from V_A to $V_B = V_A + \Delta V$

$$\theta = \frac{\Delta t}{t_A} = \frac{t_A - t_B}{t_A} = \frac{\frac{l}{V_A} - \frac{l}{V_B}}{\frac{l}{V_A}} = \frac{V_B - V_A}{V_B} \cong \frac{\Delta V}{\overline{V}} \qquad (1)$$

where the average velocity is $\overline{V} = (V_A + V_B)/2$. Eq. (1) shows that the slope of time lags θ is equal to the relative change in velocity $\Delta V/\overline{V}$ between signals A and B.

[1]Ph.D. Candidate, School of Civil and Environmental Engineering, Georgia Institute of Technology, 790 Atlantic Drive, Atlanta, GA 30332-0355 (corresponding author). E-mail: sheng.dai@gatech.edu

[2]Professor, Geomechanics, Civil Engineering, Bauhaus-Universität Weimar, 99423 Weimar, Germany. E-mail: frank.wuttke@uni-weimar.de

[3]Professor, School of Civil and Environmental Engineering, Georgia Institute of Technology, Atlanta, GA 30332-0355. E-mail: jcs@gatech.edu

Note. This manuscript was submitted on January 30, 2012; approved on November 26, 2012; published online on November 28, 2012. Discussion period open until February 1, 2014; separate discussions must be submitted for individual papers. This paper is part of the ***Journal of Geotechnical and Geoenvironmental Engineering***, Vol. 139, No. 9, September 1, 2013. ©ASCE, ISSN 1090-0241/2013/9-1504–1511/$25.00.

J. Geotech. Geoenviron. Eng. 2013.139:1504-1511.

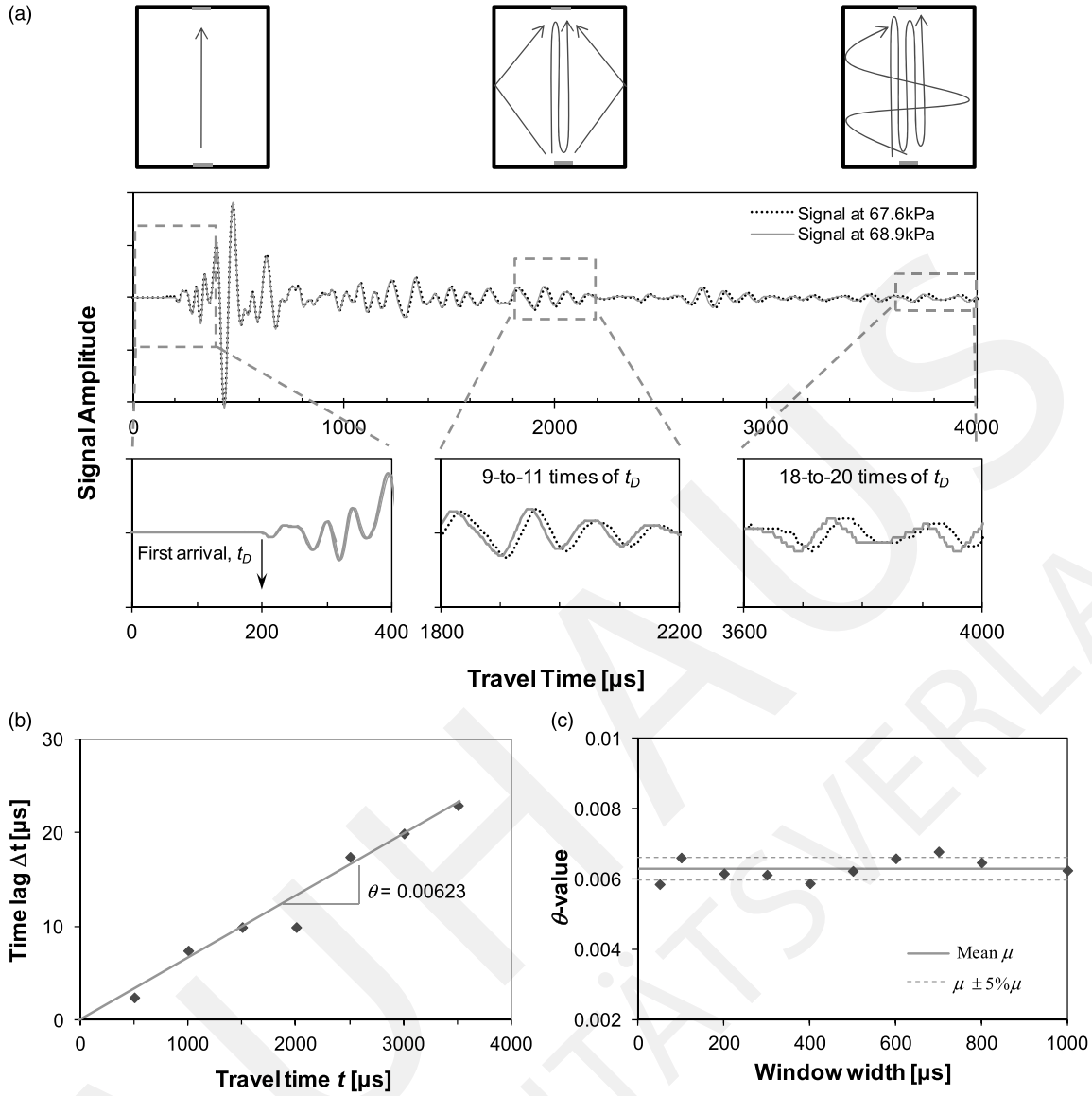

Fig. 1. Schematic illustration of seismic coda analysis; (a) the first arrival of a wave signature reflects the fastest wave pathway (Fermat's principle); events that have experienced multiple reflections arrive later in the coda. Therefore, codas accumulate differences in propagation velocity; (b) time lag Δt between two signals increases almost linearly with propagation time t; the slope θ is the stretching factor; (c) the value of θ varies slightly with window width in time-windowed cross correlations; differences in θ values attributable to the window width are mostly within 5%

It follows from Eq. (1) that a certain event at time t_A in signal A appears at a stretched time $t_B = t_A(1 + \theta)$ in signal B. Thus, the slope θ is herein referred to as the stretching factor. Three different methods to determine the stretching factor θ are presented next.

Method 1: Short-Time Cross Correlation

Short-time windows are extracted from the full signals A and B, and the relative time lag Δt between the windowed signals is determined by cross correlation (Snieder et al. 2002; Santamarina and Fratta 2005; Wuttke et al. 2012). Multiple time lags are obtained by repeating time windowing and cross correlation at different positions along the signals. The time lag Δt determined for each window position is plotted versus the window central time t_W to determine θ, as shown in Fig. 1(b). Window width and superposition must be selected a priori. Computed θ values vary slightly with window width, as shown in Fig. 1(c).

Method 2: Time-Stretched Cross Correlation

The linear increase in time lag Δt with travel time t for corresponding events in signals A and B implies that waveforms can overlap by linearly stretching the timescale of the faster one, say signal B (Sens-Schönfelder and Wegler 2006). The procedure consists of four steps: (1) select a value for θ; (2) time-stretch the faster signal B using $t_B = t_A(1 + \theta)$; (3) compute the cross correlation between the full-length signals, that is, the original signal A and the stretched signal B; (4) repeat steps 1 through 3 for other θ values. The sought value of θ is the one that renders the highest cross correlation, as shown in Fig. 2(a). Note that time-stretching requires resampling: new signal values at all times t_i are obtained by interpolating between stretched signal values that fall immediately above and below t_i (we use linear interpolation).

Signal amplitudes decrease with time; thus, cross correlation values are biased by the earlier higher energy events in the signals.

J. Geotech. Geoenviron. Eng. 2013.139:1504-1511.

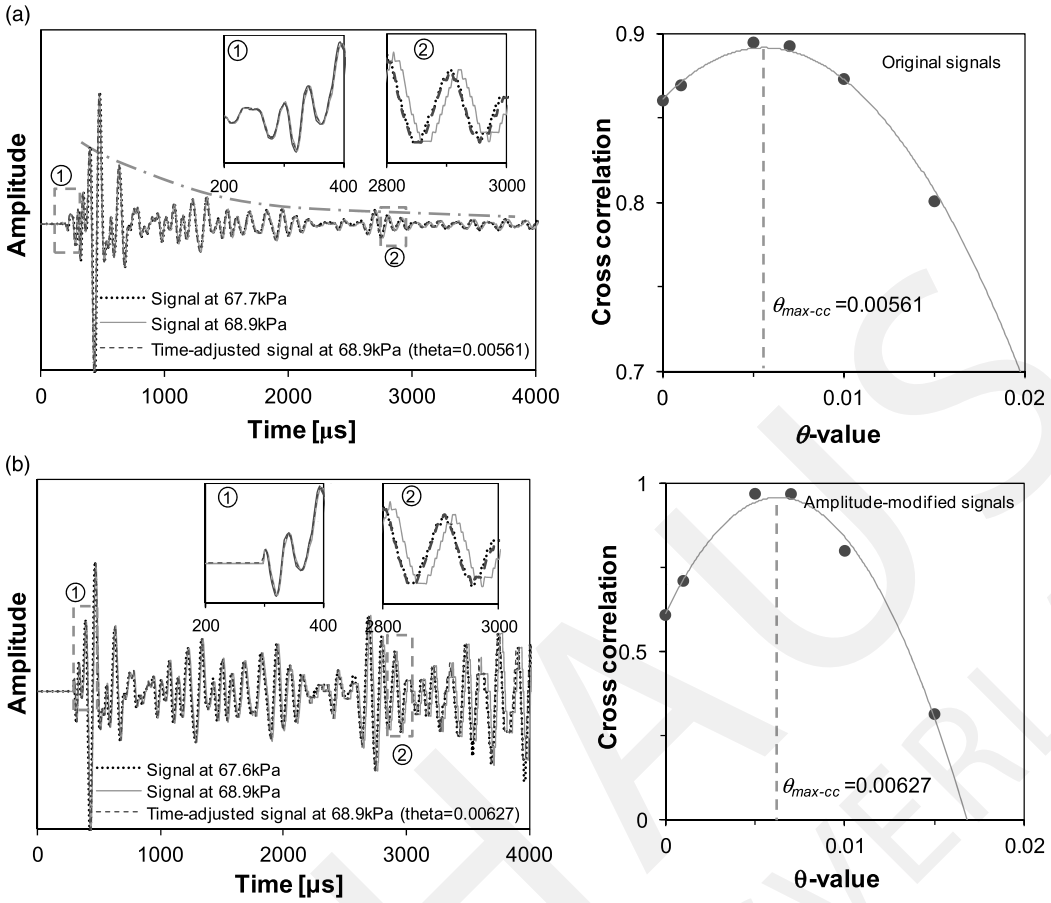

Fig. 2. Time-stretched cross correlation: full-signal based determination of the stretching factor θ in the time domain; (a) computations using original signals; (b) both signals are exponentially amplified [dashed-dotted line in (a)] to obtain constant energy content in time before computing the cross correlation: the signal value x_i at time t_i is amplified by a factor $e^{\alpha t i}$ where α is constant for all t_i and equal for both signals; inserts show amplified signal windows (denoted as 1 and 2)

This bias is overcome by premultiplying both signals A and B by the same exponential amplifier, as shown by the dashed-dotted line in Fig. 2(a), to yield signals with constant energy content in time, as shown in Fig. 2(b): the signal value x_i at time t_i is amplified by a factor $e^{\alpha t i}$, where α is constant for all t_i and equal for both signals.

Method 3: Frequency-Stretched Spectra

Two signals A and B with a linear increase in time lag can be regarded as the same signal but sampled with two different sampling intervals: signal A using Δt, and signal B with $(1 \pm \theta)\Delta t$. In other words, their amplitudes are identical when the discrete time $t_A = i \times \Delta t$ equals $t_B = i \times [(1 \pm \theta)\Delta t]$, where i is an integer. Therefore, in the frequency domain, the spectral magnitude for signal A at frequency $\omega_A = 2\pi u/(N \times \Delta t)$ equals that for signal B at $\omega_B = 2\pi u/[N \times (1 \pm \theta)\Delta t]$, where the integer u is the frequency counter and N is the number of discrete points in the sampled signal. Then, the stretching coefficient can be determined in the frequency domain as follows: (1) compute the frequency spectrum for both signals A and B; (2) linearly stretch the spectrum of the slower signal until both spectra match best (i.e., cross correlation—note that this requires interpolation to compute stretched spectral values at frequencies ω_u); (3) the sought value of θ is the one that corresponds to the best match between the two spectra. The results are shown in Fig. 3 for the same signal pair used earlier.

Comparison

The values in Figs. 1, 2, and 3 were obtained for the same signal pair. The computed stretching factors are (a) short-time cross correlation $\theta = 0.00623$ ($\pm 5\%$ for different window widths), (b) amplitude-adjusted time-stretched cross correlation $\theta = 0.00627$; and (c) cross correlation of the frequency-stretched spectra $\theta = 0.00628$. From Eq. (1), the stretching factor is $\theta = \Delta V/V$, hence, θ-values measured in this example indicate that a 0.6% velocity change has taken place in the medium between signals A and B (i.e., a 1.4 kPa isotropic stress increase).

Experimental Study: P Wave Velocity in Dry Sand

The purpose of this experimental study is to explore the potential of coda wave analysis in detecting very small velocity changes. We study two cases: velocity changes due to small changes in effective stress, and the more challenging case of velocity changes during creep aging.

Experiment Design

Specimen

A cylindrical soil specimen (radius $R = 17.5$ mm and height $H = 74.4$ mm) is confined by a latex membrane and subjected to isotropic stress in a triaxial chamber (Fig. 4). The soil selected for this study is Ottawa-20/30 sand (quartzitic; median grain size $d_{50} = 0.72$ mm;

J. Geotech. Geoenviron. Eng. 2013.139:1504-1511.

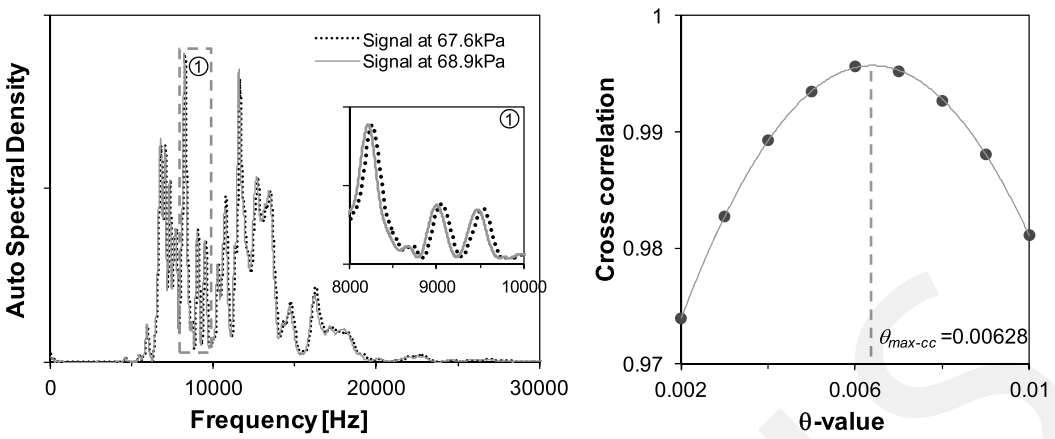

Fig. 3. Stretched spectra: full-signal-based determination of the stretching factor θ in the frequency domain

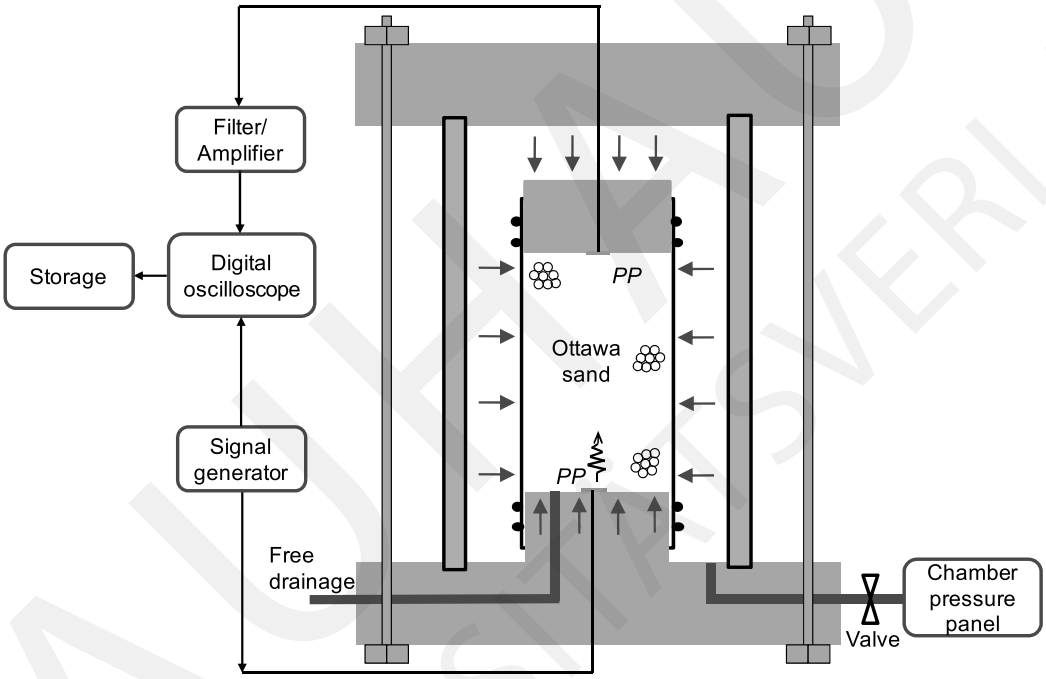

Fig. 4. Experimental configuration; stiffness evolution in uniform quartzitic dry sand subjected to isotropic gas confinement (as illustrated with the arrows); P waves are generated and detected using piezopads (*PP*)

coefficient of uniformity $C_u = 1.2$; roundness $R = 0.9$; sphericity $S = 0.9$; packing $e_{\max/\min} = 0.742/0.502$).

Testing Procedure

The load history involves three stages. (1) Loading: the confining stress is gradually increased from 0 kPa until 68.9 kPa, in 1.4 kPa steps (note that the confining stress is actually measured in PSI and converted into kPa; the loading is increased from 0 to 10 psi, in 0.2 psi steps). (2) Creep: the applied confining stress is held constant at 68.9 kPa for approximately 8 h. (3) Unloading: the confining stress is gradually decreased back to 0 kPa in -1.4 kPa steps.

Wave Propagation

Piezopads are installed on the caps of the sample to monitor the evolution of P wave velocity in the sand. Received wave signals are recorded at each loading step and periodically during creep.

Data Reduction

The reference first arrival travel time is determined for the signal gathered at isotropic confinement $\sigma' = 34.5$ kPa in this study, where the first arrival is very clear. All other travel times are compared to this one through consecutive stretching coefficients $t_B = t_A(1 + \theta)$, as discussed earlier.

Test Results

The complete cascade of 110 signals recorded during loading, creep, and unloading stages is shown in Fig. 5. The horizontal axis shows the wave travel time and the vertical axis shows the waveforms cascading in chronological sequence from the beginning of the test until the end. Signal amplitude is captured with gray intensity: white denotes waveform peaks and black denotes troughs. Travel times shorten during loading and creep. Particularly during creep, differences in first arrival times cannot be visually distinguished (in

J. Geotech. Geoenviron. Eng. 2013.139:1504-1511.

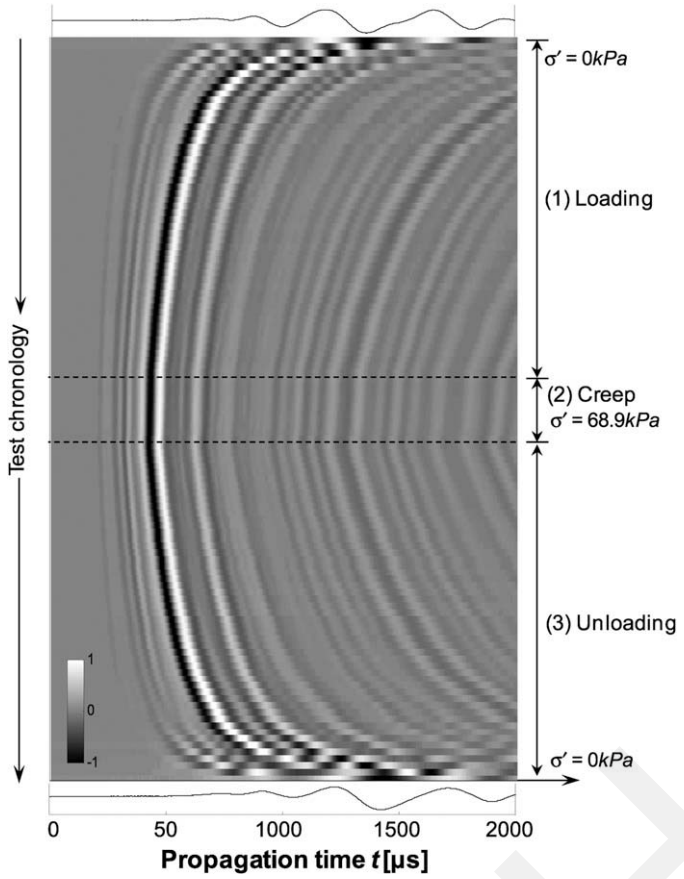

Fig. 5. Cascade of received wave signals (in total 110 waveforms; the first and last signals are shown at the top and bottom of the signal cascade); the signal amplitude is illustrated in gray intensity, where white represents peaks and black troughs; (1) loading from self-weight $\sigma' = 0$ kPa to $\sigma' = 68.9$ kPa in $\Delta\sigma' = 1.4$ kPa (0.2 psi) increments; (2) creep at constant confining pressure ($\sigma' = 68.9$ kPa); (3) unloading from $P = 68.9$ kPa to self-weight in $\Delta\sigma' = -1.4$ kPa drops; note the increasing gradient of peaks and troughs in wave codas recorded during the creep stage

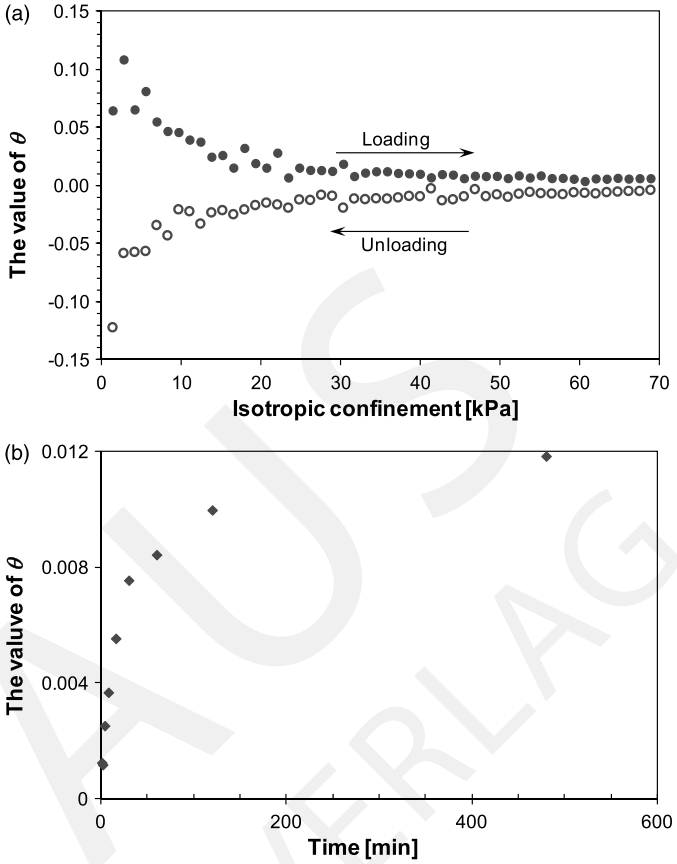

Fig. 6. Computed θ values (a) during loading and unloading; (b) during creep

fact, they may be smaller than the sampling interval $\Delta t = 0.25$ μs). However, codas show clear time shifts of peaks and troughs, even during the creep stage.

Fig. 6 shows computed θ values for all consecutive signals using the short-time cross-correlation method. Computed P wave velocities during the three experimental stages are then presented in Fig. 7(a). The initial P wave velocity of the specimen under self-weight is 110.0 m/s. Velocity increases with confining stress to reach 292.2 m/s at 68.9 kPa, and decreases during unloading to a final value of 119.0 m/s. Fig. 7(b) shows the time-lapse velocity change for the Ottawa sand specimen during creep under constant isotropic confinement $\sigma' = 68.9$ kPa (note that the velocity is plotted in high resolution). The increase in velocity due to creep is $\Delta V_P \approx 1.5\%$ within 8 h of monitoring, and velocity changes as small as $\Delta V/V < 0.1\%$ are detected between consecutive signals.

Analysis

Velocity-Stress Response

Velocity-Stress Power Relationship

A power-type Hertzian relationship adequately captures velocity stress in soils (Santamarina et al. 2001)

$$V = \alpha \left(\frac{\sigma'}{\sigma'_{\text{ref}}} \right)^{\beta} \tag{2}$$

where α is the soil wave velocity when σ' equals the reference effective stress σ'_{ref}, and β reflects the dependency of velocity on effective stress σ' in the direction of wave propagation. Wave velocities measured at $\sigma' > 10$ kPa are well fitted with Eq. (2) ($\alpha = 93.0$ m/s and $\beta = 0.27$ during loading, and $\alpha = 98.0$ m/s and $\beta = 0.26$ during unloading). Stiffness hysteresis in quartzitic sands subjected to isotropic loading is easily missed in standard visual signal interpretation. However, this is clearly seen in the coda-based data plotted in Fig. 7(a). This hysteresis behavior may possibly be due to slight changes in fabric and/or interparticle contact behavior.

Self-Weight Effect

Measured velocities at lower confinement stresses (i.e., $< \sim 10$ kPa in this study) deviate from the velocity-stress power relationship. This is because soil self-weight induces an inhomogeneous stress distribution inside of the specimen that has not been captured in the velocity-stress relationship.

At zero confinement ($\sigma' = 0$), the vertical effective stress in the sediment increases linearly with depth due to self-weight, from $\sigma'_z = \sigma_{\text{cap}}$ (top cap at $z = 0$) to $\sigma'_z = \sigma_{\text{cap}} + \gamma_s H$ at the bottom of the specimen (height H and unit weight γ_s). This stress field must be accounted for during the analysis of P wave velocity data obtained at very low confining stress. Travel time is an integral of slowness $1/V_z$ along the specimen height H

J. Geotech. Geoenviron. Eng. 2013.139:1504-1511.

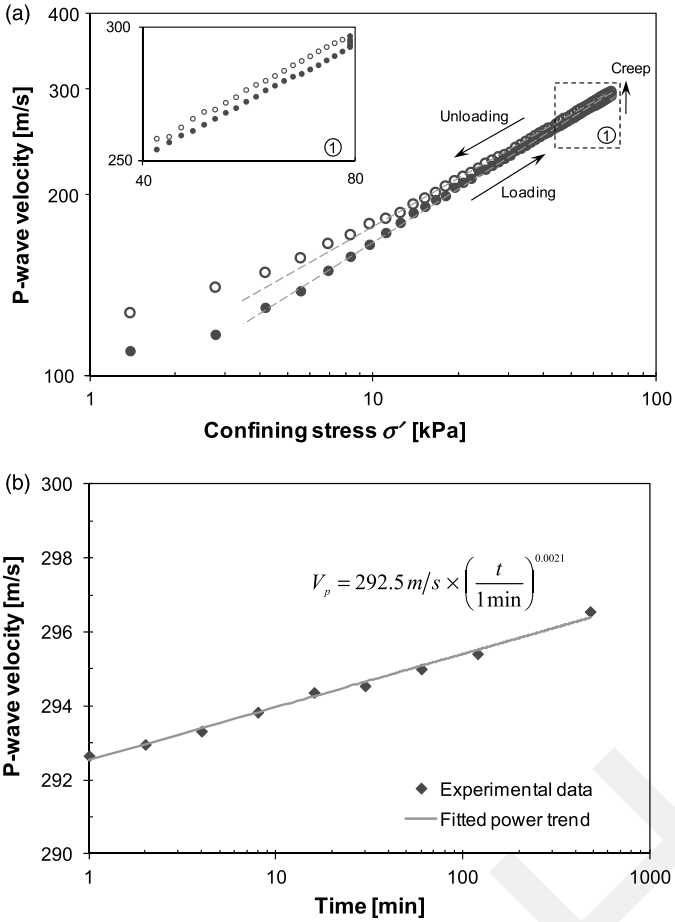

Fig. 7. P wave velocity evolution (a) as a function of applied confining stress σ' during loading (solids) and unloading (circles) stages; the insert amplifies changes in stiffness due to creep during sustained loading $\sigma' = 68.9$ kPa; (b) as a function of time during creep (diamonds) at constant confining stress $\sigma' = 68.9$ kPa

$$t = \int_0^H \frac{dz}{\alpha\left(\frac{\sigma'_z}{\sigma'_{\text{ref}}}\right)^{\beta}} = \int_0^H \frac{dz}{\alpha\left(\frac{\sigma'_0 + \sigma_{\text{cap}} + \gamma_s z}{\sigma'_{\text{ref}}}\right)^{\beta}}$$

$$= \frac{1}{\alpha\gamma_s(1-\beta)}\left[\left(\frac{\sigma'_0 + \sigma_{\text{cap}} + \gamma_s H}{\sigma'_{\text{ref}}}\right)^{1-\beta} - \left(\frac{\sigma'_0 + \sigma_{\text{cap}}}{\sigma'_{\text{ref}}}\right)^{1-\beta}\right] \tag{3}$$

where σ'_0 is the applied isotropic confining stress. Travel times determined using coda analysis are plotted as a function of isotropic confining stress in Fig. 8. We concluded that when self-weight is accounted for at low confining stress, the power velocity-stress relation [Eq. (2)] properly reproduces the complete data set [cf. Figs. 7(a) and 8].

If self-weight is neglected, predicted travel times t_p are much longer than measured times-t_m at low confinement (Fig. 8). For a given sediment with parameters α and β, the ratio t_p/t_m is a function of the ratio between self-weight and confining stress, $\gamma_s H/(\sigma'_0 + \sigma_{\text{cap}})$. From Eq. (3)

$$\frac{t_p}{t_m} = \frac{\frac{\gamma_s H}{\sigma' + \sigma_{\text{cap}}}(1-\beta)}{\left(1 + \frac{\gamma_s H}{\sigma'_0 + \sigma_{cap}}\right)^{1-\beta} - 1} \tag{4}$$

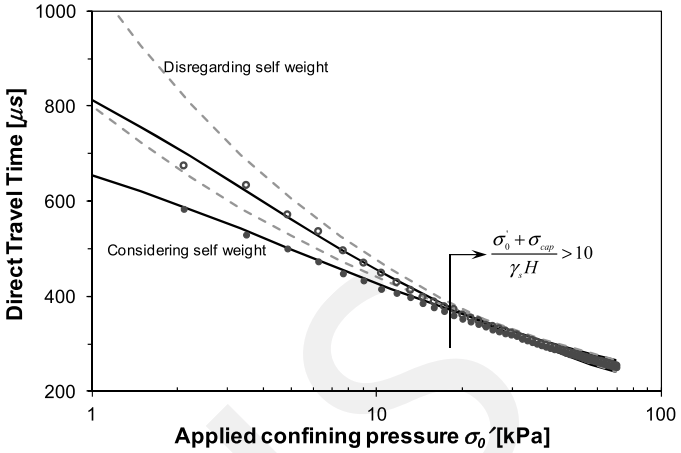

Fig. 8. Predicted (solid lines: considering the self-weight effect; dashed lines: disregarding the self-weight effect) versus measured (dots) direct travel time as a function of applied confining pressure σ'_0; accounting for self-weight requires time integration along the specimen

For $\beta = 0.25$, the error in travel time due to self-weight is less than 1% when $(\sigma'_0 + \sigma_{\text{cap}})/(\gamma_s H) > 10$. In other words, the effect of self-weight on soil stiffness can be negligible when the confining stress is at least 10 times larger.

Velocity-Stress Parameter β and the Stretching Factor θ

The stretching factor θ between two consecutive signals gathered at stresses σ'_A and σ'_B reflects the stress-dependent velocity change. Indeed, combining Eqs. (1) and (2) yields

$$\theta = 1 - \left(\frac{\sigma'_B}{\sigma'_A}\right)^{\beta} \tag{5}$$

This result anticipates the ability of coda waves to resolve changes in mean stress smaller than 1% in uncemented sands (assuming $\theta = 0.001$ and $\beta = 0.25$).

Creep in Dry Sandy Specimen

Computed wave velocities in the sand specimen tested during the creep stage follow a power law with time, as shown in Fig. 7(b)

$$V_{\text{P}} = a\left(\frac{t}{t_{\text{ref}}}\right)^{b} = 292.5\left(\frac{t}{1\ \text{min}}\right)^{0.0021} \tag{6}$$

where the parameter a is the P wave velocity under constant confinement at the reference time t_{ref} (in this case, $t_{\text{ref}} = 1$ min), and the exponent b reflects the rate of creep-dependent stiffening. Both a and b are experimentally determined parameters, and are inherently governed by confining conditions and sediment characteristics.

The creep strain rate $\dot{\varepsilon}$ of a particulate medium at constant effective stress is a function of stress σ' and time t (Singh and Mitchell 1968; Mitchell and Soga 2005)

$$\dot{\varepsilon} = k\left[\frac{\sigma'}{\sigma'_{\text{ref}}}\right]^{m}\left[\frac{t_{\text{ref}}}{t}\right]^{n} \tag{7}$$

where k, m, and n are sediment-dependent parameters, and σ'_{ref} and t_{ref} are the reference stress and time. At the particle level, the tangential normal stiffness E_{T} in a Hertzian system can be related to the

J. Geotech. Geoenviron. Eng. 2013.139:1504-1511.

axial strain ε_z as (simple cubic packing, Richart et al. 1970; Cascante and Santamarina 1996)

$$E_T = \frac{G_m}{1 - \nu_m} \varepsilon_Z^{1/2} \tag{8}$$

where G_m and ν_m are the shear modulus and Poisson's ratio of the material that makes the grains. The strain at time t is obtained by integrating Eq. (7), and it is replaced in Eq. (8) to obtain a general expression for the evolution of velocity during soil creep as a function of stress σ' and time t

$$V_P = \sqrt{\frac{E}{\rho}} = \sqrt{\frac{G_m}{\rho(1-\nu_m)}} \left(\frac{k t_{ref}}{1-n}\right)^{\frac{1}{4}} \left(\frac{\sigma'}{\sigma'_{ref}}\right)^{\frac{m}{4}} \left(\frac{t}{t_{ref}}\right)^{\frac{1-n}{4}} \tag{9}$$

Most soils have an n value that ranges between 0.75 and 1 (Singh and Mitchell 1968; lower values reported in Singh and Mitchell 1969; Campanella and Vaid 1974). The fitted n value for the quartzitic sand tested in this study is $n = 0.9916$ [cf. Eqs. (6) and (9)], indicating a slow velocity change with time under a confinement of 68.9 kPa.

Discussion: Underlying Assumptions in Coda Analysis

Basic coda analysis presumes that changes in the medium cause identical proportional velocity changes $\Delta V/V$ on all wave paths and propagation modes. In particular, P wave and S wave velocities must be equally affected by the process, that is, V_P/V_S remains constant and θ values for P and S components are identical, θ_P/θ_S. This condition applies to dry or unsaturated soils. In saturated soils, the P wave velocity is primarily controlled by the fluid bulk modulus; thus, only a minor increase in $\Delta V_P/V_{P_0}$ takes place during loading, while the change in $\Delta V_S/V_{S_0}$ can be large.

We highlight that basic coda analysis reveals the relative stretching factor between two waveforms. An absolute wave travel time is required as reference value to determine velocity and velocity changes. Typically, the waveform with the clearest first arrival is selected to determine the reference travel time.

Conclusions

Slight velocity changes in a soil specimen that cause undetectable changes in the first arrival may be measured using coda wave analysis. Values smaller than $\Delta V/V < 0.1\%$ were detected in this study.

The proportional change in velocity is mathematically equal to the stretching factor $\theta = \Delta V/V$. There are robust signal processing algorithms to determine the stretching factor θ between consecutive signals. They involve the cross correlation of either (1) short-time windows, (2) time-stretched signals, or (3) frequency-stretched spectra.

Basic coda wave analysis applies to systems with homogeneous velocity changes and constant V_P/V_S ratio. This is the case in dry and partially saturated soils.

The high velocity resolution attained with coda wave analysis allows for the determination of wave velocities during small stress changes, creep, diagenesis, and aging, where subtle contact-level processes can only be detected by high resolution signal interpretation. Coda wave analysis can resolve a $\Delta\sigma'/\sigma < 1\%$ change in mean effective stress.

Self-weight induces an inhomogeneous stress distribution inside of a specimen. Data reduction must consider gravity effects when the boundary effective stress is less than 10 times the gravity-induced stress.

In agreement with existing creep models, experimental results show that velocity increases during soil creep under constant confinement and follows a power law as a function of time. The exponent can be readily measured using coda wave analysis even when stable quartzitic sands are tested for a relatively short duration.

Acknowledgments

Support for this research was provided by the Chevron-managed DOE/NETL Methane Hydrate Project DE-FC26-01NT41330 and Gulf of Mexico Gas Hydrate Joint Industry Project; R&D Program Geotechnologien funded by the German Research Foundation and German Ministry of Education and Research (Grant 03G0636B), as well as the European Regional Development Fund (Grant FKZB715-09010). Additional funding was provided by the Goiuzeta Foundation.

References

Aki, K. (1969). "Analysis of seismic coda of local earthquakes as scattered waves." *J. Geophys. Res.*, 74(2), 615–631.

Aki, K., and Chouet, L. B. (1975). "Origin of coda waves: Source, attenuation, and scattering effects." *J. Geophys. Res.*, 80(23), 3322–3342.

Arroyo, M., Muir Wood, D., Greening, P. D., Medina, L., and Rio, J. (2006). "Effects of sample size on bender-based axial G_0 measurements." *Geotechnique*, 56(1), 39–52.

Cascante, G., and Santamarina, J. C. (1996). "Interparticle contact behavior and wave propagation." *J. Geotech. Engrg.*, 122(10), 831–839.

Campanella, R. G., and Vaid, Y. (1974). "Triaxial and plane strain creep rupture of an undisturbed clay." *Can. Geotech. J.*, 11(1), 1–10.

Gret, A. A. (2004). "Time-lapse monitoring with coda wave interferometry." Ph.D. thesis, Colorado School of Mines, Golden, CO.

Lee, J. S., and Santamarina, J. C. (2005). "Bender elements: Performance and signal interpretation." *J. Geotech. Geoenviron. Eng.*, 131(9), 1063–1070.

Mitchell, J. K., and Soga, K. (2005). *Fundamentals of soil behavior*, 3rd Ed., Wiley, Inc., New York.

Otheim, T. L., Adam, L., van Wijk, K., Batzle, M. L., McLing, T., and Podgorney, R. (2011). "CO_2 sequestration in basalt: Carbonate mineralization and fluid substitution." *The Leading Edge*, 30(12), 1354–1359.

Richart, F. E., Jr., Hall, J. R., and Woods, R. D. (1970). *Vibration of soils and foundations*, Prentice Hall, Englewood Cliffs, NJ.

Santamarina, J. C., and Fratta, D. (2005). *Discrete signals and inverse problems: An introduction for engineers and scientists*, Wiley, Chichester, U.K.

Santamarina, J. C., Klein, K. A., and Fam, M. A. (2001). *Soils and waves: Particulate materials behavior, characterization and process monitoring*, Wiley, Chichester, U.K.

Schurr, D. P., Kim, J. Y., Sabra, K. G., and Jacobs, L. J. (2011). "Damage detection in concrete using coda wave interferometry." *NDT Int.*, 44(8), 728–735.

Shapiro, N. M., Campillo, M., Stehly, L., and Ritzwoller, M. H. (2005). "High-resolution surface-wave tomography from ambient seismic noise." *Science*, 307(5715), 1615–1618.

J. Geotech. Geoenviron. Eng. 2013.139:1504-1511.

Sens-Schönfelder, C., and Wegler, U. (2006). "Passive image interferometry and seasonal variations of seismic velocities at Merapi Volcano, Indonesia." *Geophys. Res. Lett.*, 33(21), L21302.

Singh, A., and Mitchell, J. K. (1968). "General stress-strain-time function for soils." *J. Soil Mech. and Found. Div.*, 94(1), 21–46.

Singh, A., and Mitchell, J. K. (1969). "Creep potential and creep rupture of soils." *Proc., 7th Int. Conf. on Soil Mechanics and Foundation Engineering*, Socieded Mexicana de Mecanica de Suelos, Mexico City, 379–384.

Snieder, R. (2006). "The theory of coda wave interferometry." *Pure Appl. Geophys.*, 163(2–3), 455–473.

Snieder, R., Grêt, A., Douma, H., and Scales, J. (2002). "Coda wave interferometry for estimating nonlinear behavior in seismic velocity." *Science*, 295(5563), 2253–2255.

Wuttke, F., Asslan, M., and Schanz, T. (2012). "Time-lapse monitoring of fabric changes in granular materials by coda wave interferometry." *J. ASTM Geotech Test.*, 35(2), 353–362.

Youn, J. U., Choo, Y. W., and Kim, D. S. (2008). "Measurement of small-strain shear modulus G_{max} of dry and saturated sands by bender element, resonant column, and torsional shear tests." *Can. Geotech. J.*, 45(10), 1426–1438.

J. Geotech. Geoenviron. Eng. 2013.139:1504-1511.

Geotechnical Testing Journal, Vol. 35, No. 5
Paper ID GTJ103727
Available online at: www.astm.org

F. Wuttke,[1] *K. Markwardt,*[2] *and T. Schanz*[3]

Dispersion Analysis in Geotechnical Laboratory Tests: Time-frequency and Time-scale Signal Transforms

ABSTRACT: Signal processing techniques are very important for the analysis of dispersion characteristics in geotechnical laboratory applications. The scope of this paper includes the study of advanced time-frequency and time-scale methods with regard to the development of an efficient method of group velocity determination based on the time-frequency behavior of propagating wave fields. The paper analyzes different time-frequency and time-scale transform methods for further use in group velocity determination as alternatives to conventional techniques. Besides the alternative itself, the presented scheme overcomes some existing problems of conventional methods in velocity determination. The advantages and disadvantages of the time-frequency and time-scale methods are presented and discussed. Finally, the applicability of given time-frequency and time-scale methods is validated by synthetic and experimental data.

KEYWORDS: small strain stiffness, time-frequency signal transform, time-scale signal transform, wave field analysis

Introduction and Motivation

The application of wave field analysis to geotechnical laboratory experiments has been in use for a while (Santamarina and Fratta 2005). Most publications focus on the detection of realistic travel times of shear or compression waves (Arulnathan and Boulanger 1998; Jovicic et al. 1996; Ismail and Rammah 2005; Youn et al. 2008). Often only a first break arrival method is proposed, although the detection of the first arrival in the wave field is often a nontrivial task; see Fig. 1. In that figure it is obvious that different crossover points between the normal and the inverse polarized signal exist. Different phenomena, such as near field effects, P-wave noise, and others, sometimes compounded, can appear, so that the choice of a first arrival becomes very subjective.

For improving the objectivity of the method, some automated signal treatment procedure would be welcome. Some studies exist that propose different cross correlation methods (Arulnathan and Boulanger 1998; Greening and Nash 2004). However, the application of cross correlation methods based on impulse signals (Arunathan and Boulanger 1998) is non-trivial because of the dispersive behavior of waves and often insufficient signal coherence. In an attempt to overcome these problems, a more promising method was presented by Greening and Nash (2004). Using a Chirp signal, they successfully applied the phase difference method, in that sufficient coherence between the signals could be shown. The phase difference method had also the advantage of being more general in scope: a whole dispersion curve (phase velocity versus frequency) is obtained, not a single velocity value.

However, the phase difference method suffers from uncertainties and resolution problems in the low and high frequency ranges outside the excitation range. This behavior is well known from the application of the phase difference method in spectral analysis of surface waves (Nazarian 1984). A chain of wrong results can follow from the wrong initial detection of phase changes (Nazarian et al. 1994; Yuan and Nazarian 1993; Wuttke 2005).

Figure 2 illustrates the problems encountered during application of a phase difference method of propagating sweep signals. The experiment shown in Fig. 2 was done in a triaxial cell with a transmitter and a receiver in the top and bottom plates. The signal itself is a linear sweep signal with a starting frequency of 1 kHz and an end frequency of 20 kHz. A large coherence value was confirmed, but strong signal noise outside of the excited frequency range always exists.

Figure 2(*a*) shows the transmitted and received signals. The second plot shows the coherence between transmitted and received signals. Figure 2(*c*) shows the phase spectra of the cross correlated signal, and the unwrapped phase of those spectra is visible in Fig. 2(*d*). The phase velocity is shown in the last plot. Figure 2(*c*) shows the bad quality of the cross correlated phase function in frequency ranges lower than 5 kHz and higher than 15 kHz. The number of initial phase changes influences the initial rise gradient of the unwrapped phase function, as shown in Fig. 2(*d*). However, the unwrapped phase function is the basis for the value of the phase velocity shown in Fig. 2(*e*).

The major objective of this study is to present a methodology based on time-frequency and time-scale transform methods to reduce or overcome the described problems in dispersion analyses, thus providing a method that is more reliable and less

Manuscript received December 23, 2010; accepted for publication June 4, 2012; published online August 2012.

[1]Modeling in Geomechanics, Bauhaus-Univ. Weimar, 99423 Weimar, Germany (Corresponding author), e-mail: frank.wuttke@uni-weimar.de

[2]Institute of Mathematics and Physics, Bauhaus-Univ. Weimar, 99423 Weimar, Germany, e-mail: klaus.markwardt@uni-weimar.de

[3]Chair of Foundation Engineering, Soil and Rock Mechanics, Ruhr-Univ. Bochum, 44780 Bochum, Germany, e-mail: tom.schanz@rub.de

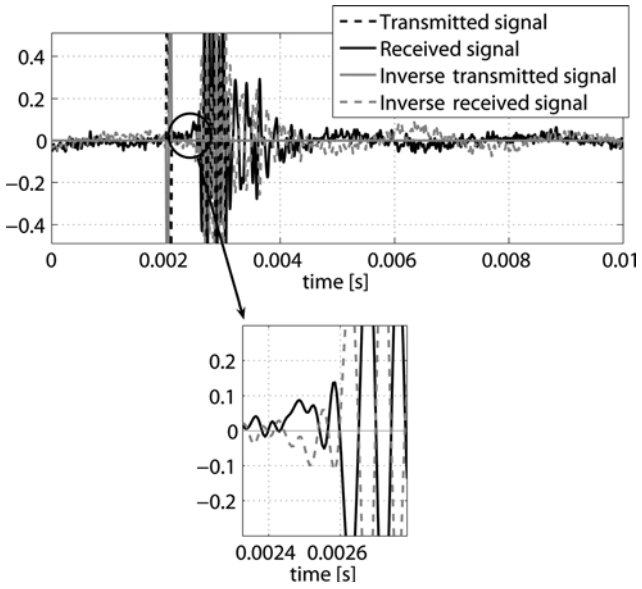

FIG. 1—*Difficulties in first arrival detection by crossover points.*

subjective in the signal processing of dispersion analysis. With the analysis of time-frequency dependence, the group velocity c_{gr} between the transmitted and received signal can be determined. Using the well-known relations between group and phase velocity (e.g., Greening and Nash 2004), the phase velocity then can be determined from the group velocity.

The paper itself contains in the current section an introduction to the topic, its importance to geotechnical laboratory testing, and the objective of the presented investigations in geotechnics. In particular, the development of an objective method with some automated signal treatment procedure is needed in order to overcome the problems with existing methods. In practice, the existing wave-based laboratory signal analysis methods often have the drawback of unreliable results. Besides the already existing method, the investigation focuses on geotechnical non-conventional treatments.

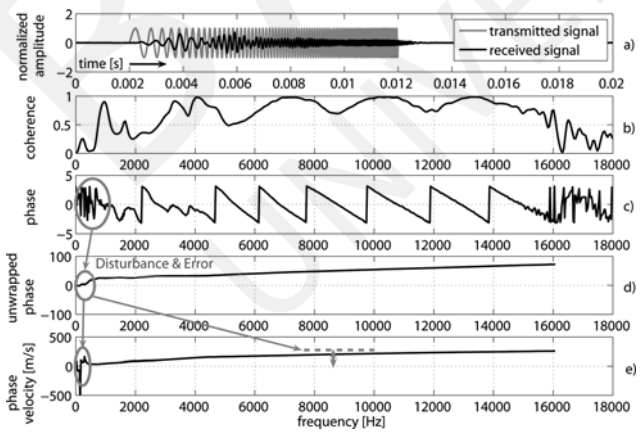

FIG. 2—*Existing low quality of multiples of 2π in low frequency range in phase difference method and the resulting error in the unwrapping phase, as well as the calculated phase velocity.*

Prior to implementing an appropriate time-frequency or time-scale method, one has to study the transform family. Not all methods are able to deliver the same time-frequency sharpness of data density. Therefore, the choice of the right method for further work is very important and valuable. This paper presents the major time-frequency and time-scale transforms with emphasis on their applicability. To compare the different time-frequency and time-scale methods, a common mathematical base is used in the paper and is described in the sections titled "Time-scale Transform Methods" and "Time-frequency Transform Methods."

After the described signal analysis tools are employed, their utility is proven and validated as shown in the section "Determination of Group Velocity by the Use of Time-frequency and Time-scale Methods." Based on the described time-frequency and time-scale methods, a new method of determining the group velocity in geotechnical laboratory tests is presented. The validation is done initially with some synthetic test examples and subsequently with several experimental tests using various granular materials. Finally, the experimental tests are compared with conventional methods, such as first arrival or phase difference methods. The study also explicitly illustrates the strong influence on practical application of the trust interval of the analyzed results.

Time-scale Transform Methods

After first applications in time-frequency analysis during the 1970s (Bath 1974) with short-term Fourier analysis, the wavelet transform as a time-scale transform method was developed during the 1990s. Several authors were using and applying the continuous wavelet transform (Mallat 1998; Santamarina and Fratta 2005; Gucunski and Shokouhi 2004). In practical and theoretical application, the continuous wavelet transform was described in detail (Cattani and Rushchitsky 2007; Allen and Mills 2004). The fast wavelet transform (FWT) is rarely used in foregoing application fields. Furthermore, in the field of non-destructive testing, advanced methods for the time-frequency analysis of non-stationary signals were developed, too. To identify the dispersion characteristics of a signal, different time-frequency signal transforms and time-scale signal transforms were used (Hammond and White 1996; Mallat 1998; Niethammer and Jacobs 2001; Narasimhan and Nayak 2003; Wuttke et al. 2009a; Wuttke et al. 2009b; Wuttke et al. 2010).

The first developments in time-frequency analysis were methods of short-time frequency or Gabor transform. By petroleum seismologists and mathematicians, the basics of the continuous wavelet transform were discovered. Scale and dilatation parameters, instead of the traditional frequency variable, were used in this transform. In wavelet transforms, different problems arise because of the scale of the signal features. In the approaches of Grossmann and Morlet, the wavelet transform uses scaled and translated wavelets in a Hilbert space inner product to convert time-varying signals into functions of two variables. The produced wavelet system $\psi_{[s,\tau]}$ can be interpreted as a multiple copy of the original wavelet ψ rescaled by s and centered around the time shift τ, if the mother wavelet is centered around 0.

Continuous Wavelet Transform

By following the statements given in the Appendix, one can define the associated continuous wavelet transform (CWT) for $s > 0$, $\tau \in \mathbb{R}$, depending on the analyzed wavelet ψ, as

$$W(s,\tau) = W\{f\}(s,\tau) = \frac{1}{\sqrt{s}}\int_{-\infty}^{\infty} f(t)\,\psi^*\left(\frac{t-\tau}{s}\right)dt, \quad s > 0 \quad (1)$$

where:

s = scaling parameter, and

τ = shifting parameter.

The factor $1/\sqrt{s}$ is required in order to normalize the wavelets' respective energy contents. After normalized dilatation and reflection, the CWT (Eq 1) is defined by

$$\Psi_{[s]}(t) = \frac{1}{\sqrt{s}}\psi\left(\frac{-t}{s}\right) \Rightarrow W\{f\}(s,\tau) = \left(f * \Psi^*_{[s]}\right)(\tau) \quad (2)$$

If the CWT is represented as a parameter-dependent convolution (Eq 2), the following definition is achieved via Eq A13:

$$\begin{aligned} F_\tau\{W(s,\tau)\}(\xi) &= F\{f\}(\xi)\cdot F_t\left\{\frac{1}{\sqrt{s}}\psi^*\left(\frac{-t}{s}\right)\right\}(\xi) \\ &= \hat{f}(\xi)\cdot\sqrt{s}\,\hat{\psi}(s\xi) \end{aligned} \quad (3)$$

With the assumption that the amplitude spectra $|\hat{\psi}(\xi)|$ of the mother wavelet ψ is sufficiently localized in a frequency band, the application of CWT for each fixed $s > 0$ equals a frequency band filter.

For the purpose of signal analysis, the CWT is more suitable (Farge 1992), because the CWT keeps redundancies of the signal, and thus there is an increase in the resolution. As described before, there exist real and complex valued types of mother wavelets. The complex valued type is more suitable for the analysis of wave fields. Because of the existence of real and imaginary parts, appearing wavelet oscillations are eliminated when the magnitude of the wavelet transformed result is used. In the presented derivations, the complex Morlet wavelet was chosen as the mother wavelet. The base of this wavelet is a modulated Gauss function, whereas in the following the Morlet wavelet as a standard normed version is used.

$$\begin{aligned} \psi_M(t) &= \pi^{-1/4}e^{j\omega_c t}e^{-(1/2)t^2}, \\ \omega_c &= 2\pi\xi_c,\ |\psi_M(t)|^2 = \frac{e^{-t^2}}{\sqrt{\pi}},\ \|\psi_M\| = 1 \end{aligned} \quad (4)$$

If Eq 4 is used in CWT 1, the original equation (Eq 1) becomes

$$W_{s,\tau} = \pi^{-1/4}s^{-1/2}\int_{-\infty}^{\infty} f(t)\,e^{-j\omega_c[(t-\tau)/s]}e^{-1/2[(t-\tau)/s]^2}dt \quad (5)$$

If one wishes to discretize the transform into a numerical integration, the following substitutions can be made: $t \mapsto t_i = i\cdot\Delta t, \tau \mapsto \tau_b = b\cdot\Delta t, s \mapsto s_a = a\cdot\Delta t, f_i = f(i\cdot\Delta t)$.

$$\begin{aligned} W_{s_a,\tau_b} &= \pi^{-1/4}\left(\frac{\Delta t}{a}\right)^{1/2}\sum_{i=0}^{N-1} f_i e^{j\omega_c[(b-i)/a]}e^{1/2[(b-i)/a]^2}, \\ & a \in \mathbb{N},\ b \in \mathbb{N}_0 \end{aligned} \quad (6)$$

This transform is performed with the new scaling parameter a and time parameter b. The oscillation in the real and imaginary parts and the smooth magnitude $|W_{s,\tau}|$ are shown in Fig. 3, an analysis of a synthetic wave field.

The relation of scale parameters s_a to frequency parameters f_i through the center frequency gives the time-frequency representation or (τ,ξ)-spectrum of the signal f. Despite its good resolution of the time-dependent frequency change, the application of the CWT is time consuming. For records with more than 5000 samples, the CWT becomes impractical. The speed can be increased considerably by mapping the wavelet transform in the Fourier space (Torrence and Compo 1998). A more suitable way involving the use of formula 3 is shown in the following subsection.

During the analysis of time-frequency dependences, one needs to consider the time-frequency uncertainty after Heisenberg. The behavior of inherent duality is a direct consequence of the Fourier transform definition. The time-frequency resolution is always larger than $1/4\pi$. For the case of a sharper time resolution, only a more blurred frequency resolution is obtained, and vice versa. The following equation describes the uncertainty relation between time and frequency:

$$\Delta t\cdot\Delta f \geq \frac{1}{4\pi} \quad (7)$$

Continuous Wavelet Transform in Frequency Domain

To reduce the time and effort involved in the evaluation of the CWT, the CWT can be computed in the frequency domain using a modification of Eq 3. The Morlet wavelet can be represented in the Fourier domain with $\omega = 2\pi\xi$ and $\omega_c = 2\pi\xi_c$ (ξ_c is the center frequency) by

$$\hat{\psi}_M\omega = \pi^{-1/4}\int_{-\infty}^{\infty} e^{-1/2}e^{j\omega_c-\omega t}dt = F_t\left\{\pi^{-1/4}e^{-(1/2)t^2}\right\}2\pi\xi - \xi_c$$

with the argument of $\omega-\omega_c$ instead of ω. Using $\hat{\psi}_M(\omega) = \sqrt{2}\sqrt[4]{\pi}\exp[-(\omega-\omega_c)^2/2]$, Eq 3 is given in frequency scale to $F_\tau\{W(s,\tau)\}(\xi) = \sqrt{2s}\sqrt[4]{\pi}\hat{f}(\xi)\exp[-4\pi^2(s\xi-\xi_c)^2/2]$. With the discretization of s, the new scaling parameter a is provided in time steps Δt, where $s = a\cdot\Delta t$, the frequency representation.

$$(FW)\{f\}(f,a) = \sqrt[4]{\pi}\sqrt{2\Delta t}\sqrt{a}\hat{f}(\xi)\exp\left(-2\pi^2(a\Delta t\xi-\xi_c)^2\right)$$

For every fixed scaling parameter a, a frequency band-pass filtering of the signal f (liked with special co-domain filtering) is performed. In practical applications, the fast Fourier transform is employed to back transform in the time domain $W_{(s,\tau)}$.

Discrete Wavelet Transform

With Eq 2 and the discretization $\tau_k = k\Delta t, t_\nu = \nu\Delta t, f_\nu = f(t_\nu)$, $\Psi_i = \{\Psi_{i,\nu}\} = \{\Psi_{[s_i]}(t_\nu)\}$ under the use of Eq A9, a system of discrete convolution terms is considered.

$$W(s_i,\tau_k) \approx \Delta t(f*\Psi_i)(k) = \frac{\Delta t}{\sqrt{s_i}}\sum_{\nu=0}^{N-1} f(t_\nu)\psi^*\left(\frac{t_\nu-\tau_k}{s_i}\right) \quad (8)$$

The above discrete convolutions are realized under the use of fast Fourier transform. With the use of the Mallat algorithm, the discrete wavelet transform can be realized as an FWT (Markwardt

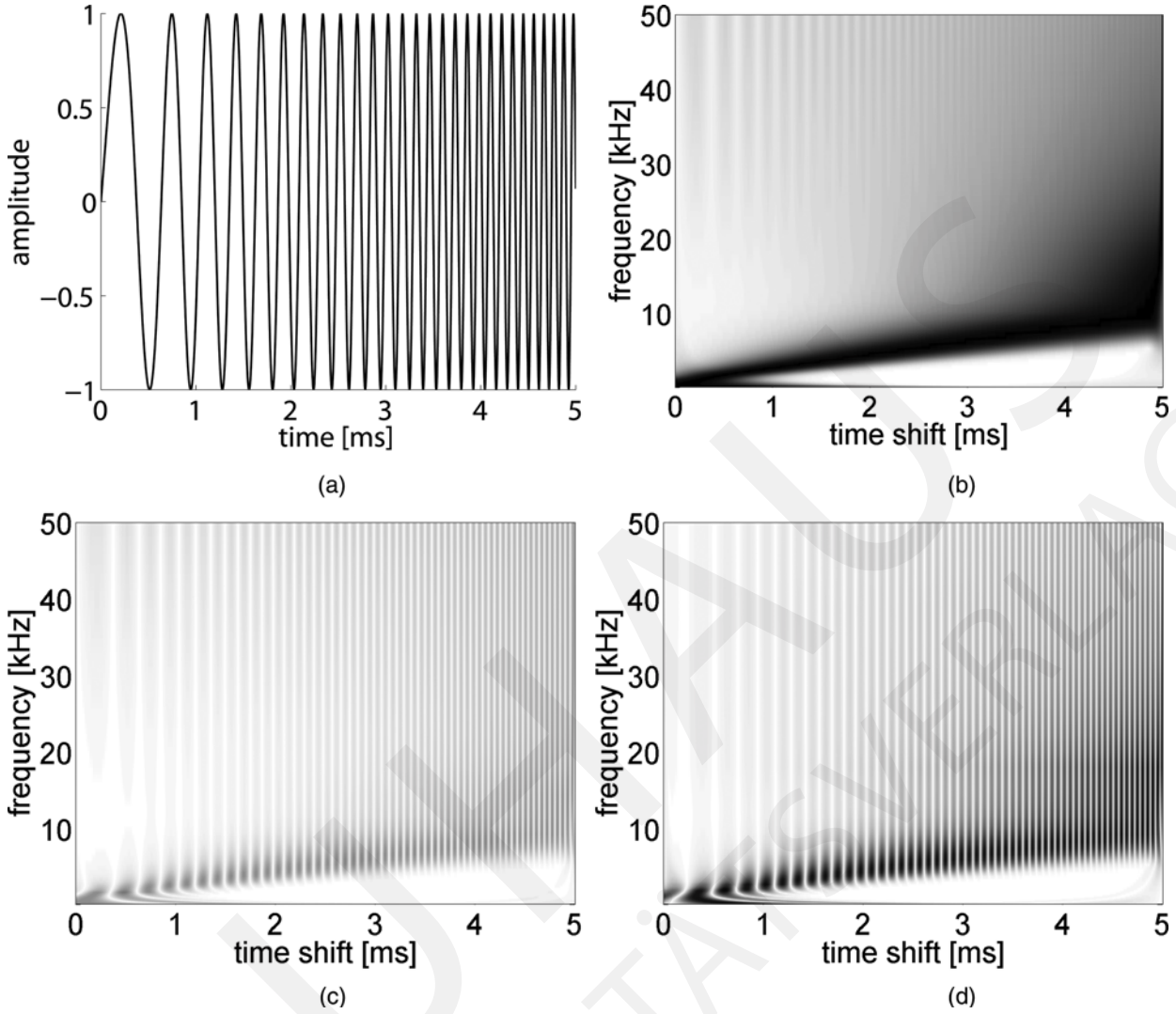

FIG. 3—*Wavelet transform of given sweep signal: (a) time history (sweep), (b) module, (c) real part of $W_{s,\tau}$, and (d) imaginary part of $W_{s,\tau}$.*

2006; Brehm et al. 2005). As is visible in Fig. 4, the discrete wavelet transform shows a crude resolution in opposition to the continuous transform. The grid structure visible in Fig. 4(*c*),

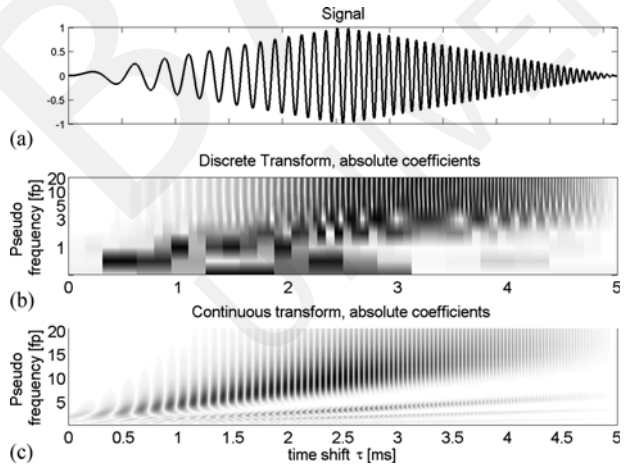

FIG. 4—*Wavelet transformed signal (biorthogonal mother wavelet): (a) time history (sweep), (b) absolute value of discrete wavelet transform, and (c) absolute value of continuous wavelet transform.*

which shows the surface plot of the continuous transform of the signal, is achieved via the use of a real valued biorthogonal mother wavelet.

Time-frequency Transform Methods

The foregoing time scale methods use, similar to the windowed Fourier transform, a scaled window or "atom" to analyze the frequency dependence of the signal. Thus, the resolution of the foregoing transforms depends on the time-frequency resolution of the used window function. In the time-frequency signal transform, there is no dependence of the resolution on the window function. This family is generally known as quadratic time-frequency transforms. One member of this family is the so-called Wigner–Ville distribution (WVD) or Wigner–Ville transform, one of the first time-frequency transforms. In the analysis of pure monochromatic waves or linear chirps (sweep signals), the Wigner–Ville transform is one of the most optimal methods.

In contrast to short-time Fourier transforms, in which small overlapping windows are the basis of analysis, the WVD is a Fourier transform with respect to τ in $x[t + (\tau/2)]x^*[t - (\tau/2)]$, which

is the inner product described by the current autocorrelation function. The autocorrelation is the inverse Fourier transform of the energy density $S_{xx}^{E}(\xi)$ after the theorem of Parseval (Kiencke et al. 2008).

$$r_{xx}^{E}(\tau) = \int_{-\infty}^{\infty} X(\xi)\, e^{j2\pi\xi\tau} X^{*}(\xi) d\xi = F_{\xi}^{-1}\left\{S_{xx}^{E}(\xi)\right\} \tag{9}$$

To determine the amount of similarities in a time and frequency shifted signal relative to the original signal, the shift is separated into two symmetric parts before and after the time or frequency point. This two-dimensional Fourier transform regarding the time and frequency shift is the WVD. The WVD corresponds to a time- and frequency-dependent power spectral density,

$$W_{xx}(t,\xi) = F_{\tau}\left\{x\left(t+\frac{\tau}{2}\right)x^{*}\left(t-\frac{\tau}{2}\right)\right\} \tag{10}$$

regarding the time shift

$$W_{xx}(t,\xi) = \int_{-\infty}^{\infty} \underbrace{\int_{-\infty}^{\infty} A_{xx}(\tau,\vartheta) e^{-j2\pi\vartheta t} d\vartheta}_{x\left(t+\frac{\tau}{2}\right)x^{*}\left(t-\frac{\tau}{2}\right)}\; e^{-j2\pi\xi\tau} d\tau \tag{11}$$

or regarding the frequency shift

$$W_{xx}(t,\xi) = \int_{-\infty}^{\infty} \underbrace{\int_{-\infty}^{\infty} A_{xx}(\tau,\vartheta) e^{-j2\pi\xi\tau} d\tau}_{x\left(t+\frac{\vartheta}{2}\right)x^{*}\left(t-\frac{\vartheta}{2}\right)}\; e^{-j2\pi\vartheta t} d\vartheta \tag{12}$$

In numerical applications, the discrete WVD is used by substituting $t = n \cdot t_S$, where t_S is the sample time and $\xi = k\xi_s/N$, where ξ_s is the sample frequency to

$$W_{xx}(n,k) = 2 \sum_{m=-(N-1)}^{N-1} x(n+m)x^{*}(n-m)\, \exp(-j4\pi km/N) \tag{13}$$

The resolution of the WVD is documented in Fig. 5. It is visible that the method is well suited to image linear time-frequency dependent signals, even in the lower or higher frequency range.

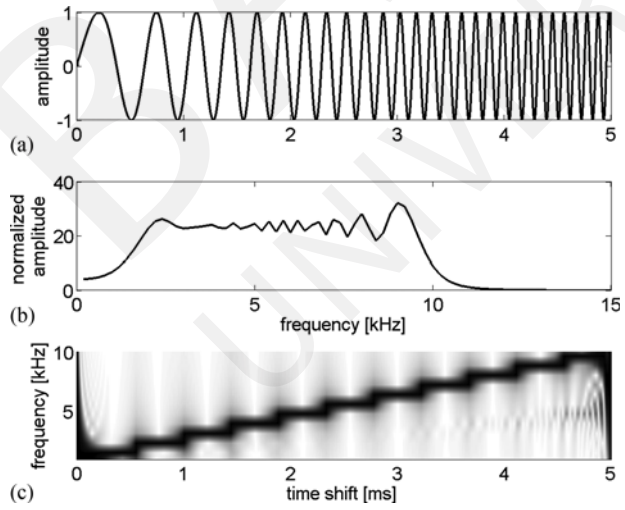

FIG. 5—*Wigner–Ville transform of given sweep signal: (a) time history (sweep), (b) magnitude of the frequency spectra, and (c) time-frequency dependent module (magnitude).*

The same sweep signal as in Fig. 3 was used during the simulation. In addition to the WVD, several other types of time-frequency signal transform methods exist. Further conclusions and derivations related to quadratic transforms and contained types are given in the cited references (Kiencke et al. 2008; Hammond and White 1996; Mallat 1998; Huerta-Lopez et al. 2000).

Determination of Group Velocity via Time-frequency and Time-scale Methods

The outcome of both time-scale and time-frequency transform methods is the imaging of the time-frequency signature of the signal. Via examination of this signature, the group velocity can be determined by comparing the center times and frequencies of the time-frequency surface plot (Fig. 6).

Based on the specific time-frequency and time-scale transforms, the frequency bands (Eq 5) or sample shifts (Eq 13) are used to detect the time-frequency behavior of a signal. The presented velocity analysis is based on center or peak points of compared small wave groups in terms of time and frequency. Therefore, the determined velocity is a group velocity and not a phase velocity. The proposed analysis uses the determined time shift between transmitted and received signals Δt at the relevant center frequency and the distance between the receivers Δs. Based on that information, the group velocity $c_{gr} = \Delta s/\Delta t$ (Fig. 6) is examined at every frequency. The absolute value of the group velocity spectra is mathematically linked with the phase velocity of the wave train.

Validation of the Suggested Approach

To validate the applicability of the proposed approach, two synthetic and different laboratory examples are analyzed. A schematic setup of the experimental devices was presented by Wuttke et al. (2010). For the first synthetic example, a linear sweep signal was used that propagated along a wave path length of 0.2 m at a

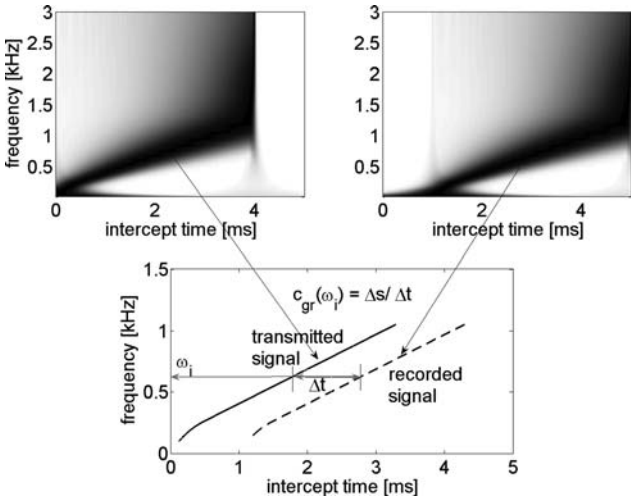

FIG. 6—*Time-frequency dependence of transmitted and received signals and determination of the group velocity c_{gr}.*

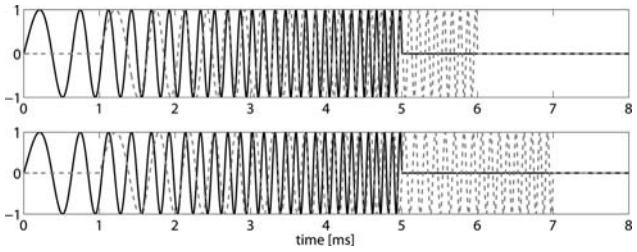

FIG. 7—*The given synthetic sweep signals for (a) constant velocity and (b) a stretched signal due to the dispersive behavior of the velocity.*

constant wave velocity of 200 m/s. The wave propagates without dispersion; this means all frequencies in the signal should be shifted by the same time delay (see the upper plot of Fig. 7).

The expected output of the synthetic test gives information about the ability of the analyzed time-frequency and time-scale transforms. As result of this case, the numerical dispersion induced by the methods can be analyzed. It is visible from Fig. 8 that the given constant wave velocity of 200 m/s is perfectly retrieved by the WVD and the wavelet transform (WT). The methods show no numerical dispersion in the analyzed signal. The resolution of the WT in the lower frequency range is much more stable and accurate for this synthetic example than the WVD, but in general both methods are able to determine the right velocity over the complete frequency range.

The second synthetic example considers a decrease of wave velocity from 200 m/s at 1 kHz to 100 m/s at 10 kHz, whereby dispersion during wave propagation is simulated (see the lower

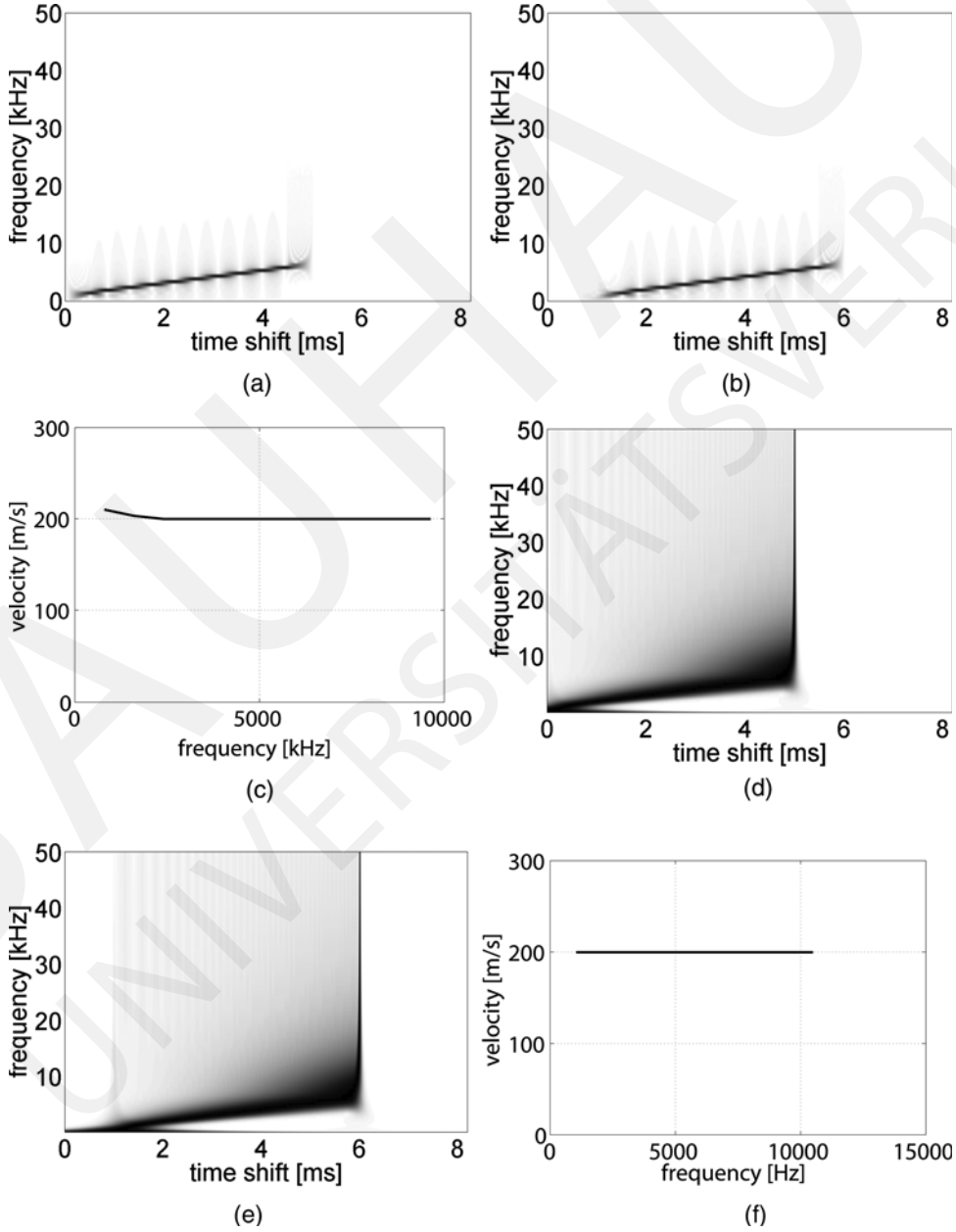

FIG. 8—*Wigner–Ville distribution (WVD) and wavelet transform (WT) of given propagating synthetic sweep signal of constant velocity: (a) module of the transmitted signal, WVD; (b) module of the transmitted signal, WT; (c) module of the received signal, WVD; (d) module of the received signal, WT; (e) group velocity, WVD; and (f) group velocity, WT.*

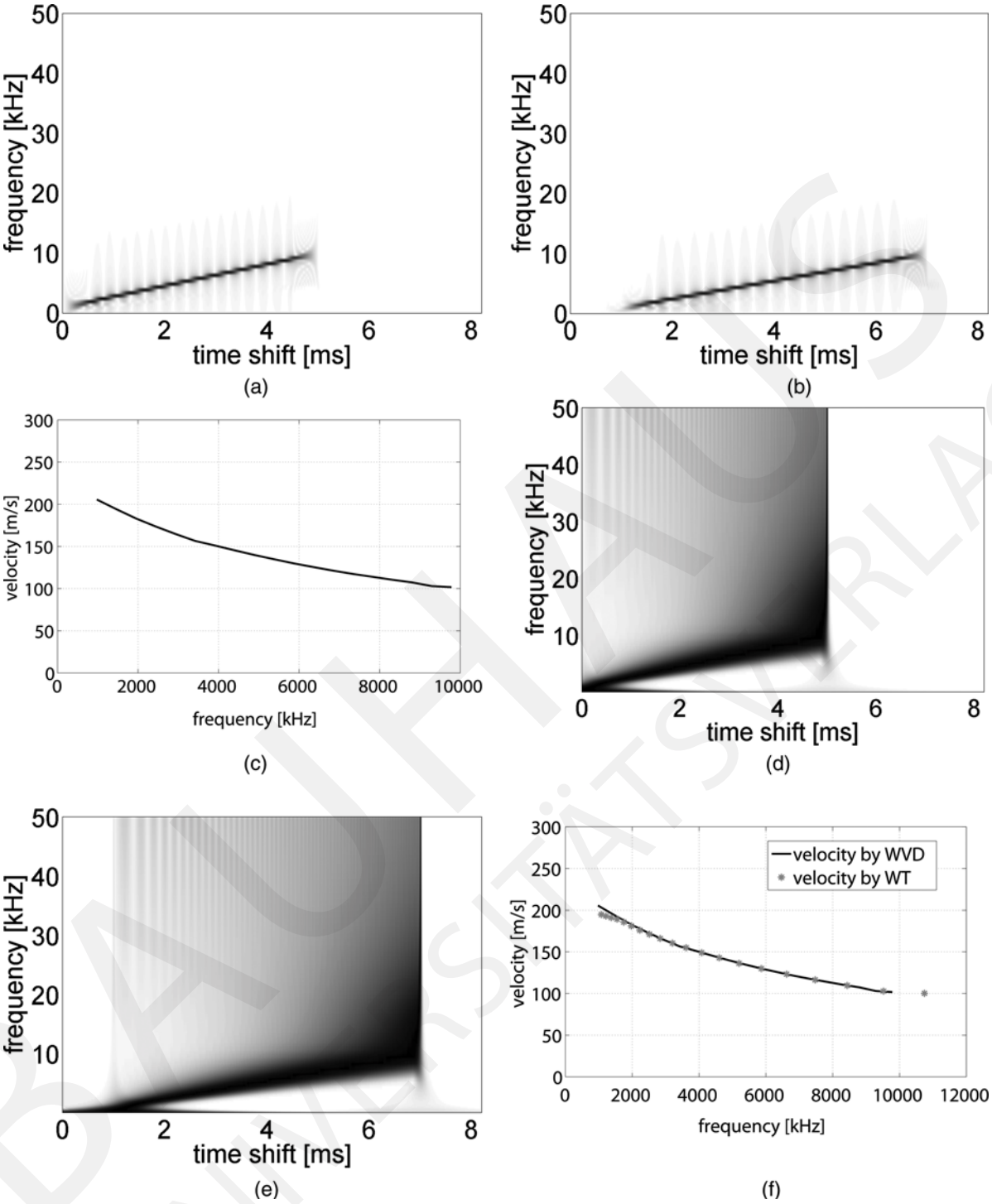

FIG. 9—*Wigner–Ville distribution (WVD) and wavelet transform (WT) of given propagating synthetic sweep signal of dispersive velocity: (a) module of the transmitted signal, WVD; (b) module of the transmitted signal, WT; (c) module of the received signal, WVD; (d) module of the received signal, WT; (e) group velocity, WVD; and (f) group velocity, WT, compared to the WVD group velocity.*

plot of Fig. 7). The distance between receiver and transmitter is the same as in the preceding example. The expected output of this second synthetic test is the ability of the time-frequency and time-scale transforms to analyze dispersion in signals. If one assumes the "transmitting" input signal is a linear sweep over a time of 0.005 s in a frequency range of 1 to 10 kHz, the "recorded" output signal is a linear sweep lasting 0.006 s for the constant velocity signal and 0.007 s as a stretched signal for the dispersive velocity signal, both in the same frequency range. The output dispersion should be a nonlinear dispersion function. Both the transmitted and the dispersed signal are shown in Fig. 7 (lower plot).

The results of the analysis of the second synthetic example are shown in Fig. 9. On the left-hand side in Fig. 9, the results for the time-frequency analysis are presented; the right-hand side shows

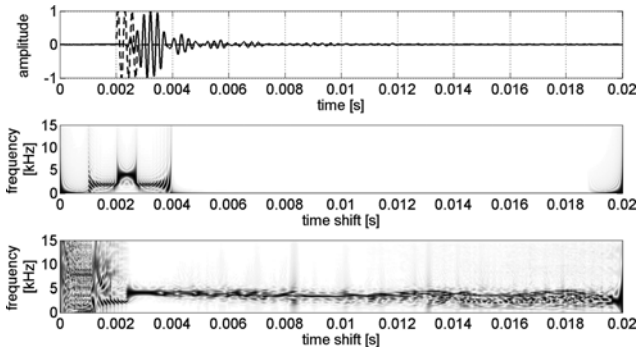

FIG. 10—*Application of the WVD at a given harmonic signal of three periods for dry glass beads of 1.5 mm diameter in a triaxial cell and an isotropic confining pressure of 10 kPa.*

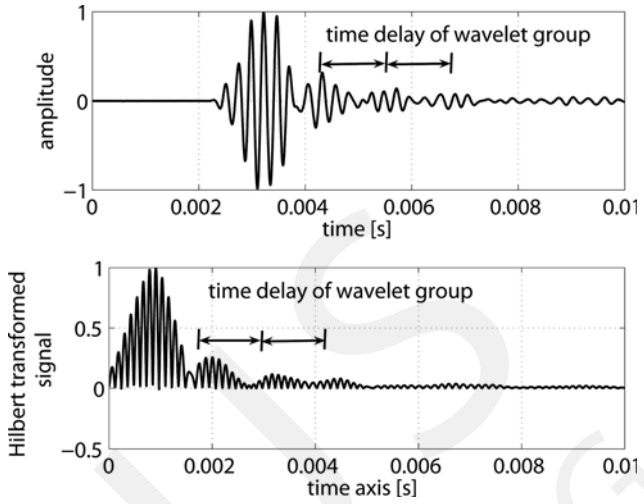

FIG. 11—*Determination of group velocity from the reflected wavelet groups in the recorded signal in a triaxial cell with dry glass beads of 1.5 mm diamter and an isotropic confining pressure of 10 kPa.*

the results for the time-scale transform. The plot in Fig. 9(*f*) also includes a comparison between both analysis methods. They are equal for the given linear sweep signals, and both methods are able to determine the correct velocity over the complete frequency range.

To further check the validity, different laboratory validation tests were done in a triaxial cell with mounted piezo-elements in the top and bottom plates. As a piezo-element for shear wave excitation, a parallel type bender element was used so as to avoid induced charge cross-talk. The piezo-electrical elements are from the German company PiCeramic and were mounted in water resistant epoxy. There are element couples with different lengths between 0.5 and 1 cm. The laboratory equipment was controlled using LabView. To generate and record the seismic signals during laboratory tests, an extended function generator for sweep signals and polarization change of the signal was implemented in Labview. As a data logger, an NI-USB 6251 with a maximal sample rate of 1 MHz was used. The bender elements were impinged by a voltage range of ±10 V, and the input signal was in the lower range of millivolts. The data logger was prefixed by a charge amplifier.

The relevant frequency ranges for measurements are given in terms of their dependence on the sample size and grain size. The laboratory specimens had a diameter of 0.1 m and a tip-to-tip bender element distance of $\Delta s = 0.057$m. The isotropic confining pressure was 10 or 50 kPa, as depicted in the figure legend.

The test in the triaxial samples shows disturbances of the propagating wave field. The lateral boundaries reflect the wave field into the propagating field, and back and forward propagating wave fields can interfere. In general, the resolution of the measurement is reduced, and the signal quality decreases. In some cases of short harmonic impulse excitation, the back and forward propagating wave group is clearly visible in the record and can be used for analysis. In the case of long harmonic or sweep signals, the sample will respond in motion in coincidence with the free flexural eigenmodes of the system (see Arroyo 2007). If test equipment without similar geometrical boundaries is used, the different influences described before are not present, and a potential material dispersion can be analyzed in a direct way. For comparison, the first arrival detections are plotted into the time-frequency dependent results.

The first laboratory test was performed in order to study the propagation of a short harmonic signal in glass beads (density = 1.485 t/m^3); see Fig. 10. This multi-periodical impulse and its reflected signals are to be detected in the output signal. In that first test, a three-period sinus signal of 4 kHz was transmitted. As is visible in the output signal, several reflected wave packages (running up and down) exist. The second plot in Fig. 10 shows the analysis regarding the time-frequency dependence of a transmitted signal with a constant frequency over 0.0075 s. The third plot in Fig. 10 shows the time-frequency analysis of the output signal. As expected, the excitation frequency is visible over the whole time history as a result of the reverberating wave packages. However, the largest amplitudes of the output signal show sharp contrast. Through the use of the Hilbert transformed signal to determine the envelope of the signal, the time delay (approximately 0.001 s) of the reflected wavelet groups was detected (Fig. 11). From this, the group velocity of these packages (double length between elements/plates) could be determined as 114 m/s and used as a comparison value for further tests. For the signal processing of the amplitude envelope, the Hilbert transformed signal was used (see Santamarina and Fratta 2005; Wuttke 2005; Dziewonski et al. 1969).

The second test employs as the transmitted signal a sweep of the same duration as the previous signal (0.0075 s). The frequency increased linearly from 3 to 6 kHz over the interval. As is visible in second plot of Fig. 12, the increase in frequency in the given interval is obvious. The third plot shows the time-frequency plot of the output signal, which does not have the same slope. The fourth plot shows a small dispersion of the group velocity. Because of the limited excitation range of the analyzed time-frequencies in the second and third plots, this velocity can be determined only in a certain range, the trust interval. The trust interval in the presented spectra is defined by the frequency excitation range of the signal. Frequency dependent velocities outside of that range are not representative and reliable. Comparison with the group velocity in Fig. 11 shows good agreement at 4 kHz.

The third test was done using Hostun sand with an initial void ratio *e* of 0.83. In analogy to the foregoing examples, a short sweep signal between 4 and 6 kHz was transmitted (see the

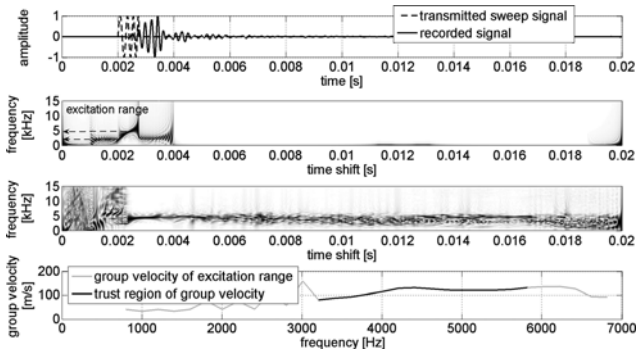

FIG. 12—*Application of WVD using a short sweep signal in dry glass beads of 1.5 mm diameter in a triaxial cell and with an isotropic confining pressure of 10 kPa.*

second plot in Fig. 13). As in the analysis of the glass beads, the Hostun sand shows the same behavior in a lower gradient between time and frequency in the output signal. The last plot in Fig. 13 shows a comparison between the trust interval of the group velocity between 4 and 6 kHz and the velocities from first arrival analysis. For the Hostun sand, additional measurements using a series of single-period sinus signals with frequencies varying between 3 and 7 kHz were taken. From those measurements, the time-of-flight (TOF) was determined; it is used for comparison.

Finally, a long sweep signal was applied to the sand sample to determine the group velocity from the shift of the time-frequency relation (Fig. 6). The signal was excited to between 3 and 10 kHz; the excitation time was 0.01 s. During the long excitation time, the transmitted and reflected wave fields interfere and reduce the resolution quality. The third plot in Fig. 14 shows the scattered signal due to these disturbances caused by reflections and interferences. Between 4 and 6 kHz, the signal quality of the output is still acceptable as a trust interval. To allow visualization of the comparison at a larger scale, a zoom of Fig. 13 and Fig. 14 is shown in Fig. 15.

The performed tests show dispersion probably caused by geometrical boundary conditions. Arroyo (2007) presented a theoretical study of existing dispersion branches excited by the sample geometry. He mentioned the likelihood that flexural eigenmodes are stimulated when axially mounted bender elements are used on cylindrical samples. In consideration of Figs. 14 and 15 and the foregoing statement of Arroyo (2007), the up and down wave field

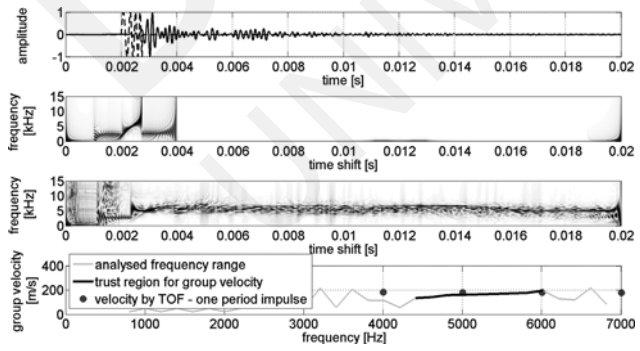

FIG. 13—*Application of WVD using a short sweep signal of 4 to 6 kHz in dry Hostun sand in a triaxial cell and with an isotropic confining pressure of 50 kPa.*

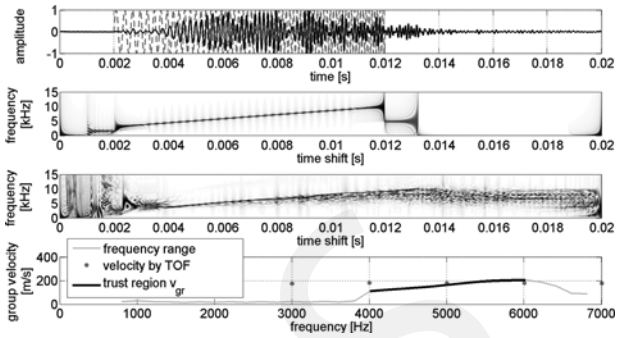

FIG. 14—*Application of WVD using a sweep signal of 3 to 10 kHz in dry Hostun sand in a triaxial cell and with an isotropic confining pressure of 50 kPa.*

is carried by flexural dispersion branches in the range of substantial excitation, the trust region. Figures 16(*a*) and 16(*b*) show the theoretically determined group and phase velocities as numerical solutions of the given experimental sample. The simulation was done using a modified open source program, pcdisp (Seco and Jiménez 2012). The parameters of bar speed and geometry were used based on the detected values of the measurement and the given experimental setup. Figure 16(*a*) shows the phase velocity of a cylinder 10 cm in diameter and 20 cm in height. As material parameters, a Poisson ratio of 0.1 and a bar shear wave speed of 200 m/s, as detected by TOF, were used. In addition to the foregoing phase velocities, the group velocity dispersion branches were determined [Fig. 16(*b*)]. Figure 17 shows branch parts of the excited region, the trust region (grey part). It can be seen that the branch function follows the detected group velocity shape. In order to identify the sample velocities from the detected group velocity, further study of numerical simulations including source excitation and an inversion procedure is necessary. In that sense, the time-frequency and the time-scale transform methods provide a valuable tool for studying dispersion branches in relation to material parameters of the sample.

The reliable and fast determination of wave velocities in materials is an important task in geotechnical engineering. Existing methods have different disadvantages and uncertainties in the determination of wave velocities. The TOF is easy and widely used, but sometimes it involves such strong uncertainties that a determination of the wave velocity is very unreliable. Phase difference methods are powerful, but uncertainties in the initial phase

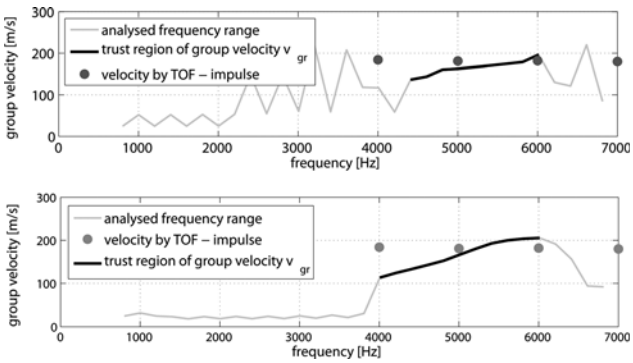

FIG. 15—*Zoomed view of the group velocities compared to TOF of Fig. 13 and Fig. 14.*

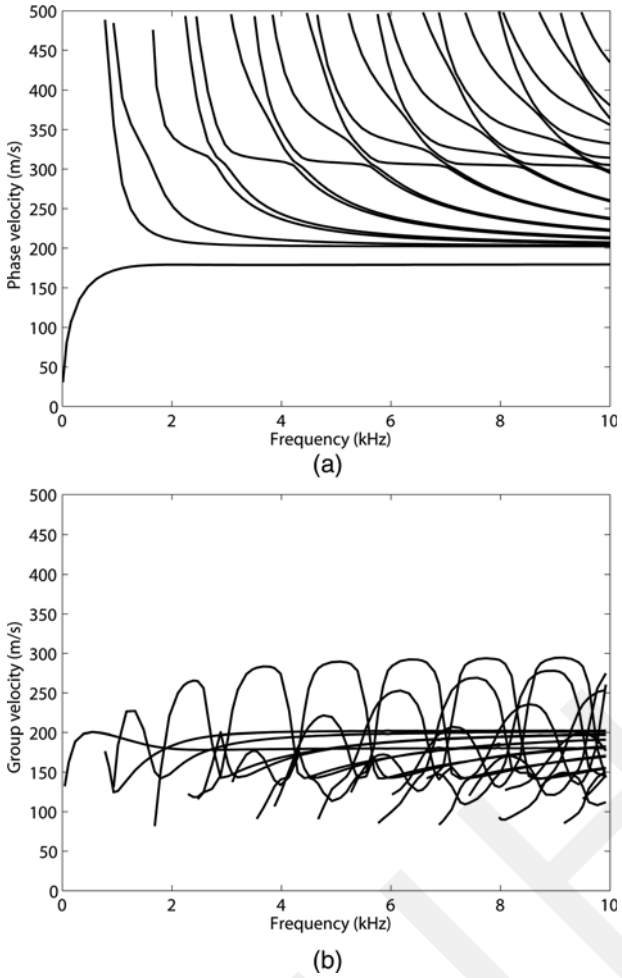

FIG. 16—*Theoretical dispersion branches of (a) phase and (b) group velocities for the given sample. As the material wave velocity, the detected shear wave velocity of 200 m/s and a Poisson ratio of 0.1 were used to compare the simulation with the experiment. The simulation geometry was an infinite bar of 10 cm diameter.*

function of the cross correlated functions pose important problems, as shown before. Thus neither method is always applicable, and even when they can be used, it is desirable to have a further method for comparison. This is the reason for the development of a method to study the wave velocities with a robust and stable process, without subjective influences, such as a subjective choice of crossover points or subjective choice of initial phase change. Of course, the presented method is also not a perfect method. Each method has advantages and disadvantages. The developed method is a promising tool for analyzing wave velocities and reducing uncertainties. Finally, coupled interpretations of experimental signals under the use of different analysis tools will provide the highest trust in the obtained results.

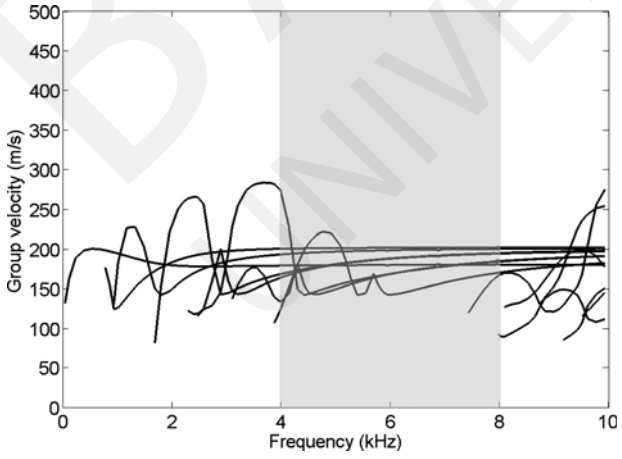

FIG. 17—*Theoretical dispersion branches of selected group velocities in the trust region (grey range) of the experiment.*

Concluding Remarks

The present paper analyzes a variety of time-frequency and time-scale transform methods that are appropriate for determining time-frequency characteristics by means of analyzing wave based testing procedures. It is clearly shown that the continuous wavelet transform (CWT) and the Wigner–Ville distribution (WVD) give better resolution than the fast wavelet transform (FWT), which was developed for a minimum of signal redundancy. Based on the more suitable CWT and WVD methods, a scheme to determine the group velocity was developed. The outlined method was validated using synthetic and laboratory tests that show the applicability of the proposed approach.

The resolution of the tested time-frequency methods was in general sufficient, but the FWT needs further pre-processing in order to achieve similar good resolution. To increase the CWT speed, the transform is performed in the frequency domain. The WVD has high speed and sharp resolution at all considered frequencies. The wavelet transform (WT) method yields increased fuzziness with increasing frequency. Increased resolution is very important for calculating the exact time difference between the transmitted and received signals. This means, in particular, that a small difference in time at high frequencies can mean a large difference in velocity.

The robustness of the WT and WVD was illustrated with synthetic tests, and the WVD was faster for the same resolution. The advantage of the WT is the analytical structure of the transform, which allows the WT to be applied to specific boundary conditions. That process is not possible with the time-frequency transforms (WVD). Using that method only the core or kernel function can be modified, but the method itself is not as flexible as WT. Nevertheless, training and understanding are needed with regard to both transforms, and the paper contributes to this.

During the application of experimental signals, further problems might arise, such as transmitter resonance and boundary and near-field effects, which influence the propagating wave field. To validate the presented method, different laboratory experiments were performed. The equipment employed (bender elements on a triaxial sample) has certain geometrical characteristics that can cause reflections and interferences in the wave field.

Reverberation of quasi-harmonic excitation signals might blur the time frequency signature of the received signal, making travel time identification impossible in the time-frequency maps. In the case discussed here, the Hilbert transform was successfully applied to establish a group velocity.

With the use of short sweep signals, an easy and straightforward calculation of the group velocity was possible. It could be demonstrated that an automatized algorithm can be used for data analysis and no "subjective" choices are necessary. Even if the excitation time becomes large, as shown for the last example, the resolution of the time-frequency signature is clear enough. The last excitation case contains boundary effects, reflections, and interferences, so a decrease in resolution is observed. Additionally, it is to be considered that a large excitation time causes structural responses at flexural eigenmodes. Investigation (Arroyo 2007) shows theoretical group velocity dispersion modes that seem similar, but to deal with a larger frequency range showing strong dispersion behavior, further studies are needed. In general, and from the experience with the strong dispersion of the seismic surface waves, it seems possible to use experimental and theoretical group velocities in identification processes.

Acknowledgments

The writers acknowledge the support of the R & D Programme GEOTECHNOLOGIEN, funded by the German Ministry of Education and Research (BMBF) and the German Research Foundation (DFG) (Grant No. 03G0636B). Further thanks for stimulating discussions on that topic are given to J. Carlos Santamarina from Georgia Institute of Technology and Marcos Arroyo from Technical University of Catalonia. The writers also thank the reviewers for their useful and critical comments.

APPENDIX: MATHEMATICAL BASICS AND NOTATIONS

In the following, the mathematical basics and used notations of signal processing in time-frequency and time-scale transforms are presented; therefore, this appendix is recommended reading for those attempting to understand the used theories and numerical solutions.

Definitions and Transforms in Signal Processing

With g^* or $\bar{g}$, the conjugate complex of a function g is denoted. By use of the scalar product in Hilbert space,

$$L^2(\mathbb{R}) : \langle f, g\rangle = \int_{-\infty}^{\infty} f(t) g^*(t) dt \tag{A1}$$

and the scalar product in sequence space,

$$l^2(\mathbb{Z}) : \langle f, g\rangle = \sum_{k=-\infty}^{\infty} f_k g_k^* \tag{A2}$$

the corresponding norms and energy expressions are obtained.

$$E(f) = \|f\|^2 = \langle f, f\rangle < \infty \tag{A3}$$

$|f(t)|^2 = f(t)f^*(t)$ is often used as the energy density per time. The Fourier transform is defined as

$$\hat{f}(\xi) = F\{f\}(\xi) = \int_{-\infty}^{\infty} f(t)\, e^{-j2\pi\xi t} dt \tag{A4}$$

where the frequency is $\xi \in \mathbb{R}$. By substituting $\xi = \omega/2\pi$ in Eq A4, the often used notation $F\{f\}(\omega)$ with angular frequency scaling of the independent variable is achieved. Subsequent formulas in this study would be modified. Under the use of Eq A4, Parseval's theorem is defined as

$$\left\langle \hat{f}, \hat{g} \right\rangle = \langle f, g\rangle \tag{A5}$$

Formula A4 provides a unitary transformation. The energy of the original time signal is preserved by this type of Fourier transform. If f depends on more than one variable, we define the Fourier transform regarding one related variable (here t) as follows:

$$F_t\{f(s,t)\}(\xi) = \int_{-\infty}^{\infty} f(s,t)\, e^{-j2\pi\xi t} dt \tag{A6}$$

For such a function, the scalar product of Eq A1 regarding one selected variable can be defined as

$$\langle f(s,t), g(t,u)\rangle_t = \int_{-\infty}^{\infty} f(s,t) g^*(t,u) dt \tag{A7}$$

Convolution and Correlation in Signal Processing

In particular, the following definitions are essential for the objectives explained above:

$$\text{Convolution} : (f * g)(\tau) := \int_{-\infty}^{\infty} f(t) g(\tau - t) dt \tag{A8}$$

$$\text{Discrete convolution} : (f * g)(k) := \sum_{\nu=-\infty}^{\infty} f_\nu g_{k-\nu}, \quad k \in \mathbb{Z} \tag{A9}$$

$$\text{Cross-correlation} : (f \otimes g)(\tau) := \int_{-\infty}^{\infty} f^*(t) g(\tau + t) dt \tag{A10}$$

$$\text{Discrete cross} - \text{correlation} : (f \otimes g)(k) := \sum_{\nu=-\infty}^{\infty} f_\nu^* g_{k+\nu} \tag{A11}$$

From the foregoing equations, it follows that

$$(f * g)(\tau) = \int_{-\infty}^{\infty} f(t-\tau) g(t) dt = \{f^*(-t) * g(t)\}(\tau) \tag{A12}$$

It is known that the following convolution theorem (cross correlation theorem) is valid (cp. Eq A12):

$$F\{f * g\} = F\{f\} \cdot F\{g\} \qquad \left(F\{f \otimes g\} = \overline{F\{f\}} \cdot F\{g\}\right) \tag{A13}$$

Under the use of a CWT, the following notation of a chosen mother wavelet ψ is defined:

$$\psi_{[s,\tau]}(t) = \frac{1}{\sqrt{s}} \psi\left(\frac{t-\tau}{s}\right), \quad s > 0,\ \tau \in \mathbb{R} \tag{A14}$$

This definition is used to distinguish further between CWT and discrete wavelet transform.

References

Allen, R. L. and Mills, D., 2004, *Signal Analysis: Time, Frequency, Scale and Structure*, IEEE, Piscataway, NJ.

Arroyo, M., 2007, "Wavelet Based Analysis of Pulse Tests in Soil Samples," *Rivista Italiana di Geotecnica*, Vol. 2, pp. 25–38.

Arulnathan, R. and Boulanger, R., 1998, "Analysis of Bender Elements," *Geotech. Test. J.*, Vol. 21(2), pp. 120–131.

Bath, M., 1974, *Spectral Analysis in Geophysics, Developments in Solid Earth Geophysics*, Vol. 7, Elsevier Science, New York, Amsterdam.

Brehm, M., Markwardt, K., and Zabel, V., 2005, "Applications of Wavelet Packets in System Identification," *Jahrestagung der Gesellschaft für Angewandte Mathematik und Mechanik e.V. (GAMM)*, Luxembourg City, Luxembourg.

Cattani, C. and Rushchitsky, J., 2007, *Wavelet and Wave Analysis as Applied to Materials with Micro or Nanostructure*, World Scientific, River Edge, NJ.

Dziewonski, A., Bloch, S., and Landisman, M., 1969, "A Technique for the Analysis of Transient Seismic Signals," *Bull. Seismol. Soc. Am.*, Vol. 59(1), pp. 427–444.

Farge, M., 1992, "Wavelet Transforms and Their Application to Turbulence," *Annu. Rev. Fluid Mech.*, Vol. 24, pp. 395–457.

Greening, P. and Nash, D., 2004, "Frequency Domain Determination of G_0 Using Bender Elements", *Geotech. Test. J.*, Vol. 27(3), pp. 288–294.

Gucunski, N. and Shokouhi, P., 2004, "Detection and Characterization of Cavities under the Airfield Pavements by Wavelet Analysis of Surface Waves," *FAA Worldwide Airport Technology Transfer Conference*, NJ.

Hammond, J. and White, P., 1996, "The Analysis of Non-stationary Signals Using Time-frequency Methods," *J. Sound Vib.*, Vol. 190(3), pp. 419–447.

Huerta-Lopez, C., Shin, Y., Powers, E., and Roesset, J., 2000, "Time-frequency Analysis of Earthquake Records," *12th World Conference of Earthquake Engineering*, January, Auckland, New Zealand.

Ismail, M. and Rammah, K., 2005, "Shear-plate Transducers as a Possible Alternative to Bender Elements for Measuring G_{max}," *Geotechnique*, Vol. 55(5), pp. 403–407.

Jovicic, V., Coop, M., and Simic, M., 1996, "Objective Criteria for Determining G_{max} from Bender Element Tests," *Geotechnique*, Vol. 46(2), pp. 357–362.

Kiencke, U., Schwarz, M., and Weickert, T., 2008, *Signalverarbeitung: Zeit-Frequenz-Analyse und Schaetzverfahren* [Signal Processing: Time-Frequency Analysis and Assessment Methods], Oldenbourg.

Mallat, S., 1998, *A Wavelet Tour of Signal Processing*, Academic Press, San Diego.

Markwardt, K., 2006, Application of Fast Wavelet Transformation in Parametric System Identification, Vol. XIV of Applied and Numerical Harmonic Analysis, Wavelet Analysis and Applications, Birkhäuser Verlag, Basel/Switzerland, chapter 3: Fractal and Multifractal Theory, Wavelet Algorithm, Wavelet in Numerical Analysis, pp. 247–254.

Narasimhan, S. and Nayak, M. B., 2003, "Improved Wigner-Ville Distribution Performance by Signal Decomposition and Modified Group Delay," *Signal Process.*, Vol. 83, pp. 2523–2538.

Nazarian, S., 1984, "In Situ Determination of Elastic Moduli of Soil Deposits and Pavement Systems by Spectral-Analysis-of-Surface-Wave Method," Ph.D. thesis, University of Texas at Austin, TX.

Nazarian, S., Yuan, D., and Baker, M. R., 1994, "Automation of Spectral Analysis of Surface Wave Method," *Dynamic Geotechnical Testing II*, R. J. Ebelhar, V. P. Drevinch, and B. L. Kutter, Eds., pp. 88–100.

Niethammer, M. and Jacobs, L. J., 2001, "Time-frequency Representations of Lamb Waves," *J. Acoust. Soc. Am.*, Vol. 109(5), pp. 1841–1847.

Santamarina, J. and Fratta, D., 2005, *Discrete Signals and Inverse Problems*, John Wiley and Sons, New York.

Seco, S. and Jiménez, A. R., 2012, "Modelling the Generation and Propagation of Ultrasonic Signals in Cylindrical Waveguides," *Ultrasonic Waves*, Intech Open Access Publisher, pp. 1–28.

Torrence, C. and Compo, G., 1998, "A Practical Guide to Wavelet Analysis," *Bull. Am. Meteorol. Soc.*, Vol. 79(1), pp. 61–78.

Wuttke, F., 2005, "Site Identification by Use of Surface Waves," dissertation, PhD dissertation, Bauhaus-Universität Weimar, Germany [in German].

Wuttke, F., Asslan, M., and Schanz, T., 2010, "Determination of G_0 via High Resolution Time-frequency Analysis in Dry, Saturated and Partially Saturated Sands," *Proceedings of the 5th UNSAT International Conference on Unsaturated Soils*, CRC Press, Boca Raton, FL.

Wuttke, F., Markwardt, K., and Schanz, T., 2009a, "Application of Time-frequency Methods, Wavelet Analysis, Conventionally Strategies and Coda Wave Interferometry to Monitor the Wave Velocities due to Parameter Changes in Granular Multiphase Materials," *National Congress of Theoretical and Applied Mechanics*, August, 2009, Borovets, Bulgaria.

Wuttke, F., Markwardt, K., and Schanz, T., 2009b, "Application of Wavelet Transforms in Soil Dynamics—Ex and In Situ Investigations," *3rd Congress on Structural Dynamics*, Kassel, Germany, Association of German Engineers, VDI.

Youn, J.-U., Choo, Y.-W., and Kim, D.-S., 2008, "Measurement of Small-strain Shear Modulus gmax of Dry and Saturated Sands by Bender Element, Resonant Column and Torsional Shear Tests," *Can. Geotech. J.*, Vol. 45, pp. 1426–1438.

Yuan, D. and Nazarian, S., 1993, "Automated Surface Wave Method: Inversion Technique," *J. Geotech. Engrg.*, Vol. 119(7), pp. 1112–1126.

Zustandsänderungsmonitoring von granularen, mehrphasigen Böden mittels Codawellen-Interferometrie

Process monitoring in granular, multiphase soils by use of coda wave interferometry

Author: Prof. Dr.-Ing. **F. Wuttke**, Bauhaus-Universität Weimar, Juniorprofessur für Modellierung in der Geomechanik, Coudraystrasse 11c, 99423, Weimar

Co-author: Prof. Dr.-Ing. habil. T. Schanz, Ruhr-Universität Bochum, Lehrstuhl für Grundbau, Boden- und Felsmechanik, Universitätsstrasse 150, 44780 Bochum

Kurzfassung

Das Monitoring von Strukturänderungen ist für die Detektion einer Schädigung, einer beabsichtigten oder zwangsweise ablaufenden Strukturänderung in Materialien eine wichtige Zielgröße in der Strukturidentifikation. Sind diese Änderungen sehr klein, kann die Detektion eine große Herausforderung mit herkömmlichen dynamischen oder akustischen Methoden darstellen. In dem folgenden Beitrag soll die Anwendung der Codawellen-Interferometrie auf granulare und mehrphasige Materialien diskutiert werden. Es soll anhand von Beispielen aus der Geotechnik die Sensitivität der Methodik und die Möglichkeiten der Zustandsableitung gezeigt werden. Im Rahmen der vorgestellten Versuche und Analysen, wird die Methode genutzt, um kleinste Änderung im Spannungszustand nach geringen Belastungsänderungen von granularen Materialien, nach Kriechvorgängen im Material unter konstanter Belastung bzw. nach Änderung der Materialfeuchtigkeit zu detektieren. Durch Simulation der Wellengeschwindigkeiten bzw. deren Geschwindigkeitsgradienten unter Nutzung modifizierter Hertz-Mindlin-Kontaktmodelle konnte eine Randbedingungsänderung durch die Methodik simuliert und somit für Identifikationsaufgaben herangezogen werden. Für die Versuche wurden sowohl modifizierte, mit Piezosensorik ausgerüstete, geotechnische Laborgeräte als auch eine spezielle, nichtberandete und damit reflexionsfreie Großversuchszelle genutzt. In allen betrachteten Fällen konnte die auf die geomechanischen Fragestellungen angepasste Interferometrie sehr gute, subjektiv unbeeinflusste und damit eindeutige Ergebnisse erzielen.

1. Einleitung und Motivation

Die Charakterisierung von natürlichen Bodenmaterialien ist durch die komplexe Partikelstruktur eine Herausforderung insbesondere wenn der Prozess der Strukturänderung im Focus des Interesses liegt. Elastische Wellen stellen für diese Zielstellung ein wertvolles Werkzeug für Informationen über die Veränderung der Bodenstruktur dar. Beispiele dafür sind die Bestimmung der ‚*small-strain*' Steifigkeit,

der Dämpfung und räumlichen Heterogenität und Strukturänderungen durch innere oder durch Randbedingungen induzierte Prozesse. Oftmals werden für diese Messungen einfache Ersteinsatzmessungen angewendet, wobei die Durchführung bzw. die Bestimmung der Ersteinsatzzeit ein wesentliches Problem darstellen kann. Eine Vielzahl von Wissenschaftlern hat eine ebenso große Anzahl von unterschiedlichen Verfahren zu Bestimmung der Ersteinsatzzeit publiziert.

Problematisch werden die bislang verfügbaren Messungen, wenn die Veränderungen in der Struktur oder Randbedingungen so klein sind, dass die Detektion dieser versagt und sich erst über einen langen Zeitraum akkumuliert, wie Diagenese, Kriechen oder Alterung.

Für ein Prozess-Monitoring in solchen Fällen kann die Codawellen-Analyse bzw. Codawellen-Interferometrie erfolgreich angewendet werden. Die Coda selber beinhaltet die mehrfach reflektierten und zerstreuten Wellensignale am Ende des gesamten Wellenzuges [14]. Durch die längeren Laufzeiten und mehrfach reflektierten Wellenwege und Trajektorien ist das durch das Medium laufende Signal in der Lage die inhärenten Informationen superpositioniert zu speichern. Die Codawellen-Analyse analysiert ebendiesen Teil des Wellenfeldes, um die gespeicherten Informationen in verwertbare Wellengeschwindigkeiten zu transformieren. Anwendungen dazu finden sich im Erdbebeningenieurwesen, dem Vulkan- und Verwerfungsmonitoring als auch in der Materialcharakterisierung [14], [5], [12], [13], [10], [15], [4].

In dieser Studie werden neben den Grundlagen der Codawellen-Interferometrie unterschiedliche Untersuchungen zur hochauflösenden Abbildung und Modellierung von Spannungsänderungen, von Kriechvorgängen in granularen Materialen und zur Evolution der Wellengeschwindigkeit bzw. Steifigkeit in Abhängigkeit vorhandener Saugspannungen in teilgesättigten Materialien durchgeführt.

2. Codawellen-Analyse

Das grundlegende Konzept der Codawellen-Analyse nutzt zwei aufeinanderfolgende, durch eine kleine Strukturstörung, getrennte Wellensignale. Durch die eingetragene Störung wird in dem nachfolgenden Signal ein kontinuierlich zunehmender Phasenversatz in der Coda induziert. Dieser kontinuierlich zunehmende Phasenversatz stellt die Grundlage der Methode dar: mit zunehmenden Laufweg, durch Reflexionen u.a., wird die Information in einer linear zunehmenden Phase innerhalb der Coda gespeichert, siehe Bild 1a. In der Kreuzkorrelation des gleitenden Fensters ergibt sich dadurch ein linear ansteigende Zeitversatz, Bild 1b, bzw. der Verlauf des Gradienten über die Zeit, Bild 1c.

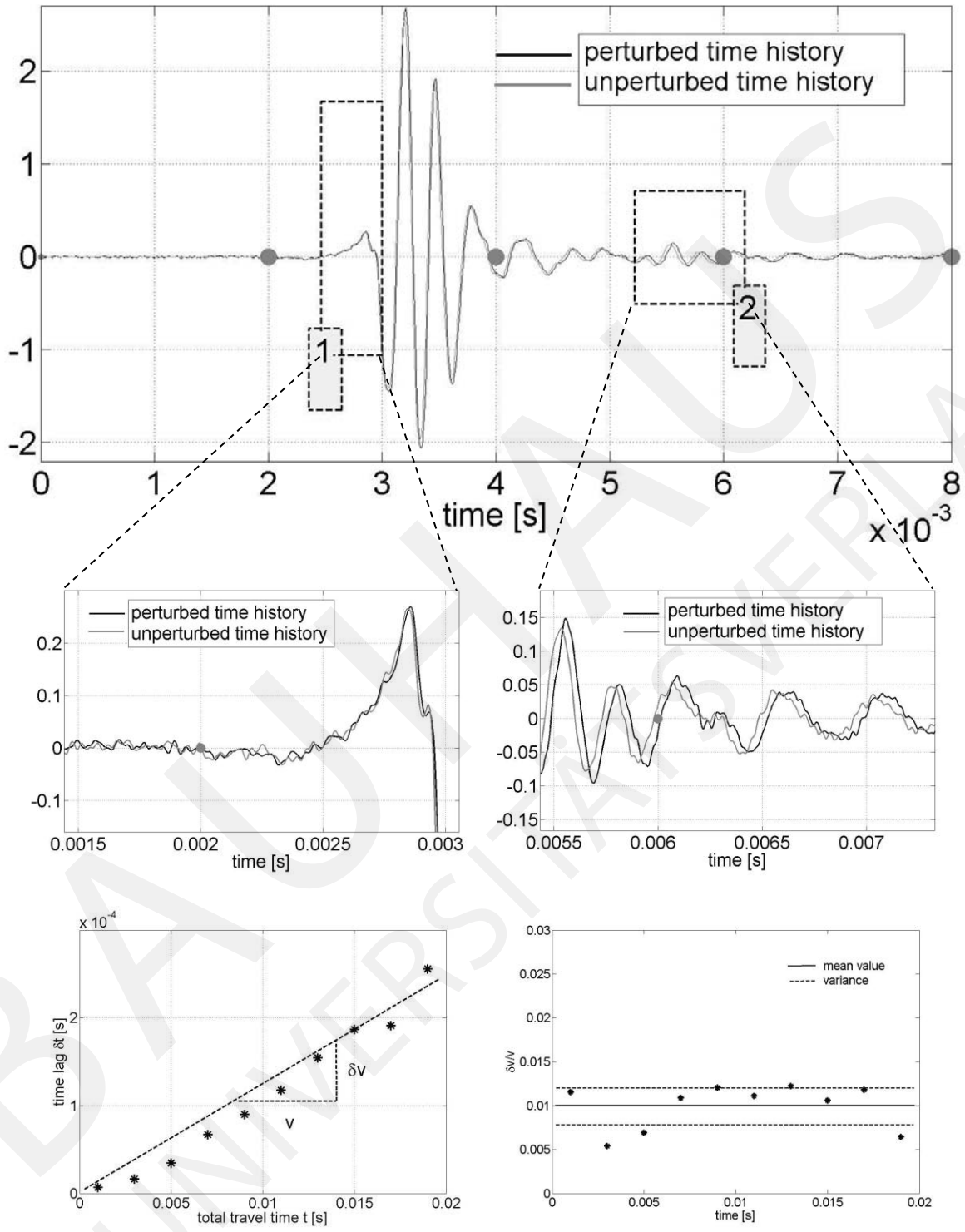

Bild 1: Schematische Darstellung der Codawellenanalyse: I) Zeitversatz mit zunehmender Zeit in der Wellencoda, II) Abbildung des linear zunehmenden Zeitversatzes bzw. konstanten Anstiegs und III) Abbildung der des Anstiegswertes in jedem Zeitfenster und Mittelwert über die Zeitfenster.

Analysemethoden

1) Die übliche Codawellenanalyse beruht auf der Anwendung von einer normierten Kreuzkorrelation definierter, aufeinanderfolgender Zeitfenster zwischen dem Signal des ungestörten Systems, u_{unp}, und dem Signal des gestörten Systems, u_{per}, zur Bestimmung der Zeitverschiebung δt ([13]; [14]; [15]).

$$R^{t,T}(t_s) := \frac{\int_{t-T}^{t+T} u_{unp}(t')\, u_{per}(t'+t_s)\, dt'}{\left[\int_{t-T}^{t+T} u_{unp}^2(t')dt' \int_{t-T}^{t+T} u_{per}^2(t')dt'\right]^{\frac{1}{2}}}$$

2) In einer Erweiterung der Codawellenanalyse wird anstelle der gefensterten Zeitabschnitte das komplette Signal des gestörten Systems um einen konstanten Gradienten gedehnt, [11]. Der Wert des Gradients wird variiert, bis die Kreuzkorrelation maximiert ist. Eine Verbesserung der in der Signalanalyse kann zusätzlich durch die Überlagerung des Signals mit einer Normierungsfunktion bezüglich eines konstanten Signal-Energiegehaltes erreicht werden, [4].

$$R^{t}(\varepsilon) := \frac{\int_{t_1}^{t_2} u_{unp}(t)\, u_{per}\left(t(1-\varepsilon)\right) dt}{\left[\int_{t_2}^{t_2} u_{unp}^2(t)dt \int_{t_1}^{t_2} u_{per}^2\left(t(1-\varepsilon)\right)dt\right]^{\frac{1}{2}}}$$

3) Eine weitere Möglichkeit der Analyse besteht in der Signalauswertung im Frequenzbereich, [4]. Dabei wird analog der Dehnung im Zeitbereich das Signalspektrum im Frequenzbereich um einen konstanten Gradienten im Frequenzbereich gedehnt bis eine maximale Übereinstimmung gefunden ist.

Ein Vergleich der unterschiedlichen Methoden, siehe [4], zeigte für die analysierten Signale eine sehr gute Übereinstimmung der jeweiligen Gradienten.

3. Hertz-Kontaktmodelle

Für die Interpretation und Übertragung der Ergebnisse aus den experimentellen Codawellen-Analysen ist die Nutzung von Hertzkontaktmodellen hervorragend geeignet, da das physikalische Verhalten durch die Änderungen in der Mikrostruktur dominiert sind. Diese Informationen sind in der Wellencoda gespeichert und gut in die obigen Theorien übertragbar, anpassbar und erweiterbar. Ausgehend von den Definitionen der modifizierten Hertz-Mindlin Theorie [2] kann die gemittelte Inter-Partikel

Normalkraft $\langle N \rangle$ für eine isotrope Zufallsanordnung von mono-dispersen Partikeln wie folgt definiert werden:

$$\langle N \rangle = \frac{4\pi R_g^2 \sigma_0}{cn(1-n)},$$

wobei R_g den idealisierten Radius des Kornes, σ_0 der isotrope Umgebungsdruck, n die Porenzahl und cn die Koordinationszahl beschreibt, [5], [8]. Mit den eingehenden Normal- und Scherkräften am Kornkontakt, S_n und S_t, sowie dem sphärischen Kontaktradius r_c

$$S_n = \frac{4r_c\mu}{1-\nu},\ S_t = \frac{8r_c\mu}{2-\nu},\ r_c = \sqrt[3]{\frac{3NR_c(1-\nu)}{8\mu}},\ R_c^{-1} = 0.5\left(R_1^{-1} + R_2^{-1}\right)$$

und m und n als Kornsteifigkeit, das Poissonverhältnis ν sowie der Schubmodul des Korns μ, ergibt sich die Scherwellengeschwindigkeit c_s zu

$$c_s = \sqrt{\frac{1}{\rho_b} \cdot \frac{cn(1-n)}{20\pi R_g}\left(S_n + 1.5S_t\right)}.$$

Mit der Verschiebung Δ zwischen zwei Partikeln von $\Delta = 2r_c^2 / R_c$, kann mit den obigen Gleichungen die Kraft-Verschiebung bzw. die Spannung-Deformations-Beziehung in Form der exponentiellen Gleichung $N = ar^\theta$, wobei a und θ Konstanten darstellen, abgebildet werden [9]. Die Definition der Steifigkeit als Ableitung der Kraft-Verschiebungsrelation, kann nach [7] ohne Verlust der Allgemeinheit die Spannungs-Deformationsbeziehung bzw. unter Einbeziehen der Partikelmasse die allgemeine Spannungs-Geschwindigkeitsrelation aufgestellt werden $c_s = \alpha\sigma^{(\theta-1)/2\theta} = \alpha\sigma^\beta$, siehe [3], [9]. Die Konstanten α und β enthalten dabei die obigen Terme zu Kornradius R_g, Poissonverhältnis n und den Kornmodul μ. Für die folgenden Analysen wird die verallgemeinerte Kurzform herangezogen.

4. Analyse / Prozessmonitoring

In einer ersten Studie an mono-dispersen Glasperlen (3.5mm) wurde die Sensitivität der Codawellen-Analyse bezüglich des Geschwindigkeitsgradienten mit stufenweise erhöhten isotropen Zelldrücken (Druckstufe 1kPa). Dabei wurden die experimentellen Messwerte entsprechenden synthetischen ‚*Messwerten*' unter Nutzung der obigen Hertz-Mindlin--Gleichungen gegenübergestellt, siehe Bild 2. In den Bildern ist deutlich die hochauflösende Abbildung der Gradienten zu den entsprechenden Druckstufen zu sehen, mit konventionellen Analysen, z. B. Ersteinsatz, waren die Unterschiede in der Wellengeschwindigkeit zwischen den engen Druckstufen nicht abbildbar.

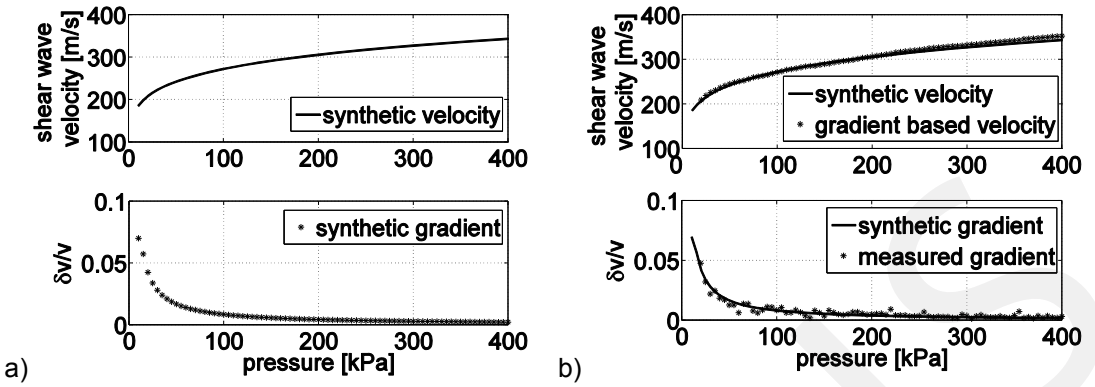

Bild 2: a) Synthetische Wellengeschwindigkeit und Geschwindigkeitsgradient für 3.5mm Glasperlen nach Hertz-Mindlin Theorie, b) Vergleich der gemessenen und synthetisch berechneten Wellengeschwindigkeiten und Geschwindigkeitsgradienten

Um in weiteren Studien das Verhalten von unterschiedlichen Sanden hinsichtlich innerer Strukturänderungen und der inneren Spannung- und Steifigkeitsänderung unter Berücksichtigung eines mehrphasigen Boden zu analysieren, werden unterschiedliche natürlich anstehende Böden mit der Codawellenanalyse näherer untersucht. Bild 3 zeigt die typische Gradientenentwicklung mit zunehmender Spannung. Um die absoluten Wellengeschwindigkeiten aus den Gradientenentwicklungen zu bestimmen, muss ein ‚Einhängewert' einer absoluten Geschwindigkeit genutzt werden (siehe nachfolgende Gleichung).

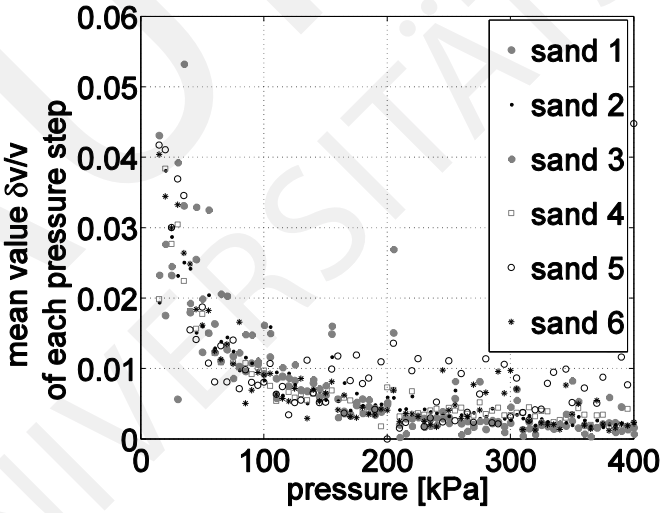

Bild 3: a) Synthetische Wellengeschwindigkeit und Geschwindigkeitsgradient für 3.5mm Glasperlen nach Hertz-Mindlin Theorie, b) Vergleich der gemessenen und synthetisch berechneten Wellengeschwindigkeiten und Geschwindigkeitsgradienten

Dabei muss zur Berücksichtigung unterschiedlicher Verhaltensweisen im Bodenmaterial, welche eine Zu- und Abnahme der Geschwindigkeitsgradienten beinhalten können, der Gradient mit dem entsprechenden Vorzeichen berücksichtigt werden.

$$c_{s,abs,i+1} = c_{s,abs,i} + c_{s,abs,i} \cdot \chi_i \quad \text{mit} \quad \chi_i := \left\{ \frac{\delta c_s}{c_s} \right\}_i$$

In der nachfolgenden Studie soll die Detektion einer isotropen Spannungsevolution (Isotrope Zelldruckänderung) in einer Triaxialversuchs-Belastungszyklus mit Codawellen analysiert und ausgewertet werden [15]. In Bild 4a ist der Verlauf der Gradientenevolution mit konstant zunehmender Spannung abgebildet. Deutlich sichtbar ist die sehr gute Nachrechnung unter Nutzung eines Exponenten von 1/4, welcher für eckige Kornformen anstelle des Exponenten von 1/6 für runde Kornformen in den Hertz'schen Gleichungen genutzt wird [4]. Der Absolutwert der Spannung ergibt sich in diesem Fall durch den Startpunkt Null. Im Falle einer inhärenten isotropen Spannung, muss dieser Wert durch anfängliche Messungen bekannt sein oder durch entsprechende Modell bestimmt werden. Alle nachfolgenden Spannungsanalysen gelten hierbei für den kleinen Dehnungsbereich, da Porenraumänderungen in diesen Studien nicht berücksichtigt wurden.

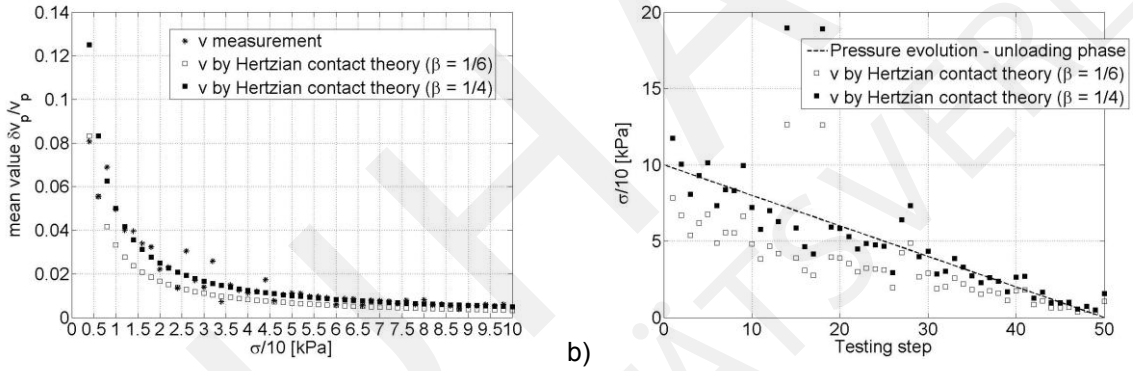

Bild 4: a) Vergleich der Geschwindigkeitsgradienten zwischen Messung und Prognose unter Nutzung von des Exponenten β = 1/6 für elastische, sphärische Körner und β = 1/4 für eckige Körner (Belastungsphase); b) Nachrechnung der Spannungsevolution unter Nutzung der gemessenen Geschwindigkeitsgradienten und Exponenten β = 1/6 für elastische, sphärische Körner und β = 1/4 für eckige Körner (Belastungsphase)

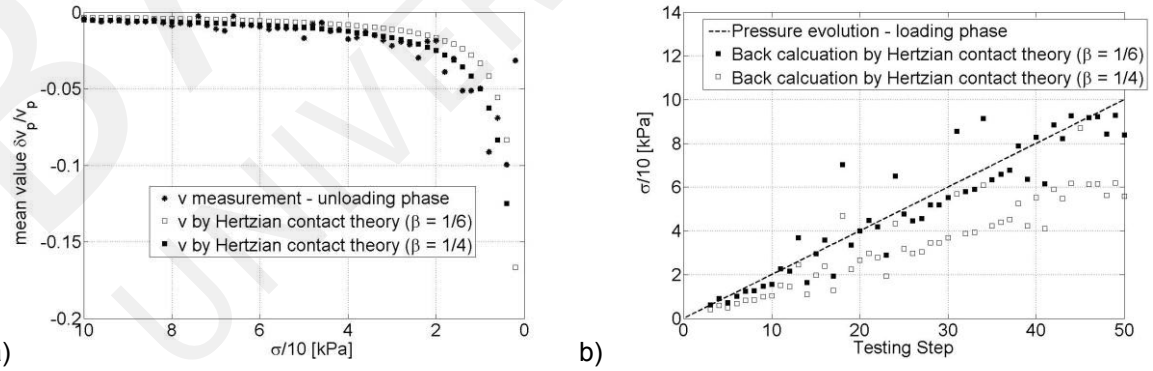

Bild 5: a) Vergleich der Geschwindigkeitsgradienten zwischen Messung und Prognose unter Nutzung von des Exponenten β = 1/6 für elastische, sphärische Körner und β = 1/4 für eckige Körner (Entlastungsphase); b) Nachrechnung der Spannungsevolution unter Nutzung der gemessenen Geschwindigkeitsgradienten und

Exponenten β = 1/6 für elastische, sphärische Körner und β = 1/4 für eckige Körner (Entlastungsphase)

Bild 4b zeigt die aus den Geschwindigkeitsgradienten bestimmten Spannungswerte. Unter Nutzung der obigen Hertzkontakt-Gleichungen kann der Gradient der isotropen Spannungen bzw. die isotrope Spannung aus dem Geschwindigkeitsgradienten über folgenden Gleichungen abgebildet werden [4]

$$\frac{\delta v}{v} = \left(\frac{\delta \sigma}{\sigma} \right)^{\beta}$$

In Bild 5a und 5b ist die Entlastungsast des Versuches mit der Evolution des Geschwindigkeits-gradienten und der Gegenüberstellung der rückgerechneten und der tatsächlichen Spannungs-evolution abgebildet. Wiederum ist sichtbar, dass die Exponenten ¼ den Verlauf besser wiedergegeben.

Für die Analyse der ‚small-strain' Steifigkeit- bzw. der Wellengeschwindigkeitsabhängigkeit von der Teilsättigung im Bodenmaterialien wurde eine Spezialtriaxialzelle zur Kontrolle der Saug- und Umgebungsspannungen konzipiert. Neben den Messungen innerhalb der Spezialtriaxialzelle erfolgte die Bestimmung der Saugspannung-Sättigungs-Kurve (SWCC) zur Interpretation des Einflusses von auftretenden Saugspannungen in Abhängigkeit von der vorhandenen Materialsättigung. Beide Messungen sind in Bild 6 gegenübergestellt und bilden die Grundlage für die Ableitungen dieser Analyse.

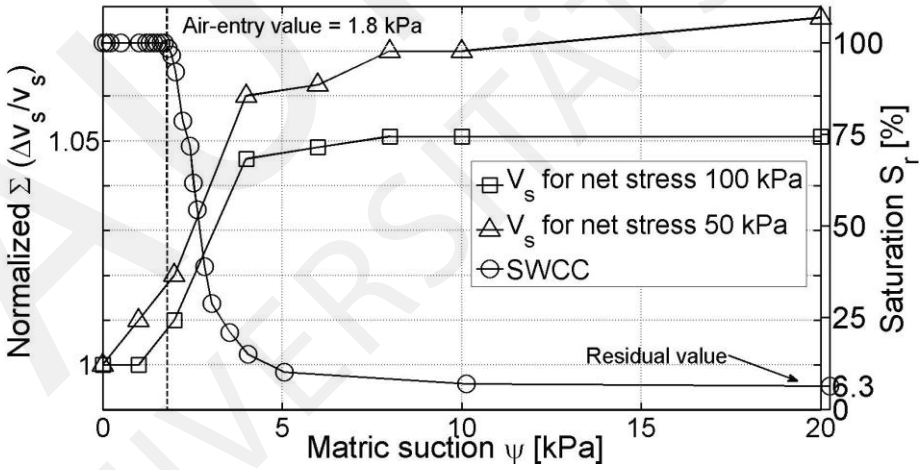

Bild 6: Summierter Geschwindigkeitsgradient versus Saugspannung und SWCC von Hostun-Sand zu zwei unterschiedlichen Netzspannungen

Ausgehend von Bild 6 werden der akkumulierte Geschwindigkeitsgradient und der akkumulierte Gradient der SWCC – Kurve in Abhängigkeit von der Saugspannung gegenübergestellt, siehe Bild 7. Der gleiche Verlauf der akkumulierten Gradienten beider Funktionen zeigt den deutlichen Einfluss der Saugspanungen auf die Geschwindigkeits- bzw. ‚small-strain' Steifigkeitsevolution des untersuchten Bodenmaterials, [1].

Legt man dem SWCC Verlauf eine Van Genuchten Gleichung zugrunde [4],

$$\theta\left(\psi\right) = \left[1 + \left(\alpha\psi\right)^{n}\right]^{-m}$$

mit θ als volumetrischer Wassergehalt, ψ als Saugspannung und *n*, *m* als konstitutive Parameter, so kann der Wellengeschwindigkeitsgradient aus dem Saugspannungsgradienten $\delta\theta/d\psi$ und damit die Wellengeschwindigkeit bzw. die Steifigkeit in Abhängigkeit von der Saugspannung bestimmt werden:

$$\frac{\delta v}{v} = \frac{\delta\theta}{\theta} = 1 - \frac{\left(1 + \alpha\psi_1^n\right)^m}{\left(1 + \alpha\psi_{i+1}^n\right)^m}.$$

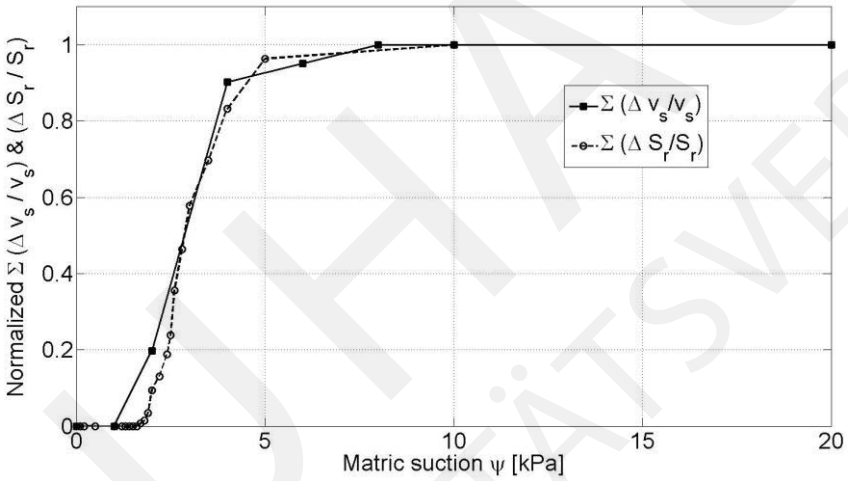

Bild 6: Normierten akkumulierten Geschwindigkeitsgradienten (100 kPa) Netzspannung versus normierten akkumulierten Gradienten der Saugspannungskurve

5. Zusammenfassung

In dem vorliegenden Beitrag wurde ein neues Monitoringverfahren, die Codawellen Interferometrie, vorgestellt und auf ein verschiedenes geomechanische Strukturmonitoring erweitert und angepasst. Zum hochauflösenden Monitoring der kleinen Strukturstörungen wurden die entsprechenden Gleichungen abgeleitet und dargestellt. An verschiedenen Fallbeispielen ist das Potential der Methodik dargestellt. Neben der Spannungsevolution konnte die Abhängigkeit der Wellengeschwindigkeiten von der Saugspannung ausgehend von der Saugspannungs-Sättigungs-Kurve abgeleitet werden. Dadurch ist es möglich, mittels vorhandenem Wissen über zu dem Saugspanungs-Sättigungsverhalten die ‚small-strain' Steifigkeiten in Abhängigkeit vom Sättigungsgrad zu prognostizieren und damit einen sehr wertvollen Beitrag für die Eingangswerte in Entwurfs- und Bemessungsverfahren zu liefern.

6. Literaturverzeichnis

[1] Asslan, M. and F. Wuttke (2012). Wave velocity change and small-stain stiffness in unsaturated soils: experimental investigation, European Unsaturated Soil Conference, Naples

[2] Bachrach, R.,Dvorkin, J. and Nur, A. (2000), "Seismic velocities and poisson's ratio of shallow unconsolidated sands", Geophysics, Vol. 65, No. 2, pp. 559–564.

[3] Cascante, G. and J. C. Santamarina (1996). Interparticle Contact Behavior and Wave Propagation. ASCE Geotechnical Journal, 122(10): 831-839.

[4] Dai, S., F. Wuttke, F. and J. C. Santamarina (2012). Coda Wave Analysis to Monitor Processes in Soils. Journal of Geotechnical and Geoenvironmental Engineering (submitted in 2012).

[5] Gret, A. A. (2004). Time-lapse monitoring with coda wave interferometry. Colorado School of Mines, Ph.D thesis.

[6] Marion, D. (1990), Acoustical, Mechanical and Transport Properties of Sediments and Granular Materials, PhD thesis, Stanford University.

[7] Richart, Jr., F. E., J.R. Hall, and R.D. Woods. (1970). Vibration of soils and foundations. Prentice hall, Inc., Englewood Cliffs, N.J.

[8] Saadatfar, M., Kabla, A., Senden, T. and Aste, T. (2005), The Geometry and the Number of Mono disperse Sphere Packs Using X-Ray Tomography, Vol. 1, A. A. Balkema, pp. 33–36.

[9] Santamarina J.C., K.A. Klein, and M.A. Fam (2001). Soils and waves: Particulate Materials Behavior, Characterization and Process Monitoring. J. Wiley and Sons, Chichester, UK

[10] Schurr, D.P., J.Y. Kim, K.G. Sabra, and L.J. Jacobs (2011). Damage detection in concrete using coda wave interferometry. NDT&E International, 44: 728-735.

[11] Sens-Schönfelder, C., and U. Wegler (2006). Passive image interferometry and seasonal variations of seismic velocities at Merapi Volcano, Indonesia. Geophysical Research Letters, 33(21), L21302.

[12] Shapiro, N. M., M. Campillo, L. Stehly, and M.H. Ritzwoller (2005). High-Resolution Surface-Wave Tomography from Ambient Seismic Noise. Science, 307(5715): 1615-1618.

[13] Snieder, R. (2002). Coda wave interferometry and the equilibration of energy in elastic media. Physical Review E, 66(4): 046615.

[14] Snieder, R. (2006). The Theory of Coda Wave Interferometry. Pure and Applied Geophysics, 163(2): 455-473.

[15] Wuttke, F., M. Asslan, and T. Schanz (2012). Time-lapse monitoring of fabric changes in granular materials by Coda Wave Interferometry. Geotechnical Testing Journal, 35(2), doi 10.1520/GTJ103546.

Geotechnical Testing Journal, Vol. 35, No. 2
Paper ID GTJ103546
Available online at: www.astm.org

F. Wuttke,[1] *M. Asslan,*[2] *and T. Schanz*[3]

Time-Lapse Monitoring of Fabric Changes in Granular Materials by Coda Wave Interferometry

ABSTRACT: The determination of wave velocities in soils captures an important role for small-strain parameter in constitutive modeling as well as in monitoring processes of the state. The wave velocity differs substantially with the porosity, surrounding pressure, degree of saturation and other parameters in soils. In particular when the environmental conditions are non-stationary. For studying the change of state parameters in granular materials, the identification of the velocity evolution can be a challenge in particular if the perturbations are small. We discuss the application of a new seismic method for geotechnical experiments—the Coda wave interferometry. The method is used to detect the wave velocities change related to small soil perturbations. Whereas the perturbations are caused by small changes in stress and void ratio. Different material, well-known sands and artificial glass beads are analysed in this experimental study by conventional volume measurements and seismic methods to detect the stress and porosity changes. The wave excitation and recording was done by piezoceramic bender elements. In result of the tests, the coda wave interferometry emphasized its large potential for the time-lapse monitoring of soils.

KEYWORDS: coda wave interferometry, wave propagation, bender element tests, granular materials

Introduction

Geotechnical Motivation and Current State of the Art

The determination of material parameters and there change in the small-strain range, depending on environmental conditions, is a basic task in the description of strain-dependent material behavior of soils. For the determination of small-strain shear stiffness, different *in situ* and *ex situ* methods are available in Geoscience. The performance of laboratory tests permits an extensive study under controlled conditions. The study of the acoustical characteristics of granular material in laboratory experiments has been technically realized since many years, (e.g., Lee and Santamarina 2004; Santamarina and Fratta 2005). By far, most of the literature is related to different interpretation of time-of-flight measurements (travel time difference) as base for small-strain shear modulus assessment (Arulnathan and Boulanger 1998; Jovicic et al. 1996; Ismail and Rammah 2005; Youn et al. 2008). Due to several superimposed effects on the wave path, the determination of wave velocity is often a non-trivial task. During the laboratory tests, straightforward methods as peak or crossover point differences were applied (Blewett et al. 2000) as well as the more suitable application of cross correlation methods (Arulnathan and Boulanger 1998). Both of them can be difficult to interpret due to inherent dispersion characteristics in granular material, the cylindrical shapes of the test specimen and often insufficient signal coherence. A further method was presented by Greening and Nash (2004). Based on a sweep signal, the phase difference method between the transmitter and receiver signal was successfully applied over a wide frequency range. However from SASW method, where the phase difference method is a basis, the large uncertainties and assignment problems in the low frequency range are known (Nazarian et al. 1994; Yuan and Nazarian 1993). All of these methods are not suitable to detect small material perturbations in a satisfying way, to detect small changes in void ratio and associated stresses.

In geophysics, there has been for some years of developments in theory and application of the multi-scattered waves by the coda wave interferometry (CWI). Snieder (2002,2006) developed the theoretical background of the CWI, in a strongly scattering medium. Whereas the idea to use the sensitivity of the coda wave is not new and variously used before in a more or less empirical sense for seismology applications (see Poupinet et al. 1984). During the last decade, the CWI was several times used in material science and illustrated the extreme sensitivity of multiple scattered waves (Cowan et al. 2002; Grèt et al. 2006) to small perturbations. In this sense the method was used to analyze the change of rock properties (Grèt 2004; Grèt et al. 2006) under different influences. The use of CWI in geotechnical related tasks is still open, but the method can be a useful tool in monitoring states or parameter. The current paper deals with the application of the CWI to monitor the change of stress and void ratio during isotropic pressure change. As the results show, the method gives an excellent impression and a more sensitive view on the evolution of stress changes during experiments. Additionally, the results of

Manuscript received November 2, 2010; accepted for publication August 15, 2011; published online September 2011.

[1]Modeling in Geomechanics, Bauhaus-Univ. Weimar, 99423 Weimar, Germany, (Corresponding author), e-mail: frank.wuttke@uni-weimar.de

[2]Modeling in Geomechanics, Bauhaus-Univ. Weimar, 99423 Weimar, Germany, email: milad.asslan@uni-weimar.de

[3]Chair of Foundation Engineering, Soil and Rock Mechanics, Ruhr-Univ. Bochum, 44780 Bochum, Germany, e-mail: tom.schanz@rub.de

the glass bead measurements fit in a good manner with the calculated velocity gradient of Hertzian Contact models.

Physical Background

From the point of view of granular materials, it is essential to interpret the excited and transmitted records in more general context to determine the velocities or to monitor the material perturbations. This paper tries to consider microscopic influences during the propagation of a wave train in a granular material. From numerical simulations (Lomax 1999; Somfai et al. 2005), it was ascertained that the transmitted acoustic signal can be separated into an initial coherent part and a subsequent randomly or noisy part (coda) influenced by multiple scattering through the granular media. The initial coherent part is linked to the first arrival and the wave group containing the main energy. Whereas the coda behind the coherent part represent the superimposed wave part.

In soil mechanics, literature on wave propagation is chiefly concerned with the measurement of macroscopic elastic modules. To achieve this objective, the wave velocity is extracted from the coherent part of the signal. The remaining part is discarded as scattering and other effects. It can be postulated that a granular assembly can be considered as an effective medium for the transmission of a wave train, if the tests were done on sufficiently large scales and pressures and if the focus is on the initial coherent part of the response. The noisy part arrives after this wave front, which is more sensitive to small changes in the stress, structure, and packing details. Any measurements which are dominated by this noisy part will be influenced by the granular structure and its constituents, like density, grain size, grain shape, water content, and others and not by an average effective parameter of the media.

For the identification of material parameter and stages both the initial coherent and superimposed, noisy part provides valuable information. The initial coherent part provide absolute wave velocity values to characterize the media. In opposite to that the noisy part, the coda is very sensitive to determine the wave velocity gradient between two stages in the material, before and after a small change or perturbation.

Analysis of Absolute Wave Velocities

Many measurements concerning the detection of the time-of-flight (TOF) were done in the past. Most of them tried to find the right point of the incoming wave train, whereas all analyses were related to first coherent part of the wave train and the determination of the effective modules in the material. The objective of research was mostly the investigation of different impulse functions, different impulse shapes, lengths, frequency content, and others. Greening and Nash (2004) used a spectrum analyzer to investigate sweep signals for further phase velocity calculations based on the phase difference method (PD method). The results show differences between the TOF velocity and the phase velocity. In general the phase velocity as a consistent velocity linked with the wave length seems more suitable to explain the complex wave behavior in granular materials than the sharp wave front (TOF) of the ballistic wave. Additionally, the phase velocity beside the group velocity are connected to the energy transport in a wave package. Due to this feature, the group and phase velocity are more sensitive to characterize a dispersive material. Between the phase v_{ph} and group velocity, v_{gr}, with $f, k \in R$ exist the following relations, Eq 1

$$v_{ph} = \frac{\omega}{k} = \lambda \cdot f \quad \text{and} \qquad v_{gr} = \frac{\partial \omega}{\partial k} = v_{ph} + k \cdot \frac{\partial v_{ph}}{\partial k} \tag{1}$$

where λ is wavelength, f frequency, ω angular frequency, and k the wave number. The phase velocity v_{ph} used in (Greening and Nash 2004) can be calculated by using following relations, Eq 6. In Eqs 4 and 5 the terms describe the unwrapped phase function $\varphi_{ij}(f)$, the cross -correlated function r_{ij} in time domain, Eq 2

$$(f \otimes g)(\tau) := \int_{-\infty}^{\infty} f^*(t) g(\tau + t) dt \tag{2}$$

between the transmitted and received signals f and g, respectively, as well as L the distance between transmitter and receiver. By applying the Fourier transform rules to Cross-Correlation, the following relation is given

$$\mathfrak{F}(f \otimes g) = (\mathfrak{F}\{f\})^* \cdot (\mathfrak{F}\{g\}) \tag{3}$$

where the phase to a given frequency f_i of the cross-correlated function is defined as

$$\varphi_{ij}(f) = \tan^{-1} \frac{\Im\left[r_{ij}(f_i)\right]}{\Re\left[r_{ij}(f_i)\right]} \tag{4}$$

and the velocity of a given frequency f_i is determined by

$$v_{ph}(f_i) = L \frac{2\pi f_i}{\varphi(f_i)} \tag{5}$$

To calculate the group velocity of a given frequency f_i and phase v_{ph}, the following equation can be used (Greening and Nash, 2003)

$$v_{gr}(f_i) = 2\pi L \frac{df}{d\varphi(f_i)} \tag{6}$$

Another way to determine the group velocity of propagation waves during laboratory measurements is the application of time-frequency and time scale methods (Arroyo 2007) and (Wuttke et al. 2010). For that objective, a sweep-signal excitation can be used to overcome the problems in the phase difference and TOF methods and to determine wave velocities as well as the dispersion characteristics. The time scaled signal transform methods like continuous wavelet transform (Santamarina and Fratta 2005; Gucunski and Shokouhi 2004; Mallat 1998) were successfully applied also to further tasks. The continuous wavelet transform is defined for $s > 0$, $\tau \in R$ and the chosen wavelet function ψ to Eq 7

$$W(s, \tau) = \frac{1}{\sqrt{s}} \int_{-\infty}^{\infty} f(t) \psi^* \left(\frac{t - \tau}{s} \right) dt \tag{7}$$

where s is the scaling, τ the shifting parameter and ψ^* is noted the conjugate complex of the function ψ. Beside this signal transform methods, in material science, the time-frequency signal transform methods or time-frequency distributions are often used to analyse the wave fields and dispersion characteristics. The application of

the time-frequency and time-scaled methods are described in detail in (Wuttke et al. 2010).

Analysis of Wave Velocity Gradients by Small Perturbations

Theoretical Background of CWI

As explained before, the complete wave train consists of an initial coherent part followed by a noisy tail, the coda. The coda itself is compounded by different scattering effects, where the waves are interfered from different wave paths along the grain contacts (Snieder 2002) and (Snieder 2006). Due to this behavior, the small material changes accumulate in this superimposed diffuse wave field; consequently, the coda is extremely sensitive to any packing details. The base of the CWI is the determination of the velocity gradients between two stages of the system, before and after a small perturbation, as, e.g., stress or density change, change of suction or water content. By use of the gradient function in combination with an absolute velocity as a start value, see Eq 14, the approach is able to give an exact and sensitive information about the absolute velocity changes. Whereas these information are directly aligned with the whole range of stress and porosity change. The theoretical background of the scattered waves is the Feynman path summation (Lomax 1999) and (Snieder 2006) which describes stochastic arbitrary wave paths through a granular media and the genesis of a wave train as superimposed different wave fields. The analysis of this part is achieved by using the normalized windowed cross correlation (NWCC) in Eq 8

$$R^{t,T}(t_s) := \frac{\int_{t-T}^{t+T} u_{unp}(t')u_{per}(t'+t_s)dt'}{\left[\int_{t-T}^{t+T} u_{unp}^2(t')dt' \int_{t-T}^{t+T} u_{per}^2(t')dt'\right]^{\frac{1}{2}}} \tag{8}$$

in which u_{unp} represents the wave field in the unperturbed and u_{per} represents the wave field in the perturbed system, T represents the window length and t_s represents the time markers. The detected time delay in the shifted and cross correlated windows shows a more or less linear gradient with the total time t. In more current publication a so-called stretched CWI is used (Sens-Schönfelder and Larose 2008)

$$R^{t}(\varepsilon) := \frac{\int_{t_1}^{t_2} u_{unp}(t)u_{per}[t(1-\varepsilon)]dt}{\left[\int_{t_2}^{t_2} u_{unp}^2(t)dt \int_{t_1}^{t_2} u_{per}^2[t(1-\varepsilon)]dt\right]^{\frac{1}{2}}} \tag{9}$$

were ε is the gradient of the velocity $\varepsilon = dv/v$, see (Hadziioannou et al. 2009). The application of ε corresponds with the stretching of the time axis, whereas the value of ε is to be determined by application of a grid search or optimization strategies to find the maximum in the cross correlation coefficient. The stretching itself assumes a linear time shift over the time axis, which might be not always the case.

Numerical Analysis of CWI

The steps to calculate conventionally CWI are shown in Fig. 1 and can be enumerate in general following items.

1. Measurement of the time histories always at the same point in the granular material (before and after the perturbation).
2. Subdivision of the time histories in suitable time windows (subdivision in 10 till 15 windows of the time history).
3. Application of across-correlation for each window; a normalized cross correlation will provide additionally the stochastically knowledge of the velocity gradient.
4. Assignment of the time delays of each window to the mean running time of the time history.
5. The gradient between the time lag and total travel time represents the velocity gradient between two stages of the granular material.
6. With repeating of the foregoing procedure to stages after a perturbation in the material, the evolution of the gradient can be shown.

With the plots in Fig. 1, the different steps should be visualized. The gray dots in Fig. 1(*a*) denote the used time windows for the analysis. The normalized cross correlation is applied to each window in Fig. 1(*a*) consequently, with in creasing time an increasing time delay in the respective cross correlation function is to be registered. In Fig. 1(*b*) the initial coherent part is shown, where the stack of superimposed waves is still small and following no time lag is between the unperturbed and perturbed time history visible.

In opposite to Fig. 1(*b*), Fig. 1(*c*) shows a window from the coda, where the time lag between the unperturbed and perturbed time history is obvious. With application of the cross correlation to these two time histories the time lag is found in Fig. 1(*d*). With application of the cross correlation to each window the time lags δt yield a linear function, see Fig. 1(*e*). The representative time lag or peak point of the cross-correlated function is shifted along the time axis for each increasing time window too.

With determination of $\delta t/\Delta t$ the respective gradient for each window is found, where Δt means the medium time value of each window. By taking the mean value of the determined gradients, the mean gradient as well as the variance of the gradient is found, see Fig. 1 (*f*). The normalized cross correlation (NCC) provides the statistical variance of each velocity gradient through the value of spectral magnitude. In Fig. 2 the definition of the velocity gradient $\delta v/v$ itself is given inside of the time lag-travel time plot.

To use the CWI in order to monitor the change in stress or void ratio, the velocity gradient is to be determined for each small step of pressure or void ratio change. An automatic series of pulses during the slow measurement is to be applied. The present study analyzes a stacked time history every 5 kPa as base for the signal procedures. If the signal-to-noise-ratio was showing an insufficient value, the data was band-pass filtered.

Experimental Setup, Analysis, and Results

Experimental Setup

Laboratory equipment in this study was controlled by LabView 8.2. To generate and record the seismic signals during laboratory tests, a function generator was implemented. The signal shapes cover harmonic, impulse and sweep signals, simultaneously and

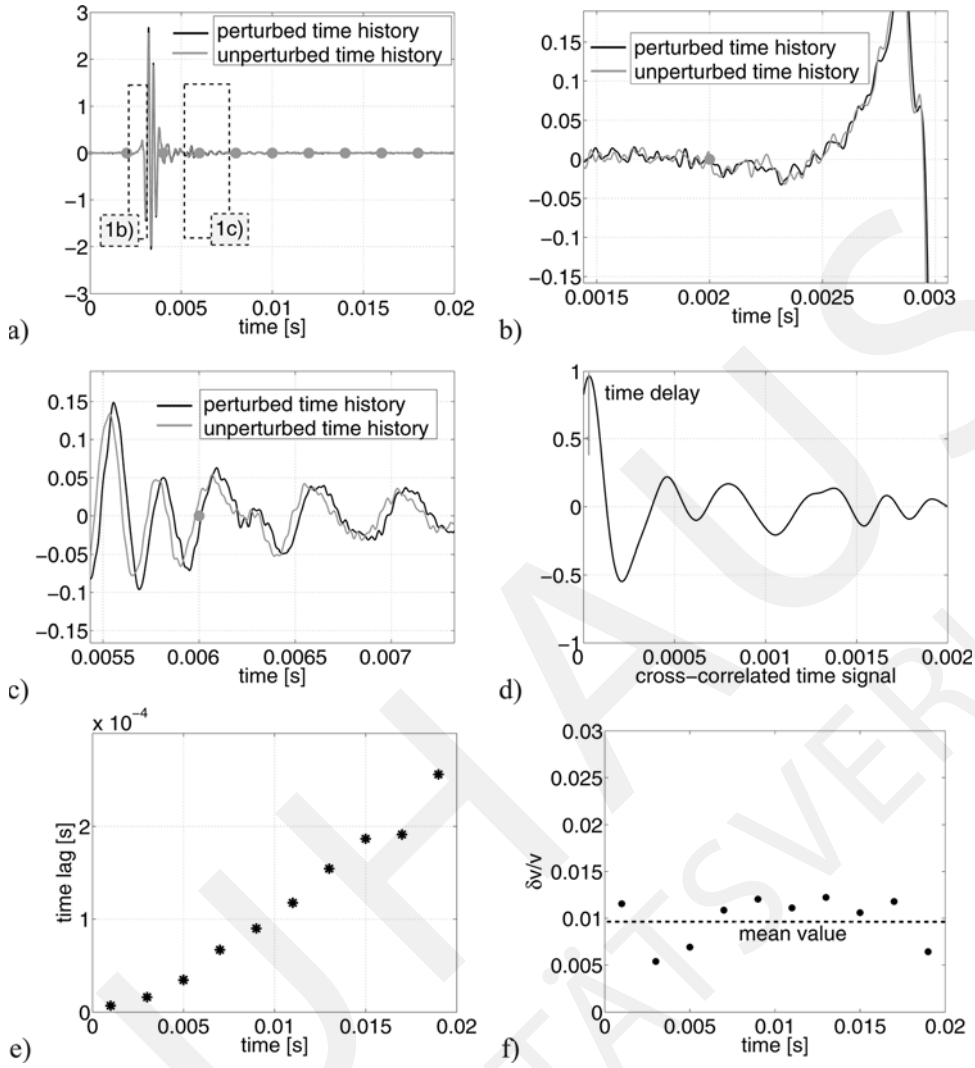

FIG. 1—*Scheme of velocity gradient determination: (a) complete time history in the unperturbed and perturbed material with the selected window distances, (b) zoom of the coherent wave field within a window, (c) zoom of the scattered wave field within a window, (d) Normalized windowed cross correlation of one window, (e) time lag of the windows over time history, (f) mean value of the velocity gradient between the unperturbed and perturbed wave field.*

the change of polarization is possible for each signal. Additionally, a data logger NI-USB 6251 with a maximal sampling rate of 1 MHz was used. The bender elements were excited by a voltage range of ±10V. For the test a parallel type of bending elements was used to avoid the electrical cross-talk phenomenon. To amplify the low voltage of the received signal, the data logger was prefixed by a charge amplifier. The relevant frequency ranges for measurements are given according to the specimen size and grain size. The laboratory specimens were prepared in a triaxial cell with a height of 0.2 m and a diameter of 0.1 m, whereas the distance between the bender elements is L = 0.184 m. The cell consist of a plastic top and steel bottom plate, where porous plates and piezo-elements are implemented. The cell itself was a calibrated cell to control and measure the volume change during the applied pressure steps under constant environment temperatures. For the analyzed frequency range, a band between 3 and 30 kHz was used. To prove the applicability of the method for the given objective, the time lapse monitoring of fabric changes, different tests at sands, sand-kaolin mixtures, and glass beads were done (see Fig. 3).

To study the fabric change during laboratory tests, the confining pressure was increased in steps of 5 kPa from 10 up to 400 kPa to monitor the small change in stress and porosity. All tests were done under dry and saturated conditions, the relevant results to monitor the fabric change are shown in this paper. To analyse the saturated soil samples, the saturation was done at the beginning of the test procedure. The test was performed under drained conditions to avoid pore water pressures during the increase of the cell pressures. During the whole tests the sample was either dry or fully saturated. There was no change in saturation level.

Experimental Analysis

In the following sections, eight different materials are analyzed in detail—five different Sands; one Sand-Kaolin Mixture and two mono-disperse glass beads of diameter 3.5 and 8 mm. To compare the determined velocities, based on the determination of the TOF, phase velocity and the velocity gradients, a comparison of all

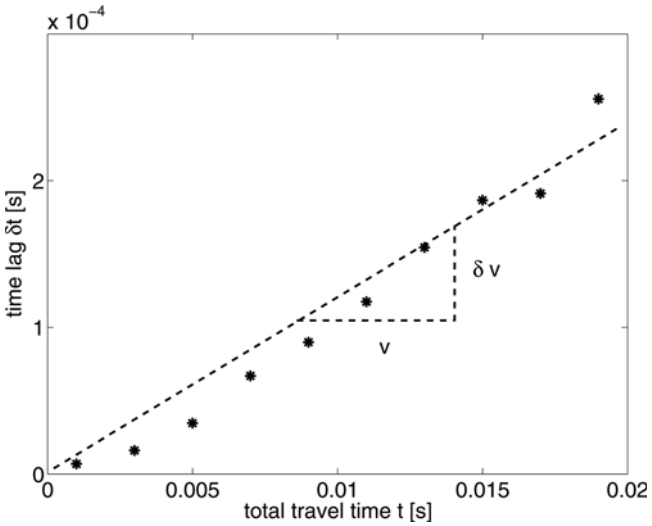

FIG. 2—*Definition of velocitygradient by the ratio dv/v between the total time t and the time lag δt of the shifted windows in the coda wave interferometry.*

results are given. For improvement of TOF picking, the transmitter signal was used twice in normal deviation and inverse polarized deviation, see Fig. 4(*a*).

As described above, the signal can be separated into two parts; the initial coherent part and the noisy, super imposed part—the coda of the time history (see Fig. 4(*a*)).

This second part, the coda, was subject of CWI to determine the velocity gradients. In opposite of the impulse excitation in Fig. 4(*a*) additionally a sweep signal was used to determine the phase velocity, see Fig. 4(*b*). In both figures, Fig. 4(*a*) and 4(*b*) a typical plot of the transmitted and recorded signal is shown, which are the base for TOF, PD, and CWI analysis. Also, both excitations were used to determine absolute wave velocities for comparison to the velocity gradient based calculations. To achieve the objective, which is monitoring of small changes/perturbations in soil specimen by CWI, the state change monitoring is reduced in this paper to monitor the change of stress or void ratio during the pressure change with comparison to conventional volume change measurements.

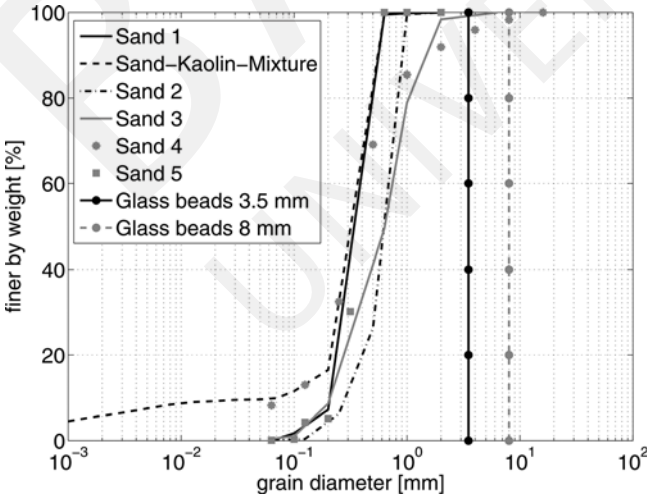

FIG. 3—*Grain size distribution of tested materials.*

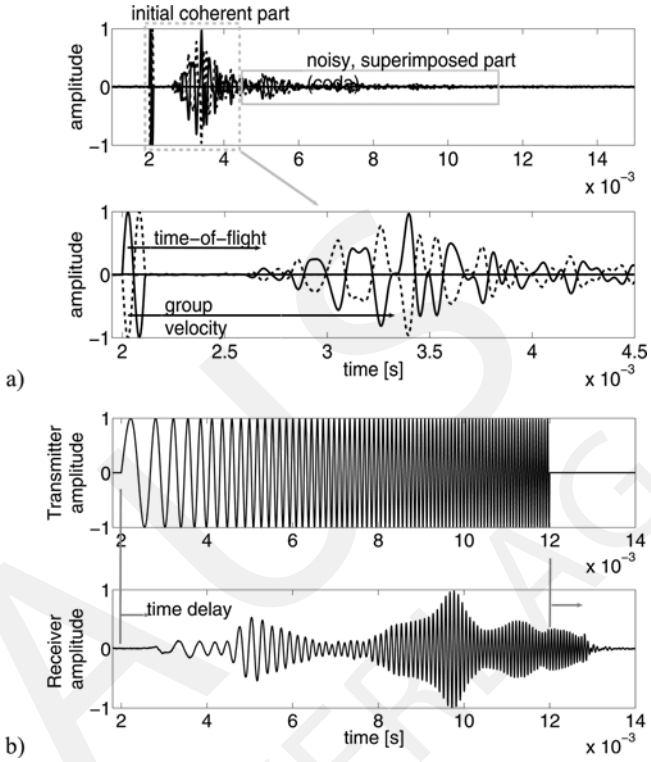

FIG. 4—*(a) Impulse signals to determine TOF, (b) Sweep signal to determine the phase and group velocity.*

Related to this objective, Fig. 5 shows examples of the velocity gradients evolution with pressure steps. It is visible that the change is primarily a function of the change in contact pressure between the grains. By use of the scattered wave field analysis, a smooth and detailed information about the velocity changes with increasing pressure results. Under consideration of the well-known problems in the identification of the first arrival in TOF methods, the application of the CWI is more reliable, because the cross-correlated function shows one time-dependent peak in the cross-correlated function - the time delay between both time histories in the given window.

In Figs. 5 and 6 it is visible that void ratio curves have a decimal power less amplitude evolution and has a much more rough shape, which suggests that the evolution of velocity gradients is influenced by the contact stresses of the grains. To study that influence of the contact stresses between the grains, several monodisperse glass beads specimen were analyzed by the CWI. The change in the void ratio by using mono-disperse glass beads equals zero. Hence, the influence of the contact stresses could be analyzed, see Fig. 7. The evolution of the velocity gradients between Figs. 6 and 7 is quite similar, which confirms the assumption that primarily the contact stresses are responsible for the evolution of the measured velocity gradients in the compacted specimen with low porosity change.

Evolution of the Wave Gradients by Contact Stresses

To substantiate the interpretation of the experimental velocity gradient evolution, a comparison with synthetic generated results

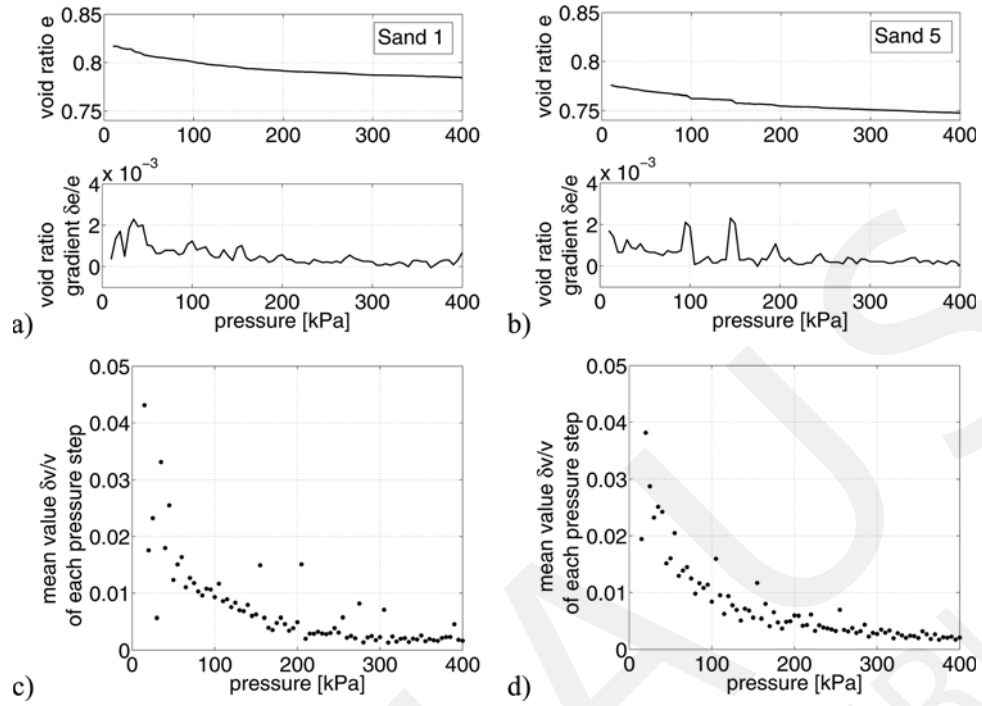

FIG. 5—*(a) and (b) Evolution of void ratio change for Sand 1 and 5; (c) and (d) Evolution of velocity gradient for Sand 1 and 5.*

based on a Hertzian contact models is analyzed. Accordingly, the argumentation of (Bachrach et al. 2000) and (Brandt 1955) for the definition of a modified Hertz-Mindlin Theory, the interparticle normal skeletal average force for an isotropic random assembly of mono disperse spherical particles, $\langle N \rangle$, is defined as

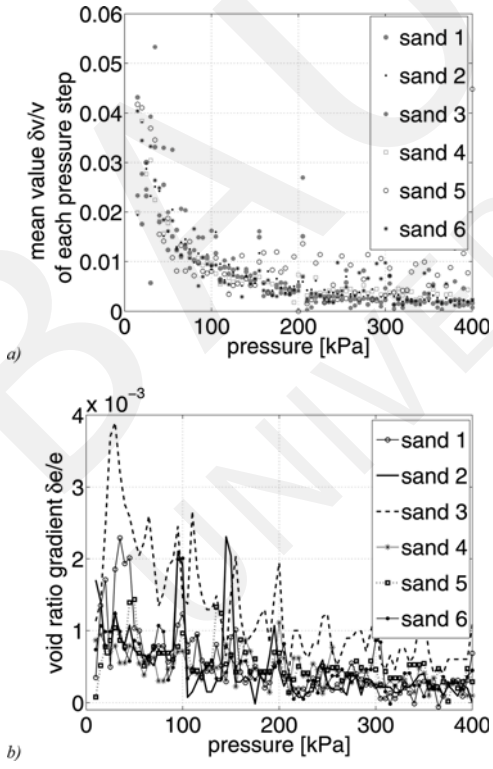

FIG. 6—*(a) Evolution of velocity gradients for all Sands, (b) Evolution of void ratio change for all Sands.*

$$\langle N \rangle = \frac{4\pi R_g^2 \sigma_0}{cn(1-n)} \tag{10}$$

where Rg is defined as in Fig. 8, σ_0 is the isotropic confining pressure, n is the porosity and cn is the coordination number, which describes the average number of contacts per grain, (Marion 1990) and (Santamarina et al. 2001). The average force $\langle N \rangle$ applying on each contact point contains the assumptions that the contacts are distributed with a uniform probability of the sphere surface, the contacts deform identically and forces are conform to normal forces.

After (Saadatfar et al. 2005), the coordination number can differ between 6.9 and 8.2. Based on the accomplishments of (Bachrach et al. 2000), the Hertz-Mindlin model contains two contact models for the normal S_n and shear S_t stiffness

$$S_n = \frac{4 r_c \mu}{1-\nu} \text{ and } S_t = \frac{8 r_c \mu}{2-\nu} \tag{11}$$

$$r_c = \sqrt[3]{\frac{3NR_c(1-\nu)}{8\mu}} \text{ with } R_c^{-1} = 0.5\left(R_1^{-1} + R_2^{-1}\right) \tag{12}$$

where μ and ν are the grain shear stiffness and the Poisson's ratio, respectively. The radii R_1 and R_2 are local radii of two grains, see Fig. 8. The shear wave velocity c_S can finally defined to Eq 13

$$c_s = \sqrt{\frac{1}{\rho_b} \cdot \frac{cn(1-n)}{20\pi R_g}(S_n + 1.5 S_t)} \tag{13}$$

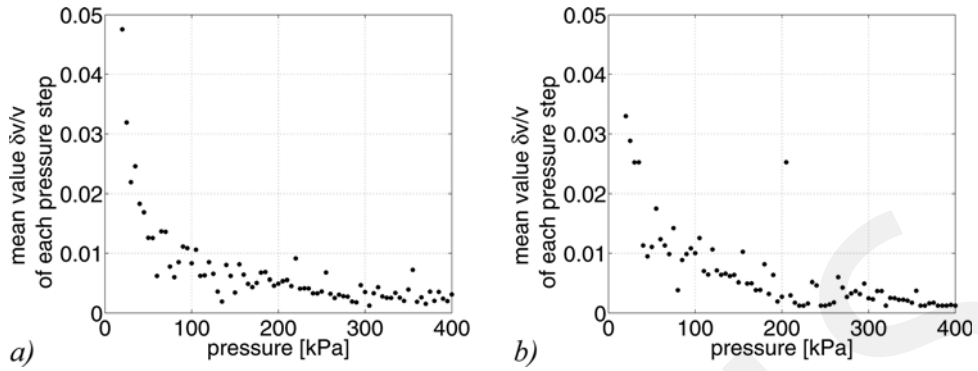

FIG. 7—*Evolution of velocity gradients under increasing pressure steps for monodisperse glass beads: (a) 3.5 mm and (b) 8 mm diameter.*

where ρ_b is the bulk density. Following material parameter for glass beads were used for the synthetic calculation of the shear wave velocities: $E_g = 104$ GPa, $G_g = 31$ GPa, $\nu_g = 0.21$, $\rho_g = 2.5$ t/m^3, $R_g = R_c = 3.5/8$ mm, $n = 0.41$, $\rho_{skel} = 1.485$ t/m^3, $cn = 6$. The results of the synthetic calculation are shown in Fig. 9. In Fig. 9 the comparison between the synthetic calculation and the measured data are shown. It is obvious that the measured and synthetic data fit quite excellent. From the measured velocity gradient of the glass beads of 3.5 mm, the velocities were determined by using the initial value of the synthetic velocities and calculating the further velocities by increasing pressure with use of Eq 14

$$c_{s,abs,i+1} = c_{s,abs,i} + c_{s,abs,i} \cdot \chi_i, \text{ where } \chi_i := \left\{ \frac{\delta c_s}{c_s} \right\}_i \tag{14}$$

By applying Eq 14, the absolute shear wave velocities in Fig. 9(*b*) for the synthetic data and the calculated values from CWI should be similar because the gradients of both data are close. This point confirms the assumption that the changes in velocity of the skeleton of glass beads under increasing pressure only affects the interparticular stress without change in volume. This behavior underlies the fact that the CWI monitors the velocity changes in a realistic manner. By applying this knowledge and assuming of the Hertz-Mindlin-Theory to the measurements of the experimental tests with visible influence of the void ratio, it should be possible to separate the influence of the confining pressure and the volume change during the tests with sand material. Whereas in opposite to the analyzed glass beads the velocity change accumulated in natural sands is associated with both the stress and porosity change. In terms of micro-mechanical description, that means, beside the pressure change there is a change in the number of contacts and radii between the grains.

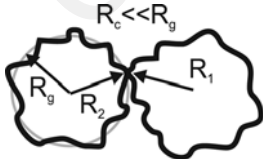

FIG. 8—*Contact definitions between two angular grains, after Bachrach (2000).*

Comparison of Absolute Wave Velocities Determined by CWI, TOF, and PD Method

In following section different velocities will be compared to separate the relation of the CWI to the absolute velocity detection methods. For this objective all methods, the TOF, PD, CWT, and CWI were applied to each pressure step under use of an impulse and wavelet or sweep excitation. In a first step the TOF velocities and the calculated absolute velocities from the velocity gradient by using initial values of the absolute velocity measurements (see Eq 14) are compared for dry and saturated sand, see Fig. 10(*a*) and 10(*b*). It is visible that the trends between TOF and CWI shows differences. A straight forward link between these two methods seems impossible from the physical point of view. The TOF is based on a ballistic wave front, where in the optimal case no reflected or interfered waves are stored. The ballistic wave "feels" the material as a continuum and not as a particular media; otherwise the ballistic wave front will be strongly scattered by the particles. In opposite to the ballistic wave front, the coda has no fixed wave front. The coda is generated by different interfering and reflecting wave fronts with increasing time in the time history on the recording point. Hence the coda is becoming more and more sensitive to the material structure with increasing time. This behaviour is obvious in Fig. 2. Hence, the coda and therefore the CWI depends on scattered, reflected and superimposed multi-directional wave field.

In difference to the foregoing comparison between TOF and CWI, the phase velocities v_{ph} show a better agreement to calculated absolute velocities based on CWI. This is shown in Fig. 11. In Fig. 11 on the right hand side the evolution starts from the initial value of the phase velocity at 5 kHz. With this initial value the evolution was calculated by Eq 14. to determine the absolute velocity values over the pressure range. The methodologies of phase velocities and group velocities determination are analyzed more in detail in Wuttke et al. (2010). It was found that for the performed tests, the frequency dependent phase and group velocity function corresponds to the eigenvalues of torsional modes. These effects were theoretically analyzed in Arroyo (2007) and Arroyo et al. (2002).

By following the argumentation of Hadziioannou et al. (2009), the scattered waves are more sensitive to small variations than ballistic waves. Whereas the small variations cause a velocity change in the medium by which the small continuous phase

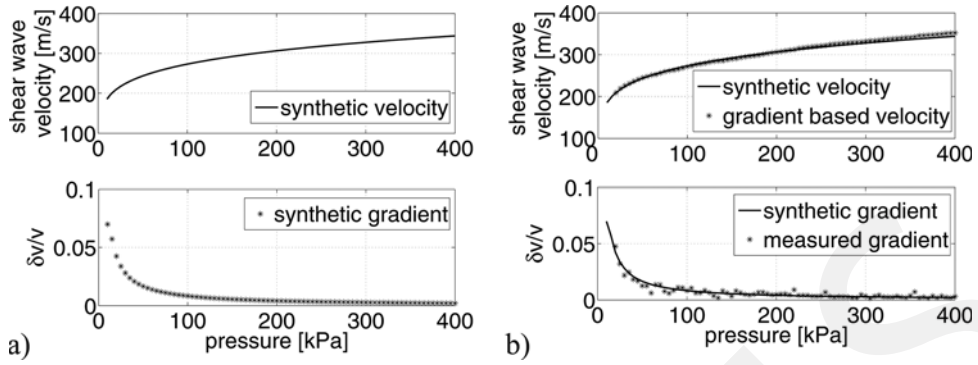

FIG. 9—*(a) Synthetic Wave velocity and velocity gradient for glass beads 3.5 mm after Hertz-Mindlin Theory, (b) Comparison between measured and calculated wave velocity and velocity gradient.*

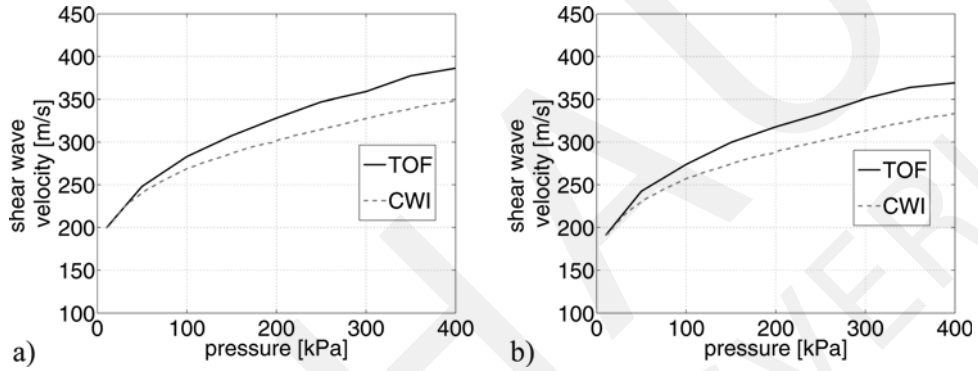

FIG. 10—*Comparison between TOF and Shear wave velocity determined from the velocity gradient, (a) Sand 2, dry and (b) Sand 2, saturated.*

changes in the coda are caused. This argumentation highlights that the evolution of the velocity gradients is more close to the phase velocity results than phase differences, which is reflected in Fig. 11 too.

Advantages and Limitations of CWI

To conclude the CWI following statements regarding the advantages of CWI can be done. The CWI offers a very useful tool for a sensitive monitoring of structure changes. The coda itself has a direct sensitivity to the inter-particle structure change. That is obvious, because the CWI is based on the scattered and superimposed wave field in stochastical, heterogeneous media. With the performed test it could be shown that the CWI is able to give a smooth and well described evolution function. With application of absolute wave velocity determination methods, the general trend of absolute velocity change can be monitored very well. Hence, the CWI method has the potential to be a essential tool for civil health and structural monitoring.

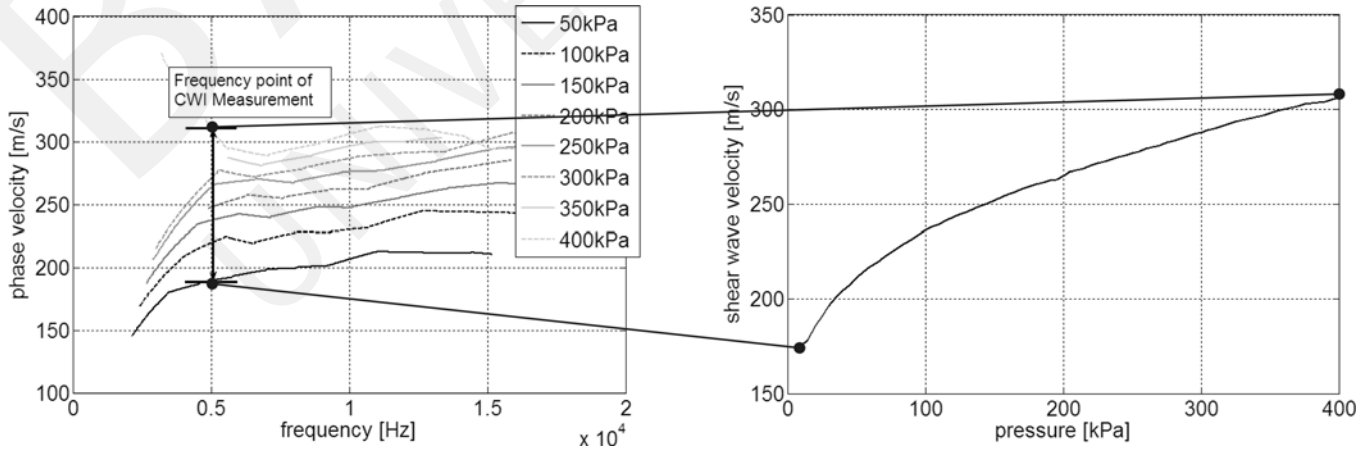

FIG. 11—*(left) Phase velocity curves for Sand 2, (right) Absolute wave velocity calculated by use of velocity gradients and a start value (lowest vph to 5 kHz) after Eq 14.*

A disadvantage of the CWI is its limitation to velocity gradients. To determine further material parameter, like small strain shear stiffness, always a joint application of an absolute velocity method and the CWI is necessary. A further limitation is the arbitrary multi-directional superimposed wave fields in the current application. These multi-directional superimposed wave fields do not allow to separate any anisotropic change in the material. In particular the structure change due to anisotropic stress is possible to indicate in general but not related to the principle directions. A further limitation is the integral value of the velocity gradient. Hence a localization of the change is not possible. Applying this method in tomographical arrays a trace directed allocation should be possible. A further problem rises in the microscopic allocation or correlation if different microscopic phenomenon cause a change in the structure at the same time. One example is the existence of increasing inter-particle stresses and crushing particle edges or contact points. The final gradient is an integral gradient of the complete structure change. An anisotropic allocation would be useful in that case but is not possible yet. A more numerical limitation of the CWI is the focus on small perturbations. If stronger changes are present, both coda signals are not coherent in their shape, and the windowed cross correlation becomes difficult in the length of the windows. In this case the stretched cross correlation can be useful.

Conclusions

The objective of this paper was to analyse a new tool to determine the velocity gradients due to a small change in the structure or pressure. It was found that the coda wave interferometry can be a powerful tool to monitor these very small changes. Compared to an absolute velocity, the accumulated gradient function in Eq 14 is able to describe the velocity change in granular material in a sensitive and detailed manner. As the experiment validated, the CWI is more robust and reliable during the application than absolute wave velocity methods, because only one absolute maximum value exists in the cross-correlation function to determine the time delay. Additionally, the method is suited for an automation in laboratory measurements. To provide information about material values in small strain range, like small strain stiffness a start value of an absolute velocity is needed to initialize the wave velocity function based on a gradient.

During the study of mono-disperse artificial glass beads, the gradient described perfectly the velocity change due to the isotropic pressure change. The evolution of the measured and synthetically calculated gradients based on the modified Hertz-Mindlin Theory has shown good agreement. Whereas the pressure or pressure change are directly related with the velocity or velocity change. The presented results show a non-linear trend because the compared values are velocities or velocity gradients. If the comparison would be done with the applied stresses the same linear trend would be visible. The non-linearity is not caused by a physical path effect. The reason for the non-linear trend is the exponential relation of stresses to the shear wave velocity.

It was shown that the method can give additional information about the velocity evolution in a very sensitive manner; hence the method has the potential to act as a monitoring tool for changes in material, structure, field conditions, and stresses. A further important point is the reliability of velocity gradient determination. Hence, the sensitive and reliable monitoring of small fabric changes in granular materials is realized by the coda wave interferometry.

Acknowledgments

The writers acknowledge the support of the R and D-Program GEOTECHNOLOGIEN funded by the German Ministry of Education and Research (BMBF) and German Research Foundation (DFG), Grant 03G0636B.

References

Arroyo, M., 2007, "Wavelet Based Analysis of Pulse Tests in Soil Samples," *Riv. Ital. Geotec*., Vol. 2, pp. 25–38.

Arroyo, M., Medina, L., and Muir Wood, D., 2002, "Scale Effects in Bender-Based Pulse Tests," *Numerical methods in Geomechnics*, *NUMOG VIII*, G. N. Pande and S. Pietruszczak, Eds., Balkema, Rome, Italy, pp. 589–595.

Arulnathan, R., and Boulanger, R., 1998, "Analysis of Bender Elements," *Geotech. Test. J.*, Vol. 21, No. 2, pp. 120–131.

Bachrach, R., Dvorkin, J., and Nur, A., 2000, "Seismic Velocities and Poisson's Ratio of Shallow Unconsolidated Sands," *Geophysics*, Vol. 65, No. 2, pp. 559–564.

Blewett, J., Blewett, I., and Woodward, P. K., 2000, "Phase and Amplitude Response Associated With the Measurement of Shear-Wave Velocity in Sand by Bender Elements," *Canadian Geotechnical Journal*, Vol. 37, pp. 1348–1357.

Brandt, H., 1955, "A Study of the Speed of Sound in Porous Granular Media," *J. Appl. Mech.*, Vol. 22, pp. 479–485.

Cowan, M., Jones, I., and Weitz, D., 2002, "Diffusing Acoustic Wave Spectroscopy," *Phys. Rev. E*, Vol. 65, 066605.

Greening, P., and Nash, D., 2004, "Frequency Domain Determination of G_{max} Using Bender Elements," *Geotech. Test. J*., Vol. 27, No. 3, pp. 288–294.

Grèt, A. A., 2004, "Time-Lapse Monitoring With Coda Wave Interferometry," Ph.D. thesis, Center of Wave Phenomena, Colorado School of Mines, Golden, CO.

Grèt, A., Snieder, R., and Scales, J., 2006, "Time-Lapse Monitoring of Rock Properties With Coda Wave Interferometry," *J. Geophys. Res.*, Vol. 111, B03305.

Gucunski, N., and Shokouhi, P., 2004, "Detection and Characterization of Cavities Under the Airfieldpavementsby Wavelet Analysis of Surface Waves," *FAA Worldwide Airport Technology Transfer Conference*, Atlantic City, NJ.

Hadziioannou, C., Larose, E., Coutant, O., Roux, P., and Campillo, M., 2009, "Stability of Monitoring Weak Changes in Multiply Scattering Media With Ambient Noise Correlation: Laboratory Experiments," *J. Acoust. Soc. Am.*, Vol. 125, No. 6, pp. 3688–3695.

Ismail, M., and Rammah, K., 2005, "Shear-Plate Transducers as a Possible Alternative to Bender Elements for Measuring G_{max}," *Géotechnique*, Vol. 55, No. 5, pp. 403–407.

Jovicic, V., Coop, M., and Simic, M., 1996, "Objective Criteria for Determining G_{max} From Bender Element Tests," *Géotechnique*, Vol. 46, No. 2, pp. 357–362.

Lee, J.-S., and Santamarina, J., 2004, "Bender Elements: Performance and Signal Interpretation," *J. Geotech. Geoenviron. Eng.*, Vol. 131, No. 9, pp. 1063–1070.

Lomax, A., 1999, "Path-Summation Wave Forms," *Geophys. J. Int.*, Vol. 138, pp. 702–716.

Mallat, S., 1998, *A Wavelet Tour of Signal Processing*, Academic Press, San Diego, CA.

Marion, D., 1990, "Acoustical, Mechanical and Transport Properties of Sediments and Granular Materials," Ph.D. thesis, Stanford Univ., Palo Alto, CA.

Nazarian, S., Yuan, D., and Baker, M. R., 1994, "Automation of Spectral Analysis of Surface Wave Method," *Dynamic Geotechnical Testing II*, R. J. Ebelhar, V. P. Drevinch and B. L. Kutter, Eds., pp. 88–100.

Poupinet, G., Ellsworth, W., and Frechet, J., 1984, "Monitoring Velocity Variations in the Crust Using Earthquake Doublets: An Application to the Calaveras Fault, CA," *J. Geophys. Res.*, Vol. 89, No. B7, pp. 5719–5731.

Saadatfar, M., Kabla, A., Senden, T., and Aste, T., 2005, "The Geometry and the Number of Mono Disperse Sphere Packs Using X-Ray Tomography," *Powders and Grains*, Vol. 1, A. A. Balkema, pp. 33–36.

Santamarina, J., and Fratta, D., 2005, *Discrete Signals and Inverse Problems*, John Wiley and Sons, New York.

Santamarina, J., Klein, K., and Fam, M. A., 2001, *Soils and Waves*, Wiley, New York.

Sens-Schönfelder, C., and Larose, E., 2008, "Temporal Changes in the Lunar Soil From Correlation of Diffuse Vibrations," *Phys. Rev. E*, Vol. 78, 045601.

Snieder, R., 2002, "Coda Wave Interferometry and Equilibrium of Energy in Elastic Media," *Phys. Rev.*, Vol. 66, No. 4, pp. 1–8.

Snieder, R., 2006, "The Theory of Coda Wave Interferometry," *Pure Appl. Geophys.*, Vol. 163, pp. 455–473.

Somfai, E., Roux, J., Snoeijer, J., VanHecke, M., and Van Saarloos, W., 2005, "Elastic Wave Propagation in Confined Granular Systems," *Phys. Rev. E*, Vol. 72, pp. 1539–3755.

Wuttke, F., Markwardt, K., and Schanz, T., 2010, "Application of Time-Frequency and time-Scale Signal Transform to Analyse Dispersion Characteristics in Granular Materials: Theory," (submitted).

Youn, J.-U., Choo, Y.-W., and Kim, D.-S., 2008, "Measurement of Small-Strains Hear Modulus G_{max} of Dry and Saturated Sands by Bender Element, Resonant Column and Torsional Shear Tests," *Can. Geotech. J.*, Vol. 45, pp. 1426–1438.

Yuan, D., and Nazarian, S., 1993, "Automated Surface Wave Method: Inversion Technique," *J. Geotech. Eng.*, Vol. 119, No. 7, pp. 1112–1126.

Wave velocity analysis of state parameter changes in multi-phase granular materials

F. Wuttke
Bauhaus-Universität Weimar, Chair and Laboratory of Soil Mechanics, Germany

M. Asslan
Bauhaus-Universität Weimar, Chair and Laboratory of Soil Mechanics, Germany

T. Schanz
Ruhr-Universität Bochum, Chair of Foundation Engineering, Soil and Rock Mechanics, Germany

ABSTRACT: The determination of wave velocities in soils captures an important role for initials parameter in constitutive modelling as well as in monitoring processes as state indicator nowadays. The wave velocity differs substantially with the porosity, surrounding pressure, degree of saturation and other parameters in soils. To determine the wave velocity in soils, different methods in situ and ex situ exist. For studying the behaviour of waves under different conditions, the laboratory methods are indispensable, but the identification of the correct velocity can be a large challenge particularly if the perturbations are small. We discusses existing methods in time, frequency and time-frequency space and applying of the coda wave interferometry to determine the wave velocity in dependence of small soil perturbations. During measurements, the application shows uncertainties and mistakes in identification of wave velocities. In comparison to conventional methods, like first arrival measurement, the advantages of extended methods as wavelet transforms and time-frequency distributions are shown. To study the dependency of wave velocities caused by small perturbations, as hydro-mechanical changes, the coda wave interferometry was used. The laboratory tests were done on different type of sands with well known hydro-mechanical parameter. In result of the tests, the coda wave interferometry emphasized its large potential for the time-lapse monitoring of soils.

1 INTRODUCTION

1.1 *Geotechnical motivation and current state*

The determination of initial states, like initial shear stiffness, is a basic part in the description of strain-dependent material behaviour of soils. For the determination of initial shear stiffness, different in- and ex-situ methods are available. The performance of laboratory tests permits an extensive study under controlled conditions. The study of the acoustical characteristics of granular material in laboratory experiments is technically realized since many years (e.g. Lee & Santamarina 2004, Santamarina & Fratta 2005). Most of the literature is related to different interpretation of time-of-flight measurements (travel time difference) as base of initial shear modulus assessment (Arulnathan & Boulanger 1998, Jovicic, Coop & Simic 1996, Ismail & Rammah 2005, Youn, Choo & Kim 2008). Due to several superimpose effects on the wave path the determination of wave velocity is a non-trivial task. During the laboratory tests, straight forward methods as peak or cross-over point differences were applied (Blewett, Blewett & Woodward 2000) as well as the more suitable application of cross-correlation methods (Arulnathan & Boulanger 1998). Both of them can be difficult to interpret due to inherent dispersion characteristics in granular material and often insufficient signal coherence. A further, more advanced method was presented by Greening & Nash 2004. Based on a sweep signal, the phase difference method between the transmitter and receiver signal was successfully applied over a wide frequency range. However from SASW method, where the phase difference method is a basis, the large uncertainties and assignment problems in the low frequency range are known (Nazarian, Yuan & Baker 1994, Yuan & Nazarian 1993).

1.2 *Physical background*

From the point of view of granular materials, it is essential to interpret the signals in more general context to determine the velocities or to monitor the material perturbations. This paper tries to consider

microscopical influences during the propagation of a wave train in a granular material. From numerical simulations (Lomax 1999, Somfai et al. 2005) it was ascertain that the transmitted acoustic signal can separated into an initial coherent part and a subsequent randomly or noisy part (coda) influenced by multiple scattering through the granular media. The soil mechanics literature on wave propagation is chiefly concerned with the measurement of macroscopical elastic modules under specific soil conditions. In particular, under multi-phase conditions (Alramahi et al. 2008). After extraction of the wave velocity from the coherent part of the signal, as discussed, the remaining part is discarded as scattering and other effects. It can be postulated that a granular assembly can be considered as an effective medium for the transmission of a wave train, if the tests were done on sufficiently large scales and pressures and if the focus is on the initial coherent part of the response. After this wave front follows the noisy part, which is sensitive to small changes in the structure and packing details. Any measurements which are dominated by this noisy part will be influenced by the granular structure and its constituents, like density, grain size, shape, water content and others and not by an average effective parameter of the media.

2 ASSIGNMENT OF ABSOLUTE VELOCITY LEVEL

2.1 *Conventional methods*

Many measurements concerning the determination of the right time-of-flight (TOF) were done in the past. Most of them tried to find the right point of the incoming wave train, whereas all analyses were related to first coherent part of the wave train and the determination of the effective modules in the material. The objective of research was mostly the investigation of different impulse functions, different impulse shapes, lengths, frequency content and others. Greening and Nash (2004) used a spectrum analyser to investigate sweep signals for further phase velocity calculations. The results show differences between the TOF velocity and the phase velocity. In general the phase velocity as a consistent velocity linked with the wave length is much more suitable to explain the complex wave behaviour in granular materials as the sharp wave front (TOF). Additionally, the phase velocity is beside the group velocity connected to the energy transport, hence more sensitive to characterize a dispersive material and accordingly gives more realistic wave velocities.

2.2 *Time-scale and Time-frequency signal transforms*

In following, the sweep-signal excitation was used to find opportunities to overcome the problems in the phase difference and TOF methods and to determine wave velocities as well as the dispersion characteristics in multi-phase material. The used sweep-signal was a linear time-frequency function. Besides, the phase difference method, time-frequency and time-scale transform methods were used in this study to analyse the time-dependent signal. By using these methods the group velocity is calculated. The application of the easy short-term Fourier transform in time domain (Bath 1974) or similar methods, as multiple filter methods (Dziewonski, Bloch & Landisman 1969), fails because the resolution of this method is quite poor. The time scaled signal transform methods like continuous wavelet transform (Santamarina & Fratta 2005, Gucunski & Shokouhi 2004, Mallat 1998) were successfully applied to other tasks. Beside this signal transform methods, in material science the time-frequency signal transform methods or time-frequency distributions (Hammond & White 1996, Mallat 1998, Niethammer & Jacobs 2001, Narasimhan & Nayak 2003) are often used to analyse the wave fields and dispersion characteristics.

In own laboratory tests, the continuous wavelet transform (CWT) was required to keep a sufficient level of redundancy in the transformed signal. Due to this demand the use of the CWT during running laboratory tests requires a further special mathematical treatment to avoid a huge calculation time effort. To apply the CWT in laboratory tests the CWT (eq.1) was transformed into the frequency domain. As suitable mother wavelet for vibration analyses, the Morlet wavelet was used.

$$W_{s,\tau} = \frac{1}{\sqrt{|s|}} \int_{-\infty}^{\infty} f(t)\psi^*\left(\frac{t-\tau}{s}\right)d\tau \rightarrow \mathfrak{F}\left(W_{s,\tau}\right) \qquad (1)$$

The given variables are *f(t)* time history, ψ wavelet function, *s* scaling factor, τ shift variable, * nominates the complex conjugated term and $\mathfrak{F}$ the Fourier transformed function. By using the rules of the discrete Fourier Synthesis, the decomposed Wavelet transformed signal in time and frequency is given by eq.2, see Torrence 2005.

$$W_{s,\tau} = \sum_{0}^{N-1} \mathfrak{F}\left\{f(t)\right\}\mathfrak{F}\left\{\psi^*\left(\omega_k, \omega_0, a, b, \Delta t\right)\right\} e^{j\omega_k b\Delta t} \qquad (2)$$

Different to the time-scale transform methods, the time-frequency transform methods are less analytical from the mathematical point of view and therefore more limited, but faster in use. The Wigner-Ville distribution is often used representative of Cohen's class, which are the general class of the quadratic time-frequency formulations. The basis for the high resolution in time and frequency is the current autocorrelation of the time history itself, see eq.3.

$$W(t,\omega)=\int_{-\infty}^{\infty} f\left(t+\frac{\tau}{2}\right)f^{*}\left(t-\frac{\tau}{2}\right)e^{-j\pi ft}d\tau \qquad (3)$$

The entity of both the time-scale and time-frequency transform methods is the imaging of the dependency between time and frequency. Therefore, by comparison of the time-frequency dependence of a transmitted and a received signal, the group velocity can be determined, see figure 1. The absolute value of the group velocity is given by the dark lines in the surface plot of 3D time-frequency spectra and mathematically linked with the phase velocity of the wave train.

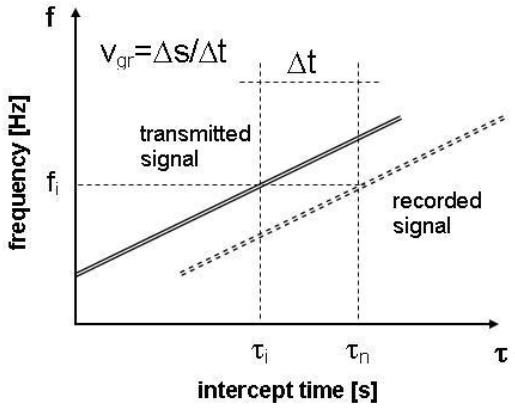

Figure 1. Time-frequency dependence of transmitted and received signal by using a sweep excitation and a time-scale or time-frequency transform method.

The difference in the detected velocity between the first arrival or time-of-flight methods velocities is given due to the dispersion, attenuation and scattering characteristics in granular multi-phase materials.

3 ASSIGNMENT OF VELOCITY GRADIENTS

3.1 *Diffuse Waves & Coda wave interferometry*

As explained before, the complete wave train consists of an initial coherent part followed by a noisy tail, the coda. The coda itself is compounded by different scattering effects, where the waves are interfered from different wave paths along the grain contacts (Snieder 2002, Snieder 2006). But due to this many different superimposed influences (accumulation of small changes), this part of the wave front is sensitive to any packing details and called diffuse waves. The base of the coda wave interferometry (CWI) is the determination of the velocity gradients between two stages of the system, before and after a small perturbation, as e.g. density change, change of suction or water content. This characteristics promises to find a sensitivity sensor for further monitoring studies. In combination of absolute velocity assessment methods with velocity gradient methods, the absolute velocity can be given by adding the gradient to an initial value in a sensitive manner. The theoretical background of the diffuse waves is the Faynman path summation (Lomax 1999) which describes stochastically arbitrary wave paths through a granular media and the genesis of a wave train as superimposed different wave fields. The analysis of this part is realised by using the normalized windowed cross correlation (CC) in eq. 4

$$R^{(t,T)}(t_s)=\frac{\int_{t-T}^{t+T} u_{unp}(t')u_{per}(t'+t_s)dt'}{\left(\int_{t-T}^{t+T} u_{unp}^2(t')dt'\int_{t-T}^{t+T} u_{per}^2(t')dt'\right)^{1/2}}, \qquad (4)$$

in which u_{unp} represents the wave field in the unperturbed und u_{per} in the perturbed system, T the window length and t_s the time markers. The detected time delay in the shifted and cross correlated windows shows a more or less linear gradient with the total time t. In ratio to the time lag δt the gradient of the velocity $\delta v/v$ is defined, see figure 2. The normalised CC gives additionally a trust value in the statistical sense.

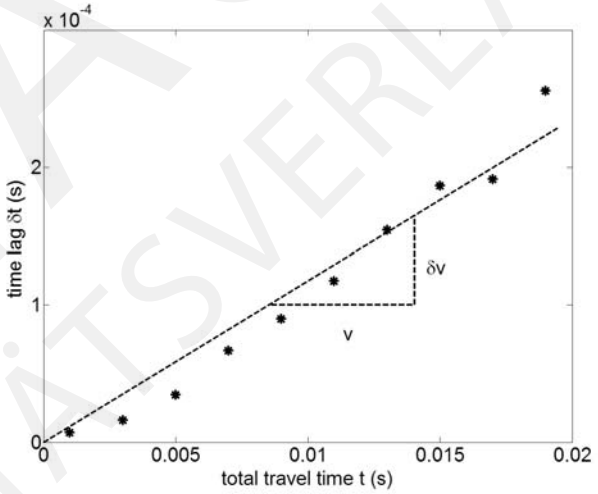

Figure 2. Definition of velocity gradient by the ratio $\delta v/v$ between the total time t and the time lag δt of the shifted windows in the coda wave interferometry.

4 EXPERIMENTAL STUDIES

4.1 *Experimental Setup*

The control of the laboratory equipment takes place by LabView 8.2. To generate and record the seismic signals during laboratory tests, an extended function generator was implemented in Labview. The content of signal shapes covered harmonic, impulse and sweep signals whereas the change of polarization is possible for each signal. To record the transmitted and received signals at the same time was the most difficult point. As data logger a NI-USB 6251 with a maximal sample rate of 1MHz was used. The bender elements were impinged by a voltage range of ±10V. Because the input signal was in the lower range of mV, the data logger was prefixed by a charge amplifier. The relevant frequency ranges for measure-

ments are given in dependence on the sample size and grain size. The laboratory specimens were prepared in a triaxial cell with a height of 0.2 m and a diameter of 0.1 m whereas the distance between the elements is Δs = 0.184m. The analysed frequency range was between 3 kHz to 30 kHz. The tests were done on seven different sands as shown in figure 3 and glass beads with four different diameters (0.6, 1.0, 3.5 and 8 mm).

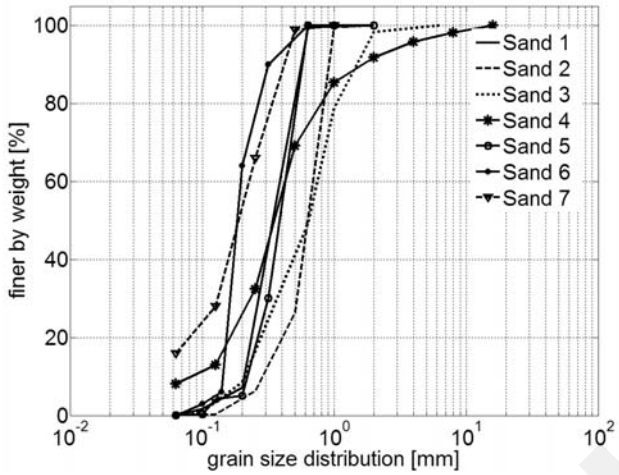

Figure 3. Grain size distribution of test sands

During the laboratory tests, the confining pressure was increased in steps of 5 kPa from 100 kPa up to 400 kPa to detect small changes in porosity of the structure. The tests were done under dry and saturated conditions, whereas the study of partially saturated conditions with same material is not finished yet, due to the time effort to achieve the hydraulic equilibrium in the media.

4.2 *Experimental analyses*

Three different materials are analysed in detail here, Sand 5 and 6 and glass beads of 3.5 mm diameter. A comparison of all material is given at the end. In the following paragraphs the results of the time-of-flight (TOF), phase and group velocity as well as the velocity gradients are presented and discussed. For improvement of TOF picking, the transmitter signal was used twice in normal deviation and inverse polarised deviation, see figure 4. The signals shown in figure 4 can separated into the mentioned above two parts – the initial coherent part and the noisy, superimposed part – the coda. The second part of the given tests was subject of CWI to determine the velocity gradients.

In opposite to the impulse excitation, the sweep signal is used to determine the phase and group velocity, see figure 5. Figure 6 shows the surface plot of figure 5 for the transformed transmitter and receiver signal in time-frequency range.

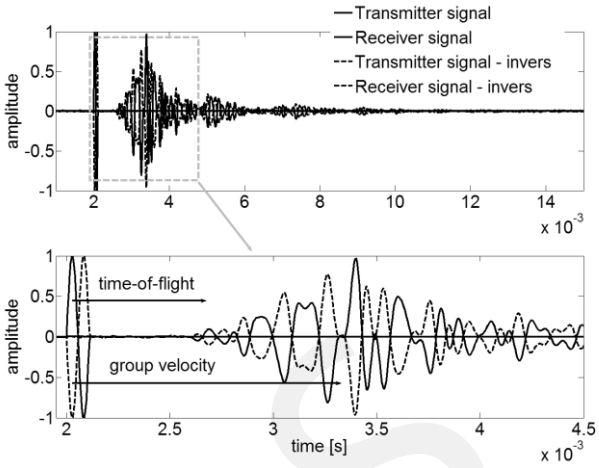

Figure 4. Typical impulse signals to determine TOF, here for dry sand – 100 kPa and 9 kHz.

From the time delay between both transformed signals, the group velocity was calculated. However, the determination of the phase or group velocity needs an excellent signal quality because these methods are more sensitive to noise and disturbances.

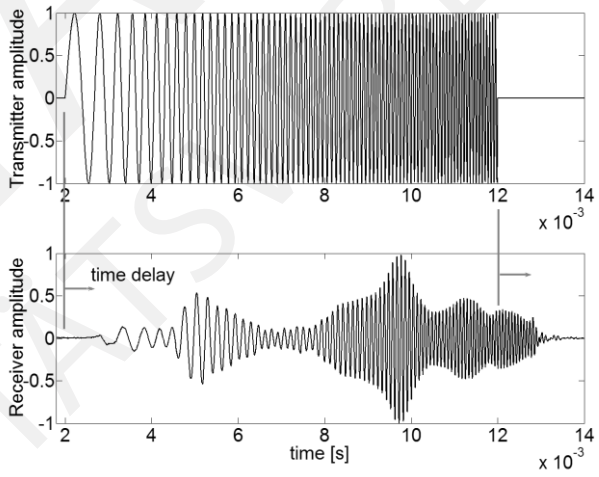

Figure 5. Used sweep signals to determine the phase and group velocity in the same sample as well as the time delay between the transmitter and receiver signal

The advantage of these complex and sensitive methods is directly linked to the wave length. Furthermore, the presented group velocity analysis gives a completion to the TOF and phase difference method. This analysis gives an extension of information and an option to overcome or to reduce the existing problems in velocity determination.

Figure 7 shows the comparison between the phase, group and TOF - velocity in a dry and saturated sample. To validate the measured group velocity, the relationship between group and phase velocity was used to determine numerically the group velocity from phase velocity measurements.

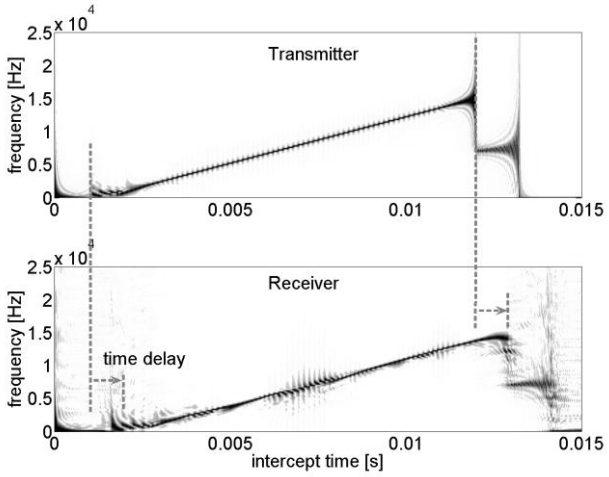

Figure 6. Surface plot of the transformed transmitter and receiver signal

It is obvious that the numerical and measured group velocities are very close. The frequency trend is similar for both cases – dry and saturated material. But the TOF values are higher than the phase or group velocity. With presence of a fluid, the phase velocity and TOF velocity is decreasing. In general, the velocity is decreasing from 10 up to 15 percent after sample saturation. In comparison to analysis of the initial coherent part, the analysis of the second part gives much more detailed information about small changes in the structure.

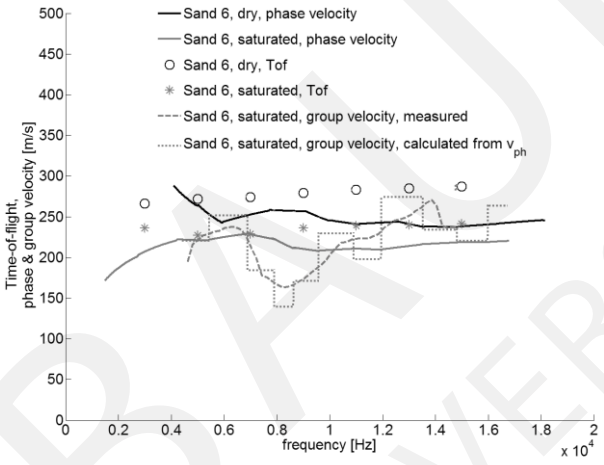

Figure 7. Comparison between TOF, phase and group velocity

As shown in figure 8, the evolution of the velocity gradient over the pressure steps is equivalent to the change of porosity. It is visible that the test sand no. 6 has a different behaviour in the evolution of the velocity gradient after the saturation. The reason was found after more detailed investigation of the void ratio, see figure 9. In comparison between the gradient of void ratio evolution, as derivation of the void ratio in figure 9, and the gradient of velocity, in figure 8, it is visible that there is a direct link between both gradients; see figure 10 and figure 11. The void ratio was determined by measurement of cell water change after each pressure step.

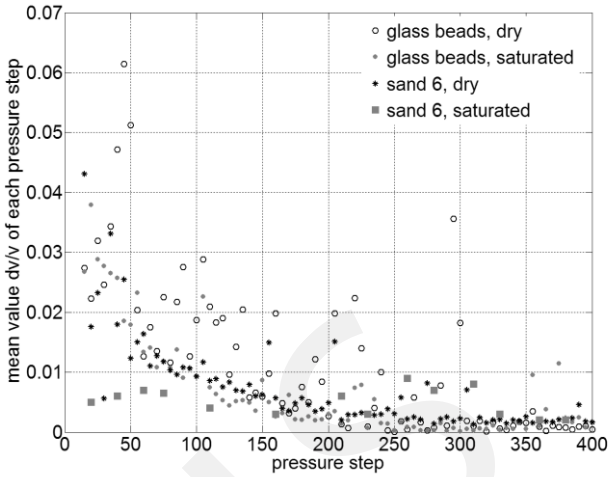

Figure 8. Evolution of the velocity gradient under increasing pressure steps.

This procedure gives the more or less rough void ratio curves in figure 9.

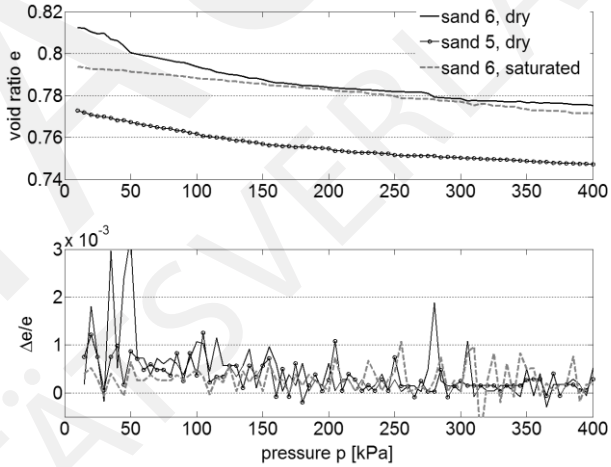

Figure 9. Evolution of the void ratio change with pressure

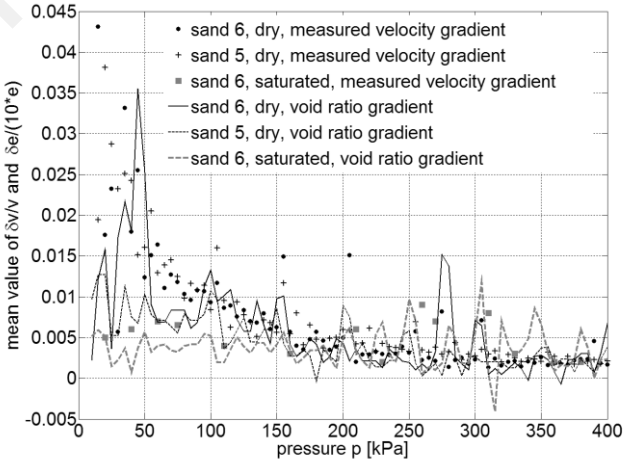

Figure 10. Comparison between the velocity and the void ratio gradient of dry and saturated sand.

By using this not-well-smoothed curve for derivation of the void ratio gradients, the spikes in figure 9 appear. To compare both gradients, a trend function for the void ratio gradient is to be used. Figures 10 and 11 show impressively the sensitivity of velocity gradients for small perturbations. By summation of all

velocity gradients to an accumulated function a link to the accumulated volume change is given.

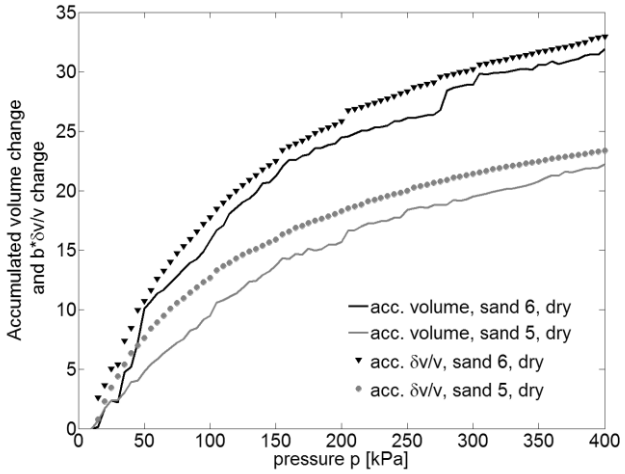

Figure 11. Comparison between the shape of the accumulated volume change and accumulated velocity gradient of the sands.

Figure 11 shows a comparison between both accumulated functions. Whereby the velocity gradient is multiplied by a constant factor b (60.0 / 40.0) for comparison between the accumulation shapes.

4.3 *Conclusions*

The objective of the presented paper was to analyse tools to assess granular material under field influences (pressure, fluid). To determine initial states in these media or to monitor small changes in a sensitive manner – different information can be extracted from a wave train propagating through a porous media. The methods were validated at dry and saturated material and currently the partially saturated material is under study. It was shown that the methods can give additional information about the dispersion characteristics as well as the accumulated changes due to small changes in porosity, inter-particle pressures and others like water content.

5 ACKNOWLEDGMENT

The authors acknowledge the support of the R&D-Programme GEOTECHNOLOGIEN funded by the German Ministry of Education and Research (BMBF) and German Research Foundation (DFG), Grant 03G0636B.

6 REFERENCES

Alramahi, B., Alshibli, K.A., Fratta, D., Trautwein, S. 2008. A Suction-control apparatus for the measurement of P- and S-Wave velocity in soils. *Geotechnical Testing Journal*. 31(1):12-24

Arulnathan, R. & Boulanger, R. 1998. Analysis of bender elements. *Geotechnical Testing Journal*, 21(2): 120–131.

Blewett, J., Blewett, I.J. & Woodward. 1999. Measurement of shear wave velocity using phase-sensitive detection techniques. *Canadian Geotechnical Journal*. 36:934-939.

Bath, M. 1974, Spectral analysis in geophysics. Developments in geophysics 7, Elsevier Scientific Publishing

Dziewonski, A., Bloch, S. & Landisman, M. 1969. A technique for the analysis of transient seismic signals. *Bulletin of Seismological Society of America*. 59(1): 427–444.

Farge, M. 1992, Wavelet transforms and their application to turbulence. *Annual Review of Fluid Mechanics.* 24, 395–457.

Greening, P. & Nash, D. 2004. Frequency domain determination of G_0 using bender elements. *Geotechnical Testing Journal* 27(3): 288–294.

Gucunski, N. & Shokouhi, P. 2004. Detection and characterization of cavities under the airfield pavements by wavelet analysis of surface waves, in *FAA Worldwide Airport Technology Transfer Conference*, New Jersey, USA.

Hammond, J. & White, P. 1996. The analysis of non-stationary signals using time-frequency methods. *Journal of Sound and Vibration* 190(3): 419–447.

Ismail, M. & Rammah, K. 2005. Shear-plate transducers as a possible alternative to bender elements for measuring gmax. *Geotechnique*. 55(5): 403–407.

Jovicic, V., Coop, M. & Simic, M. 1996. Objective criteria for determining gmax from bender element tests. *Geotechnique*. 46(2): 357–362.

Lee, J.-S. & Santamarina, J., C. 2004. Bender elements: perfocmance and signal interpretation. *Journal of Geotechnical and Geoenvironmental Engineering*. 131(9):1063-1070

Lomax, A. 1999. Path-summation waveforms. *Geophysical Journal International*. 138:702-716

Mallat, S. 1998. A wavelet tour of signal processing, Academic Press.

Narasimhan, S. & Nayak, M. B. 2003. Improved Wigner-Ville Distribution performance by signal decomposition and modified group delay. *Signal Processing*. 83: 2523–2538.

Nazarian, S., Yuan, D. & Baker, M. R. 1994. Automation of spectral analysis of surface wave method, in Ebelhar, Drevinch & Kutter, (eds), *Dynamic Geotechnical Testing II*, 88–100.

Niethammer, M. & Jacobs, L. J. 2001. Time-frequency representations of lamb waves. *Journal of Acoustical Society of America* 109(5): 1841–1847.

Santamarina, J. & Fratta, D. 2005. Discrete Signals and Inverse Problems, John Wiley and Sons.

Snieder, R. 2002. Coda Wave Interferometry and equilibrium of energy in elastic media. *Physical Review*. E 66(046615):1-8

Snieder, R. 2006. The theory of Coda Wave Interferometry. *Pure and Applied Geophysics*. 163:455-473

Somfai, E., Roux, J.N., Snoeijer, J.H., Van Hecke, M. & Van Saarloos, W. 2005. Elastic wave propagation in confined granular systems. *Physical review*. E 72: 1539-3755.

Torrence, C. & Compo, G. 1998, A practical guide to wavelet analysis. *Bulletin of the American Meterological Society* 79(1): 61–78.

Youn, J.-U., Choo, Y.-W. & Kim, D.-S. 2008. Measurment of small-strain shear modulus gmax of dry and saturated sands by bender element, resonant column and torsional shear tests. *Canadian Geotechnical Journal*. 45:1426–1438.

Yuan, D. & Nazarian, S. 1993. Automated surface wave method: Inversion technique. *Journal of Geotechnical Engineering*. 119(7): 1112–1126.

Publikationen zum Kapitel 3

Macroelement for Statically Loaded Shallow Strip Foundation Resting on Unsaturated Soil

F. Wuttke[1]; B. Kafle[2]; Y. Lins[3]; and T. Schanz[4]

Abstract: The load deformation and failure behavior of shallow footings can be described in a macroelement formulation. This paper deals with the study of the failure surface and the definition and validation of plastic load deformation by single surface hardening models. The straightforward application of the plasticity theory to the soil-foundation system makes it possible to extend the given expression for the case of unsaturated soils. This paper studies a small-scale footing test on unsaturated sand for the formulation of the elastoplastic macroelement of shallow footings under a centrally applied vertical load. The influence of soil suction on different parameters associated with the macroelement is studied and calibrated against experimental results. The presented model shows good agreement with the experimental results. Finally, the limitations and still open questions of the approach are discussed in detail. **DOI: 10.1061/(ASCE)GM.1943-5622.0000254.**

CE Database subject headings: Unsaturated soils; Shallow foundations; Calibration; Static loads.

Author keywords: Unsaturated soils; Shallow foundation; Macroelement; Calibration.

Objective and Introduction

This paper provides a framework for the development of a macroelement for a vertical statically loaded shallow strip foundation resting on unsaturated soil. The objective is to present a closed set of equations based on the theory of elastoplasticity. Following the former solution of Nova and Montrasio (1991), the development was done as an extension of that formulation by considering the influence of soil suction in relationship to the soil-water characteristic curve (SWCC) as the hydraulic core relationship of the given load-displacement behavior.

Bearing Capacity of Unsaturated Soils

The determination of the bearing capacity occurs frequently in geotechnical engineering, because it is the key parameter required when designing foundations. The theory of bearing capacity on saturated soil has been under development for several decades by many researchers, whereas the theory of bearing capacity on unsaturated soils is rarely investigated.

Prandtl (1921) was the first to study the penetration of a hard body into a softer material, which is similar to a footing on soil. Among others, bearing-capacity analysis was most prominently developed by Terzaghi (1943), Meyerhof (1951), Vesic (1973), and Bolton (1986).

Based on the assumption that a soil is either fluid saturated ($S = 1.0$) or dry ($S = 0$), several researchers, for instance Prandtl (1921), Terzaghi (1943), and Meyerhof (1951), proposed approaches for the estimation of the ultimate bearing capacity. The solution for a vertically and centrally loaded rough strip footing over the homogeneous soil by Terzaghi (1943) has been accepted for decades

$$q_u = N_c \times c' + N_q \times q + \frac{1}{2} B \times N_\gamma \gamma \tag{1}$$

where q_u = ultimate bearing capacity; N_c, N_q, and N_γ = nondimensional bearing-capacity factors depending on friction angle ϕ, providing the contributions of the cohesion in the soil, surcharge, and unit weight, respectively; c' = effective cohesion; q = overburden pressure; γ = unit weight of the soil; and B = width of the footing. Bearing-capacity factors based on different assumptions were proposed by several researchers (Terzaghi 1943; Meyerhof 1951; Kumbhojkar 1993; Zhu et al. 2001).

Most shallow foundations are typically located above the groundwater table, which requires an understanding of bearing capacity on unsaturated soils (i.e., $0 < S < 1$). Very few experimental investigations on the influence of suction on the bearing capacity have been undertaken thus far. For instance, Broms (1963) found the influence of suction on the bearing capacity of flexible pavements, and Oloo et al. (1997) determined the influence of suction of unpaved roads and presented a procedure for the determination of the bearing capacity in pavement systems. Plate-load tests were conducted by Steensen-Bach et al. (1987), Costa et al. (2003), and Rojas et al. (2007) on unsaturated sand, lateritic soils, and lean clay, respectively. Their experimental results showed an increase of the bearing capacity with increasing suction. During testing of a square model footing on an unsaturated coarse-grained soil, Mohamed and Vanapalli (2006) and Vanapalli and Mohamed (2007) found that the bearing capacity measured for an unsaturated specimen was approximately five times higher than the bearing capacity for a saturated specimen.

[1]Chair of Geomechanical Modeling, Bauhaus-Universität Weimar, 99423 Weimar, Germany (corresponding author). E-mail: frank.wuttke@uni-weimar.de

[2]Chair of Geomechanical Modeling, Bauhaus-Universität Weimar, 99423 Weimar, Germany.

[3]Chair of Foundation Engineering, Soil and Rock Mechanics, Ruhr-Universität Bochum, 44780 Bochum, Germany.

[4]Chair of Foundation Engineering, Soil and Rock Mechanics, Ruhr-Universität Bochum, 44780 Bochum, Germany.

Note. This manuscript was submitted on October 12, 2011; approved on September 12, 2012; published online on September 18, 2012. Discussion period open until March 1, 2014; separate discussions must be submitted for individual papers. This paper is part of the ***International Journal of Geomechanics***, Vol. 13, No. 5, October 1, 2013. ©ASCE, ISSN 1532-3641/2013/5-557–564/$25.00.

Int. J. Geomech. 2013.13:557-564.

Limited investigation has been carried out until now for predicting the bearing capacity of foundations on unsaturated soils using analytical methods. Using the term that describes the nonlinear behavior of unsaturated shear strength from the laboratory test results for a square footing, Vanapalli and Mohamed (2007) proposed an equation to predict the bearing capacity of unsaturated soil.

Macroelement for Shallow Foundations

The macroelement formulation consists of a coupled system of a structural component, an elastoplastic soil half-space, and the boundary between them, as shown in Fig. 1. This coupled system of soil and structure is able to describe the observed phenomenon of load displacement by including soil-structure interaction. Ticof (1977) has shown that the locus of the bearing-capacity failure of the footing under the action of combined horizontal and vertical loads is a parabola, as further used in macroelement modeling. Nova and Montrasio (1991) have outlined that the linear elasticity is not successful in predicting settlements because of the assumption that the effect of the horizontal and vertical components of inclined loading can be considered separately during the process of macroelement modeling. Fig. 1 shows the pictorial representation of the macroelement consisting of forces from the structure and the arbitrary elastoplastic region of the soil. By the use of an incremental plasticity model consisting of a constitutive law accounting for interaction between the forces on the structure and the plastic displacement, it is possible to develop an elastoplastic strain-hardening macroelement, which can reproduce the complex behavior of the soil-structure interaction (Nova and Montrasio 1991).

Constitutive Modeling in Single-Phase Materials

Theory of the Elastoplastic Strain-Hardening Macroelement

Studies of the failure surface, notably those by Nova and Montrasio (1991) and Butterfield and Gottardi (1994), have suggested a parabolic failure surface for the coupled forces acting on the foundation. The different forces and displacements associated with the model can be expressed mathematically as the generalized force vector $\mathbf{Q}$ and the associated displacement vector $\mathbf{q}$. From Nova and Montrasio (1991)

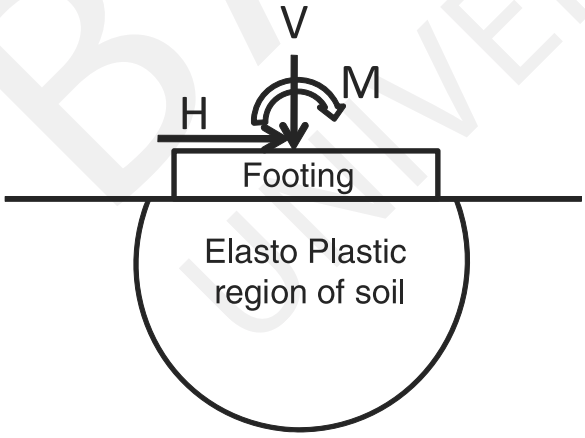

Fig. 1. Pictorial representation of the macroelement of shallow foundation (data from di Prisco 2002)

$$\mathbf{Q} = \begin{Bmatrix} \xi \\ h \\ m \end{Bmatrix} = \frac{1}{V_m} \begin{Bmatrix} V \\ H/\mu \\ M/\psi_m B \end{Bmatrix} \tag{2}$$

$$\mathbf{q} = \begin{Bmatrix} \eta \\ \varepsilon \\ \zeta \end{Bmatrix} = V_m \begin{Bmatrix} v \\ \mu u \\ \psi \theta_m B \end{Bmatrix} \tag{3}$$

where H = horizontal load; M = generated moment; V = vertical load, V_m = maximum centric vertical load capacity of the macroelement; μ = slope of the failure envelope at the origin in the H-V plane; ψ_m = slope of the failure envelope at the origin in the M-V plane; B = width of the foundation; v = displacement in the vertical direction; u = displacement in the horizontal direction; and θ_m = angle of rotation, see Fig. 2.

In Eq. (2), forces are normalized with the limiting uniaxial vertical force, and the moment is normalized by the foundation width to obtain dimensional homogeneity. Similarly, in Eq. (3), the displacement parameters are scaled by limiting the uniaxial vertical force for the fulfillment of the criterion on conjugate work (Prager 1955)

$$w = \mathbf{Q}^T \mathbf{q} = Vv + Hu + M\theta_m \tag{4}$$

The three-dimensional failure surface of the macroelement is expressed as

$$h^2 + m^2 - \xi^2(1-\xi)^{2\beta} = 0 \tag{5}$$

where β = constitutive parameter, which controls the shape of the failure envelope as shown in Fig. 3.

The loading function of the macroelement is postulated as the function of the load vector $\mathbf{Q}$ and the history of the macroelement ρ_c as

$$f(\mathbf{Q}, \rho_c) = h^2 + m^2 - \xi^2 \left[1 - \frac{\xi}{\rho_c}\right]^{2\beta} = 0 \tag{6}$$

The variable ρ_c lies in the interval $(0, 1] = \{\rho_c \in \mathbb{R} | 0 < \rho_c \leq 1\}$. When $\rho_c = 1$, the loading function coincides with the failure surface.

Evolution of the Yield Surface and the Plastic Flow

Experimental evidence of the yield surface has not been ascertained (Ghaboussi and Momen 1982). A yield surface with the same shape as the failure envelope is purposed. The flow rule from Nova and Montrasio (1991) for the single surface hardening model can be defined step wise as follows:

1. When $f(\mathbf{Q}, \rho_c) < 0$, that is, the current stress state is located inside the yield surface such that the strain increment is reversible, then no permanent deformation occurs, that is, $d\mathbf{q} = 0$.
2. When $f(\mathbf{Q}, \rho_c) = 0$, that is, the stress state is located on the yield surface and the stress increment is inward, $df(\mathbf{Q}, \rho_c) < 0$, the generalized strain is reversible and no permanent deformation takes place, that is, $d\mathbf{q} = 0$.
3. When $f(\mathbf{Q}, \rho_c) = 0$, the stress state is located on the yield surface and the stress increment is outward, $df(\mathbf{Q}, \rho_c) = 0$, the elastic domain grows in such a way that the new stress state $\mathbf{Q} + d\mathbf{Q}$ lies on the new surface given by Eq. (6) and the value of ρ_c attains a new value $\rho_c + d\rho_c$.

Int. J. Geomech. 2013.13:557-564.

By inserting the plastic potential denoted by g, the expression for the increment of the plastic strain ($d\mathbf{q}^p$) for a given state of stress $\mathbf{Q}$ and the current value of memory function ρ_c the given stress increment $df(\mathbf{Q}, \rho_c)$ is obtained from Mestat et al. (2002) as

$$d\mathbf{q}^p = \Lambda \frac{\partial g}{\partial \mathbf{Q}} \tag{7}$$

where Λ = plastic multiplier and is a nonnegative scalar. The plastic potential that defines the direction of the plastic strain can be defined as

$$g(\mathbf{Q}) = \lambda^2 h^2 + \chi^2 m^2 - \xi^2 \left[1 - \frac{\xi}{\rho_g}\right]^{2\beta} = 0 \tag{8}$$

where $\lambda = \mu/\mu_g$, $\chi = \psi_m/\psi_g$, and ρ_g = scaling factor and its numerical value has no significance in the flow rule. The variables μ_g and ψ_g are constitutive parameters. If λ and χ are both equal to unity, then $f(\mathbf{Q})$ and $g(\mathbf{Q})$ are equal and the plastic potential coincides with the failure envelope and the flow rule becomes associative.

The plastic multiplier Λ is a function of the load increment and the history of the macroelement contained in the hardening modulus. The scalar function commonly known as the hardening modulus is introduced such that

$$H\Lambda = \frac{\partial f}{\partial \mathbf{Q}} d\mathbf{Q} \tag{9}$$

By introducing a hardening function ρ_c the hardening modulus can be expressed as

$$H = -\left[\frac{\partial f}{\partial \rho_c}\right]\left[\frac{\partial \rho_c}{\partial \mathbf{q}}\right]\left[\frac{\partial g}{\partial \mathbf{Q}}\right] \tag{10}$$

where the hardening function ρ_c is expressed as

$$\rho_c = 1 - \exp\left(-\frac{R_0\sqrt{v^2 + (\alpha_h u)^2 + (\gamma_h B\theta_m)^2}}{V_m}\right) \tag{11}$$

where α_h and γ_h = nondimensional constitutive parameters, and R_0 = initial slope of the tangent of the force-displacement curve. By combining Eqs. (7), (9), and (10), the increment of the plastic strain ($d\mathbf{q}^p$) for a given state of stress is obtained as

$$d\mathbf{q}^p = -\frac{\frac{\partial \mathbf{f}}{\partial \mathbf{Q}^T}\frac{\partial \mathbf{g}}{\partial \mathbf{Q}} d\mathbf{Q}}{\left[\frac{\partial f}{\partial \rho_c}\right]\left[\frac{\partial \rho_c}{\partial |\mathbf{q}^T|}\right]\left[\frac{\partial g}{\partial \mathbf{Q}}\right]} \tag{12}$$

Experimental and Laboratory Study for Multiphase Granular Materials

Material, Testing Procedure, and Unsaturated Hydraulic Behavior

The laboratory program includes the determination of the SWCC and the bearing capacity on saturated and unsaturated sand. The material used is Hostun sand (Flavigny et al. 1990). According to the Unified Soil Classification System, Hostun sand is poorly graded sand (SP). The main parameters of Hostun sand are provided in Table 1. The main parameters of Hostun sand are provided in Table 1 and visible in the grain-size distribution in Fig. 4.

The SWCC of the tested Hostun sand was determined using a modified pressure-plate apparatus (Lins et al. 2009; Schanz et al. 2011) and is visible in Fig. 5. The modified apparatus allows for the application of small suction pressure steps using the adjustable hanging water column system connected to the water reservoir below the ceramic disk. An air pressure control system is connected to the top of the cell, which allows the application of large suction steps using air pressure via the top porous stone. The sand specimen is saturated from the bottom, allowing water to flow through the ceramic disk using the water column system.

The SWCC of the saturated sand specimen is determined using two different techniques. The hanging water column technique is used to measure the SWCC for low suction values (i.e., 0–3.0 kPa) by applying negative water pressure, u_w, to the specimen. The second technique is useful for measuring the SWCC for suction values from 3 to 100 kPa by applying air pressure, u_a, to the top cap of the cell. The water pressure at the bottom of the ceramic stone is kept equal to the atmospheric pressure (i.e., $u_w = 0$) when using this technique. During the testing procedure, the amount of water drained from the specimen under each applied suction value, ($\psi = u_a - u_w$), is measured.

After finishing the test, the specimen is dismantled and the gravimetric water content is measured by oven drying. The volumetric water content, θ, corresponding to the applied suction values was computed from back calculations.

The measured SWCC of Hostun sand is shown in Figs. 2–5. For fitting the experimental data of the SWCC, the Fredlund and Xing (1994) equation was used. From the SWCC, the sand desaturates at a faster rate because the sand is poorly graded. The air-entry value, ψ_{aev}, of the material is approximately 1.9 kPa, and residual suction, ψ_r, was obtained at approximately 3.3 kPa. Drainage and imbibition cycles show the hysteresis phenomenon in the tested Hostun sand.

Table 1. Properties of Hostun Sand

Properties	Hostun sand
Specific gravity	2.65
Coefficient of uniformity, C_u	1.50
Coefficient of curvature, C_c	1.11
Classification (Unified Soil Classification System)	SP
D_{50} (mm)	0.35

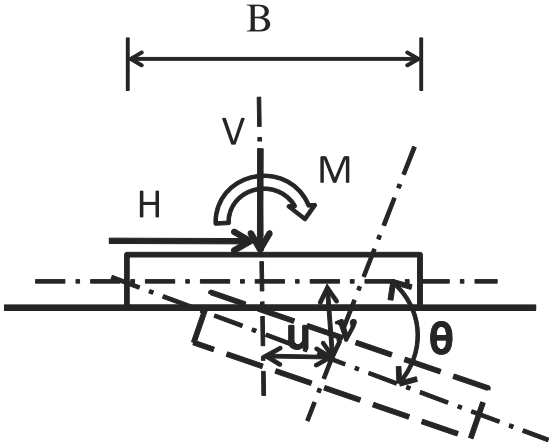

Fig. 2. Forces acting over the macroelement and the associated displacement (data from di Prisco 2002)

Int. J. Geomech. 2013.13:557-564.

The values of the parameter associated with the Fredlund and Xing (1994) equation are searched to fit the experimental result. The Fredlund and Xing (1994) equation of the SWCC for Huston sand is expressed as

$$\theta = \theta_r + \frac{(\theta_s - \theta_r)}{\left[\ln\left(e + \left(\frac{\psi}{\alpha}\right)^n\right)\right]^m} \tag{13}$$

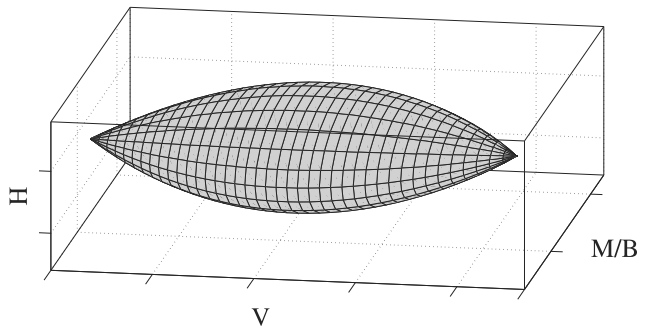

Fig. 3. Three-dimensional failure envelope in the V, H, and M/B space obtained from Eq. (5)

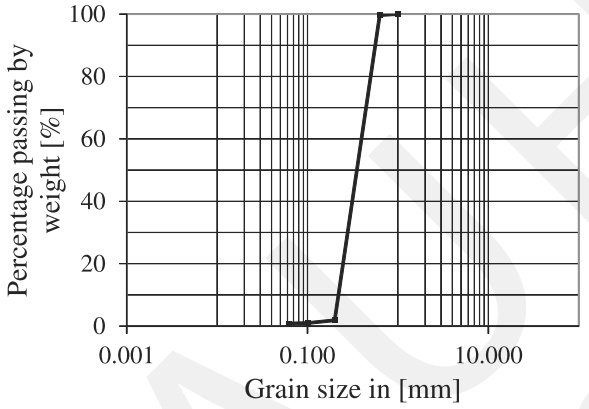

Fig. 4. Grain-size distribution of Hostun sand used in the experiment

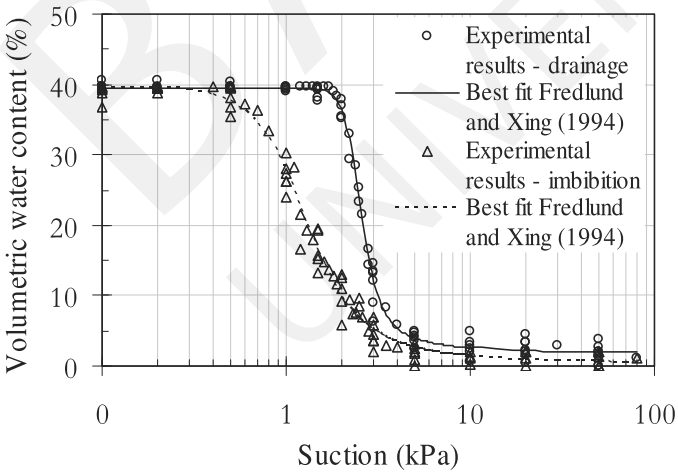

Fig. 5. Soil-water characteristic curve of Hostun sand (Lins et al. 2009)

where θ = volumetric water content; ψ = suction; $\theta_r = 1.7$ is the residual volumetric water content; $\theta_s = 39.5$ is the saturated volumetric water content; n, m, and α = constants whose values are 9.95, 1.4, and 2.4, respectively.

Bearing Capacity

The bearing capacity of a surface model strip footing was determined in a specially designed box, as shown in Fig. 6. The box is 1,000 mm in length, 500 mm in height, 500 mm in width, and consists of an outer frame made of stable wood and an inner tank made of plexiglass. The outer frame avoids lateral bending deformations that may occur because of loading the model footing in the tank. The tank has four openings (two on each side) with attached burettes that are used for allowing water to flow into the box. Also, a predetermined value of suction can be achieved in the sand-filled bearing-capacity box by the hanging water column technique using these burettes (one on each side). A tentative suction was obtained by measuring the location of the water table from the surface of the specimen with the help of the burette attached to the openings at the bottom of the box. Precise measurement of the suction is done by use of a tensiometer located at different depths from the surface. The suction of the specimen was obtained as an average value of suction at the bottom of the foundation and at the depth of $1.5B$ from the bottom of the foundation.

The dimensions of the model strip footing are 477 mm in length, 79 mm in width, and 45 mm in height. From studies of scale effects on the bearing capacity of granular soil, a notable effect on the bearing capacity of the model footings has been observed from numerical and experimental results. Herle and Tejchman (1997), Bolton and Lau (1988), and Cerato and Lutenegger (2006) have shown that the threshold values of B/D_{50} exist above which there in is no effect of particle size on model test results. In separate studies, Kusakabe (1995) and Herle and Tejchman (1997) recommended the threshold value of $B/D_{50} \geq 100$ to avoid particle-size effects on model test results. For the model test, the ratio of $B/D_{50} = 225$, which is greater than the threshold value of 100; therefore, the particle-size effect in the model test can be neglected. The dimensions of the box were estimated based on consideration of the failure mechanism because of the loading of the strip footing. The friction angle, ϕ', was measured under plane-strain loading conditions using a double-wall cell (Schanz and Alabdullah 2007; Alabdullah et al. 2009).

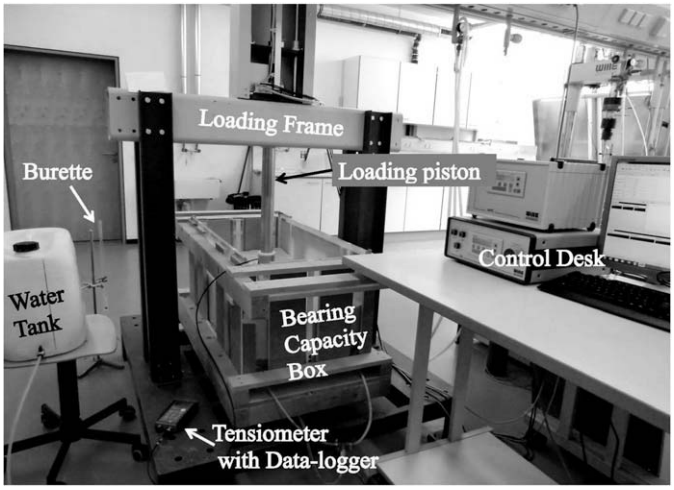

Fig. 6. Bearing-capacity loading device with bearing-capacity box

Int. J. Geomech. 2013.13:557-564.

The calculation using Terzaghi's failure mechanism for shallow foundations and the determined friction angle $\phi' = 46.9°$ was conducted for a failure zone of a length approximately equal to 460 mm and a maximum depth to 95 mm. The bearing-capacity box was placed in a loading frame, and the surface footing was loaded at a constant rate of 0.002 mm/s. The footing settlements were measured with a resolution equal to 0.001 mm, and the accuracy of the applied load was equal to 0.05%. A data logging system was used to collect all the experimental data.

Fig. 7 summarizes the results of load versus settlement, and Fig. 8 summarizes suction versus maximum load measurements from bearing-capacity tests conducted on unsaturated specimens with different average suction values below the model strip footing.

Fig. 8 shows that the ultimate bearing capacity increases with an increase in average suction and attains maximum value. After attaining this maximum value, the ultimate bearing capacity decreases with a further increase in suction. For a fluid saturated sample, the bearing capacity was found to be 60% of the dry specimen.

Extended Macroelement Definition for Multiphase Granular Material

Implementation of Unsaturated Behavior of Soil in an Elastoplastic Strain-Hardening Macroelement

The effect of soil suction on the maximum vertical load capacity of a footing, V_m, has been experimentally verified by several researchers,

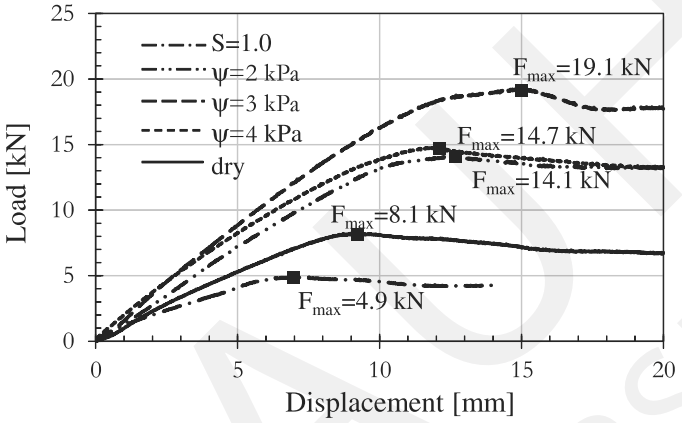

Fig. 7. Experimental results of load versus settlement tests

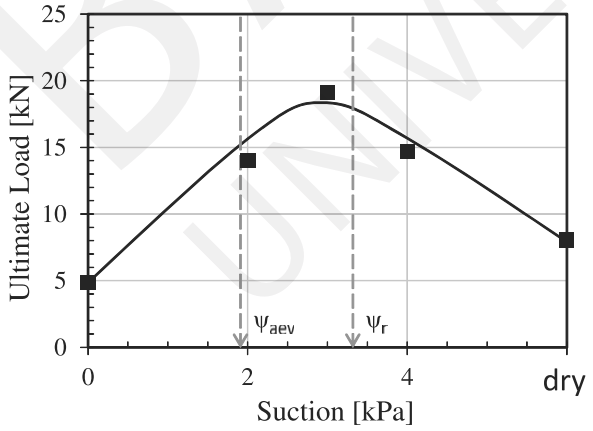

Fig. 8. Variation of ultimate load with suction

including Vanapalli and Mohamed (2007) for a square footing, and Lins et al. (2009) and Schanz et al. (2011) for a strip footing on Huston sand. The experimental effect of soil suction on V_m can be observed in Fig. 8. The semiempirical mathematical formulation of the bearing capacity for an unsaturated soil extended from the classical bearing-capacity equation of Terzaghi (1943) as a function of soil suction was notably done by Vanapalli and Mohamed (2007). This equation has been used for the prediction of the bearing capacity of footing over sand by Schanz et al. (2011).

The failure criteria for the macroelement, Eq. (5), which consists of forces normalized by V_m and parameter β, can be generally extended to account for suction ψ as follows:

$$f(\mathbf{Q},\psi) = \left[\frac{H}{\mu V_m(\psi)}\right]^2 + \left[\frac{M}{V_m(\psi)\psi_m(\psi)B}\right]^2 - \left[\frac{V}{V_m(\psi)}\right]^2\left[1-\frac{V}{V_m(\psi)}\right]^{2\beta(\psi)} = 0$$
$$= [h(\psi)]^2 + [m(\psi)]^2 - [\xi(\psi)]^2[1-\xi(\psi)]^{2\beta(\psi)} = 0 \quad (14)$$

where $h(\psi)$ = function of the normalized horizontal force for unsaturated soil, $m(\psi)$ = function of the normalized moment for unsaturated soil, $\xi(\psi)$ = function of the normalized vertical force for unsaturated soil, and $\beta(\psi)$ = function of the parameter-controlling shape of the interaction function between different forces acting on foundation over unsaturated soil. The loading function for the unsaturated soil is obtained by introduction of the parameter ρ_c, which is independent of suction and is the memory parameter for the macroelement. The loading function for unsaturated soil is defined as

$$f(\mathbf{Q},\rho_c,\psi) = [h(\psi)]^2 + [m(\psi)]^2 - [\xi(\psi)]^2\left[1-\frac{\xi(\psi)}{\rho_c}\right]^{2\beta(\psi)} = 0 \quad (15)$$

The plastic potential for an unsaturated soil can be formulated in a similar way, which is defined as

$$g(\mathbf{Q},\psi) = [\lambda \times h(\psi)]^2 + [\chi(\psi) \times m(\psi)]^2 - [\xi(\psi)]^2\left[1-\frac{\xi(\psi)}{\rho_g}\right]^{2\beta(\psi)} = 0 \quad (16)$$

The hardening function of the macroelement, expressed in Eq. (11), is controlled by different parameters, including R_0, γ_h, and V_m, which are functions of the soil suction for an unsaturated soil $R_0 \rightarrow R_0(\psi)$, $\psi \in \mathbb{R}$, $\psi \geq 0$, $\gamma_h \rightarrow \gamma_h(\psi)$, $\psi \in \mathbb{R}$, $\psi \geq 0$, and $V_m \rightarrow V_m(\psi)$, $\psi \in \mathbb{R}$, $\psi \geq 0$. The hardening function for unsaturated soil can be expressed as

$$\rho_c(\psi) = 1 - \exp\left(-\frac{R_0(\psi)\sqrt{\upsilon^2 + (\alpha_h u)^2 + (\gamma_h(\psi) \times B\theta_m)^2}}{V_m(\psi)}\right) \quad (17)$$

where $R_0(\psi)$ = initial slope of the tangent of the force-displacement curve for an unsaturated soil. The plastic incremental displacement for the unsaturated soil can be formulated as an extended form of Eq. (12) and is expressed as

Int. J. Geomech. 2013.13:557-564.

$$d\mathbf{q}^p(\psi) = -\frac{\dfrac{\partial \mathbf{f}(\psi)}{\partial \mathbf{Q}(\psi)^T}\dfrac{\partial \mathbf{g}(\psi)}{\partial \mathbf{Q}(\psi)}d\mathbf{Q}(\psi)}{\left[\dfrac{\partial f(\psi)}{\partial \rho_c}\right]\left[\dfrac{\partial \rho_c(\psi)}{\partial |\mathbf{q}(\psi)^T|}\right]\left[\dfrac{\partial g(\psi)}{\partial \mathbf{Q}(\psi)}\right]} \tag{18}$$

Vanapalli and Oh (2010) and Oh et al. (2009) have interpreted the effect of soil suction on the modulus of elasticity of sandy soil. Oh et al. (2009) used the modulus of elasticity of saturated soil as a reference value to obtain the modulus of elasticity of unsaturated soil.

The extension of the existing formulas [Eqs. (6), (8), and (11)] by the matric suction has notable influence on the failure surface (Fig. 9). Besides the strong dependency of the vertical failure load V_m on the suction, the initial slope R_0 of the vertical forces and displacements is also influenced by suction (Fig. 10). This reveals that the vertical load capacity and the moment capacity both depend on soil suction, although the horizontal load capacity of the foundations resting on the soil surface are assumed to be independent of the soil suction.

In Figs. 11 and 12, the initial slope of tangent R_0 increases, attaining the maximum value in the vicinity of the residual suction ψ_r in the transition zone of the SWCC. After attaining the maximum value, R_0 rapidly decreases nonlinearly. In the residual zone, R_0 decreases slowly to attain an asymptote parallel to the suction axis.

Calibration of the Constitutive Parameter

Oh et al. (2009) have shown that the experimental results of the modulus of elasticity are well expressed numerically as the function of matric suction and the degree of saturation. The values of $R_0(\psi)$ derived from experimental results are expressed in Fig. 11. By plotting $R_0(\psi)$ against suction, similar behavior, as observed by Oh et al. (2009), can be seen in Fig. 12. To describe the dependency of $R_0(\psi)$ and $V_m(\psi)$, an empirical relationship based on the experimental results was derived. $R_0(\psi)$ can be expressed as a function of the degree of saturation and suction as

$$R_0(\psi) = R_{\text{sat}}\left(1 + a\psi^b S^c\right) \tag{19}$$

where R_{sat} = initial slope of the tangent of the force-displacement curve of saturated soil; ψ = value of suction; S = degree of saturation; and a, b, c = constants.

To obtain the appropriate values of different parameters associated with Eq. (19), a global optimization using the particle swarm optimization (Kennedy and Eberhart 1995; Branke 1999; van Soest and Casius 2003; Schutte et al. 2004) was done to obtain the best fit for the experimental results. By the use of the particle swarm optimization, the following values for the constants a, b, and c obtained consideration from the given experimental data: $a = 4.1 \times 10^{-5}$,

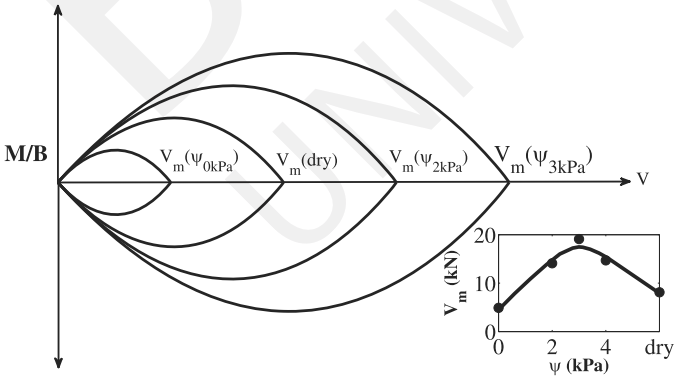

Fig. 9. Dependency of failure envelope on soil suction

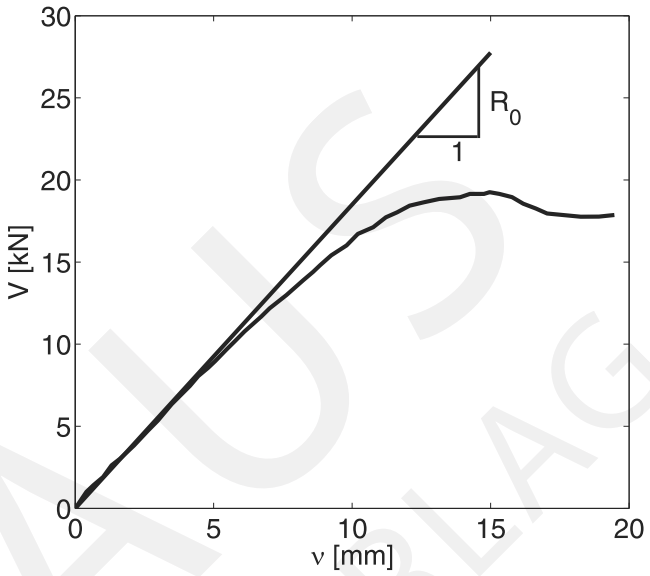

Fig. 10. Slope of initial tangent R_0 obtained from the load-displacement curve for a given suction

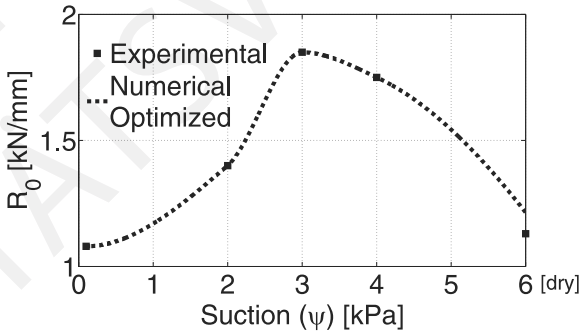

Fig. 11. Relationship between the slope of the initial tangent R_0 and the soil suction

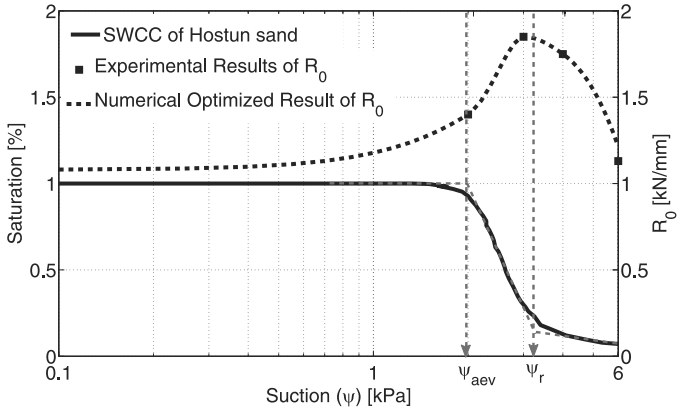

Fig. 12. Variation of the initial slope of the tangent with variation of the soil suction over different zones of the soil-water characteristic curve

Int. J. Geomech. 2013.13:557-564.

$b = 13.59$, and $c = 4.17$. The fitted function of the experimental results and the numerical optimized results are expressed in Figs. 11 and 12, respectively. The numerically optimized result of $R_0(\psi)$ showed a good fit with the experimental result.

Values of parameter β, which is crucial to define the shape of the loading function and the failure envelope, expressed by Eqs. (14) and (15), were searched by the use of particle swarm optimization. Values of β were searched by implementing values from Eq. (19) and the constitutive parameters from Table 2. With 70 particles and 1,000 iteration steps, the values of β were searched in the domain (0.6, 1.4) for the best-fitting value to obtain the minimum deviation of the numerical results from the experimental result. The searched values of β for different suctions are shown in Fig. 13. The values of β for different suctions show nonlinear behavior with the soil suction, which increases until the air-entry value is attained. Beyond the air-entry value, the value of β gradually decreases. The arithmetic mean of the values of β for different soil suctions was obtained to be $\beta_{mean} = 0.932$, as shown in Fig. 13. The variation of β with suction reveals that the shape of the failure envelope changes with the change in suction.

Numerical Study and Results

The macroelement for unsaturated soil was implemented numerically, as shown in Figs. 14 and 15, by the use of the optimized function from Eq. (19), values obtained experimentally and expressed in Fig. 8, and the values of $\beta(\psi)$ obtained from the optimization expressed in Fig. 13. The remaining constitutive parameters from Nova and Montrasio (1991) used in the implementation of the macroelement for the centric vertical load are listed in Table 2.

Comparison of the effect of $\beta(\psi)$ on the model response for different soil suction is illustrated in Fig. 14, where the macroelement is implemented for varying values of $\beta(\psi)$ with soil suction expressed in Fig. 13 and $\beta = 0.95$, as recommended by Nova and Montrasio (1991). The model response is observed to be the same when $\beta(\psi)$ or a constant value of $\beta = 0.95$ is used. A comparison between the experimental and numerical results by varying $\beta(\psi)$ with the soil suction is shown in Fig. 15. The experimental values in Fig. 15 are truncated beyond the ultimate load to facilitate rapid and precise optimization. Clear evidence of the dependency of the load-displacement behavior of footing on soil suction can be observed through Figs. 14 and 15. From Fig. 15, the numerical results have good agreement with the experimental results, and the static elastoplastic macroelement of the unsaturated soil developed herein is capable of reproducing the main features of the behavior of unsaturated soil under the footing.

Conclusions

An elastoplastic strain-hardening macroelement for strip foundations considering unsaturated soil behavior was formulated for static loading. Numerical output was validated with the experimental results. The dependency of different parameters associated with the macroelement formulation under the influence of soil suction was conceptualized. The function correlating the initial tangent of the load-displacement curve for unsaturated soil with soil suction was rationally formulated. Different parameters associated with this function were searched by global optimization to minimize the discrepancies between experimental and theoretical results.

Dependency of $\beta(\psi)$ on soil suction was realized by optimization of numerical results with experimental results. The variation of $\beta(\psi)$ has no significant effect on the model response. Numerical implementation of the macroelement for unsaturated soil by incorporating different

Table 2. Constitutive Parameters for Hostun Sand

Parameter	Result
α	3
λ	1/3
μ	0.802

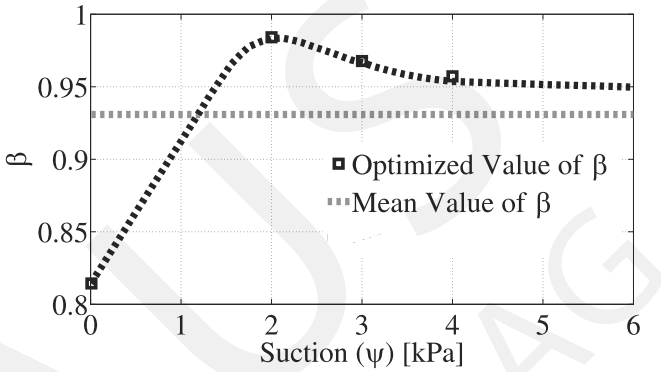

Fig. 13. Variation of parameter β and soil suction (ψ)

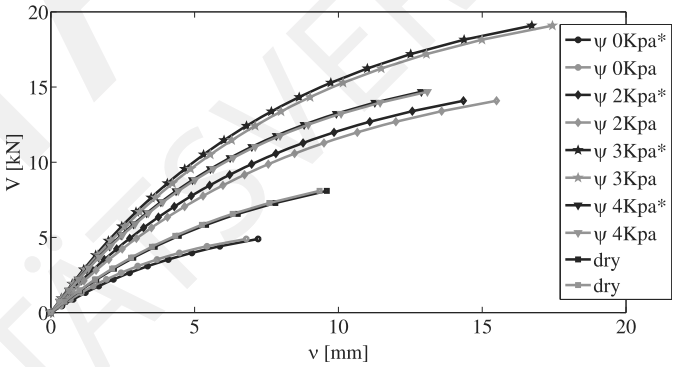

Fig. 14. Numerical results for simulation of failure loads with constant $\beta = 0.95$ (gray line) and variable optimized β (black lines with *) depending on different soil suction; each black line follows the relationship in Fig. 13

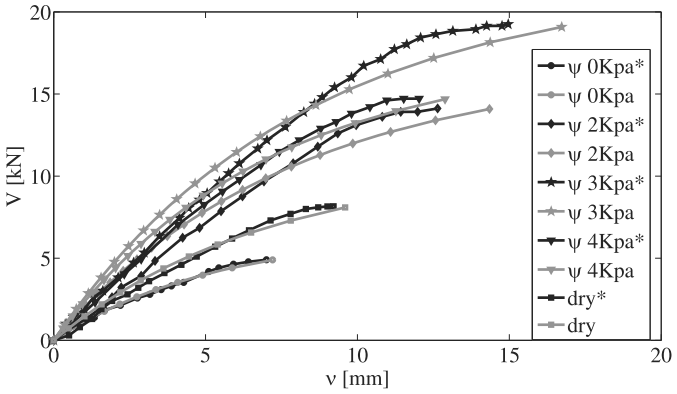

Fig. 15. Experimental (black lines with *) and numerical results of the macroelement (gray line) for the load-displacement curve for varying suction

Int. J. Geomech. 2013.13:557-564.

parameters associated with unsaturated soil showed a good agreement with the experimental results. A strong contribution of the development of the macroelement for unsaturated soil has been verified. The developed model was capable of reproducing nonlinear load-displacement behavior of footing on unsaturated soil for static loading.

Because of the choice of a single type of material for these experimental studies, the range of the values of the parameter searched may not be large enough to represent a variety of existing soil types. To increase the field of application of this model, additional experiments should be undertaken to define the range of parameters associated with the model to obtain a higher quality of model response and to generalize the model.

Acknowledgments

The authors thank the German Research Foundation for funding the Research Training Group 1462, the Free State of Thuringia and the European Regional Development Fund for funding of experimental devices (Grant No. FKZ B 715-09010), and the NATO (Grant No. CLG984136).

References

Alabdullah, J., Lins, Y., and Schanz, T. (2009). "Shear strength of unsaturated sand under plane strain conditions." *Proc., 4th Asia-Pacific Conf. on Unsaturated Soils*, O. Buzzi, S. Fityus, and D. Sheng, eds., Taylor & Francis, London, 129–133.

Bolton, M. D. (1986). "The strength and dilatancy of sands." *Geotechnique*, 36(1), 65–78.

Bolton, M. D., and Lau, C. K. (1988). "Scale effects arising from particle size." *Proc., 12th Int. Conf. on Soil Mechanics and Foundation Engineering*, J. F. Corté, ed., Balkema, Rotterdam, Netherlands, 127–131.

Branke, J. (1999). "Memory enhanced evolutionary algorithms for changing optimization problems." *Proc., IEEE Congress on Evolutionary Computation*, IEEE Xplore Digital Library, Washington, DC, 1875–1882.

Broms, B. B. (1963). "The effect of degree of saturation on the bearing capacity of flexible pavements." *Highw. Res. Rec.*, 71, 1–14.

Butterfield, R., and Gottardi, G. (1994). "A complete three dimensional failure envelope for shallow footings on sand." *Geotechnique*, 44(1), 181–184.

Cerato, A. B., and Lutenegger, A. J. (2006). "Bearing capacity of square and circular footings on a finite layer of granular soil underlain by a rigid base." *J. Geotech. Geoenviron. Eng.*, 132(11), 1496–1501.

Clerc, M. (2006). *Particle swarm optimization*, Wiley-ISTE, London.

Costa, Y. D., Cintra, J. C., and Zornberg, J. C. (2003). "Influence of matric suction on the results of plate load tests performed on a lateritic soil deposit." *J. ASTM Geotech Test.*, 26(2), 219–226.

di Prisco, C., Nova, R., and Sibilia, A. (2002). "Analysis of soil-structure interaction of towers under cyclic loading." *Proc., Numerical Models in Geomechanics (NUMOG) VIII*, G. N. Pande and S. Pietruszczak, eds., Swets & Zeitlinger, Lisse, Netherlands, 637–642.

Flavigny, E., Desrues, J., and Player, B. (1990). "Note technique, le sable d'hostun RF." *Revue Française de Geotechnique*, 53, 67–70 (in French).

Fredlund, D. G., and Xing, A. (1994). "Equation for soil water characteristics curve." *Can. Geotech. J.*, 31(4), 440–448.

Ghaboussi, J., and Momen, H. (1982). "Modeling and analysis of cyclic behaviour of sands." Chapter 12, *Soil mechanics—Transient and cyclic loads*, G. N. Pande and O. C. Zienkiewicz, eds., Wiley, New York, 313–342.

Herle, I., and Tejchman, J. (1997). "Effects of grain size and pressure level on bearing capacity of footings on sand." *Proc., IS-Nagoya'97: Deformation and Progress. Failure in Geomech*., A. Asaoka, T. Adachi, and F. Oka, eds., Elsevier Science, London, 781–786.

Kennedy, J., and Eberhart, R. C. (1995). "Particle swarm optimization." *Proc., IEEE Int. Conf. Neural Networks*, IEEE, Piscataway, NJ, 1942–1948.

Kumbhojkar, A. S. (1993). "Numerical evaluation of Terzaghi's Nγ." *J. Geotech. Eng.*, 119(3), 598–607.

Kusakabe, O. (1995). "Foundations." Chapter 6, *Geotechnical centrifuge technology*, R. N. Taylor, ed., Blackie, London, 120–172.

Lins, Y., Schanz, T., and Vanapalli, S. K. (2009). "Bearing capacity and settlement behavior of a strip footing on an unsaturated coarse-grained soil." *Proc., 4th Asia-Pacific Conf. on Unsaturated Soils*, O. Buzzi, S. Fityus, and D. Sheng, eds., Taylor & Francis, London, 443–448.

Mestat, P., Bourgeois, E., and Reiffsteck, P. (2002). "Elastoplastic modeling of soils: Monotonous loadings." Chapter 3, *Constitutive modeling of soils and rocks*, P. Y. Hicher and J. F. Shao, eds., Wiley-ISTE, London, 77–142.

Meyerhof, G. G. (1951). "The ultimate bearing capacity of foundations." *Geotechnique*, 2(4), 301–332.

Mohamed, F. M. O., and Vanapalli, S. K. (2006). "Laboratory investigations for the measurement of the bearing capacity of an unsaturated coarse-grained soil." *Proc., 59th Can. Geotech. Conf.* (CD-ROM), Canadian Geotechnical Society, Vancouver, Canada, 219–226.

Nova, R., and Montrasio, L. (1991). "Settlement of shallow foundations on sand." *Geotechnique*, 41(2), 243–256.

Oh, W. T., Vanapalli, S. K., and Puppala, A. J. (2009). "Semi-empirical model for the prediction of modulus of elasticity for unsaturated soils." *Can. Geotech. J.*, 46(8), 903–914.

Oloo, S. Y., Fredlund, D. G., and Gan, J. K.-M. (1997). "Bearing capacity of unpaved roads." *Can. Geotech. J.*, 34(3), 398–407.

Prager, W. (1955). "The theory of plasticity: A survey of recent achievements." *Proc., Inst. Mech. Eng.*, 169(1), 41–57.

Prandtl, L. (1921). "Uber die eindringungsfestigkeit (harte) plastischer baustoffe und die festigkeit von schneiden." *Z. Angew. Math. Mech.*, 1(1), 15–20 (in German).

Rojas, J. C., Salinas, L. M., and Seja, C. (2007). "Plate-load tests on an unsaturated lean clay." *Conf. on Experimental Unsaturated Soil Mechanics*, T. Schanz, ed., Springer Proceedings in Physics, Vol. 112, 445–452.

Schanz, T., and Alabdullah, J. (2007). "Testing unsaturated soil for plane strain conditions: A new double wall biaxial device." *Conf. on Experimental Unsaturated Soil Mechanics*, T. Schanz, ed., Springer Proceedings in Physics, Vol. 112, 169–178.

Schanz, T., Lins, Y., and Vanapalli, S. K. (2011). "Bearing capacity of a strip footing on unsaturated sand." *Proc., 5th Int. Conf. Unsaturated Soils*, Taylor and Francis, Barcelona, Spain, 1195–1200.

Schutte, J. F., Reinbolt, J. A., Fregly, R. T., and George, A. D. (2004). "Parallel global optimization with the particle swarm algorithm." *Int. J. Numer. Methods Eng.*, 61(13), 2296–2315.

Steensen-Bach, J. O., Foged, N., and Steenfelt, J. S. (1987). "Capillary induced stresses—Fact or fiction?" *Proc., 9th European Conf. Soil Mech. Found. Eng.*, E. T. Hanrahan, T. L. L. Orr, and T. F. Widdis, eds., Balkema, Dublin, Ireland, 83–89.

Terzaghi, K. (1943). *Theoretical soil mechanics*, Wiley, New York.

Ticof, J. (1977). "Surface footings on sand under general planer loads." Ph.D. thesis, Southampton Univ., Southampton, U.K.

van Soest, A. J., and Casius, L. J. R. (2003). "The merits of a parallel genetic algorithm in solving hard optimization problems." *J. Biomech. Eng.*, 125(1), 141–146.

Vanapalli, S. K., and Mohamed, F. M. O. (2007). "Bearing capacity of model footings in unsaturated soil." *Conf. on Experimental Unsaturated Soil Mechanics*, T. Schanz, ed., Springer Proceedings in Physics, Vol. 112, 483–493.

Vanapalli, S. K., and Oh, W. T. (2010). "A model for predicting the modulus of elasticity of unsaturated soils using the soil-water characteristic curve." *Int. J. Geotech. Eng.*, 4, 425–433.

Vesic, A. S. (1973). "Analysis of ultimate loads of shallow foundations." *J. Soil Mech. and Found. Div.*, 99(1), 45–73.

Zhu, F., Clark, J. I., and Phillips, R. (2001). "Scale effect of strip and circular footings resting on dense sand." *J. Geotech. Geoenviron. Eng.*, 127(7), 613–621.

Int. J. Geomech. 2013.13:557-564.

Vibration induced building settlement assessment and calculation

Wuttke, F.[1], Schmidt, H.-G.[1], Zabel, V.[2], Kafle, B.[3], Stade, I.[2]
[1] Chair of Soil Mechanics, Bauhaus-University Weimar, Coudraystrasse 11C, D-99423 Weimar, Germany
[2] Institute of Structural Mechanics, Bauhaus-University Weimar, Marienstrasse 15, D-99423 Weimar, Germany
[3] Graduated Student, Bauhaus-University Weimar, Coudraystrasse 11C, D-99423 Weimar, Germany

email: frank.wuttke@uni-weimar.de, schmidt25@uni-weimar.de, volkmar.zabel@uni-weimar.de, binod.kafle@uni-weimar.de, ingmar.stade@uni-weimar.de

ABSTRACT: Vibration induced settlements are one of the major issues in vibration analysis. The realistic determination of the right amplitudes is still a very complex task with many uncertainties. The presented study analyses several theories of cyclic accumulation of settlements at an existing building with considerable settlements, road traffic close to the building and weak soil beneath the building. In general, the historical building originated in the 15th century is sensitive with respect to settlements due to several modifications in its history. In several investigations at the historical building several experimental and theoretical studies such as detailed soil investigations, extensive vibration measurements, recording of damage patterns and a traffic survey were performed. Different methods can be used for the assessment of the accumulated settlements - implicit and explicit methods. The explicit models describe the evolution of stresses or the accumulation of strains in dependence of the number of cycles. The implicit method describes the accumulation of plastic strains by means of stress and strain increments in every single hysteresis loop. These calculations methods by using FEM models and different material laws are time-consuming, especially in cases of a great number of load cycles. To circumvent this drawback a Macro Element Model was tested too. In a first step of this case study the building was modelled using finite elements to assess the risk of cyclic induced settlements. The traffic induced excitations were measured and simulated by wave propagation through a layered half space. For the simulation of the cyclic interaction between building and soil, several theories were extensively analysed. In the following the results of different material laws were compared and evaluated.

KEY WORDS: Cyclic Settlements; Cyclic Accumulation; Vibration induced settlement.

1 INTRODUCTION TO CYCLIC SETTLEMENT ANALYSIS

In many cases traffic loading is the reason for damages in historical buildings. For an existing old building with diverse crack patterns the possibility of causation by traffic loading induced permanent settlements is examined. Cyclic stresses and strains caused by traffic loadings will be transported in different propagation directions. The induced vibrations cause volume change in soil, in which the volume change generated by shear strain is dominant. Pore water pressure built up or volumetric strains takes place in dependence of the saturation and the drainage. Precondition for the development of strains are drained soil conditions. On the other hand, without drainage the development of pore water pressure can cause the risk of liquefaction.

In level ground with approximately homogeneous soil the developed volumetric strain causes deformations only in the vertical direction only. For both cases – accumulation or settlements or liquefaction risk assessments - the evaluation of the volumetric strains is needed. Different methods can be used for the study of the accumulated volumetric strains (see fig.1). Explicit or N-type models have a good suitability for the assessment of permanent deformation in the soil. Implicit or hysteretic models describe the material behaviour on the base of incremental stress-strain-constitutive laws, used for each single cycle. Some numerical programs (FE, ME) are available with several implemented constitutive relations. Under consideration of a large number of cycles and often a large amount of constitutive parameters the use of these programs for the engineering practice is limited. To assess the effects of cyclic shear strains on the cyclic soil behavior threshold shear strains are introduced by Vucetic 1994: the linear cyclic threshold shear strain γ_{tl} and the volumetric cyclic threshold shear strain γ_{tv}. These strains represent the boundaries for fundamentally different categories of cyclic soil behavior (see fig.1).

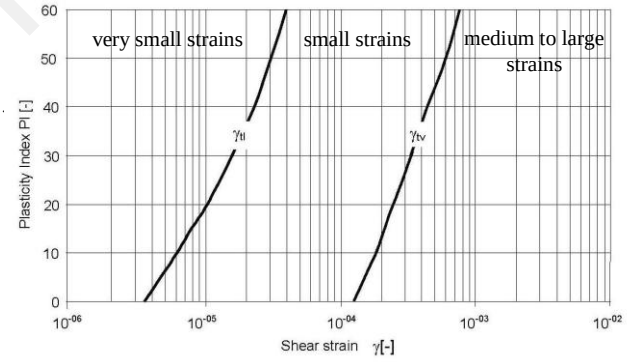

Figure. 1: Threshold cyclic shear strains after Vucetic 1994

Following practical ranges of the cyclic shear strain γ_c will be distinguished for soil dynamic problems (Vucetic 1994):

1. $\gamma_c < \gamma_{tl}$: practically linear–elastic soil behaviour, pore water pressure development and permanent volume change are negligible with no change of soil stiffness.
2. $\gamma_{tl} < \gamma_c < \gamma_{tv}$: nonlinear, slightly elasto-plastic soil behaviour, in soils with drainage a permanent volume change accumulates.

3. $\gamma_c > \gamma_{tv}$: nonlinear, elasto-plastic soil behaviour, permanent degradation of soil stiffness, further development of permanent cyclic pore water pressure and volume change accumulation.

2 OBJECT OF RELEVANCE – DAMENSTIFT OF CITY WASUNGEN

The building site is located in a small town of Wasungen 270 m above sea level in Thüringen, Germany. It is situated on the bank of river Werra. The building "Damenstift" is a historical building, from 1586, and one of the oldest buildings in the city. The federal highway No.19 runs through the centre of the city and from the front side of the building and the river Werra runs by the close distance from the back side of the building. The points of interest and investigation are numerous strong cracks in the building walls. It was not known whether the cracks are coming from the traffic or other reasons. To identify the true reasons different investigation were done by the Bauhaus-University Weimar including a cyclic accumulation study which is described in this paper.

Figure 2. Damenstift Wasungen road side.

Figure 3. Damenstif Wasungen cross section

3 SITE AND VIBRATION INVESTIGATION

3.1 Geotechnical Site Investigation

The field investigation to determine the engineering characteristics of the subsurface materials included Dynamic Probing and obtaining samples. Laboratory tests were carried out in soil samples obtained from the sampler in order to acquire necessary information with regards to the physical and mechanical properties of the soil layers and further on to evaluate and determine the parameters required for the calculations. Around the building several exploring points were done. Figure 4 is showing soil profile which was used for further analysis. As it is shown under the artificial fill (0-1.5m) there is a 1.5 m clay-type layer of very soft conscience and high amount of organic components.

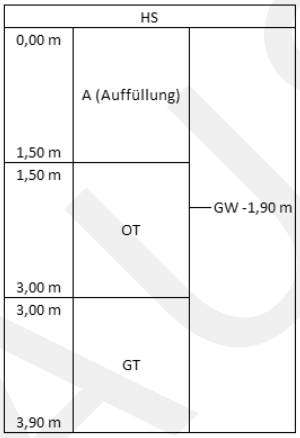

Organic Clay:
very soft and high mass of organic components
I_p = 42.6%,
w_l = 93,3%,
between 1.5 - 2m
Layer thickness

Figure 4. Soil profile under the building

3.2 Site Vibration Measurements

On site there were different vibration measurements to get the base time histories in the ground and building for vibration and cyclic assessments. In the first step the wave propagation from the road to the building were measured to find the particle velocity at the building and ground.

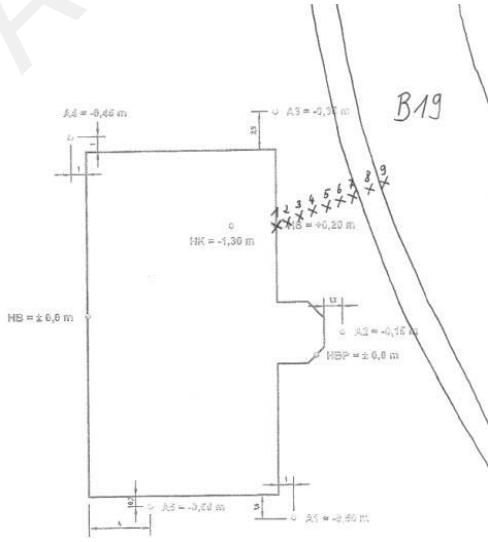

Figure 5. Geophone trace between building and road

Figure 4 is showing the placed geophones between the road and building on the distance of 5 m. The measured amplitudes over the time are given in figure 5. It is visible that the amplitude is not more than 0.5 mm/s close to the building. In a next step an elicitation to number of cars and trucks to determine the number of loading cycles under the building was performed. From this elicitation a numbers of

extrapolated cycles are visible in table 1. For simplicity each car is taken as one cycle.

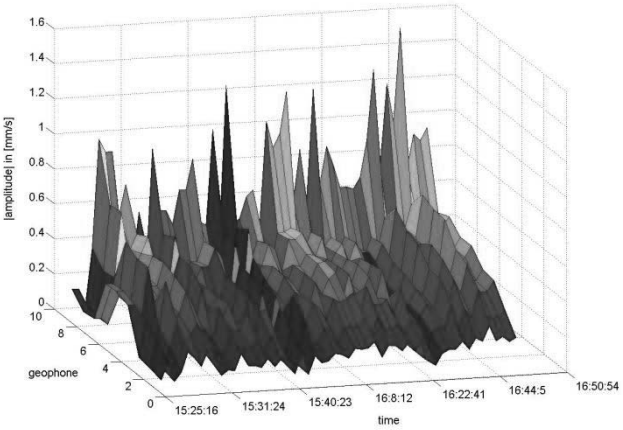

Figure 6. Measured amplitude degradation between road and building.

Table 1. Number of cycles under the building

Mesh size	General No. of Cars /24h	Trucks / 24h
elicitation	23952	3140
1st Year	8742480	1146100
2nd Year	17484960	2292200
5th Year	43712400	5730500
10th Year	87424800	11461000

4 MODELLING

From the above investigations and building model was done to analyse the reactions, load and deformation behaviour in the building, see Figure 6.

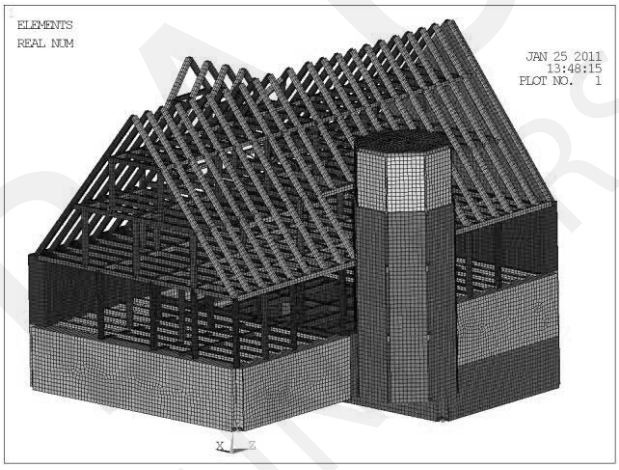

Figure 7. 3D FE Model of building Damenstift

The load distribution on the foundation, figure 8, and the acceleration time histories, figure 9, gives the cyclic loads which interact with cyclic load amplitude on the soil.

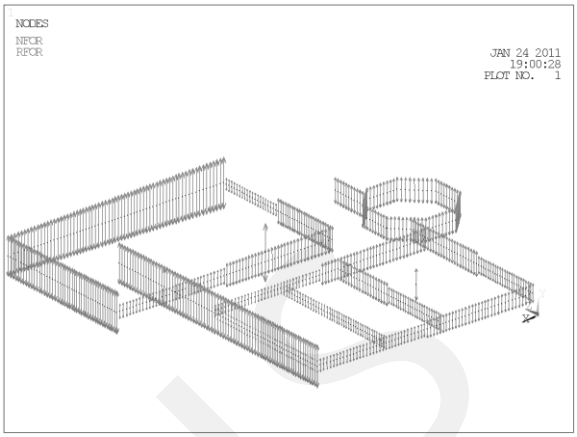

Figure 8. Force distribution under building foundation as input for the accumulation calculation.

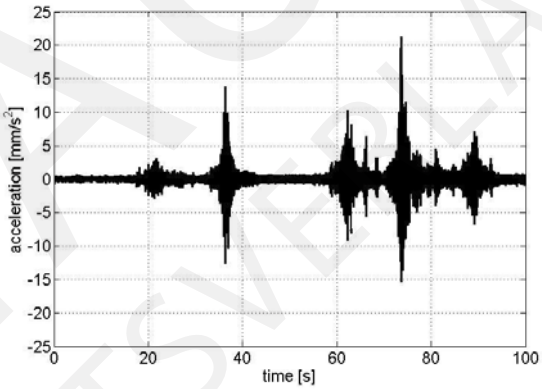

Figure 9. Acceleration time histories at the foundation as input for the accumulation calculation.

5 CYCLIC SETTLEMENT ANALYSIS

5.1 Empirical relation and results

In the literature numerous proposals for the assessment of the accumulation of settlements due to cyclic or dynamic loadings are given, e.g. Monosmith, C.L., N. Ogawa, C.R. Freeme (1975); Tokimatsu, A.M., H. B. Seed (1987): Byrne, P.M., J. McIntyre (1994): Li, D., E.T. Selig (1996); Pradel, D. (1998); Chai, J.C., N. Miura (2002); Stewart, J.P., D.H. Whang (2003); Karg, C.(2007).

Excited wave fields caused by traffic loadings contains different stress and strains in different propagation directions. Acting cyclic shear strains have a dominant influence of the soil volume change and the development of volumetric strains. In level ground with approximately homogeneous soil the developed volumetric strain causes strains in only vertical direction. Precondition for the development of strains are drained soil conditions. On the other hand, without drainage the development of pore water pressure can cause the risk of liquefaction. For both cases the evaluation of the volumetric strains is needed. Due to cyclic loadings accumulation models are developed to predict the accumulation of permanent volumetric strains: the hysteretic and the N-type models, see figure 2.

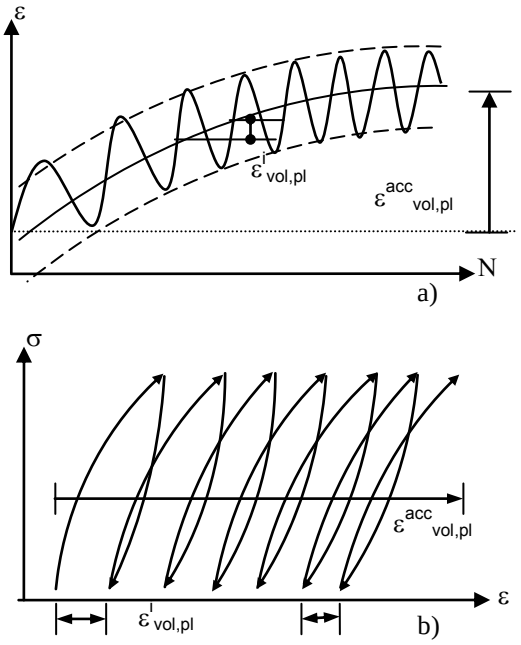

Figure 10. Accumulation models a) N-type model (implicit), b) hysteretic model (explicit)

For the assessment of the accumulated volumetric strains during a large number of cycles the hysteretic models are not practicable. For the description of the development of permanent strains in each hysteretic slope constitutive material laws are needed, in most of the cases with a many unknown material parameters. In contrast, the N-type accumulation models can easily be used to assess the accumulation of strains for a great number of cycles. In order to assess the accumulation of permanent strains during traffic loadings the N-type model after Monosmith (1975), improved by Li & Selig (1996) and Chai & Miura (2002) will be used. With this N-type model used for cohesive and fine-grained soils the accumulated volumetric strains are investigated to

$$\varepsilon^{acc}_{vol,pl} = 0{,}01 \cdot a(\tau_d / \tau_f)^m \cdot (1+\tau_s / \tau_f)^n \cdot N^b \qquad (1)$$

with
N – number of cycles
a, b, m, n – different parameters after Li&Selig 1996
τ_d – dynamic shear stress
τ_s – static shear stress
τ_f – shear strength.

The influence of the actual static shear stress and the shear strengths is taken into account. In this case study the following site data are used:
- thickness of the soft organic clay layer is nearly 2,0 meters, density ρ = 1,4 t/m^3, LL 93%, , PI = 42.6%, shear wave velocity c_s= 45 m/s, angle of friction φ'= 17,5°, cohesion c = 10 kPa.
- greatest measured vibration velocity v_0= 0.3mm/s (particle velocity).

The acting cyclic shear stress is calculated with
$\tau_d = \gamma \cdot G_0 = \rho \cdot c_s \cdot v_0$ = 0,002 kPa. Further used are the static shear stress τ_s = 5,25 kPa and the shear strength τ_f = 21,0 kPa. In the equation above these parameters after Li&Selig are introduced:
- a= 3,5 (influenced the magnitude of accumulated strains)
- m= 1,2 (influenced the distribution of accumulated strains with the depth)
- n =1 (linear relation between stresses and strains)
- b = 0,34 (in dependence of the soil type).

The accumulated cyclic volumetric strain after 10 years is given by $\varepsilon_{vol,acc}$= 3,279·10^{-4}. For multidirectional shearing (use of the double volumetric strain $\varepsilon_{vol,acc}$) the cyclic induced permanent settlement of the 2m-layer is obtained by s_{cyc}= 1,3 mm. This very small magnitude of settlement is also explained by using the threshold shear strains in fig. 1. The activated cyclic shear strain $\gamma \approx 7{,}0 \cdot 10^{-07}$ is smaller than the linear cyclic threshold shear strain γ_{tl} for cohesive soils (see fig.6).

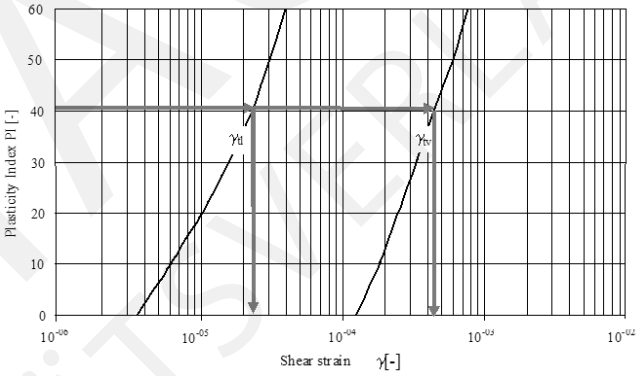

Figure 11. Likelihood distribution of settlement accumulation after Vucetic. y_{tl} defines the threshold between linear-elastic and nonlinear-elastic material behaviour. y_{tv} defines the threshold from low settlement accumulation to significant settlement accumulation

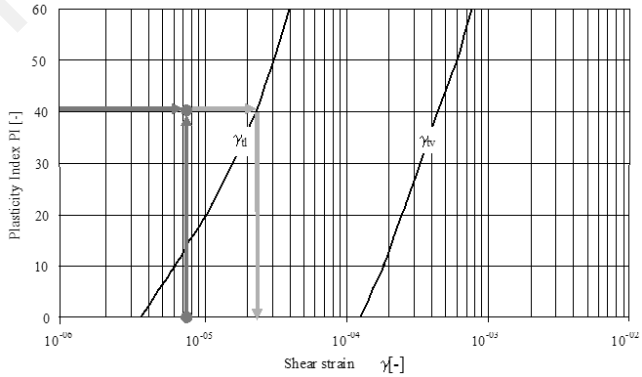

Figure 12. Likelihood of settlement accumulation after empirical assessments for the given site. Red dot indicate a shear strain of $\gamma = 6{,}6 \cdot 10^{-06}$

5.2 Constitutive relation and results

Assessment of accumulation of cyclic displacement on the foundation can be done by the use of constitutive models which are capable of defining elasto-plastic strain hardening theory. One of them is the model in which the general coupling behaviour of soil and structure during cyclic loading

in the form of spring and dash-pods can be simplified by the use of strain hardening elasto-plastic theory. The system of spring can be substituted in the form of macroelement formulated by (Nova, R. and Montrasio, L., 1991) which connects generalized forces and generalized displacements (di Prisco, C., Nova, R.and Sibilia, A., 2002). It is possible to account the mechanical disapiation of energy during cyclic loading generated by accumulation behaviour of displacement. It is done by slecting precisely the different constitutive parameters introduced to account for the cyclic loading. By assuning that the hysterretic plastic generalized strain (displacements and rotations) takes place during the cyclic loading within the bounding surface it is possible to simulate the realastic foundation behaviour for cyclic loads with an ease. Similarly di Prisco, et al., 2003 has shown that dynamic soil structure interaction can be correctly implemented by the use of elasto plastic macroelement to account for material damping through the accumulation of plastic displacement and the radiation damping by the help of dash pods.

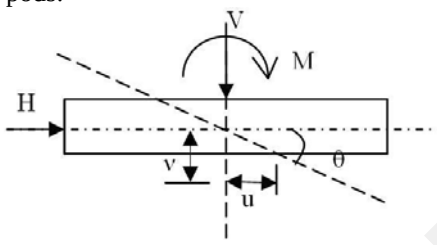

Figure 13. Definition of forces acting over macroelement with corresponding displacements.

General form of 3-D macroelement developed from constitutive modelling as expressed in; (Nova, R. and Montrasio, L., 1991)

$$f\left(Q,\rho_c\right)=h^2+m^2-\xi^2\left[1-\frac{\xi}{\rho_c}\right]^{2\beta}=0 \qquad (2)$$

where $h=H/(\mu V_m)$
$m= M/(\psi B V_m)$
$\xi = V/V_m$
ρ_c= Loading history parameter
H= Horizontal load
M= Generated moment
V= Vertical force
V_m=Maximum centric vertical load capacity of macroelement
μ= Slope of failure envelope in the H-V plane
ψ=Slope of failure envelope in the M-V plane
B=Breadth of foundation
β=Constitutive parameter which controls the shape of the failure envelope

Failure envelope defined by eq. 2 is a parabolic locus in H-V plane and is a elliptical locus in M-H plane which is expressed in Fig. 14 (a) and (b).
The complete 3-D failure envelope represented by eq. 2 is expressed in figure 15.

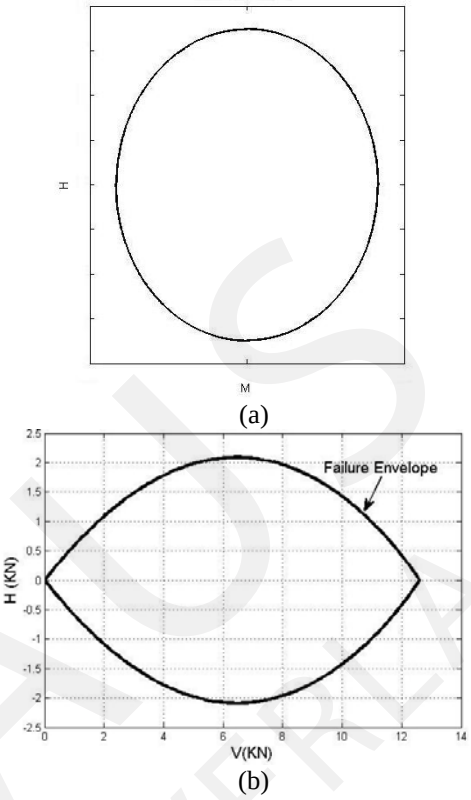

Figure 14 Elliptical failure envelope in M-H plane (a) and parabolic failure envelope in V-H plane (b)

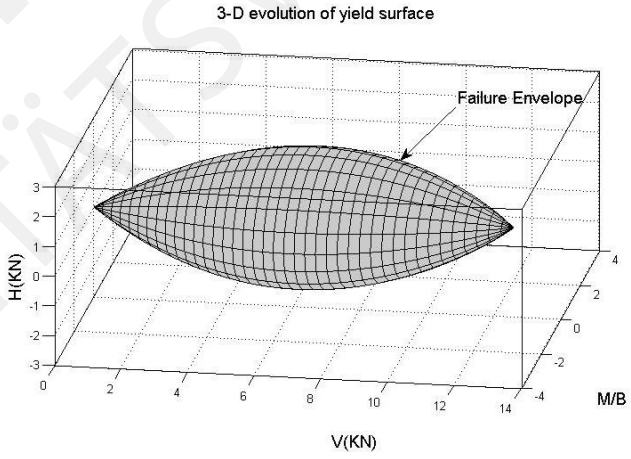

Figure 15. 3-D failure envelope in V, H, M/B space

For the case of cyclic loading an additional terms are needed to simulate the elasto-plastic history of loading and unloading and the accumulation of permanent plastic deformation as well. The evolution of plastic deformation under cyclic loads is separated into racheting or shakedown behaviour as shown in figure 16.

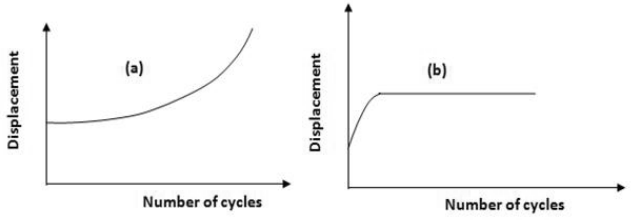

Figure 16. Racheting and Shakedown behaviour during cyclic loading.

During the cyclic loading the value of stiffness goes on changing. This is due to the volumetric change of the soil during repeated loading. More over the energy induced by the cyclic loading is used to do work for the relocation of soil particles. Models defining the cyclic loading are capable to define many behavioral changes of the soil, but it is seen that one single model is not capable to define all the behavioral changes taking place on the soil during cyclic loading. Due to which combination of different models are needed to correctly obtain realistic behaviour of the soil during cyclic loading. Defining complete behaviour of cyclic loaded macroelement by the use of one plasticity model is literally not possible till date. So we will be combining the bubble model proposed by (Al-Tabbaa, A. and Wood, D.M., 1989) and the bounding surface plasticity model proposed by (Dafalias, Y.F. and Herrmann, L.R., 1982) as done by (di Prisco, et al., 2002) for the application of macroelement to the experimental data of cyclic loaded footing over sand.

Different assumptions for the implementation of cyclic load are discussed herein. The method from (di Prisco, et al., 2002) is followed with some amendment on it to describe the cyclic phenomenon more precisely. A bounding surface with the same shape that of yield surface is located in between failure envelope and origin of V axis. Current stress point p lies well within the region of bounding surface. The cap of the cone is spherical and is connected with the cone fulfilling C_1 continuity, which states that for the function whose second derivative exists, in addition to the function value the first derivative is also continuous at the element transition.

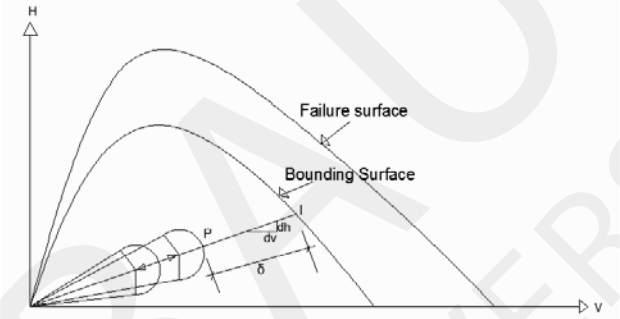

Figure 17. Extended bounding surface model for cyclic loading, (di Prisco et al. 2002).

It assumed that the cone evolves during the monotonic loading and remains in elastic state and can change in shape and size while maintaining the elastic state. Cone is fixed at the origin i.e. at H=0, M=0, V=0. The cap situated on the top of the cone maintains elastic state inside it where as outside the cap plastic state exists. If the point is on the surface of cap it will deliver plastic strain, see figure 17. When the image point is located on the bounding surface whose position is obtained by extending line joining origin and current stress point, cyclic loading in such condition will fluctuate both horizontal and vertical force as shown in figure 18.

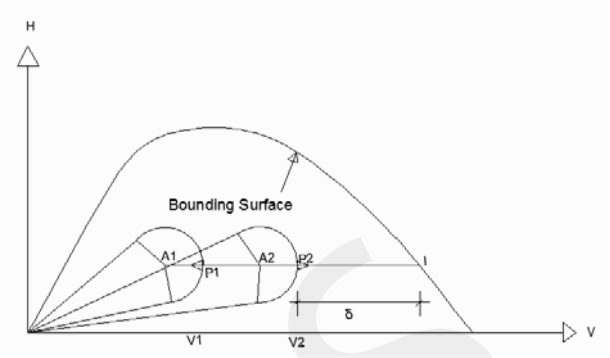

Figure 18. Position of cone during Vertical cyclic load

The general definitions for forces **Q** and dispacements **q** of the soil-structure-interaction system are given by

$$\mathbf{Q}=\begin{bmatrix}\xi\\ h\\ m\end{bmatrix}=\frac{1}{V_m}\begin{Bmatrix}V\\ \frac{H}{\mu}\\ \frac{M}{\psi B}\end{Bmatrix} \quad \text{and} \quad q=\begin{bmatrix}\eta\\ \varepsilon\\ \varsigma\end{bmatrix}=V_m\begin{Bmatrix}\upsilon\\ \mu u\\ \psi\theta B\end{Bmatrix}. \qquad (3)$$

Both vectors are linked with a compliance matrix **C** to load-displacement system.

$$d\mathbf{q}=Cd\mathbf{Q} \qquad (4)$$

The plastic potential for non-associated flow can be determined from,

$$g\left(Q,\rho_g\right)=\lambda^2h^2+\chi^2m^2-\xi^2\left[1-\frac{\xi}{\rho_g}\right]^{2\beta}=0\,. \qquad (5)$$

By following di Prisco 2002 the gradient of eq. (5) defines the generalized strain increment

$$d\rho_c=\left(1-\rho_c\right)\frac{R_0}{V_m^2}\left[d\eta+\alpha\frac{d|\varepsilon|}{\mu}+\gamma\frac{d|\varsigma|}{\psi}\right] \qquad (6)$$

and for cyclic updating memory parameter ρ_k is introduced in (6) by replacing ρ_c.

$$d\rho_k=\left(1-\rho_k\right)\frac{R_0}{V_m^2}\left[d\eta+\alpha\frac{d|\varepsilon|}{\mu}+\gamma\frac{d|\varsigma|}{\psi}\right]. \qquad (7)$$

The modification of the constitutive law regarding cycling loading is done in the equation for the generalized plastic strains obtained from (Nova, R. and Montrasio, L., 1991, di Prisco et al. 2002):

$$dq^p=\Lambda\left(\mathbf{Q}_I\right)\phi_c\left(\delta,\rho_k\right)\frac{\partial g}{\partial\mathbf{Q}}\mathbf{Q}_I\,. \qquad (8)$$

Where subscript I represent the value at the image point. The term ϕ_c considers the cyclic behaviour during cyclic loading and can be expressed in matrix form as

$$\phi_{cii} = \begin{bmatrix} e^{-\left[\varsigma_\eta \sqrt{\frac{\delta\rho_c}{\xi}} + \kappa_\eta \rho_k\right]} & 0 & 0 \\ 0 & e^{-\left[\varsigma_\varepsilon \sqrt{\frac{\delta\rho_c}{\xi}} + \kappa_\varepsilon \rho_k\right]} & 0 \\ 0 & 0 & e^{-\left[\varsigma_\varsigma \sqrt{\frac{\delta\rho_c}{\xi}} + \kappa_\varsigma \rho_k\right]} \end{bmatrix} \quad (9)$$

The term ϕ_c consists of the constitutive parameters ς, κ and the memory parameter ρ_k. ρ_k is updated when a new memory surface is reached during cyclic loading. Hence the plastic deformation can be expressed by the follow generalized plastic strain (di Prisco 2002):

$$dq^p = \begin{bmatrix} \partial\eta \\ \partial\varepsilon \\ \partial\varsigma \end{bmatrix} = \Lambda_I \begin{bmatrix} \phi_{c11} & 0 & 0 \\ 0 & \phi_{c22} & 0 \\ 0 & 0 & \phi_{c33} \end{bmatrix} \begin{bmatrix} \frac{\partial g}{\partial \xi} \\ \frac{\partial g}{\partial h} \\ \frac{\partial g}{\partial m} \end{bmatrix} \begin{bmatrix} \xi & h & m \end{bmatrix}_I . \quad (10)$$

For the follow simulation different parameter are measured and assumend to determine all required input parameter [16, 17] and [18, 19]. Form the Building mass and the maximal measured accelaration of 20 mm/s², figure 9, the cyclic force amplitude was determined. The measured cyclic amplitude was 0.05 kN/m. The static load of the building was obtained to be 50 KN/m. The number of cycles was assumed to be 87424800 in ten years. From the foregoining described geotechnical site invesitgation a bearing capacity of 375 kN/m was determined.

Table 2: Parameters for implementation of cyclic macroelement

ϕ	β	R_0 (KN/mm)	λ	α	V_m
22.5	0.95	1.685	0.12	2.81	375 (KN)
μ	B(m)	ς_η(L)	κ_η(L)	ς_η(u)	κ_η(u)
3.106	1	2	5	5	2

(L) Loading, (u) Unloading.

The prognosis of accumulation of settlement was observed from numerical implementation by the use of parameters expressed in Table 2. In this process implicit method for the determination of settlement was used. The amplitude of the cyclic force is 0.013% of the bearing capacity. And the associate average displacement per cycle is 5.6 x 10^{-8}mm, which is very less. To obtain a complete accumulated curve showing an asymptotic behaviour was not possible due to the computational barrier of the machines. Nevertheless we were able to simulate the cyclic behaviour of the traffic load as shown in Fig.(19) and accumulation behaviour of settlement for low number of cycles as shown in Fig.(20).

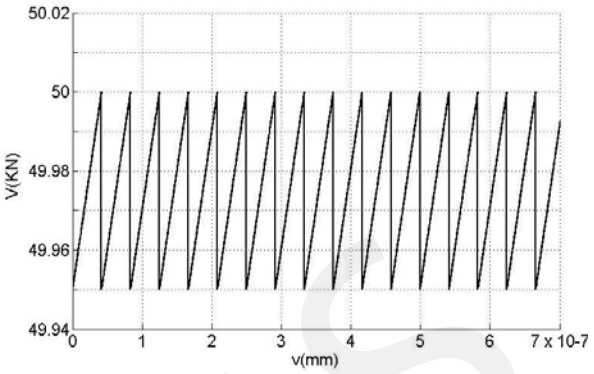

Figure 19. Simulated cyclic load after eq. (8)

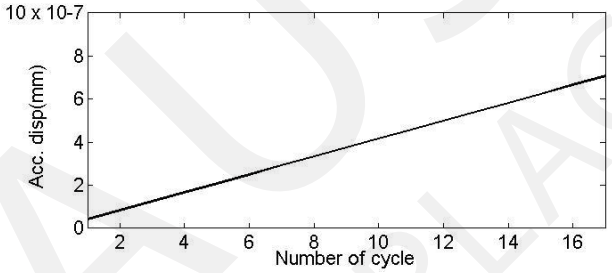

Figure 20. The accumulated settlement under use of elasto-plastic macro-element modelling.

ACKNOWLEDGMENTS

This optional section contains acknowledgments.

REFERENCES

[1] Byrne, P.M., J. McIntyre (1994): Deformation in granular soils due to cyclic loading, Geotechnical Special Publication No. 40, Ed. Jeung / Félio: Settlement´94, Texas A&M University

[2] Chai, J.C., N. Miura (2002): Traffic load induced permanent deformation of road on soft subsoil, J. Geotech. and Geoenv. Engrg., ASCE, 128 (11),907–916

[3] Karg, C.(2007): Modelling of strain accumulation due to low level vibrations in granular soils, PhD Thesis University Gent

[4] Li, D., E.T. Selig (1996): Cumulative plastic deformation for fine-grained subgrade soils, Journal Geotechnical Engineering, ASCE, 122 (12),1005–1013

[5] Monosmith, C.L., N. Ogawa, C.R. Freeme (1975): Permanent deformation characteristicsof subgrade soil due to repeated loading", Transp. Res. Rec. No. 537, Transportation Research Board, Washington D.C. pp. 1–17

[6] Pradel, D. (1998): Procedure to evaluate earthquake induced settlements in dry sandy soils, J. Geotech. and Geoenv. Engrg., ASCE, 124 (4),364–368

[7] Stewart, J.P., D.H. Whang (2003): Simplified procedure to estimate ground settlements from seismic compression in compacted soils, 2003 Pacific Conference on Earthquake Engineering, paper no. 046

[8] Tokimatsu, A.M., H. B. Seed (1987): Evaluation of settlements in sands due to earthquake shaking, J. Geotech. Engrg., ASCE, 113 (8),861–878

[9] Vucetic, M. (1994): Cyclic threshold shear strains in soils, J. Geotech. Engrg., ASCE, 120 (12),2208–2228

[10] Nova, R. and Montrasio, L. Settlement of shallow foundaitons on sand [Journal]. - [s.l.] : Geotechnique, 1991. - 2 : Vol. 41. - pp. 243-256.

[11] di Prisco C., Nova R. and Sibilia A. Shallow footing under cyclic loading experimental behaviour and constitutive modelling [Report] /

Milan University of Technology (Politecnico). - Milan, Italy : [s.n.], 2002.

[12] di Prisco C., 2003 (unpublished reports & private communication)

[13] Al-Tabbaa, A. and Wood, D.M. An experimentally based bubble model for clay [Journal] // Numerical Models in geomechanics, NUMOG III / ed. Pietruszczak S. and Pande, G.N.. - Niagara Falls : Elsevier applied science, 1989. - pp. 91-99.

[14] Dafalias, Y. F.and Popov, E. P. A model of nonlinearly hardening materials for complex loading [Journal] // Acta Mechanica. - [s.l.] : Springer-Verlag, 1975. - Vol. 21. - pp. 173-192.

[15] Dafalias, Y.F. and Herrmann, L.R. Bounding surface formulation [Book Section] // Soil Mechanics-Transient and cyclic loading / ed. Pande G.N. and Zeinkiewicz, O.C.. - [s.l.] : John Wiley and Sons Ltd, 1982.

[16] Rütz, D., Report – Geotechnical Site Investigation, Damenstift Wasungen, Bauhaus-University Weimar, 2010 unpublished

[17] Könke, C., Final Report, Damenstift Wasungen, Bauhaus-University Weimar, 2010, unpublished

[18] Zabel, V., Report – Vibration Measurement Damenstift Wasungen, Bauhaus-University Weimar, 2010, unpublished

[19] Wuttke, F., Report – Settlement Accumulation Damenstift Wasungen, Bauhaus-University Weimar, 2010, unpublished

Cyclic macroelement for shallow footing over unsaturated soil

B. Kafle & F. Wuttke
Geomechanical Modeling, Faculty of Civil Engineering, Bauhaus-Universität Weimar, Weimar, Germany

ABSTRACT: Settlement behaviour of foundation over unsaturated soil under the action of cyclic loading can be described by the inclusion of soil structure interaction considering nonlinear soil behaviour by the use of Macroelement formulation. The aim of this paper is to develop a framework of macroelement consisting of coupled system of forces, foundation and the nonlinear behaviour of multiphase granular soil. The model simulates the ratchetting behaviour during cyclic loading of multiphase soil. This is achieved by modifying the bounding surface to account for the change in hardening behaviour of the soil during cyclic loading. The mathematical control over the ratchetting behaviour is established by obtaining the distance of the current stress state from the established image point. The modification of bounding surface as a mathematical control is done to simulate the cyclic accumulation of displacement for the soil under multiphase condition.

1 INTRODUCTION

1.1 *Macroelement for shallow foundation*

Macroelement is a space constituting coupled system of forces from super structure, soil half space and the boundary between them. The complex behaviour of soil structure interaction can be conceived by the use of elastoplastic strain hardening macroelement constituting the interaction between different structural forces acting on foundation. The use of granular model like macroelement constituting of few constitutive parameter and capable of delivering high ended results of Soil structure interaction reduces the ambiguity of model response and the complexity in the analysis of the system under consideration. Figure 1. shows the pictorial representation of macroelement consisting of forces from structure and the arbitrary elasto-plastic region of soil under consideration of macroelement.

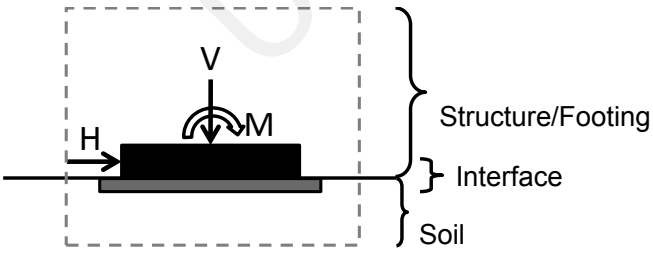

Figure 1. Pictorial representation of macroelement of shallow footing (after di Prisco & Pisano 2011).

Macroelement for the dry sand has been proposed by several authors including (Gottardis & Butterfield 1988, Nova & Montrasio 1991, Butterfield and Gottardi 1994, Houlsby & Cassidy 2002, Grange 2008, Chatzigogos et al. 2009 etc.).

Macroelement for unsaturated soil has been proposed by (Wuttke et al. 2012) in which the model from (Nova and Montrasio 1991) has been extended to acount for multiphase behaviour.

1.2 *Macroelement for cyclic loading*

The repeating behaviour of cyclic loading leads to the several unique behavioral changes in the properties of soil. The small and repeated cycles with very low frequency gives rise to the behaviour of cyclic loading under drained condition. Whereas the rapid and transient cyclic loading leads to the similar behaviour as that of cyclic loading under undrained condition. Accumulation of strain during the cyclic loading is taken as the fundamental soil properties for the prognosis of structural resilience. A macroelement capable to simulate cyclic loading will take into account of several important features of soil structure interaction including interaction of forces from structures, nonlinear soil behaviour, interaction of the soil structure interface. (di prisco et al. 2002), proposed the cyclic macroelement model as an extension of static macroelement model from(Nova & Montrasio 1991) by combining two constitutive model, bubble model proposed by (Al-Tabbaa, &

Wood 1989) and the bounding surface model proposed by (Dafalias & Herrmann 1982). The proposed model is able to simulate the behaviour of foundation under cyclic loading and is also able to provide the prognosis of accumulation of cyclic strain.

This paper proposes a cyclic macroelement for multiphase granular soil by the modification of constitutive parameters of (Nova & Montrasio 1991) as proposed by (Wuttke et. al. 2012) and introducing it in the cyclic macroelement as proposed by (di prisco et al. 2002) to account for the prognosis of accumulation of cyclic displacement with the change in soil suction.

2 EXPERIMENTAL STUDIES FOR MULTIPHASE GRANULAR MATERIAL

2.1 *Properties of Material used*

The material used for the present investigation is Hostun sand (Flavigny et al. 1990). According to the USCS classification Hostun sand is poorly graded sand (SP). Main parameters of Hostun sand are provided in Table 1 and the grain size distribution is shown in Figure 2.

Table 1. Properties of Hostun Sand.

Properties	Hostun sand
Specific gravity	2.65
C_u	1.50
C_c	1.11
Classification(USCS)	SP
D_{50}	0.35mm

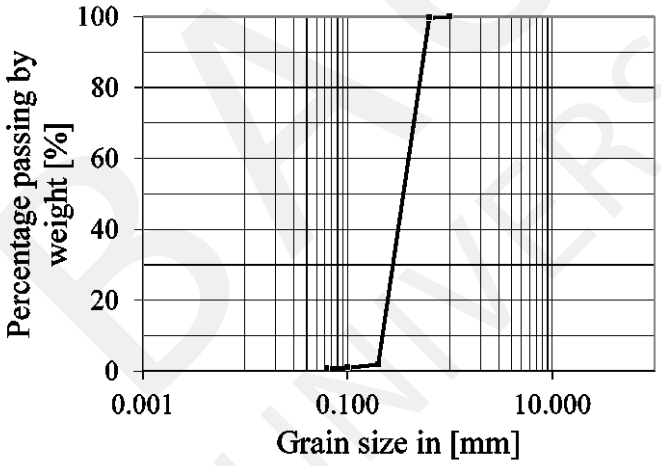

Figure 2. Grain size distribution of hostun sand used in the experimental investigation

The SWCC of the Hostun sand was determined in the laboratory using modified pressure plate apparatus (Schanz et al. 2011) Figure 3. The modified pressure plate is able to measure soil suction in small steps by using hanging water column connected to the base of the pressure plate. The low suction values were determined by the hanging water column technique. For the higher suction values from 3 to 100 kPa the air pressure is applied from the top and the water drained from the bottom of the sample is measured for the balanced atmospheric pressure.

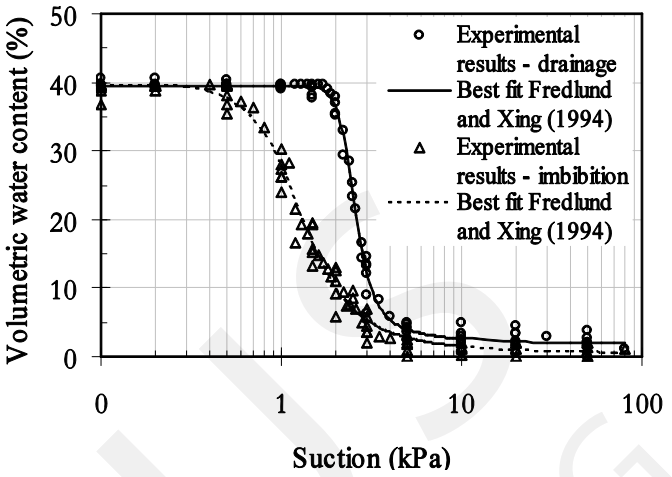

Figure 3. Soil-water characteristic curve of Hostun sand (Wuttke et al. 2012)

The volumetric water content, θ corresponding to the applied suction values was computed from back calculations. Air-entry value ψ_{aev} and residual suction ψ_r is approximated to 1.9 kPa and 3.3 kPa respectively from SWCC of hostun sand presented in Figure 3.

2.2 *Bearing capacity test*

Being capacity of a rough surface model square footing with the size 100mm x 100mm was determined in a box, shown in Figure 4.

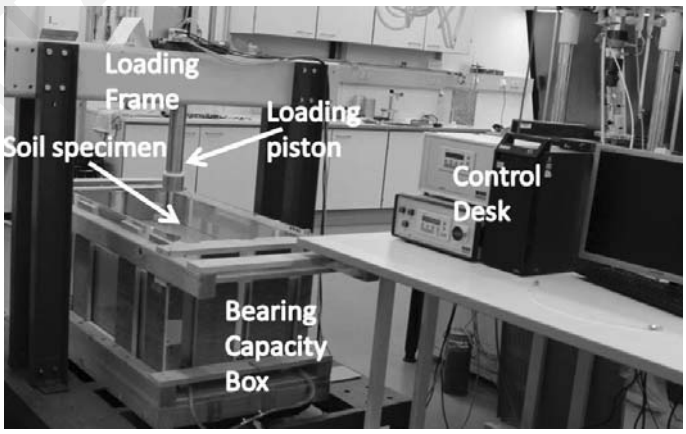

Figure 4. Experimental setup for bearing capacity test

The box is capable of draining water from four of its opening located at the bottom so as to obtain desired suction in the specimen. The box has the dimension of 980 mm in length, 480mm in height and 480mm in width. Tentative value of suction was obtained by measuring the location of water table on the specimen from the surface. Precise measurement of suction is done by the use of tensiometer located at the different depth of the specimen from the surface.

(Bolton & Lau 1988, Cerato & Lutenegger 2006) performed study of scale effect on the bearing capacity of granular soil. A notable effect on the bearing capacity of model footing was observed from numerical and experimental results. (Kusakabe 1995, Herle & Tejchamn 1997) proposed the threshold value of $B/D_{50} \geq 100$ to avoid particle size effect on model test. With the dimension of footing 100mm x 100mm and D_{50}=0.35mm; B/D_{50} of used hostun sand is greater than the threshold value for the effect of particle size on the bearing capacity test. The height of the specimen is obtained by considering the general shear failure mechanism under the static vertically loaded footing such that the failure mechanism due to the footing will occur within the box and the boundary effect in the vertical direction can be ignored.

The sample was prepared by filling the sand in layers and compacted to obtain same void ratio of 0.7±0.02 in each test. After the preparation of the sample de-aired water was slowly filled from bottom of the specimen to obtain saturated specimen. Form the saturated specimen, water was drained to set the water table to a desired level from the surface. The suction of the specimen was measured by the use of tensiometer embedded in the specimen at different depth. The average value of measured suction up to the depth of 1.5B is calculated to homogenize the soil suction over the depth of specimen and designated as the suction of specimen. During the test the suction is precisely controlled and kept constant in the soil sample by connecting the box with the water reservoir. The friction angle of the specimen (Hostun Sand) is obtained from (Schanz & Vermeer 1996) for non-lubricated foundation with the friction angle $\phi = 41.8^{\circ}$. Automated data logging system was used to collect all the experimental data. Figure. 5. summarizes the test result for load versus settlement curve.

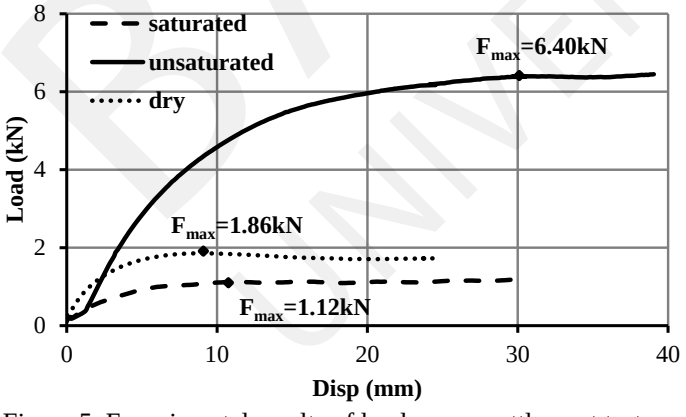

Figure 5. Experimental results of load versus settlement tests

The bearing capacity box was placed in a loading frame as shown in Figure 4. Three different specimen; dry, saturated and unsaturated with an average suction of 2.1kPa (approximately. equal to ψ_{aev})was prepared. Displacement controlled loading with the constant rate of 0.0025 mm/s was applied on the footing until a failure load was reached.

3 CONSTITUTIVE MODEL

Assessment of cyclic displacement on the foundation can be done by the use of constitutive models which uses general coupling behaviour of soil and structure during cyclic loading in the form of spring and dash-pods and can be simplified by the use of strain hardening elasto-plastic theory. The system of springs can be substituted by elastoplastic macroelement from (Wuttke et al. 2012) which takes into account of multiphase soil behavour. The different forces acting over the foundation and their corresponding displacement are shown in Figure 6.

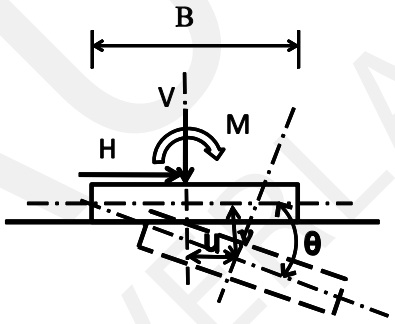

Figure 6. Forces acting over macroelement and the associated displacement (Wuttke et al. 2012)

The different forces and displacement associate with macroelement can be expressed mathematically as generalized force vector $\boldsymbol{Q}$ and the associated displacement vector $\boldsymbol{q}$. The forces in generalized force vector are normalized with uniaxial limiting vertical force and moment is normalized additionally by width to obtain dimensional homogeneity Eq.(1). For the fulfillment of criteria of work conjugate, associated displacement vector is scaled with uniaxial limiting vertical force Eq.(2). The generalized force and displacement vectors and the extended formulation of macroelement for unsaturated soil from (Wuttke et al. 2012) is expressed as,

$$\mathbf{Q}(\psi) = \begin{Bmatrix} \xi(\psi) \\ h(\psi) \\ m(\psi) \end{Bmatrix} = \frac{1}{[V_m(\psi)]} \begin{Bmatrix} V \\ H/\mu \\ M/\left(\psi_M(\psi).B\right) \end{Bmatrix} \tag{1}$$

$$\mathbf{q}(\psi) = \begin{Bmatrix} \eta(\psi) \\ \varepsilon(\psi) \\ \zeta(\psi) \end{Bmatrix} = [V_m(\psi)] \begin{Bmatrix} v \\ \mu u \\ \psi_M(\psi).\theta.B \end{Bmatrix}, \tag{2}$$

where, (ψ) represents suction dependency of parameters, H denotes horizontal load, M, generated moment, V, vertical load and $V_m(\psi)$ maximum centric uniaxial vertical load capacity of

macroelement for particular soil suction. μ, slope of failure envelope at the origin in H -V plane, $\psi_M(\psi)$, slope of failure envelope at the origin in M-V plane, *B*, width of foundation, *v* and *u* are displacement in vertical and horizontal direction and θ angle of rotation.

3-D failure surface of macroelement for multiphase soil from (Wuttke et al. 2012) is expressed as

$$[h(\psi)]^2 + [m(\psi)]^2 - [\xi(\psi)]^2 \left[1 - \xi(\psi)\right]^{2\beta(\psi)} = 0. \quad (3)$$

where, $\beta(\psi)$ is a constitutive parameter which controls the shape of the failure envelope.

The loading function of macroelement for multiphase soil is postulated as the function of load vector $\boldsymbol{Q}$, the history of macroelement ρ_c and the soil suction as;

$$f(\mathbf{Q}, \rho_c, \psi) = \left[h(\psi)\right]^2 + \left[m(\psi)\right]^2 - \left[\xi(\psi)\right]^2 \left[1 - \frac{\xi(\psi)}{\rho_c}\right]^{2\beta(\psi)} = 0. \quad (4)$$

The ρ_c lies in the interval $(0,1] = \{\rho_c \in R | 0 < \rho_c \leq 1\}$. When $\rho_c = 1$ loading function coincides with failure surface.

The plastic potential which defines the direction of plastic strain is defined as function of load vector varying with soil suction as,

$$g(\mathbf{Q}, \psi) = \left[\lambda \cdot h(\psi)\right]^2 + \left[\chi(\psi) \cdot m(\psi)\right]^2 - \left[\xi(\psi)\right]^2 \left[1 - \frac{\xi(\psi)}{\rho_g}\right]^{2\beta(\psi)} = 0. \quad (5)$$

where, $\lambda = \mu/\mu_g$, $\chi(\psi) = \psi_M/\psi_g$ and ρ_g is a dummy variable and its numerical value has no significance in flow rule. μ_g and ψ_g are constitutive parameters. Hardening function ρ_c is introduced containing nondimensional constitutive parameters α and γ, and the initial slope of the tangent of force displacement curve for centric vertically loaded foundation, $R_0(\psi)$ *as*, Eq.(6),

$$\rho_c(\psi) = 1 - \exp\left(-\frac{R_0(\psi)\sqrt{v^2 + (\alpha u)^2 + (\gamma(\psi) B\theta)^2}}{[V_m(\psi)]}\right). \quad (6)$$

The incremental plastic strain $d_{\boldsymbol{q}}{}^p(\psi)$ for a given state of stress is obtained as, Eq.(7),

$$d\mathbf{q}^p(\psi) = \Lambda(\psi) \frac{\partial g(\psi)}{\partial \mathbf{Q}(\psi)}, \quad (7)$$

In formulating cyclic behaviour we need to have parameters which can define several behaviours observed during cyclic loading. For this achievement we need to modify the constitutive relation which is capable of generating realistic cyclic behaviour. The model from (di Prisco et al., 2002) is followed with amendment on it to describe the cyclic phenomenon of multiphase soil. A bounding surface with the same shape that of yield surface is assumed to be located in between failure envelope and origin Figure 7. The co-ordinates of Current stress point *p* lies well within the region of bounding surface. The cap of the cone is assumed to be spherical. The cone evolves during the monotonic loading and remains in elastic state and can change in shape and size while maintaining the elastic state. The cap of the cone maintains the boundary between the elastic and plastic state of stress. By locating the image point on the bounding surface which is obtained by connecting the current state of stress with the path of the cyclic stress and introducing a parameter which locates the distance of current state of stress from image point, plastic accumulated strain during the cyclic loading when the current state of stress is well within the bounding surface can be obtained.

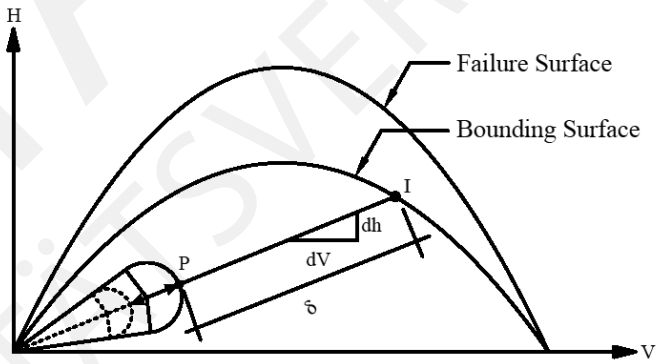

Figure 7. Extended bounding surface with current state of stress and location of image point for cyclic loading, (di Prisco et al. 2002)

The modified plastic generalized strain proposed by (di Prisco et al. 2002) is further extended with the proposed formulation from (Wuttke et al. 2012) to account for the cyclic loading under multiphase soil as,

$$\mathrm{dq}(\psi)^{\mathrm{p}} = \Lambda_{\mathrm{I}}(\psi)\phi_{\mathrm{c}}\left(\delta, \rho_{\mathrm{k}}, \psi\right)\left(\frac{\partial \mathrm{g}(\psi)}{\partial \mathbf{Q}(\psi)}\right)_{\mathrm{I}} \quad (8)$$

Where subscript *I* represent the value at the image point. The term $\phi_c(\psi)$ considers the cyclic behaviour of soil during cyclic loading and can be expressed in matrix form as,

$$\phi_{cii}(\psi) = e^{-\left[\varsigma_i(\psi)\sqrt{\frac{\delta(\psi)}{\frac{\xi(\psi)}{\rho_c(\psi)}}} + \kappa_i(\psi)\rho_k(\psi)\right]} \quad (9)$$

The term $\phi_{cii}(\psi)$ consists of the constitutive parameters $\varsigma(\psi)$, $\kappa(\psi)$ and the memory parameter $\rho_k(\psi)$

expressed in Eq.(10) which is updated when a new memory surface is reached during cyclic loading. The extended ρ_k from (di Prisco et al. 2002) to account for the memory retaining properties during cyclic loading for multiphase soil is expressed as;

$$d\rho_k(\psi) = (1-\rho_k(\psi))\frac{R_0(\psi)}{\left[V_m^2(\psi)\right]}\left[d\eta + \alpha\frac{d|\varepsilon|}{\mu} + \gamma(\psi)\frac{d|\zeta|}{\psi_M(\psi)}\right] \quad (10)$$

4 NEUMERICAL RESPONSE

Numerical response of unsaturated soil is obtained by extracting the model dependency parameters from the experimental results. As outlined by (Wuttke et al. 2012) few of the model parameters are influenced by the multiphase behaviour of the soil and other parameters can be taken as a constant as forwarded by (Montrasio & Nova 1997). The parameters influnced by multiphase condition of soil are $V_m(\psi)$ and $R_0(\psi)$. $V_m(\psi)$ and $R_0(\psi)$ are obtained from the experimental result as outlined in Figure 5 and Figure 8. respectively. The different values of $R_0(\psi)$ and $V_m(\psi)$from experimental results obtained from Figure 5 are presented in Table 2.

Table 2. Variation of ultimate load and slope of initial tangent with soil suction (From Figure 5).

Suction (kPa)	V_m (kN)	R_0 (kN/mm)
0	1.12	0.252
2.1	6.4	0.822
Dry	1.86	0.533

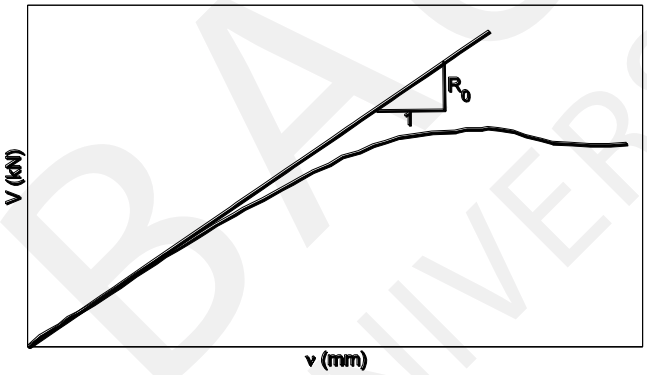

Figure 8. Slope of initial tangent R_0 for the centric vertical loading for the a particular value of suction (Wuttke et al. 2012)

For the numerical simulation of cyclic loading amplitude of 0.1kN with the static load of 0.8kN was used. The initial displacement corresponding to the static load of 0.8kN obtained from experimental results from Figure 5. was used as the starting point of the cyclic load. The model is simulated to obtain the response for the small frequency and for the drained condition. The ratchetting behaviour and the accumulation of plastic displacement for saturated, dry and unsaturated sand are shown in Figure 9-14. The values of cyclic parameters associated with the model are presented in Table 3.

Table 3. Parameters associated with the model

			$\zeta(\psi)$			$\kappa(\psi)$		
λ	α	β	Sat.	Dry	Unsat.	Sat.	Dry	Unsat.
1/3	3	0.95	50	50	8	8	8	50

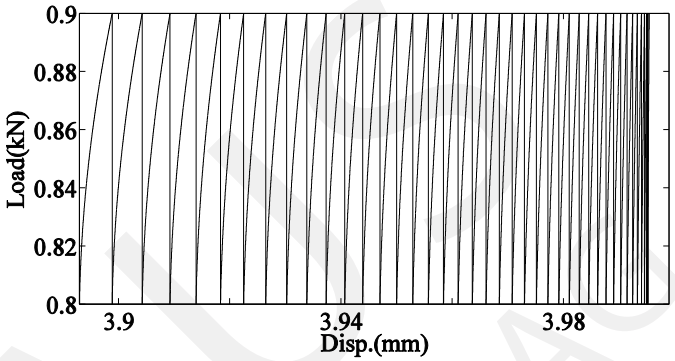

Figure 9. Numerical response of ratchetting behaviour of saturated sand

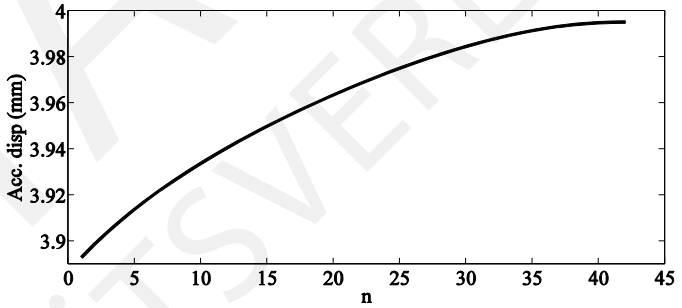

Figure 10. Numerical response of accumulation of plastic displacement of saturated sand with number of cycles (n).

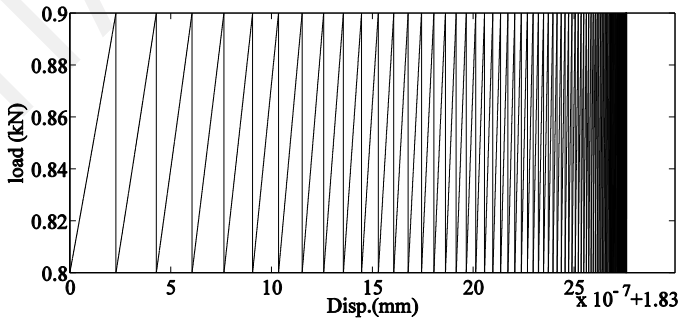

Figure 11. Numerical response of ratchetting behaviour of unsaturated sand with suction 2.1kPa

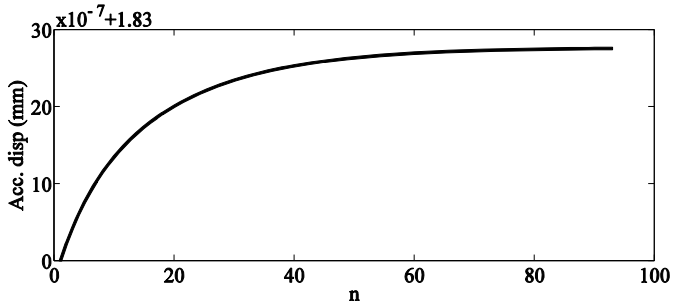

Figure 12. Numerical response of accumulation of plastic displacement of unsaturated sand (2.1kPa) with number of cycles (n).

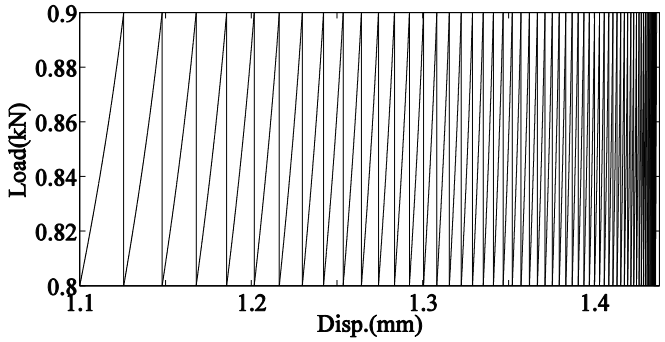

Figure 13. Numerical response of ratchetting behaviour of dry sand

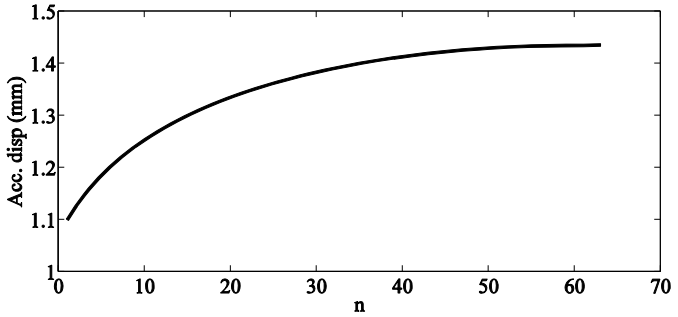

Figure 14. Numerical response of accumulation of plastic displacement of dry sand with number of cycles (n).

5 CONCLUSION

The Numerical model formulated herein was able to simulate the ratchetting behaviour of sand under the saturation of different fluid and unsaturated condition for small amplitude under drained condition. The influence of the suction dependent soil parameters $R_0(\psi)$ and $V_m(\psi)$ over the ratchetting behaviour was observed from the accumulation curve. The unsaturated sand has quantitatively lower accumulation of plastic displacement compared to water saturated and air saturated sand. The higher value of ultimate load $V_m(\psi)$ and the slope of initial tangent $R_0(\psi)$ for the unsaturated sand have shown the significant influence on the accumulation behaviour of the plastic strain during cyclic loading. The influence of soil suction on the cyclic constitutive parameters of the model, $\zeta(\psi)$ and $\kappa(\psi)$ is also observed. The model has shown its competence for simulating the cyclic accumulation of plastic displacement for the change in soil suction. However due to the small number of experimental result the values of constitutive parameters is not obtained for the wide range of suction and for the variety of existing soil type.

6 ACKNOWLEDGEMENTS

The authors would like to thank the support of the German Research Foundation DFG for funding the Research Training Group GRK 1462.

7 REFERENCES

Al-Tabbaa, A. & Wood, D. M. 1989. An experimentally based bubble model for clay, Pietruszczak, S. and Pande, G.N. (eds.), *NUMOG III*: 91-99. Niagara Falls: Elsevier applied science.

Bolton, M. D. & Lau, C. K. 1988. Scale effects arising from particle size. Corte´ J. F. (ed.), *Centrifuge 88*: 127-131. Rotterdam: Balkema,

Butterfield, R. & Gottardi, G. 1994. A complete three dimensional failure envelope for shallow footings on sand. *Geotechnique* 44: 181-184.

Cerato, A. B. & Lutenegger, A. J. 2006. Bearing capacity of square and circular footings on a finite layer of granular soil underlain by a rigid base. *J. Geotech. Geoenviron. Eng., ASCE* 132(11): 1496-1501.

Chatzigogos, C.T., Pecker, A. & Salencon, J. 2009. Macroelement modeling of shallow foundations. *Soil Dynamics and Earthquake Engineering* 29: 765–781

Dafalias, Y.F. & Herrmann, L.R. 1982. Bounding surface formulation. Pande G.N. and Zeinkiewicz, O. C. (eds.), *Soil Mechanics-Transient and cyclic loading*: John Wiley and Sons Ltd,

di Prisco, C., Nova, R. & Sibilia, A. 2002. Analysis of soil-structure interaction of towers under cyclic loading. Pande, G.N. and Pietruszczak, S. (eds.), *NUMOG VIII*: 637-642. Rome: Rotterdam: Balkema.

di Prisco, C. & Pisano, F. 2011. Seismic response of rigid shallow footings. di Prisco, M., La Borderie, C. & Nicot, F. (eds.), *European Journal of Environmental and Civil Engineering*: 185-221. Paris: Lavoisier.

Flavigny, E., Desrues, J. & Player, B. 1990. note technique, le sable d'hostun RF. *Revue Française de Geotechnique* 53: 67-70.

Gottardis, M. & Butterfield, R. 1988. Displacements of footing on sand under eccentric and inclined loads, *Can. Geotech. J.* 25(2), 199-212.

Grange, S. 2008. Modélisation simplifiée3Dde l'interaction sol-structure: application au génie parasismique. Ph. D. Thesis.

Herle, I. & Tejchman, J. 1997. Effects of grain size and pressure level on bearing capacity of footings on sand. Asaoka, A., Adachi, T. & Oka, F. (eds.), *IS-Nagoya'97: Deformation and progressive failure in geomechanics*: 781-786 Pergamon.

Houlsby, G.T. & Cassidy, M.J. 2002. A plasticity model for the behaviour of footings on sand under combined loading, *Geotechnique* 52(2): 117-129.

Kusakabe, O. 1995. Foundations. *Geotechnical centrifuge technology*, R. N.Taylor, (eds.), Blackie Academic and professional, London

Montrasio, L. & Nova, R. 1997. Settlement of shallow foundations on sand: geometrical effects, *Geotechnique* 47(1): 49-60.

Nova, R. & Montrasio, L. 1991. Settlement of shallow foundations on sand. *Geotechnique*, 41(2): 243-256.

Schanz, T., Lins, Y. & Vanapalli, S. K. 2011. Bearing capacity of a strip footing on unsaturated sand. *Proc., 5th Int. Conf. on Unsaturated soils*: 1195-1200. Barcelona, Spain: Taylor and Francis Group.

Schanz, T. & Vermeer, P. A. 1996. Angles of friction and dilatancy of sand, *Geotechnique* 46(1): 145-151

Wuttke, F., Kafle, B., Lins, Y. & Schanz, T. 2012. A macroelement for statically loaded shallow strip foundation resting on unsaturated soil. *Int. J. Geomech.* (in Press).

A hybrid very small to large strain stiffness macro-element model for shallow foundations

F. Wuttke[a,*], B. Kafle[a]

[a]*Bauhaus-Universitaet Weimar, Geomechanical Modeling, Coudraystreet 11c, 99423, Weimar*

Abstract

To improve the accuracy of the model prediction an existing elasto-plastic hardening macro-element formulation is extended for the small-strain behavior. The novelty is able to consider different shape of degradation curves by optimizing the constitutive parameter of the chosen hyperbolic function based on measured and well defined degradation curves. Therefore the specific soil behaviour can be considered by uniquely choosing the different parameters of the stiffness degradation curve. Following the Hueckel postulation an hybrid model is presented, which is able to bridge between both constitutive descriptions.

Keywords: Macroelement theory, Small-strain Stiffness, Shallow foundation, Bearing capacity, Constitutive models

1. Objective and Introduction

This paper provides a framework for the development of a hybrid small-to-large strain Macro-element for a vertical statically loaded footing resting over a granular material. The objective is to present a closed set of equations based on the theory of elasto-plasticity. Following the former solution of Nova (1991), the development was done as an extension of that formulation by considering the influence of the small-strain behaviour of the given load-displacement behaviour.

*Corresponding author

Email addresses: frank.wuttke@uni-weimar.de (F. Wuttke), binod.kafle@uni-weimar.de (B. Kafle)

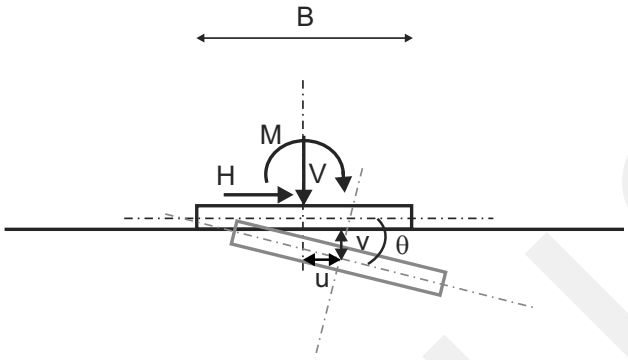

Figure 1: The possible direction of motion for the defined macro element with vertical, horizontal forces and moment(after Wuttke et. al. 2012).

Load-Deformation Behaviour of Footing Systems The load-deformation behaviour of footing systems is covered by a very small deformation to large elasto-plastic deformation range including failure. The modeling of elasto-plastic load deformation behaviour is limited by conventional measurements from a strain level of 10^{-3} to the failure strain level of 10^{-1}. Most of the existing constitutive models are formulated only for this range. In contrast to the incremental load-deformation behavior and modeling, there exist different hyperbolic description for static and dynamic loading since several years, Butterfield (1986), Prevost (1990), Fahey (1993), Puzrin (1996) and Atkinson (2000). To analyses the load-deformation behavior of footing the deformation have to be described over the full range of strain. For this objective this paper deals with a hybrid method which can be used for the development in the full strain range.

Static Macroelement for shallow foundations The Macroelement formulation consists of a coupled system of following components - elasto-plastic soil half space, the interface between structure, soil and footing, see Fig. 1. This coupled system is able to describe the experimental load-deformation behavior under consideration of soil-structure interaction. Under consideration of an incremental elasto-plastic constitutive model, the elasto-plastic strain-hardening description by an macro-element can reproduce the complex behavior of soil structure interaction.

2. Single Surface hardening Model

Theory of elasto-plastic strain hardening Macroelement Following the studies of Nova (1991) and Butterfield (1994) the failure surface can be described by a parabolic surface for the coupled forces acting on the foundation. The forces and displacements can be expressed as a generalized force vector $\mathbf{Q}$ and the associated displacement vector $\mathbf{q}$ as follows,

$$\mathbf{Q} = \begin{Bmatrix} \bar{V} \\ \bar{H} \\ \bar{M} \end{Bmatrix} = \frac{1}{V_m} \begin{Bmatrix} V \\ \frac{H}{\mu} \\ \frac{M}{\psi_m} B \end{Bmatrix} \text{and} \, \mathbf{q} = \begin{Bmatrix} \bar{v} \\ \bar{u} \\ \bar{\theta} \end{Bmatrix} = V_m \begin{Bmatrix} v \\ \mu u \\ \psi_m \theta_m B \end{Bmatrix}, \quad (1)$$

where, H denotes horizontal load, M the generated moment, V the vertical load, V_m the maximum centric vertical load capacity of the Macroelement,μ slope of failure envelope at the origin in the $H-V$ plane, ψ_m the slope of failure envelope at the origin in the $M-V$ plane, B width of foundation, ν the displacement in vertical direction, u displacement in horizontal direction and θ_m the angle of rotation. In Eq.1 forces are normalized by failure vertical load and moment additionally is normalized by the foundation width to obtain dimensionless moments. Similarly, in Eq.1 displacement parameters are also scaled by failure vertical load from the principle of work conjugate Prager (1955), load and deformation should comply,

$$w = \mathbf{Q}^T \mathbf{q} = Vv + Hu + M\theta_m. \quad (2)$$

The 3-D failure surface of macro-element is expressed as,

$$\bar{H}^2 + \bar{M}^2 - \bar{V}\left(1 - \bar{V}\right)^{2\beta} = 0, \quad (3)$$

where, β is a constitutive parameter to control the shape of failure envelope. The loading function of macro-element is postulated as

$$f\left(Q, \rho_c\right) = \bar{H}^2 + \bar{M}^2 - \bar{V}\left(1 - \frac{\bar{V}}{\rho_c}\right)^{2\beta} = 0, \quad (4)$$

where ρ_c is the hardening function whose value lies in the interval $(0, 1] = \{\rho_c \in \mathbb{R} | \, 0 < \rho_c \leq 1\}$.

Evolution of yield surface and plastic flow For the yield surface same shape as the failure envelope is purposed and the flow rule from the single surface hardening model of Nova (1991) is used. By the introduction of the plastic potential g, the increment of plastic strain (dq^p) for a given state of stress $\mathbf{Q}$ and for the hardening function ρ_c, the given force increment $df\,(Q, \rho_c)$ is obtained from Mestat (2002)

$$dq^p = \Lambda \frac{\partial g}{\partial Q}, \tag{5}$$

where, Λ is the plastic multiplier. The plastic potential which defines the direction of plastic strain is expressed as,

$$g\,(Q) = \lambda^2 \bar{H}^2 + \xi^2 \bar{M}^2 - \bar{V}\left(1 - \frac{\bar{V}}{\rho_g}\right)^{2\beta} = 0, \tag{6}$$

where, $\lambda = \mu/\mu_g$, $\xi = \psi_m/\psi$ and ρ_g is a scaling factor and is without any numerical significance and μ_g and ψ_g are constitutive parameters. If λ and ξ are both equal to unity then $f(Q)$ and $g(Q)$ are equal and the plastic potential coincides with the failure envelope and the flow rule becomes associative, else it is non-associative. The plastic multiplier Λ is a function of the load increment whereas the hardening modulus captures the history of macro-element. The hardening modulus follows a scalar function of the form,

$$H\Lambda = \frac{\partial f}{\partial Q} dQ. \tag{7}$$

Under consideration of a hardening function ρ_c, the hardening modulus is expressed as

$$H = -\left[\frac{\partial f}{\partial \rho_c}\right]\left[\frac{\partial \rho_c}{\partial q}\right]^T\left[\frac{\partial g}{\partial Q}\right]. \tag{8}$$

where the hardening function ρ_c is expressed by an exponential function explaining the relation between force and deformation

$$\rho_c = 1 - exp\left(-\frac{R_0\sqrt{v^2 + (\alpha_h u)^2 + (\gamma_h B\theta_m)^2}}{V_m}\right). \tag{9}$$

The terms α_h and γ_h are non-dimensional constitutive parameters and R_0 is the initial slope of the tangent of the force displacement curve, hence the

stiffness modulus. By combining Eqs.6, 8 and 9, the increment of plastic strain (dq^p) for a given state of stress is defined

$$dq^p = -\frac{\frac{\partial f}{\partial Q^T}\frac{\partial g}{\partial Q}dQ}{\left[\frac{\partial f}{\partial \rho_c}\right]\left[\frac{\partial \rho_c}{\partial q}\right]^T\left[\frac{\partial g}{\partial Q}\right]}. \tag{10}$$

3. Small-Strain Load-Deformation Behavior

Hyperbolic Strain Description The small-strain-load deformation behavior has been studied since several years. To improve the ability of models for realistic prognosis of deformation small strain behavior plays an important role in engineering design Atkinson (2000). The study of the small-strain behavior was done by many authors Butterfield (1986), Prevost (1990), Fahey (1993) and Puzrin (1996). Conventional constitutive models consider the strain range larger than 10^{-3}. Only few models are able to consider the behavior in small strain range, Benz (2007), Elhakim (2005) and Houlsby (2006). The mathematical description of soil behavior in small strain range is different from the ordinary constitutive model. The soil behavior is governed by hyperbolic description of stiffness degradation, whereas elasto-plastic model is based on incremental load or deformation steps.

The hyperbolic constitutive material description was analyzed by different authors for a large range of soil types and boundary condition. In principle there exist an well documented 'library' about this soil behavior. The most prominent one were Duncan (1970) and Houlsby (2006) with different descriptions for the small up to large strain behavior. Therefore the objective should be to adapt the constitutive modeling for the macro-element in such a case that any different hyperbolic description can be used to formulate the reduction of the stiffness with strain. That can be done by fitting constitutive parameter in an easy hyperbolic description on the exact G or E degradation curve. A hyperbolic description proposed by Bai (2011) for granular material was used to achieve this objective

$$\frac{E}{E_{max}} = \frac{1}{a + b\epsilon^m}. \tag{11}$$

The parameters a, b, and$m$ are fitting parameter and the strain ϵ is a function of deformation v which controls the degradation.

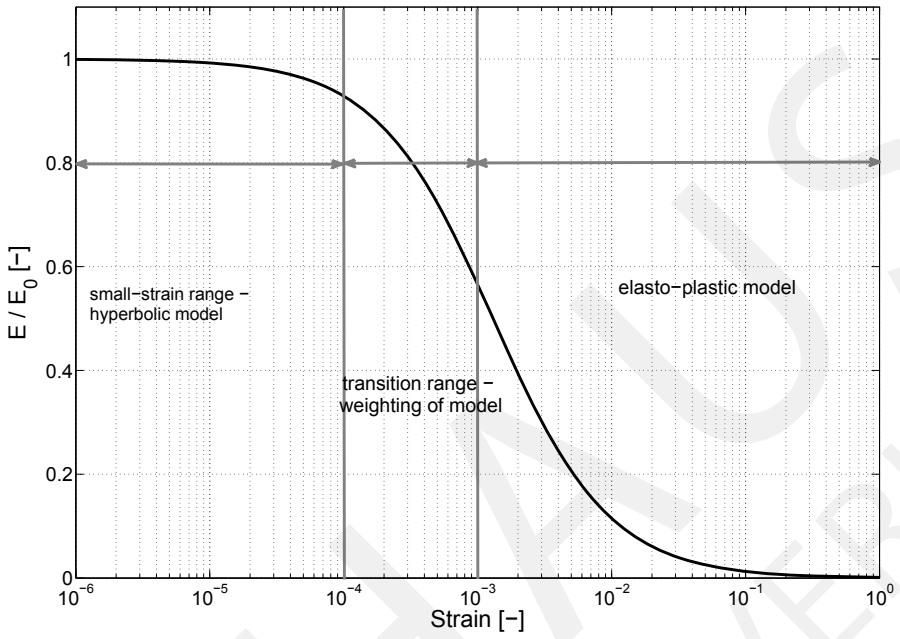

Figure 2: Definition of overlapping range - transition range between the small-strain behavior and elasto-plastic behavior citation needed (Niemunis 2011)

4. Hybid macro-element definition considering small-strain deformation and large strain deformation

The development of the hybrid constitutive macro-element is based on the statement of Hueckel (1979) that in the small-strain range, the strain is micro-plastic. Therefore the complete plastic strain is given as a sum of micro-plastic and plastic strain.

$$\epsilon = \underbrace{\epsilon^{elastic} + \epsilon^{mirco-plastic}}_{\text{small-strain range}} + \epsilon^{plastic}. \tag{12}$$

By Niemunis (2011) there exists a coupling of the hypo-plastic constitutive modeling with the para-elastic definition by weighting functions. Fig.4 shows the three weighting ranges chosen by the authors in comparison Fig.4 shows the weighting amplitude in the transition range. The weighting function is controlled by the strain ϵ as function of deformation $\epsilon\left(\frac{\delta v}{v}\right)$ and thresholds d_L and d_0

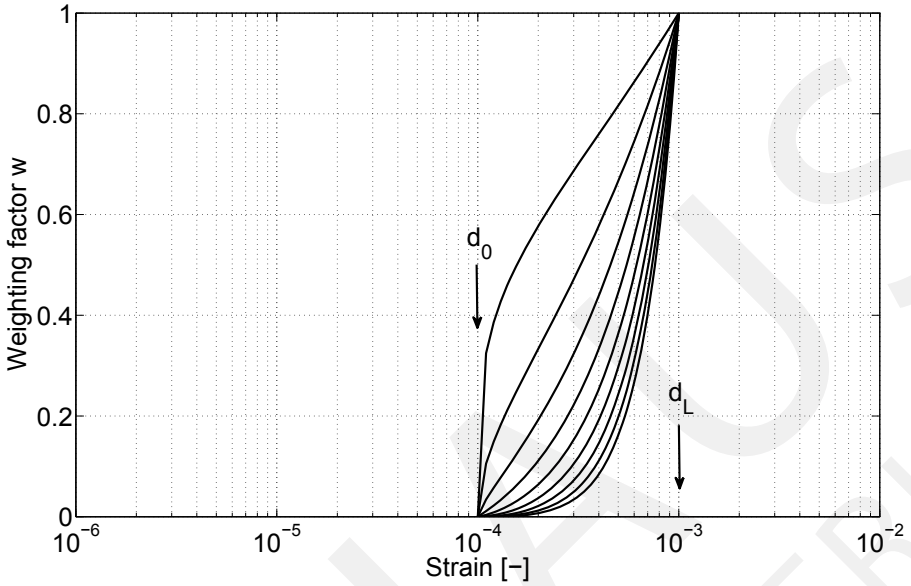

Figure 3: Weighting function w in Eq.13 after Niemunis (2011)

$$w = \left(\frac{\epsilon - d_0}{d_L - d_0}\right)^{\Delta} = \left(\frac{\epsilon - d_0}{d_L - d_0}\right)^{\Delta}. \tag{13}$$

The associated flow rule is valid in the small-strain range Houlsby (2006). Whereas the elasto-plastic region is governed by the non associated flow rule. The transition zone in between the small strain range and the elasto-plastic region acts as the bridging zone of the two different soil behavior. By the use of weighting function from Eq. 13 the smooth transition takes place from the small strain range following associated flow rule to the elasto-plastic region following the non-associate flow rule. The value of constitutive parameter w can be searched for the needed form of transition. Under this consideration of the definition the plastic deformation after eq. (12) with a smooth transition is defined as,

$$dq^p = (1-w)\left(\Lambda\frac{\partial g}{\partial Q}\right)^{associated} + w\left(\Lambda\frac{\partial g}{\partial Q}\right)^{non-associated} \tag{14}$$

From Eq. (14) the elastic deformation in the small strain range from the associative flow rule is obtained. In the transition zone the micro plastic

deformation is obtained from the combination of two different phenomenon, associative and non associative flow of micro-plastic deformation. The associative part of displacement decreases with the increase in the value of weighting function w which is the function of displacement. On the other-hand the elasto-plastic deformation obeying non associative flow rule increases with the increase of the displacement. At the end of the transition zone displacement is fully elasto-plastic in nature following the non associative flow rule. To control the small-strain behavior, the loading function respective of the hardening function has to be modified. Under consideration of the hyperbolic description of the hardening function the evolution of yield surface is the logarithmic description of the stiffness degradation as the displacement increases from very small strain range to the large strain range. In the small strain range where the associated flow rule is valid, only the plastic multiplier in Eq.(6) is depended on the hardening function. Following the one-dimensional hardening function from Nova (1991)

$$\frac{V}{V_m} = 1 - exp\left(-\frac{R_0 v}{V_m}\right), \tag{15}$$

the definition of the new hardening function should take into account the phenomenon of exponential increment of the displacement v. As definition of the new 1D hardening function following changes in control of the load-displacement behaviour was done.

$$\rho_c = 1 - \underbrace{\left(\frac{1}{a + bv^m}\right)}_{\text{scaling factor}} \cdot \underbrace{\left(\frac{E_{max} v_r}{V_m}\right)}_{\text{magnitudes}}. \tag{16}$$

where the magnitudes v_r and V_m are constant values. v_r is derived from the stiffness degradation curve as the boundary between the small strain range-hyperbolic model and transition range, see figure 4. The term V_b^{III} is described by the failure of the foundation under centric vertical load and mathematically equal to V_m, figure 4. The boundary between these ranges follow the C1 continuity such that the plastic flow is continuous during the evolution of the yield surface. Both terms v_r, V_b are described at the boundary of each range $V_b^I, V_b^{II}, V_b^{III}$ which acts as the mathematical control of respective zones. The plastic deformation in different zones is achieved by the replacement of V_m by V_b, eq.1 which controls the hardening behavior depending on the change in soil stiffness within the given strain boundaries,

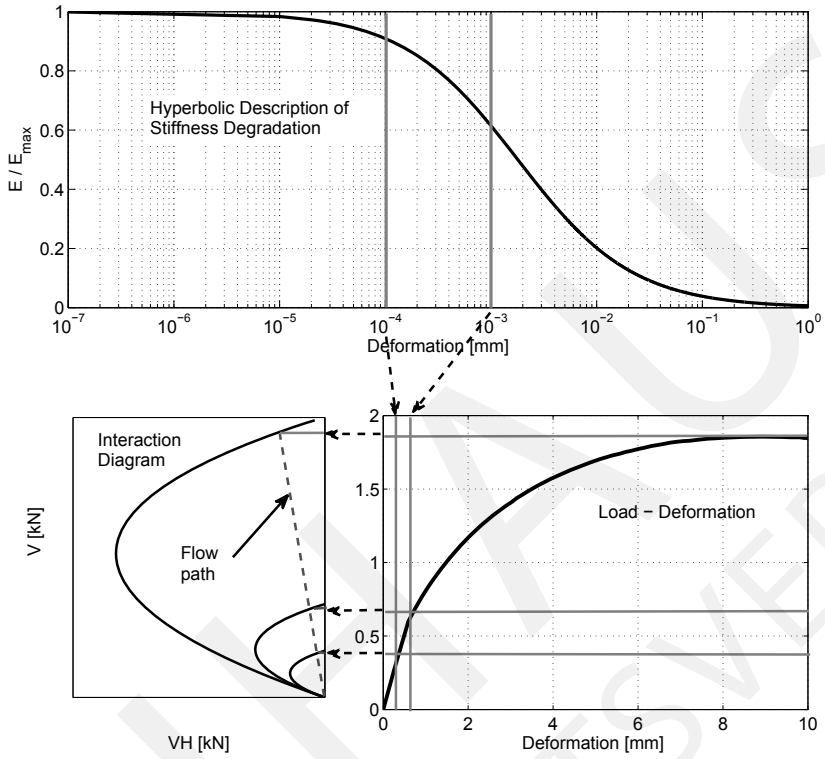

Figure 4: Defined boundaries of strain ranges for numerical calculation within the hybrid macro-element

allowing the model to capture the different soil behaviors in the different regions.

and is replaced by V_m ref. Eq. 1 when the current state lies within the respective boundaries. This allows to capture the different soil behavior in the different region described by the hardening function which depends on the change in soil stiffness. For the different types of degradation curves the terms can be determined with the monotonic variation in the respective control point of the curve, see point V_b^I and V_b^{II}. With this definition the elasto-plastic equation and numerical implication is unique for each of those three ranges.

The hardening function is extended from 1D description to 3D description

by

$$\rho_c = 1 - \frac{E_{max}}{a + b\left(\frac{1}{V_m}\sqrt{\bar{v}^2 + \bar{u}^2 + \bar{\theta}^2}\right)^m} \cdot \frac{v_r}{V_m}. \tag{17}$$

For all other definition the equation of Nova (1991) are valid and will be used for calculation of the force-deformation relation.

5. Numerical study

To validate the hybrid model different numerical studies is undertaken and also validated against the experimental results. The study was done to show the differences between the hardening functions, the load-deformation behavior and the coupled load behavior. Fig. 5 shows the hardening function of the new model including small-strain behavior and the former elasto-plastic definition after Nova (1991). It is evident that the new hardening function is much more steep at the beginning as compared to elasto-plastic hardening function.

The fitted parameter for the new hyperbolic model during the numerical study are: $E_{max} = 0.1kN/mm^2$, $V_m = V_b^{III} = 1.86kN$, $a = 0.00538$, $b = 0.04$, $m = 0.8$, $v_r = v_{threshold}/V_m$ and $v_{threshold} = 0.1mm$. The value of initial Stiffness for Hostun sand E_{max} was determined from the experimental data of the mean wave velocity for the strain-range of 10^{-7}[%].The constitutive parameter $\Delta = 0.75$ is selected for the smooth transition via weighting function w. An experimental result from the static centric vertical loading of 10 cm square rigid shallow footing resting over dry Hostun sand with void ratio of 0.7 is used.

The deformation corresponding to the different boundaries in the strain plane is obtained by the assumption that the normal sample height of the triaxial specimen to obtain the stiffness degradation curve is of the order of 100-200mm. The displacement corresponding to the respective axial strain in stiffness degradation curve is obtained by increasing the value by the factor of 100mm.The values of the different boundary in the load space is obtained from the experimental load displacement curve for corresponding boundary of the three different zones Fig. 4 in displacement plane. C1 continuity in the boundary between transition and elasto-plastic region, is ascertained by the continuity of stiffness at the end of the iteration step in transition zone

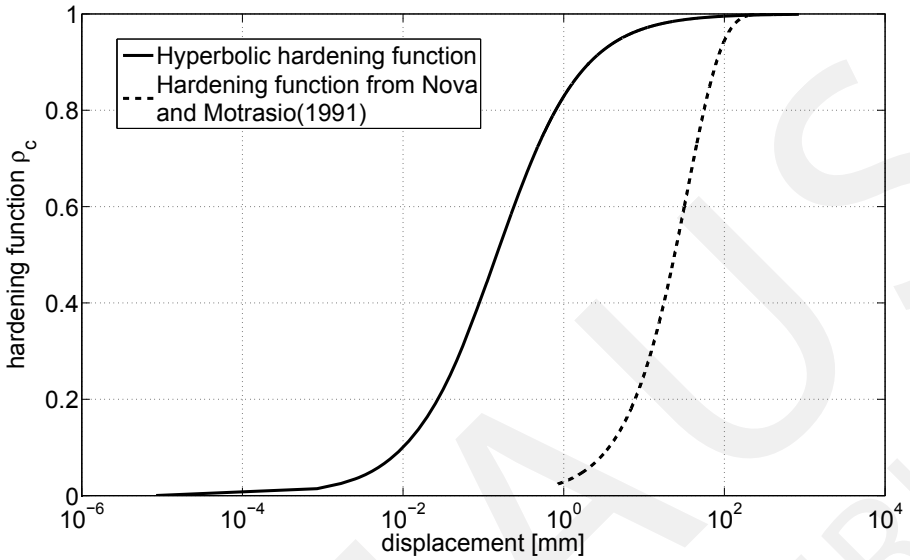

Figure 5: Comparision of the exponential hardening function by Nova (1991) and the proposed new hyperbolic hardening function to describe the *small-strain* behaviour.

as the value of R_0 Eq. 15. The macroelement from Wuttke (2012) is used to simulate the load displacement behaviour for complete range.
Figure 6 shows the evolution of the vertical load against vertical deformation behavior under the application of proposed hybrid very small strain to large strain stiffness macro-element and former pure elasto-plastic load-deformation behavior. Both were compared with the experimental results. The similar trend of the hardening function, where reduced deformation or stiffer answer in the low-deformation range is obtained due to the higher stiffness. This provides the background for stiffer behavior in the small-strain range, as the small-strain behavior was excluded in the model proposed by foregoing researchers. The hybrid model is able to explain the much stiffer soil behavior in the very small strain range. Figure 7 is showing a detailed view of the load-deformation function at the very-small strain range. A sharp transition in the different boundaries can be observed. This change depends on the choice of the weighting function controlled by Δ and therefore the transition can be smooth or sharp according to the value of Δ. The reasonable advantage of the presented model is the use of stiffness degradation behavior from very-small to large value of stiffness in contrast to the former

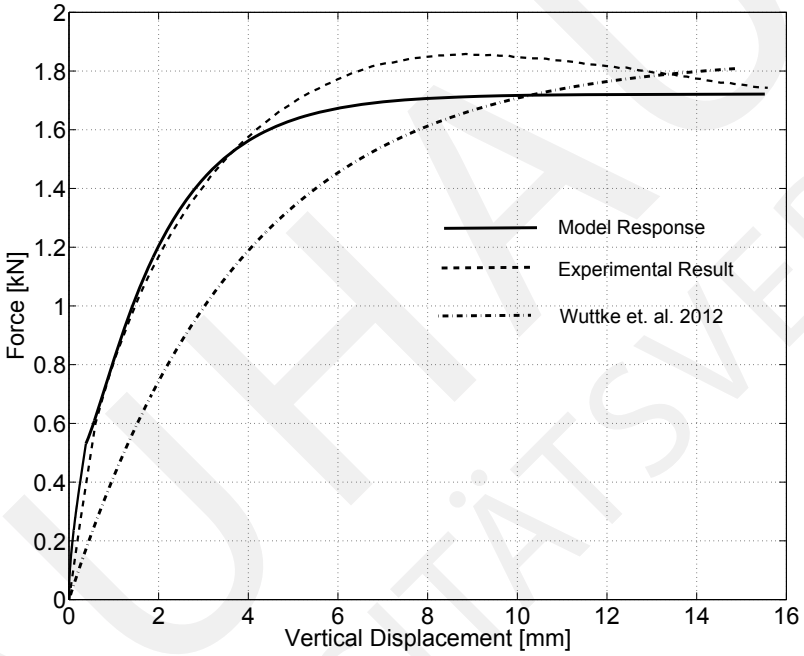

Figure 6: Comparison of response of proposed hybrid model and existing elasto-plastic model from Nova (1991) with the experimental data.

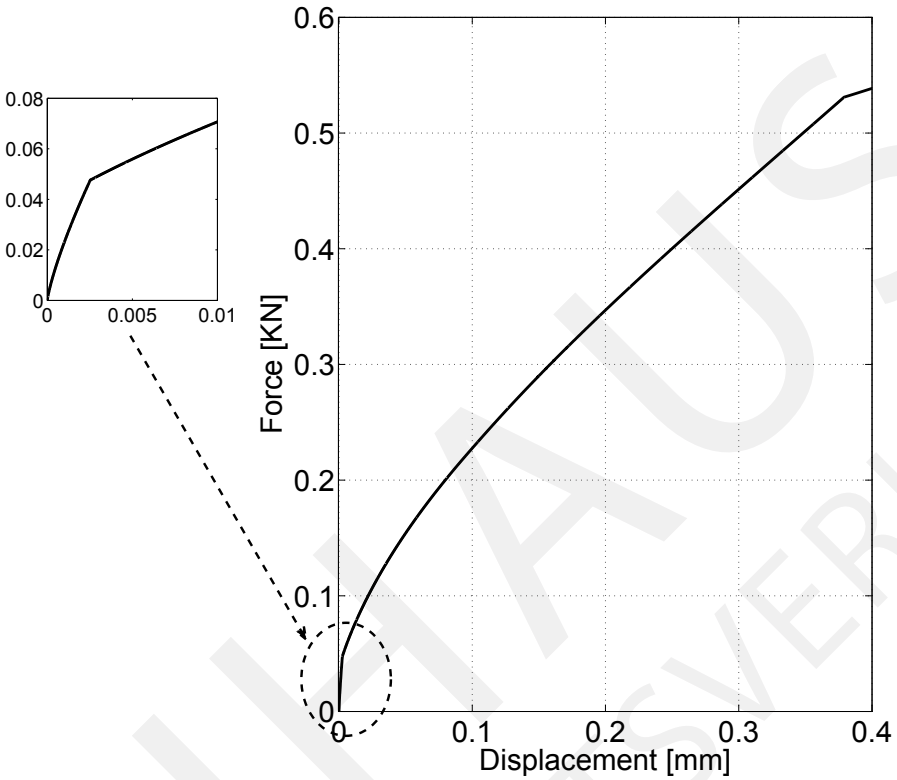

Figure 7: Transition of pure small-strain to transition range with rapit change of inclination due depending of the chosen weighting function.

choice of the value of R_0 as a constant slope parameter in the hardening function.

6. Conclusions

The existing elasto-plastic hardening model was extended by small-strain deformation characteristics. By choosing the hardening function dependent on the stiffness degradation curve, the constitutive parameter controlling the shape of degradation can be fitted by experimental results. Hence, any stiffness degradation curve can be numerically embedded in the model to obtain the response of the model in a coupled field of macro-element at very small

strain range. Finally the proposed hybrid macro-element is able to simulate the behavior of soil in the very small strain range showing a stiffer load deformation behavior in this range. The model is also competent in the large strain range and provides a good agreement with the experimental result. Common available experimental deformation measuring devices are not able to determine the precise deformation in very-small strain range. Hence the stiffness determined based on the measurements are not able to explain the realistic load-deformation behavior in this range. In particular the need of realistic realization of deformation at small strain range for various kind of natural or artificial load generated in the soil or structure needs formulation for very-small strain behavior of soil for the prediction of the prognosis of the displacement.

7. Acknowledgment

The authors would like to thank the support of the German Research Foundation for funding the Research Training Group 1462, the support of the the European Regional Development Fund for funding of experimental devices with grand no. FKZ B 715-09010 and the support of the DAAD under the grant number ID54712913.

8. Appendix

To fulfill the requirements of the plastic multiplier, the partial derivation has to be given. Hence the partial derivation $\frac{\partial \rho_c}{\partial \bar{v}}$, $\frac{\partial \rho_c}{\partial \bar{u}}$ and $\frac{\partial \rho_c}{\partial \bar{\theta}}$ is defined to

$$\begin{aligned} \rho_c &= 1 - \frac{E_{max}}{a + b\left(\frac{1}{v_m}\sqrt{\bar{v}^2 + \bar{u}^2 + \bar{\theta}^2}\right)^m} \cdot \frac{v_r}{v_m} \\ &\mapsto \frac{E_{max}}{a + b\left(\frac{1}{v_m}\sqrt{\bar{v}^2 + \bar{u}^2 + \bar{\theta}^2}\right)^m} \cdot \frac{v_r}{v_m} = 1 - \rho_c \end{aligned}$$

$$\begin{aligned} \frac{\partial \rho_c}{\partial \bar{v}} &= \frac{E_{max} v_r}{v_m}\left[a + b\left(\frac{1}{v_m}\sqrt{\bar{v}^2 + \bar{u}^2 + \bar{\theta}^2}\right)^m\right]^{-2} \cdot m\ b \cdot \\ &\left(\frac{1}{v_m}\sqrt{\bar{v}^2 + \bar{u}^2 + \bar{\theta}^2}\right)^{m-1} \cdot \frac{\bar{v}}{v_m}\left(\bar{v}^2 + \bar{u}^2 + \bar{\theta}^2\right)^{-0.5} \end{aligned}$$

$$= \frac{mb\bar{v}}{v_m} \frac{1-\rho_c}{\left[a+b\left(\frac{1}{v_m}\sqrt{\bar{v}^2+\bar{u}^2+\bar{\theta}^2}\right)^m\right]} \cdot \frac{\left(\frac{1}{v_m}\sqrt{\bar{v}^2+\bar{u}^2+\bar{\theta}^2}\right)^{m-1}}{\left(\bar{v}^2+\bar{u}^2+\bar{\theta}^2\right)^{0.5}}$$

$$\frac{\partial \rho_c}{\partial \bar{u}} = \frac{mb\bar{u}}{v_m} \frac{1-\rho_c}{\left[a+b\left(\frac{1}{v_m}\sqrt{\bar{v}^2+\bar{u}^2+\bar{\theta}^2}\right)^m\right]} \cdot \frac{\left(\frac{1}{v_m}\sqrt{\bar{v}^2+\bar{u}^2+\bar{\theta}^2}\right)^{m-1}}{\left(\bar{v}^2+\bar{u}^2+\bar{\theta}^2\right)^{0.5}}$$

$$\frac{\partial \rho_c}{\partial \bar{\theta}} = \frac{mb\bar{\theta}}{v_m} \frac{1-\rho_c}{\left[a+b\left(\frac{1}{v_m}\sqrt{\bar{v}^2+\bar{u}^2+\bar{\theta}^2}\right)^m\right]} \cdot \frac{\left(\frac{1}{v_m}\sqrt{\bar{v}^2+\bar{u}^2+\bar{\theta}^2}\right)^{m-1}}{\left(\bar{v}^2+\bar{u}^2+\bar{\theta}^2\right)^{0.5}}$$

References

Nova, R. and Montrasio, L. (1991), 'Settlement of shallow foundations on sand', *Geotechnique* **41**(2), 243-256.

Butterfield, R. and Gottardi, G. (1991), 'A complete three dimensional failure envelope for shallow footings on sand', *Geotechnique* **44**, 181-184.

Jardine, R.J. and Potts, D.M. and Fourie, A.B. and Burland, J.B. (1991), 'Studies of the influence of non-linear stress-strain characteristics in soil-structure interaction', *Geotechnique* **36**, (3) 377-396.

Niemunis, A. and Prada-Sarmiento, L. F. and Grandas-Tavera, C. E. (1991), 'Paraelasticity', *Acta Geotechnica* **36**,(6) 67-80.

Hueckel, T. and Nova, R. (1991), 'Some hysteresis effects of the behaviour of geological media', *International Journal of Solids and Structures* **15**,(6) 625-642.

Duncan, J.M. and Chang, C.Y. (1991), 'Nonlinear analysis of stress and strain in soils', *Journal of Geotechnical and Geoenvironmental Engineering* **96**,(5) 1629-1653.

Atkinson, J.H. (1991), 'Non-linear soil stiffness in routine design', *Geotechnique* **50**,(5) 487-508.

Puzrin, A.M., and Burland, J.B. (1991), 'Non-linear model of small-strain behavior of soils', *Geotechnique* **48**,(2) 217-233.

Prager, W. (1955), 'The theory of plasticity: a survey of recent achievements', *James Clayton Lecture* **Proc. Inst. Mech. Engrs.**,(169) 41-57.

Prevost, J.H. and Keane, C.M. (1990), 'Elastoplastic modeling of soils: Monotonous loadings', *in Constitutive modeling of soils and rocks* **John Wiley**,(8) 77-142.

Mestat, P. and Bourgeois, E. and Reiffsteck, P. (2002), 'Shear stress-strain curve generation from simple material parameters', *Journal of Geotechnical and Geoenvironmental Engineering* **116**,(8) 1250-1254.

Wuttke, F. and Kafle, B. and Lins, Y. and Schanz, T. (2012), 'A macro-element for static loaded shallow strip foundation resting on unsaturated soil', *ASCE International Journal of Geomechanics* http://dx.doi.org/10.1061/(ASCE)GM.1943-5622.0000254).

Fahey, M. and Carter, J.P. (1991), 'A finite element study of the pressuremeter test in sand using a nonlinear elastic plastic model ', *Canadian Geotechnical Journal* **30**,(2) 348-362.

Houlsby, G.T. and Puzrin, A.M. (2006), *Principles of Hyperplasticity*, Springer.

Benz, T. (1990), Small strain stiffness of soils and its numerical consequences, PhD thesis, Universität Stuttgart.

Elhakim, A. F. (1990), Evaluation of shallow foundation displacement using soil small-strain stiffness, PhD thesis, Georgia Institute of Technology.

Bai, L. (1990), Preloading Effects on Dynamic Sand Behaviour by Resonant Column Tests, PhD thesis, Technische Universität Berlin.

Publikationen zum Kapitel 4

Soil Dynamics and Earthquake Engineering 41 (2012) 102–118

Contents lists available at SciVerse ScienceDirect

Soil Dynamics and Earthquake Engineering

journal homepage: www.elsevier.com/locate/soildyn

Elastic wave scattering and stress concentration effects in non-homogeneous poroelastic geological media with discontinuities

Petia S. Dineva [a,*], Frank Wuttke [b], George D. Manolis [c]

[a] Institute of Mechanics, Bulgarian Academy of Sciences, 1113 Sofia, Bulgaria
[b] Chair of Geomechanical Modeling, Bauhaus University, 99421 Weimar, Germany
[c] Department of Civil Engineering, Aristotle University, 54124 Thessaloniki, Greece

ARTICLE INFO

Article history:
Received 13 February 2012
Received in revised form
7 May 2012
Accepted 9 May 2012

ABSTRACT

In this work, we investigate elastic wave propagation in complex geological media that exhibit material inhomogeneity in the form of depth-dependent material parameters and heterogeneity in the lateral direction. In addition, we consider a layered structure with non-parallel interfaces, free-surface relief, plus the presence of different type of discontinuities such as interface and/or internal cracks. The seismic load comprises incident, time-harmonic pressure (P) and vertically polarized shear (SV) waves, thus covering the plane strain case. Next, the computational technique developed herein is a hybridization of the semi-analytical wave number integration method (WNIM) with the boundary element method (BEM) cast in the frequency domain for solving 2D problems of elastodynamics. Transient response to this problem is recovered through standard Fourier synthesis of the frequency domain results. In essence, the present modeling effort interfaces continuum mechanics with linear fracture mechanics, since it focuses on wave scattering by cracks in complex geological regions. Material behavior is reproduced by the viscoelastic equivalent to Biot's poroelasticity. More specifically, by assuming saturated geomaterials, Bardet's model is introduced in the analysis as the computationally efficient viscoelastic isomorphism to Biot's equations of dynamic poroelasticity, thus replacing the original two-phase material by a single phase one. Finally, the role of stationary cracks in poroelastic materials is investigated through an extensive series of parametric studies, whereupon these discontinuities act as both wave scatterers and stress concentrators. In sum, our simulations serve to quantify the sensitivity of the near field stress intensity factors (SIF) and of the far field free surface motions to incoming wave characteristics, surface and underground topography, and mechanical properties of the geological deposits.

1. Introduction

Site effects are responsible for modifications imparted on the seismic signal at a "reference" site, i.e., a station on rock outcrop far away from the epicenter. More specifically, the combined influence of various geological factors on the seismic signal makes it difficult to separate and identify key parameters that should be considered in earthquake engineering practice [1]. Site effects still need to be examined in more detail and quantified in order to be used for earthquake-resistant design. As a step towards this direction, the present work considers the combined influence of surface relief, non-parallel layers, internal and interface geological cracks, wave path inhomogeneity, and material poroelasticity on the seismic response of 2D geological configurations. The aim here is to model and subsequently quantify these combined site effects and track elastic waves travelling upwards from a buried source in both frequency and time domains. The following brief state-of-the-art review on seismic wave propagation in geological regions will help define the aforementioned problem.

1.1. Wave propagation in geological media with various types of heterogeneities

Propagation of seismic waves through heterogeneous geological structures causes reflection, refraction, diffraction and scattering phenomena that are difficult to quantify. In addition, different types of discontinuities such as cracks, cavities and inclusions further complicate the overall picture by acting as scatterers and stress concentrators. These heterogeneities may generate large amplification as well as spatial variations in the seismic motions, which have important repercussions in the analysis of large infrastructure such as dams, bridges, pipelines, tunnels, etc. The literature is quite rich in

* Corresponding author. Tel.: +30 2310 995707; fax: +30 2310 995769.
E-mail address: petia@imbm.bas.bg (P.S. Dineva).

0267-7261/$ - see front matter © 2012 Elsevier Ltd. All rights reserved.
http://dx.doi.org/10.1016/j.soildyn.2012.05.009

terms of results obtained for various cases of surface and subsurface topography as well as for shallow sedimentary basins [2–8], irregular soil layers [9–11], geological cracks [12–17], buried cavities [18–22] and tunnels [23–27]. The computational methods employed to study the underlying elastic wave propagation phenomena in these types of heterogeneous media can be classified as follows:

1.1.1. Analytical methods

Commonly used analytical and semi-analytical methods include ray theory and its modifications [28,29], matrix methods, reflectivity methods and wave number integration methods (WNIM) [30–32] and finally mode matching methods [33]. In general, all these methods are restricted to inhomogeneous media with simple geometries (circle, cylinder, and sphere) and to a heterogeneity length scale that is considerably larger than the predominant wavelengths. This limits their use to urban zoning-type studies.

1.1.2. Numerical methods

These are suitable for analyzing complex heterogeneous media, but require much computational effort in terms of computer run-time and memory. Most numerical methods assume seismic loads in the form of incident body waves, but may also handle artificial or historical seismic records. Among all numerical methods, we mention the Boundary Element Method (BEM) that has become rather popular over the last decade because of efficient modeling of infinite and semi-infinite domains [34,35]. This gives the BEM a marked advantage over finite difference and finite element methods, namely the reduction in dimensionality of a given problem since only surfaces (and not interior regions) need to be modeled. In addition, the BEM is well suited for problems where stress gradients are manifested, as for instance in fracture mechanics. Dynamic analysis using BEM in both time and frequency domains is possible, provided the proper fundamental solutions (or Green's functions) are a priori available.

1.1.3. Hybrid techniques

The key idea behind hybrid techniques is to use standard numerical methods for the strongly heterogeneous part of the local geology and try to model the surrounding medium, which may be quasi-homogeneous, by analytical or semi-analytical means. Although the BEM is a good candidate for a hybrid technique, there are relatively few hybrid schemes using it for the seismic response of heterogeneous geological profiles [36–40]. In sum, there is a lack of hybrid techniques that can model all three basic components of the problem, namely (a) seismic source, (b) wave path from source to surface and (c) details of the local, finite geological region of interest with its nonparallel layers, free surface relief and inclusions. In the presence of cracks, the problem becomes even more complex because the conventional, displacement-based BEM degenerates [41] and alternative formulations must be developed. In this direction, we have the multi-domain BEM [42], the displacement discontinuity method which is essentially an indirect-type BEM [43], the non-hypersingular, traction-based BEM that derives from the two-state conservation law of elastodynamics in its integral form [44], and finally the dual BEM that combines the displacement-based BEM on one of the crack's surfaces with the hypersingular traction-based BEM on the other surface [45–47]. In previous work [14–15], the authors developed a BEM combining both displacement and traction integral formulations for the analysis of time-harmonic waves propagating through cracked, multi-layered geological regions with surface topography, where the local geological region rests on a homogeneous half-plane. More recently, a hybrid WNIM and displacement-based BEM technique was developed [48] to study seismic wave propagation in a geological inclusion embedded in an inhomogeneous half-plane containing a seismic source. This last technique has now been extended in here to include cracks in the geological inclusion.

1.2. Seismic wave propagation in poroelastic geological media

Poroelasticity is a continuum mechanics theory for materials comprising an elastic matrix with fluid-saturated pores. The presence of the fluid stiffens the material, but also results in diffusion between regions of higher to lower pressure. Since Biot [49] proposed a phenomenological model for dynamic poroelasticity over 50 years ago, the problem of wave propagation in two-phase materials has been extensively studied. Regarding use of the BEM in poroelasticity, we note the key role played by the fundamental solution (or Green's function) in reducing a given boundary-value problem (BVP) into a system of integral equations along the boundaries. Unsurprisingly, much research work has been directed towards the derivation of fundamental solutions for the governing partial differential equations of poroelasticity [50–54]. A comprehensive review of poroelastodynamics along with the analytical and numerical solutions that have been developed to date can be found in Schanz [55]. So far, the BEM has seen limited application to seismic wave propagation in saturated heterogeneous geological media due to the multiphase nature of the problem. There is, however, a marked similarity between poroelastic and viscoelastic materials in terms of their dynamic response, a fact that suggests the possibility to use a single phase model with special, augmented properties in lieu of the multiphase one. This idea was promulgated by Bardet and Morochnik [56–58], who proposed an equivalent viscoelastic solid to model saturated poroelastic materials governed by Biot's theory. Specifically, the speed and attenuation of the longitudinal and transverse waves in soils described by viscoelastic isomorphism are related to Biot's material parameters in a way that equates the viscoelastic and poroelastic wave numbers. Parametric studies [58] have shown that viscoelastic isomorphism gives solutions practically identical to those of the original poroelastic problem for a specific range of material parameters.

Recently, the authors [59] successfully used Bardet's model in conjunction with the conventional displacement BEM to study seismic wave propagation in a non-homogeneous soil inclusion resting on the homogeneous poroelastic half-plane. This work will now be extended to include heterogeneities such as parallel and non-parallel soil layers, free-surface relief, interface and internal cracks, plus the presence of a seismic source whose signal travels along an inhomogeneous path. This will allow us to examine the dual role of cracks acting as scatterers and stress concentrators in poroelastic media by solving a series of BVP. The first such case describes seismic wave propagation in a finite, laterally inhomogeneous cracked soil stratum rested on a horizontally layered half-plane that contains a seismic source. Additional cases include a crack in (i) an infinite poroelastic plane, (ii) a finite poroelastic region, (iii) a finite laterally inhomogeneous poroelastic inclusion resting on a homogeneous half-plane, all subjected to incoming P- or SV-waves, and (vi) a poroelastic, horizontally layered half-plane containing a seismic source within a layer.

Briefly, the paper is structured as follows: Section 2 defines the BVP for seismic wave propagation in a cracked, laterally non-homogeneous complex region embedded within an inhomogeneous half-plane containing a seismic source. The hybrid computational model is then developed in Section 3. Next, Section 4 presents numerical results for an extensive series of parametric studies, while a list of conclusions is given in Section 5. All results presented herein are to be understood within the framework of the viscoelastic to

poroelastic similarity and are subject to the constraints that this entails.

2. Problem formulation

2.1. Governing equation of motion and boundary conditions

As shown in Fig. 1, the mechanical model comprises a finite local geological region Ω_{LGR} embedded in an inhomogeneous (with depth) half-plane. The half-plane itself is modeled by a stack of M horizontal layers $\cup_{i=1}^{M}\overline{\Omega}_i$, with the first layer being $\overline{\Omega}_1$. The bottom layer $\overline{\Omega}_M$ rests on the homogeneous half-plane, while a seismic source is placed at an intermediate layer $\overline{\Omega}_i$. Plane strain conditions are assumed to hold. Next, the local region $\Omega_{LGR}=\cup_{i=1}^{N}\Omega_i$ contains N layers with non-parallel boundaries and a free-surface relief, plus interface and internal cracks. The external boundaries of the local geological region Ω_{LGR} comprise the traction-free surface plus the enclosing boundary Λ. Without loss of generality, we assume an interface crack FE of length l_{FE} plus an internal crack CD of length l_{CD}. We consider the case where the local geological region Ω_{LGR} is located within the first, deep layer of the horizontally layered half-plane. The main objective here is to obtain synthetic seismograms at receiver points along the free surface of the local geological region.

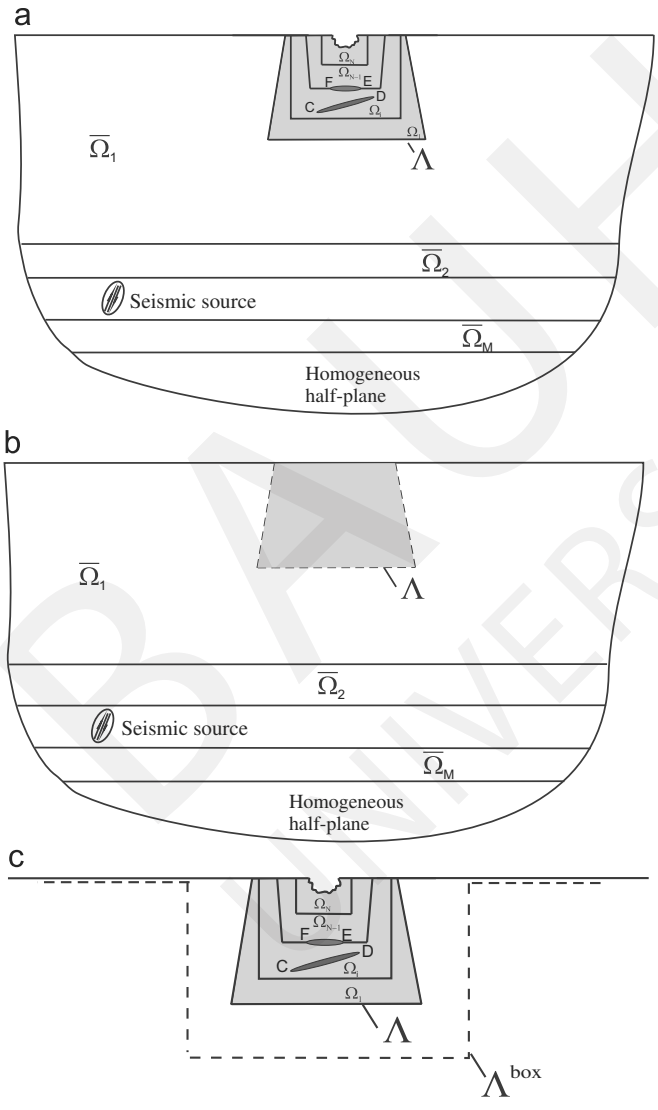

Fig. 1. (a) Problem configuration solved by the hybrid WNIM-BEM; (b) WNIM computation of the free field motions along Λ for the background model; (c) BEM computation of the total wave field inside and outside Λ.

The geomaterial in each layer is homogeneous, isotropic and water saturated, while its mechanical properties are described by Bardet's model [56], which represents the poroelastic material as one-phase viscoelastic one of the Kelvin–Voigt type. After applying the Fourier transform to the time-dependent governing equations of motion of the geological continuum and using the correspondence principle of viscoelasticity [60], the governing equation for each layer in the frequency ω domain is as follows:

$$(k_S^2/k_P^2-1)(u_{z,xz}+u_{x,xx})+u_{x,xx}+u_{x,zz}=-k_P^2u_x$$
$$(k_S^2/k_P^2-1)(u_{x,xz}+u_{z,zz})+u_{z,xx}+u_{z,zz}=-k_S^2u_z \quad (1)$$

In the above, u_i, $i=x,z$ are displacement vector components in the horizontal and vertical directions, respectively, while k_P and k_S are the corresponding complex-valued wave numbers for P- and S-waves. Each layer has different values, which for a linear Kelvin–Voigt viscoelastic model assume the form

$$k_P^2=\omega^2/(\alpha^*)^2;\quad k_S^2=\omega^2/(\beta^*)^2 \quad (2)$$

$$(\alpha^*)^2=\alpha^2(1-i\omega\xi_P);\quad (\beta^*)^2=\alpha^2(1-i\omega\xi_S) \quad (3)$$

where $\alpha=\sqrt{(\lambda+2\mu)/\rho}$, $\beta=\sqrt{\mu/\rho}$ are the elastic P- and S-wave velocities. We have that λ,μ are the real parts of the complex-valued Lame constants λ^*,μ^* of the viscoelastic medium and ρ is its density. Also, ξ_P,ξ_S are the respective P- and S-wave attenuation coefficients (or ratios) that account for a small amount of viscous damping. In the low frequency range, i.e., $\omega\xi_P,\ \omega\xi_S\ll 1$ Eq. (3) simplifies as

$$k_P\approx\omega(1+0.5i\xi_P)/\alpha;\quad k_S\approx\omega(1+0.5i\omega\xi_S)/\beta \quad (4)$$

The general viscoelastodynamic BEM formulation can be found in Schanz [61]. Also, frequency domain viscoelastic BEM for solving dynamic problems were used by Manolis and Beskos [62] in connection with the differential operator form of the constitutive equations, by Kobayashi [63] in connection with the integral form of the constitutive equations, and by Abascal and Dominguez [64] and Beskos et al. [65] in connection with the simple hysteretic damping model.

The BVP under consideration is now defined by governing Eq. (1) and the following frequency-dependent boundary conditions, see Fig. 1: (a) zero tractions at the free surface; (b) displacement compatibility and traction equilibrium conditions at the interfaces between layers in the local region; (c) zero tractions on the crack surfaces and a crack opening displacement $\Delta u_i=u_i^+-u_i^-$, which represents the displacement discontinuity on the crack surface $S_{cr}=S_{cr}^+\cup S_{cr}^-$; (d) compatibility and equilibrium conditions for displacements and tractions at the interface between the homogeneous and inhomogeneous part of the half-plane; (e) exclusion of incoming waves into the upper inhomogeneous part of the half-plane (the seismic bed) in the absence of any seismic sources embedded in the lower homogeneous part (i.e., a Sommerfeld radiation condition).

This BVP is solved in the low frequency range and a numerical, inverse fast Fourier transformation (FFT) is applied in order to obtain the corresponding time-dependent solution. The displacement is a vector-valued function satisfying the following continuity condition: $u_i(x,z,\omega)\in C^2(\Omega_B)\cap C^1(S_B)$, where S_B is the surface (closure) of volume Ω_B. Correspondingly, the traction at surface point $r=(x,z)$ with normal vector $n_i(r)$ is given as $p_i(r)=\sigma_{ij}(r)n_j(r)=P'_{ik}(n_r,\partial_r)u_k(r)$, where σ_{ij} is the stress tensor. The traction operator is defined as $P'_{ik}(n_r,\partial_r)=\lambda^*n_i(r)\partial_k+\mu^*n_k(r)\partial_i+\mu^*\delta_{ik}n_l(r)\partial_l$, where $\partial_k=\partial/\partial r_k$, Finally, the tractions satisfy a continuity condition $p_i(x,z,\omega)\in C^1(\Omega_B)\cap C^0(S_B)$, where $C^k(\Omega_B)$ is the set of k-continuously differentiable functions in Ω_B.

2.2. The Bardet viscoelasticity model

This model was developed by Bardet [56–58], while its validation and use for seismic wave propagation in saturated geomaterials has also been discussed by the authors [59]. For completeness purposes, we now present the key idea behind this model, mainly its isomorphism to Biot's theory [49]. Consider a representative volume V of the two-phase, solid-fluid system with isotropic elastic skeleton and porosity $n=V_p/V$, where V_p describes the volume of the pores. The relevant parameters are the following three bulk modulus/density pairs: K_{dry}, ρ_{dry} for dry material, K_g, ρ_g for the solid grains and K_f, ρ_f for the fluid. The saturated material density is given by the following equation: $\rho_{sat}=\rho_{dry}+n\rho_f=(1-n)\rho_g+n\rho_f$. The shear stiffness of the porous material is provided by the solid skeleton alone and is not affected by fluid saturation, since fluids (in our case water) sustain dilatational deformation only. Due to this fact, both dry and saturated materials have one and the same shear modulus, namely $\mu_{dry}=\mu_{sat}$ and hitherto denoted by just μ. Bardet [56] solved the Biot dynamic poroelasticity equations for time-harmonic plane waves and obtained analytical expressions for the P- and S-wave numbers. Next, he introduced the idea of poroelastic-viscoelastic similarity by equating the Biot wave numbers with the viscolelastic ones given in Eq. (4). As a result, the following expressions were obtained for the wave velocities and attenuation factors:

$$\alpha=\sqrt{P+2Q+R/\rho_{sat}};\ \ \beta=\sqrt{N/\rho_{sat}};$$
$$\xi_P=\frac{\rho_{sat}}{b}\left(\frac{Q+R}{P+2Q+R}\frac{n\rho_f}{\rho_{sat}}\right)^2;\ \ \xi_S=\frac{\rho_{sat}}{b}\left(\frac{n\rho_f}{\rho_{sat}}\right)^2 \tag{5}$$

In the above, we have that

$$P=\frac{3(1-v)}{1+v}K_{dry}+\frac{Q^2}{R};\ \ Q=\frac{n(1-n-K_{dry}/K_g)}{1-n-K_{dry}/K_g+nK_g/K_f}K_g;$$
$$R=\frac{n^2K_g}{1-n-K_{dry}/K_g+nK_g/K_f}$$
$$N=\frac{3}{2}\frac{1-2v}{1+v}K_{dry};\quad K_{dry}=\frac{2}{3}\ \frac{\mu(1+v)}{1-2v};$$
$$\lambda_{sat}=\lambda_{dry}+\frac{Q^2}{R}=\frac{3v}{1+v}K_{dry}+\frac{Q^2}{R} \tag{6}$$

Furthermore, v is Poisson's ratio for the dry skeleton, $b=(n^2g\rho_f/\hat{k})$ is the viscous dissipation coefficient, g is the acceleration of gravity and $\hat{k}$ is the material permeability with values in the range $10^{-10}-10^{-2}$ m/s. It should be mentioned here that Eqs. (5) and (6) are valid under the restriction $\omega\rho_{sat}/b)\ll 1$, which is satisfied in the frequency range exhibited by most typical earthquakes and also for commonly encountered fluid conductivity values.

The Bardet model matches Biot's theory within its range of applicability. Additional restrictions imposed by this model are: (a) the relative motion of the fluid in the pores is laminar flow described by Darcy's law; (b) the single-phase material assumption precludes the recovery of information on the fluid pressure and its influence on overall material deformation; (c) the second (slow) P-wave predicted by Biot's theory cannot be evaluated; (d) the model is valid in the low frequency range, as defined above. Despite these shortcomings, the main advantage of the Bardet model is that it easy can be incorporated within existing BEM software codes, in contrast to the Biot model which requires computation of complicated Green's function that are difficult to evaluate numerically.

Following Bardet's model, dependence of the longitudinal α and shear β wave speeds on the porosity for both dry and saturated materials is depicted in Figs. 2 and 3, respectively. These results are for values of Poisson's ratio ranging as $v=0.1-0.4$. The reference geological material examined here is sandstone with $K_g=36{,}000$ MPa; $\rho_g=2650$ kg/m^3; $K_f=2000$ MPa;

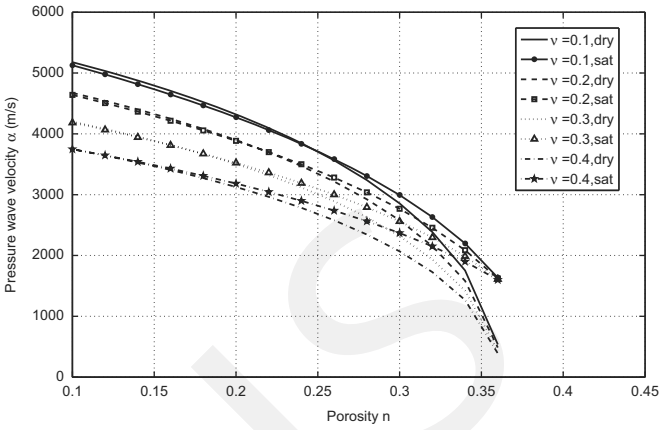

Fig. 2. P-wave velocity α following Morochnik and Bardet [58] for dry and saturated materials versus porosity.

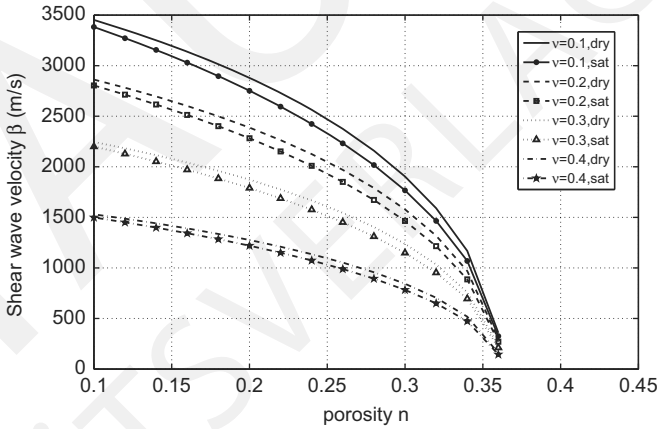

Fig. 3. S-wave velocity β following Morochnik and Bardet [58] for dry and saturated materials versus porosity.

$\rho_f=1.000$ kg/m^3, see Lin et al. [66]. The dry bulk modulus is calculated from the expression proposed below [66] that derives from experimental data, with $K_{cr}=200$ MPa the bulk modulus at critical porosity $n_{cr}=0.36$:

$$K_{dry}=K_{cr}+(1-n/n_{cr})(K_g-K_{cr}) \tag{7}$$

The following conclusions can now be drawn:

(1) The P- and S-wave speeds decrease with increasing porosity. For example, at a fixed Poisson ratio value of $v=0.1$, and as porosity increases from $n=0.10$ to 0.36, α values drop (compared to the starting values) to 1/10 for the dry and to 1/3 for the saturated material, respectively. The β values are somewhat insensitive to the presence of the fluid, since the drop (from staring values) with increasing porosity is about 1/10 for both dry and saturated material.
(2) For small porosity values around $n=0.10$ and for $(K_{dry}/K_f)=13$, there is little difference between P-wave speeds for dry and saturated geomaterials, and this remains true up to $n=0.20$ and for $(K_{dry}/K_f)=8$. In these cases, the stiffness of the dry skeleton is much greater than the compressibility of the fluid, which has no further influence on the material properties.
(3) For high porosity values, when $(K_{dry}/K_f)=1.0$ at $n=0.34$ and $(K_{dry}/K_f)=1.0$ at $n=0.36$, rock poroelasticity is noticeable and the influence of the fluid becomes important.
(4) The presence of fluids stiffens a poroelastic material, as the pore pressure induced by the excitation helps resist the external compression. The shear stiffness in Biot porous

media is provided by the solid skeleton and it is not affected by fluid saturation: $\mu_{sat}=\mu_{dry}$, while the Lame coefficient changes to $\lambda_{sat}=\lambda_{dry}+(Q^2/R)$, where the Biot coefficients Q and R are functions of porosity n and of the bulk moduli of the solid skeleton K_{dry}, the solid grain K_g, and the fluid K_f.

(5) The fluid in the pores also acts as a damper, because we have viscous-type flow from regions of higher pressure to those of lower pressure, i.e., a diffusion process.
(6) For small porosity $n=0.10$ and dry materials, we recover the purely elastic case.
(7) As Poisson's ratio v_{dry} increases, the P- and S-wave speeds decrease in the range of small porosities. As porosity increases, the difference between wave speed values at different Poisson ratios decreases. For example, at $n=0.10$ the percentage difference between P-wave speeds for saturated materials at $v=0.1$ and at $v=0.4$ is 304%, while at $n=0.36$ this difference becomes only 2%.

3. Hybrid computational model combining the WNIM and BEM

Modeling of seismic wave propagation in geological media must include the source, the travel path and the receiving site. Two basic types of models can be distinguished here, namely:

(a) The all-in-one, source-path-site single computational method demanding an extreme amount of computer memory and time, especially for cases where the source-to-receiver distance is measured in the tens of km.
(b) The hybrid approach, which is based on a two-step procedure that combines both the source and path effects as computed by one type of method, with the local site effects evaluated by another method. The latter method uses the wave field produced by the former one as input, and the two methods are connected by a wave-injection boundary that is perfectly permeable to the waves scattered from the local near field.

Hybrid methods are appropriate when one part of the full model (usually the smaller local field) exhibits a complex topography and is embedded in a much larger far field containing the source and path effects. The main disadvantage of these two-step models, which have been developed over the years by many researchers, is that the second step of the solution neglects any interaction between the backscattered waves coming from the local region with the incoming waves travelling through the layers of the surrounding half-space. In practice, this approach is applicable when the local field is embedded within a thick homogeneous layer, so that any backscattering effects from the local geological profile dampen out before reaching the boundaries of the deeper layers comprising the half-space. This is the key idea behind the concept of the "excitation box" proposed by most researchers who use the two-step hybrid approach. As a matter of fact, the second step uses information obtained from the first step directly as a boundary condition to model wave propagation in the truncated "excitation box" comprising the near field geological region.

The hybrid two-step WNIM and displacement-based BEM was developed in previous work by the authors [48] for the synthesis of seismic signals in laterally non-homogeneous geological inclusions within a horizontally layered half-plane containing a seismic source. In here, we augment this hybrid formulation by introducing discontinuities and poroelastic material behavior.

3.1. Hybrid computational technique

3.1.1. The WNIM

We define the "free-field" displacements u_i^{fr} and tractions p_i^{fr} as the response of the layered half-plane without the lateral inhomogeneity (i.e., the local geological inclusion Ω_{LGR}) that is subjected to elastic waves radiating from the seismic source, see Fig. 1(b). The external boundary of the local geological region Ω_{LGR}, denoted by Λ, is shown in Fig. 1(b) by a broken line because in the first step of the two-step hybrid model this boundary is fictitious. The free-field is the solution of the BVP posed by Eq. (1) plus the following boundary conditions: (a) zero tractions on the horizontal free surface; (b) satisfaction of both displacement continuity and traction equilibrium across any two consecutive horizontal layers; (c) the same conditions hold true for the seismically active homogeneous background ("seismic bed") at its interface with the non-homogeneous part of the half-plane; and (d) Sommerfeld's radiation condition at infinity. The WNIM is used to compute the free-field motion, which is stored along the boundary Λ. Since the WNIM is known [32,48], it is unnecessary to describe it here. It is sufficient to say that it is an analytical approach based on Luco and Apsel's work [30,31] for deriving Green's functions for a layered half-plane.

3.1.2. The BEM

After dispensing with the seismic source, we focus on the truncated domain comprising the area inside the BEM box, see Fig. 1(c). Between the external boundary Λ of the local geological region Ω_{LGR} and the first layer of the half-plane we introduce by broken line the fictitious boundary Λ^{box} of the truncated domain denoted as the "BEM box". Using the BEM, we solve for both the internal and the external problems, corresponding to the continuum inside and outside the local geological region Ω_{LGR}, but still inside the BEM box. The size of this BEM box depends of the distance after which the elastic waves scattered by the local region Ω_{LGR} dampen out.

3.1.3. The hybridization procedure

The total wave field is the sum of the free and the scattered wave fields, i.e.,

$$u_i=u_i^{fr}+u_i^{sc},\quad p_i=p_i^{fr}+p_i^{sc} \tag{8}$$

Inside local region Ω_{LGR} we have the total wave field, while outside boundary Λ just the scattered one. These fields are coupled by means of boundary conditions relating the "inside" field u_i, p_i with the "outside" field $u_i^{sc}=u_i-u_i^{fr}$, $p_i^{sc}=p_i-p_i^{fr}$. The free-field computed from the first step is used as the boundary condition on Λ. Of course, truncation of the computational model, see Fig. 1(c), neglects any interaction with the scattered wave emanating from the underlying, deeper layers. As a consequence, truncation limits the amount of interaction between the geological structure of interest and its surrounding medium in terms of the incoming ("background") elastic wave field, which may include surface and body waves that are influenced by the seismic source, the wave path followed and by localized interface effects. In sum, multiple reflections of the scattered elastic waves that occur between the local excitation domain and the geological region beyond it, can be modeled properly only by an optimal choice of the truncated domain, as dictated by validation studies.

3.2. The combined BEM approach

The combined BEM simultaneously computes the total wave field inside region Ω_{LGR} and the scattered wave field outside boundary Λ in the following way:

(1) For any layer Ω_n, $n=1, 2, 3,\ldots N$, inside Ω_{LGR}, the following system of boundary integral equations with respect to the total wave field must be satisfied along the layer interfaces

Γ_n, provided no internal cracks are present:

$$c_{ij}\, u_j(r,\omega) = \int_{\Gamma_n} U^*_{ij}(r,r_0,\omega)\, p_j(r_0,\omega)\, d\Gamma - \int_{\Gamma_n} P^*_{ij}(r,r_0,\omega) u_j(r_0,\omega)\, d\Gamma \quad (9)$$

In the above, U^*_{ij}, P^*_{ij} are the displacement and traction fundamental solutions of Eq. (2), c_{ij} are jump terms depending on the surface geometry at the field (or collocation) point $r=(x,z)$, while $r_0=(x_0,z_0)$is the source point.

(2) For a layer Ω_n with an internal crack present, the regularized hypersingular traction-based BEM along the boundary Γ_n is used. This alternative BEM formulation derives from computational fracture mechanics, and some of the surface integrals are hypersingular. To circumvent this difficulty, the regularization technique of Sladek and Sladek [67] is used. Simply stated, this regularization procedure is based on integration by parts so as to shift the spatial derivatives from the strongly singular fundamental traction solution to the unknown displacements, including the crack-opening displacements $\Delta u^k_i(\eta,\omega)$ (note that η is a local coordinate). As a result, we have

$$\begin{aligned} p_l(r,\omega) = & \int_{\Gamma_n} P'_{lk} U^*_{ks}(r_0,r,\omega) p_s(r_0,\omega) d\Gamma \\ & + c_{lpjr} n_p(r) \left\{ c_{iskt} \left[\int_{S^+_{cr}} \Delta K^i_{rs} D_t U^*_{kj}(r-r_0,\omega)\, dS_\eta \right. \right. \\ & \left. + \int_{\Gamma_n} K^i_{rs} D_t U^*_{kj}(r-r_0,\omega)\, d\Gamma \right] \\ & - \rho\,\omega^2 \left[\int_{S^+_{cr}} \Delta u_i(r_0,\omega) n_r(r_0) U^*_{ij}(r-r_0,\omega)\, dS_\eta \right. \\ & \left. \left. + \int_{\Gamma_n} u_i n_r(r_0) U^*_{ij}(r-r_0,\omega)\, d\Gamma \right] \right\} \end{aligned} \quad (10)$$

In the above, $c_{ijkl}=\lambda^*\delta_{ij}\delta_{kl}+\mu^*(\delta_{ik}\delta_{jl}+\delta_{il}\delta_{kj})$, $K^i_{rs}=[n_r(\eta)D_s - n_s(\eta)D_r]u_i(\eta,\omega)$, $\Delta K^i_{rs}=[n_r(\eta)D_s - n_s(\eta)D_r]\Delta u_i(\eta,\omega)$, $D_r=(\partial/\partial\eta_r)$ is a spatial derivative along crack surface S_{CR}. As mentioned previously, λ^*, μ^* are the complex-valued Lame constants of the viscoelastic medium and ρ is the density. Finally, U^*_{ij}, P^*_{ij} are the same displacement and traction fundamental solutions of Eq. (2) as before.

(3) Along boundary Λ, the following BEM system of equations is satisfied with respect to the scattered wave field:

$$\begin{aligned} c_{ij}(u_j(r,\omega)-u^{fr}_j(r,\omega)) = & \int_\Lambda U^*_{ij}(r,r_0,\omega)(p_j(r,\omega)-p^{fr}_j(r,\omega))d\Gamma \\ & - \int_\Lambda P^*_{ij}(r,r_0,\omega)(u_j(r,\omega)-u^{fr}_j(r,\omega))d\Gamma \end{aligned} \quad (11)$$

Thus, the external problem outside the boundary Λ can be solved, with the size of the excitation box chosen so that the backscattered wave field along Λ^{box} is minimized.

The system of Eqs. (9)–(11), together with the boundary conditions described in Section 2.1, constitute a BVP for the unknown displacements and tractions $u_i(r,\omega)$, $p_i(r,\omega)$ on surfaces Γ_n, $n=1,2,\ldots,N$ and the crack opening displacement $\Delta u^k_i(\eta,\omega)$ on the S^+_K crack. The first step is to obtain the free-field wave solution by the WNIM. Next, numerical treatment of the remaining problem follows standard BEM procedure based on collocation of the field variables (displacements and tractions) at pre-defined nodal points. Specifically, the entire boundary is discretised into 1D line elements using a polynomial approximation for the surface geometry and the field variables. Conventional three-node quadratic boundary elements (BE) are employed on smooth surfaces, while the presence of cracks requires use of two special crack-tip boundary elements. These are the quarter point element (QP-BE) for modeling asymptotic behavior in the displacement field as $u_i \approx O(\sqrt{r})$ near the crack-tip, and the traction singular quarter-point boundary element (SQP-BE) for interface cracks to model the asymptotic behavior in the traction field as $p_i \approx O(1/\sqrt{r})$. Collocation points are defined at the mid-point and edges of a given BE with the possibility of shifting odd-numbered edge nodes. More specifically, the shifted point method is used [68] that avoids placing nodes directly on irregular locations such as crack tips and corners. Following discretization of all surfaces, the kernels of the boundary integrals exhibit singularities of the type

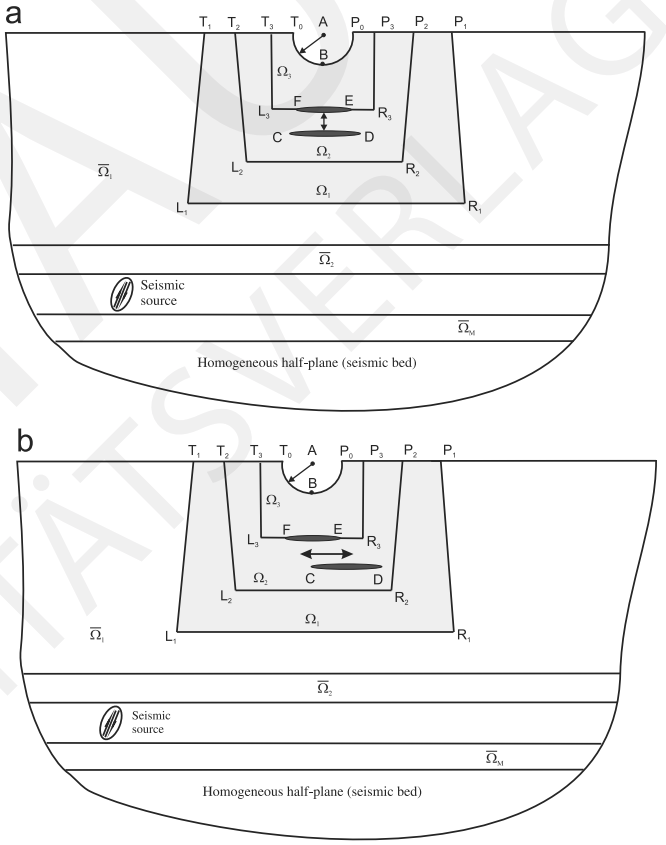

Fig. 4. Geometry of geological region used in Example 4.1 for three different crack configurations: (a) Cases 1 and 2 with depth of internal crack at 120 m and 170 m, respectively; (b) case 3 with internal crack offset to the right by 42 m.

Table 1
Properties of the layered half-space in Example 4.1.

Soil layer $\overline{\Omega}_i$	Thickness (km)	Depth to top (km)	Density ρ_i (kg/m^3)	S-wave speed β_i (m/s)	P-wave speed α_i (m/s)
1	5.0	5.0	2750	3500	6100
2	8.0	13.0	2900	3600	6200
3	4.0	17.0	3200	4100	7650
4	2.0	19.0	3200	4200	7500
5	2.0	21.0	3200	4200	7650
6	2.0	23.0	3200	4300	7800
7	5.0	28.0	3300	4350	8000
8	22.0	50.0	2900	3800	6800
Bedrock	∞	∞	3350	4600	8200

$O(1/(c\pm\xi))$, for $c\in[-1,+1]$, which lead to CPV integrals and singularities of the type $O(\ln(c\pm\xi))$, for $c\in[-1,+1]$, which lead to non-singular integrals (note that ξ is a local coordinate). The latter regular integrals are computed numerically by special log-weighted Gaussian quadrature, while the former singular ones are computed analytically, using asymptotic solutions of the Green's functions for small argument. After application of the collocation method, the BEM transforms into system of linear algebraic equations for the unknown displacement and tractions in the Fourier domain. Finally, in order to obtain displacements and tractions as functions of time, the inverse FFT is employed.

Table 2
Real and imaginary parts of the displacement vector obtained by the MS-FDM [69], the MS-BEM [69] and the WNIM-BEM in the frequency domain at receiver point (0, 30 m).

Frequency (Hz)	Method	Real part u_x	Imaginary part u_x	Real part u_z	Imaginary part u_z
0.5	MS-FDM	−0.551	+1.101	−0.483	−0.623
	MS-BEM	−0.501	+1.098	−0.476	−0.619
	WNIM-BEM	−0.533	+1.105	−0.480	−0.621
1.0	MS-FDM	−1.111	−0.963	−0.503	+1.322
	MS-BEM	−1.097	−0.958	−0.498	+1.320
	WNIM-BEM	−1.105	−0.968	−0.501	+1.318
1.5	MS-FDM	+0.607	−0.532	−0.481	−0.722
	MS-BEM	+0.598	−0.530	−0.479	−0.698
	WNIM-BEM	+0.610	−0.534	−0.480	−0.718
2.0	MS-FDM	−0.081	−0.056	−0.463	+0.462
	MS-BEM	−0.078	−0.055	−0.460	+0.459
	WNIM-BEM	−0.080	−0.057	−0.465	+0.460
3.0	MS-FDM	−0.709	+0.013	+0.253	+0.419
	MS-BEM	−0.705	+0.015	+0.251	+0.421
	WNIM-BEM	−0.711	+0.013	+0.255	+0.420

4. Numerical results

In this section, we apply the hybrid computational scheme to solve the problem outlined in Section 3 and comprising three basic parts, namely seismic source, wave path and local geological inclusion with discontinuities. The aim is to investigate the dependence of the elastic wave field that develops in the discontinuous poroelastic geological region to the material and geometric parameters of the problem, including the presence of cracks that act both as stress concentrators and as wave scatterers. In accordance to these aims, the following numerical examples are solved: (a) synthesis of seismic signals in a finite, laterally inhomogeneous poroelastic cracked geological inclusion surrounded by a horizontally layered half-plane containing a seismic source by the hybrid WNIM–BEM; (b) synthesis of seismic signals in a poroelastic, horizontally layered half-plane containing a seismic source by the WNIM; (c) SIF computation for a single crack in a poroelastic medium under incident P- or SV-waves by the BEM; (d) SIF computation for a finite rectangular block of poroelastic material with a centered crack

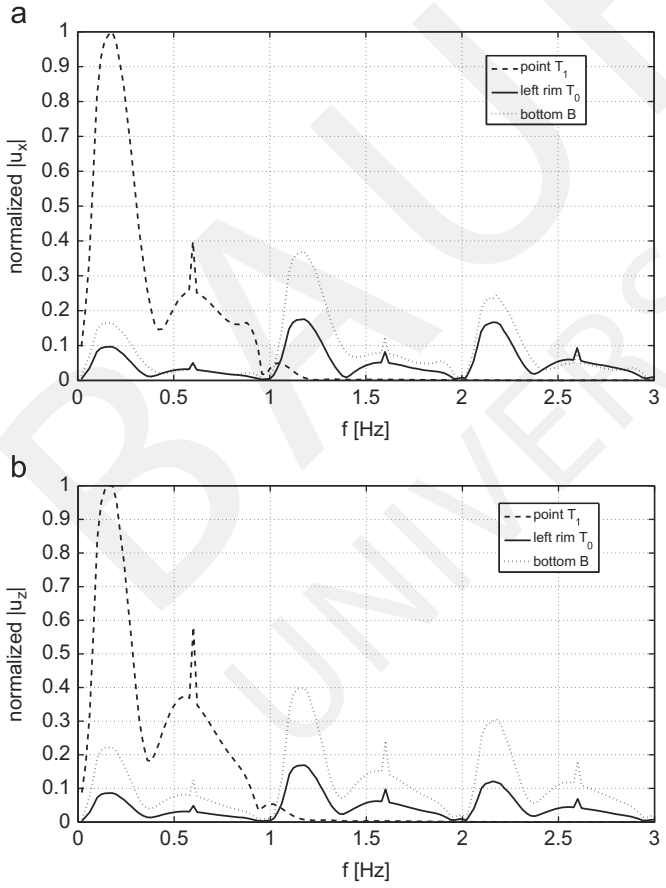

Fig. 5. Normalized (a) horizontal and (b) vertical displacement amplitude versus frequency at receiver points along the free surface and the canyon for a crack-free local geological region.

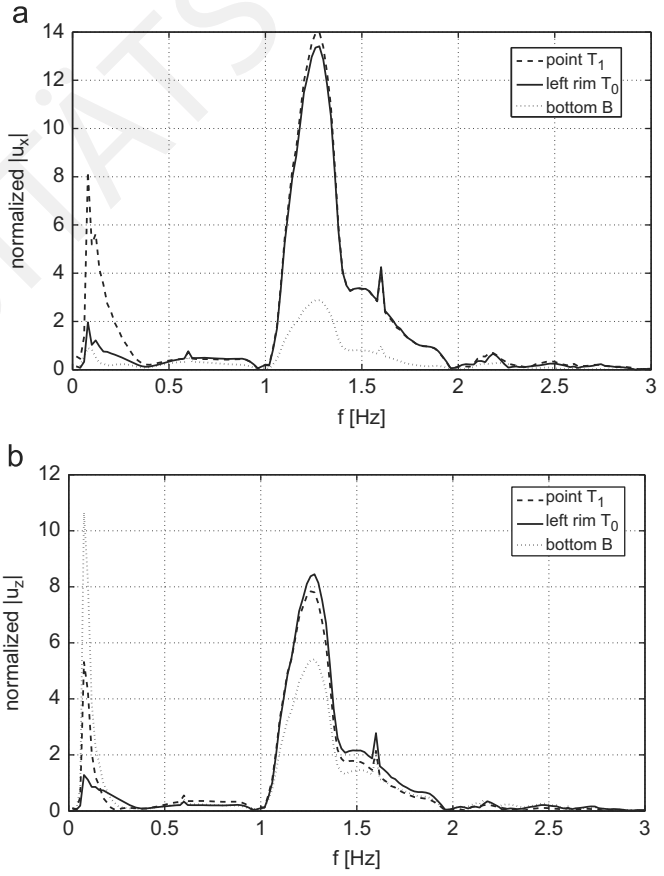

Fig. 6. Normalized (a) horizontal and (b) vertical displacement amplitude versus frequency at receiver points along the free surface and the canyon for a cracked geological region (Case 1).

subjected to time-harmonic loads by BEM; and (e) synthesis of seismic signals in a finite, laterally inhomogeneous poroelastic geological inclusion with cracks surrounded by a homogeneous half-plane under P- or SV-waves by BEM.

4.1. Finite laterally non-homogeneous cracked geological inclusion in a horizontally layered half-plane containing a seismic source

The geometry for this numerical example is shown in Fig. 4, where the local geological region Ω_{LGR} is situated in the first horizontal layer $\overline{\Omega}_1$ of the embedding half-plane. The local region itself comprises three non-parallel layers and has a free-surface relief in the form of a semi-circular canyon of radius $A=30\,m$. The coordinates of the points delineating the local region boundaries (in m) are as follows:

Upper left side is $T_0(30,0), T_3(60,0), T_2(90,0), T_1(100,0)$
Upper right side is $P_0(-30,0), P_3(-60,0), P_2(-90,0)$, $P_1(-100,0)$
Left side is $L_1(110,270), L_2(90,180), L_3(60,90)$
Right side is $R_1(-110,270), R_2(-90,180), R_3(-60,90)$.

There is also an interface crack *EF* between the second and third layers (length=75 m, depth=90 m), plus an internal crack *CD* inside the second layer (length=120 m; depth=120 m for Case 1; depth=170 m for Case 2). Finally, we have Case 3 where the internal crack is shifted to the right (offset=42 m; depth=120 m). The mechanical properties of the elastic halfspace are presented in Table 1, with the density and wave speed values in the three layers of local region Ω_{LGR} as follows:

$\rho_1=2750\ \text{kg}/m^3;\quad \alpha_1=6100\ m/s;\quad \beta_1=3500\ m/s$
$\rho_2=2485\ \text{kg}/m^3;\quad \alpha_2=4674\ m/s;\quad \beta_2=2862\ m/s$
$\rho_3=2155\ \text{kg}/m^3;\quad \alpha_3=2579\ m/s;\quad \beta_3=1579\ m/s$

Finally, a buried vertical line seismic source is located at $x=2$ km to the left of the vertical axis and at depth $y=2.0$ km from the surface of the geological deposit.

The adequacy of the BEM mesh used to solve this problem was examined in previous work [14,15], where the local region rests on a homogeneous half-plane. As previously mentioned, the mesh used for discretizing all surfaces of the aforementioned geological region utilizes standard quadratic BE, except near the crack-tips. There, both the QP-BE and the SQP-BE are, respectively, used to model the asymptotic behavior of the displacements as $\sqrt{r}$ and of the tractions as $1/\sqrt{r}$ near the crack-tip, where r is the radial in a local polar coordinate system centered at the crack-tip itself. The rule-of-thumb relations between the minimum-allowed BE length, the maximum-allowed BE length and the incident wavelength are $l_{BE}^{\min}=\lambda_{SV}/23$ and $l_{BE}^{\max}=\lambda_{SV}/10$, which serve to gage the total number of elements necessary for configuring an acceptable mesh. Typical such meshes require about 140 nodes for the layers including the free surface, 13 nodes for the internal crack and 17 nodes for the interface crack.

Furthermore, the hybrid WNIM-BEM technique was applied to the same example, but in the absence of cracks. Calibration of the mesh used followed guidelines established in recent work by the authors [48]. The size of the external region, as delineated in Fig. 1(c), is deemed to be optimal in the sense that the total elastic

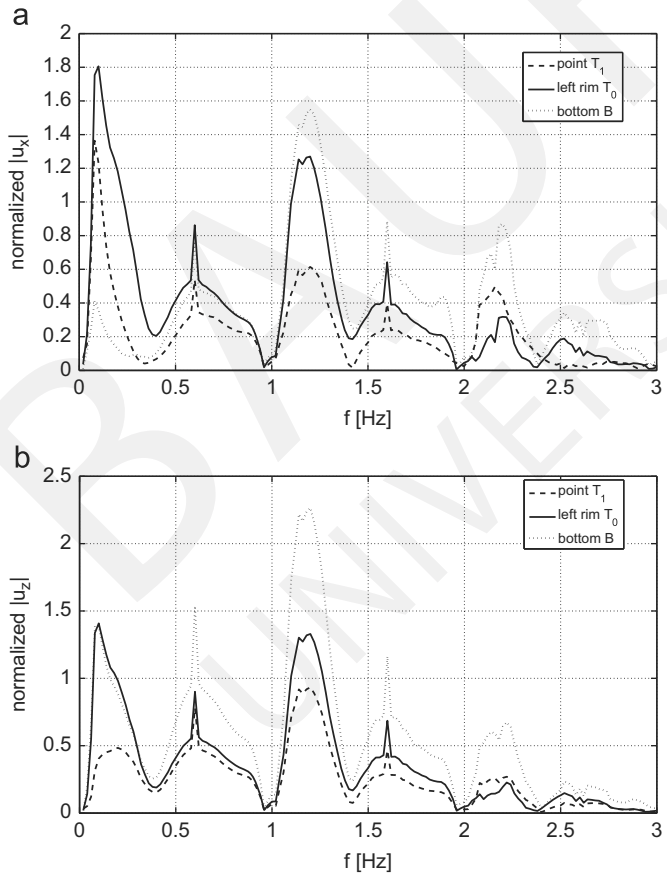

Fig. 7. Normalized (a) horizontal and (b) vertical displacement amplitude versus frequency at receiver points along the free surface and the canyon for a cracked geological region (Case 2).

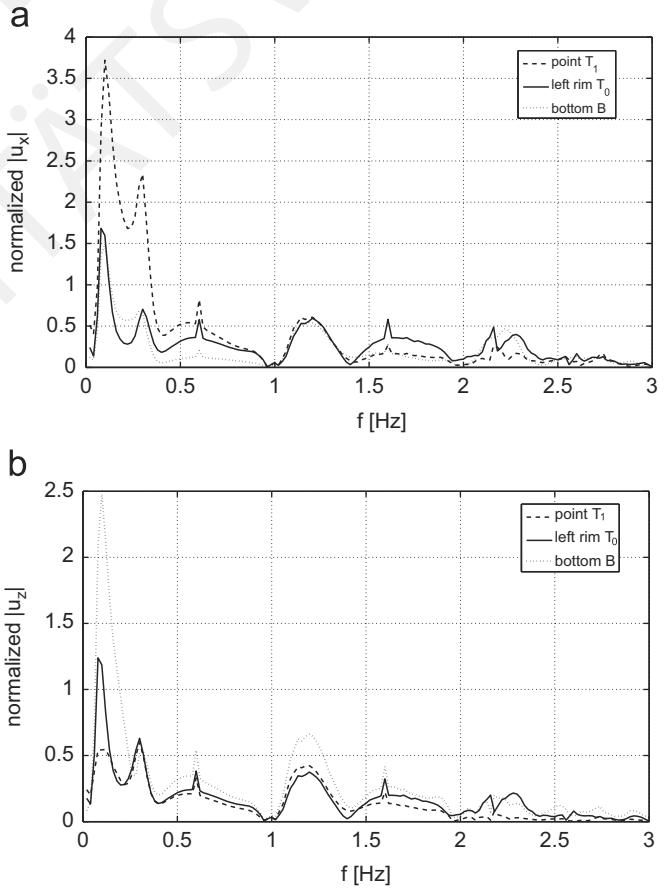

Fig. 8. Normalized (a) horizontal and (b) vertical displacement amplitude versus frequency at receiver points along the free surface and the canyon for a cracked geological region (Case 3).

wave field outside this region essentially replicates the "background" solution to within an accuracy level of 7%–9%. This implies minimal interaction between the scattered wave field and the geological structure that lies below the excitation region. In earlier work [69], the same numerical example, but without cracks, was solved using two different hybrid techniques. These were the modal summation-finite difference method (MS-FDM) and the modal summation-boundary integral equation method (MS-BIEM). More specifically, the MS and the BIEM were, respectively, used as the first and second steps comprising this particular hybrid computational technique. A detail validation study of the hybrid MS-BIEM technique is presented in Ref. [69] on the basis of a comparison with the MS-FDM. In here, we add our WNIM-BEM technique to the aforementioned comparison study and collect results in Table 2, which shows the normalized displacement components at receiver point with coordinates (0, 30 m) (i.e., the bottom of the canyon). The normalization is done by dividing through with the maximum absolute value of the specific displacement component recorded across the frequency response spectrum. In this particular test case, an instantaneous seismic source corresponding to a pure double couple is buried in the half-space at a depth of 2 km and an epicenter distance of 10 km. The dip angle is $\delta=60^\circ$, the rake angle is $\psi=90^\circ$ and the strike angle is $\Phi=30^\circ$, while the seismic moment magnitude at the source is equal to 10^{13} N-m.

Fig. 5 plots the normalized displacement amplitudes versus excitation frequency (in Hz) at three selected receiver points, namely at T_1(100,0), at the left rim of the canyon T_0 (30,0)and at the bottom B (0,30) in the absence of cracks. Amplitude normalization is with respect to the maximum values recovered for each of the two corresponding displacement components that were computed from the bedrock reference model. Next, Figs. 6–8 plot the same normalized amplitudes but for Cases 1–3, respectively, which involve the presence of geological cracks in the inclusion region Ω_{LGR}. Normalization in these figures is now made with respect to the corresponding maximum displacement amplitude of the corresponding crack-free case, i.e., Fig. 5 results. At first, we observe in the spectra of Fig. 5 that the distribution of natural frequencies for this complex geological structure is very roughly spaced in the pattern $f_n=0.25+n\cdot 0.50, n=0,1,2,\ldots$(Hz), as would be expected in a typical layered structure [70]. The most pronounced response is observed at point T_1 outside the canyon, while the response recorded at the left rim T_0 and at the bottom of the canyon is almost an order of magnitude less. As the frequency increases, the canyon response across its perimeter begins to converge, implying that the overall dimensions of the canyon start to become irrelevant at high wave numbers. Next, Figs. 6–8 clearly demonstrate the sensitivity of the synthetic seismic signals along the free surface to the presence of cracks and to their relative position on this surface. Two basic trends are observed, namely (a) the response recorded at the three control points starts to exhibit a similar pattern, with the displacement magnitudes becoming comparable, and (b) the peaks in the response show a shift towards higher frequencies. Specifically, the most critical case is when an interface and an internal crack are closely spaced directly below the canyon (Case 1), where amplification factors ranging from *8* to 14 for the horizontal and vertical magnitudes,

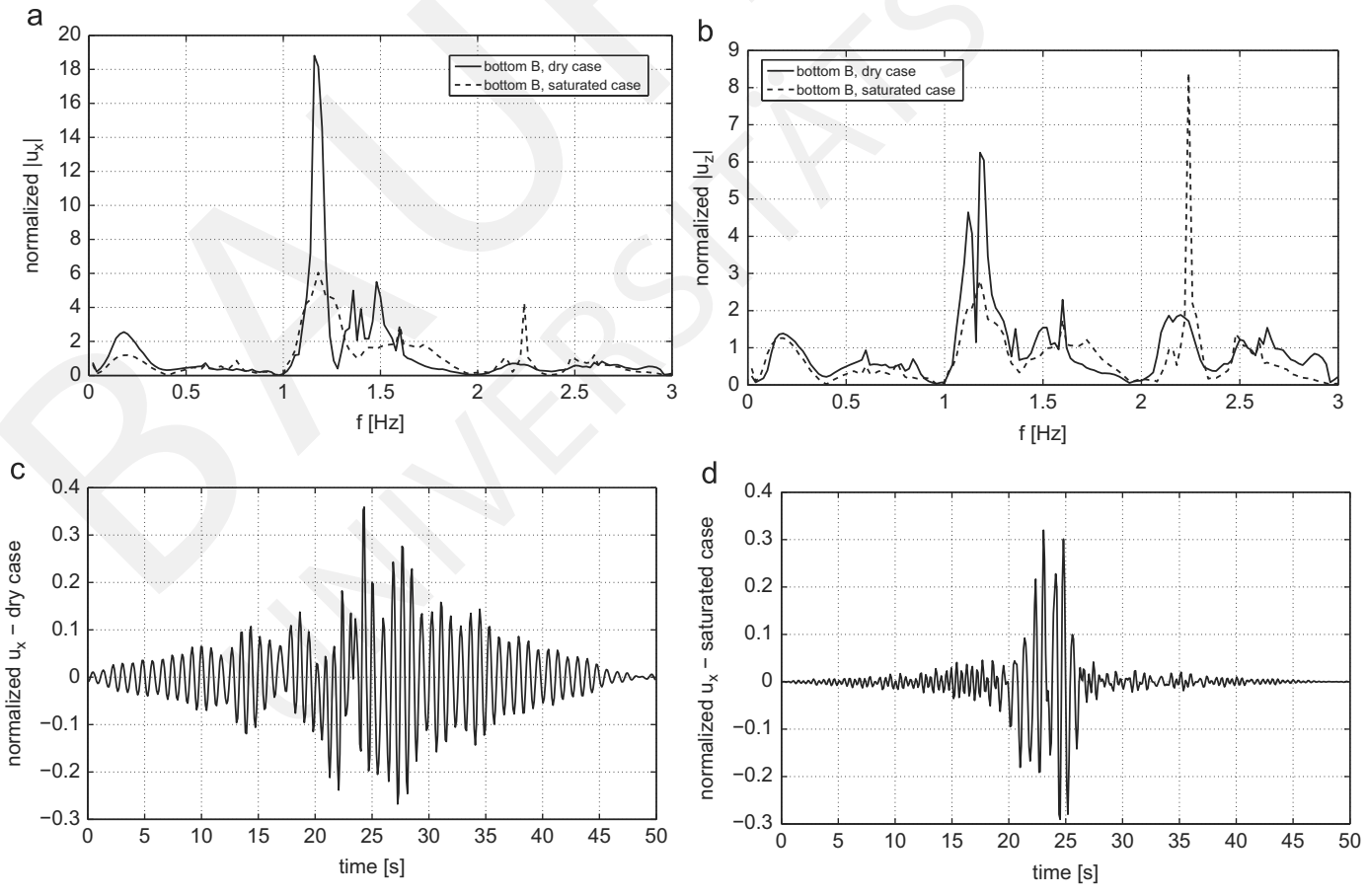

Fig. 9. Normalized displacement components at bottom of the canyon for the cracked dry and saturated local geological region of Case 1: Normalized (a) horizontal and (b) vertical displacement amplitude versus frequency. Transient time signals for the horizontal displacement component in the case of (c) dry and (d) saturated materials.

Table 3
Properties of the layered half-space in Example 4.2 with four Poisson ratio v values.

Soil layer $\overline{\Omega}_i$	Thickness (km)	Depth (km)	Density ρ_i (kg/m^3)		Porosity n_i	Poisson ratio v_{dry}	S-wave speed β_i (m/s)		P-wave speed α_i (m/s)	
			Dry	Sat.			Dry	Sat.	Dry	Sat.
1	2	1	1696	2056	0.36	0.1	358	325	538	1634
2	2	2	1722	2072	0.35	0.1	869	792	1304	1939
3	2	3	1749	2089	0.34	0.1	1168	1069	1752	2198
4	3	4	1775	2105	0.33	0.1	1398	1284	2097	2426
5	5	5	1802	2122	0.32	0.1	1590	1465	2385	2632
6	7	7	1828	2138	0.31	0.1	1756	1624	2634	2819
Bedrock	∞	∞	1855	2155	0.3	0.1	1904	1766	2856	2993
1	2	1	1696	2056	0.36	0.2	297	270	485	1621
2	2	2	1722	2072	0.35	0.2	721	657	1177	1870
3	2	3	1749	2089	0.34	0.2	968	886	1582	2087
4	3	4	1775	2105	0.33	0.2	1159	1064	1893	2280
5	5	5	1802	2122	0.32	0.2	1318	1215	2153	2456
6	7	7	1828	2138	0.31	0.2	1456	1617	2378	2546
Bedrock	∞	∞	1855	2155	0.3	0.2	1579	1864	2578	2767
1	2	1	1696	2056	0.36	0.3	233	211	436	1609
2	2	2	1722	2072	0.35	0.3	565	515	1058	1810
3	2	3	1749	2089	0.34	0.3	760	695	1421	1988
4	3	4	1775	2105	0.33	0.3	909	835	1701	2149
5	5	5	1802	2122	0.32	0.3	1034	935	1935	2297
6	7	7	1828	2138	0.31	0.3	1142	1056	2137	2433
Bedrock	∞	∞	1855	2155	0.3	0.3	1238	1149	2317	2560
1	2	1	1696	2056	0.36	0.4	158	144	389	1599
2	2	2	1722	2072	0.35	0.4	385	351	944	1757
3	2	3	1749	2089	0.34	0.4	517	473	1268	1899
4	3	4	1775	2105	0.33	0.4	619	569	1518	2030
5	5	5	1802	2122	0.32	0.4	704	649	1726	2151
6	7	7	1828	2138	0.31	0.4	778	719	1907	2263
Bedrock	∞	∞	1855	2155	0.3	0.4	844	783	2067	2369

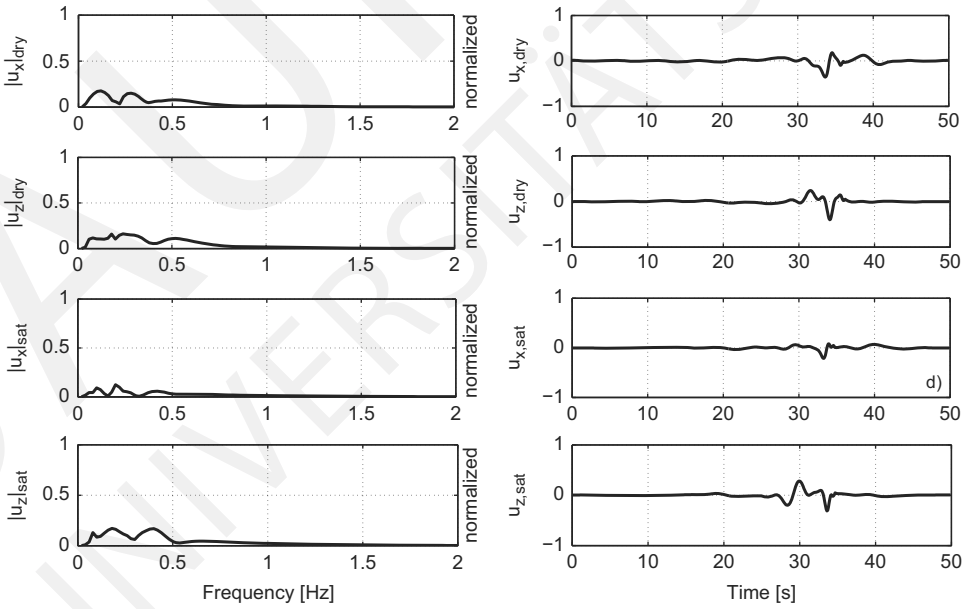

Fig. 10. Layered half-plane displacements versus frequency and time for both dry and saturated soil; Poisson ratio is $v=0.1$.

respectively, are observed at $f=1.25$ Hz. This situation ameliorates as crack spacing increases (Case 2) or as the bottom crack starts to move away from the seismic source position (Case 3).

Finally, Fig. 9 plots the frequency spectra for both displacement components and the transient seismic signals (i.e., displacements in the horizontal direction versus time) observed at the bottom of the canyon for the problem defined in Fig. 4 as before, but with the following modifications: The first layer (subscript 1) of the inclusion Ω_{LGR} stays as is, while the second and third layers (subscripts 2,3) are now poroelastic sandstones with material properties derived from Section 2.2 (also see for Figs. 2 and 3), where two porosity values are considered ($n_2=0.34$; $n_3=0.30$) and a common Poisson's ratio is retained ($v_2=v_3=0.25$). Displacement normalization in Fig. 9 is with respect to the maximum amplitude observed for these components when the geological deposit is crack-free and linear elastic in terms of its mechanical

behavior. As far as the crack configuration is concerned, we retain Case 2. When the signals that develop in the dry and saturated material are contrasted, the influence of poroelasticity in the presence of discontinuities is still clearly visible: (a) the dominant frequencies shift to higher values in the presence of poroelastic layers, i.e., a stiffening effect is observed; (b) the transient signals become damped (i.e., take longer to develop and die out faster) and their magnitude is somewhat reduced.

4.2. Horizontally layered poroelastic half-plane containing a seismic source

The layered half-plane comprises seven layers and contains a seismic source with the following characteristics:

depth $z=2$ km; *offset* $z=2$ km;

seismic moment $M_0=5.98\cdot10^{14}$ *N-m*

corner frequency $f_C=5.0$ Hz;

strike angle $\phi=151^\circ$; *dip angle* $\delta=83^\circ$; *rake angle* $\theta=7^\circ$

The porosity changes from the bottom upwards to the free-surface, in increments of $\Delta n=0.01$ starting from $n_7=0.3$. The material properties for this layered structure are given in Table 3 for four values of Poisson's ratio. The density and wave speeds for dry and saturated material are all computed using Bardet's model of Section 2.2.

Figs. 10–13 plot the seismic signals at the control point (i.e., the origin of coordinates) for both cases of a dry rock layered configuration and its corresponding saturated one, as obtained by the WNIM. All time histories and frequency spectra for the horizontal and vertical displacement components at the free surface for the saturated material are normalized with respect to their corresponding maximum (absolute) values observed in dry case.

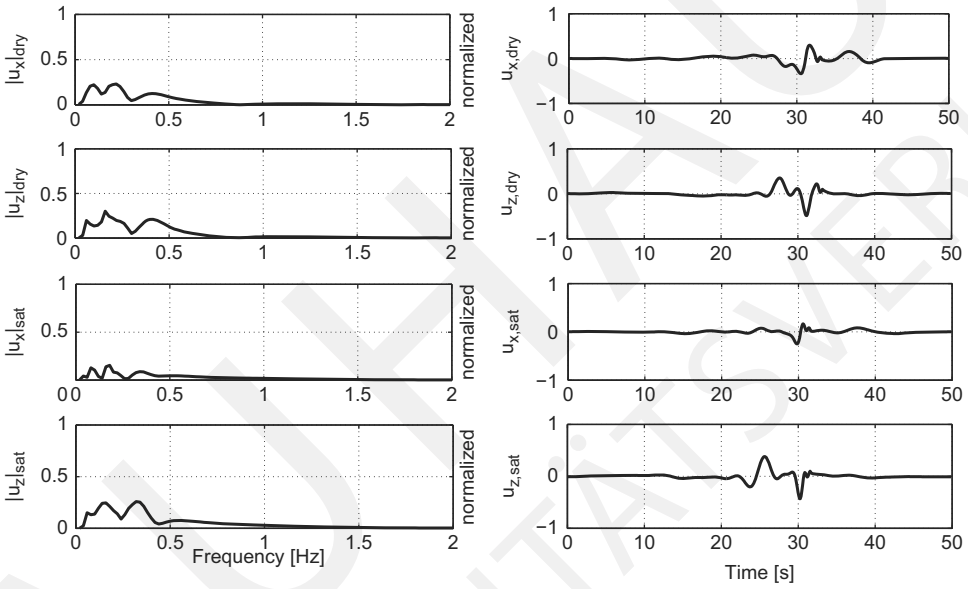

Fig. 11. Layered half-plane displacements versus frequency and time for both dry and saturated soil; Poisson ratio is $\nu=0.2$.

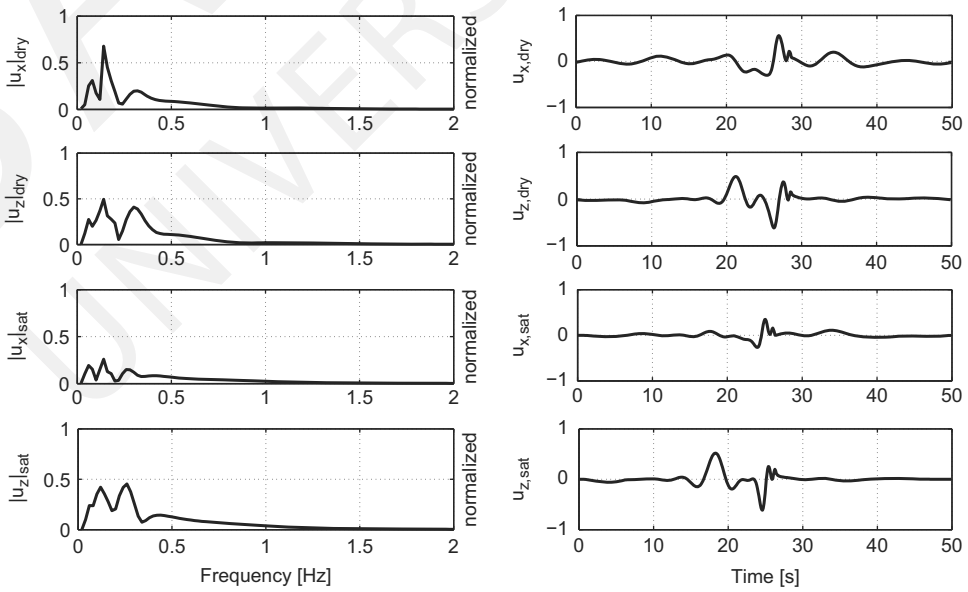

Fig. 12. Layered half-plane displacements versus frequency and time for both dry and saturated soil; Poisson ratio is $\nu=0.3$.

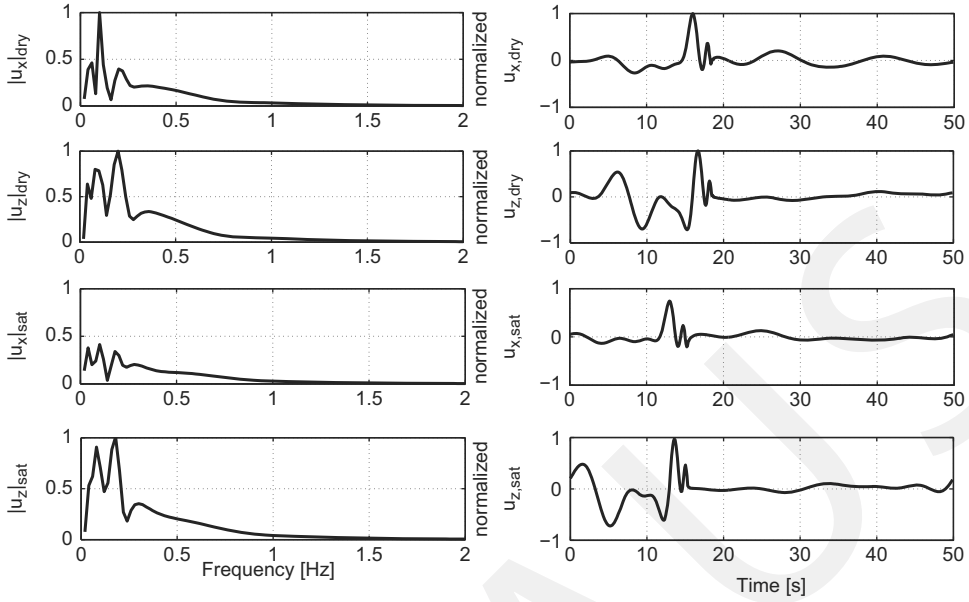

Fig. 13. Layered half-plane displacements versus frequency and time for both dry and saturated soil; Poisson ratio is $v=0.4$.

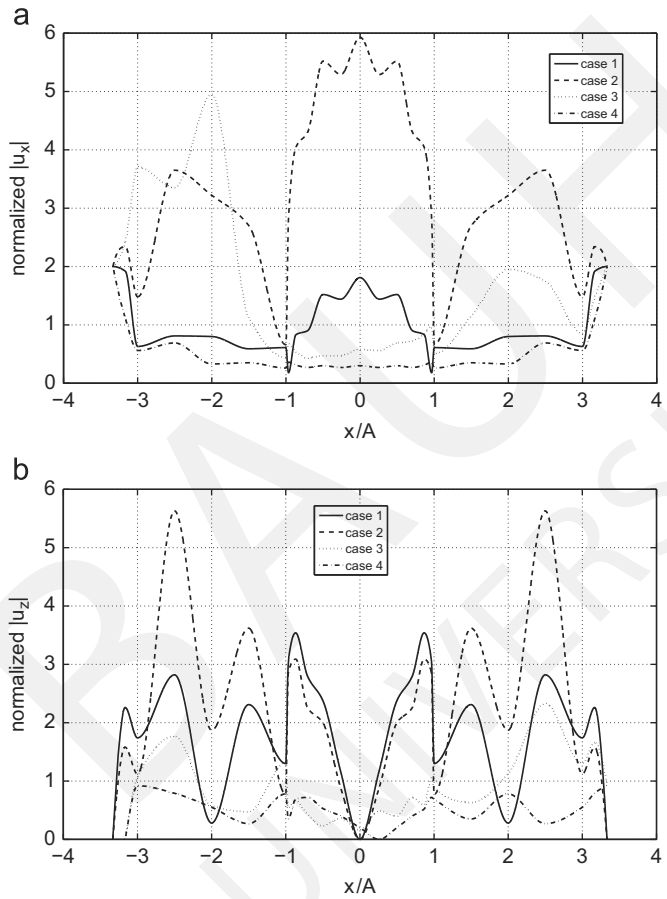

Fig. 14. Normalized (a) horizontal and (b) vertical displacement amplitudes at the free surface of the embedded geological region for SV-wave incidence at $f=5$ Hz.

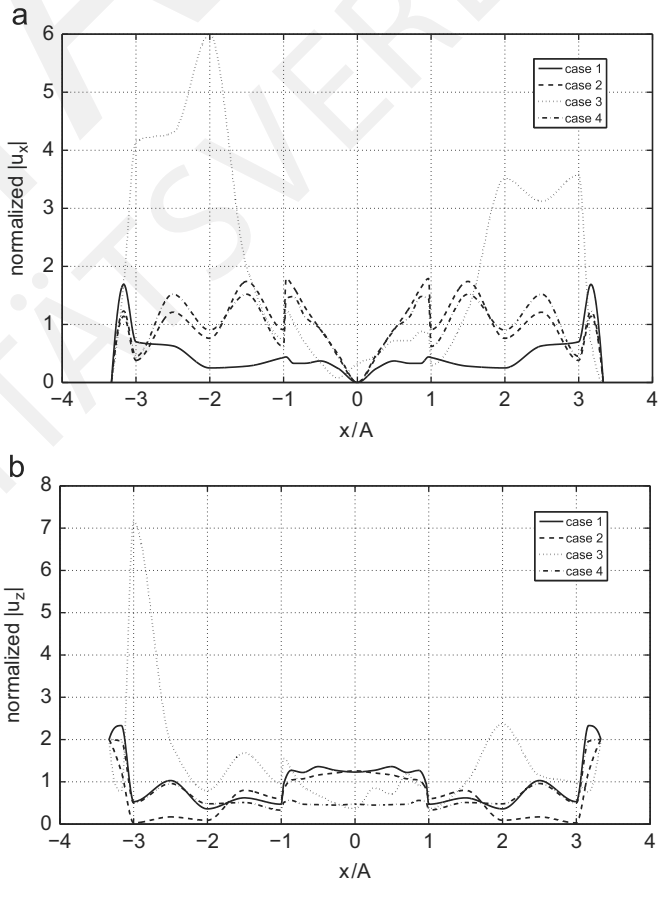

Fig. 15. Normalized (a) horizontal and (b) vertical displacement amplitudes at the free surface of the embedded geological region for P-wave incidence at $f=5$ Hz.

At first, we observe that for a Poisson ratio of $v=0.1$ in Fig. 10, the transient response is basically "flat" in all cases, i.e., very little happens until 30 s have elapsed and then a small disturbance registers. The difference between dry and saturated conditions is thus minimal: the frequency response spectra show some minor peaks around $f=0.1$ s and $f=0.3$ s for both cases. At the other extreme end of Poisson's ratio of $v=0.4$ in Fig. 13, large deviations between dry and saturated cases begin to show. In reference to the time signals, the dry case registers the arrival of P- and S-wave signals at roughly 3 and 6 s, respectively. For a source-to-receiver

distance of 2.82 km, this implies average wave speeds of about $\alpha=1000$ and $\beta=500$ m/s. When the material is saturated, these arrival times drop to 2 and 5 s, respectively, implying average wave speeds of about $\alpha=1400$ and $\beta=600$ m/s. In reference to the frequency response spectra, the dry material shows multiple peaks, but the two most pronounced ones are at around $f=0.1$ and $f=0.2$ Hz. These values still register when the material is saturated, albeit with lower spectral values that are now roughly one-half than before. In sum, the transient displacement response in the saturated case dampens out fast after 15 s have elapsed, and its magnitude prior to that time is smaller compared to dry case.

4.3. Poroelastic cracked geological inclusion in a homogeneous half-plan swept by elastic waves

For this numerical example, we use the same geological deposit as in Example 4.1 containing the laterally non-homogenous inclusion Ω_{LGR}. The incoming elastic waves emanating from the underlying homogeneous half-plane are P- and SV-waves with unit amplitude, while the material in the half-plane is sandstone with properties listed in Section 2.2. The following cases are considered: (a) Case 1 is the saturated half-plane with porosity $n=0.34$ and a surface relief in the form of a semi-circular canyon; (b) case 2 deals with the crack-free inclusion Ω_{LGR} in a dry half-plane; (c) case 3 is as the previous second case, but for a saturated half-plane with porosity $n=0.34$, and three saturated layers in Ω_{LGR} with porosities $n_1=n_2=0.34$; $n_3=0.20$, respectively, from top to bottom; (d) case 4 is as the previous third case, but with the crack pattern in Ω_{LGR} being that of Fig. 4(a).

Figs. 14 and 15 plot the displacement amplitudes at the free-surface of the embedded geological region versus x/A, (where A is the radius of the canyon) for incident SV- and P-waves, respectively. Specifically, both horizontal and vertical displacement components are depicted at a fixed frequency of 5 Hz. In the former case, Poisson's ratio is $v=0.30$ for all layers, while in the latter case, this value is $v=0.25$ for all layers. At first, both figures clearly show the effect of porosity in a crack-free environment. In particular, the peak values in this frequency spectrum decrease when the material is saturated compared to what happens when it is dry. Despite the fact that this effect is frequency-dependent, it is evident that the pore pressure induced by the elastic waves as they sweep the poroelastic deposit helps resist the induced loads and indirectly tends to stiffen the elastic skeleton. In addition, the pore fluid acts as a viscous damper. Finally, the existence of discontinuities such as cracks completely alters the aforementioned pattern to the point where it is not possible to discern any definite trends in the frequency spectra.

4.4. Single crack in poroelastic material under incident elastic waves

This numerical example considers a single line crack with a half-length a in a poroelastic material under incident P- and SV-waves. We assume a vacuum inside of the crack. The aim here is to quantify how poroelastic material properties presented by the viscoelastic Bardet model influence the dynamic stress concentration field formation in the vicinity of a crack-tip, as measured by the computed SIF of classical fracture mechanics. This particular problem is solved using the hyper-singular, traction-based BEM. Consider a crack length of $2a=10$ m along the O x-axis, spanning the interval $(-5,+5)$.

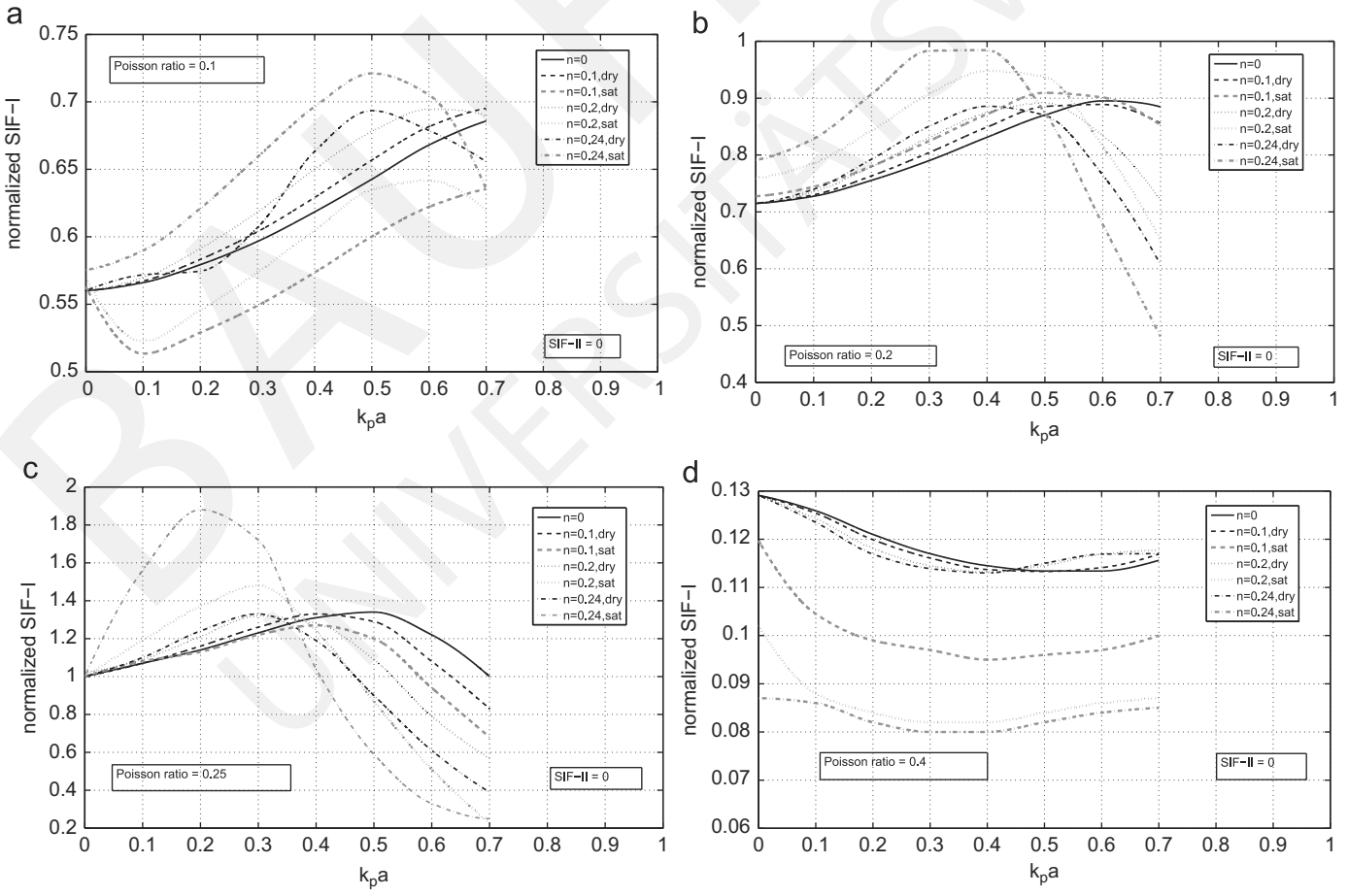

Fig. 16. Normalized *SIF-I* versus normalized frequency k_pa for a single crack in the infinite poroelastic plane under incident normal P-wave for Poisson's ratio (a) $v=0.1$; (b) $v=0.2$; (c) $v=0.25$ and (d) $v=0.4$.

The number of BE used to model the crack is seven, with the first and last ones (moving from the left and right, respectively) being QP-BE that are adequate for modeling the asymptotic behavior of displacements as $\sqrt{r}$, r being the distance to the crack-tip in a reference polar coordinate system centered at the crack-tip. Figs. 16 and 17 present a rather detailed study of the normalized SIF for mode-I and mode-II cracks versus normalized frequency ($k_P a = (\omega a/\alpha^{EL})$, $k_S a = (\omega a/\beta^{EL})$) for both the dry and the saturated material. The former figure is for a normally incident P-wave, while the latter one is for the SV-wave. Also, α^{EL}, β^{EL} are the P- and S-wave speeds for a purely elastic material at zero porosity. The plots are parametric in terms of the porosity, which ranges as $n=0.1$; 0.2; 0.24 and in terms of Poisson's ratio, which ranges as $v=0.1$; 0.2; 0.25; 0.4. The background material is sandstone with mechanical properties given in Section 2.2, following Bardet's equivalent viscoelastic model. The SIF is computed from the following fracture mechanics traction formula [71]:

$$K_{I,II} = \lim_{x \to \pm a} p_{z,x} \sqrt{2\pi(x \mp a)} \tag{12}$$

where $p_{z,x}$ is the corresponding traction at point $(x,0)$ close to the crack-tip and is subsequently normalized by its static stress value, i.e., $\sigma = \mu\,(k_S^{el})^2 \sqrt{\pi a}$, $k_S^{el} = (\omega/\beta^{el})$.

At first, we mention that the results appearing in Figs. 16(c) and 17(c) and pertaining to a Poisson's ratio of $v=0.25$ and porosity $n=0$ were validated here through comparison with the analytical solution of Chen and Sih [72] for the purely elastic case. Next, the influence of the poroelastic continuum on the dynamic stress concentration fields near the crack-tips is obvious. For an incident P-wave and low Poisson's ratios, high porosity values give lower SIF for all frequencies (and vice-versa), as compared to the purely elastic case. As Poisson's ratio is increased, this remains true up to a specific wave number, past which the trend reverses. At the highest Poisson's ratio, all poroelastic SIFs are lower compared to the purely elastic ones. In order to give a sense of measure, at a dimensionless frequency $k_P a=0.7$ in Fig. 16(c), the difference (as a percentage) in the SIF between purely elastic case and a saturated one with porosity $n=0.24$ is about 83%, while as the frequency drops to $k_P a=0.6$, this difference is almost three-fold. For incident SV-waves and the lower range of Poisson's ratio, poroelastic SIFs overshoot their corresponding purely elastic values at high porosity levels (and vice-versa), but there exists a turning frequency past which the situation reverses. At the highest Poisson's ratio value, SIFs for all cases show small relative differences, but a divergence begins past the dimensionless frequency of $k_S a=0.5$, where all poroelastic SIFs now begin to overshoot their purely elastic values.

4.5. Finite rectangular poroelastic domain with a centered crack subjected to time-harmonic load

This problem examines a rectangular domain of poroelastic sandstone with a centrally-placed geological crack of half-length a subjected to uniform time-harmonic tension $\sigma \cdot \exp(-i\omega t)$ applied on two opposite horizontal sides, as shown in Fig. 18. The amplitude of the time-harmonic load is $\sigma\,(kN/m^2)$ and ω (rad/sec) is the excitation frequency. Due to symmetry, only one-quarter of the region is considered, and the displacement-based BEM is used to solve for the SIF at the crack tip. The overall

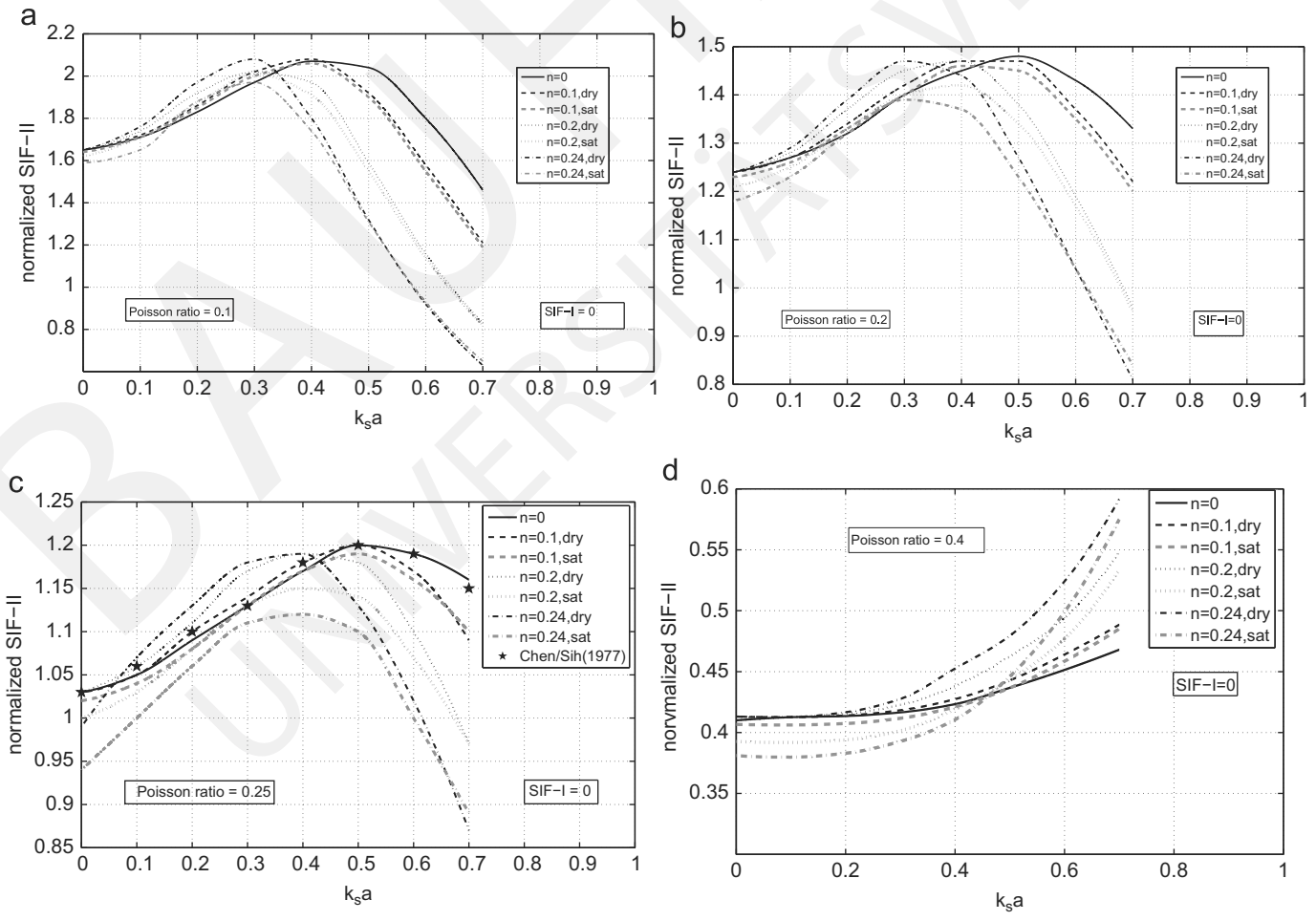

Fig. 17. Normalized *SIF-I* versus normalized frequency $k_S a$ for a single crack in the infinite poroelastic plane under an incident normal SV-wave for Poisson's ratio (a) $v=0.1$; (b) $v=0.2$; (c) $v=0.25$ and (d) $v=0.4$.

size of the poroelastic domain is 20 m × 40 m and the crack length is $2a=5(m)$. The basic BEM mesh consists of 18 quadratic BE for the geometry in Fig. 18, while a finer mesh is used near and along the crack line. In order to model the asymptotic behavior of the displacements and tractions near the crack-tip, we, respectively, use one QP-BE on the right end and one SQP-BE on the left end of the crack, with five more BE in between.

We mention here that the BEM solution for this problem, when the rectangular domain is a purely elastic material, has been validated in previous work by the authors [68], where detailed information on the size and density of BEM mesh is furnished. The aim here is to show how material poroelasticity described by the viscoelastic Bardet model influences the computed SIF values. More specifically, Fig. 19 shows how the SIF changes as a function of material porosity, and for the following range of porosity: $n=0.24; 0.30$. As before, material properties for the sandstone material derive from Section 2.2. The SIF is computed from the well-known displacement formula of fracture mechanics [71]:

$$K_I = \mu/2(1-\nu)\sqrt{2\pi/l_{QP}}(4u_z^2-u_z^1) \tag{13}$$

In the above, l_{QP} is the length of the QP-BE applied at the crack-ends, while u_z^2, u_z^1 are the displacements computed at the second and first nodes of the QP-BE, respectively. Also, SIF normalization is carried out by division with the term $\sigma\sqrt{\pi\, a}$. The basic feature observed in Fig. 19 is that the maximum SIF values, as functions of dimensionless frequency, are shifted to the left of the spectrum (i.e., to lower values) in the presence of material porosity, irrespective of the value of Poisson's ratio. Regarding the SIF magnitude, we observe that a near doubling occurs for a low Poisson's ratios and a high porosity values, i.e., for $\nu=0.10$; $n=0.30$. For the next increment in Poisson's ratio, this overshoot is about 25% for large porosity, i.e., for the combination $\nu=0.20$; $n=0.30$. Any further increase in Poisson's ratio, irrespective of porosity, yields SIF values that never exceed the purely elastic SIF value.

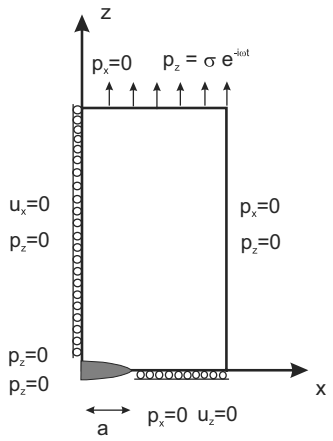

Fig. 18. Poroelastic region containing a centrally placed geological crack: the quarter-sized domain is solved due to symmetry.

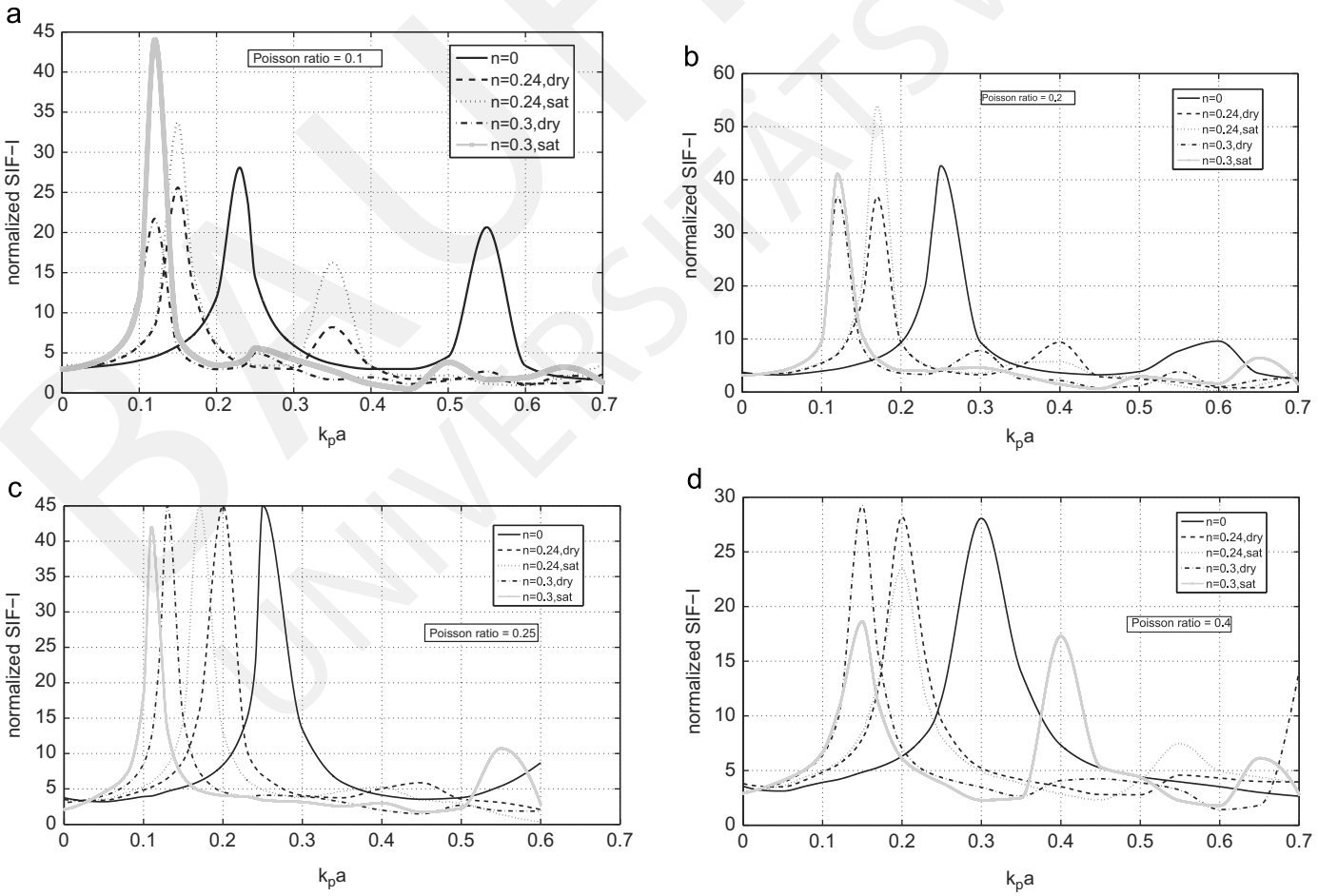

Fig. 19. Normalized SIF versus frequency for a centrally cracked poroelastic plate under uniform time-harmonic tension: (a) $\nu=0.1$; (b) $\nu=0.2$; (c) $\nu=0.3$; and (d) $\nu=0.4$.

5. Conclusions

In here, we studied in-plane elastic wave propagation in a laterally non-homogeneous, cracked geological inclusion embedded in a vertically inhomogeneous half-plane containing a buried seismic source. Furthermore, material behavior is modeled by Bardet's viscoelastic isomorphism to Biot's dynamic poroelasticity equations. The results obtained for dynamic stress concentrations near cracks are thus within the framework of linear fracture mechanics for viscoelastic materials. Insofar as Bardet's model applies to one-phase materials only, there are limitations in the evaluation of fracture states for poroelastic media, because it cannot take into account time-dependent pore pressure diffusion at the crack tip and pore pressure conditions on the crack faces.

In terms of analysis, we developed a hybrid computational technique combining the semi-analytical WNIM with the BEM. Each of the two constituent schemes is applied to that part of the numerical model where it is best suited. Specifically, the former scheme is used for the background geology to simulate wave propagation from the source to the external boundary of the geological inclusion, while the latter scheme is applied to the inclusion itself and yields synthetic seismograms along its free surface. Also, when layers in the inclusion are free of internal cracks, the displacement-based BIEM is used, while the hyper-singular, traction-based BIEM is used if such cracks are present.

The numerical simulations clearly demonstrate that wave field development in the geological inclusion is indeed complex and depends on a number of factors such as: (a) seismic source location; (b) material inhomogeneities encountered along the wave path; (c) geometry of the geological inclusion and (d) presence of free-surface relief, non-parallel layering and geological cracks. The latter feature plays a dual role in the wave propagation phenomenon; cracks scatter the incoming wave field and at the same time produce a non-uniform, local stress distribution with pronounced concentration effects. In sum, the methodology developed herein is a useful tool for future soil-structure-interaction studies of complex urban settings whose infrastructure comprises tunnels, rail lines, conduits, underground storage facilities, foundation systems, above ground structures, etc.

Acknowledgment

The first author wishes to acknowledge support provided through the MC-IEF Grant No. PIEF-GA-2010-270889. Also, the second and third authors acknowledge NATO Collaborate Linkage Grant No. CLG-984136.

References

[1] CEN Eurocode 8. Design of structures for earthquake resistance. Part 1: General rules. Brussels: Seismic Actions and Rules for Buildings. European Committee for Standardization; 2003.
[2] Chen JT, Lee JW, Wu CF, Chen IL. SH-wave diffraction by a semi-circular hill revisited: a null-field boundary integral equation method using degenerate kernels. Soil Dynamics and Earthquake Engineering 2011;31:729–36.
[3] Gatmiri B, Arson C, Nguyen KV. Seismic site effects by an optimized 2D BE/FE method I: Theory, numerical optimization and application to topographical irregularities. Soil Dynamics and Earthquake Engineering 2008;28(8): 632–45.
[4] Gatmiri B, Arson C. Seismic site effects by an optimized 2D BE/FE method II: Quantification of site effects in two-dimensional sedimentary valleys. Soil Dynamics and Earthquake Engineering 2008;28(8):646–61.
[5] Alvarez-Rubio S, Benito JJ, Sanchez-Sesma FJ, Alarcon E. The use direct boundary element method for gaining insight into complex seismic site response. Computers and Structures 2005;83:821–35.
[6] Alvarez-Rubio S, Sanchez-Sesma FJ, Benito JJ, Alarcon E. The direct boundary element method: 2D site effects assessment on laterally varying layered media (methodology). Soil Dynamics and Earthquake Engineering 2004;24: 167–80.
[7] Trifunac MD. Scattering of plane SH wave by a semi-cylindrical canyon. Earthquake Engineering and Structural Dynamics 1972;1:267–81.
[8] Todorowska MI, Lee VW. Surface motion of shallow circular alluvial valleys for incident plane SH waves-analytical solution. Soil Dynamics and Earthquake Engineering 1991;10:192–200.
[9] Liu E, Zhang Zh, Yue J, Dobson A. Boundary integral modeling of elastic wave propagation in multi-layered 2D media with irregular interfaces. Communications in Computational Physics 2008;3(1):52–62.
[10] Bouchon M, Coutant O. Calculation of synthetic seismograms in a laterally varying medium by the boundary element-discrete wavenumber method. Bulletin of the Seismological Society of America 1994;84:1869–81.
[11] Chen X. Seismograms synthesis for multi-layered media with irregular interfaces by global generalized reflection/transmission matrices method Part III:Theory of 2D P-SV case. Bulletin of the Seismological Society of America 1996;86:389–405.
[12] Rodrıguez-Castellanos A, Luzon F, Sanchez-Sesma FJ. Diffraction of seismic waves in an elastic, cracked half-plane using a boundary integral formulation. Soil Dynamics and Earthquake Engineering 2005;25:827–37.
[13] Liu E, Zhang ZJ. Numerical study of elastic wave scattering by distributed cracks or cavities using the boundary integral method. Journal of Computational Acoustics 2001;9(3):1039–54.
[14] Dineva P, Manolis GD. Scattering of seismic waves by cracks in multi-layered geological regions: I. Mechanical model. Soil Dynamics and Earthquake Engineering 2001;21:615–25.
[15] Dineva P, Manolis GD. Scattering of seismic waves by cracks in multi-layered geological regions: II. Numerical results. Soil Dynamics and Earthquake Engineering 2001;21:627–41.
[16] Liu E, Crampin S, Hudson JA. Diffraction of seismic wave by cracks with application to hydraulic fracturing. Geophysics 1997;62:253–65.
[17] Achenbach JD, Lin W, Keer LM. Surface waves due to scattering by a near-surface parallel crack. IEEE Transactions of Sonics and Ultrasonics 1983;SU-30:270–5.
[18] Hal L, Lee VW, Liang J. Anti-plane (SH) waves diffraction by an underground semi-circular cavity: analytical solution. Earthquake Engineering and Engineering Vibration 2010;9:385–96.
[19] Wang G, Liu D. Scattering of SH-wave by multiple circular cavities in half space. Earthquake Engineering and Engineering Vibration 2002;1(1):36–44.
[20] Lee VW, Manoogian ME. Surface motion above an arbitrary shape underground cavity for incident SH waves. Journal of European Earthquake Engineering 1995;7(1):3–11.
[21] Lee VW, Sherif RI. Diffraction around circular canyon in elastic wedge space by plane SH waves. Journal of Engineering Mechanics ASCE 1996;122(6): 539–44.
[22] YH Pao, CC Mow, Diffraction of elastic waves and dynamics stress concentrations; New York, 1971.
[23] Lee VW, Hao L, Liang J. Diffraction of anti-plane SH waves by a semi-circular cylindrical hill with an inside concentric semi-circular tunnel. Earthquake Engineering and Engineering Vibration 2004;3(2):249–62.
[24] Liang JW, Luo H, Lee VW. Scattering of plane SH waves by a circular-arc hill with a circular tunnel. Acta Seismological Sinica 2004;17(5):549–63.
[25] Manoogian ME. Scattering and diffraction of SH waves above an arbitrarily shaped tunnel. ISET Journal of Earthquake Technology 2000;1-3:11–26.
[26] Lee VW, Chen S, Hsu IR. Anti-plane diffraction from canyon above subsurface unlined tunnel. Journal of Engineering Mechanics ASCE 1999;125(6):668–75.
[27] Lee VW, Trifunac MD. Response of tunnels to incident SH waves. Journal of the Engineering Mechanics Division ASCE 1970;105:643–59.
[28] Babich VM. Ray method for the computation of the intensity of wavefronts. Moscow: Nauka; 1956.
[29] Pao YH, Gajewski RG. The generalized ray theory and transient response of layered elastic solids. In: Thurston RN, Mason WP, editors. Physical Acoustics. New York: Academic Press; 1977. p. 183–265.
[30] Luco JE, Apsel RJ. On the Greens functions for layered half-space: Part I. Bulletin of the Seismological Society of America 1983;73:909–29.
[31] Apsel RJ, Luco JE. On the Greens functions for layered half-space: Part II. Bulletin of the Seismological Society of America 1983;73:931–51.
[32] Wuttke F Advanced site investigation by use of surface waves. PhD thesis. Bauhaus University, Weimar; 2005.
[33] Fah D A hybrid technique for the estimation of strong ground motion in sedimentary basins. PhD thesis. ETH no. 9767, Swiss Federal Institute of Technology, Zurich; 1992.
[34] Manolis GD, Beskos DE. Boundary element methods in elastodynamics. London: Allen and Unwin; 1987.
[35] Dominguez J. Boundary elements in dynamics. Amsterdam: Elsevier; 1993.
[36] Panza GF, Paskaleva I, Dineva P, Mura C. Earthquake site effects modeling by hybrid MS-BIEM: the case study of Sofia, Bulgaria. Rendiconti di Scienze Fisiche, Accademia dei Lincei 2009;20(2):91–116.
[37] Gil-Zepeda SA, Montalvo-Arrieta JC, Vai R, Sanchez-Sesma FJ. A hybrid indirect boundary element-discrete wave number method applied to simulate the seismic response of stratified alluvial valleys. Soil Dynamics and Earthquake Engineering 2003;23:77–86.
[38] Zhang B, Papageorgiou AS, Tassoulas JL. A hybrid numerical technique, combining the finite element and boundary element methods for modeling the 3D response of 2D scatterers. Bulletin of the Seismological Society of America 1998;88:1036–50.

[39] Yokoi T, Sanchez-Sesma FJ. A hybrid calculation technique of the indirect boundary element method and the analytical solution for three dimensional problems of topography. Geophysical Journal International 1998;133: 121–39.
[40] Moczo P, Bystricky E, Kristek J, Carcione M, Bouchon M. Hybrid modeling of P-SV seismic motion at inhomogeneous viscoelastic topographic structures. Bulletin of the Seismological Society of America 1997;87(5):1305–23.
[41] Cruse TA, Two-dimensional BIE. Fracture mechanics analysis. Applied Mathematical Modelling 1978;2:287–93.
[42] Lachat JC, Watson JO. Effective numerical treatment of boundary integral equation. International Journal for Numerical Methods in Engineering 1976; 10:991–1005.
[43] Crouch SL. Solution of plane elasticity problems by the displacement discontinuity method. International Journal for Numerical Methods in Engineering 1976;10:301–43.
[44] Zhang C, Gross D. On wave propagation in elastic solids with cracks. Southampton: Computational Mechanics Publication; 1998.
[45] Portela A, Aliabadi MH, Rooke DP. Dual boundary element method: efficient implementation for cracked problems. International Journal for Numerical Methods in Engineering 1992;33:1269–87.
[46] Aliabadi MH. A new generation of boundary element methods in fracture mechanics. International Journal of Fracture 1997;86:91–125.
[47] Chen WH, Chen TC. Efficient dual boundary element technique for two-dimensional fracture problem with multiple cracks. International Journal for Numerical Methods in Engineering 1995;38:1739–56.
[48] Wuttke F, Dineva P, Schanz T. Seismic wave propagation in laterally inhomogeneous geological region via a new hybrid approach. Journal of Sound and Vibration 2011;330:664–84.
[49] Biot M. Theory of propagation of elastic waves in a fluid-saturated porous solid. Journal of Acoustical Society of America 1956;28(4):168–91.
[50] Manolis GD, Beskos DE. Integral formulation and fundamental solutions of dynamic poroelasticity and thermoelasticity. Acta Mecanica 1989;76: 89–104.
[51] Cheng AHD, Badmus T, Beskos DE. Integral equation for dynamic poroelasticity in frequency domain with BEM solution. Journal of Engineering Mechanics ASCE 1991;117:1136–57.
[52] Burridge R, Vargas CA. The fundamental solution in dynamic poroelasticity. Geophysical Journal of the Royal Astronomical Society 1979;58:61–90.
[53] Norris AN. Radiation from a point source and scattering theory in a fluid-saturated porous solid. Journal of the Acoustical Society of America 1985;77:2012–23.
[54] Schanz M, Diebels S. A comparative study of Biot's theory and the linear theory of porous media for wave propagation problems. Acta Mechanica 2003;161:213–35.
[55] Schanz M. Poroelastodynamics: linear models, analytical solutions and numerical methods. Applied Mechanics Reviews 2009;62(3) 030803-1-030803-15.
[56] Bardet JP. A viscoelastic model for the dynamic behaviour of saturated poroelastic soils. Journal of Applied Mechanics 1992;59:128–35.
[57] Bardet JP. The damping of saturated poroelastic soils during steady-state vibrations. Applied Mathematics and Computation 1995;67:3–31.
[58] Morochnik V, Bardet JP. Viscoelastic approximation of poroelastic media for wave scattering problems. Soil Dynamics and Earthquake Engineering 1996;15:337–46.
[59] Dineva P, Datcheva M, Manolis GD, Schanz T. Seismic wave propagation in laterally inhomogeneous porous media by BIEM. International Journal for Numerical and Analytical Methods in Geomechanics 2012;36:111–27.
[60] Christensen RM. Theory of viscoelasticity. New York: Academic Press; 1971.
[61] Schanz M. Wave propagation in viscoelastic and poroelastic continua: a boundary element approach. In: Pfeiffer F, editor. Lecture Notes in Applied Mechanics, Vol. 2. Berlin: Springer; 2001 Series.
[62] Manolis GD, Beskos DE. Dynamic stress concentration studies by boundary integrals and Laplace transform. International Journal for Numerical Methods in Engineering 1981;17:573–99.
[63] Kobayashi S. Elastodynamics. In: Beskos DE, editor. BEM in Mechanics; 1987. p. 191–255.
[64] Abascal R, Dominguez J. Vibrations of footings on zoned viscoelastic soils. Journal of Engineering Mechanics ASCE 1986;112:433–47.
[65] Beskos DE, Dasgupta B, Vardoulakis IG. Vibration isolation using open or filled trenches. Part 1: 2D homogeneous soil. Computational Mechanics 1986;1:43–63.
[66] Lin CH, Lee VW, Trifunc MD. The reflection of plane waves in a poroelastic half-space saturated with inviscid fluid. Soil Dynamics and Earthquake Engineering 2005;25:205–23.
[67] Sladek V, Sladek J. Transient elastodynamic three-dimensional problems in cracked bodies. Applied Mathematical Modelling 1984;8:2–10.
[68] Rangelov T, Dineva P, Gross D. A hypersingular traction boundary integral equation method for stress intensity factor computation in a finite cracked body. Engineering Analysis with Boundary Elements 2003;27(1):9–21.
[69] Dineva P, Vaccari F, Panza G. Hybrid modal summation-BIE method for site effect estimation of a seismic region in a laterally varying media. Journal of Theoretical and Applied Mechanics 2003;33(4):55–88.
[70] Kausel E. Fundamental solutions in elastodynamics: a compendium. Cambridge: Cambridge University Press; 2006.
[71] Aliabadi MH, Rooke DP. Numerical fracture mechanics. Southampton: Computational Mechanics Publication; 1991.
[72] Chen EP, Sih GC. Scattering waves about stationary and moving cracks. In: Sih GC, editor. Mechanics of Fracture: Elastodynamic Crack Problems. Leyden: Noordhoff; 1977. p. 119–212.

Journal of Theoretical and Applied Mechanics, Sofia, 2012, vol. 42, No. 3, pp. 75–100

COMBINED FIELDS

ELASTIC WAVEFIELD EVALUATION IN DISCONTINUOUS POROELASTIC MEDIA BY BEM: SH-WAVES*

Petia S. Dineva
Institute of Mechanics, Bulgarian Academy of Sciences, Acad. G. Bonchev St., Bl. 4, 1113 Sofia, Bulgaria,
e-mail: petia@imbm.bas.bg

Frank Wuttke
Chair of Geomechanical Modeling, Bauhaus University 99421 Weimar, Germany,
e-mail: frank-wuttke@uni-weimar.de

George D. Manolis
Department of Civil Engineering, Aristotle University, 54124 Thessaloniki, Greece,
e-mail: gdm@civil.auth.gr

[Received 21 April 2012. Accepted 14 May 2012]

Abstract. This work examines the anti-plane strain elastodynamic problem for poroelastic geological media containing discontinuities in the form of cavities and cracks. More specifically, we solve for: (*i*) a mode III crack; (*ii*) a circular cylindrical cavity, both embedded in an infinite poroelastic plane; and (*iii*) a mode III crack in a finite-sized poroelastic block. The source of excitation in all cases are time-harmonic, horizontally polarized shear (SH) waves. These three cases depict a situation whereby propagating elastic waves are diffracted and scattered by the presence of discontinuities in poroelastic soil, and this necessitates the computation of stress concentration factors (SCF) and stress intensity factors (SIF). Thus, the sensitivity of the aforementioned factors to variations in the material parameters of the surrounding poroelastic continuum must be investigated. Bardet's model is introduced by assuming saturated soils as the computationally efficient viscoelastic isomorphism

*The first author (PSD) wishes to acknowledge financial support provided through the MC-IEF Grant No. PIEF-GA-2010-270889. Also, the other two authors (FW, GDM) acknowledge the NATO Collaborate Linkage Grant No. CLG-984136.

Corresponding author e-mail: petia@imbm.bas.bg

to Biot's equations of dynamic poroelasticity, and stress fields are then evaluated for an equivalent one-phase viscoelastic medium. The computational tool employed is an efficient boundary element method (BEM) defined in terms of the non-hypersingular, traction-based formulation. Finally, the results obtained herein demonstrate a marked dependence of the SIF and the SCF on the mechanical properties of the poroelastic continuum, while the advantages of the proposed method as compared to alternative analytical and/or numerical approaches are also discussed.
KEY WORDS: SH-waves, cavities, cracks, poroelasticity, Bardet's model, anti-plane strain, stress concentration factor, stress intensity factor, boundary element method.

1. Introduction

Elastic wave propagation phenomena in geological media involve a number of important factors such as material inhomogeneity, the presence of a second liquid phase in the soil, the presence of discontinuities, the existence of buried seismic sources, and finally the presence of a free-surface relief within layered soil deposits. Various numerical simulations and measurements have clearly demonstrated the influence of all the above factors on the resulting scattered wave field, and identified the generation of localized stress concentration phenomena [1]. In here, we examine time harmonic, anti-plane strain wave motion in poroelastic geological media with discontinuities in the form of cylindrical cavities and mode III cracks. The purpose is to quantify the influence of soil poroelasticity on the SCF that develops at the cavity perimeter and of the SIF at the crack tips. The soil is approximated as a single-phase material with mechanical properties computed on the basis of the viscoelastic-poroelastic similarity.

Dynamic stress concentrations around discontinuities comprise an important class of problems in solid mechanics [2]. Diffraction of seismic waves around buried cavities and geological cracks has also been a research topic of interest to earthquake engineering [3]. Elastostatic analysis of these problems, as given in the classical treatises of Neuber [4], Muskhelishvili [5], Savin [6] and Timoshenko and Goodier [7] is valid only when mass inertia effects are unimportant. In recent years, research activity on dynamic stress concentration has greatly accelerated, resulting in a plethora of papers starting with the works of Pao and Mow [2], Achenbach [8], Miklowitz [9] and Zhang and Gross [10] among others. Various specialized computational methods were also developed and are classified here as follows: (a) quasi-analytical methods such as the wave function expansion [2], the matched asymptotic expansion [11], and the complex function method [12–14]; (b) numerical methods such as var-

ious boundary element techniques, see Refs. [15–20]. The benchmark problem of an embedded cavity in the infinite space engulfed by body waves has been solved by Pao and Mow [2], Datta and Shah [11] and Kobayashi and Nishimura [15] among others. Another such benchmark, namely the cavity and/or tunnel buried in a half-space has been studied by various researchers, see Refs. [15, 17, 21]; the case of multiple circular holes can be found in Providakis et al. [19]. Finally, a comprehensive study of dynamic fracture in elastic isotropic homogeneous media containing cracks can be found in Zhang and Gross [10].

The problems of computing stress concentration effects becomes much more difficult when discontinuities occur in two-phase media such as water-saturated soils. As a consequence, relatively few results have been obtained, such as those of Kattis et al. [22] and Wang et al. [23], who studied diffraction of elastic waves around cavities in a poroelastic medium, and of Liang et al. [24–26] who presented results for a cavity in a poroelastic half-space under incident pressure and shear waves based on Biot's [27] theory. The behaviour of cracked poroelastic media is recognized as an area of high interest in geomechanics although somewhat ignored from a research viewpoint and in applications such as energy recovery from geological formations, see Refs. [28–30].

In a series of papers, Bardet [31, 32] demonstrated the applicability of the viscoelastic behaviour equivalent to Biot's [27] model of dynamic poroelasticity (i.e., viscoelastic isomorphism) in the development of computational techniques for a well defined range of material parameters and in the low frequency response range. More specifically, viscoelastic isomorphism was used by Morochnik and Bardet [33] in the solution of wave scattering problems involving pressure waves by a spherical poroelastic inhomogeneity, and results obtained by both Biot and Bardet models were nearly identical in regions away from the immediate vicinity of the inhomogeneity. More recently, a series of solutions conducted by the authors [34] using the Bardet model show nearly identical results with those obtained by the Biot's model for some benchmark type of boundary-value problems (BVP).

In the following, the advantages and disadvantages of viscoelastic isomorphism of Bardet are briefly discussed, since this is the preferred constitutive law for a boundary element method (BEM) treatment of elastic wave propagation problems.

(1) The main advantages of viscoelastic isomorphism is a mechanical simplicity (a one-phase instead of two-phase material) and a mathematical simplicity in terms of the resulting wave equation and its fundamental solution. These allow for approximate solutions of complex BVP on seismic wave

propagation in fluid-saturated strata.

(2) The limitations of the Bardet model are (a) it is valid in the low frequency range, which however is typical for seismic waves, (b) it cannot account for the second (slow) longitudinal wave that dampens out very fast; (c) it is not possible to account for boundary conditions involving pore fluid pressure; and (d) the consolidation process due to fluid-skeleton interaction is expressed by a time-dependent deformation process that cannot be modelled by viscoelasticity. More specifically, fracture in poroelastic media is governed by a time-dependent pore pressure diffusion at the crack-tips, coupled with a corresponding time-dependent deformation of the soil skeleton. This process yields a SIF that depends on the pore pressure boundary conditions along the crack faces.

We conclude adding up these limitations, that modelling fracture behaviour of poroelastic media with viscoelastic isomorphism hinges on the use of the equivalent material parameters, which capture the basic characteristics of the problem but cannot account for time-dependent interaction between solid and fluid.

The basic BEM formulation using the linear elastic, anisotropic constitutive law has been presented in recent publications by the authors [35, 36] for anti-plane and in-plane strain problems. The novelty here is an extension of this BEM formulation to water-saturated soil media described by Bardet's viscoelastic isomorphism model. Briefly, the paper is structured as follows: Section 2 defines the BVP for elastic waves propagating under anti-plane strain conditions in a poroelastic region containing discontinuities in the form of cracks and cavities. Next, the computational BEM model is discussed in Section 3, while Section 4 presents validation examples plus numerical results from a series of parametric studies. Finally, the paper ends with interpretation of the obtained results and a list of conclusions and a blueprint for future work in this area .

2. Problem formulation

2.1 Governing equation of motion and boundary conditions

In general, a mechanical model appropriate for soil-structure-interaction (SSI) phenomena comprises a finite local geological inclusion with discontinuities, embedded in a stack of soil layers, which in turn rests on the homogeneous half-space [37]. In here, however, we examine a series of sub-problems which comprise the general case, so as to separately examine the influence of discontinuities on SH-waves propagating through a poroelastic continuum. In the

Cartesian coordinate system $Oxyz$ we consider a finite geological region with external boundary S swept by time harmonic SH-waves with a frequency ω (rad/sec), as shown in Fig. 1. The material is homogeneous, isotropic and water saturated with its mechanical properties described by Bardet's [31] model, which represents poroelasticity as a single-phase, Kelvin-Voigt viscoelastic material, as discussed in the next section. The material now possesses complex-valued Lame constants λ^*, μ^* and ρ is the (real) density based on the correspondence principle of viscoelasticity [38].

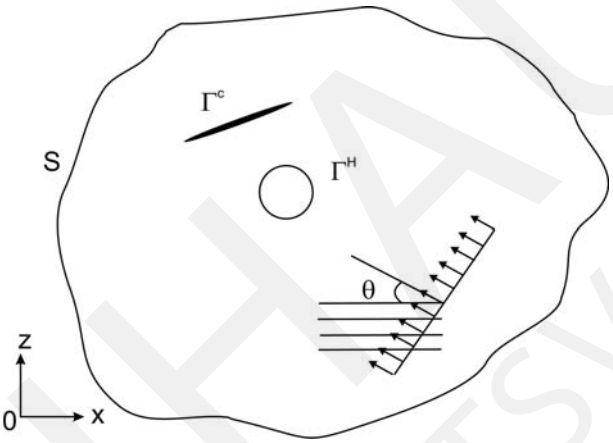

Fig. 1. Finite geological region with boundary$S$ containing discontinuities, such as a mode III crack with boundary Γ^c and a cylindrical cavity with boundary Γ^H, under incident SH waves

Frequency domain viscoelastic BEM for solving dynamic problems was used by Manolis and Beskos [39] in connection with the differential operator form of the constitutive equations, by Kobayashi [40] in connection with the integral form of the constitutive equations, and by Abascal and Dominguez [41] and Beskos et al. [42] in connection with the simple hysteretic damping model.

Non-zero field quantities for the anti-plane case with respect to the plane $y = 0$ are a displacement component $u_y(x, z)$ and two shear stress components $\sigma_{yx}(x, z)$, $\sigma_{yz}(x, z)$. The corresponding traction is defined as $p_y = \sigma_{yx} n_x + \sigma_{yz} n_z$, where (n_x, n_z) is the outward pointing normal vector at all surfaces, namely the external boundary of the finite domain, the crack line and the cavity perimeter. The common multiplier $\exp(i\omega t)$ is suppressed through-out the analysis since time-harmonic response is assumed. As a consequence, the governing equation of motion in the frequency domain simplifies

to:

$$\sigma_{iy,i} + \mu^* k_{SH}^2 u_y = 0, \quad i = x, z \tag{2.1}$$

In the above, $k_{SH} = \dfrac{\omega}{c_{SH}}$ is the SH wave number with phase velocity c_{SH}, subscript commas denote spatial derivatives, vector quantities are denoted through the use of indices $(i, j = x, z)$ and the summation convention over repeated indices is implied.

The boundary conditions prescribed along the outer surface S is either a displacement $u_y(\mathbf{x}) = \bar{u}_y(\mathbf{x})$ for $\mathbf{x} \in S_U$ or a traction $p_y(\mathbf{x}) = \bar{p}_y(\mathbf{x})$ for $\mathbf{x} \in S_P$, where $S = S_U \cup S_P$ and $S_U \cap S_P = \emptyset$. The region may contain cracks and/or cavities (holes), in which case traction-free conditions are satisfied along the crack lines $\Gamma^c = \Gamma^{+c} \cup \Gamma^{-c}$ and hole perimeter Γ^H. Sommerfeld's radiation condition must also be satisfied if an infinite region is under consideration to preclude waves moving into the core region from infinity.

2.2. Bardet's viscoelastic isomorphism

In poroelasticity, we define a representative volume V for the solid-fluid continuum, which comprises an elastic, isotropic solid skeleton (matrix) with porosity $n = V_P/V$, where V_P is the pore volume. This volume may be filled with a fluid (water) or may be empty (vacuum). We consider here fully saturated soil, which is a two-phase material since all pores are filled with fluid. Unsaturated soils are three-phased materials since air is also present in the pores, but this is beyond the scope of this work. The "dry rock" approximation is the case of an air-filled solid skeleton, while the "solid grain" characteristics are the properties of the skeleton material. The following terminology is now used for the components of the two-phase system: (a) dry rock (or soil), (b) solid grain and (c) fluid. The elastic bulk modulus and density respectively are K_{dry}, $\rho_{dry} = (1-n)\rho_g$; K_g, ρ_g; K_f, ρ_f, while the solid-fluid system density is $\rho_{sat} = \rho_{dry} + n\rho_f = (1-n)\rho_g + n\rho_f$. Next, the shear strength of the porous material is provided by the solid skeleton and is not affected by the fluid, since fluids sustain dilatational deformations only. Thus, both dry and saturated soils are described by the same shear modulus, namely $\mu = \mu_{dry} = \mu_{sat} = \dfrac{3(1-2\nu)}{2(1+\nu)} K_{dry}$, and ν is Poisson's ratio for the dry skeleton.

The equation governing time-harmonic wave propagation in fluid-saturated soils considered as two-phase materials was derived by Biot [27]. A characteristic equation for the wave numbers can be obtained [31, 43] by substituting the plane wave expansions for the displacements into Biot's wave

equation without body forces. Three solutions to Biot's wave equation have been identified, corresponding to (a) a shear wave S transmitted through the solid skeleton, (b) a fast dilatational wave P1 and (c) a slow dilatational wave P2. The corresponding wave velocities are complex and frequency dependent, hence they correspond to dissipative and dispersive waves. Finally, the solid and fluid dilatations are in phase for the first arriving P1 wave, and in reverse phase for the slower P2 wave, which damps out quickly. As mentioned previously, Bardet [31] proposed a single-phase viscoelastic material representation for saturated soils. At first, the viscoelstic Lame constants are complex-valued with the same real part as in their elastic counterparts. The same holds true for the governing viscoelastic wave equation, with wave numbers which are complex-valued, frequency dependent functions that satisfy causality conditions. More specifically, for a Kelvin-Voigt model, the wave numbers are $k_P^2 = \dfrac{\omega^2}{c_P^2\,(1 - i\omega\xi_P)}$; $k_S^2 = \dfrac{\omega^2}{c_S^2\,(1 - i\omega\xi_S)}$, where c_P, c_S are (approximately) the real part of the P- and S-wave velocities, while ξ_P; ξ_S are the corresponding attenuation coefficients representing a small amount of hysteretic damping. In the low frequency range, i.e., $\omega\xi \ll 1$, the wave numbers reduce to:

$$k_P \approx \frac{\omega\,(1 + 0.5\omega\xi_P)}{c_P}; \quad k_S \approx \frac{\omega\,(1 + 0.5\omega\xi_S)}{c_S}, \tag{2.2}$$

Bardet [31] introduced a poroelastic-viscoelastic isomorphism by equating the wave numbers in Biot's poroelastic model with the above viscoelastic ones. This process gives the following equivalence relations between poroelastic and viscoelastic materials:

$$c_P = \sqrt{\frac{P + 2Q + R}{\rho_{sat}}}; \quad c_S = \sqrt{\frac{\mu}{\rho_{sat}}}; \tag{2.3}$$

$$\xi_P = \frac{\rho_{sat}}{b}\left(\frac{Q + R}{P + 2Q + R} \cdot \frac{n\rho_f}{\rho_{sat}}\right)^2; \quad \xi_S = \frac{\rho_{sat}}{b}\left(\frac{n\rho_f}{\rho_{sat}}\right)^2. \tag{2.4}$$

We now have the various poroelastic material parameters related as follows:

$$P = \frac{3\,(1 - \nu)}{1 + \nu}K_{dry} + \frac{Q^2}{R}; \quad Q = \frac{n\,(1 - n - K_{dry}/K_g)}{1 - n - K_{dry}/K_g + nK_g/K_f}K_g;$$

$$R = \frac{n^2 K_g}{1 - n - K_{dry}/K_g + nK_g/K_f},$$

$$N = \frac{3}{2}\frac{1-2\nu}{1+\nu}K_{dry}; \quad K_{dry} = \frac{2}{3}\frac{\mu(1+\nu)}{1-2\nu}; \tag{2.5}$$
$$\lambda_{sat} = \lambda_{dry} + \frac{Q^2}{R} = \frac{3\nu}{1+\nu}K_{dry} + \frac{Q^2}{R}.$$

Furthermore, $b = n^2 g\rho_f/\hat{k}$ is the viscous dissipation coefficient, g is the acceleration of gravity and $\hat{k}$ is the soil permeability with values in the range $10^{-10} - 10^{-2}\ m/\sec$.

Morochnik & Bardet [33] obtained the above approximate expressions for frequency values satisfying the condition $(\omega\,\rho_{sat}/b) << 1$. This condition is easily fulfilled for the frequency range considered important in earthquake engineering since permeability values for most soils is small (e.g., for sand $\hat{k} = 10^{-6} - 10^{-4}$m/sec). The proposed model can also account for soil stiffening, in as much as the pore pressure induced by seismic loads helps in resisting the compressive loads. This can be ascertained by inspecting Eq. (2.3) for the P and S wave velocities, and Eq. (2.5) that shows increased λ_{sat} values compared to λ_{dry}. The equivalent model also predicts changes in the damping mechanism for a poroelastic material. This is clearly evident from Eq. (2.4) and (2.5), where phase velocities and attenuation coefficients for the propagating waves depend on porosity, bulk modulus of the dry skeleton, solid grain and fluid, and on soil hydraulic conductivity.

Finally, all numerical simulations presented in section 4 are for sandstone, with $K_g = 36.000$ MPa; $\rho_g = 2.650$ kg/ m^3; $K_f = 2.000$ MPa; $\rho_f = 1.000$ kg/m^3; see Lin et al. [43], who used the original 3D Biot model applied to the homogeneous half-plane. The soil dry bulk modulus is calculated using an analytical expression derived from experimental data, with $K_{cr} = 200$ MPa being the bulk modulus at critical porosity $n_{cr} = 0.36$:

$$K_{dry} = K_{cr} + (1 - n/n_{cr})\,(K_g - K_{cr})\,. \tag{2.6}$$

An earlier validation study of Bardet' model [34] showed the wave field that develops in the homogeneous poroelastic half-plane is nearly identical with the solution obtained by using the Biot model. We demonstrate in Fig. 2 the dependence of the sandstone shear wave phase velocity of Eq. (2.3), for both

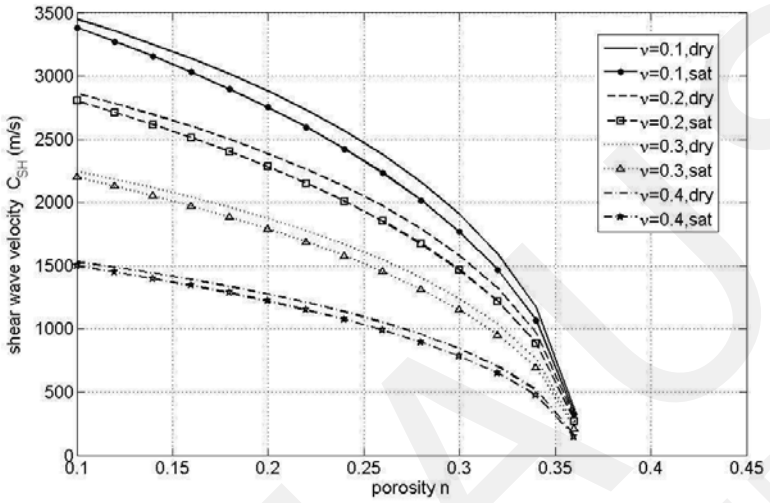

Fig. 2. SH-wave velocity variation with porosity for dry and saturated soil as computed by Bardet's model

dry and saturated conditions, on the porosity n, where we observe the rapid drop of c_{SH} as the porosity increases.

2.3. Fundamental solution of the governing equation

The key role played by the fundamental solution in a BEM formulation is to reduce a given BVP to a system of boundary integral equations through use of a reciprocal theorem [44]. The displacement fundamental solution U_y^* for the SH-wave problem satisfies the following partial differential equation:

$$\sigma_{iy,i}^* + \mu^* k_{SH}^2 U_y^* = -\mu^* \delta(\boldsymbol{\zeta} - \boldsymbol{\zeta}_0); \quad i = x,\, z \tag{2.7}$$

In the above, the viscoelastic stress is defined as $\sigma_{iy}^* = \mu^* U_{y,i}^*$ and $\delta(\boldsymbol{\zeta} - \boldsymbol{\zeta}_0)$ is the Dirac (generalized) delta function for a field and source point configuration. This fundamental solution for the general anisotropic medium was derived in Manolis et al. [35] using the Radon transform. More specifically, after application of this transformation to Eq. (2.7), an ordinary differential equation is obtained and the fundamental solution U_y^* is derived in a closed form, followed by the inverse Radon transform. Problems involving cracked anisotropic media have been successfully solved in the past by the authors [35, 36], who also obtained results by Radon-type fundamental solutions.

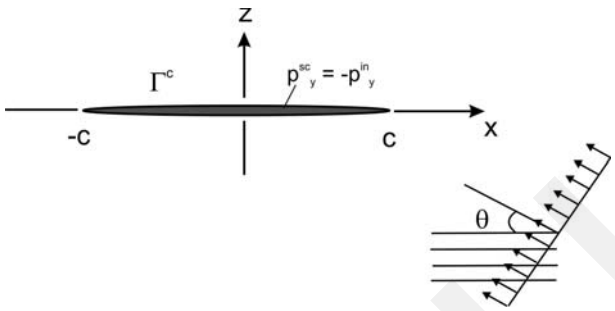

Fig. 3. Scattering of SH- waves by a mode III crack of length $2c$ in the Oxz plane

3. BEM computational model

We use the non-hypersingular, traction-based BEM in the presence of cracks with the frequency-dependent fundamental solution obtained in closed form by the Radon transform, as previously mentioned. This type of computational method was first proposed for elastic, isotropic and homogeneous cracked solids by Zhang and Gross [10] based on the J-integral for time-harmonic elastodynamics. The reason it becomes necessary to switch to a non-hypersingular traction BEM is because the conventional displacement-based BEM degenerates in the presence of crack lines.

A BEM formulation for a bounded domain that is equivalent to the BVP defined by Eq. (2.1) plus the relevant boundary conditions is obtained as follows: First, the boundary of a given problem is represented as $\Gamma = S \cup \Gamma^H \cup \Gamma^c$, where S is the external boundary of the continuous medium containing a cavity and/or a crack. Note, that a crack line is specified as $\Gamma^c = \Gamma^{+c} \cup \Gamma^{-c}$, where Γ^{+c} and Γ^{-c}represent the upper and lower lines of the crack, see Fig. 3. The non-hypersingular traction BEM is defined as:

$$\frac{1}{2}p_y^0(\boldsymbol{\zeta}) = \mu^* n_i(\boldsymbol{\zeta}) \int\limits_S \Big[\big(\sigma^*_{\eta y}(\boldsymbol{\zeta}, \boldsymbol{\zeta}_0, \omega) u^0_{y,\eta}(\boldsymbol{\zeta}_0)$$

$$-\rho\omega^2 U^*_y(\boldsymbol{\zeta}, \boldsymbol{\zeta}_0, \omega) u^0_y(\boldsymbol{\zeta}_0)\big)\, \delta_{i\lambda} - \sigma^*_{\lambda y}(\boldsymbol{\zeta}, \boldsymbol{\zeta}_0, \omega) u^0_{y,i}(\boldsymbol{\zeta}_0) \Big] n_\lambda(\zeta_0) dS \tag{3.1}$$

$$- \mu^*\, n_i(\boldsymbol{\zeta}) \int\limits_S U^*_{y,i}(\boldsymbol{\zeta}, \boldsymbol{\zeta}_0, \omega) p^0_y(\boldsymbol{\zeta}_0) dS, \quad \boldsymbol{\zeta} \in S,$$

for the outer boundary only. Also, the BEM equations in the presence of discontinuities are:

(3.2)

$$
\begin{aligned}
p_y(\boldsymbol{\zeta}) = \mu^* n_i(\boldsymbol{\zeta}) \int\limits_S \Big[& (\sigma^*_{\eta\, y}(\boldsymbol{\zeta}, \boldsymbol{\zeta}_0, \omega) u^c_{y,\eta}(\boldsymbol{\zeta}_0) - \rho\omega^2 U^*_y(\boldsymbol{\zeta}, \boldsymbol{\zeta}_0, \omega) u^c_y(\boldsymbol{\zeta}_0)) \delta_{i\lambda} - \\
& - \sigma^*_{\lambda\, y}(\boldsymbol{\zeta}, \boldsymbol{\zeta}_0, \omega) u^c_{y,i}(\boldsymbol{\zeta}_0) \Big] n_\lambda(\boldsymbol{\zeta}_0) dS - \\
& - \mu^* n_i(\boldsymbol{\zeta}) \int\limits_S U^*_{y,i}(\boldsymbol{\zeta}, \boldsymbol{\zeta}_0, \omega) p^c_y(\boldsymbol{\zeta}_0) dS + \\
& + \mu^* n_i(\boldsymbol{\zeta}) \int\limits_{\Gamma^{+c}} \Big[(\sigma^*_{\eta\, y}(\boldsymbol{\zeta}, \boldsymbol{\zeta}_0, \omega) \Delta u^c_{y,\eta}(\boldsymbol{\zeta}_0) - \rho\omega^2 U^*_y(\boldsymbol{\zeta}, \boldsymbol{\zeta}_0, \omega) \Delta u^c_y(\boldsymbol{\zeta}_0)) \delta_{i\lambda} - \\
& - \sigma^*_{\lambda\, y}(\boldsymbol{\zeta}, \boldsymbol{\zeta}_0, \omega) \Delta u^c_{y,i}(\boldsymbol{\xi}_0) \Big] n_\lambda(\boldsymbol{\zeta}_0) d\Gamma^{+c} + \\
& + \mu^* n_i(\boldsymbol{\zeta}) \int\limits_{\Gamma^H} \Big[(\sigma^*_{\eta\, y}(\boldsymbol{\zeta}, \boldsymbol{\zeta}_0, \omega) u^c_{y,\eta}(\boldsymbol{\zeta}_0) - \rho\omega^2 U^*_y(\boldsymbol{\zeta}, \boldsymbol{\zeta}_0, \omega) u^c_y(\boldsymbol{\zeta}_0)) \delta_{i\lambda} - \\
& - \sigma^*_{\lambda\, y}(\boldsymbol{\zeta}, \boldsymbol{\zeta}_0, \omega) u^c_{y,i}(\boldsymbol{\zeta}_0) \Big] n_\lambda(\boldsymbol{\zeta}_0) d\Gamma^H - \\
& - \mu^* n_i(\boldsymbol{\zeta}) \int\limits_{\Gamma^H} U^*_{y,i}(\boldsymbol{\zeta}, \boldsymbol{\zeta}_0, \omega) p^c_y(\boldsymbol{\zeta}_0) d\Gamma^H, \\
& \boldsymbol{\zeta} \in \Gamma = S \cup \Gamma^{+c} \cup \Gamma^H,
\end{aligned}
$$

involving boundaries S, Γ^H and one side of the crack line, namely Γ^{+c}. In the above, we have that the free traction term in the boundary integral equations is:

(3.3)

$$
\begin{aligned}
& p_y(\boldsymbol{\zeta}) = -\frac{1}{2} p^c_y(\boldsymbol{\zeta}),\ \boldsymbol{\zeta} \in S; \quad p_y(\boldsymbol{\zeta}) = -\frac{1}{2} p^0_y(\boldsymbol{\zeta}),\ \boldsymbol{\zeta} \in \Gamma^H; \\
& p_y(\boldsymbol{\zeta}) = -\frac{1}{2} p^0_y(\boldsymbol{\zeta}),\ \boldsymbol{\zeta} \in \Gamma^{+c}.
\end{aligned}
$$

Next, $\Delta u_y^c = u_y^c\big|_{\Gamma^{+c}} - u_y^c\big|_{\Gamma^{-c}}$ denotes the crack opening displacement (COD), n_i are all outward unit normal vectors at the surfaces, $\boldsymbol{\zeta}(x,z)$ and $\boldsymbol{\zeta}_0(x,z)$ are the observation and the source points, respectively. Furthermore, $U_y^*(\boldsymbol{\zeta},\boldsymbol{\zeta}_0,\omega)$ is the fundamental displacement solution of Eq. (2.1). u_y^0, p_y^0 denote displacements and tractions in terms of prescribed boundary conditions that encompass all external loads across the boundary S of the region free of holes or cracks. In the presence of discontinuities, u_y^c, p_y^c are the fields induced by the loads $p_y^c = -p_y^0$ acting on the cavity perimeter Γ^H and/or the crack lines Γ^c, along with zero boundary conditions on the external boundary, i.e., $u_y^c(\boldsymbol{\zeta}) = 0$, $\boldsymbol{\zeta} \in S_u$ and $p_y^c(\boldsymbol{\zeta}) = 0$, $\boldsymbol{\zeta} \in S_P$. This breakdown is a consequence of the principle of superposition that is valid for linear problems and addition of the BVP components yields the correct boundary conditions along all surfaces of the problem.

The total wave field u_y, p_y is a sum of the incident wave field for displacement and traction u_y^{in}, p_y^{in} and the scattered wave field u_y^{sc}, p_y^{sc}, i.e. $u_y = u_y^{in} + u_y^{sc}$, $p_y = p_y^{in} + p_y^{sc}$ in the case when we consider inhomogeneities such as cracks and/or cavities in an infinite domain. The incident wave displacement satisfies the governing equation (2.1), while the scattered wave displacement satisfies the wave equation (2.1), the boundary condition along the inhomogeneity's perimeter $p_y = 0$ and the Sommerfeld radiation condition at infinity.

The integro-differential system of Eqs. (3.1)–(3.2) is defined with respect to the unknown field quantities u_y^0, p_y^0, u_y^c, p_y^c and Δu_y^c for the general BVP, which involves a finite external region with boundary S that encompasses a mode III crack and/or a cylindrical cavity. In the case of problem (i) for a crack in the infinite plane, the BIE (3.1)–(3.2) are reduced since there are no integrals along the external boundary S and along the cavity perimeter Γ^H. The only unknowns here are the CODs. Next, when we solve problem (ii) for a circular cylindrical cavity embedded in the infinite poroelastic plane, then integrals along S and Γ^{+c} are absent and the only unknowns are displacements along the cavity perimeter. Finally, for case (iii) the BIE along Γ^H are not used. An algebraic system of equations is obtained following discretization of all surfaces with quadratic (i.e., three-node) boundary elements (BE) and special quarter-point boundary elements (QP–BE) that capture the asymptotic behaviour of displacements and stresses near the crack tips by use of special interpolation functions. This system is in terms of the aforementioned unknowns and is completely equivalent to Eq. (3.1)–(3.3). It is then solved using nodal collocation for a discrete spectrum of frequency values. The following principles hold true in the approximation of the displacement u_y and traction

p_y across a BE: (a) Hölder continuity conditions are satisfied at least at the collocation points $u_y \in C^{1,\alpha}(S)$; $p_y^{\in} C^{0,\alpha}(S)$; ($b$) near the crack-tip, the asymptotic expressions for the displacement and for the traction is well known from linear fracture mechanics, i.e. $u_y \approx O(\sqrt{r})$ and $p_y \approx O(1/\sqrt{r})$, where r is the distance from the crack-tip; (c) points at which the boundary is not smooth, and correspondingly the normal vector does not exist, or the Hölder conditions fails, are defined as "irregular" points. The crack-tips in a cracked body and the sharp corners in a body containing crack or hole are particular examples of irregular points. These irregular points should not be used as collocation points since the traction boundary integral equations exist only at the points where the interpolation functions are (Hölder) continuously differentiable and the boundary is smooth. This problem is circumvented by using the shifted node concept [45], where odd-numbered nodes are offset from by a small distance so that nodal collocation can proceed unimpeded; they still remain at these locations for geometry interpolation purposes.

It should be mentioned that the COD plays a key role in dynamic fracture analysis. More specifically, all other field quantities at any arbitrary internal point can be easily evaluated from the relevant integral representation formulas of elastodynamics if the COD's and the displacements along the cavity perimeter have been computed from the BEM system of Eq. (3.1)–(3.2). Thus, both near- and far- field solutions can be determined, with the former yielding information on the dynamic stress concentration distribution and the latter showing the influence of discontinuities at the outer boundaries, which in the case of seismic wave propagation correspond to the motions observed along the free surface of geological media [1].

The singular integrals in Eq. (3.1)–(3.2) converge in the Cauchy principal value sense, if the appropriate smoothness requirements in the approximation of the displacement and stress fields are fulfilled. The disadvantage of the standard quadratic approximation built within the ordinary BE is that it cannot impose smoothness at irregular points such as crack-tips, corner points and generally odd-numbered nodes of the mesh, which delineate the two ends of a given element. This problem is overcome by the use of the 'shifted point' method, as mentioned previously.

Finally, the most essential quantities that characterize the stress concentration phenomena are the SIF for cracks and the SCF for cavities. The former are obtained directly from the nodal values of the traction ahead of the crack-tip as $SIF_{III} = \underbrace{\lim}_{x_1 \to c} p_y \sqrt{2\pi(x_1 \mp c)}$, where c is the half-length of the crack (see Fig. 3) and the crack is orientated along the Ox axis and the

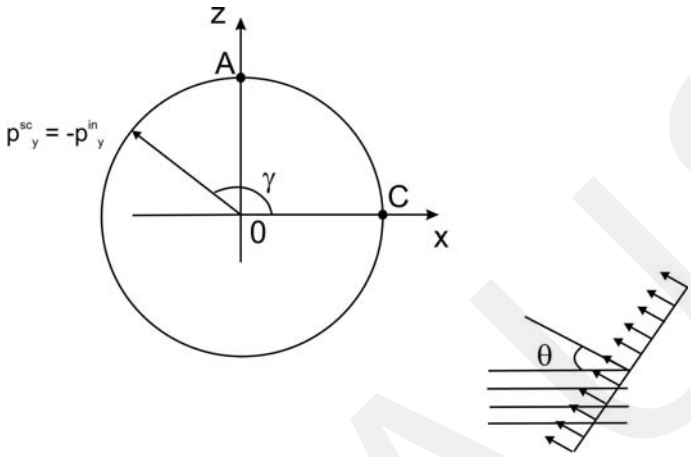

Fig. 4. Scattering of SH- waves by a circular cylindrical cavity of radius $r = c$ in the Oxz plane

center at the origin O. They are subsequently normalized by the maximum amplitude value for the traction resulting from the incident wave. The SCF are defined as the ratio of the stress along the circumference of a cavity to the maximal amplitude of the incident stress field at the same point (see Fig. 4). More specifically, the normalized dynamic SCF $|\sigma_{\theta\gamma}/\tau_0|$ is computed by using the formula $\sigma_{\theta\gamma} = -\sigma_1 \sin(\theta - \gamma) + \sigma_2 \cos(\theta - \gamma)$, where $\sigma_1 = \sigma_{xy} + \sigma^{in}_{xy}$, $\sigma_2 = \sigma_{zy} + \sigma^{in}_{zy}$ and $\tau_0 = \omega\sqrt{\mu\rho}$ is the amplitude of the maximum shear stress of the incident SH-wave for the isotropic homogeneous case. Also, γ is the angle of the observation point along the cavity perimeter with respect to the horizontal direction and θ is the incident angle of the incoming wave, see Fig. 4.

4. Numerical examples

In this section we distinguish two parts, one focusing on validation-type studies, while another collects the results of parametric studies for both cracks and cavities in the poroelastic continuum, which is modeled as a single-phase, viscoelastic material.

4.1. SH-wave scattering by a finite line crack in the infinite poroelastic plane

This problem is depicted in Fig. 3, where a mode III crack of half-length c is located in the Oxz infinite plane and swept by an SH-wave propagating at an incident angle θ with respect to the horizontal axis. Values for the shear

modulus and density of this elastic plane are as follows:

$$\mu = 2.71 \times 10^{10}\ \mathrm{N/m^2}; \quad \rho = 7.550\ \mathrm{kg/m^3}. \tag{4.1}$$

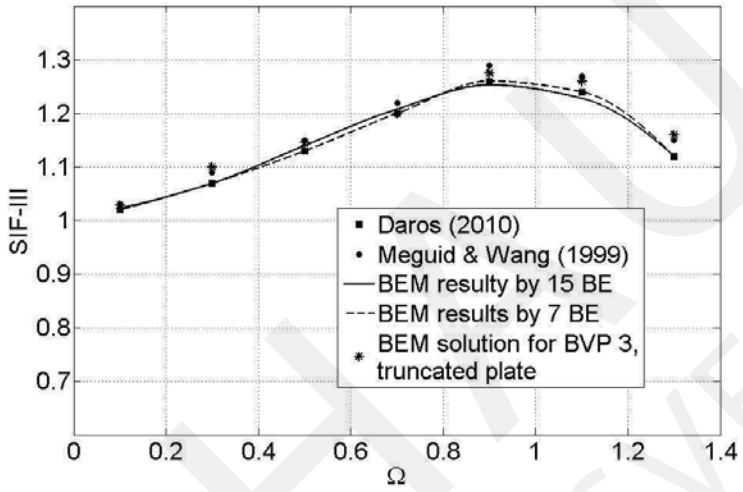

Fig. 5. Normalized dynamic SIF validation for a single mode III crack versus normalized frequency Ω for a normally incident SH-wave propagating in the homogeneous, isotropic plane

At first, we have the results of a validation study for the linear elastic, homogeneous isotropic background material. More specifically, Fig. 5 plots the SIF at the crack tip versus normalized frequency $\Omega = (\omega c/c_S)$, where c_S (m/sec) is the elastic wave speed. The results are parametric in terms of the number of the number of BE used for modelling the crack surface. These comprise both conventional three-node quadratic BE on the regular surfaces, plus the special quarter point element (QP–BE) for modelling asymptotic behaviour in the displacement field as $u_i \approx O(\sqrt{r})$ near the crack tip. Figure 5 demonstrates the high accuracy achieved by the use of only seven BE, (five regular plus two special), which is further improved as the number of BE increases to fifteen. Concurrently, the results shown in Fig. 5 are obtained by Daros [46], who used a non-hypersingular, traction-based BEM, along with those of Meguid and Wang [47] who used a singular integral equation method. We conclude that the accuracy of our proposed traction-based BEM is satisfactory.

Next, Fig. 6 plots the same SIF, but for a poroelastic material obeying

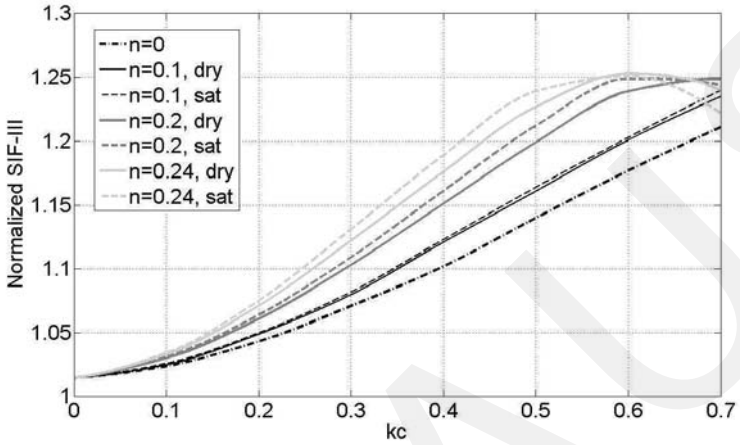

(a)

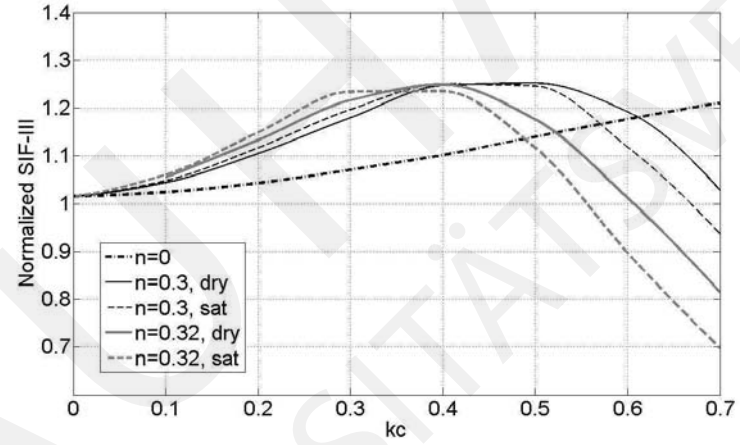

(b)

Fig. 6. Normalized SIF versus normalized frequency kc for a single mode III crack in an infinite poroelastic plane under an incident SH-wave: (a) small and (b) large porosity n values for both dry and saturated soil

the Bardet viscoelastic isomorphism model. We show two sets of results in this figure, one for porosity $n < 0.25$ and another for $n > 0.30$, while Poisson's ratio is fixed at $\nu = 0.10$. The value of the normalized SIF increases in the former plot of Fig. 6(a) with increasing dimensionless frequency to values that exceed the elastic SIF by about 10%, and then starts to taper off. Porosity values of around $n = 0.25$ serve as an upper bound for this type of behaviour,

while low ones of $n = 0.10$ give results that run roughly parallel and slightly above those of the elastic SIF. Also, the difference between dry and saturated soil at the same porosity value is rather small. Similar behaviour as before is observed in Fig. 6(b) up to a dimensionless frequency value of $\Omega = 0.40$, past which the SIF drops sharply, irrespective of what the porosity value is.

4.2. SH-wave scattering by a circular cavity in the infinite poroelastic plane

Figure 4 depicts the problem, where a circular cylindrical cavity of radius $r = c$ is embedded in the infinite elastic Oxz plane and swept by a harmonic SH-wave. The boundary of the cavity is traction-free and the incoming wave scatters on the perimeter, producing a non-zero displacement field. The BVP is solved by the BEM for the scattered wave field, whereupon the incident wave produces a traction field along the cavity's perimeter, with its negative value (i.e., opposite direction) imposed as a load. This way, the sum of incident and scattered traction fields along the perimeter is zero, which is the correct boundary condition, with the BEM yielding the scattered displacement field.

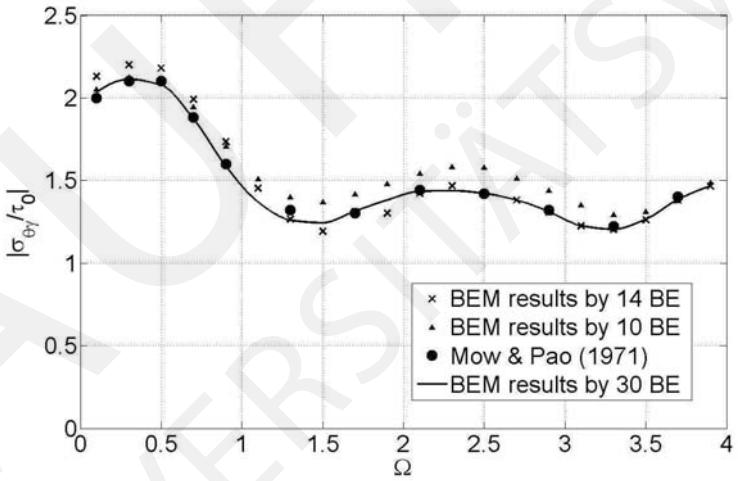

Fig. 7. Dynamic SCF validation at a point A on the perimeter of the circular cavity versus normalized frequency Ω for an incoming SH-wave with incidence angle $\theta = 0$

Figure 7 plots the dynamic SCF on the cavity perimeter as a function of the incoming wave frequency (the non-dimensional value Ω is used), along with the classical results of Pao and Mow [2]. The SCF is normalized by the magnitude of the stress value τ_0 carried by the SH-wave. This validation

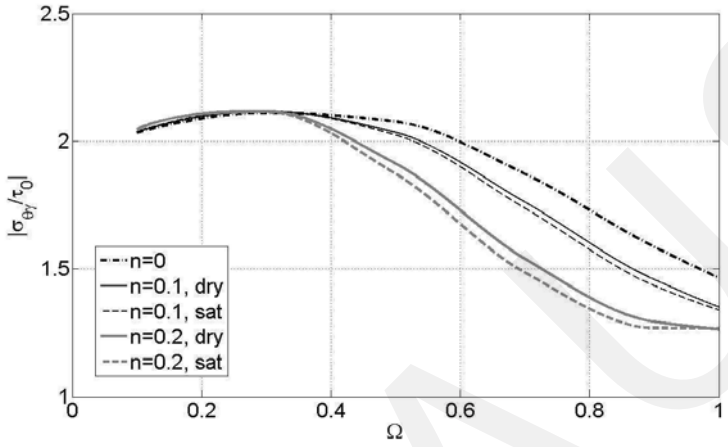

(a)

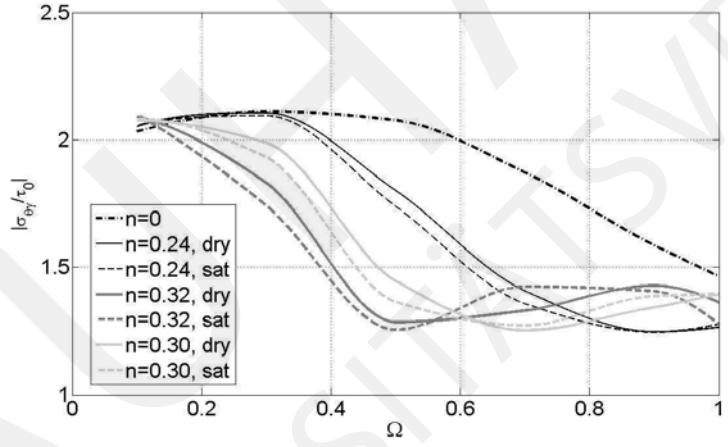

(b)

Fig. 8. Dynamic SCF at a point A on the perimeter of the circular cavity versus normalized frequency Ω for an incoming SH-wave with incidence angle $\theta = 0$: (a) small and (b) large porosity n values for both dry and saturated soil

study assumes the surrounding material to be linearly elastic. The excellent convergence of the BEM as a function of a small number of BE is clearly shown in Fig. 7, where just ten BE along the perimeter produces acceptable results, while thirty BE gives a nearly perfect match. Next, Fig. 8 is the same plot, but for a surrounding material that is poroelastic and represented by Bardet's viscoelastic isomorphism. We show two sets of results as in the previous sub-

section, one for porosity $n < 0.20$ and another for $0.24 < n < 0.30$, while Poisson's ratio is fixed at $\nu = 0.10$. The poroelastic SCF drops off smoothly (maximum drop in the neighborhood of 15–20%) in the former case of Fig. 8(a), with increasing frequency as compared to the elastic values. This drop is more pronounced with higher porosity values, and the difference between dry and saturated soil for the same porosity remains quite small. We observe in Fig. 8(b) that at higher porosities, the poroelastic SCF drops very rapidly to values that are about 80% less compared to the elastic SCF and remain low at around $SCF = 1.2$. This drop is more rapid as the porosity increases to $n = 0.30$.

4.3. Cracked finite poroelastic region subjected to time-harmonic tractions

A finite elastic region contains a centrally placed, mode III crack and is subjected to a uniform time-harmonic traction along its horizontal boundaries, as shown in Fig. 9. A validation study for this example is performed using truncation, i.e., by increasing the size of the material surrounding the crack until the outer boundary has practically no influence on the SIF that develops at the crack tip. We converge to a finite square region of size $2a$, and given the mode III crack of half-length c, we require that $a > 10c$. In this case, the outer boundary no longer influences the elastic wave field, insofar that waves

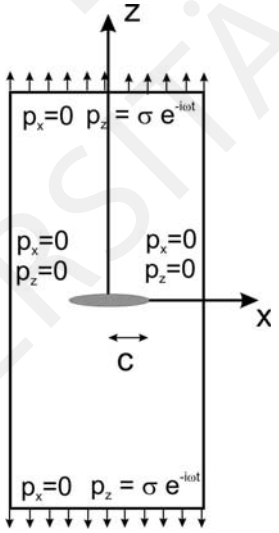

Fig. 9. Finite rectangular poroelastic region with a centered crack with half-length c under uniform, time-harmonic traction $p_y = \sigma$, where σ is the load stress amplitude

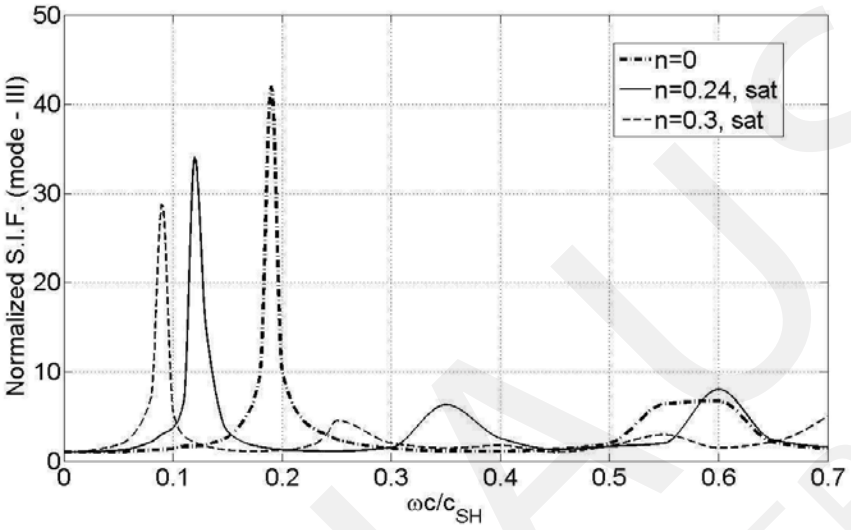

Fig. 10. Normalized dynamic SIF versus normalized frequency Ω for a mode III centred crack in a rectangular poroelastic region as a function of porosity n

scattered by the crack dampen out before reaching the perimeter of the BEM mesh. The results are now the same as those recovered in sub-section 4.1 for a crack in infinite plane, see Fig. 5. The boundary element mesh consists of 7 BE along the crack and 20 BE along the external boundary in the BEM simulations.

Next, Fig. 10 plots the normalized SIF versus dimensionless frequency Ω for the poroelastic region of finite size 20x40 (m), parametric in terms of porosity values n. We first observe that there is a definite pattern of peaks in the SIF frequency response, caused by the finite size of the dry 'box', namely a sharp one at $\Omega = 0.2$ and a lesser one at $\Omega = 0.6$. These indicate very strong resonance effects, and the former SIF overshoots its static value for the infinite region forty-fold. The latter one is milder and the overshoot is roughly five-fold. The presence of a water phase in the saturated soil acts as a damping mechanism and causes a frequency shift to lower values for the SIF peaks (i.e., to less than $\Omega = 0.1$ depending on the porosity for the first peak and to $\Omega = 0.55$ for the second peak). It also causes a substantial drop in these peak SIF values, to about thirty-fold in the former case and to a just a doubling in the latter case.

5. Interpretation of results

In this work, we focus on elastic wave propagation in a poroelastic continuum with discontinuities under anti-plane strain conditions. The objective was to study the development of the SIF at the tip of a crack and of the dynamic SCF in the perimeter of a cavity, when the surrounding medium is water saturated soil, and the excitation are incoming SH- axes. Based on the result presented herein, the following points can now be summarized:

(1) For small values of porosity around one-tenth, there are minor differences in the SIF values at the crack-tips between dry and saturated soils. This difference, however, also increases and starts to depend on the frequency of excitation as porosity increases.
(2) Up to porosity values of one-quarter, the SIF values increase, both with respect to increasing frequency and porosity values.
(3) For high porosity values of over one-third, there exists a 'turning' frequency past which the SIF starts to drop after having reached is maximum value. This 'turning' frequency starts to shift to the left in the spectrum (i.e., decreases) with increasing porosity.
(4) In a finite-sized region, resonance effects are observed and very high SIF values result, with the presence of the fluid phase acting as a damping mechanism that ameliorates this effect.
(5) For both dry and saturated soils with low porosities, the SCFs are lower than those observed for a purely elastic material, and this reduction is proportional with the frequency (at least in the frequency interval considered herein).
(6) Also, the SCF computed for both dry and saturated soils with porosities higher than one-quarter are lower than the corresponding elastic SCF in the low (dimensionless) frequency range up to $\Omega = 0.5$. Past that value, they start to exhibit an oscillatory behaviour with increasing frequency.

At this point, we stress that insofar as the Bardet model for one-phase materials is concerned, it cannot take into account the time-dependent pore pressure diffusion process at the crack-tip, nor the pore pressure boundary conditions along crack faces. Thus, there are limitations when the aforementioned model is applied to fracture in poroelastic media, but it is still useful for engineering practice. More specifically, the viscoelastic-poroelastic similarity is useful for extracting approximate solutions that can be used as benchmark cases to calibrate the accuracy of more advance (in terms of constitutive laws) computational methods applied to wave propagation problems in fluid-saturated soils. In sum, the dynamic mode III crack SIF is higher that the correspond-

ing static one for a wide range of frequencies of excitation, which means the inertial properties of the material should be taken into consideration. Most important, however, is the presence of the fluid phase in the soil that alters the SIF values dramatically and its influence cannot be easily surmised, unless the appropriate computations are performed. The same comments hold true for the SCF that develops in the perimeter of buried cavities.

6. Conclusions

The novelty in the present work stems from the incorporation of the viscoelastic isomorphism concept in a mesh-reducing numerical method such as the BEM as a way of examining the dynamic response of fractured and/or discontinuous poroelastic media. This offers the following computational advantages:

(a) The modelling of a two-phase material by a single-phase viscoelastic one. This simplifies the governing equation and allows for recovery of its fundamental solution, which is the key ingredient in a BEM formulation. This opens the gateway to study fracture in poroelastic media given the complexity of BVP in fracture mechanics. At the same time, the equivalent model can account for changes in the stiffness and damping mechanism in the porous soil, since Bardet's equivalence formulas for the phase velocities show explicit dependence on the porosity, the bulk modulus of the dry skeleton, of the solid grain and of the fluid components, and on the hydraulic conductivity.

(b) The use of the BEM also carries computational advantages in comparison with other analytical or numerical methods, such as (i) a drop in the dimensionality of the problem with a corresponding reduction in the size of the resulting algebraic system following surface discretization; (ii) solution at prescribed internal points in the domain is selectively performed based on the boundary values without recourse to domain discretization (e.g., finite elements or finite differences); (iii) high accuracy in the results due to the semi-analytical character of the method insofar as it is based on the fundamental solution of the underlying wave equation; (iv) the high level of accuracy is maintained because numerical quadrature is directly applied to the boundary integral equations, which are an exact solution statement; (v) the satisfactory solution of problems exhibiting stress gradient fields is possible.

In sum, the present BEM development using viscoelastic isomorphism gives approximate solutions for complex BVP involving wave propagation in

fluid-saturated media. High accuracy in the BEM solution is maintained following this viscoelastic approximation, along with a very efficient use of CPU time and memory because of the mesh-reduction character of the BEM.

REFERENCES

[1] Helbig, K. (editor), Modelling the Earth for Oil Exploration, London, Pergamon Press, 1994.

[2] Pao, Y. H., C. C. Mow. Diffraction of Elastic Waves and Dynamic Stress Concentration, New York, Crane Russak, 1971.

[3] Villaverde, R. Fundamentals Concepts of Earthquake Engineering, Florida, Boca Raton, CRC Press, 2009.

[4] Neuber, H. Theory of Notch Stresses, Principles for Exact Stress Calculation, David Taylor Model Basin Report, DC, Washington, US Navy Department, 1945.

[5] Muskhelishvili, N. I. Some Basic Problems of the Mathematical Theory of Elasticity, Groningen, Noordhoff, 1953.

[6] Savin, G. Stress Concentration around Holes, London, Pergamon Press, 1961.

[7] Timoshenko, S. P., J. N. Goodier. Theory of Elasticity, 3rd Editon, New York, McGraw-Hill, 1970.

[8] Achenbach, J. D. Wave Propagation in Elastic Solids, Amsterdam, North-Holland, 1973.

[9] Miklowitz, J. Elastic Waves and Waveguides, Amsterdam, North-Holland, 1984.

[10] Zhang, C. H., D. Gross. Wave Propagation in Elastic Solids with Cracks, Southampton, Computational Mechanics Publications, 1998.

[11] Datta, S. K., A. H. Shah. Scattering of SH-waves by Embedded Cavities. *Wave Motion,* **4** (1982), No. 3, 265–283.

[12] Liu, D. Dynamic Stress Concentration Around a Circular Hole due to SH-wave in Anisotropic Media. *Acta Technica Sinica,* **4** (1988), 146–155.

[13] Liu, D., F. Han. The Scattering of Plane SH-waves by Noncircular Cavity in Anisotropic Media. *Journal of Applied Mechanics*, **60** (1993), 769–772.

[14] Liu, D., H. Lin. Scattering of SH-waves by a Shallow Buried Cylindrical Cavity and the Ground Motion. *Explosion and Shock Waves*, **23** (2003), No. 1, 6–12.

[15] Kobayashi, S., N. Nishimura. Analysis of Dynamic Soil-structure Interactions by Boundary Integral Equation Method, In Numerical Methods in Engineering, edited by P. Lascaux, Paris, Pluralis, 1983, 353–362,

[16] Manolis, G. D. A Comparative Study in Three Boundary Element Method Approaches to Problems in Elastodynamics. *International Journal of Numerical Methods in Engineering,* **19** (1983), 73–91.

[17] Luco, J. E., F. C. P. De Barros. Dynamic Displacements and Stresses in the Vicinity of a Cylindrical Cavity embedded in a Half-space. *Earthquake Engineering and Structural Dynamics,* **23** (1994), 321–340.

[18] Wang, Y. H., Y. K. Cheung, C. W. Woo. The Stress Intensity Factor of a Crack emanating from a Circular Hole in a Finite Plate by Boundary Collocation Method. *International Journal of Fracture,* **43** (1990), No. 2, 97–108.

[19] Providakis, C. P., D. A. Sotiropoulos, D. E. Beskos. BEM Analysis of Reduced Dynamic Stress Concentration by Multiple Holes. *Communications in Numerical Methods in Engineering,* **9** (1993), 917–924.

[20] Liaw, B. M., M. Kamel. A Crack Approaching a Curvilinear Hole in an Anisotropic Plane under General Loadings. *Engineering Fracture Mechanics,* **40** (1991), 25–35.

[21] Lee, V. W., M. D. Trifunac. Response of Tunnels to Incident SH-waves. *Journal of Engineering Mechanics of ASCE,* **105** (1979), 643–659.

[22] Kattis, S. E., D. E. Beskos, A. H. D. Cheng. 2D Dynamic Response of Unilined and Lined Tunnels in Poroelastic Soil to Harmonic Body Waves. *Earthquake Engineering and Structural Dynamics,* **32** (2003), 97–110.

[23] Wang, J. H., X. L. Zhou, J. F. Lu. Dynamic Stress Concentration Around Elliptic Cavities in Saturated Poroelastic Soil under Harmonic Plane Waves. *International Journal of Solids and Structures,* **42** (2005), 4295–4310.

[24] Liang, J., Z. Ba, V. W. Lee. Scattering of Plane P-waves around a Cavity in Poroelastic Half-space: I. Analytical Solution. *Earthquake Engineering and Engineering Vibration,* **27** (2007), No. 1, 1–6.

[25] Liang, J., Z. Ba, V.W. Lee. Scattering of Plane P-waves around a Cavity in Poroelastic Half-space: II. Numerical Results. *Earthquake Engineering and Engineering Vibration,* **27** (2007), No. 1, 7–11.

[26] Liang, J., Z. Liu. Diffraction of Plane SV Waves by a Cavity in Poroelastic Half-space. *Earthquake Engineering and Engineering Vibration*, **8** (2009), No. 1, 29–46.

[27] Biot, M. Theory of Propagation of Elastic Waves in a Fluid-saturated Porous Solid. *Journal of Acoustical Society of America,* **28** (1956), No. 4, 168–191.

[28] Mahyari, A. T. Computational Modelling of Fracture and Damage in Poroelastic Media, PhD Thesis, Canada, Montreal, McGill University, 1997.

[29] Charlez, P. A. Rock Mechanics, Vol. 2, Petroleum Applications, Paris, Editions Technip, 1997.

[30] Fjaer, E., R. M. Holt, P. Horsrud, A. M Raaen, R. Risnes. Petroleum Related Rock Mechanics, 2nd Edition, Amsterdam, Elsevier, 2008.

[31] Bardet, J. P. A Viscoelastic Model for the Dynamic Behaviour of Saturated Poroelastic Soils. *Transactions of the ASME,* **59** (1992), 128–135.

[32] Bardet, J. P. The Damping of Saturated Poroelastic Soils during Steady-state Vibrations. *Applied Mathematics and Computation,* **67** (1995), 3–31.

[33] Morochnik V., J. P. Bardet. Viscoelastic Approximation of Poroelastic Media for Wave Scattering Problems. *Soil Dynamics and Earthquake Engineering,* **15** (1996), 337–346.

[34] Dineva, P., M. Datcheva, G. D. Manolis, T. Schanz. Seismic Wave Propagation in Laterally Inhomogeneous Poroelastic Media via BIEM. *International Journal for Numerical and Analytical Methods in Geomechanics,* **36** (2012), 111–127.

[35] Manolis, G. D., P. S. Dineva, T. V. Rangelov. Dynamic Fracture Analysis of a Smoothly Inhomogeneous Plane containing Defects by BEM. *Engineering Analysis with Boundary Elements*, **36** (2012), 727–737.

[36] Dineva, P., T. Rangelov, D. Gross. BIEM for 2D steady-state problems in cracked anisotropic materials. *Engineering Analysis with Boundary Elements,* **29** (2005), 689–698.

[37] Johnson, J. J. (editor) Soil-Structure-Interaction: The Status of Current Analysis Methods and Research, Research Report NUREG CR-1780, DC, Washington, Nuclear Regulatory Commission, 1981.

[38] Christensen, R. Theory of Viscoelasticity: An Introduction, New York, Academic Press, 1971.

[39] Manolis, G. D., D. E. Beskos. Dynamic Stress Concentration Studies by Boundary Integrals and Laplace Transform. *International Journal of Numerical Methods in Engineering,* **17** (1981), 573–599.

[40] Kobayashi, S. Elastodynamics, In: *BEM in Mechanics*, edited by D. E. Beskos, Amsterdam, North Holland, 1987, 191–255.

[41] Abascal, R., J. Dominguez. Vibrations of Footings on Zoned Viscoelastic Soils. *Journal of Engineering Mechanics ASCE,* **112** (1986), 433–447.

[42] Beskos, D. E., B. Dasgupta, I. G. Vardoulakis. Vibration Isolation using Open or Filled Trenches. Part 1: 2D homogeneous soil. *Computational Mechanics,* **1** (1986), 43–63.

[43] Lin, C. H., V. W. Lee, M. D. Trifunac. The Reflection of Plane Waves in a Poroelastic Half-space Saturated with Inviscid Fluid. *Soil Dynamics and Earthquake Engineering,* **25** (2005), 205–223.

[44] Dominguez, J. Boundary Elements in Dynamics, Southampton, Computational Mechanics Publication, 1993.

[45] Rangelov, T., P. Dineva, D. Gross. A Hypersingular Traction Boundary Integral Equation Method for Stress Intensity Factor Computation in a Finite Cracked Body. *Engineering Analysis with Boundary Elements,* **27** (2003), No. 1, 9–21.

[46] Daros, C. H. On Modelling SH Waves in a Class of Inhomogeneous Anisotropic Media via the Boundary Element Method. *ZAMM,* **90** (2010), No. 2, 113–121.

[47] Meguid, S. A., X. D. Wang. Wave Scattering From Cracks and Imperfectly Bonded Inhomogeneities in Advanced Materials. *Mechanics of Materials,* **31** (1999), 187–195.

Journal of Sound and Vibration ▮ (▮▮▮▮) ▮▮▮–▮▮▮

Contents lists available at ScienceDirect

Journal of Sound and Vibration

journal homepage: www.elsevier.com/locate/jsvi

Seismic wave propagation in laterally inhomogeneous geological region via a new hybrid approach

F. Wuttke [a,*], P. Dineva [b], T. Schanz [c]

[a] Laboratory of Soil Mechanics, Bauhaus-University, 99421 Weimar, Germany
[b] Department of Continuum Mechanics, Institute of Mechanics, Bulgarian Academy of Sciences, 1113 Sofia, Bulgaria
[c] Chair of Foundation Engineering, Soil and Rock Mechanics, Ruhr-University, 44780 Bochum, Germany

ARTICLE INFO

Article history:
Received 15 May 2008
Received in revised form
17 August 2010
Accepted 28 August 2010
Handling Editor: A.V. Metrikine

ABSTRACT

2D seismic wave propagation in a local multilayered geological region rested in an inhomogeneous half-space with a seismic source is studied. Plane strain state is suggested. The vertical variation of the soil properties in the half-space is modelled by a set of horizontal flat isotropic, elastic and homogeneous layers. The finite local region is with non-parallel layers and free surface relief. Efficient hybrid wavenumber integration-boundary integral equation method (WNI-BIEM) is proposed, validated and applied for synthesis of seismic signals in the finite soil stratum. The numerical simulation reveals that the developed hybrid method is able to demonstrate the sensitivity of the obtained synthetic signals to the seismic source properties, to the heterogeneous character of the wave path and to the relief peculiarities of the local stratified geological deposit. The advantages and disadvantages of the proposed method are discussed.

1. Introduction

A way to shed light on seismic wave propagation in complex geological profile, consists in developing of high-performance tools to simulate seismic signals. A detailed overview of the approaches developed in the field is given by Sanchez-Sesma [1]. Essentially three main groups of methodologies treat the problem and they are analytical, numerical and hybrid methods. Analytical methods are mainly based on the ray theory, mode matching methods and integral representation theorems. Ray theory [2] and its modifications such as the Maslov asymptotic theory [3], the Kirchhoff–Helmholtz methods [4], Gaussian beams [5], generalized ray method [6] and the Born approximation method [7] are restricted to media with simple geometry. Mode matching techniques are based on the fact that the unknown wave fields are built up by superposition of normal modes of the considered medium. The problem is reduced to the evaluation of a set of coefficients needed for the expansion of the wave field by the normal nodes at a given frequency by satisfy the correct boundary conditions. The modal summation is very useful for synthesizing long-period seismograms. Alternative techniques are the reflectivity method [8] and the generalized R/T coefficient method [9,10] as wavenumber integration method (WNIM) that can compute numerical signals for both long- and short-period signals. A satisfactory agreement between theoretical seismograms obtained by generalized ray method and WNIM is presented in Burdik and Orcutt [11].

The modelling of seismic wave propagation in geological media includes the source, the travel path and the receiving site (see Fig. 1a). It comprises two types of models: (a) all-in-one source–path-site single computational tool demanding an

* Corresponding author.
E-mail addresses: frank.wuttke@uni-weimar.de (F. Wuttke), petia@imbm.bas.bg (P. Dineva), tom.schanz@rub.de (T. Schanz).

0022-460X/$ - see front matter © 2010 Elsevier Ltd. All rights reserved.
doi:10.1016/j.jsv.2010.08.042

Nomenclature

Latin characters

C_{ij}	free term coefficients in BIEs depending on the local geometry
$\mathbf{C}$	vector of unknown constants of the analytical solution of ordinary differential equation for the motion-stress vector
D	damping ratio
$\mathbf{E}$	known structure matrix of the layer in the system for the motion-stress vector
L, h	half-width, depth of a semi-elliptical valley
l_{BE}	length of the boundary element
M_{ij}	seismic moment, with ith arm and jth force direction ($i,j = x,z$)
M_0	seismic scalar moment
M	number of layers in vertically inhomogeneous half-space Ω_0
N	number of layers in laterally inhomogeneous geological region Ω_{LGR}
$\mathbf{p}$	traction vector, $p_j = \sigma_{ij} n_j$, where σ_{ij} and n_j are the components of the stress tensor and the outward normal of the surface element
P_j	components of the seismic unit line source described by the term ΔQ
$\mathbf{P}^*$	traction fundamental solution
$\mathbf{R}$	modified reflection coefficient matrix
$\widehat{\mathbf{R}}$	generalized reflection coefficient matrix (cumulative coefficient)
S	depth (z=S) of the seismic source
t	time variable
$\mathbf{T}$	modified transmission coefficient matrix
$\widehat{\mathbf{T}}$	generalized transmission coefficient matrix (cumulative coefficient)
$\mathbf{u}$	displacement vector
$\ddot{\mathbf{u}}$	acceleration vector
$\mathbf{U}^*$	displacement fundamental solution

Greek characters

α	compressional wave velocity
β	shear wave velocity
δ	dip angle of the fault
ρ	density
ζ	wavenumber
θ	slip or rake angle of the fault
Θ	incident angle of P-wave
λ, μ	lame constants
λ_S	length of the shear wave
Λ	common boundary between Ω_{LRG} and Ω_0
$\mathbf{\Lambda}$	exponential matrix in the system for the motion-stress vector
σ_{ij}	stress tensor
$\mathbf{\Sigma}$	vector of stress components
ϕ	strike angle of the fault
ω	circle frequency

Sub- and Superscripts

(x,z)	position of the observer
$\mathbf{T}^l_{d/u}$	transmission coefficients for plane P- and SV-waves impinging on the lth interface from above and below
$\mathbf{R}^l_{d/u}$	reflection coefficients for plane P- and SV-waves impinging on the lth interface from above and below
$\widehat{\mathbf{T}}^l_{d/u}$	generalized transmission coefficients for plane P- and SV-waves, including multiple reflections, conversions and transmissions on the layers above and below the lth interface
$\widehat{\mathbf{R}}^l_{d/u}$	generalized reflection coefficients for plane P- and SV-waves, including multiple reflections, conversions and transmissions on the layers above and below the lth interface
$\mathbf{\Lambda}^l_{d/u}$	the submatrices representing the upgoing/downgoing waves within the lth layer
$\mathbf{C}^l_{d/u}$	the unknown coefficients of analytical solution of ordinary differential equation for the motion-stress vector inside lth layer, representing the upgoing/downgoing waves within the lth layer
$\mathbf{C}^l_{Pd/Pu}$	the unknown coefficients of analytical solution of ordinary differential equation for the motion-stress vector inside lth layer, representing of upgoing/downgoing P-waves within the lth layer
$\mathbf{C}^l_{Sd/Su}$	the unknown coefficients of analytical solution of ordinary differential equation for the motion-stress vector inside lth layer, representing of upgoing/downgoing SV-waves within the lth layer

Abbreviations and Notations

$\Delta\mathbf{Q}$	stress-discontinuity representing the seismic source
$\Omega_{\mathrm{LGR}} = \bigcup_{i=1}^{N} \Omega_i$	finite local geological region with N non-parallel layers Ω_i
$\Omega_0 = \bigcup_{k=1}^{M} \Gamma_k$	vertically inhomogeneous half-space modelled by a series of M homogeneous flat layers Γ_i, parallel to free surface
BIEM	boundary integral equation method
CPV integral	Cauchy principal value integral
FFT	fast Fourier transformation
MS-BIEM	modal summation-boundary integral equation method
WNIM	wavenumber integration method
WNI-BIEM	wavenumber integration-boundary integral equation method
MSM	modal summation method
MS-FDM	modal summation-finite difference method
FE-BEM	finite element-boundary element method

Please cite this article as: F. Wuttke et al., Seismic wave propagation in laterally inhomogeneous geological region via a new hybrid approach, *Journal of Sound and Vibration* (2010), doi:10.1016/j.jsv.2010.08.042

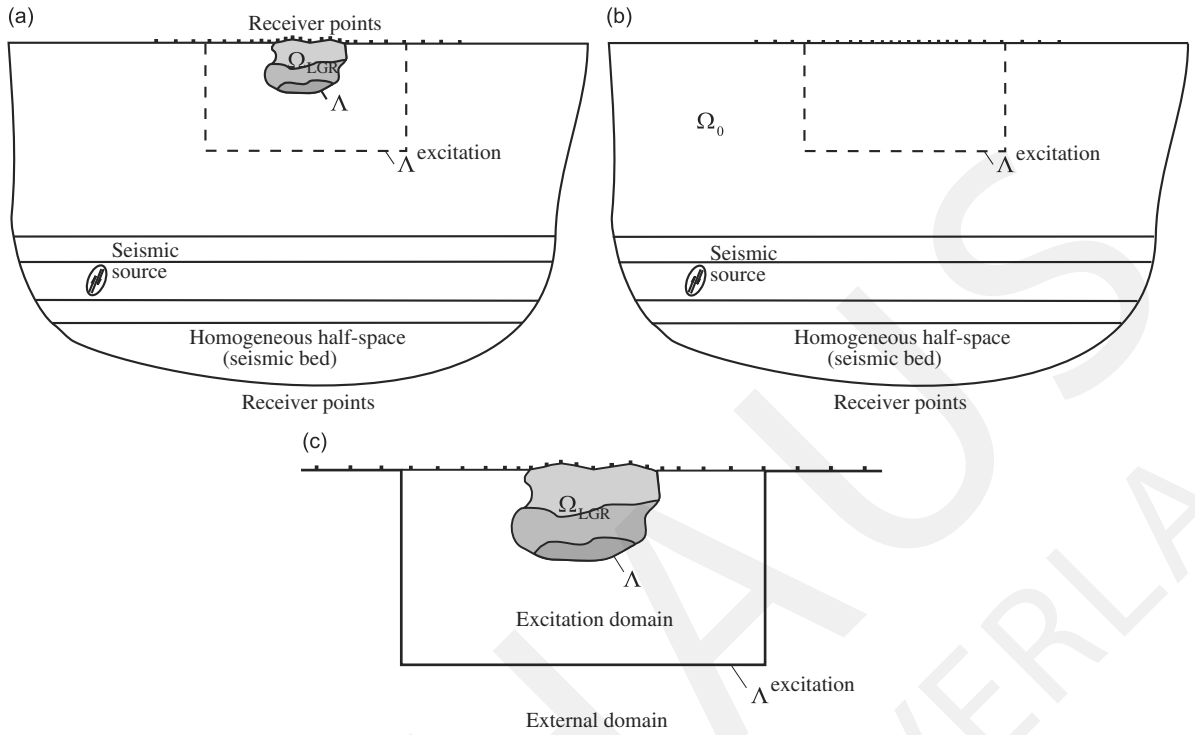

Fig. 1. Scheme of the hybrid WNI-BIEM: (a) original problem configuration; (b) first step: background model and WNIM computation of the free field motion along $\Lambda^{\text{excitation}}$; (c) second step: BIEM computation of the total wave field inside the excitation region and the scattered wave field outside $\Lambda^{\text{excitation}}$.

extreme computer memory and time, especially in the cases the source–receiver distance is measured in dozens of km and (b) hybrid approach based on a two-step procedure that combines the source and path effects (see Fig. 1b) computed by one method and local site effects (see Fig. 1c) evaluated by other method using the first method's wave field as input and basing on the fact that the connection between the two methods keeps the formal wave-injection boundary perfectly permeable for the wave scattered by the local structure. The hybrid methods are especially appropriate when a certain (smaller) part of the model is with more complex topography and geometry than others and it is situated in a large and deep regional model including the source and path effects. The hybrid two-step technique originates by [12] as a domain-coupling technical algorithm. This algorithm was developed and extended further in: (a) [13–16], where the modal summation and finite difference technique is used in the first and second step correspondingly; (b) [17–21] combining the discrete wavenumber method for the regional computation (first step), finite element method for topographic surface parts and finite difference method for localized structures with a flat free surface embedded in a background medium. The same philosophy dates back to works [22,23]. The term "wave injection" was introduced in [24,25]. An efficient seismic modelling requires various methods to be combined, each one being applied just for a single task at which the method performs best. In that way, the individual advantages are enhanced, and the limitations are reduced.

As a whole, the analytical methods are restricted to inhomogeneous media with simple geometry (for example, parallel, horizontal layers in the half-space) and heterogeneity with dimension considerably larger than the prevailing wavelengths and therefore they are only of limited use for zoning studies. This is the reason to use the analytical WNIM to model the wave propagation in inhomogeneous in depth half-space with a seismic source in it. As an analytical tool, the WNIM can give solutions for depths of hundred kilometers without limitations due the CPU time and memory. This is not true for the BIEM, because as a numerical method it has limitations concerning the CPU time and memory. Of course, one of the main advantages of the BIEM is that the fundamental solution used in the construction of the boundary integral equations obeys the radiation condition and thus infinitely extended boundaries are automatically incorporated. In opposite to the BIEM other numerical methods have to use special transmitting, silent and non-reflecting viscous boundaries to satisfy the Sommerfeld's radiation conditions. This very important property is used in the hybrid method essentially as far as the direct BIEM solves both internal and external problems in the second step of the hybrid algorithm. On the boundary between homogeneous and inhomogeneous parts of the half-space, the satisfaction of the Sommerfeld's radiation condition by the WNIM solution has no difficulties. Most of the papers consider analytical approach for solution of the background model and numerical procedure for treating the lateral near-surface soil deposit, see [12–21,25]. Other reasons to use the BIEM to model the wave motion in the local stratified, geological area are the rest of the advantages of this tool: (a) reduce the size of the problem dimensionality and the size of the resulting algebraic system in contrast to other

Please cite this article as: F. Wuttke et al., Seismic wave propagation in laterally inhomogeneous geological region via a new hybrid approach, *Journal of Sound and Vibration* (2010), doi:10.1016/j.jsv.2010.08.042

numerical domain methods; (b) possibility to model lateral inhomogeneity in contrast to WNIM and other analytical approaches; (c) solution at each internal point in the domain is expressed in terms of boundary values without recourse to domain discretization and this main facility is very important when wave propagation problems are being solved in multilayered solids, because only the boundaries between layers are discretized, not their volumes as it is when domain discretization methods as finite element or finite difference methods are used; (d) flexibility to model relief peculiarities in contrast to analytical methods and finite difference method having problems with implementing conditions on boundaries of complex geometric shapes, see [18]; (e) the possibility to obtain directly, with no other intermediate source of error, the dynamic regime — displacements and tractions; (f) the semi-analytical character of the method as far as it is based on Green's function of the considered problem; (g) high level of accuracy is achieved since numerical quadrature techniques are directly applied to the boundary integral equations, which are an exact solution of the considered problem.

Although the advantages of the BIEM are well known, there is still a lack of hybrid methods that are based on this method. Up to now, few BIEM-based hybrid schemes, such as Bard and Bouchon [26,27], Bravo et al. [28], Kawase [29], Bouchon et al. [30], Kawase and Aki [31], Papageorgiou and Kim [32], Zhang et al. [33], Gil-Zepeda et al. [34], Nguyen and Gatmiri [35] have been presented for seismic response analysis of topographic structures. The coupled BIEM with finite element and finite difference methods are proposed in [36–40]. In [41–43], a hybrid approach in which an internal region including the valley under harmonic plane waves is modeled by finite elements, while the exterior region is modeled by the BIE-method. The accuracy and efficiency of the hybrid indirect BIE-Born approximation method is studied in [44]. Gil-Zepeda et al. [34] proposed a hybrid indirect BIEM-discrete wavenumber method and applied it to model the ground motion of stratified alluvial valleys under incident plane SH waves from an elastic homogeneous half-space. An efficient hybrid MS-BIE method based on the modal summation and the direct boundary integral equation technique is developed in [45].

We conclude that there is a lack of hybrid models based on BIEM that allow to take into consideration the properties of all three components: seismic source, inhomogeneous in depth wave path and finite laterally inhomogeneous soil stratum. The majority of the computational tools use the body plane waves as input of the seismic motion in the lateral inhomogeneous geological site. That is not adequate to the real seismic scenarios.

The objective of the present paper is to combine the facilities of both analytical WNI and numerical BIE methods in order to develop an accurate and efficient hybrid approach for synthesis of theoretical seismograms in a laterally varying near-surface seismic region embedded in a deep horizontally layered half-space with a seismic source in one of the layers, accounting for: (a) the seismic source characteristics; (b) the inhomogeneous wave path from the source to the area of interest; (c) the local geological media with the complex mechanical and geometrical properties and (d) the existence of free surface relief peculiarities.

The proposed hybrid technique is based on the WNIM for investigating wave propagation in the background structure, while BIE method is used for synthesis of theoretical seismograms on the free surface of the local finite near-surface soil stratum with or without relief. The hybrid method, as proposed in this paper is most closely resembles to the method discussed in [12–21,25]. The paper has following content: Starting with the problem description in Section 2, followed by the hybrid computational tool presented and discussed in Section 3. The validation study of the computational technique is presented in Section 4. Finally, numerical examples for different seismic scenarios are solved and simulation study is given in Section 5, followed by conclusions in the last Section 6.

2. Problem statement

Consider in-plane seismic wave propagation problem in a near-surface finite local multilayered geological region Ω_{LGR} embedded in a deep first layer of an inhomogeneity in depth, presented by a stack of horizontal layers, which rest on the homogeneous half-space, see Fig. 1a. Plane strain state is suggested. Non-parallel isotropic, elastic and homogeneous layers Ω_i, $i=1,\ldots,N$ are situated in the local soil stratum Ω_{LGR}. The mechanical properties for the inhomogeneity in depth, Ω_0 are modelled with series of M elastic isotropic homogeneous and horizontal layers Γ_i. These layers are parallel to the free surface and overlay the homogeneous half-space — the seismic bed. A seismic source is located in one of the flat layers of the vertical layered part Ω_0 of the half-space. Three types of free surface geometry of the local soil deposit Ω_{LGR} are considered: (a) uniform surface model; (b) canyon model; (c) hill-like model, correspondingly. The objective is to obtain the synthetic seismograms in some receiver points along the free surface of the local near-surface region Ω_{LGR}. The governing wave equations for the lth layer are the following partial differential equations:

$$(\alpha_l^2-\beta_l^2)u_{j,ji}(x,z,t)+\beta_l^2 u_{i,jj}(x,z,t)=\ddot{u}_i(x,z,t) \quad \text{in } Q_B=\Omega_B\ x(0,T) \tag{1}$$

In Eq. (1) commas indicate spatial derivatives, while vectorial quantities are denoted through the use of indices ($i,j=x,z$) and Ω_B comprises the range inside the local geological region and the layered part of the half-space outside it. Longitudinal and shear wave velocities, α_l,β_l, are different for different soil layers in Ω_{LRG}, where $l=1,2,\ldots,N$, and in the layered part of the half-space, where $l=1,2,\ldots,M$, T is the duration of the seismic load, u_i is the displacement, $\ddot{u}_i$ is the acceleration, $i=x,z$. In order to exclude the time variable t and to solve the boundary-value problem in the frequency ω domain a Fourier transform is applied to the time variable. The governing partial differential equation for each lth layer is now of

Please cite this article as: F. Wuttke et al., Seismic wave propagation in laterally inhomogeneous geological region via a new hybrid approach, *Journal of Sound and Vibration* (2010), doi:10.1016/j.jsv.2010.08.042

elliptic type:

$$\left(\frac{(\zeta_s^l)^2}{(\zeta_p^l)^2}-1\right)(u_{z,xz}+u_{x,xx})+u_{x,xx}+u_{x,zz}=-(\zeta_p^l)^2u_x$$

$$\left(\frac{(\zeta_s^l)^2}{(\zeta_p^l)^2}-1\right)(u_{x,xz}+u_{z,zz})+u_{z,xx}+u_{z,zz}=-(\zeta_s^l)^2u_z \quad (2)$$

where $\zeta_p^l=\omega/\alpha_l$ and $\zeta_s^l=\omega/\beta_l$. The boundary-value problem consists of the governing Eq. (2) and the following frequency-dependent boundary conditions, see Fig. 1a: (a) the traction at the free surface is zero; (b) displacement compatibility and traction equilibrium conditions at the boundary between each two layers are satisfied; (c) modeling of the seismic bed by homogeneous half-space with compatibility and equilibrium conditions for displacements and traction at the interface between the homogeneous and inhomogeneous part of the half-space; (d) exclusion of incoming waves into the inhomogeneous part of the half-space out of depth (seismic bed) in the case of absence of a seismic source embedded in homogeneous half-space (Sommerfeld radiation condition). The BVP is solved for a sufficient number of values of frequency and a numerical inverse fast Fourier transformation (FFT) is applied in order to obtain the time-dependent solution. The solution of the boundary-value problem is a vector-value function $u_i(x,z,\omega)$, which complies the Hölder continuity on the boundary $\overline{Q}_B$ and satisfies the system (2) and the boundary conditions given above.

3. Hybrid wavenumber integration — BIE method

3.1. The essence of the hybrid approach

The hybrid WNI-BIEM computation scheme is subdivided into two steps. In the first step, the background 1D-wave field $u_i^{\rm fr}$, $p_i^{\rm fr}$ in the stack of horizontal, isotropic layers due to a seismic source in one of them is computed. Complete seismograms are stored at the selected locations along an excitation boundary $\Lambda^{\rm excitation}$, see Fig. 1b. The quantities of $u_i^{\rm fr}$, $p_i^{\rm fr}$ are named "*free-field motion*" in [23,34,46], "*background wave*" in [17], "*source radiation and wave propagation in the background 1D medium*" in [47], "*mean wave field obtainable as the response solution for the layered half-space without the lateral inhomogeneity*" in [48,49]. In spite of the used different notations, the mechanical sense is one and the same. It is a wave field corresponding to the 1D medium with no additional local 2D heterogeneity. The 1D model usually represents a stack of flat layers overlaying a half-space, see [47]. This is true in our case, also. Background model solution is the response solution for the horizontally layered half-space *without the lateral inhomogeneity* $\Omega_{\rm LGR}$ and *subjected to seismic waves radiate from the seismic source*, see Fig. 1b. It satisfies the elastodynamic wave equation and the following boundary conditions: (a) tractions are zero on the flat free surface; (b) displacement compatibility and traction equilibrium conditions at the boundary between each two flat layers are satisfied; (c) modelling of the seismic bed by homogeneous half-space with displacement compatibility and traction equilibrium conditions at the interface between the homogeneous and inhomogeneous part of the half-space; (d) exclusion of incoming waves into the inhomogeneous part of the half-space out of the depth (seismic bed) in the case of absence of a seismic source embedded in the homogeneous part of the half-space (Sommerfeld radiation condition). The near-surface local geological $\Omega_{\rm LGR}$ region is situated entirely inside the excitation domain which is bounded by the excitation boundary $\Lambda^{\rm excitation}$ and the free surface, see Fig. 1c. In [17–21], the authors named it the excitation box. The seismic source is placed outside the excitation region, see Fig. 1a,b. Inside the excitation region, the medium surrounding the local geological region $\Omega_{\rm LGR}$ has the same mechanical properties as in the background field calculation. The free field motion (the background) part is calculated by WNIM, described shortly below. In the second step the seismic source is no longer present and the medium is truncated in a domain comprising the area inside the excitation region and outside the excitation boundary $\Lambda^{\rm excitation}$ in its close vicinity, see Fig. 1c. The second step modelling comprises detailed local structure with the strongest inhomogeneity and occupies only a fraction of the background model considered in the first step, see [17–21]. The BIEM computes simultaneously the total (complete) wave field $u_i^{\rm total}$, $p_i^{\rm total}$ in the interior of the excitation region and the scattered $u_i^{\rm sc}$, $p_i^{\rm sc}$ wave field outside the excitation boundary $\Lambda^{\rm excitation}$. The quantities of $u_i^{\rm sc}$, $p_i^{\rm sc}$ are named "*diffracted waves*" in [34–43,46], "*residual field*" in [17,18,23] and "*scattered wave field called also perturbation due to the lateral inhomogeneity*" in [48,49]. In spite of the used different notations, the mechanical sense is one and the same and it is the scattered by the local inhomogeneity wave. The scattered wave field is defined by the difference $u_i^{\rm sc}=u_i^{\rm total}-u_i^{\rm fr}$, $p_i^{\rm sc}=p_i^{\rm total}-p_i^{\rm fr}$. The complete wave field inside the excitation region (internal problem) and the scattered wave field outside the excitation boundary (external problem) are computed by the BIEM simultaneously. These fields are coupled by means of the boundary conditions relating $u_i^{\rm total}$, $p_i^{\rm total}$ on the inner side of the excitation boundary with scattered wave $u_i^{\rm sc}$, $p_i^{\rm sc}$ on the outer side of the boundary, satisfying the welded contact. The saved and recorded background wave field in the first step $u_i^{\rm fr}$, $p_i^{\rm fr}$ is used as "implemented" boundary conditions on the excitation boundary to generate the wave field as if it enters the excitation region outside. The truncation of the background model is an approximation that neglects interaction of the scattered wave with cropped parts of the 1D model (stack of horizontal, isotropic layers) as deeper layers. The obtained solution does not contain information about the interactions between the residual wave field and the structural features deeper than the BIEM domain, see [17–21]. The excitation domain is chosen to encompass the local structure of interest. The outside of the excitation domain with further interfaces and inhomogeneities is truncated and only the necessary volume defined after validation study is left.

Please cite this article as: F. Wuttke et al., Seismic wave propagation in laterally inhomogeneous geological region via a new hybrid approach, *Journal of Sound and Vibration* (2010), doi:10.1016/j.jsv.2010.08.042

So, the truncation limits the interactions between the structure of interest and the outer medium to the interaction with contents of the incoming background wave field, i.e. it may include surface and body waves influenced by the source, wave path and the structure around (in close vicinity of) the excitation domain. The multiple reflections of the scattered wave between the local structure of interest inside the excitation domain and the regional structure outside it can be modelled properly by the optimal choice of the truncated domain based on the validation study.

3.2. WNIM–BIEM coupling

The key point of the hybrid method is the presentation of the total wave field by a sum of the free field (background) and the scattered parts: $u_i^{\text{total}}=u_i^{\text{fr}}+u_i^{\text{sc}}$, $p_i^{\text{total}}=p_i^{\text{fr}}+p_i^{\text{sc}}$. The total wave field is inside the excitation domain, while the scattered wave field is propagating outside of the excitation domain. The boundary conditions relating the total wave field on the inner side of the excitation boundary with scattered wave *on the outer side of the boundary*, *satisfying the welded contact*. The hybrid coupling keeps the excitation boundary fully transparent in the second step. The scattered wave field penetrates freely out of the excitation domain and, if reflected by an inhomogeneity, it freely propagates through the excitation boundary back into the local structure. Oprsal et al. [19] discussed clearly the essence of the generalized hybrid approach of wave injection based on binding two sub-volumes treated by arbitrary wave propagation methods. The decomposition of the total wave field into a sum of free field motion and the scattered wave is commented in the same manner in [60] for the case of the seismic response of a foundation rested in a non-homogeneous half-space.

3.3. WNIM solution for free field wave motion u_i^{fr},p_i^{fr}

In the first step, the seismic source radiation and wave propagation in the horizontally layered background medium Ω_0 is calculated by the WNIM, and the computed background wave field $\mathbf{U}^{\mathbf{fr}}$ (called free-field) is recorded along the excitation boundary $\Lambda^{\text{excitation}}$, see Fig. 1b. The WNIM solves the problem for wave propagation in horizontally layered media with a seismic source at a given level $z=S$ and rested on homogeneous half-space, where radiation condition is satisfied. The unknowns are displacements $u_i^{l,\text{fr}}(x,z,t)$ and traction $p_i^{l,\text{fr}}(x,z,t)=\sigma_{ij}^{l,\text{fr}}n_j$ in each lth layer, where $i=x,z$. The basic equations (1) are decoupled by application of the Helmholtz decomposition theorem into potentials, see [8]. Since the elastic properties do not depend on horizontal position, we use the Fourier transforms over time and the horizontal coordinate to reduce the partial differential equations of motion to a set of ordinary differential equations according to the displacement $\mathbf{u}^{l,\text{fr}}(\zeta,z,\omega,S)$ and stress $\mathbf{\Sigma}^{l,\text{fr}}(\zeta,z,\omega,S)$ vectors which depend on the frequency ω , wavenumber ζ, location of the observer z and source depth S. After applying the inverse Fourier transformation to the wavenumber ζ, unknown displacement and stresses are obtained in the frequency-space domain. The frequency-domain formulation is based on the representation of the complete response in terms of semi-infinite integrals with respect to the wavenumber. The integrands for each wavenumber and frequency are determined by an efficient factorization in terms of generalized transmission and reflection coefficients which are calculated by an iterative scheme. As far as we consider the case, when the lateral inhomogeneous soil deposit is situated in the first layer of the horizontally layered half-space (see Fig. 1a) we need the WNIM solutions for displacement $\mathbf{u}^{l,\text{fr}}(x,z,\omega)$ and stress $\mathbf{\Sigma}^{l,\text{fr}}(x,z,\omega)$ vectors in the first layer $l=1$. Following notation and mathematical description in [9,10,52,54,55,70], these analytical expressions are given as follows:

$$\mathbf{u}^{1,\text{fr}}(x,z,\omega,S)=\frac{1}{2\pi}\int_{-\infty}^{\infty}(\mathbf{E}_{11}^1\mathbf{\Lambda}_d^1\widehat{\mathbf{R}}_u^0+\mathbf{E}_{12}^1\mathbf{\Lambda}_u^1)\widehat{\mathbf{T}}_u^1\widehat{\mathbf{T}}_u^2\ldots\widehat{\mathbf{T}}_u^{S-1}(\mathbf{B}^{S+}\mathbf{D}^S-\mathbf{B}^{S-})^{-1}\Delta\mathbf{Q}\mathrm{e}^{(\mathrm{i}\zeta x)}\,\mathrm{d}\zeta \tag{3}$$

$$\mathbf{\Sigma}^{1,\text{fr}}(x,z,\omega,S)=\frac{1}{2\pi}\int_{-\infty}^{\infty}(\mathbf{E}_{21}^1\mathbf{\Lambda}_d^1\widehat{\mathbf{R}}_u^0+\mathbf{E}_{22}^1\mathbf{\Lambda}_u^1)\widehat{\mathbf{T}}_u^1\widehat{\mathbf{T}}_u^2\ldots\widehat{\mathbf{T}}_u^{S-1}(\mathbf{B}^{S+}\mathbf{D}^S-\mathbf{B}^{S-})^{-1}\Delta\mathbf{Q}\mathrm{e}^{(\mathrm{i}\zeta x)}\,\mathrm{d}\zeta \tag{4}$$

The integrands in Eqs. (3) and (4) are functions of wavenumber ζ and depend on the characteristics of the soil stratum, frequency, the depth of the seismic source and the location of the observer. In the above equations the generalized reflection/transmission (R/T) coefficients are denoted by $\widehat{\mathbf{R}}_u^l=\mathbf{R}_u^l+\mathbf{T}_d^l\widehat{\mathbf{R}}_u^{l-1}\widehat{\mathbf{T}}_u^l$ and $\widehat{\mathbf{T}}_u^l=(\mathbf{I}-\mathbf{R}_d^l\widehat{\mathbf{R}}_u^{l-1})^{-1}\mathbf{T}_u^l$, $l=1,\ldots,S-1$ for the layers above the source and $\widehat{\mathbf{R}}_d^l=\mathbf{R}_d^l+\mathbf{T}_u^l\widehat{\mathbf{R}}_d^{l+1}\widehat{\mathbf{T}}_d^l$ and $\widehat{\mathbf{T}}_d^l=(\mathbf{I}-\mathbf{R}_u^l\widehat{\mathbf{R}}_d^{l+1})^{-1}\mathbf{T}_d^l$, $l=M-1,\ldots,S$ for the layers below the source. For $l=M$ the generalized reflection coefficients are $\widehat{\mathbf{R}}_d^l=\mathbf{R}_d^M$ and $\widehat{\mathbf{T}}_d^M=\mathbf{T}_d^M$, where $\mathbf{R}_d^M$ and $\mathbf{T}_d^M$ are the modified R/T coefficients for the layer M. The index l of layers is running from 1 to M, and the seismic bed is homogeneous half-space and denoted by $M+1$. The term $\widehat{\mathbf{R}}_u^{l-1}=\widehat{\mathbf{R}}_u^0$ is the reflection coefficient at the free surface as the upper boundary of the first layer. The seismic line source in vertical or horizontal direction is described by the term $\Delta\mathbf{Q}=[-P_x,0]^T$ and $\Delta\mathbf{Q}=[0,-P_z]^T$, where P_x and P_z are unit line loads in horizontal and vertical directions. Matrix $\mathbf{I}$ describes the unit matrix, while the power of -1 means the inverse of a matrix. The matrices $\mathbf{E}$ contain the variables excluding exponents and amplitudes of the analytical solution for each layer. The matrix expressions for displacements and stresses are as follows:

$$\mathbf{u}^{l,\text{fr}}(\zeta,z,\omega)=\mathbf{E}_{11}^l\mathbf{\Lambda}_d^l\mathbf{C}_d^l+\mathbf{E}_{12}^l\mathbf{\Lambda}_u^l\mathbf{C}_u^l \tag{5}$$

$$\mathbf{\Sigma}^{l,\text{fr}}(\zeta,z,\omega)=\mathbf{E}_{21}^l\mathbf{\Lambda}_d^l\mathbf{C}_d^l+\mathbf{E}_{22}^l\mathbf{\Lambda}_u^l\mathbf{C}_u^l \tag{6}$$

Please cite this article as: F. Wuttke et al., Seismic wave propagation in laterally inhomogeneous geological region via a new hybrid approach, *Journal of Sound and Vibration* (2010), doi:10.1016/j.jsv.2010.08.042

where the terms $\mathbf{\Lambda}^l_{d/u}$ describe the wave propagation in positive (down) and negative (up) directions in the lth layer. The submatrices $\mathbf{\Lambda}^l_{d/u}$ and $\mathbf{E}^l_{ij}$, i=1,2, j=1,2, are functions of shear modulus μ^l, shear β^l and compressional α^l wave velocities, wavenumber ζ, frequency ω and $z \in (z^{l-1}, z^l)$. The terms $\mathbf{C}^l_{Pd/Pu}$ and $\mathbf{C}^l_{Sd/Su}$ are the unknown constants of the solution of the ordinary differential equation, in the lth layer that describe up and down going P- and SV-wave propagation, see [9,53]. The quality factor or its inverse the dissipation factor describing the material attenuation in soil is defined by the material damping ratio that in the numerical studies here is assumed to be depth dependent. For layers embedded in a depth smaller than 1 km the material damping ratio is 1%, in a depth between 1 and 5 km the material damping ratio is 0.5% and for layers in a depth more than 5 km the damping ratio is 0.25%. By following the definition of the complex velocities [9], the singular points of the integrals in Eqs. (5) and (6) are shifted slightly from the wavenumber real axis in the complex plane. The numerical integration along the real wavenumber axis can be done without singularities. Finally, the displacement function in the frequency and space domain is obtained after integration over all wavenumbers along the integration path. The displacements in the time and space domain are obtained by inverse Fourier transformation procedure.

3.4. BIEM solution in the second step

In this second step, the BIEM computes simultaneously the total (complete) wave field in the interior of the excitation region and the scattered wave field outside the excitation boundary. The following system of boundary integral equations according to the total wave field is satisfied along the boundaries of the layers inside the excitation region:

$$C_{ij}u_i(x,z,\omega) = \int_{\Omega_m} U^*_{ij}(x,z,x_0,z_0,\omega)p_j(x_0,z_0,\omega)\,\mathrm{d}\Gamma - \int_{\Omega_m} P^*_{ij}(x,z,x_0,z_0,\omega)u_j(x_0,z_0,\omega)\,\mathrm{d}\Gamma \tag{7}$$

m=1,2,3,…,N here, and C_{ij} are the constants depending on the geometry at the collocation point (x,z); (x_0,z_0) denotes the position vector of the source point; Γ_{Ω_m} is the boundary of the Ω_m layer; u_i and p_j are the unknown total displacements and tractions on the boundaries Γ_{Ω_m}; U^*_{ij}, P^*_{ij} are the displacement and traction frequency-dependent fundamental solutions of Eq. (2), given in [50]. The BIE on the external boundary $\Lambda^{\text{external}}$ is added and it is according to the scattered wave field, which in this case is $u_i^{\text{sc}}=u_i^{\text{total}}-u_i^{\text{fr}}$, $p_i^{\text{sc}}=p_i^{\text{total}}-p_i^{\text{fr}}$.

$$C_{ij}(u_j^{\text{total}}(x,z)-u_j^{\text{fr}}(x,z))|_{\Lambda^{\text{external}}} = \int_{\Lambda^{\text{external}}} U^*_{ij}(x,z,x_0,z_0,\omega)(p_j^{\text{total}}(x_0,z_0)-p_j^{\text{fr}}(x_0,z_0))\,\mathrm{d}\Gamma - \int_{\Lambda^{\text{external}}} P^*_{ij}(x,z,x_0,z_0,\omega)(u_j^{\text{total}}(x_0,z_0)-u_j^{\text{fr}}(x_0,z_0))\,\mathrm{d}\Gamma \tag{8}$$

The system of BIE (7) and (8) is according to the unknown displacement u_i^{total} and traction p_i^{total} on the boundaries of the layers in the local geological structure, on the boundary of the excitation region and on the observer points on the free boundary. In order to solve this system of BIEs we need to know the free field motion u_i^{fr}, p_i^{fr} at the boundary nodes on the external boundary $\Lambda^{\text{external}}$. The values for u_i^{fr}, p_i^{fr} in the boundary nodes on $\Lambda^{\text{external}}$ are obtained as solution of the background problem by WNIM. The usual numerical procedure of BIEM is applied. The boundary is discretized into elements using piecewise polynomial approximations of the boundary geometry, displacement and traction. The mesh discretization is made via the quadratic boundary element method. After discretization, in the Fourier transformed domain the kernels of the obtained integrals have singularities like (a) $O(1/c\pm\xi)$, for $c\in[-1;+1]$ that lead to the *Cauchy principal value* (CPV) integrals and (b) singularities like $O(\ln(c\pm\xi))$ for $c\in[-1;+1]$ that lead to non-singular integrals. The regular integrals are computed employing the Gaussian 32-point quadrature scheme and boundary element subdivision, while the singular integrals are solved analytically, using the asymptotics of the fundamental solutions for small arguments, see [51]. After application of discretization procedure, the system of boundary integral equations is transformed into an algebraic system for the unknown displacement and traction in the Fourier domain. To obtain displacements and tractions as functions of time, the inverse Fourier transformation is applied.

4. Validation study

The aim of the validation study is to establish the error bounds of the proposed hybrid tool and to evaluate its accuracy on the base of solution of several benchmark examples. The validation of the proposed hybrid solution is based on the comparison to pure analytical or numerical methods or other hybrid computational techniques. The first example validates the proposed hybrid WNI-BIEM technique by solution of specially selected benchmark example which can be solved by the pure analytical methods and by the proposed hybrid method. The second and the third numerical examples validate the accuracy of the BIEM that is one of the base components of the proposed hybrid technique.

The fourth test example concerns comparison of the numerical results obtained by the proposed WNI-BIEM with two other hybrid techniques as modal summation-BIEM (MS-BIEM) and modal summation-finite difference method (MS-FDM).

Test example 1. As a first test example a structural model given in Fig. 2a is used.

The local geological region Ω_{LGR} in Fig. 2a is a valley $L_1R_1T_1P_1$ and it is situated in the first layer of a layered half-space. The coordinates of the corner points (in meters) are: $T_1(100,0)$, $P_1(-100,0)$, $L_1(110,270)$, $R_1(-110,270)$. The mechanical properties of the local geological region are the same as the first layer in the horizontally layered half-space. In this case it

Please cite this article as: F. Wuttke et al., Seismic wave propagation in laterally inhomogeneous geological region via a new hybrid approach, *Journal of Sound and Vibration* (2010), doi:10.1016/j.jsv.2010.08.042

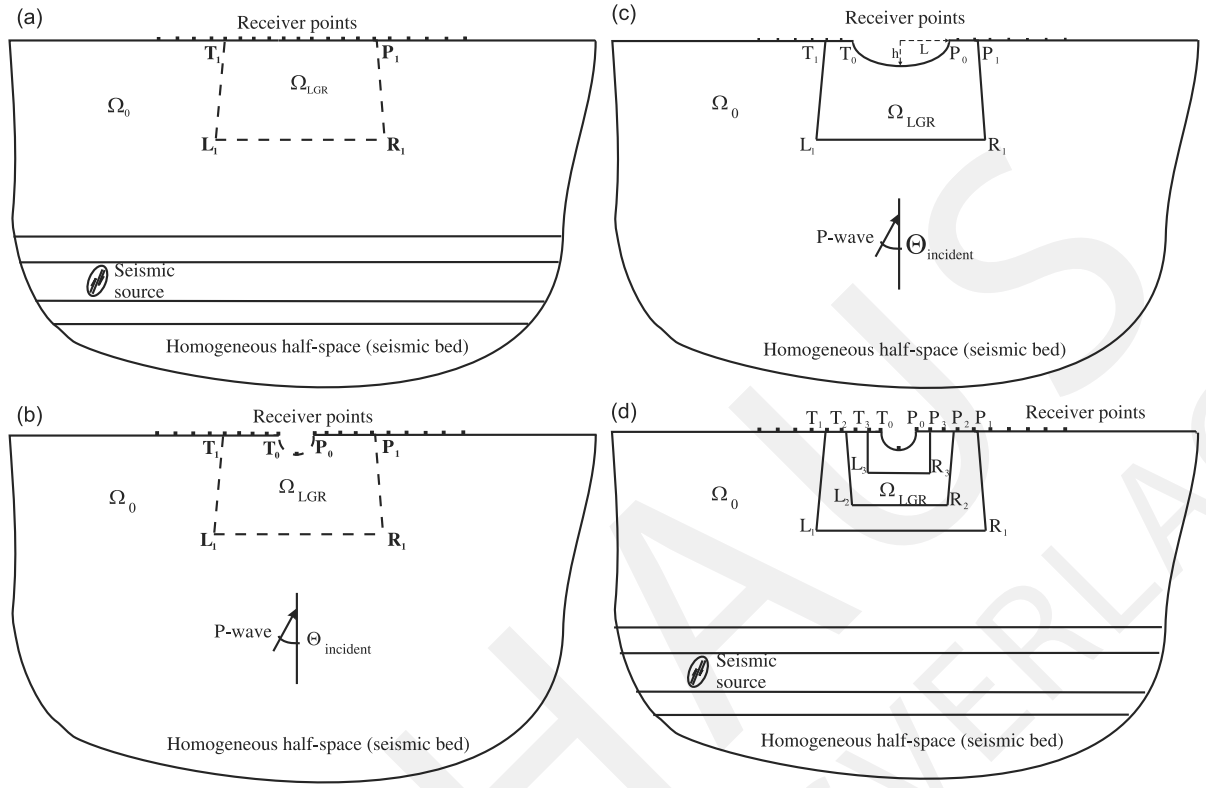

Fig. 2. The geometry of the numerical examples: (a) test example 1; (b) test example 2; (c) test example 3; (d) test example 4.

is possible to solve the problem by both methods—by the pure WNIM and by the proposed hybrid WNI-BIEM. The comparison between studied hybrid solutions against pure WNIM results can evaluate and place the accuracy bounds of the developed hybrid computational technique. The same validation philosophy can be seen in [14], where the proposed hybrid modal summation-finite difference method (MS-FDM) is verified by solution of the background 1D model (background model is the same as in our case: horizontal flat layers with a seismic source in one of them) by both the pure analytical modal summation method (MSM) and the hybrid MS-FDM. The density ρ_i, the longitudinal wave velocity α_i, the shear wave velocity β_i and the depth of the layers presenting a non-homogeneous in depth half-space are given in Table 1. Two wave paths (1 and 2) are considered with different mechanical properties. A buried vertical line source is defined in wave path 1 at $x=2$ km and at a depth of 2 km and in wave path 2 at $x=2$ km and at a depth of 6 km. Figs. 3a–h show that frequency-dependent displacement components at receiver point (0, 0), obtained by the WNIM and by the hybrid computational tool, are almost identical for both wave paths. The hybrid numerical scheme perfectly replicates the background wave field and this fact demonstrates that the proposed hybrid method works accurately. It is necessary to execute the validation study for each new seismic scenario, because the comparison between the pure analytical method and the proposed hybrid method allows establishing control over the accuracy of the BIEM part of calculations that depends on the correct mesh discretization. The accuracy condition in the BIEM discretization procedure requires that $(\lambda_S/l_{\mathrm{BE}}) \geq 10$, where l_{BE} is the length of the boundary element, λ_S is the shear wavelength. So, special attention is needed at high frequencies and for very soft soil layers, where the wave length is small. It is clear that to reach high-numerical accuracy in these cases a very fine BEM mesh is necessary.

Test example 2. The elastic half-plane with surface topography subjected to incident longitudinal time-harmonic P-wave.

In this test example, the pure BIEM is used to compute the free surface displacement components in a homogeneous half-plane with surface topography in the form of circular cylindrical canyon subjected to incident longitudinal P-wave. This problem was solved analytically in [56] for cylindrical canyons with variable width-to-depth ratios. In particular, we focus on the case where this ratio is equal to 1.0, the incident wave angle is 60°, Poisson's ratio for the homogeneous half-plane is 0.25, longitudinal wave velocity is of 5277 m/s, the value of the dimensionless parameter $\eta = 2A/\lambda_s$ is 0.25, where $r=A$ is the canyon radius. Fig. 2b shows the geometry of this analyzed example. The local geological region is the trapezoidal value $T_1P_1L_1R_1$ that is as those in the test example 1, but on the free surface there is a semi-circular canyon and the prescribed material properties are the same as in the homogeneous half-space, considered in this case. This example evaluates the convergence of the BIEM solution by comparison of the authors' results with the analytical solution in [56]. The necessary accuracy was reached at discretization mesh of 64 boundary elements of quadratic type and Figs. 4a and b show comparison of the surface displacement

Please cite this article as: F. Wuttke et al., Seismic wave propagation in laterally inhomogeneous geological region via a new hybrid approach, *Journal of Sound and Vibration* (2010), doi:10.1016/j.jsv.2010.08.042

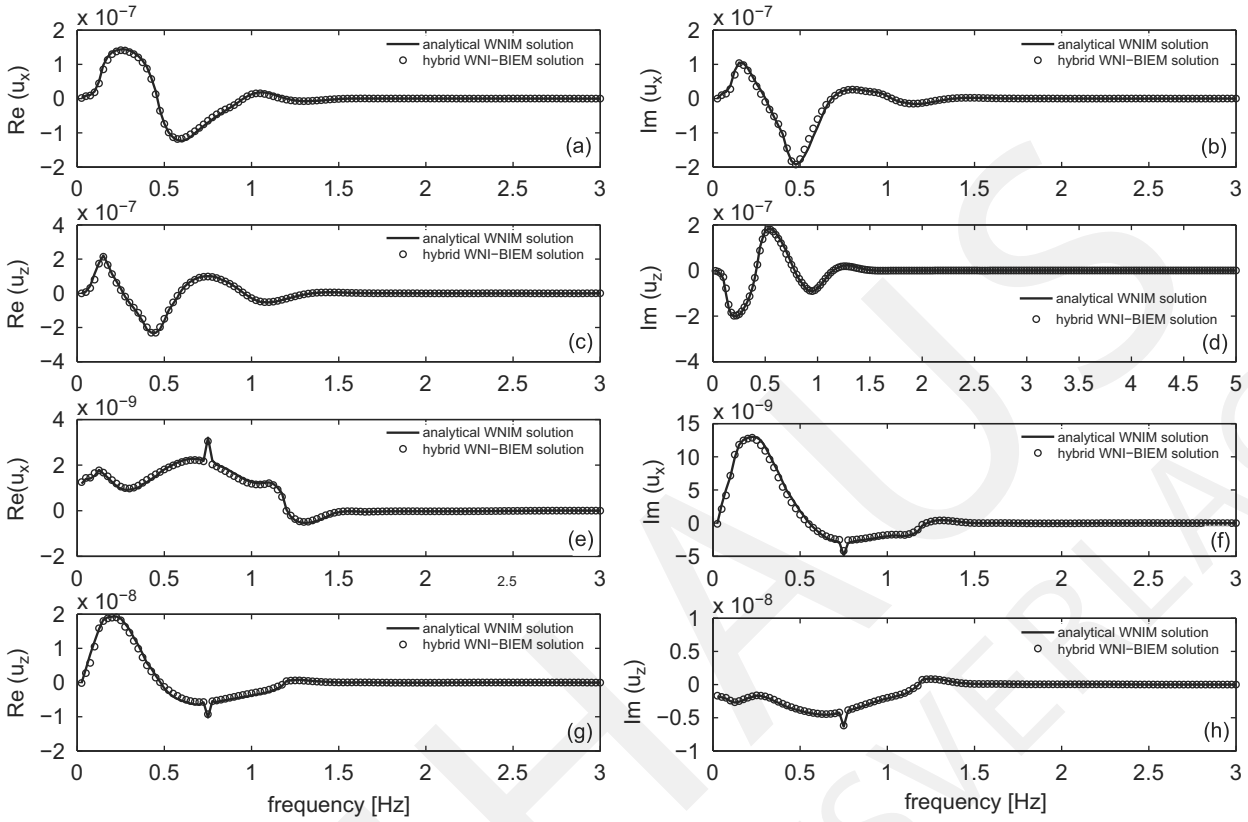

Fig. 3. Real and imaginary part of displacement components vs frequency at receiver point (0, 0): (a)–(d) for wave path 2; (e)–(h) for wave path 1.

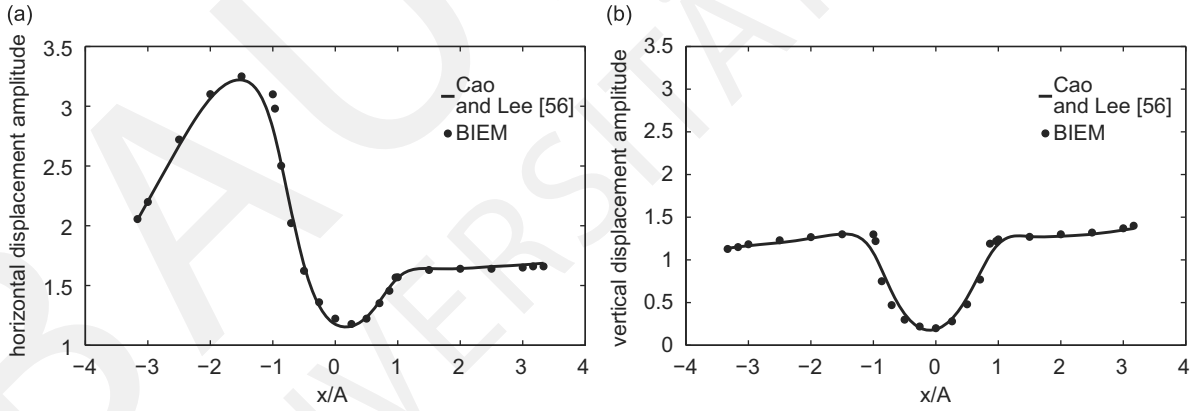

Fig. 4. Surface displacement amplitudes vs x/A on the free surface of homogeneous half-space with a circular canyon of radius $r=A$ under incident longitudinal P-wave: (a) horizontal component; (b) vertical component.

components obtained by BIEM and in [56] vs value of x/A. The both results are very close and this shows that the BIEM works accurately and the chosen discretization mesh gives the convergence results. The similar validation strategy aiming to evaluate the accuracy of other hybrid technique, the hybrid finite element-boundary element method (FE-BEM), was solved in [39], where the diffraction of a plane SV wave of vertical incidence by a semi-circular canyon in an elastic half-space is considered. However, according to the authors, the validation study of the proposed here hybrid WNI-BIEM should be completed by considering more complex benchmark example for a finite soil stratum with non-parallel interfaces situated in an inhomogeneous in depth part of the half-space and this is done in the test examples 3 and 4 as follows.

Test example 3. A semi-elliptical valley rested in a homogeneous half-space subjected to incident longitudinal time-harmonic plane P-wave, see Fig. 2c.

Please cite this article as: F. Wuttke et al., Seismic wave propagation in laterally inhomogeneous geological region via a new hybrid approach, *Journal of Sound and Vibration* (2010), doi:10.1016/j.jsv.2010.08.042

There is no exact solution for this benchmark example. In [57,58] are presented BIEM results for two-dimensional case of a semi-elliptical valley with half-width L, depth h, shape ratio h/L, shear wave velocity in the valley v_s^{valley} situated in a homogeneous half-space with shear wave velocity $v_s^{\text{half-space}}$ and subjected to P- and SV-time-harmonic waves with prescribed incident angle Θ, frequency ω and unit amplitude. Soil is assumed to be isotropic, homogeneous and linear elastic. The contact between valley and half-space is assumed to be perfectly bonded. Comparison between results obtained by Fishman and Ahmad [58] and the BIEM authors' results is presented in Figs. 5a,b in order to evaluate the accuracy of the one of the base tools build up the proposed hybrid technique. Parameters are as follows: dimensionless frequency $\eta = \omega L/\pi v_s$ is 0.5, shape ratio h/L is 0.5, $v_s^{\text{half-space}} = 2v_s^{\text{valley}}$, Poisson's ratio is $\frac{1}{3}$, mass density ratio is $\rho^{\text{valley}}/\rho^{\text{half-space}} = \frac{2}{3}$, incident angle according to axis Oy is $\Theta = 0^\circ$. The displacement amplitude at the free surface is plotted

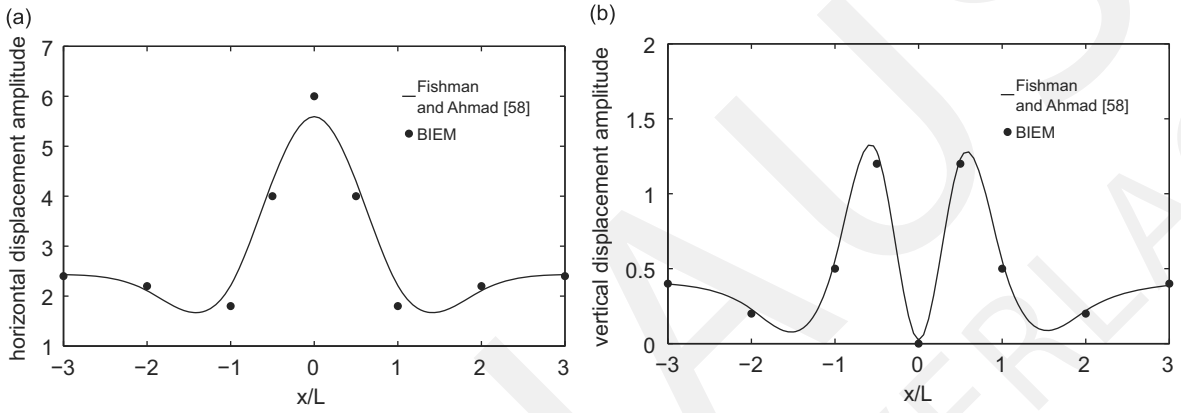

Fig. 5. Displacement amplitudes u_x (case a) and u_z (case b) on the surface of a semi-elliptical valley with shape ratio h/L = 0.5 rested in homogeneous half-space vs dimensionless distance x/L for dimensionless frequency $\eta = 0.5$ at normal incident longitudinal P-wave.

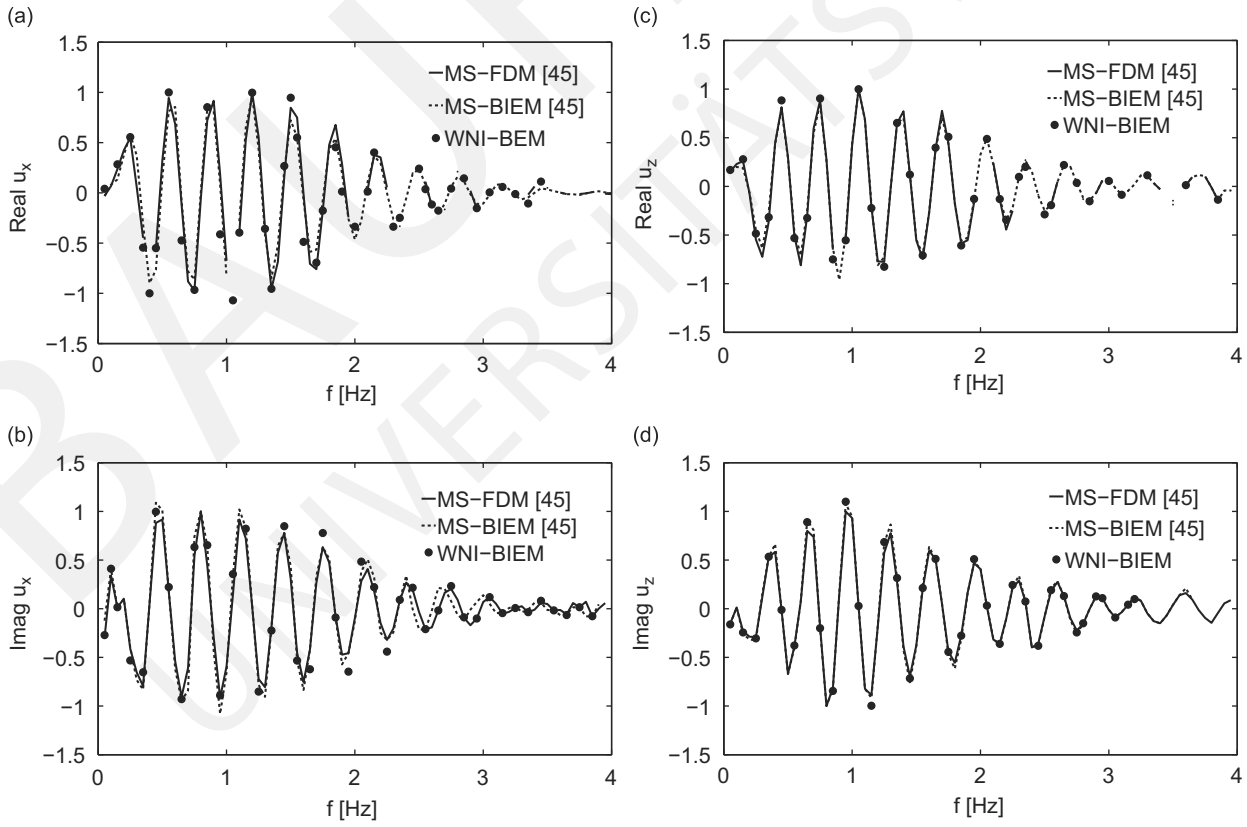

Fig. 6. The real and imaginary part of the displacement components u_x (a, b) and u_z (c, d) obtained by the MS-FDM [45], the MS-BIEM [45] and the WNI-BIEM in the frequency domain at receiver point (0, 30).

Please cite this article as: F. Wuttke et al., Seismic wave propagation in laterally inhomogeneous geological region via a new hybrid approach, *Journal of Sound and Vibration* (2010), doi:10.1016/j.jsv.2010.08.042

vs the dimensionless distance x/L. It is obvious that the obtained authors' results are in agreement with those obtained by Fishman and Ahmad in [58].

Test example 4. Seismic response of a finite local geological region with relief peculiarities and non-parallel layers rested in an inhomogeneous-in-depth half-space presented by a stack of flat horizontal layers with a seismic source in one of them.

The geometry of this benchmark example is given in Fig. 2d. The finite local soil stratum Ω_{LGR} is situated in the first layer of the half-space and it has three layers with non-parallel interfaces. There is a free-surface relief in the form of a semi-circular canyon of radius $r=A=30$ m. The coordinates of the points indicating the geometrical boundaries of the layers are: $T_0(30,0)$; $T_3(60,0)$; $T_2(90,0)$; $T_1(100,0)$; $P_0(-30,0)$; $P_3(-60,0)$; $P_2(-90,0)$; $P_1(-100,0)$; $L_1(110,270)$; $R_1(-110,270)$;

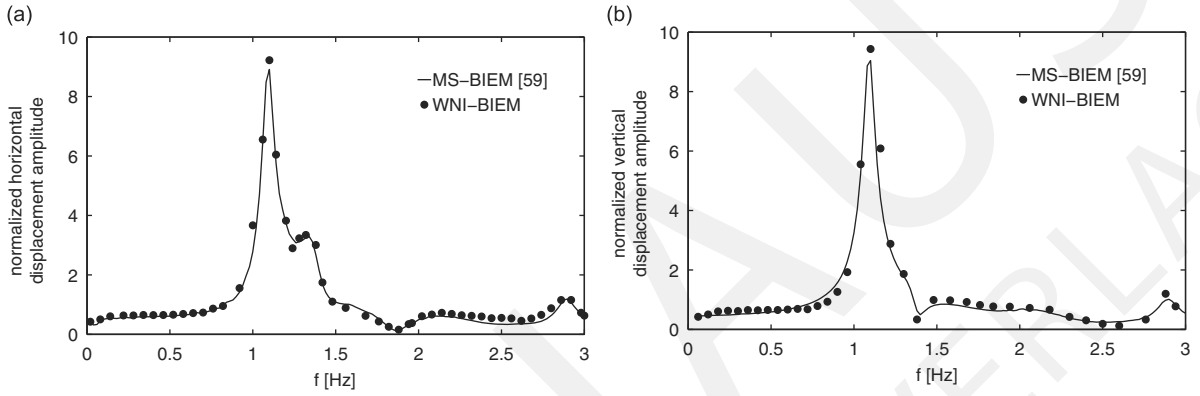

Fig. 7. Normalized displacement components obtained by MS-BIEM [59] and WNI-BIEM in the frequency domain at receiver point (−30, 0.0).

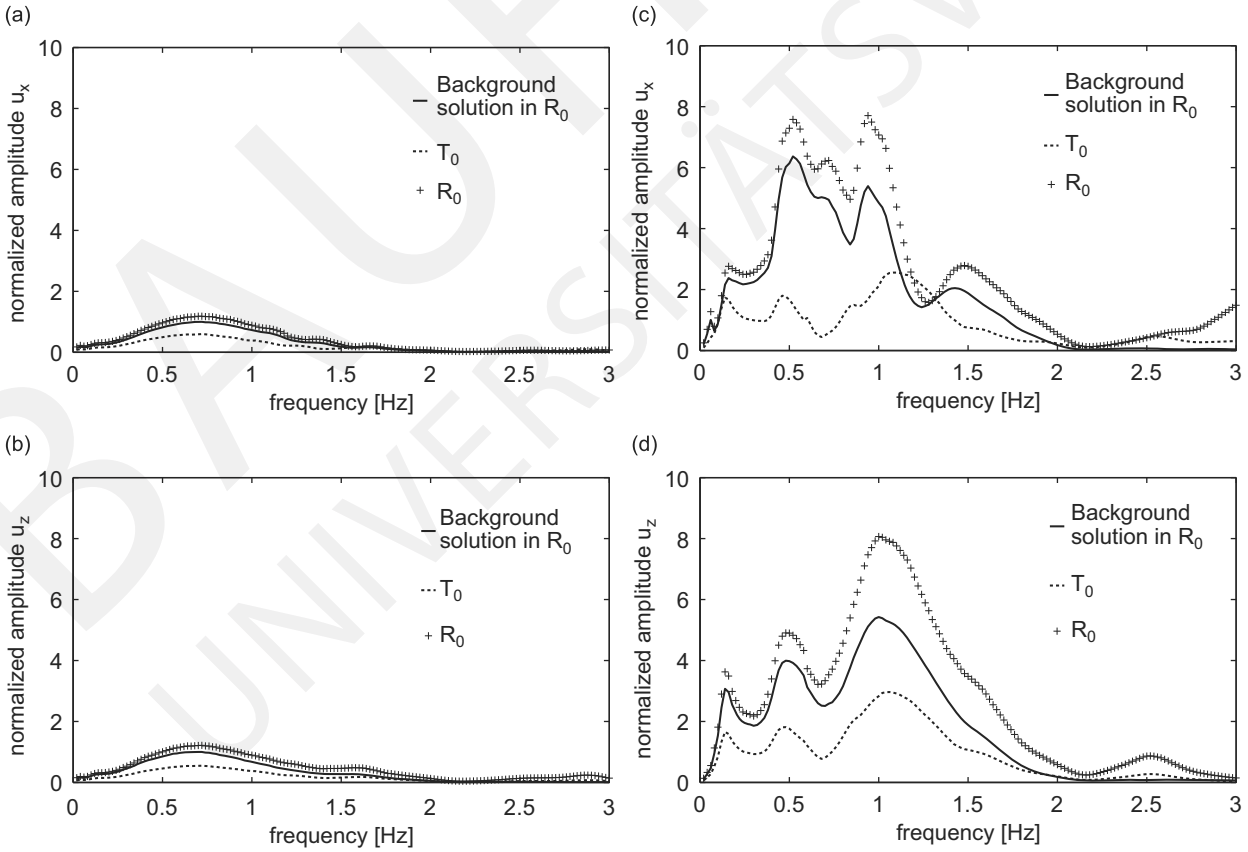

Fig. 8. Normalized displacement amplitudes vs frequency at receivers $T_0(30,0)$ and $R_0(0,30)$ for buried line seismic source at depth of 6 km and for two wave paths: (a) and (b) wave path 1; (c) and (d) wave path 2.

Please cite this article as: F. Wuttke et al., Seismic wave propagation in laterally inhomogeneous geological region via a new hybrid approach, *Journal of Sound and Vibration* (2010), doi:10.1016/j.jsv.2010.08.042

$L_2(90,180)$; $R_2(-90,180)$; $L_3(60,90)$; $R_3(-60,90)$. The mechanical properties of the background model are presented in Table 1a. The density ρ, longitudinal α and shear β wave velocities of the layers in Ω_{LGR} are as follows: $\rho_3 = 2400\,\mathrm{kg/m^3}$; $\alpha_3 = 5000\,\mathrm{m/s}$; $\beta_3 = 2900\,\mathrm{m/s}$; $\rho_2 = 2800\,\mathrm{kg/m^3}$; $\alpha_2 = 4500\,\mathrm{m/s}$; $\beta_2 = 2430\,\mathrm{m/s}$; $\rho_1 = 2800\,\mathrm{kg/m^3}$; $\alpha_1 = 5500\,\mathrm{m/s}$; $\beta_1 = 2970\,\mathrm{m/s}$. An instantaneous source corresponding to a pure double couple is in the half-space at depth of 2 km and epicentre distance of 10 km. The dip angle δ is 60°, the rake angle θ is 90° and the strike angle ϕ is 30°. The seismic moment of the source is taken to be 1×10^{13}N m. The discretization mesh consists of 170 quadratic boundary elements and the discretization along the boundaries T_1L_1, L_1R_1, R_1P_1 and T_0P_0 is the same as those at solution of the test examples 1 and 2. The same numerical example was solved in [45] by the usage of other two hybrid techniques as the modal summation-finite difference method (MS-FDM) and the modal summation-BIEM (MS-BIEM). The numerical results of the proposed WNI-BIE method are compared with the results presented in [45] and obtained by the usage of two different hybrid numerical schemes. Figs. 6a–d show the comparison of the solutions for normalized displacement components at the receiver point (0,30) (the bottom of the canyon) obtained by three different hybrid computational tools. The normalization is done by the maximal absolute value of the corresponding displacement component. These figures show very close solutions in the frequency domain. The shapes of the wavelets coincide for all three techniques and the differences in amplitudes are of the order of average percentage error about 8%. The test example with the same geometry is solved in [59] by the hybrid MS-BIEM with the data for the case study of the capital city of Bulgaria, Sofia. The bedrock model is with mechanical characteristics for the Sofia region [61], the seismic source is with the following characteristics: the dip angle δ is 44°, the rake angle θ is 309°, the strike angle ϕ is 21°, the magnitude is 3.7, the source depth is 12 km and the epicentre distance is 20 km. The mechanical constants of the layers in the local geological region are taken from [59] for a sandstone formation to: $\rho_3 = 1749\,\mathrm{kg/m^3}$; $\alpha_3 = 1582\,\mathrm{m/s}$; $\beta_3 = 969\,\mathrm{m/s}$; $\rho_2 = 1696\,\mathrm{m/s}$; $\alpha_2 = 486\,\mathrm{m/s}$; $\beta_2 = 300\,\mathrm{m/s}$; $\rho_1 = 2650\,\mathrm{kg/m^3}$; $\alpha_1 = 5700\,\mathrm{m/s}$; $\beta_1 = 3290\,\mathrm{m/s}$. Figs. 7a,b present a comparison between normalized seismograms obtained by both hybrid methods WBI-BIEM and MS-BIEM at receiver $(-30, 0)$ (the edge of the canyon). Normalization is made with respect to the amplitude of the corresponding displacement component of the bedrock reference regional model. Fig. 7 demonstrates that the results for the seismic response obtained by both hybrid methods are very close. The obtained results in the validation study show that the proposed hybrid WNI-BIEM works with high accuracy and we will use it in our simulation study presented in the following section. The created FORTRAN program code has the following parameters: at a fixed frequency the CPU time is 7 min, the peak memory is 3524K, for AMD Athlon (TM), 1.60 GHz, 512 MB RAM.

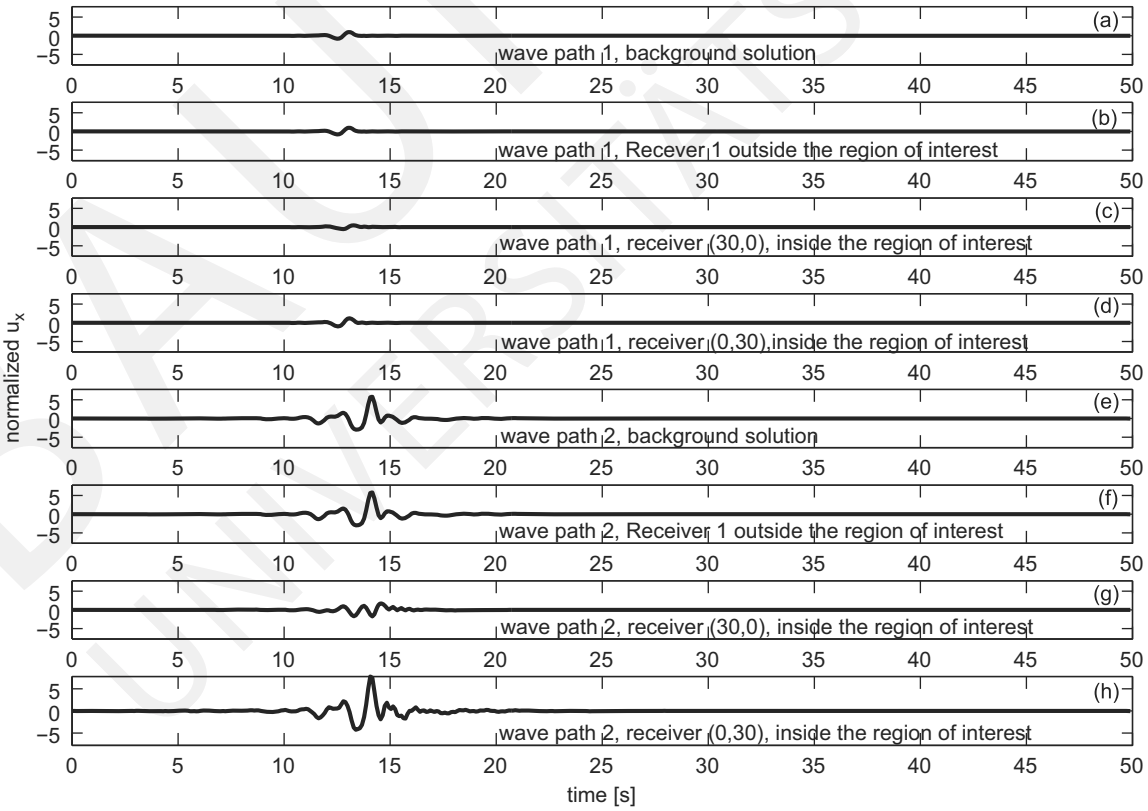

Fig. 9. Normalized horizontal displacement vs time at receivers $T_0(30,0)$ and $R_0(0,30)$ for buried line vertical seismic source at x=2 km, depth of z=6 km, and for two wave paths: (a)–(d) wave path 1; (e)–(h) wave path 2.

Please cite this article as: F. Wuttke et al., Seismic wave propagation in laterally inhomogeneous geological region via a new hybrid approach, *Journal of Sound and Vibration* (2010), doi:10.1016/j.jsv.2010.08.042

5. Numerical simulations

In order to illustrate the efficiency of the proposed hybrid method, the response of a multilayered region with geometry given in the test example 4 (Fig. 2d) is analyzed. Three types of the free-surface geometry relief are considered: (a) flat model; (b) semi-circle canyon with radius $r=A=30$ m; (c) semi-circle hill with radius $r=A=30$ m. The mechanical properties of the finite geological region are given in Table 2. The aim of the simulation study is to demonstrate that the synthetic signals, obtained through the proposed hybrid WNI-BIEM, depend on: (a) wave path inhomogeneity; (b) relief existence on the free surface; (c) mechanical properties of the local finite soil stratum and lateral inhomogeneity of the local geological region; (d) seismic source characteristics. Each one of these effects is considered and discussed below.

5.1. Sensitivity of the obtained synthetic seismic signals to the wave path properties

Canyon relief on the free surface of the local geological region is considered. Synthetic seismograms are obtained at two different wave paths 1 and 2 with properties given in Table 1a, b. The mechanical properties of the finite local stratum are given in Table 2. The main properties of the seismic source A are: a buried vertical line source is defined at $x=2$ km and a depth of 2 km or 6 km. The source term was assumed as a Ricker wavelet of the second order with time duration of 1.28 s and with an unit load. Two receiver points are considered: receiver $T_0(30,0)$ is the edge of the canyon and receiver $R_0(0,30)$ is the bottom of the canyon. Figs. 8a,b present the displacement amplitudes vs frequency at both receivers in the case of wave path 1. Figs. 8c,d display the same curves, but in the case of wave path 2. A comparison between the displacements in Figs. 8a,b with those in Figs. 8c,d shows the influence of wave path properties on the free surface's seismic signals. Fig. 8 demonstrates very clearly the existence of site effects and also their dependence on the type of the wave path inhomogeneity. The effect of site amplification is stronger in the case of wave path 2. The discussed simulation results demonstrate the sensitivity of the wave field to the wave path specific properties. Figs. 9 and 10 present the synthetic displacement signals in time domain. In both figures, the cases (a) and (e) present the background 1D solution, the cases (b) and (f) show the wave field in the Receiver 1 outside the excitation region, while the cases (c), (d), (g) and (h) show the wave field inside the region of interest. Receiver 1 is the first boundary node on the free surface outside the excitation region. As can be seen, the total wave field outside the region of interest replicates the background solution that demonstrate zero values of the scattered wave field outside the excitation region and this means that the minimal information about the interaction between the scattered wave field and the structural features deeper than

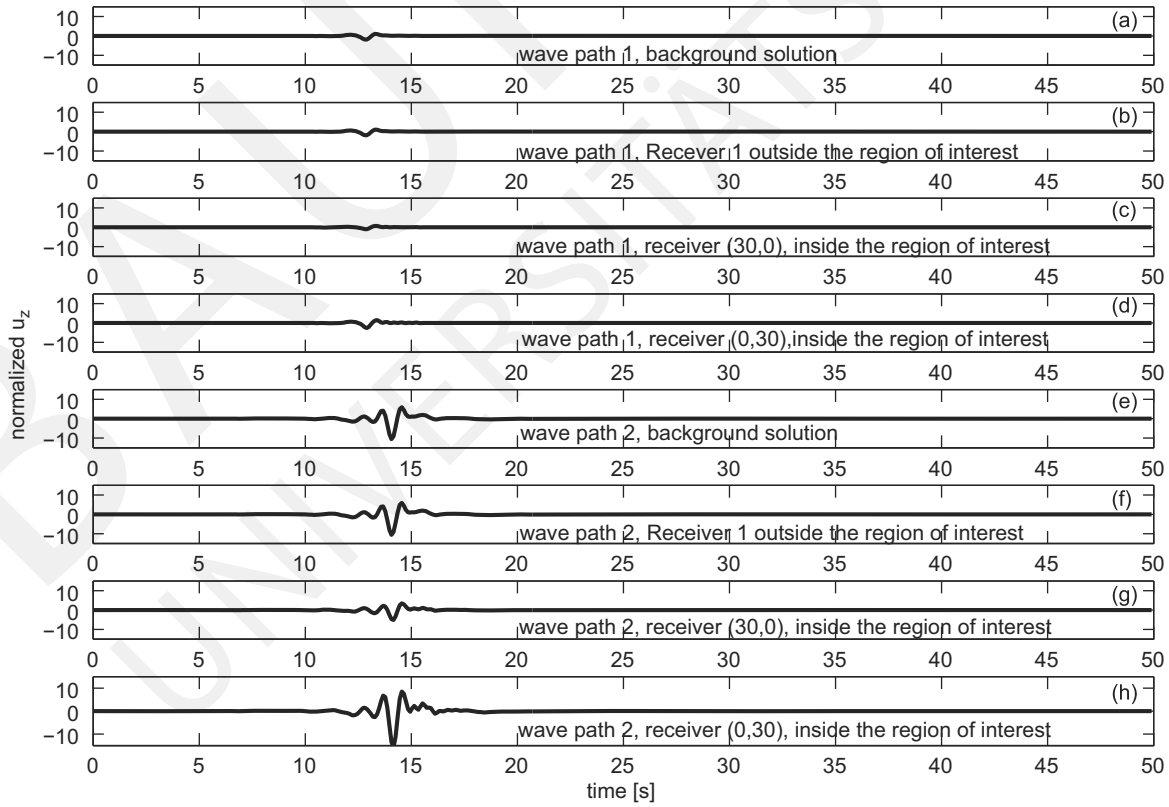

Fig. 10. Normalized vertical displacement vs time at receivers $T_0(30,0)$ and $R_0(0,30)$ for buried line vertical seismic source at $x=2$ km, depth of $z=6$ km, and for two wave paths: (a)–(d) wave path 1; (e)–(h) wave path 2.

Please cite this article as: F. Wuttke et al., Seismic wave propagation in laterally inhomogeneous geological region via a new hybrid approach, *Journal of Sound and Vibration* (2010), doi:10.1016/j.jsv.2010.08.042

the excitation region have been lost. Normalization in Figs. 8–10 is made with respect to the maximal amplitude of the corresponding displacement component, synthesized for the bedrock reference model (wave path 1). All results confirm the conclusion that wave path properties can dramatically change the character of the seismic signals.

5.2. Sensitivity of the obtained synthetic seismic signals to the free surface relief of the local geological region

The effects of surface geology can greatly enlarge the site response, exerting an important influence on the distribution of damage observed during earthquakes. In [62–64], the need of incorporating or reviewing parameters related to the local topography to account for topographical effects in the seismic response is pointed out. The role of lateral heterogeneity in

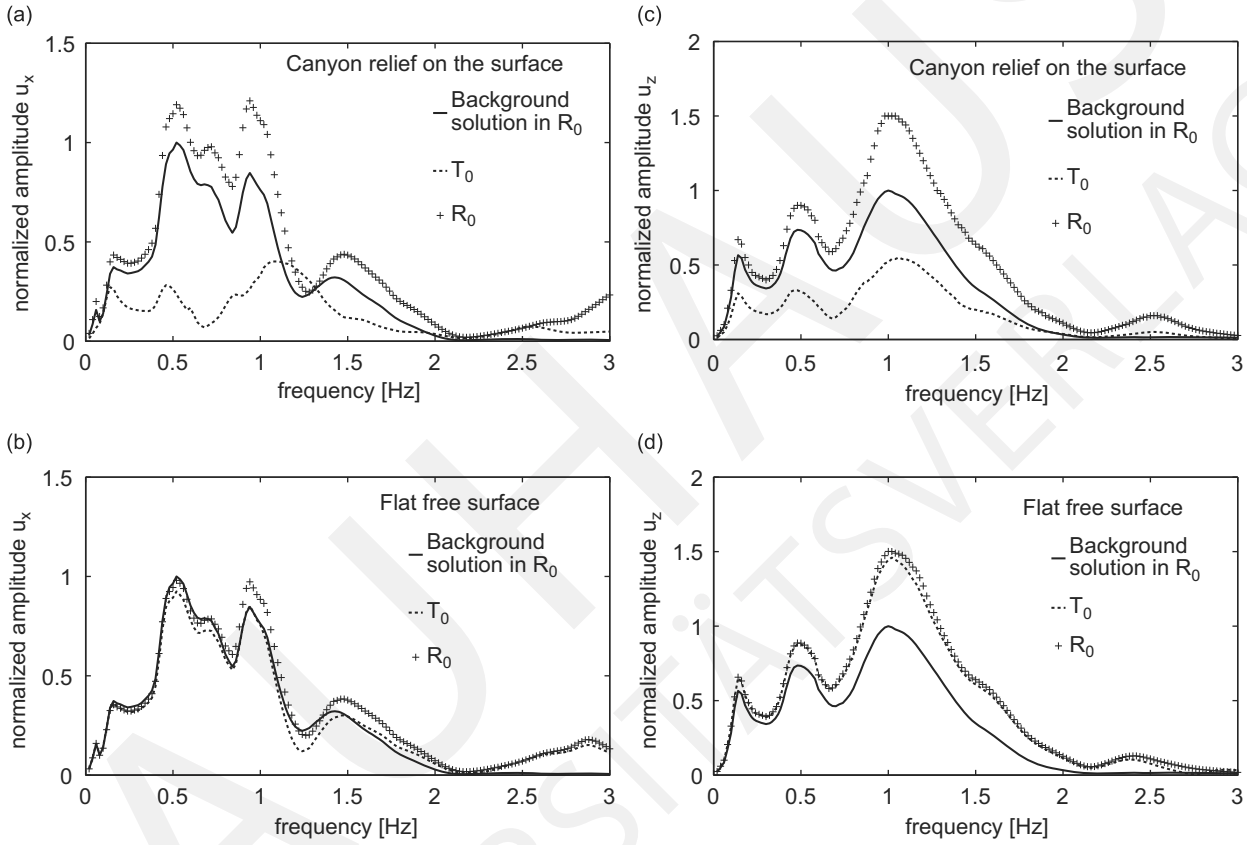

Fig. 11. Normalized displacement amplitude vs frequency at receivers $T_0(30,0)$, $R_0(0,30)$ on the free surface without and with canyon relief in the case of a buried line vertical seismic source at $x=2$ km, depth of $z=6$ km and wave path 2.

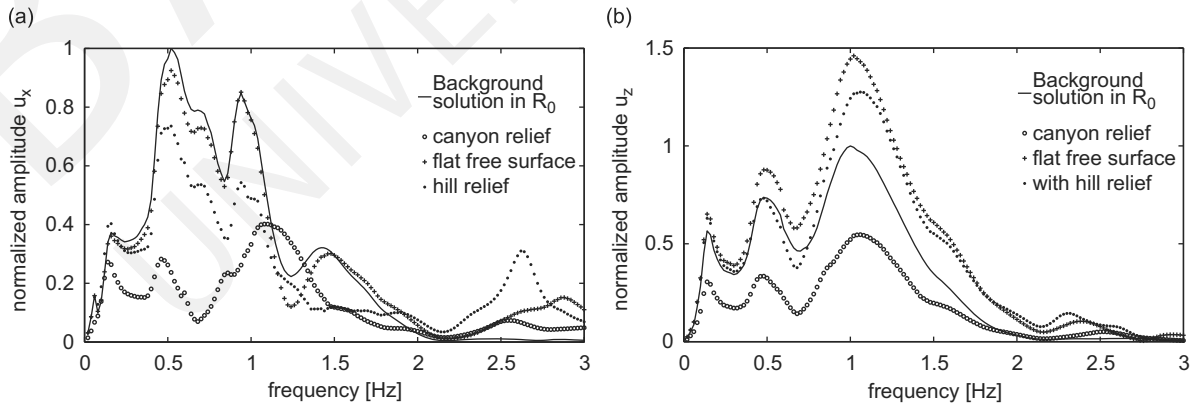

Fig. 12. Normalized displacement amplitude vs frequency at receiver $T_0(30,0)$ on the free surface without and with relief (canyon or hill) in the case of a buried line vertical seismic source at $x=2$ km, depth of $z=6$ km and wave path 2.

Please cite this article as: F. Wuttke et al., Seismic wave propagation in laterally inhomogeneous geological region via a new hybrid approach, *Journal of Sound and Vibration* (2010), doi:10.1016/j.jsv.2010.08.042

site effects, especially in small and shallow sedimentary basins has been observed in Coachella valley in California by [65], Parkway in New Zealand by [66], Colfiorito in Italy by [67,68]. The WNI-BIEM can show the influence of the relief on the computed seismic signals. Figs. 11 and 12 reveal the sensitivity of the seismic signals to the free surface relief.

The synthetic seismograms shown in Figs. 11 and 12 are obtained at wave path 2 and seismic source A at a depth of 6 km. The mechanical properties of the local soil region are given in Table 2. Three types of the free surface geometry are considered: (a) flat surface; (b) canyon relief; (3) hill-like relief, correspondingly. Normalization in Figs. 11–17 is made

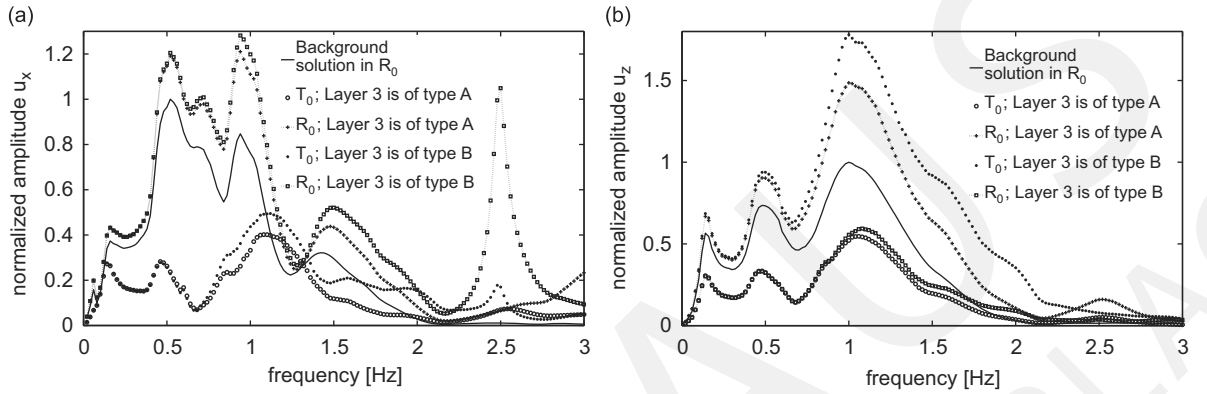

Fig. 13. Normalized displacement amplitude vs frequency at receivers $T_0(30,0)$, $R_0(0,30)$ on the free surface with canyon in the case of a buried line vertical seismic source at $x=2$ km, depth of $z=6$ km and wave path 2.

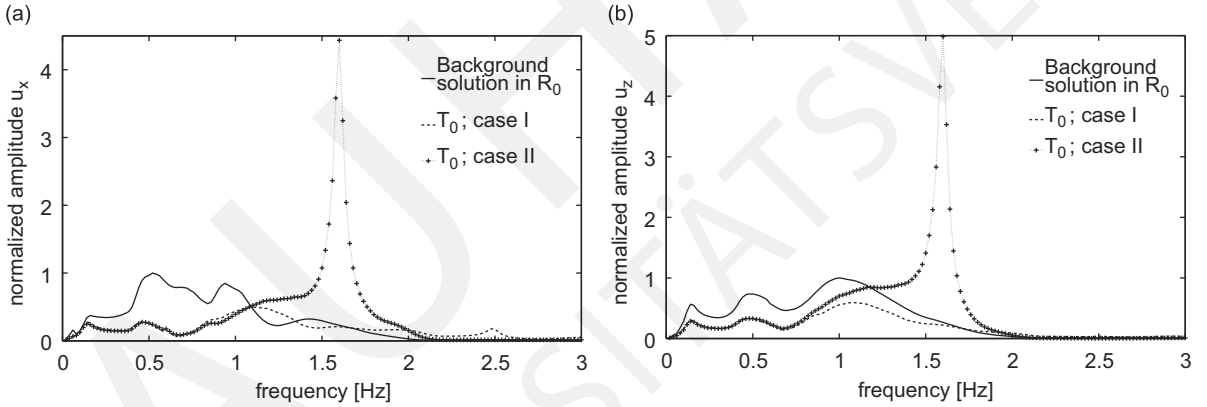

Fig. 14. Normalized displacement amplitude vs frequency at receiver $T_0(30,0)$ on the free surface of the local geological region with a semi-circle canyon in the case of a buried line vertical seismic source at $x=2$ km, depth of $z=6$ km and wave path 2 for two different cases I and II of the mechanical properties of the local soil stratum.

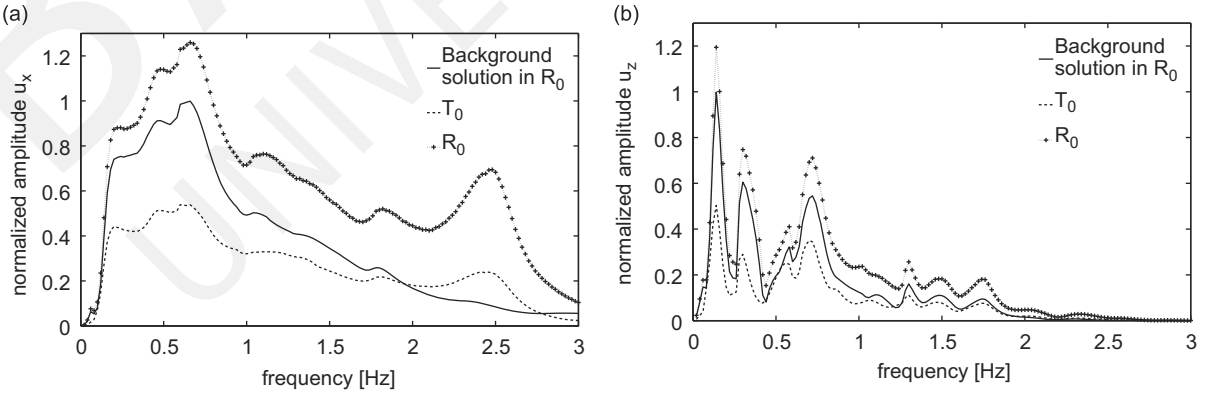

Fig. 15. Normalized displacement amplitude vs frequency at receivers $T_0(30,0)$, $R_0(0,30)$ on the free surface of the local geological region with a semi-circle canyon, at wave path 2 and a buried line vertical seismic source at $x=2$ km and depth of: (a) 2 km; (b) depth 6 km.

Please cite this article as: F. Wuttke et al., Seismic wave propagation in laterally inhomogeneous geological region via a new hybrid approach, *Journal of Sound and Vibration* (2010), doi:10.1016/j.jsv.2010.08.042

with respect to the maximal amplitude of the corresponding displacement component, synthesized for the bedrock reference model (wave path 2). Figs. 11a,b show the horizontal component of displacement amplitude in the case of local multilayered region with canyon relief and with flat free surface, correspondingly. Figs. 11c,d show the vertical component of displacement amplitude versus frequency for free surface with and without canyon relief. The discussed results reveal that the site effects are much stronger in the case of relief on the free surface, while in the case of flat free surface there is no clear presence of the site amplification. This can be explained with the complex diffraction wave picture in the case of canyon relief, i.e. with the well known edge effects. Figs. 12a,b compare the displacement amplitudes at receiver (30,0)

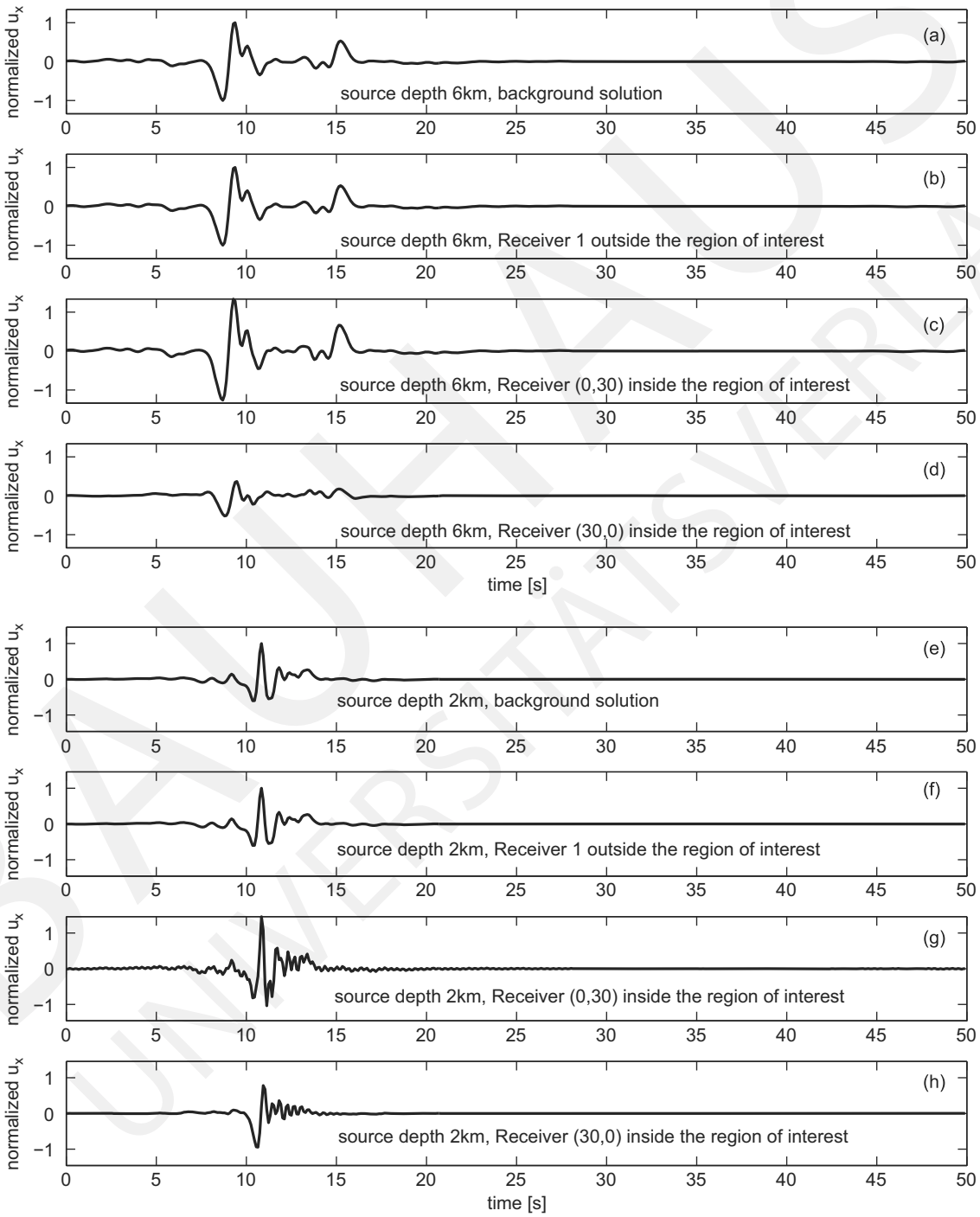

Fig. 16. Normalized horizontal displacement vs time at receivers $T_0(30,0)$ and $R_0(0,30)$. The seismic source is a double couple, situated at $x=2$ km and depth of: (a)–(d) $z=6$ km; (e)–(h) $z=2$ km.

Please cite this article as: F. Wuttke et al., Seismic wave propagation in laterally inhomogeneous geological region via a new hybrid approach, *Journal of Sound and Vibration* (2010), doi:10.1016/j.jsv.2010.08.042

(the edge of the canyon) on the free, horizontal surface and the free surface with relief (canyon or hill). In the case of canyon relief the displacement amplitudes are the smallest one, while in the case of the free, horizontal surface they are the greatest one. The complex diffraction wave picture in the case of relief peculiarities is responsible for this behavior.

5.3. Sensitivity of the obtained synthetic seismic signals to the mechanical properties of the local geological region

The mechanical properties of the local soil stratum play an important role on the specific character of the seismic signal. Fig. 13 shows displacement amplitudes at receiver $T_0(30,0)$ and receiver $R_0(0,30)$ vs frequency, at seismic source A at a

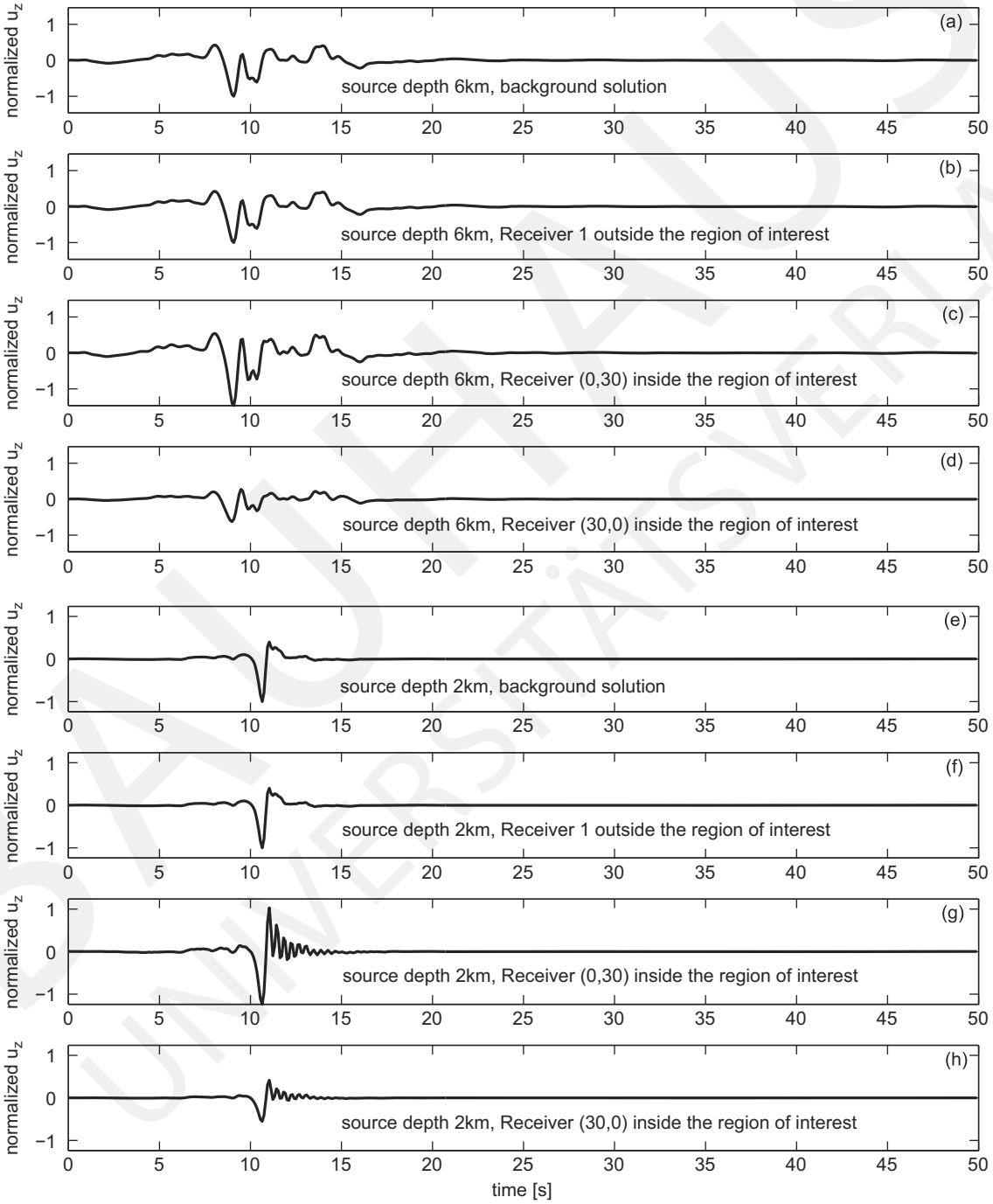

Fig. 17. Normalized vertical displacement vs time at receivers $T_0(30,0)$ and $R_0(0,30)$. The seismic source is a double couple, situated at $x=2$ km and depth of: (a)–(d) $z=6$ km; (e)–(h) $z=2$ km.

Please cite this article as: F. Wuttke et al., Seismic wave propagation in laterally inhomogeneous geological region via a new hybrid approach, *Journal of Sound and Vibration* (2010), doi:10.1016/j.jsv.2010.08.042

depth of 6 km and wave path 2. The mechanical properties of the local geological region are presented in Table 2. The third soil layer is of *type A* ($\beta_3 = 800\,\mathrm{m/s}$, $\alpha_3 = 1500\,\mathrm{m/s}$) or of *type B* ($\beta_3 = 500\,\mathrm{m/s}$, $\alpha_3 = 900\,\mathrm{m/s}$). Fig. 14 compares seismic signals obtained at receiver T_0 for two cases of mechanical properties of the finite soil profile: (a) case I — material characteristics are as those given in Table 2; (b) case II — second and third layers change their positions, i.e. second layer is with the properties of the third layer and vice versa . This leads to a complete different character of the synthetic seismograms. Figs. 13 and 14 reveal how important are the mechanical properties of the local seismic region for the characteristic peculiarities of the obtained wave signals during earthquake.

5.4. Sensitivity of the obtained synthetic seismic signals to the seismic source properties

The synthetic seismograms are obtained for seismic source B at two different depths. The rest of the data is fixed, it is considered wave path 2 and canyon relief on the free surface, while the mechanical properties of the local soil region are given in Table 2. The seismic source B used for the simulation study is the so-called double couple source. The time dependency of the seismic moment $M_0(t)$ is defined after [69]. As source parameters were chosen scalar seismic moment $M_0 = 5.98 \times 10^{14}\,\mathrm{N\,m}$, corner frequency $f_c = 5.0\,\mathrm{Hz}$, strike angle $\varphi = 151^\circ$, dip angle $\delta = 83^\circ$ and rake angle $\theta = 7^\circ$. To show the effects of different source depths this source is implemented in $x = 2\,\mathrm{km}$ and a depth of 2 km or 6 km. Figs. 15–17 demonstrate in frequency and in time domain, respectively, how sensitive are the synthetic signals to the depth of the seismic source. The discussed numerical results in this item show that the synthetic signals and the site effects depend on all essential components of the seismic wave path: seismic source located in the half-space, inhomogeneous wave path from the source to the local geological region plus the lateral inhomogeneous finite local stratum with its complex mechanical and geometrical peculiarities. The proposed, developed and validated hybrid analytically numerical tool has the possibility to account for all these important components of the seismic wave.

6. Concluding remarks

Efficient hybrid wavenumber integration-boundary integral equation method is developed, validated and applied in simulation studies. The hybrid approach combines analytical WNIM and numerical BIEM. PROS and CONS of the proposed hybrid tool are as follows: (a) it is possible to treat many soil layers due to the effective combination of both methods; (b) wave field can be evaluated for small and large distances; (c) body and surface waves are considered; (d) BIEM allows modeling of complex geometry, relief existence, non-parallel layering, inhomogeneities like cracks, inclusions, etc.; (e) capability to obtain seismograms, velocigrams and accelerograms, also response spectra, that account for the properties of the earthquake source, inhomogeneous wave path and laterally varying local geological region; (f) potential to account for geological regions with more complex mechanical behavior as anisotropy, poroelasticity, non-elasticity, etc.; (g) most of the papers in the literature take into account either one or two of the physical mechanisms controlling the seismic wave, while the hybrid WNI-BIEM has the potential to study simultaneously the combined effects of different physical properties of the system: seismic wave-geological media; (k) special attention is needed at high frequencies and for very soft soil layers, where the wavelength is small. It is clear that to reach high-numerical accuracy in these cases a very fine BEM mesh

Table 1
(a) The properties of the layered half-space (wave path 1); (b) the properties of the layered half-space (wave path 2).

Number of soil layer Γ_i	Thickness (km)	Depth (km)	Density ρ_1 (kg/m^3)	Shear wave velocity β_i (m/s)	Longitudinal wave velocity α_i (m/s)
(a)					
1	5.0	5.0	2750	3500	6100
2	8.0	13.0	2900	3600	6200
3	4.0	17.0	3200	4100	7650
4	2.0	19.0	3200	4200	7500
5	2.0	21.0	3200	4200	7650
6	2.0	23.0	3200	4300	7800
7	5.0	28.0	3300	4350	8000
8	22.0	50.0	2900	3800	6800
Seismic bed	∞	∞	3350	4600	8200
(b)					
1	0.35	0.35	2100	1400	2400
2	0.65	1.0	2200	1400	2400
3	1.5	2.5	2300	1400	2400
4	1.0	3.5	2400	1400	2400
5	1.5	5.0	2500	2200	3800
6	2.0	7.0	2600	2550	4500
7	5.0	12.0	2650	3100	5400
8	13.0	25	2750	3500	6200
9	10.0	35.0	2900	4200	7500
Seismic bed	∞	∞	3350	4600	8200

Please cite this article as: F. Wuttke et al., Seismic wave propagation in laterally inhomogeneous geological region via a new hybrid approach, *Journal of Sound and Vibration* (2010), doi:10.1016/j.jsv.2010.08.042

Table 2
The properties of the local geological region.

Number of soil layer	Density ρ_1 (kg/m^3)	Shear wave velocity β_i (m/s)	Longitudinal wave velocity α_i (m/s)
3	1800	800	1500
2	2000	1000	1700
1	2000	1400	2400

has to be used, respective this leads to high values of CPU time and memory; (l) it is necessary to establish the limits and possibilities of the proposed hybrid technique for each new seismic scenario and to this aim one-dimensional simulation experiment allows us to consider the WNIM result as one of the reference benchmark examples.

The seismic signal, obtained by the hybrid technique, can be used as a necessary base for solution of the following important geotechnical and civil engineering problems: (a) seismic wave propagation with accounting for the more complex mechanical behavior of the soil (b) soil–structure interaction and its effects on the dynamics of structures during earthquake; (c) solution of inverse problems for dynamic site characterization and identifying the soil profiles.

Acknowledgements

The authors acknowledge the support of the NATO under the Grant number CLG982064 and the *R&D*-Programme GEOTECHNOLOGIEN funded by the German Ministry of Education and Research (BMBF) and German Research Foundation (DFG), Grant 03G0636B with the publication no. GEOTECH - 320.

References

[1] F.J. Sanchez-Sesma, Strong ground motion and site effects, in: S.A. Anagnostopoulos, D. Beskos (Eds.), *Computer Analysis and Design of Earthquake Resistant Structures*, Computational Mechanics Publications, Southampton, 1996, pp. 201–239.
[2] V.M. Babich, *Ray Method for the Computation of the Intensity of Wavefronts*, Nauka, Moscow, 1956.
[3] C.H. Chapman, R. Drummond, Body-wave seismograms in inhomogeneous media using Maslov asymptotic theory, *Bulletin Seismological Society of America* 72 (1982) 277–317.
[4] N. Frazer, Quadrature of wave number integrals, in: D.J. Doornbos (Ed.), *Seismological Algorithms*, Academic Press, 1988.
[5] V. Cerveny, M.M. Popov, I. Psencik, Computation of seismic wave fields in inhomogeneous media-Gaussian beam approach, *Geophysical Journal of the Royal Astronomical Society* 70 (1982) 109–128.
[6] Y.H. Pao, R.G. Gajewski, The generalized ray theory and transient response of layered elastic solids, in: R.N. Thurston, W.P. Mason (Eds.), *Physical Acoustics*, Academic Press, New York, 1977, pp. 183–265.
[7] J.E. Gubernatis, E. Domany, J.A. Krumhansl, M. Huberman, Born approximation in the theory of scattering of elastic waves, *Journal of Applied Physics* 48 (1977) 2812–2819.
[8] B.L.N. Kennett, *Seismic Wave Propagation in Stratified Media*, vol. I, Cambridge University Press, 1983.
[9] Y. Hisada, An efficient method for computing Green's functions for a layered half-space with sources and receivers at close depths (Part 1), *Bulletin Seismological Society of America* 84 (5) (1994) 1456–1472.
[10] Y. Hisada, An efficient method for computing Green's functions for a layered half-space with sources and receivers at close depths (Part 2), *Bulletin Seismological Society of America* 85 (4) (1995) 1080–1093.
[11] L. Burdik, J. Orcutt, A comparison of the generalized ray and reflectivity methods of waveform synthesis, *Geophysical Journal of the Royal Astronomical Society* 58 (1979) 261–278.
[12] Z.S. Alterman, F.C. Karal, Propagation of elastic waves in layered media by finite difference methods, *Bulletin of the Seismological Society of America* 58 (1968) 367–398.
[13] D. Fah, P. Suhadolc, G.F. Panza, Estimation of strong ground motion in laterally heterogeneous media: modal summation-finite differences, *Proceedings of the 9th European Conference of Earthquake Engineering*, Moscow, USSR, vol. 4A, 11–16 September 1990, pp. 100–109.
[14] D. Fah, A Hybrid Technique for the Estimation of Strong Ground Motion in Sedimentary Basins, PhD Thesis, ETH Nr. 9767, Swiss Federal Institute of Technology, Zurich, 1992.
[15] D. Fah, P. Suhadolc, G.F. Panza, Variability of seismic ground motion in complex media: the case of a sedimentary basin in the Fruili Italy area, *Journal of Applied Geophysics* 30 (1993) 131–148.
[16] D. Fah, P. Suhadolc, St. Muller, G.F. Panza, A hybrid method for the estimation of ground motion in sedimentary basins: quantitative modelling for Mexico City, *Bulletin of the Seismological Society of America* 84 (2) (1994) 383–399.
[17] J. Zahradnik, P. Moczo, Hybrid seismic modelling based on discrete wave number and finite difference methods, *PAGEOPH* 148 (1/2) (1996) 21–38.
[18] P. Moczo, E. Bystricky, J. Kristek, M. Carcione, M. Bouchon, Hybrid modelling of P-SV seismic motion at inhomogeneous viscoelastic topographic structures, *Bulletin of the Seismological Society of America* 87 (5) (1997) 1305–1323.
[19] I. Oprsal, M. Pakzad, V. Plicka, J. Zahradnik, Ground motion simulation by hybrid methods, in: K. Irikura, K. Kudo, H. Okada, T. Sasatani, (Eds.), *The Effects of Surface Geology on Seismic Motion, Proceedings of ESG'98*, December 1–3, 1998, Yokohama, Japan, Vol. 2, Balkema, Rotterdam, 1998, pp. 955–960. ISBN 9058090337.
[20] I. Oprsal, V. Plicka, J. Zahradnik, Kobe simulation by hybrid methods, in: K. Irikura, K. Kudo, H. Okada, T. Sasatani, (Eds.), *The Effects of Surface Geology on Seismic Motion, Proceedings of ESG'98*, December 1–3, 1998, Yokohama, Japan, Vol. 3, Balkema, Rotterdam, 1999, pp. 1451–1456, ISBN 9058090337.
[21] I. Oprsal, J. Zahradnik, Three-dimensional finite difference method and hybrid modelling of earthquake ground motion, *Journal of Geophysical Research* 107 (B8) (2002) 16 10.1029/2000JB000082.
[22] J. Bielak, P. Christiano, On the effective seismic input for nonlinear soil structure interaction systems, *Earthquake Engineering Structural Dynamics* 12 (1984) 107–119.
[23] J. Bielak, K. Loukakis, Y. Hisada, Ch. Yoshimura, Domain reduction method for three-dimensional earthquake modelling in localized regions. Part I: theory, *Bulletin of the Seismological Society of America* 93 (2) (2003) 817–824.
[24] J.O.A. Robertsson, C.H. Chapman, An efficient method for calculating finite-difference seismograms after model alterations, *Geophysics* 65 (2000) 907–918.

Please cite this article as: F. Wuttke et al., Seismic wave propagation in laterally inhomogeneous geological region via a new hybrid approach, *Journal of Sound and Vibration* (2010), doi:10.1016/j.jsv.2010.08.042

[25] I. Oprsal, C. Matyska, K. Irikura, The source-box wave propagation hybrid methods: general formulation and implementation, *Geophysical Journal International* 176 (2009) 555–564.
[26] P.Y. Bard, M. Bouchon, The seismic response of sediment-filled valleys. Part I. The case of incident SH waves, *Bulletin of the Seismological Society of America* 70 (1980) 1263–1286.
[27] P.Y. Bard, M. Bouchon, The seismic response of sediment-filled valleys. Part II. The case of incident P and SV waves, *Bulletin of the Seismological Society of America* 70 (1980) 1921–1941.
[28] M.A. Bravo, F.J. Sanchez-Sesma, F.J. Chavez-Garcia, Ground motion on stratified alluvial deposits for incident SH waves, *Bulletin of the Seismological Society of America* 78 (1988) 436–450.
[29] H. Kawase, Time-domain response of a semicircular canyon for incident SV, P, and Rayleigh waves calculated by the discrete wavenumber boundary element method, *Bulletin of the Seismological Society of America* 78 (1988) 1415–1437.
[30] M. Bouchon, M. Campillo, S. Gaffet, A boundary integral equation discrete wavenumber representation method to study wave propagation in multilayered media having irregular interfaces, *Geophysics* 54 (1989) 1134–1140.
[31] H. Kawase, K. Aki, A study on the response of a soft basin for incident S, P and Rayleigh waves with special reference to the long duration observed in Mexico City, *Bulletin of the Seismological Society of America* 79 (1989) 136113–136182.
[32] A.S. Papageorgiou, J. Kim, Study of the propagation and amplification of seismic waves in Caracas Valley with reference to the 29 July 1967 earthquake: SH waves, *Bulletin of the Seismological Society of America* 81 (1991) 2214–2233.
[33] B. Zhang, A.S. Papageorgiou, J.L. Tassoulas, A hybrid numerical technique, combining the finite-element and boundary-element methods, for modelling the 3D response of 2D scatters, *Bulletin of the Seismological Society of America* 88 (1998) 1036–1050.
[34] S.A. Gil-Zepeda, J.C. Montalvo-Arrieta, R. Vai, F.J. Sanchez-Sesma, A hybrid indirect boundary element-discrete wave number method applied to simulate the seismic response of stratified alluvial valleys, *Soil Dynamics and Earthquake Engineering* 23 (2003) 77–86.
[35] K.V. Nguyen, B. Gatmiri, Evaluation of seismic ground motion induced by topographic irregularity, *Soil Dynamics and Earthquake Engineering* 27 (2) (2007) 183–188.
[36] G.A. Ayala, R.A. Gomes, A general procedure for solving three dimensional elasticity problems in geomechanics, in: W. Wittke (Ed.), *Numerical Methods in Geomechanics*, A. Balkema, Rotterdam, 1979.
[37] A.H. Shah, K.C. Wong, S.K. Datta, Diffraction of plane sh waves in a half-space, *Earthquake Engineering and Structural Dynamics* 10 (1982) 519–528.
[38] D.M. Cole, P.P. Kosloff, J.B. Minster, A numerical boundary integral equation for elastodynamics I, *Bulletin of the Seismological Society of America* 68 (1988) 1331–1357.
[39] B. Gatmiri, C. Arson, K.V. Nguyen, Seismic site effects by an optimized 2D BE/FE method. I. Theory, numerical optimization and application to topographical irregularities, *Soil Dynamics and Earthquake Engineering* 28 (8) (2008) 632–645.
[40] B. Gatmiri, C. Arson, Seismic site effects by an optimized 2D BE/FE method. II. Quantification of site effects in two-dimensional sedimentary valleys, *Soil Dynamics and Earthquake Engineering* 28 (8) (2008) 646–661.
[41] K.R. Khair, S.K. Datta, A.H. Shah, Amplification of oblique incident seismic waves by cylindrical alluvial valley of arbitrary cross-sectional shape: part I. Incident P and SV waves, *Bulletin of the Seismological Society of America* 79 (1989) 610–630.
[42] K.R. Khair, S.K. Datta, A.H. Shah, Amplification of oblique incident seismic waves by cylindrical alluvial valley of arbitrary cross-sectional shape: part II. Incident SH and Rayleigh waves, *Bulletin of the Seismological Society of America* 81 (1991) 346–357.
[43] S.W. Liu, S.K. Datta, M. Bouden, A.H. Shah, Scattering of oblique incident seismic waves by a cylindrical valley in a layered half-space, *Earthquake Engineering and Structural Dynamics* 20 (1991) 859–870.
[44] T. Yokoi, F.J. Sanchez-Sesma, A hybrid calculation technique of the in direct boundary element method and the analytical solution for three-dimensional problems of topography, *Geophysical Journal International* 133 (1998) 121–139.
[45] P. Dineva, F. Vaccari, G. Panza, Hybrid modal summation — BIE method for site effect estimation of a seismic region in a laterally varying media, *Journal of Theoretical and Applied Mechanics* 33 (4) (2003) 55–88.
[46] F. Luzon, L. Ramirez, F.J. Sanchez-Sesma, A. Posadas, Propagation of SH elastic waves in deep sedimentary basins with an oblique velocity gradient, *Wave Motion* 38 (2003) 11–23.
[47] F. Luzon, V.J. Palencia, J. Morales, F.J. Sanchez-Sesma, J.M. Garcia, Evaluation of site effects in sedimentary basins, *Fisica de la Tierra* 14 (2002) 183–214 ISSN:0214-4557.
[48] R. Zhang, L. Zhang, M. Shinozuka, Seismic waves in a laterally inhomogeneous layered medium, Part I: Theory, *Transactions of the ASME* 64 (1997) 50–58.
[49] R. Zhang, L. Zhang, M. Shinozuka, Seismic waves in a laterally inhomogeneous layered medium, Part II: Analysis, *Transactions of the ASME* 64 (1997) 59–65.
[50] J. Dominguez, *Boundary Elements in Dynamics. Computational Mechanics*, Elsevier, Southampton, Amsterdam, 1993.
[51] T. Rangelov, P. Dineva, D. Gross, A hypersingular traction boundary integral equation method for stress intensity factor computation in a finite cracked, *Engineering Analysis with Boundary Elements* 27 (1) (2003) 9–21.
[52] X. Chen, A systematic and efficient method of computing normal modes for multilayered media, *Geophysical Journal International* 115 (1993) 391–409.
[53] D.G. Harkrider, Surface waves in multilayered elastic media, I. Rayleigh and Love waves from buried sources in a multilayered elastic half-space, *Bulletin of the Seismological Society of America* 54 (2) (1964) 627–679.
[54] J.E. Luco, R.J. Apsel, On the Greens functions for layered half-space, Part I, *Bulletin of the Seismological Society of America* 73 (1983) 909–929.
[55] R.J. Apsel, J.E. Luco, On the Greens functions for layered half-space, Part II, *Bulletin of the Seismological Society of America* 73 (1983) 931–951.
[56] H. Cao, V.W. Lee, Scattering and diffraction of plane P waves by circular cylindrical canyons with variable depth-to-width ratios, *International Journal of Soil Dynamics and Earthquake Engineering* 9 (3) (1990) 141–150.
[57] M. Dravinski, T.K. Mossessian, Scattering of plane harmonic P, SV, and Rayleigh waves by dipping layers of arbitrary shape, *Bulletin of the Seismological Society of America* 77 (1987) 212–235.
[58] K.L. Fishman, S. Ahmad, Seismic response for alluvial valleys subjected to SH, P and SV waves, *Soil Dynamics and Earthquake Engineering* 14 (1995) 249–258.
[59] G.F. Panza, I. Paskaleva, P. Dineva, Cr. La Mura, Earthquake site effects modeling by hybrid MS-BIEM: the case study of Sofia, Bulgaria, *Rendiconti di Scienze Fisiche by the Accademia dei Lincei* 20 (2) (2009) 91–116.
[60] C.A. Brebbia, Topics in Boundary Element Research (1987), C. Brebbia (Ed.), *Applications in Geomechanics*, Vol. 4, Springer-Verlag, 1987, p. 65.
[61] I. Paskaleva, A contribution to the seismic risk assessment of the Sofia City, Report on CNR-NATO program, 65, Announcement 219.33, 2002.
[62] K. Makra, D. Raptakis, F.J. Chavez-Garcia, K. Pitilakis, How important is the detailed knowledge of a 2d soil structure for site response evaluation? in: *12th European Conference on Earthquake Engineering*, London, 2002.
[63] E. Faccioli, M. Vanini, L. Frassine, Complex site effects in earthquake ground motion, including topography, in: *12th European Conference on Earthquake Engineering*, London, 2002.
[64] R. Paolucci, Amplification of earthquake ground motion by steep topographic irregularities, *Earthquake Engineering Structural Dynamics* 31 (2002) 1831–1853.
[65] E.H. Field, Spectral amplification in a sediment filled valley exhibiting clear basin-edge-induced waves, *Bulletin of the Seismological Society of America* 86 (1996) 991–1005.
[66] F. J Chavez-Garcia, W.R. Stephenson, M. Rodrigez, Lateral propagation effects observed at Parkway, New Zealand: a case history to compare 1d versus 2d side effects, *Bulletin of the Seismological Society of America* 89 (3) (1999) 718–732.

Please cite this article as: F. Wuttke et al., Seismic wave propagation in laterally inhomogeneous geological region via a new hybrid approach, *Journal of Sound and Vibration* (2010), doi:10.1016/j.jsv.2010.08.042

[67] A. Caserta, A. Rovelly, F. Marra, F. Belluci, Strong diffraction effects at the edge of the Colfiorito, central Italy, basin, in: *Second International Symposium on the Effects of Surface Geology on Seismic Motion*, Yokohama, Balkema, 1998, pp. 435–440.
[68] A. Rovelli, L. Scognamiglio, F. Marra, A. Caserta, Edge-diffracted 1-sec surface waves observed in a small-size intermountain basin (Colfiorito, central Italy), *Bulletin of the Seismological Society of America* 91 (2) (2001) 313–334.
[69] J. Miksat, Earthquake Ground Motion Modelling from Crustal and Intermediate Depth Sources, PhD Thesis, University of Karlsruhe, 2006.
[70] F. Wuttke, Inverse site identification by use of surface waves, Ph.D. Thesis, Bauhaus-University Weimar, 2005.

Please cite this article as: F. Wuttke et al., Seismic wave propagation in laterally inhomogeneous geological region via a new hybrid approach, *Journal of Sound and Vibration* (2010), doi:10.1016/j.jsv.2010.08.042

Bei diesem Beitrag handelt es sich um einen wissenschaftlich begutachteten und freigegebenen Fachaufsatz („reviewed paper").

Hybride Modellierung seismischer Wellenausbreitung in geologischen, fluidgesättigten Materialien

F. Wuttke, T. Schanz, P. Dineva

Zusammenfassung Das Ziel dieser numerischen Studie ist die Modellierung, Validierung und Analyse von numerischen Simulationswerkzeugen zur seismischen Wellenausbreitung in einer fluidgesättigten zweidimensionalen, lokal beliebig heterogenen geologische Region, welche in einen fluidgesättigten geschichteten Halbraum eingebettet ist. Das hybride Wellenzahlintegration-Randintegral-Gleichungs-Modell (WNI-BIEM) beinhaltet eine seismische Quelle als Doppeldipol zur Simulation von geologischen Brüchen und Störungen. Die Gesamtformulierung des hybriden Modells erfolgte für den ebenen Dehnungszustand. Die lokale geologische Region wird durch nichtparallele Schichten und freie Oberfläche simuliert, während die vertikale Abfolge von isotropen, homogenen, horizontalen Schichten den umgebenden Halbraum abbildet. Das so entwickelte numerische Tool erlaubt die Simulation der Wellenausbreitung in rein elastische Materialien und in fluidgesättigten Materialien unter Ansatz eines viskoelastischen Isomorphismus der Biot'schen Poroelastizität. Die Ergebnisse der durchgeführten numerischen Simulationen zeigen deutlich den Einfluss der mehrphasigen Materialmodellierung auf die Wellenausbreitung und die Analysemöglichkeiten mit dem entwickelten hybriden Modell unter der Berücksichtigung einer entsprechenden seismischen Quelle, eines beliebigen Wellenpfads und geologischer lateraler Heterogenität, von der Oberflächentopografie und der Berücksichtigung eines gesättigten Bodenmaterials.

Hybrid modelling of transient seismic wave propagation in geological fluid saturated media

Abstract The main objective of this work is to propose, validate and apply in simulations an efficient hybrid wave number integration-boundary integral equation method (WNI-BIEM) for two-dimensional in-plane transient seismic wave propagation in a fluid saturated soil deposit rested in an inhomogeneous in depth fluid saturated half-space with a seismic source in it.

Plane strain state is suggested. The geological deposit is a finite local soil stratum with nonparallel layers and free surface relief. The vertical variation of the soil properties in the half-space is modeled by a set of horizontal flat isotropic, fluid saturated and homogeneous layers. The computational tool is based on both: (a) viscoelastic isomorphism to the Biot's dynamic poroelasticity and (b) hybrid WNI-BIEM developed and used by the authors in their previous papers ([14–15]) for pure elastic case.
The obtained numerical results demonstrate that the proposed hybrid approach has the potential to reveal how the seismic signal on the free surface of a geological region of interest depends on the seismic source characteristics, on the geological structure and material inhomogeneity of the wave path from the source till the considered receiver point, on the lateral inhomogeneoty due to the existence of relief and non-parallel layering and on the mechanical behavior of soil accounting for its fluid saturation.

Frank Wuttke
Professur Bodenmechanik /
Zentrum für Strukturdynamik und
Erdbebeningenieurwesen
Bauhaus-Universität Weimar
99421 Weimar

Tom Schanz
Lehrstuhl für Grundbau
Boden- und Felsmechanik
Ruhr-Universität Bochum
44780 Bochum

Petia Dineva
Department of Continuum Mechanics
Institute of Mechanics
Bulgarian Academy of Sciences
1113 Sofia

1 Einführung in die Thematik

Die Entwicklung hybrider Modelle mit Nutzung der Vorteile von analytischen und numerischen Methoden [1–10] ist ein zentrales Thema in der Simulation großräumiger seismischer Problemstellungen [11–16]. Derartige Modelle bieten die Möglichkeit, komplexe geologische Simulationen durchführen zu können. Neben einer komplexen geometrischen Formation besitzt der Untergrund ebenfalls eine unterschiedlich stark ausgeprägte poröse Struktur, in welcher eine Luft- und Wasserphase eingeschlossen sein kann. Die Modellierung derartiger mehrphasiger Strukturen ist seit längerem Gegenstand intensiver Forschung in der Geowissenschaft.
In der vorliegenden Studie wird der Einfluss eines Zweiphasenmodells auf die seismische Wellenausbreitung untersucht. Als Grundlage der numerischen Untersuchungen dient das Modell nach Bardet [17, 18]. Dieses wurde als viskoelastisches Analogon zu dem bekannten poroelastischen Modell nach Biot [19, 20] von Bardet entwickelt und verifiziert. Auf Basis dieser Modellierung erfolgte in der vorliegenden Studie eine vergleichende Analyse zu bereits durchgeführten Untersuchungen mit dem entwickelten hybriden Modell auf Grundlage der reinen Elastodynamik ohne Berücksichtigung von mehrphasigen Strukturen, siehe Dineva et al. [14] und Wuttke et al. [15]. Aus der Erweiterung dieser Entwicklungen mit dem benannten viskoelastischen Modell nach Bardet können die Unterschiede der beiden Modellannahmen herausgearbeitet und diskutiert werden.

2 Definition der Problemstellung

Die Wellenausbreitung wird als ebene Problemstellung in der zweidimensionalen x-z-Ebene (in-plane) betrachtet, **Bild 1.** Das gesamte Gebiet ist, wie auch schon in [14, 15] dargestellt, in eine lokale, heterogene geologische Region Ω_{LRG} und den vertikal inhomogenen Halbraum Ω_0 unterteilt. Die seismische Doppeldipolquelle ist an einer beliebigen Positi-

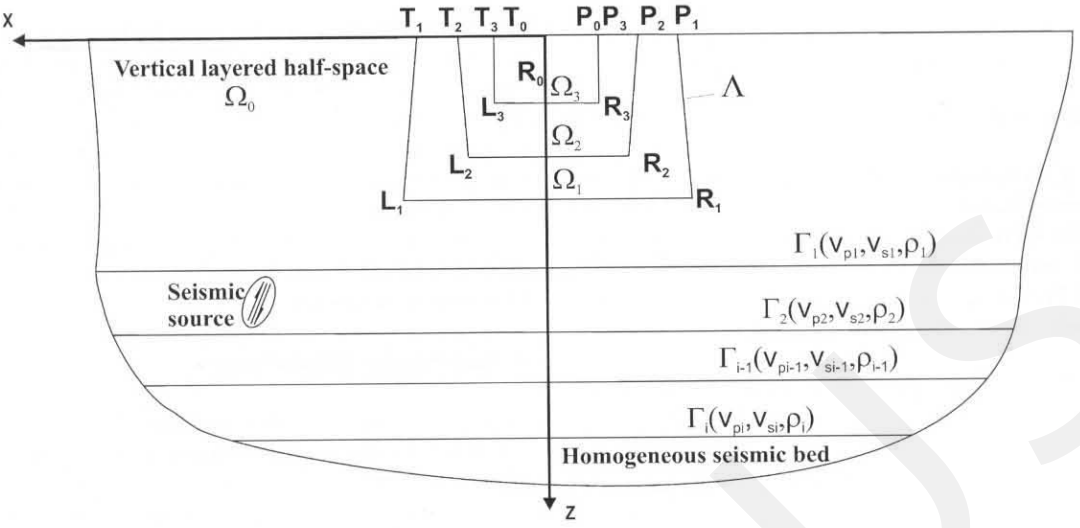

Bild 1. Hybrides Modell mit eingebetteter geologischer Region
Fig. 1. Hybrid model of the embedded geological region.

on des Halbraums Ω_0 definiert. Innerhalb des gesamten Modells wird der ebene Dehnungszustand für die Formulierungen der Wellengleichungen definiert. Die Schichten in den Regionen Ω_{LRG} und Ω_0 werden als isotrope, viskoelastische und homogene Bereiche definiert. Der viskoelastische Ansatz ist entsprechend den Ausführungen und Definitionen für eine fluidgesättigten Struktur nach Bardet [17, 18] formuliert. Die analysierten und dargestellten synthetischen Seismogramme werden an unterschiedlichen Empfängerpunkten an der freien Oberfläche der lokalen Region Ω_{LRG}, siehe Bild 1, berechnet. Für eine *l-te* Schicht kann die Wellengleichung durch folgende partielle Differentialgleichung dargestellt werden [15],

$$\left(\alpha_l^2 - \beta_l^2\right) u_{j,ji}\left(x,z,t\right) + \beta_l^2 u_{i,jj}\left(x,z,t\right) = \ddot{u}_i\left(x,z,t\right)$$
$$\text{in } Q_B = \Omega_B x \left(0,T\right) \qquad (1)$$

wobei das Gebiet Ω_B aus den Teilgebieten Ω_{LRG} und Ω_0 besteht und die Longitudinal- und Scherwellengeschwindigkeiten, α_l, β_l, unterschiedlich für die verschiedenen Schichten in Ω_{LRG}, mit $l = 1, 2, \ldots, N$, und in Ω_0, mit $l = 1, 2, \ldots, M$, sind. Die Variable T ist die Dauer der seismischen Einwirkung, u_i und $\ddot{u}_i$ sind die Verschiebung und Beschleunigung, mit $i = x, z$. Die Gleichungen werden hinsichtlich der Zeit fouriertransformiert, um die Zeitabhängigkeit zu eliminieren und das Randwertproblem im Frequenzbereich zu lösen. Das gesamte Randwertproblem besteht aus der Wellengleichung (1) und den folgenden Randbedingungen: a) Berücksichtigung einer spannungsfreien Oberfläche, b) Erfüllung der Kompatibilität der Verschiebung und Gleichgewicht der Spannungen an der Grenzfläche zwischen zwei Schichten und c) die Gültigkeit der Sommerfeld'schen Abstrahlungsbedingung im Unendlichen. Nach der Lösung des Randwertproblems für eine ausreichende Anzahl von Frequenzen ω, kann die zeitabhängige Lösung nach Anwendung der inversen Fouriertransformation wieder bestimmt werden. Hinsichtlich der ausführlichen Definition des genutzten hybriden Modells sei auf die Publikationen [14, 15, 16] verwiesen. Die dort dargestellte Modellierung bildete die Grundlage für die Erweiterung mit dem viskoelastischen Modell nach Bardet.

3 Poroelastisches Modell nach Bardet

Seit den klassischen Arbeiten zur Wellenausbreitung in poroelastischen Medien durch Biot [19, 20] auf Grundlage der Arbeiten von Frenkel [21], wurde diese Fragestellung vielfach studiert und weiterentwickelt. Etliche Autoren analysierten den Effekt eines fluidgesättigten Zweiphasenmediums auf die Wellenausbreitung in homogenen Gebieten [21–27]. Eine umfassende Abhandlung der Biot'schen Theorie gibt Schanz in [22] wieder. Die Implementation des Biot'schen Modells ist sehr komplex und infolge mangelnder Fundamentallösungen noch wenig verbreitet. Nach Simon [28] besitzt der Ansatz eines poroelastischen und viskoelastischen Materials eine ähnliche Auswirkung auf ein durchlaufendes Wellenfeld. Diese Ähnlichkeit wurde in Bardet [17, 18] genutzt, um ein viskoelastisches Modell aus den Biot'schen Ansätzen abzuleiten. Die Biot'schen Theorie basiert auf der Annahme, dass das Material eine Mixtur von Feststoffmatrix und Fluid ist, wobei die Poren der Mixtur komplett mit Fluid gesättigt sind. Durch diese gegenseitig durchdrungenen Phasen entsteht eine zusätzliche Energiedissipation während der Wellenausbreitung und neben der bekannten Logitudinal- und Scherwelle in einem rein elastischen Kontinuum, existiert eine zusätzliche, langsamere Longitudinalwelle. Verschiedene Autoren [22] untersuchten sowohl die transiente Wellenausbreitung als auch die Ausbreitung von Oberflächenwellen unter Berücksichtigung eines gesättigten poroelastischen Halbraums [29, 30]. Erste Ansätze für die Nutzung viskoelastischer Modelle in hybriden numerischen Berechnungen finden sich in [31]. Innerhalb dieses Modells ist die nunmehr komplexe Geschwindigkeit von den Materialkonstanten des Biot'schen Modells [32] abhängig. Bardet [17, 18] zeigt, dass der viskoelastische Ansatz unter den getätigen Annahmen praktisch identische Ergebnisse zum poroelastischen Zweiphasenmodell ergibt, wobei die numerische Umsetzung und Implementation weitaus einfacher ist.

Entsprechend dem Korrespondenzprinzip [33] existiert kein Unterschied zwischen elastischen und viskoelastischen Medien, wenn dynamische zeitharmonische Problemstellungen behandelt werden. Dementsprechend sind die Grundgleichungen der Elastodynamik für ein viskoelastisches Modell im Frequenzbereich definiert zu:

$$\left(k_s^2/k_p^2-1\right)\left[u_{y,xy}+u_{x,xx}\right]+\left[u_{x,xx}+u_{x,yy}\right]+k_p^2u_x=0$$
$$\left(k_s^2/k_p^2-1\right)\left[u_{x,xy}+u_{y,yy}\right]+\left[u_{y,xx}+u_{y,yy}\right]+k_p^2u_y=0 \qquad (2)$$

Darin sind k_p, k_s die komplexen Wellenzahlen der Longitudinal- und Scherwelle und u_i, $i = x, y$ die Verschiebung in x und y Richtung. Die Wellenzahlen, abhängig von der Materialstruktur, sind unterschiedlich für die jeweiligen Bodenschichten und Frequenzen ω und können über folgende Beziehung ausgedrückt werden:

$$k_p^2=\frac{\omega^2}{\left(c_p^*\right)^2}=\frac{\omega^2}{c_p^2\left(1-i\omega\xi_p\right)};\quad k_s^2=\frac{\omega^2}{\left(c_s^*\right)^2}=\frac{\omega^2}{c_s^2\left(1-i\omega\xi_s\right)} \qquad (3)$$

Die Ausdrücke c_p^* und c_s^* sind hierbei die komplexen P- und S-Wellengeschwindigkeiten des viskoelastischen Materials. Die Terme c_p und c_s repräsentieren den reellen Teil der Geschwindigkeiten und ξ_p, ξ_s korrespondieren mit dem Dämpfungstermen. Für den Fall kleiner Frequenzen und kleiner Dämpfungsterme gilt $\omega\xi_p << 1$ und $\omega\xi_s << 1$, womit die obigen Gleichungen durch die nachfolgenden Gleichungen approximiert werden können:

$$k_p^2\approx\frac{\omega}{c_p}\left(1+\frac{i}{2}\omega\xi_p\right);\quad k_s^2\approx\frac{\omega}{c_s}\left(1+\frac{i}{2}\omega\xi_s\right). \qquad (4)$$

Bardet [17, 18] postulierte eine poroelastische – viskoelastische Ähnlichkeit durch das Gleichsetzen der Wellenzahlen in (2) mit den Wellenzahlen des Biot'schen poroelastischen Modells. Daraus resultiert ein dem poroelastischen Material äquivalentes viskoelastisches Material mit Wellengeschwindigkeiten und Dämpfungstermen, die sich aus den poroelastischen Parametern zusammensetzten:

$$c_p=\sqrt{\frac{P+2Q+R}{\rho^*}};\ c_s=\sqrt{\frac{N}{\rho^*}}\ \text{und} \qquad (5)$$

$$\xi_p=\frac{\rho^*}{b}\left(\frac{Q+R}{P+2Q+R}\frac{\rho_{12}^*+\rho_{22}^*}{\rho^*}\right)^2;\ \xi_s=\frac{\rho^*}{b}\left(\frac{\rho_{12}^*+\rho_{22}^*}{\rho^*}\right) \qquad (6)$$

Hierin ist $\rho^*=(1-n)\,\rho_g+n\,\rho_f$, mit n als der Porenanteil des Festkörperskeletts, ρ_f und ρ_g sind die Fluid und Korndichten, $b = n^2\,g\,\rho_f/k$ die Dissipationskonstante, k die hydraulische Permeabilität in Böden ($10^{-2}...10^{-10}$) und $g = 9.81 m/s^2$ die Gravitationskonstante. Die Biot'schen Konstanten P, Q, N und R sind verknüpft mit dem Kompressionsmodul des trockenen Skelettes K_{dry}, dem Kompressionsmodul des Korns K_g und des Fluids (Wasser) K_f, dem Porenanteil n und der Querdehnzahl ν durch die Ausdrücke:

$$P=\frac{3(1-\nu)}{1+\nu}K_{dry}+\frac{Q^2}{R},\quad Q=\frac{n\left(1-n-K_{dry}/K_g\right)}{1-n-K_{dry}/K_g+nK_g/K_f}K_g$$

$$R=\frac{n^2}{1-n-K_{dry}/K_g+nK_g/K_f}K_g,\ K_{dry}=\frac{2}{3}\frac{\mu(1+\nu)}{1-2\nu},$$

$$\rho_{dry}=(1-n)\rho_g \qquad (7)$$

Die Scherfestigkeit des porösen Materials wird ausschließlich von dem Feststoffskelett und nicht durch das Fluid beeinflusst. Infolgedessen haben das trockene und gesättigte Material den gleichen Schermodul $\mu=\mu_{dry}$. Die obigen Beziehungen gelten nur für den Fall, wenn $\omega\rho^*/b << 1$, welches gewöhnlich für die vorhandenen Frequenzen und Permeabilitäten im Erdbebeningenieurwesen erfüllt ist. Somit ist das zweiphasige poroelastische dynamische Verhalten durch die dynamische Antwort eines Einphasen – Viskoelastischen Materials beschrieben.

4 Numerische Simulationen

Um die Effekte von fluidgesättigten porösen Materialien während der Wellenausbreitung abzubilden, wird hier ein Modell untersucht, bei dem nur zwei Schichten der geologisch heterogenen Region ausgeprägte Unterschiede in der Porosität und Sättigung besitzen. Alle weiteren Gebiete / Schichten werden als rein elastisches Medium mit konstanten Kennwerten angenommen. Die in Bild 1 dargestellten Gebiete sind wie folgt definiert: das Gebiet Ω_1 und Ω_0 als rein elastisches Material, mit einer Dichte ρ von 2750 kg/m³, einer Scherwellengeschwindigkeit β_i von 3500 m/s und einer Kompressionswellengeschwindigkeit α_i von 6100 m/s. Die Gebiete Ω_2 und Ω_3 werden als poroelastische und wassergesättigte (S = 1) oder trockene (S = 0) Materialien angenommen. Das Gebiet Ω_1 besitzt die gleichen Kennwerte wie die oberste horizontale Schicht des vertikal heterogenen Halbraums, in welche die laterale Heterogenität eingebettet ist. Die Definition der poroelastischen Parameter in Ω_2 und Ω_3 erfolgte nach Lin et. al. [27] mit folgende Annahmen: Poissonzahl ν = 0.2, Kompressonsmodul des Fluids K_f = 2000MPa, Dichte des Fluids ρ_f = 1000 kg/m³, Korndichte ρ_g = 2650 kg/m³, hydraulischer Permeabilitätskoeffizient k = 10^{-5} m/s. Nach Lin et al. [27] wurde der Kompressionsmodul nach folgender lineraren Beziehung bestimmt:

$$K_s=K_{cr}+\left(1-\frac{n}{n_{cr}}\right)\left(K_g-K_{cr}\right), \qquad (8)$$

wobei die kritische Porosität n_{cr} zu 0.36, der kritische Kompressionsmodul K_{cr} zu 200MPa und der Kompressionsmodul des Korns K_g zu 36000 MPa gesetzt wurden. Die in [27] formulierte Linearkombination zur Bestimmung des Kompressionsmoduls des Feststoffskeletts K_s erfolgt durch experimentelle Untersuchungen an porösem Sandstein.
Für die Untersuchung des Porositätseinflusses auf das Übertragungsverhalten des Wellenfeldes wurden folgende Kombinationen der Porenanteile in den Gebieten Ω_2 und Ω_3 untersucht:

- Die Porenanteile des zweiten und dritten Gebietes werden zu 0.1 ($n_2 = n_3 = 0.1$) gesetzt. Mit dieser Kombination wird den Empfehlungen nach [27] gefolgt, wonach ein Material mit diesem Porenanteil sich wie ein rein elastisches Einphasenmaterial verhalten wird.
- Der Porenanteil des zweiten und dritten Gebietes ist 0.30 ($n_2 = n_3 = 0.3$)
- Der Porenanteil des zweiten und dritten Gebietes ist 0.34 ($n_2 = n_3 = 0.34$)
- Der Porenanteil des zweiten und dritten Gebietes ist 0.356 ($n_2 = n_3 = 0.356$)

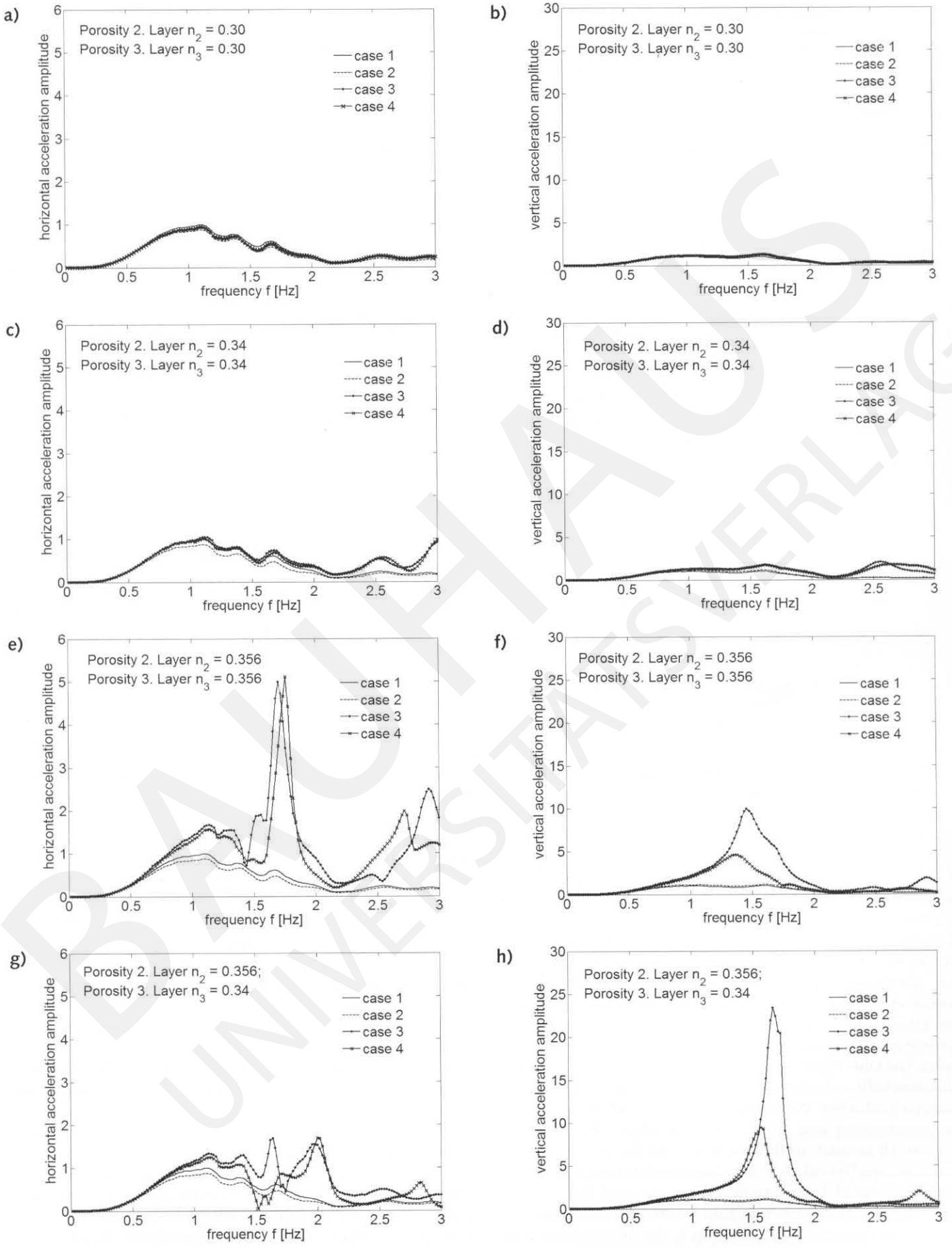

Bild 2 a-h. Synthetische Spektren der Beschleunigungszeitverläufe für den Punkt (30,0) auf der freien Oberfläche der geologisch heterogenen Region unter Berücksichtigung unterschiedlicher Porenanteile bzw. Sättigung für den Wellenpfad 1.

Fig. 2 a-h. Acceleration spectra calculated in point T_0 (30,0) on the free surface of the geological heterogeneous region and wave path 1 under consideration of different porosities and satuaration

Tabelle1a: Parameter des vertikal heterogenen Halbraums (*Bodenstruktur 1*)

Schichten Γ_i	Schicht-stärke $[km]$	Tiefe $[km]$	Dichte $\rho_i\,[kg/m^3]$	Scherwellen-geschwindig-keit $\beta_i\,[m/s]$	Kompressionswel-lengeschwindigkeit $\alpha_i\,[m/s]$
1	5.0	5.0	2750	3500	6100
2	8.0	13.0	2900	3600	6200
3	4.0	17.0	3200	4100	7200
4	2.0	19.0	3200	4200	7500
5	2.0	21.0	3200	4200	7650
6	2.0	23.0	3200	4300	7800
7	5.0	28.0	3300	4350	8000
8	22.0	50.0	2900	3800	6800
Halbraum	∞	∞	3350	4600	8200

Tabelle 1b: Parameter des vertikal heterogenen Halbraums (*Bodenstruktur 2*)

Schichten Γ_i	Schicht-stärke $[km]$	Tiefe $[km]$	Dichte $\rho_i\,[kg/m^3]$	Scherwellen-geschwindig-keit $\beta_i\,[m/s]$	Kompressionswel-lengeschwindigkeit $\alpha_i\,[m/s]$
1	0.35	0.35	2100	1400	2400
2	0.65	1.00	2200	1400	2400
3	1.50	2.50	2300	1400	2400
4	1.00	3.50	2400	1400	2400
5	1.50	5.00	2500	2200	3800
6	2.00	7.00	2600	2550	4500
7	5.00	12.0	2650	3100	5400
8	13.0	25.0	2750	3500	6200
9	10.0	35.0	2900	4200	7500
Halbraum	∞	∞	3350	4600	8200

- Der Porenanteil des zweiten Gebietes ist 0.356, während der Porenanteil des dritten Gebietes zu 0.34 gesetzt wird ($n_2 = 0.356$, $n_3 = 0.34$)

Die Ergebnisse der seismischen Signale für die unterschiedlichen Kombinationen wurden für den Punkt T_0 (30,0) in Bild 1 dargestellt. Als Eckkoordinaten (x, z) der geologischen Region wurden folgende Punkte definiert: *T_0(30,0)*; *T_3(60,0)*; *T_2(90,0)*; *T_1(100,0)*; *P_0(-30,0)*; *P_3(-60,0)*; *P_2(-90,0)*; *P_1(-100,0)*; *L_1(110,270)*; *R_1(-110,270)*; *L_2(90,180)*; *R_2(-90,180)*; *L_3(60,90)*; *R_3(-60,90)* [m]. Mit den Simulationen soll die Abhängigkeit der synthetischen Signale von der Porenanteilsänderung veranschaulicht werden. Das vorhandene Relief an der freien Oberfläche und die Charakteristiken der seismischen Quelle als Doppeldipol werden in dieser Studie konstant gesetzt. Die Oberfläche der geologischen Region erfolgte ohne Taleinschnitt – als ebene Oberfläche. Für die Simulation der unterschiedlichen Wellenpfade 1 und 2 werden die Schichtungsparameter und -abfolgen entsprechend den **Tabellen 1a** und **1b** genutzt. In **Bild 2a-h** sind die Spektren der horizontalen und vertikalen Beschleunigungskomponente für den Wellenpfad 1 dargestellt. Das zweite und dritte Gebiet der lokalen geologischen Region werden fluidgesättigt (S = 1) oder trocken (S = 0) angenommen. Die Abbildungen wurden bezüglich des Maximalwertes der numerischen Lösung des horizontal geschichteten rein elastischen Halbraums ohne laterale Heterogenität (WNIM) normiert, um den Einfluss der Porosität darzustellen.

Innerhalb der Bilder 2 bis 4 wurden folgende Modellierungsfälle unterschiedlicher Porenanteile ausgewertet:

Fall 1) Elastisch, horizontal geschichteter Halbraum ohne lateral inhomogene Region

Fall 2) Elastisch, horizontal geschichteter Halbraum mit lateral inhomogener Region, Nutzung elastodynamisches Modell mit reellen Wellenzahlen und Materialkonstanten für trockenen poroelastischen Fall mit einem Porenanteil von 0.1. Bei diesem Ansatz wird ausgenutzt, dass ein System mit geringem Porenanteil eine identische dynamische Antwort zu einem rein elastischen Einphasensystem gibt, siehe Knopoff et al. [34]

Fall 3) Poroelastisch, horizontal geschichteter Halbraum mit lateral inhomogener Region, gesättigter Zustand. Nutzung des viskoelastischen Modells mit komplexen Wellenzahlen und Wellengeschwindigkeiten nach Gleichungen (4) und (5).

Fall 4) Poroelastisch, horizontal geschichteter Halbraum mit lateral inhomogener Region, trockener Zustand. Nutzung des elastodynamischen Modells mit reellen Wellenzahlen und Materialkonstanten entsprechend λ_{dry}, μ_{dry}, ρ_{dry} und der entsprechenden Porenanteil nach Gleichung (7).

Die **Bilder 3a, b** und **Bilder 4a, b** zeigen die Spektren der horizontalen und vertikalen Komponente der Beschleunigung unter Ansatz des Wellenpfads 1 und 2. Die Porenanteile der Schichtungen wurden hier zu $n_2 = 0.356$ und $n_3 = 0.34$ gewählt. Innerhalb der Abbildungen sind die Graphen wieder-

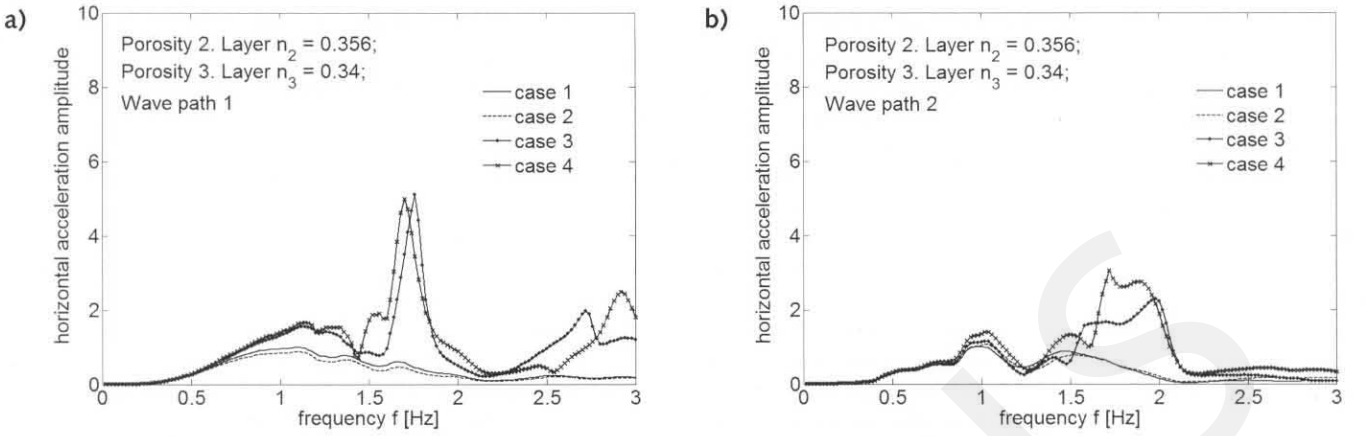

Bild 3. Einfluss der Wellenpfadeigenschaften auf die horizontale Komponente des synthetischen Spektrums der Beschleunigungen, a) Wellenpfad 1 und b) Wellenpfad 2.
Fig. 3. Influence of wave paths on the spectral horizontal acceleration component, a) wave path 1 and b) wave path 2.

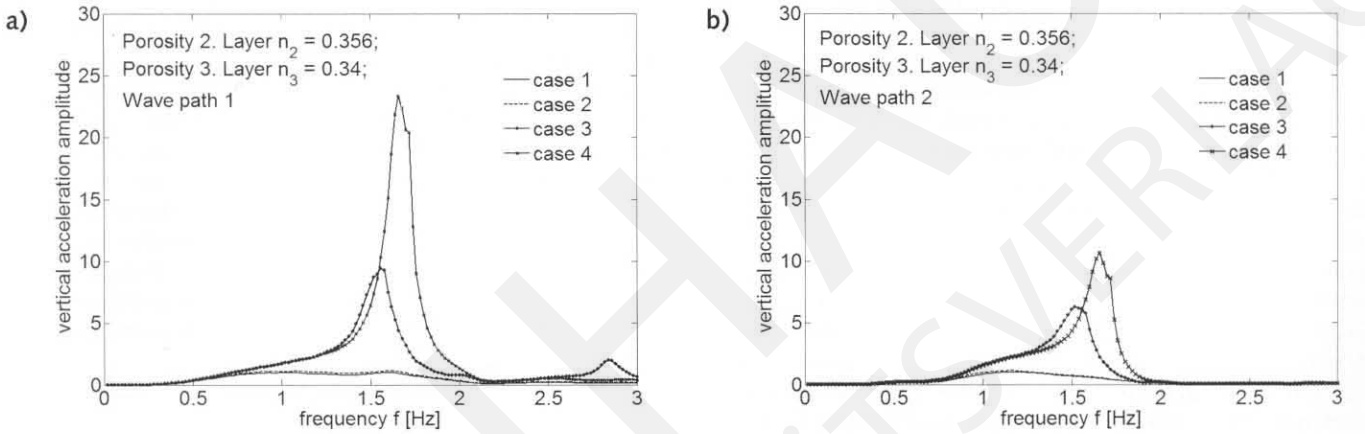

Bild 4. Einfluss der Wellenpfadeigenschaften auf die vertikale Komponente des synthetischen Spektrums der Beschleunigungen, a) Wellenpfad 1 und b) Wellenpfad 2.
Fig. 4. Influence of wave paths on the spectral vertical acceleration component, a) wave path 1 and b) wave path 2.

um bezüglich des numerischen Maximalwertes des Modellierungsfalles 1 normiert.

Einige Ausschnitte der entsprechenden Zeitverläufe, welche die Grundlage der Spektren in 2, 3 und 4 bilden, sind in **Bild 5** dargestellt. Die Ausprägung und die Form der Zeitverläufe widerspiegeln die unterschiedlichen Modellannahmen.

Die obigen Bilder 2, 3, 4 und 5 erlauben eine Diskussion hinsichtlich des Einflusses einer porösen Modellierung gegenüber einer rein elastischen Einphasen-Simulationen in einer numerischen Simulation bzw. als Interpretation zu Beobachtungen.

In Bild 2 wurde der Porenanteil innerhalb der Schichten der geologischen Heterogenität von 0.3 bis 0.356 erhöht. Der Vergleich dieser Abbildungen zeigt, dass sich der Charakter der synthetischen Signale in Abhängigkeit vom Porenanteil signifikant ändert. Der poroelastische Effekt mit der Anwesenheit eines Fluids besteht in der Versteifung des Materials, womit die Signalcharakteristik geändert wird. Die Porendrücke, induziert durch die seismischen Lasten, widerstehen einer Kompression und versteifen das Material. Die Schubsteifigkeit eines Biot'schen Materials wird nur durch das Feststoffskelett übertragen, die Anwesenheit eines Fluids hat darauf keinen Einfluss, $\mu_{sat} = \mu_{dry}$. Die Lamè-Konstante λ_{sat} ändert sich zu $\lambda_{sat} = \lambda_{dry} + Q^2/R$, worin die Biotkoeffizienten Q und R Funktionen des Porenanteils n, des Kompressionsmoduls des Feststoffskeletts K_{dry}, des Kompressi-

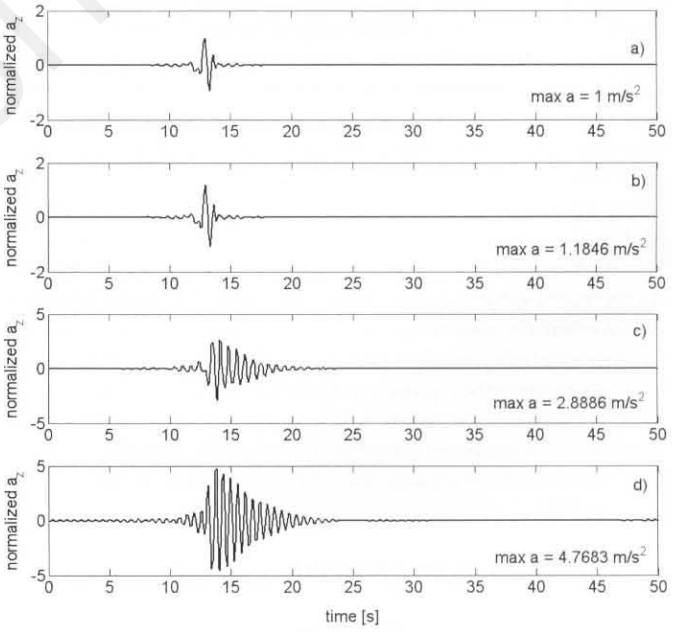

Bild 5. Vertikale Komponente der synthetischen Beschleunigungszeitverläufe für den Punkt T_0 (30,0): a) Simulation – Fall 1, b) Simulation – Fall 2, c) Simulation – Fall 3, d) Simulation – Fall 4.
Fig. 5. Vertical component of acceleration in point T_0 (30,0) for different simulation cases: a) case 1, b) case 2, c) case 3, d) case 4.

onsmoduls des Korns K_g und des Kompressionsmoduls des Fluids K_f sind. Dementsprechend hat das gesättigte Material (S=1) eine höhere Kompressionswellengeschwindigkeit als das trockene Material (S=0). Dieses kann einer der Gründe sein, warum die synthetischen Signale für höhere Porenanteile im gesättigten Modell mitunter kleineren Amplituden als für die trockene Simulation ergeben, siehe Bild 2.

Durch das gegebene komplexe Randwertproblem, mit der hybriden Struktur und porösen Materialbeschreibung, ergibt sich ein kompliziertes, von unterschiedlichen Einflüssen abhängiges Signal. Diese Einflüsse sind: a) mechanische Eigenschaften des Wellenpfads, b) Inhomogenitäten entlang des Wellenpfads, c) Quellcharakteristiken und – mechanismen, d) mechanische Eigenschaften der poroelastischen Schichtung bzw. der geologischen, poroelastischen Heterogenität. Bild 2 zeigt, dass der Effekt einer Sättigung im Material für kleinere Porenanteile gegenüber einem trockenen Material nur geringe Auswirkungen hat. Mit zunehmendem Porenanteil gewinnt der Einfluss der Sättigung in dem porösen Material an Bedeutung und die Unterschiede zwischen den Signalen eines trockenen und gesättigten Materials nehmen zu. Dieser Sachverhalt kann auch durch die Beziehungen des Kompressionsmoduls des trockenen Materials K_{dry} zu dem Modul des Fluids K_f dargestellt werden. Bei einer Porosität n = 0.1 ist der Kompressionsmodul des Skeletts $K_{dry} \sim 10\ K_f$, während bei einer Porosität n = 0.34 die Moduli fast gleich sind $K_{dry} \sim K_f$ und mit der Porosität n = 0.36 das Verhältnis der Moduli umschlägt $K_{dry} \sim 0.1\ K_f$. Zu diesem Punkt bzw. kritischem Porenanteil n_{cr}, bei dem der Kompressionsmodul des trockenen Skeletts ein Zehntel des Kompressionsmodul des Fluids beträgt, korrespondiert das Material mit einem Boden sehr geringer Steifigkeit. Nach Lin et al. [27] kann dieser Sachverhalt auch wie folgt interpretiert werden: „Die Größenordnung der Skelettsteifigkeit kontrolliert die Antwort eines fluidgesättigten Systems. In einem poroelastischen System gewinnt das Porenfluid mit zunehmender Abnahme der trockenen Skelettsteifigkeit an Einfluss."

Das Fluid in der porösen Bodenstruktur agiert ähnlich einem viskosen Dämpferelement, da es möglich ist, dass das Fluid zwischen der Regionen höherem und kleinerem Druck fließt und dadurch eine Dämpfung verursacht. Dieses Verhalten widerspiegelt sich auch in der Bild 5. Für die Simulationen mit hohem Porenanteil schwingt das Medium deutlich sichtbarer als für den Fall, dass ein rein elastisches einphasiges Material modelliert wird.

Ein weiterer wichtiger Erkenntnisgewinn, welcher aus der Analyse des Bildes 2 gewonnen werden kann, ist dass neben der Änderung der Amplituden, ebenfalls die dominanten Frequenzinhalte in den Beschleunigungszeitverläufen mit Modellierung einer porösen Struktur wesentlich verändert und verschoben werden können (gegenüber einem rein elastischen Einphasenmaterial), wobei die Anwesenheit eines Fluids diese Wirkung noch erhöhen kann, siehe auch in [35, 36, 37].

5 Schlussfolgerungen / Ausblick

In dem vorliegenden Beitrag wurde ein von den Autoren entwickeltes hybrides Wellenzahlintegrations-Randintegralgleichungs-Verfahren zur Berechnung und Analyse von seismischen Wellenfeldern in geologisch heterogenen Gebieten [15], um die Simulation eines poroelastischen Materials erweitert und validiert. Neben den Einflüssen des Wellenpfads, der seismischen Quelle und der Ausbildung der geologischen Heterogenität wurde in den vorliegenden Untersuchungen insbesondere der Einfluss einer porösen fluidgesättigten Struktur analysiert.

Die numerischen Ergebnisse zeigen, dass die Sättigung in Böden zu einem Dämpfungseffekt innerhalb der seismischen Wellenausbreitung führt. Die physikalischen Gründe für diese Effekte sind:

a) ein Dissipationsprozess infolge des viskoelastischen Verhaltens des Feststoffskelettes
b) ein Dissipationsprozess infolge des viskoelastischen Verhaltens des Fluids
c) Versteifung bezüglich der Kompressionsfähigkeit infolge der Anwesenheit des Porenfluids
d) Zunahme der Dämpfung bei Zunahme der Skelettversteifung bzw. mit Zunahme des Steifigkeitsverhältnis zwischen Skelett und Fluid

Insbesondere für oberflächennahe Bereiche – bei denen der Porenraum ausgeprägt und ein Grundwasserstand vorhanden ist – sind Simulationen ein wichtiges Hilfsmittel, um auftretende Phänomene interpretieren und weitere Aussagen für den Ingenieur ableiten zu können. Im Rahmen der Berechnungen wurde die BEM für die Modellierung der lokalen Heterogenität und die WNIM für die großskalige geologische Schichtung und die Einbindung eines Erdbebenherdes genutzt. Die vorgestellte Modellierung der Bodenstruktur stellt einen wichtigen Ausgangspunkt für weitere Ingenieuranalysen, wie Mikrozonierungs- oder Boden-Bauwerk-Wechselwirkung-Studien dar.

Danksagung

Die Autoren danken dem NATO Wissenschaftsprogramm für die Gewährung der finanziellen Unterstützung, Collaborative Linkage CLG982064.

Literatur

[1] *Fah, D., Suhadolc, P., Panza, G.F.*, Variability of seismic ground motion in complex media: The Fruili area (Italy). In: Geophysical exploration in areas of complex geology, II (R. Cassinis, K. Helbig, G.F. Panza, Eds.) Journal of Applied Geophysics, 30, 131–148, 1993

[2] *Gil-Zepeda, SA, Montalvo-Arrieta. JC, Vai, R., Sanchez-Sesma, FJ.*, A hybrid indirect boundary element–discrete wave number method applied to simulate the seismic response of stratified alluvial valleys, Soil Dynamics and Earthquake Engineering, 23, 77–86, 2003

[3] *Panza, G.F., Romanelli, F., Vaccai, Fr.*, Seismic wave propagation in laterally heterogeneous anelatic media: theory and applications to seismic zonation, Advances in Geophysics, Vol.43, 1–95, 2000

[4] *Bard, P.Y., Bouchon, M.*, The seismic response of sediment-filled valleys. Part I. The case of incident SH waves. Bulletin of the Seismological Society of America, 70:1263–1286, 1980.

[5] *Bard, P.Y., Bouchon, M.*, The seismic response of sediment-filled valleys. Part II. The case of incident P and SV waves. Bulletin of the Seismological Society of America, 70:1921–1941, 1980.

[6] *Bouchon, M., Campillo, M., Gaffet, S.*, A boundary integral equation discrete wavenumber representation method to study wave propagation in multilayered media having irregular interfaces. Geophysics, 54:1134–1140, 1989.

[7] *Nguyen, K.V., Gatmiri, B.*, Evaluation of seismic ground motion induced by topographic irregularity. Soil Dynamics and Earthquake Engineering, 27(2):183–188 , 2007

[8] *Yokoi, T. and Sanchez-Sesma, F.J.*, A hybrid calculation technique of the in direct boundary element method and the analytical solution for three-dimensional problems of topography. Geophysical Journal International, 133:121–139, 1998

[9] *Dineva, P., Vaccari, F., Panza, G.* (2003) Hybrid Modal summation-BIE method for site effect estimation of a seismic region in a laterally varying media, to appear in Journal of Theoretical and Applied Mechanics, Bulgarian Academy of Science, Volume 33(4), 55–88

[10] *Dominguez J.* (1993) Boundary elements in dynamics. Southampton/ Amsterdam: Computational Mechanics Publications/Elsevier.

[11] *Hisada, Y.*, An Efficient Method for Computing Green's Functions for a Layered Half-Space with Sources and Receivers at Close Depths (Part 1). Bulletin Seismological Society of America, 84(5):1456–1472, 1994

[12] *Chen, X.*, A systematic and efficient method of computing normal modes for multilayered media. Geophysical Journal International, 115:391–409, 1993

[13] *Luco, J.E., Apsel, R.J.*, On the Greens functions for layered half-space. Part I. Bulletin of the Seismological Society of America, 73:909–929, 1983

[14] *Dineva P., Wuttke F., Schanz, T.*, Validation study of the wave number integration-boundary integral equation method for seismic wave propagation problems, Comptes rendus de l'Academie bulgare des Sciences, Tom 59, No 9, 939–944, 2006

[15] *Wuttke, F., Dineva, P., Schanz, T.*, 2009, Seismische Wellenausbreitung in lateral inhomogenen Medien mittels eines hybriden Modells, Bauingenieur, 3:1–9

[16] *Wuttke, F. Dineva, P., Schanz, T.*, 2009, Seismic wave propagation in laterally inhomogeneous geological region via hybrid approach of wave number integration – boundary integral equation method, Journal of Sound and Vibration, (submitted 2009)

[17] *Bardet, J.P.* (1992) A viscoelastic model for the dynamic behaviour of saturated poroelastic soils, Trans. of the ASME, Vol.59, 128–135.

[18] *Bardet, J.P.* (1995), The damping of saturated poroelastic soils during steady-state vibrations, Applied Mathematics and Computation, 67:3–31

[19] *Biot, M. A.*, 1956, Theory of propagation of elastic waves in a fluid-saturated porous solid. I. Low-frquency range, Journal of the acoustical socitiety of America, Vol. 28, 2:168–178

[20] *Biot, M.A.*, 1956, Theory of propagation of elastic waves in a fluid-saturated porous solid. II. Higher-frquency range, Journal of the acoustical socitiety of America, Vol. 28, 2:179–191

[21] *Frenkel, J.*, On the theory of seismic and seismoelectric phenomena in moist soil, Journal pf Physics, Vol. 3, 4:230–241

[22] *Schanz, M.*, 2001, Wave propagation in viscoelastic and poroelastic continua. A Boundary Element Approach, Lecture Notes in Applied Mechanics, Vol.2, Springer

[23] *Schanz, M., Diebels, S.*, 2003, A comparative study of Biot's theory and the linear Theory of Porous Media for wave propagation problems, Acta Mechanica, 161, 213–235 (2003)

[24] *Schanz, M.*, 2003, On the equivalence of the linear Biot's theory and the linear theory of porous media, 16th ASCE Engineering Mechanics Conference, Washington, Seattle

[25] *Caricone, J.M.*, 1998, Viscoelastic effective rheologies for modelling wave propagation in porous media, Geophysical Prospecting, 46:249–270

[26] *Chen, J., Dargush, D.F.*, 1995, Boundary Element method for dynamic poroelastic and thermoelastic analyses, International Journal of Solids Structures, Vol. 32, 15: 2257–2278

[27] *Lin, C.-H., Lee, V.W., Trifunac, M.D.*, 2005, The reflection of plane waves in a poroelastic half-space saturated with inviscid fluid, Soil Dynamics and Earthquake Engineering, 25:205–223

[28] *Simon, B., Zienkewicz, O., Paul, D.*, 1984, An analytical solution for the transient response of saturated porous elastic solids, International Journal for Numerical and Analytical Methods in Geomechanics, 8:381–398

[29] *Schanz, M., Pryl, D.*, 2004, Dynamic fundamental solutions for compressible and incompressible modelled poroelastic continua, International Journal of Solids and Structures, 41:4047–4073

[30] *Wilmanski, K.*, 2005, Elastic modelling of surface waves in single and multicomponent systems, in Surface waves in geomechanics: Direct and inverse modelling for soils and rocks, C.G. Lai & K. Wilmanski (Eds.), Vol. 481, CISM, Springer

[31] *Panza, G., Paskaleva, I., Dineva, P., La Mura, Cr.* Earthquake site effects modelling by hybrid MS-BIEM: The case study of Sofia, Bulgaria, Rendiconti di Scienze Fisiche by the Accademia dei Lincei, (2009), Vol. 20, pp. 91–116

[32] *Morochnik, V., Bardet, J.*, 1996, Viscoelastic approximation of porous media for wave scatteing problems, Soil Dynamics and Earthquake Engineering, 15: 337–346

[33] *Christhensen, R.*, 1971, Theory of Viscoelasticity: An introduction, Academic press, New York

[34] *Knopoff, R., Fredricks, R. F., Gangi, A. F., Porter, L. D.*, 1957, Surface amplitudes of reflected body waves. Geophysics 22 (4):842–847

[35] *Dineva, P., Datcheva, M., Schanz T.*, 2006, BIEM for seismic wave propagation in fluid saturated multilayered media, in Numerical Methods in Geotechnical Engineering, ed. H.F. Schweiger, Proc. 6th European Conference on Numerical Methods in Geotechnical Engineering, 6–8 September 2006-Graz, Austria, Tayler&Francis/Balkema, pp.257–265

[36] *Todorovska, M. I., Al Rjoub, Y.*, 2006, Plain strain soil-structure interaction model for a building supported by a circular foundation embedded in a poroelastic half-space, Soil dynamics and Earthquake Engineering, 26: 694–707

[37] *Chun, L, Chopra, M. B., Dargush, G. F.*, 1999, Response of a pile to impinging seismic waves using a poroelastic Boundary Element Method, 13th ASCE Engineering Mechanics Conference, Baltimore, June 13–16